UNIVERSITÀ
DEGLI STUDI
DI MILANO

Sustainable Catalysis *via* Iron and Zinc Complexes: from Tunable Metallate Systems to Photochemical Reactivity

Ph.D. Thesis

Matteo Alberti

Ph.D. in Chemistry
Department of Chemistry

Milan, May 2026

This page intentionally left blank.

UNIVERSITÀ
DEGLI STUDI
DI MILANO

Sustainable Catalysis *via* Iron and Zinc Complexes: from Tunable Metallate Systems to Photochemical Reactivity

Ph.D. Thesis

Matteo Alberti
Student No. R13902

Supervisor: Alessandro Caselli
Full Professor, Università degli Studi di Milano

Co-supervisor: Dominika Zákutná
D11 instrument co-responsible, Institut Laue-Langevin, Grenoble; Associate Professor, Charles University, Prague

Ph.D. in Chemistry
Department of Chemistry

Thesis

Milan, May 2026

This page intentionally left blank.

Sustainable Catalysis *via* Iron and Zinc Complexes: from Tunable Metallate Systems to Photochemical Reactivity

Preparation of this work was facilitated by the use of the *IPLeiria-Thesis* template.

This page intentionally left blank.

To Marta

This page intentionally left blank.

Acknowledgements

This thesis was written for the past, present, and future students and researchers of *Lab Caselli*. The Ph.D. program has taught me many important lessons, and I have no doubt that the most valuable were the ones I learned from all of you. Therefore, most of my gratitude goes to you.

I would like to express my gratitude to Ale and Dominika. You were great supervisors, but above all, great mentors. Not only did you guide me on this scientific journey, but you also helped me grow into a better person. I also greatly appreciated the support of my group's closest collaborators: first of all, Fausto and Mario, but also Francesco, Emma, and Fabio.

I also owe gratitude to my lab colleagues, both in Milan and Prague: we shared many days together, and it felt like being part of a big, ragtag family. I am also grateful to the technicians of the University of Milan, without whom this work would not have been possible.

My appreciation also goes to my family of origin, and to Irene, my new family, for their constant support throughout these years.

My deepest and most painful thanks go to Marta. I would give anything to go back in time and live again even just one day with you and Andrea in our lab. This work is dedicated to you.

This page intentionally left blank.

Summary

This summary outlines the content of Chapters 2, 3, and 4 of the thesis. It provides a descriptive account of the research topics addressed, the systems investigated, and the results reported in each chapter.

Chapter 2 focuses on the use of iron and zinc tetrahalometallate species as catalysts for reactions involving ring-strained heterocycles. The chapter reports the preparation of homogeneous metallate salts and their immobilization on commercially available anion-exchange resins. These systems are evaluated in the dimerization of aziridines and in the cycloaddition of carbon dioxide to aziridines and epoxides, leading to the formation of oxazolidinones and cyclic carbonates, respectively. Catalytic activity is compared with that of simple iron and zinc halides. The influence of catalyst formulation, counterions, and solid supports on reaction outcome is examined. Recycling experiments are reported for selected supported catalysts, showing differences between zinc- and iron-based systems. The chapter also discusses the effect of reaction parameters such as temperature, pressure, and catalyst loading on conversion and selectivity for representative substrates. The results are presented on a case-by-case basis without extending conclusions beyond the studied systems.

Chapter 3 describes the synthesis, characterization, and reactivity of iron complexes supported by pyclen-based macrocyclic ligands. Structural characterization by single-crystal X-ray diffraction is reported for selected complexes. The chapter places particular emphasis on the use of spectroscopic techniques to assign oxidation and spin states, with Moessbauer spectroscopy used alongside magnetic measurements and UV–visible spectroscopy. Discrepancies between crystallographic metrics and electronic assignments are explicitly addressed. The chapter then examines the behavior of these iron complexes in aerobic photo-oxidation reactions under visible-light irradiation. Reactions involving benzylic substrates are described, and the influence of irradiation wavelength, catalyst loading, and reaction time on conversion and product distribution is reported. The photochemical studies are presented as extensions of the coordination chemistry rather than as a comprehensive catalytic survey.

Chapter 4 is devoted to pincer-type ligand frameworks and to the design and synthesis of a new NCN pincer ligand. The chapter begins with a literature overview of PC(sp^3)P and related pincer systems, with emphasis on C–H activation and car-

bene formation in complexes of late and first-row transition metals. The experimental part reports the synthesis of the NCN proligand **L6** starting from methylene-bridged aniline derivatives. Multiple synthetic routes are explored to functionalize the ligand and to generate metalation precursors, including methylation of anilines, directed lithiation, and radical bromination of the methylene bridge. These approaches result in either unselective reactions or undesired side products. Attempts to generate suitable intermediates for iron coordination are described, but the targeted iron pincer or carbene complexes are not obtained within the scope of the work.

Keywords: Iron Catalysis, Zinc Catalysis, Carbon dioxide utilization, Macrocyclic ligands, Photocatalysis, Metal ligand cooperation.

Abstract

This thesis investigates the use of iron and zinc complexes as sustainable catalysts for transformations of small, strained heterocycles in the field of carbon dioxide valorization, as well as the synthesis of iron complexes as catalysts for photochemical oxidation.

In the first part of the work, tetrahalometallate complexes of iron and zinc were employed as bifunctional catalysts for the cycloaddition of carbon dioxide to aziridines and epoxides, yielding oxazolidinones and cyclic carbonates, respectively. These catalysts operate through a dynamic equilibrium between a neutral metal halide acting as a Lewis acid and free halide anions acting as nucleophiles. Immobilization of these metallates on anion exchange resins generated heterogeneous catalysts that combined high activity with ease of recovery and, in some cases, improved selectivity due to cooperative effects between the support and the active species.

The second part of the thesis focuses on macrocyclic pyclen based iron complexes. These ligands stabilize iron centers in well defined oxidation and spin states, allowing detailed spectroscopic characterization and controlled photochemical reactivity. Mössbauer spectroscopy proved essential for resolving ambiguities arising from structural data and for identifying iron speciation in catalytic systems. Under visible light irradiation, iron pyclen complexes promoted aerobic oxidation of benzylic substrates, demonstrating that properly designed iron complexes can perform selective photoredox transformations.

The final part of the work explores pincer type ligand frameworks as platforms for metal ligand cooperativity. A new NCN pincer ligand was designed to extend carbene based reactivity to iron, motivated by recent advances in PC(sp^3)P systems. Although the targeted iron carbene complexes could not be obtained, the synthetic studies aims at providing a foundation for future developments.

Keywords: Iron Catalysis, Zinc Catalysis, Carbon dioxide utilization, Macrocyclic ligands, Photocatalysis, Metal ligand cooperation

This page intentionally left blank.

Contents

This page intentionally left blank.

1
Preface

The use of first row transition metals in homogeneous and heterogeneous catalysis has become a central topic of modern inorganic and organometallic chemistry, driven by concerns over sustainability, cost, and elemental abundance. Iron and zinc, in particular, are among the most attractive candidates for replacing noble metals in catalytic processes, owing to their low toxicity, high natural abundance, and rich coordination chemistry. At the same time, these metals present distinct challenges. Compared to second and third row transition metals, they exhibit harder Lewis acidity, less spin state predictability, and a greater tendency to participate in single electron and radical processes, all of which can complicate the design of selective catalytic systems.

The work described in this thesis is motivated by the question of how these intrinsic properties of iron and zinc can be converted from liabilities into advantages through appropriate catalyst design. Consequently, this work explores several complementary strategies for controlling and exploiting the reactivity of these metals, ranging from simple ion exchange resins-supported metallates to more elaborate macrocyclic complexes.

The first strategy investigated is based on tetrahalometallate species of iron and zinc, which function as bifunctional catalysts through equilibria that generate both Lewis acidic metal halides and free halide anions. These systems are particularly well suited to the activation of strained heterocycles such as aziridines and epoxides in reactions with carbon dioxide, a thermodynamically stable yet abundant one-carbon (C1) feedstock. The cycloaddition of carbon dioxide to such substrates is attractive both from a synthetic perspective and in the context of sustainable chemistry, as it proceeds with full atom economy and produces valuable heterocyclic products. By immobilizing metallate catalysts on anion exchange resins, this work further demonstrates how heterogeneous supports can be used not only for catalyst recovery, but also to introduce cooperative effects that influence activity and selectivity.

The second part of the thesis addresses a different challenge, namely the control

of the photochemical reactivity of iron complexes. Macrocyclic ligands based on the pyclen framework were employed to stabilize iron in well defined coordination environments and to allow systematic investigation of its electronic structure and reactivity. The complexes obtained in this way served as a foundation for integrating synthetic, spectroscopic, and magnetic studies, with Mössbauer spectroscopy being crucial for securing accurate assignments of oxidation and spin states. These studies showed that appropriately designed iron complexes are capable of mediating selective aerobic photo-oxidation reactions under visible light irradiation, highlighting the potential of iron as a photochemically active metal when placed in a suitable ligand.

In the final part of the thesis, the focus shifts toward pincer type ligand architectures and metal-ligand cooperativity. Recent advances in PC(sp^3)P pincer systems have demonstrated that carbene like reactivity and bond activation processes can be achieved at both noble and first row transition metals through carefully designed ligand frameworks. Motivated by these developments, a new NCN pincer ligand was designed with the aim of extending the scope of this class of molecules and the intention of producing a simpler but equally powerfull ligand. Although the targeted iron carbene complexes could not be realized within the scope of this work, this synthetic endeavor provides a robust foundation for further developments.

Taken together, the three research directions presented in this thesis reflect a progression from simple, highly robust catalytic systems to more elaborate architectures aimed at enabling increasingly demanding transformations.

Reading guidance

For ease of reference, compound abbreviations are listed in Appendix B (page 368), while general abbreviations are listed in Appendix C (page 377).

2

Non-redox Processes

2.1 Introduction

A prominent property of first-row transition metals, in contrast to those of the second and third rows, is the marked hardness of their Lewis acidity.[1] Another important feature of these first-row metals is their pronounced tendency to undergo single-electron transfer processes.[2] The most direct way to exploit these properties in catalysis is to minimize redox activity–since achieving selectivity in radical-mediated reactions is challenging–and to employ these metals in transformations where coordination by hard Lewis bases can be anticipated.

One application that has drawn considerable attention from the scientific community is the coupling of ring-strained heterocycles (mainly, aziridines and epoxides) with CO_2.

Due to the significant ring strain present in these small heterocycles, aziridines and epoxides undergo facile reactions with thermodynamically stable CO_2.[3] From the perspective of eco-sustainability, these transformations are particularly noteworthy, as the coupling proceeds with 100% atom economy and converts waste CO_2 into value-added products.[4]

Synthesis of oxazolidinones. The cycloaddition of CO_2 to aziridines to yield oxazolidinones constitutes a particularly attractive nonreductive synthetic strategy.[5] This reaction enables the incorporation of carbon dioxide into high-value heterocyclic structures that function as synthons for various pharmaceuticals[6,7] (including antibiotics,[8–11] antibacterial,[12–14] antimicrobial,[15] antithrombotic,[16] and antidepressant[17] agents) as well as versatile synthetic intermediates.[18–21] As already stated, a major challenge in CO_2 utilization lies in its intrinsic thermodynamic stability, which typically demands high-energy substrates and, in the absence of suitable catalysts, rather harsh reaction conditions. Although the coupling of aziridines with CO_2 has been shown to proceed even without a catalyst,[22–24] the use of a catalytic system with low energy input is preferable in order to comply with

green chemistry principles. A catalyst is indeed essential to surmount the enthalpic barrier associated with aziridine ring opening,[25] and a widely adopted approach relies on the synergistic action of a Lewis acid and a nucleophile: the Lewis acid coordinates to the nitrogen atom, withdrawing electron density from the C–N bond, while the nucleophile attacks one of the carbon atoms. The site of this nucleophilic attack dictates the regioselectivity of the process, introducing an additional level of complexity in the design of an efficient catalytic system.

Several studies have reported binary catalytic systems in which the primary catalyst acts as a Lewis acid, while the co-catalyst functions as the nucleophile. In most examples, the co-catalyst is an ammonium halide salt or an organic base such as DBU (1,8-diazabicyclo[5.4.0]undec-7-ene) or DMAP (4-dimethylaminopyridine). In contrast, a broad range of Lewis acids has been applied as catalysts, including Schiff base complexes,[26–29] porphyrins[30] and porphyrin complexes,[31] metal carbamates,[32] divalent lanthanides,[33] as well as heterogeneous systems based on MOFs.[34–37]

More practical approaches rely on bifunctional catalysts that combine both Lewis acidic and nucleophilic sites within a single molecule, thereby dispensing with external additives. In the most straightforward cases, simple halide salts of alkali metals have been used for this transformation.[38,39] Particularly significant in this context is the work of Pinhas and co-workers,[40] who examined the catalytic behaviour of alkali metal halides and ammonium halides. The latter, and ammonium iodide in particular, profit from their ability to form hydrogen bonds with aziridines, which improves both the efficiency and the regioselectivity of the reaction. More advanced systems comprise bifunctional metal complexes,[41,42] typically bearing ligands functionalized with ammonium or imidazolium groups that serve as the nucleophilic component. Among these, an aluminium Salphen complex[28] has been shown to be especially efficient, even in the absence of additional additives.

Synthesis of cyclic carbonates. The reactivity of epoxides in the cycloaddition of CO_2 to afford cyclic carbonates closely resembles that of aziridines. Numerous catalytic systems have been reported to promote this transformation, enabling the reaction to proceed under comparatively mild conditions.[43–57]

Within the field of heterogeneous catalysis, MOF-based hybrid materials have recently gained attention as effective catalysts for the synthesis of cyclic carbonates from CO_2, mainly due to the presence of accessible Lewis acid-base sites.[58–61] Considerable effort has also been devoted to the heterogenization of alkylammonium halides (among the most commonly employed co-catalysts for the CO_2 cycloaddition to epoxides and aziridines) by anchoring them onto high-surface-area inorganic supports such as silica or polymeric materials.[62] These heterogeneous systems allow straightforward catalyst separation and recycling; however, they typically exhibit lower activity than their homogeneous counterparts and often demand

more forcing conditions (i.e. elevated temperature, pressure, and catalyst loading).

However, an exception occurs in silica-supported aminopyridinium halides, which display enhanced catalytic performance relative to the corresponding homogeneous species. This improvement has been attributed to a synergistic interaction between the halide anion and the surface Si-OH groups, the latter acting as weak Lewis acid sites to activate the epoxide.[63]

More recently, ion exchange resin (IER)-supported zincate salts of general formula $[ZnCl_2X_2]^{2-}$ (X = Cl, Br, OAc, or NO_3) have been examined as catalytic systems.[64] Commercial IERs are attractive supports because of their low cost, ease of handling, and convenient recovery. In this context, Amberlite IRA-900 anion exchange resin was employed to retain the metallate catalyst, and the most favorable outcomes in terms of conversion and selectivity were recorded for propylene oxide as the sole substrate using the $ZnBr_2$/IER catalytic system.

Mechanism

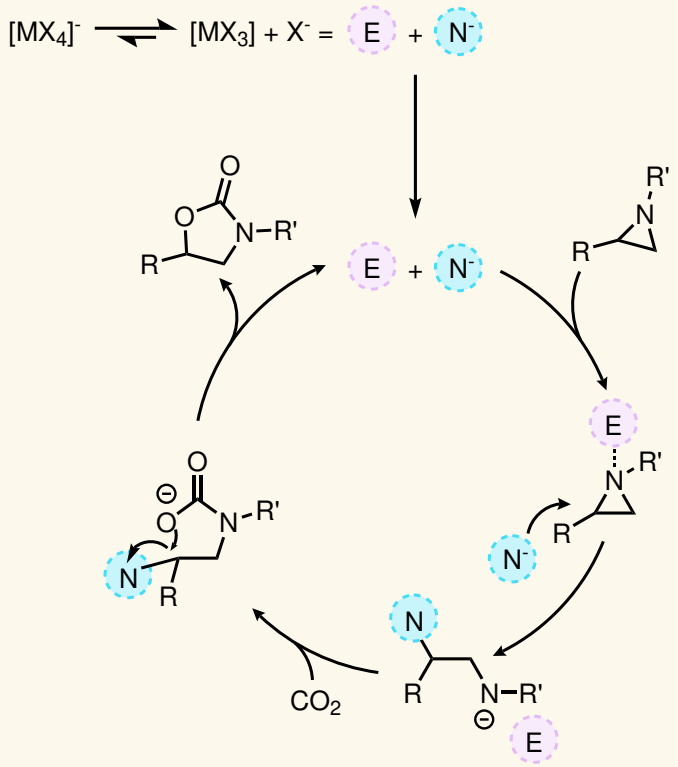

Scheme 2.1.1: *Ring opening of aziridines and insertion of CO_2 for trivalent metal halides. In the reaction of CO_2 with epoxides, the mechanism is analogous.*

During my master thesis work, I had the opportunity to study the synthesis of oxazolidinones from the coupling of aziridines with CO_2,[65] and cyclic carbonates from epoxides[66] catalyzed by ammonium ferrates and zincates. These simple yet effective systems exploit the metallate/metal halide equilibrium to generate *in situ* a halide anion that can act as a nucleophile and a neutral metal halide that can

function as a Lewis acid, activating the strained cycle and promoting ring opening (Scheme 2.1.1).

The main advantage of these catalysts is represented by their simplicity, which was deemed crucial to the sustainability of the process. To improve these systems in accordance with this principle and potentially enable their application on a larger scale, it was attempted to heterogenize the active tetrahalometallate species by generating them *in situ* on anion-exchange resins. Cross-linked polystyrene-based anion-exchange resins were selected as supports, owing to their large internal surface area[67] (ca. 2.0 m^2 g^{-1}), their known CO_2 adsorption capacity,[68] and their low cost and durability.[64] Two commercial materials were examined for comparison: Amberlyst 26-Cl, a macroreticular resin with a theoretical exchange capacity of 1.0 eq L^{-1}, and Amberlite IRA-400-Cl, a microporous resin with a theoretical capacity of 1.4 eq L^{-1}.

Due to these advantages, ferrate and zincate anions immobilized on the polymer support were synthesized by a simple ion-exchange process using readily available metal precursors. They proved to be particularly active in the synthesis of cyclic carbamates and cyclic carbonates; in the first case (cyclic carbamates), under several aspects IER-supported ferrates performed better than their homogeneous counterparts, indicating a strong synergistic effect between the polystyrene support and the active catalyst. On the other hand, in the case of cyclic carbonates, IER-supported zincates showed very good and facile recyclability, which is a major advantage for eventual future large scale applicability.

2.2 Results and discussion

2.2.1 IER-supported metallates: synthesis

The first encountered challenge was establishing a reproducible protocol for resins functionalization. The complete procedure is reported in the experimental section (Chapter 6, page 127-130).

Although the resins were commercialized in their Cl^- form, some of the samples resulted in basic solutions when dispersed in aqueous media, probably due to some residual oxhydryl. For this reason, before functionalizing the resins, it was necessary to treat them with aqueous solutions of KCl. This was achieved by filling a Versaflash® solid cartridge with the untreated resin and by recirculating overnight a concentrated aqueous KCl solution. A similar solution was adopted to introduce a bromide moiety on the catalysts (Scheme 2.2.1). Treating IRA400-Cl and A26-Cl with a concentrated solution of KBr overnight yielded fully Br-substituted **IRA400-Br** and **A26-Br**. This treatment was made for two reasons. First, in this manner, a clean and well-characterized starting material was produced, with bromine as the only counterion. SEM analyses showed a bromine surface coverage of the resin beads of 96.7% and 93.1% for **IRA400-Br** and **A26-Br**, respectively (Figures A.20 and A.21). Second, in my master thesis work[65,66] it was demonstrated that tetrabromo- and mixed chloro-bromo-metallates yielded better results in the synthesis of cyclic carbonates and carbamates from CO_2 compared to tetrachloro-metallates. Thus, I decided to introduce the bromide anion in the first part of the synthesis to make the process more cost-effective, as the metallic chlorides used in the second part of the functionalization are by far less expensive than their bromide equivalents.

Having established the pre-treatment of the chloride and bromide forms of the resins, I then moved on to grafting the iron and zinc tetrahalometallate species onto the polymer supports. For this purpose, the resins were treated either with zinc(II) chloride or iron(III) chloride, using the amount of metal salt corresponding to the maximum theoretical ion-exchange capacity of each material (1.4 meq mL^{-1} for IRA-400 and 1.0 meq mL^{-1} for A26). Different solvents were required for iron and zinc. Anhydrous $FeCl_3$ dissolved readily in acetonitrile, and treatment of the resins under these conditions provided reproducible functionalization close to the nominal loading. In contrast, anhydrous $ZnCl_2$ did not react to completion when dissolved in acetonitrile, while acetone proved to be a suitable solvent and provided higher and more consistent zinc uptake. In total, eight metallate-functionalized resins were obtained and the correct functionalization was assessed with EDX spectroscopy (Table 2.1, the spectra and micrographs are provided in the Appendix A.).

In general, iron loading was high for both resins, with particularly high uptake for sample **R2d** (A26 [$FeCl_3Br$]). In contrast, zinc incorporation in sample **R1b** (IRA400 [$ZnCl_2Br_2$]) was very low. However, to obtain quantitative metal contents, ICP-OES was elected as the most precise and reliable technique. Because cross-

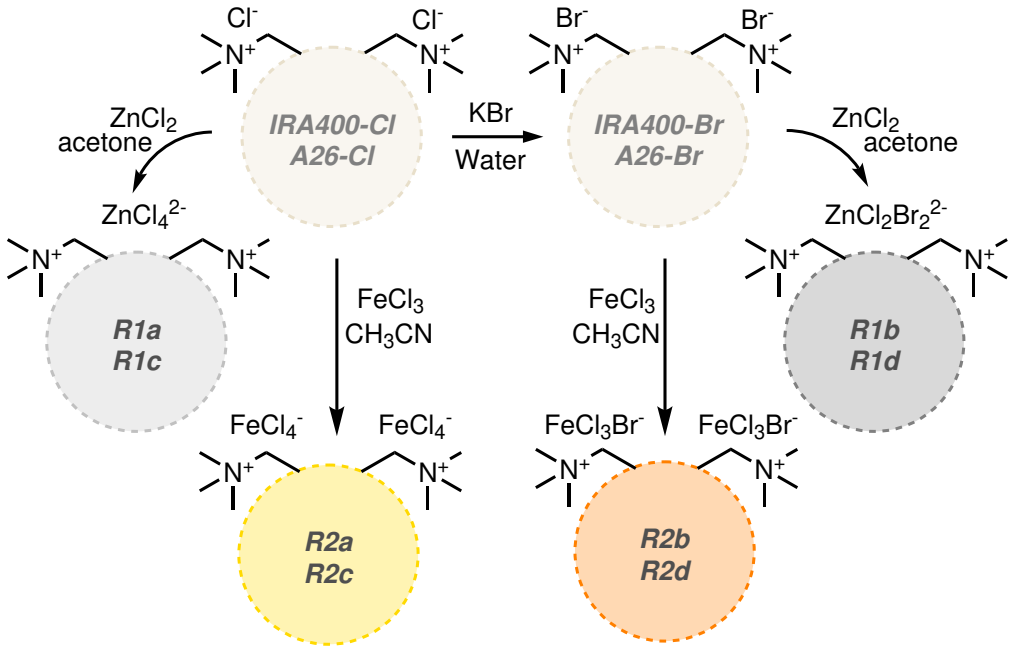

Scheme 2.2.1: *Synthesis of resins* ***R1a*****-****R2d****. Coding:* ***R1a****, IRA400* [$ZnCl_4$]; ***R1b****, IRA400* [$ZnCl_2Br_2$]; ***R1c****, A26* [$ZnCl_4$]; ***R1d****, A26* [$ZnCl_2Br_2$]; ***R2a****, IRA400* [$FeCl_4$]; ***R2b****, IRA400* [$FeCl_3Br$]; ***R2c****, A26* [$FeCl_4$]; ***R2d****, A26* [$FeCl_3Br$].

Table 2.1: *Metal content, expressed in weight fraction, for samples* ***R1b****,* ***R1d****,* ***R2b****,* ***R2c*** *and* ***R2d****.*

Sample	Iron content[a]	Iron content[b]	Metal content[c]
R1b	-	-	1.0%
R1d	-	-	7.4%
R2b	4.45%	7.0%	5.6%
R2c	6.42%	-	6.8%
R2d	6.79%	7.2%	7.4%

[a]Measured with ICP-OES for **R2b**, **R2c** and **R2d**. [b]Data obtained from ZFC curves measured with a PPMS equipped with a VSM for **R2b** and **R2d**. Details on this measurements are explained in Chapter 3. [c]Zinc content for **R1b** and **R1d**, iron content for **R2b**, **R2c** and **R2d**. Data calculated from SEM-EDS spectra, based on the maximum theoretical loading of the resins (1.4 meq mL^{-1} for IRA-400, 1.0 meq mL^{-1} for A26).

linked polystyrene is difficult to mineralize,[69] complete digestion was not achieved for zinc-containing samples. On the other hand, the Fenton process is known to facilitate complete mineralization of iron-loaded resins.[70] Thus, ICP-OES data was measured only for resins **R2b-d** and the resulting values are listed in Table 2.1. The experimental details on ICP-OES measurements are described in Chapter 6.

Magnetometry was also employed to determine the iron loading (Figure A.45 and A.46). To extract quantitative data from the ZFC and FC curves, the inverse of the magnetization was plotted as a function of temperature, and the iron content was calculated from the Curie-Weiss law fit, assuming high-spin Fe(III) ($S = 5/2$) and accounting for a temperature-independent diamagnetic contribution. Details of the calculation procedure are provided next: the molar susceptibility is related to the obtained magnetization by equation 2.1:

$$\chi_M = \frac{4\pi M}{nH} \tag{2.1}$$

with $[M]$ = emu, the measured magnetization, $[H]$ = Oe, the applied magnetic field, $[n]$ = mol. Because in the raw data the magnetization is measured in memu and the magnetic field in T (Tesla), in fact the conversion formula is the following (2.2):

$$\chi_M = \frac{4\pi M \cdot 10^{-3}}{nH \cdot 10^4} \tag{2.2}$$

Subsequently, in *non-ideal* paramagnets the molar susceptibility temperature dependence is defined by the Curie-Weiss law (equation 2.3):

$$\chi_M = \frac{\mu_0 N_A \mu_{eff}^2 \mu_B^2}{3k_B (T - \theta_{CW})} \tag{2.3}$$

with the peremability of vacuum, μ_0; Avogadro's number, N_A; effective magnetic moment, μ_{eff}; Bohr magneton, μ_B; Boltzmann's constant, k_B; and Curie-Weiss temperature, θ_{CW}. In *d*-ions, where the orbital momentum is quenched due to the strong inhomogeneous electric field, the effective magnetic moment arises only from the electron spin (equation 2.4):

$$\mu_{eff} = 2\sqrt{S(S+1)} \tag{2.4}$$

For Fe^{3+} ions in high-spin state, $\mu_{eff}(S = 5/2) = 5.91\mu_B$. Equations 2.2 and 2.3 can be joined in equation 2.5:

$$\frac{4\pi M \cdot 10^{-3}}{nH \cdot 10^4} = \frac{\mu_0 N_A \mu_{eff}^2 \mu_B^2 \cdot 10^6}{3k_B (T - \theta_{CW})} \tag{2.5}$$

With the 10^6 factor added to convert fromn CGS to SI units. Rearranging:

$$\frac{1}{M} = \frac{12k_B\pi}{nH\mu_0\mu_{eff}^2\mu_B^2 N_A \cdot 10^{13}}(T - \theta_{CW}) \tag{2.6}$$

$^1/_M$ can be plotted with T, and from the angular coefficient of the linear regression, n can be obtained. Then, it can be multiplied for the iron atomic mass and divided for the mass of the sample to obtain the weight fraction of iron in the samples.

The extracted values are compared with the ICP-OES data in Table 2.1. A systematic difference is observed between the two methods, which likely arises from the different sample treatments: magnetometry requires sample pulverization, while ICP-OES relies on complete mineralization. The magnetometry-derived values are closer to those obtained from SEM-EDS.

Raman spectroscopy was then used to qualitatively identify the tetrahalometallate species present on the resins. For the iron-functionalized materials, spectra collected at 780 nm showed five clear bands in the Fe–Cl and Fe–Br stretching region (Figure 2.1, right). In the higher-frequency region (347 and 330 cm^{-1}), the 330 cm^{-1} band matches the total symmetric stretch of $[FeCl_4]^-$ (Figure A.31). In the lower-frequency region (266, 241, 221 cm^{-1}), the weaker bands at 241 and 221 cm^{-1} can be assigned to Fe–Br stretching vibrations. These observations, together with SEM-EDS data, suggest that the samples contain mainly $[FeCl_3Br]^-$ together with minor amounts of mixed-halide species formed through halide exchange (e.g., $[FeCl_4]^-$, $[FeCl_2Br_2]^-$, $[FeClBr_3]^-$, $[FeBr_4]^-$).[71]

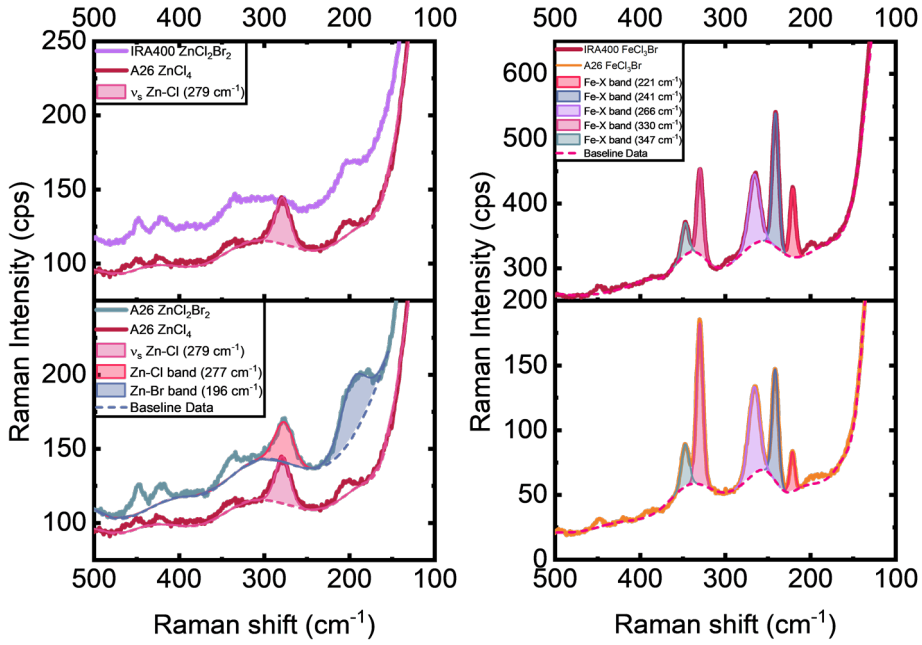

Figure 2.1: *Raman spectra of* ***R1b*** *(top left),* ***R1d*** *(bottom), superimposed with* ***R1c***, ***R2b*** *(top right) and R2d (bottom right).*

The Raman spectra of the zinc-functionalized resins were more difficult to interpret. Fluorescence of the sample under 532 nm excitation hindered data collection at that wavelength. For sample **R1b** (IRA400 $[ZnCl_2Br_2]$), the Zn–halogen region showed only very weak features, consistent with the low Zn content observed by

SEM-EDS (Figure 2.1, left). For comparison, the spectrum of **R1c** (A26[$ZnCl_4$]), prepared directly by mixing A26-Cl with $ZnCl_2$, displayed a broad Zn–Cl stretching band at 279 cm^{-1}, which is absent in the case of **R1b**. A weaker band around 200 cm^{-1} appeared in both samples, but this feature is also present in the iron-functionalized resins and was therefore attributed to the resin support. In the case of R1d (A26[$ZnCl_2Br_2$]), both a Zn–Cl stretching band at 277 cm^{-1} and a broad Zn–Br stretching band at 196 cm^{-1} were visible. Although Raman data for $[ZnCl_2Br_2]^2$ are not available in the literature, comparison with $ZnCl_2$-$ZnBr_2$ and $ZnCl_2$-KBr glasses supports these assignments, where non-bridging Zn–Br modes occur near 196 cm^{-1} and Zn–Cl modes near 279 cm^{-1}.[72]

2.2.2 Coupling of CO_2 with aziridines.[73]

Having synthesized a rather diverse group of resins, we next tested their catalytic activity in the cycloaddition of CO_2 to aziridines to form oxazolidinones. In a preliminary catalyst screening, I decided to first assess the effect of the halide, as I knew from prior experience that it exerted one of the largest (if not the largest) effect on the reactivity of the system. Moreover, as demonstrated in my previous work with ammonium ferrates and zincates,[65,66,74] iron-based catalysts were often both more efficient and selective than their zinc counterparts. With this information in mind, I selected **R2c** and **R2d** as the first two candidates, while 1-butyl-2-phenylaziridine (**S1a**) was chosen as the *benchmark* substrate for this transformation, as reported in other related works.[75] Regarding the solvent, acetonitrile appeared a promising option, as its polarity is perfectly matched to stabilize the charged intermediates of this reaction. Running the reaction for one hour at 30 °C and a CO_2 pressure of 1.6 MPa yielded mixed results.

As anticipated, the $[FeCl_3Br]^-$ functionalized resin, **R1d**, outperformed its chloride equivalent, both in yield and selectivity (compare entry 1 and 2, Table 2.2). Although selectivity was not particularly high, only 3-butyl-5-phenyl-1,3-oxazolidin-2-one, **P1a**, was detected alongside other unidentified by-products from aziridine ring opening, with no evidence of the 4-substituted isomer. With a turnover frequency (TOF) of 27 h^{-1} and a modest 71% selectivity, **R2d** performed quite remarkably as a catalyst, even in comparison with homogeneous ammonium ferrate catalysts. Under similar conditions, no reaction occurred when unfunctionalized resins were used as the sole catalyst (entries 3 and 4, Table 2.2).

Unfortunately, at the end of the reaction a yellowish tint in the reaction solvent was noticeable, suggesting partial iron leaching. To determine the actual amount of iron leached into the solution, ICP-OES analyses were conducted to assess the impact of various solvents (refer to the detailed iron leaching analysis below). Five solvents with varying polarities were evaluated, as shown in Table 6.6. Among these, the less polar dichloroethane (DCE) demonstrated optimal performance, achieving the highest yield, while minimizing iron leaching (Entry 5, Table 6.6).

Table 2.2: *Preliminary catalyst screening: effect of the anion and control experiments.*[a]

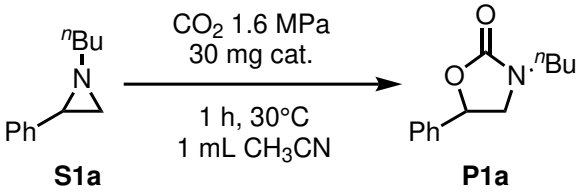

S1a **P1a**

Entry	Catalyst	Conversion (%)[b]	Yield (%)[b]	Selectivity (%)	TOF (h^{-1})[c]
1	**R2c**	53	16	30	15
2	**R2d**	99	71	71	27
3	A26-Cl	0	-	-	-
4	**A26-Br**	0	-	-	-
5	None	0	-	-	-

[a]Reaction conditions: 30 °C, 1.6 MPa CO_2, 30 mg of resin (corresponding to 3.4 mol% and 3.6 mol% for **R1c** and **R1d**, respectively, 1 h, 1 mmol of **S1a** in 1 mL of acetonitrile. [b]Conversion and yield were calculated with GC-FID, using decane as internal standard. Unidentified products derived from aziridine ring opening accounted for the rest of the mass balance. [c]Turnover frequency ($n_{\mathbf{S1a}(\text{converted})} \cdot n_{\text{cat.}}^{-1} \cdot t^{-1}$).

With these insights in mind, I then set out to optimize the reaction, using DCE as the solvent. The optimization process was carried out using Design of Experiment (DoE), which I deemed necessary to fully explore a quite complex design space and to ensure the robustness of the catalytic system. The experiment was divided in two phases:

(a) Screening phase: the design space was explored with a factorial design, which cannot offer the resolution and the prediction capabilities of a response surface method, but allows the user to quickly identify the most critical variables influencing the experiment and to exclude the least effective catalysts.
(b) Optimization phase: A response surface methodology (RSM) was applied to develop a highly predictive model

Screening phase. Among the six variables considered in the experimental design, the first one was the choice of catalyst. Resin **R2c** was not included in the study because the tetrachloroferrate anion exhibited relatively poor performance. Instead, the already efficient resin **R2d** was retained and evaluated together with two further candidates: IRA400 [$FeCl_3Br$] (**R2b**), selected to probe how resin porosity influences the reaction (as noted in section 2.1, A26 is a macroreticular resin, whereas IRA400 is microporous), and A26 [$ZnCl_2Br_2$] (**R1d**), a zinc-functionalized resin. The additional variables included in the model were CO_2 pressure (ambient or 1.6 MPa), temperature (30 or 60 °C), catalyst loading (5 mg or 30 mg of catalyst per millimole of substrate), substrate concentration (0.2 or 1 M), and reaction time (1 or 8 h). No center points were introduced, as a linear response over the selected factor ranges was assumed for the purposes of screening. A complete factorial design to cover the full experimental domain would have required 96 experiments

($3^1 \times 2^5$). To limit the experimental effort, a fractional factorial design was adopted, and the D-optimal criterion was applied to select the most informative subset of experiments. The D-optimal design maximizes the determinant of the information matrix, thereby extracting the greatest amount of information from the smallest number of runs. Ultimately, the model was constructed from 22 experiments with two replicates; the latter were included to estimate the experimental error, which was below 5% and therefore considered acceptable. The experimental outcomes are summarized in Table 6.7.

Both conversion and yield were determined, but only yield data were subjected to statistical analysis. Akaike's Information Criterion (AIC)[76] was employed to identify the statistically significant factors, which are depicted in Figure 2.2. Within the investigated range, the substrate concentration did not appear as a significant parameter, while all other main effects were statistically meaningful. Among them, the choice of catalyst emerged as the most important factor. As anticipated, higher CO_2 pressure had a pronounced positive influence on the reaction outcome. In contrast, increasing the temperature generally reduced the yield, which is consistent with expectations for high-energy substrates such as aziridines.

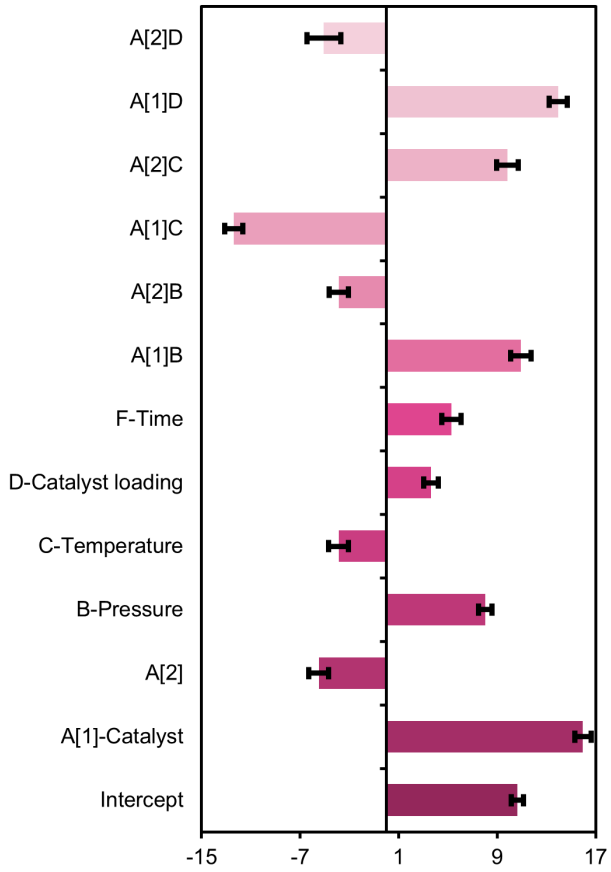

Figure 2.2: *Graphical depiction of the model's coefficient estimates for the screening experiment. Factors are coded, meaning levels are coded as -1/+1 and not as experimental values.*

The model also revealed that interactions between the catalyst choice and other

variables (pressure, temperature, and catalyst loading) played a crucial role (represented in Figure 2.2 as A[1,2]B, A[1,2]C, and A[1,2]D). In particular, the A[1,2]C interaction (catalyst and temperature) showed that lower temperatures favored catalysts **R1d** and **R2d**, whereas catalyst **R2b** performed better at 60 °C (see Figure 2.3). This behavior may be related to the distinct porosity of IRA400.

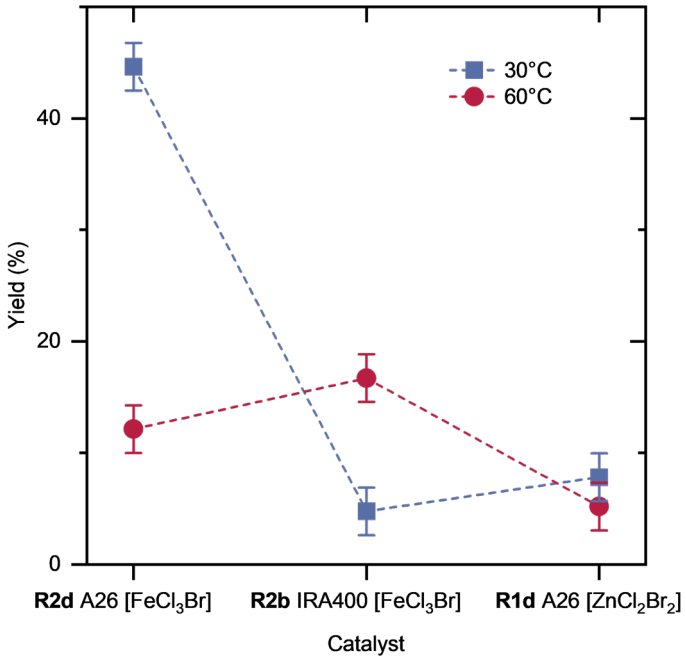

Figure 2.3: *Model prediction at two different temperatures. Reaction conditions: 0.8 MPa CO_2, 15 mg/mmol of catalyst, 8 hours of reaction time. Substrate:* ***S1a****.*

From this screening study, three main conclusions can be drawn:

1. Catalyst **R2d** is the best overall performer and was therefore chosen for subsequent optimization.
2. Within the tested range, substrate concentration is not an important factor. This agrees with my group's earlier observation that aziridine ring opening proceeds almost without barrier,[65] explaining the negligible dependence on substrate concentration under these conditions. Considering that a reaction volume of 1 mL is optimal in my experimental setup, and that a 1 M solution enables rapid and accurate substrate quantification, I selected 1 M as the working concentration.
3. Lower selectivity was observed at elevated temperatures and reduced CO_2 pressures; under these conditions, the formation of symmetrically substituted piperazines became evident.

Optimization Phase. The optimization study was designed to construct a highly predictive model capable of probing the full experimental domain and determining optimal reaction conditions, while taking into account any constraints and priorities

such as low pressure, minimal catalyst loading, and short reaction times. To achieve this, a response surface methodology (RSM) approach was applied.

The design of experiments included four factors: pressure (0.4-3.5 MPa), temperature (25-100 °C), catalyst loading (5-60 mg/mmol), and reaction time (0.5-6 h). Because the reactions were carried out in batches in an autoclave, a split-plot design was adopted, with catalyst loading treated as the only easy-to-change factor.

The runs were chosen according to the I-optimality criterion, which provided statistically sound results with a total of 28 runs organized into 14 batches, and allowing for the estimation of quadratic factor effects. In addition, two replicate experiments were included to evaluate the experimental error. The complete list of design points and the associated experimental results is reported in Table 6.10. As in the initial screening experiment, significant factors in the optimization study were determined using the Akaike Information Criterion (AIC) algorithm. The variables retained in the model are shown in Figure 2.4 (the intercept is omitted for clarity). The model reveals a strong positive correlation between reaction yield and both catalyst loading and CO_2 pressure. However, the negative quadratic terms indicate that this beneficial effect persists only up to a certain level: beyond a specific threshold in pressure or catalyst loading, the yield and hence selectivity begin to decline.

In addition, the model identifies significant negative interaction effects between reaction time and both temperature and catalyst loading. These interactions imply that extended reaction times, when combined with either high catalyst loadings or elevated temperatures, result in lower selectivity. The principal by-products, when they appear, are symmetric piperazines formed by coupling two aziridines; their formation is minimized at lower temperatures and concentrations, and under higher CO_2 pressure.[74] More details about these by-products, and an in-depth study of their formation will be discussed in the next section (page 22).

Using Response Surface Methodology (RSM), the resulting model can reliably predict reaction yield for any combination of parameters within the defined experimental experimental domain. This allows for straightforward optimization of the reaction while respecting the imposed constraints. In particular, the maximum CO_2 pressure was set at 0.8 MPa and I attempted to minimize all factors while simultaneously maximizing the reaction yield. The optimization process was weighted according to the relative importance of each factor, with the greatest emphasis placed on reducing the catalyst loading, as the reaction typically requires a comparatively high amount of catalyst. Given these constraints, the model indicated that the optimal temperature and CO_2 pressure are 25 °C and 0.8 MPa, respectively. For the remaining variables, the best conditions were determined to be a reaction time of 4.5 h and a catalyst loading of 43 mg/mmol; these optima correspond to the local maximum on the response surface shown in Figure 2.5. The predicted yield under these conditions is 93(8)%.

To verify the model, I carried out the reaction twice under the optimized con-

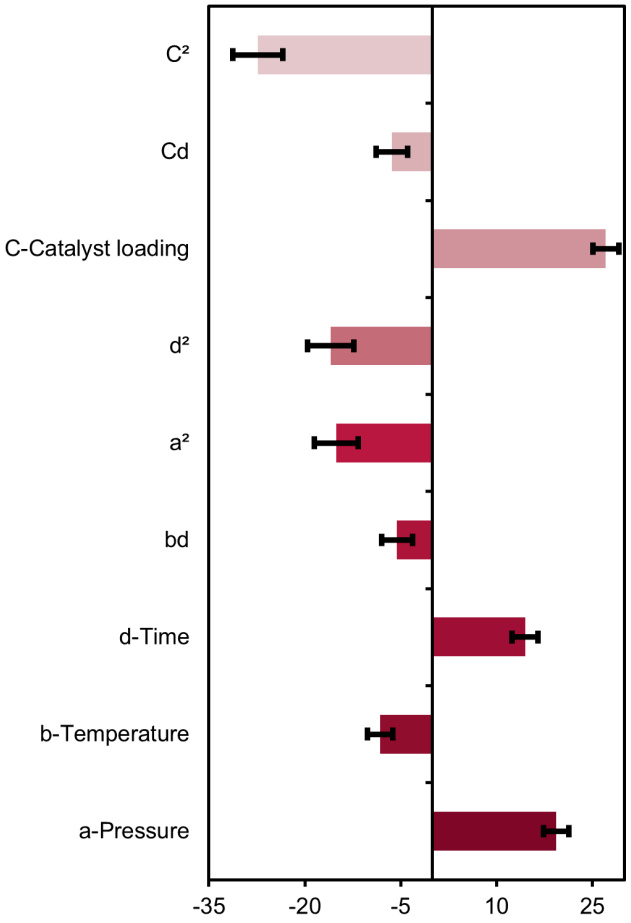

Figure 2.4: *Graphical depiction of the model's coefficients estimates for the optimization experiment. Factors are coded, meaning levels are coded as $-1/+1$ and not as experimental values. Upper case letters represent easy-to-change factors, lower case letters hard-to-change factors (HTC). The intercept was omitted for better readability.*

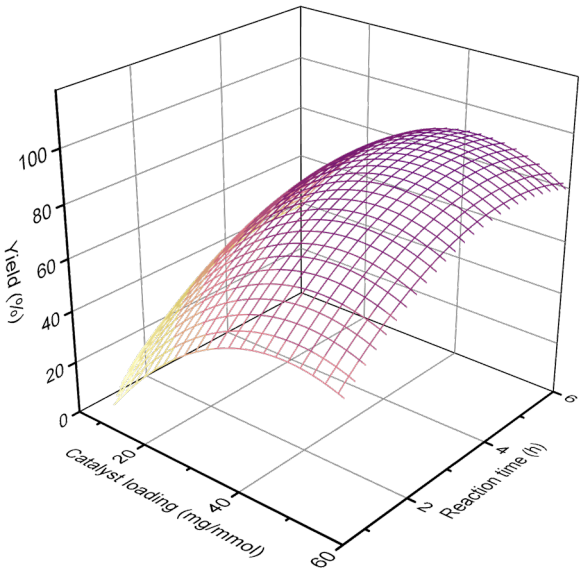

Figure 2.5: *Surface plot of the predicted yield. Reaction conditions: 0.8 MPa of CO_2 pressure, 25 °C, catalyst loading: x axis, reaction time: y axis.*

ditions, obtaining quantitative yields in both cases (Table 2.3). I then compared these results with those obtained using a homogeneous catalyst bearing the same $[FeCl_3Br]^-$ anion, namely TBA $[FeCl_3Br]$ (TBA = tetrabutylammonium, Table 2.3, entry 2), whose catalytic performance I had investigated previously. Notably, the heterogeneous catalyst **R2d** showed markedly superior performance, both in conversion (**R2d**: >99%, TBA $[FeCl_3Br]$: 75%) and in selectivity (**R2d**: >99%, TBA $[FeCl_3Br]$: 90%). This enhanced activity can be rationalized by a cooperative effect between the resin support, which is characterized by a strong CO_2 capture capability,[68] and the iron Lewis acid center, which is maintained in close spatial proximity.

Scale up and recycling test. To evaluate the scalability of the procedure, the reaction was carried out on a gram scale using the optimized conditions. Under these conditions, 1 g of **S1a** was fully converted into 3-butyl-5-phenyloxazolidin-2-one (**P1a**) within only 2 h (Table 2.3, entry 3), clearly indicating that the method can be readily scaled to larger quantities. Remarkably, **P1a** was isolated in nearly quantitative yield and in pure form after just a simple brine wash (see Chapter 6, page 151).

Because the catalyst is heterogeneous, its recovery and reuse were inherently simple. At the end of the reaction, the solid catalyst could be removed by filtration, allowing isolation of the product, and then washed with dichloromethane prior to recycling. DCM was selected in place of DCE owing to its lower boiling point. Nonetheless, the catalyst's behavior upon reuse was disappointing: after the first recycling, both conversion and yield dropped to less than half of their original values (Table 2.4, entry 2) and continued to decline in subsequent cycles. By the fifth

Table 2.3: *Validation of the optimized conditions, comparison with the homogeneous equivalent catalyst and scale up to 1 g.*[a]

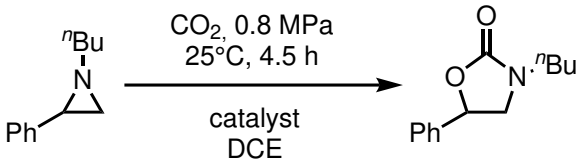

S1a **P1a**

Entry	Catalyst	Substrate (mmol)	Conversion (%)[b]	Yield (%)[b]	TOF (h^{-1})
1[c]	**R2d** 43 mg, 5.2 mol%	1	>99	>99	4.3
2	TBA [$FeCl_3Br$] (**M2b**)[d], 3.4 mol%	1	75	68	4.7
3[e]	**R2d** 245 mg, 5.2 mol%	5.7 (1 g)	>99	>99	9.6

[a]Reaction conditions: 25 °C, 0.8 MPa CO_2, 4.5 h, **S1a** 1 M in DCE. [b]Conversion and yield were calculated with GC-FID, using decane as internal standard. [c]The experiment was repeated twice, under identical conditions, leading to the same experimental result. [d] This class of compounds is described in Chapter 3. I preferred to keep the notation coherent within that chapter, and for this reason this metallate does not have code *R1a*. [e]Scale up of the reaction. Quantitative yield was obtained after 2 h.

reuse, the catalyst had become completely inactive. It is important to emphasize that the reaction maintained 100% selectivity under these conditions, demonstrating that the catalytic activity of the remaining metallate was preserved. After every catalytic run, the reaction mixture consistently displayed a bright red coloration, which we attributed to iron present in solution, most likely arising from complexation of the ferrate anion with the product **P1a**.

To verify this assumption, dedicated experiments were performed to quantify both iron retained in the spent catalyst and iron leached into the reaction mixture after a representative catalytic run (entry 1 and 2, Table 2.5), as well as to investigate the influence of the solvent (entry 3, Table 2.5), aziridine **S1a** (entry 4, Table 2.5), and the product **P1a** (entry 5, Table 2.5) on metal leaching. Notably, for experiments displaying significant iron loss, the measurements obtained from the solid and from the solution phase were in close agreement, within acceptable experimental error, underscoring the robustness of the analytical protocol.

Under catalytic conditions, approximately 25% of iron loss was observed in CH_3CN and about 20% in DCE (entries 1 and 2, Table 2.5). However, entries 3 and 4 clearly indicate that such leaching is not caused by the solvent itself nor by the presence of the starting aziridine **S1a**. In contrast, the addition of oxazolidinone **P1a** (1 M in DCE) led to a marked increase in iron solubilization (entry 5, Table 2.5), thereby confirming the hypothesis regarding complex formation with the product.

Table 2.4: *Recycling text of catalyst **R2d**.*[a]

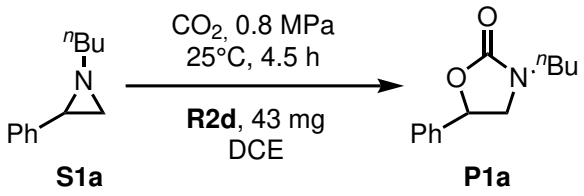

S1a **P1a**

Catalyst's cycle	Conversion (%)[b]	Yield (%)[b]
1	>99%	>99%
2	42%	42%
3	10%	10%
4	4%	4%
5	0%	0%

[a]Reaction conditions: 25 °C, 0.8 MPa CO_2, 43 mg of **R2d**, 4.5 h, **S1a** 1 M in DCE. [b]Conversion and yield were calculated with GC-FID, using decane as internal standard.

Table 2.5: *Recycling text of catalyst **R2d**.*[a]

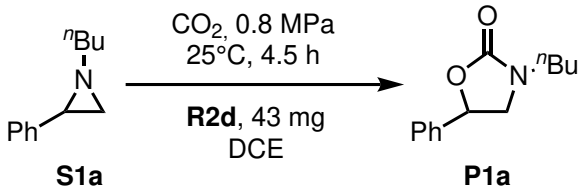

S1a **P1a**

Entry	Conditions	Fe (%) in the recovered catalyst [a]	% of Fe lost from the solid[b]	% of Fe (mg) in the residue[c]	% of Fe lost in solution[d]
1[e]	CH_3CN (after catalysis)	5.19	23.6%	0.75	26%
2[e]	DCE (after catalysis)	5.41	20.3%	0.61	21%
3[f]	DCE	6.55	3.5%	0.002	0.1%
4[f]	DCE + **S1a**	6.97	-	0.005	0.1%
5[f]	DCE + **P1a**	6.27	7.6%	0.43	15%

[a]Fe % of the recovered catalyst was calculated at the end of the treatment by ICP-OES analyses after mineralization. [b]% of iron lost calculated as the ICP-OES value before and after the treatment. [c]The amount (mg) of iron content in the solid residue was calculated at the end of the reaction by filtering the reaction mixture, evaporating the volatiles in the filtrates, and performing ICP-OES analyses after mineralization. [d]Iron lost from the fresh catalyst (%) was calculated by dividing the mg found in solution divided the total mg of iron present in the fresh catalyst. [e]Reaction conditions: 30 °C, 0.8 MPa CO_2, 43 mg of resin for 4.5 h, 1 mmol of **S1a** in 1 mL of solvent. [f]**R1d** was suspended in DCE (entry 3), DCE + 1 mmol of **S1a** (entry 4), or DCE + 1 mmol of **P1a** (entry 5) and allowed to stir at 30 °C for 14 h, after which the solid was separated from the solution by filtration. Further washing of the solid with DCE gave negligible iron content.

Substrates scope. With the optimized reaction conditions established, the substrate scope was explored along with potential limitations of the reaction. The outcomes of the screening of various aziridines are summarized in Table 2.6. Overall, the transformation proved to be broadly applicable to linear *N*-alkyl-substituted aziridines, with substrates **S1a**, **S1c**, and **S1f** affording the corresponding products in essentially quantitative yields. In every instance, the formation of the 5-phenyl-substituted oxazolidinone was completely selective, and no detectable amount of the 4-phenyl isomer was observed.

Table 2.6: *Substrate scope.*[a]

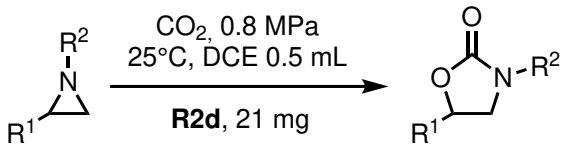

Subs.	Prod.	Scheme	Yield (%)[b]	Subs.	Prod.	Scheme	Yield (%)[b]
S1a[c]	**P1a**	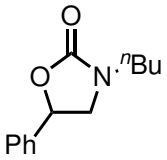	>99	**S1b**	**P1b**	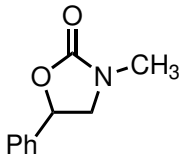	78
S1c	**P1c**	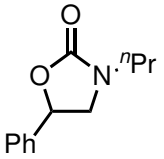	>99	**S1d**	**P1d**	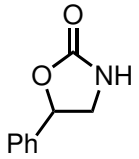	55
S1e	**P1e**	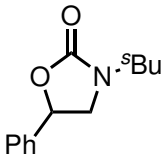	21(80)[d]	**S1f**	**P1f**	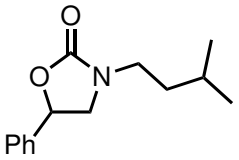	95
S1g	**P1g**	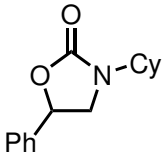	11(92)[d]	**S1h**	**P1h**	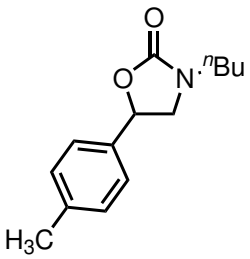	91
S1i	**P1i**	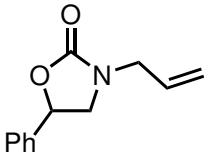	61	**S1j**	**P1j**	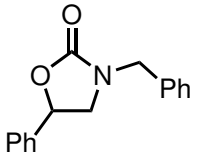	85[e]

Continues on next page

Table 2.6 – continued from previous page

Subs.	Prod.	Scheme	Yield (%)[b]	Subs.	Prod.	Scheme	Yield (%)[b]
S1k	**P1k**	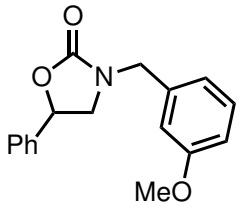	80[e, f]	**S1l**	**P1l**	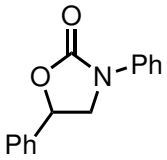	n.d.[e] (6)[d]
S1m	**P1m**	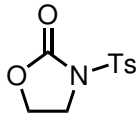	n.d. (68)[d]	**S1n**	**P1n**	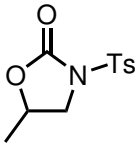	n.d. (3)[d]
					P1n'	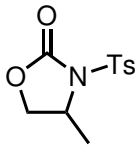	n.d. (8)[d]

[a]Reaction conditions: 25 °C, 0.8 MPa CO_2, 21 mg of **R2d**, 4.5 h, substrates: 0.5 mmol in 1 M DCE solutions. [b]Unless otherwise specified, yield refers to isolated products. In most cases an almost quantitative conversion of the aziridine was observed. When reported yields are lower than 70%, major byproducts were (±)-1,2,4,5-tetrasubstituted and meso-1,2,4,5-tetrasubstituted piperazines. Traces of benzaldehyde were detected. [c]Result of the scale up experiment (1 mmol of **S1a**). [d]Reaction conditions: 120 °C, 1.2 MPa CO_2, 21 mg of **R2d**, 16 h. [e]Yield determined by ^{1}H-NMR using dibromomethane as the internal standard. [f]3-(3-methoxybenzyl)-4-phenyloxazolidin-2-one, **P1k'**, formed in a 20:80 ratio with the desired 5-substituted product **P1k**.

A modest decrease in yield was recorded for **S1b**. 1-methyl-2-phenylaziridine is particularly prone to dimerization, forming symmetric piperazines more readily than other aziridines. In this case, both (±)-1,2,4,5-tetrasubstituted and meso-1,2,4,5-tetrasubstituted piperazines appeared as major side products. This behaviour appeared in other entries where the conversion of the starting material was high but the isolated yield of the target oxazolidinone was reduced.

The unprotected aziridine **S1d** gave less satisfactory results. Although the selectivity toward oxazolidinone **P1d** was complete, the overall conversion was limited, leading to 55% isolated yield and leaving nearly 45% of the starting aziridine unreacted. Similarly, branched *N*-alkyl aziridines **S1e** and **S1g** afforded lower yields under standard conditions, indicating that increased steric hindrance at the nitrogen atom slows the reaction. This observation supports a mechanism in which coordination of the Lewis acid catalyst to the aziridine precedes and activates nucleophilic attack.[28]

To drive these more hindered substrates to full conversion, more forcing conditions were necessary (120 °C, 1.2 MPa CO_2, 16 h), under which oxazolidinones **P1e** and **P1g** were obtained in 80 - 92% yield.

In my master thesis work it was demonstrated that an ED group on the phenyl ring accelerates the conversion rate.[65] Consistent with this, aziridine **S1h** underwent rapid transformation, though at the expense of regioselectivity, and oxazolidinone **P1h** was obtained with a 91% yield. Modifying the *N*-protecting group to allylic (**S1i**) or benzylic (**S1j** and **S1k**) units also gave satisfactory results, affording the corresponding *N*-allylic and *N*-benzylic oxazolidinones in moderate to good yields (61% - 85%). In the case of the *N*-benzylic aziridine **S1k**, the presence of an electron-donating substituent on the phenyl ring did not compromise the catalyst productivity but did diminish the typically high regioselectivity of the reaction. Thus, the 4-substituted regioisomer **P1k'** was formed in a 20:80 ratio relative to the desired 5-substituted product **P1k**.

N-aryl aziridines are well known to be particularly demanding substrates in this transformation.[77] When the reaction was carried out on 1,2-diphenylaziridine (**S1l**), the outcome was unsatisfactory, as the desired oxazolidinone was essentially not formed. Even under more forcing conditions (1.2 MPa CO_2, 120 °C), the target product **P1l** was isolated in only 6% yield, while the reaction mainly furnished 1,2,4,5-tetrasubstituted piperazines and uncharacterized oligomeric material.

In contrast, *N*-tosyl aziridines **S1m** and **S1n**, deactivated by the strongly electron-withdrawing sulfonyl group on nitrogen,[78] were unreactive at room temperature. Under harsher conditions, however, aziridine **S1m** underwent full conversion, providing 3-tosyloxazolidin-2-one in 68% yield. The major byproduct in this case most likely arose from aziridine self-opening, leading to uncharacterized oligomeric species. Conversely, the 2-methyl-substituted aziridine **S1n** remained largely unreactive even under severe conditions (120 °C, 1.2 MPa CO_2, 16 h), giving predominantly oligomeric material. Only trace amounts of the desired 3,5-disubstituted oxazolidinone **P1n** (~3%) were detected, along with 8% of the 3,4-substituted regioisomer **P1n'** (**P1n**/**P1n'** = 26:74). An inversion of regioselectivity is in line with expectations for 2-alkyl-substituted aziridines.[79]

2.2.3 Catalytic dimerization of aziridines.[74]

As discussed in the previous section (2.2.2), a common side-product of the cycloaddition of CO_2 to aziridines is the dimerization product, symmetric piperazines. Although one of the objectives of the previous work was to minimize the presence of these species in the reaction products, piperazines represent a interesting class of compounds. In a 2014 study,[80] piperazines ranked third among the 25 most frequent nitrogen heterocycles in U.S. FDA approved drugs (Figure 2.6). Their use as scaffolds in organic chemistry is not limited to the pharmaceutical industry, but spans from agrochemicals,[81] to material science,[82] and to any field that requires a rigid scaffold with diverse and tunable chemical and biological properties.[83]

Despite their simplicity, symmetric piperazines still represent irreplaceable compounds in more fundamental studies. In coordination chemistry they find use as

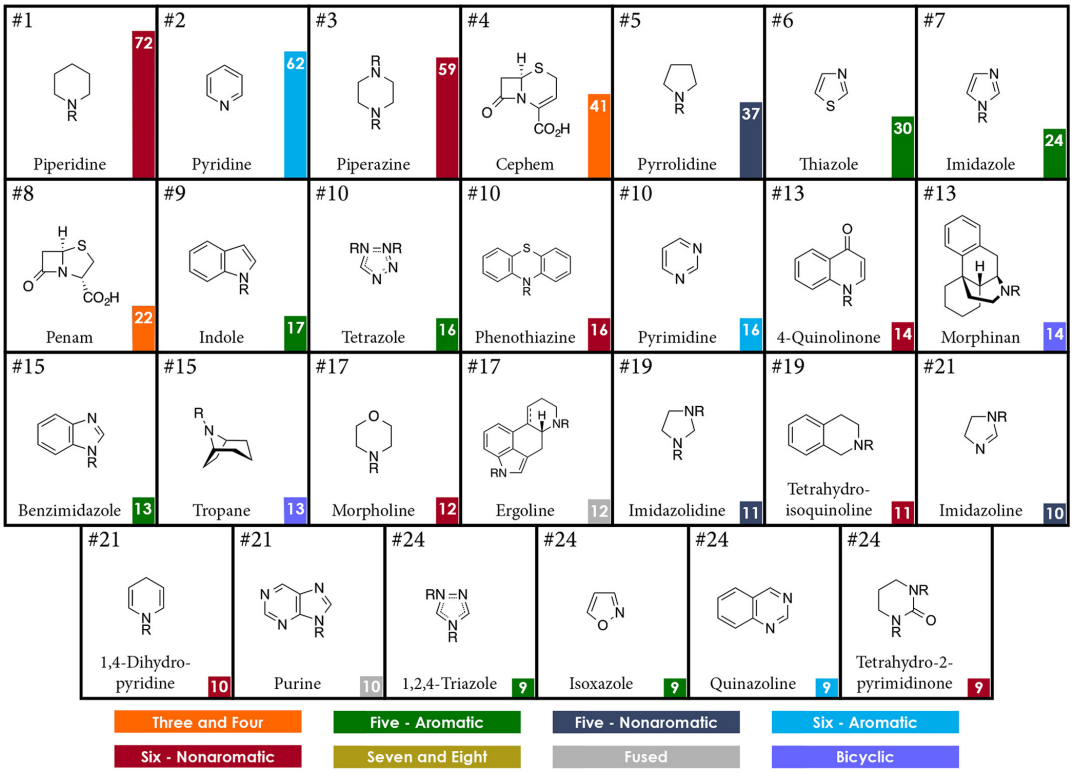

Figure 2.6: *Top 25 most frequent nitrogen heterocycles in U.S. FDA approved drugs. Image adapted from the Journal of Medicinal Chemistry.*[80]

ligands.[84] In this field, they can express their versatility by adopting either bidentate or bridging coordination modes, enabling the synthesis of monometallic and bimetallic complexes by simply controlling complexation conditions.[85] Moreover, piperazine coordination complexes are known to catalyze several reactions, among which enantioselective reduction of aldehydes,[86] asymmetric Michael additions to nitroalkenes,[87] and diaryl couplings.[88,89] Unsubstituted piperazine was also used as a cocatalyst in alkynes hydrogenation on gold nanoparticles.[90]

Most importantly, the development of efficient and selective methods for the synthesis of symmetric piperazines via aziridine dimerization remains a largely underexplored area.[91] This is rather surprising, considering that early studies had already demonstrated that LiI in refluxing THF efficiently promotes the ring-opening process, leading to the formation of a mixture of piperazine stereoisomers.[92]

As discussed above, in the carbonatation of aziridines to oxazolidinones, the homocoupling product is invariably formed at low CO_2 pressure, while elevated reaction temperatures were also found to favor the formation of piperazines. These side products are generated as four possible stereoisomers (Scheme 2.2.2), among which 2,5-disubstituted species constitute the two major isomers, consistently obtained in a 1:1 ratio.

Moreover, during my master's thesis work, I observed that alkylammonium zincates displayed a higher selectivity toward piperazine formation when compared to their alkylammonium ferrate counterparts in the CO_2 coupling of aziridines. These

observations prompted me to extend this line of investigation during my doctoral studies, focusing on tetralkylammonium zincate-catalyzed aziridine dimerization with the aim of optimizing piperazine formation and gaining deeper insight into the underlying reaction mechanism.

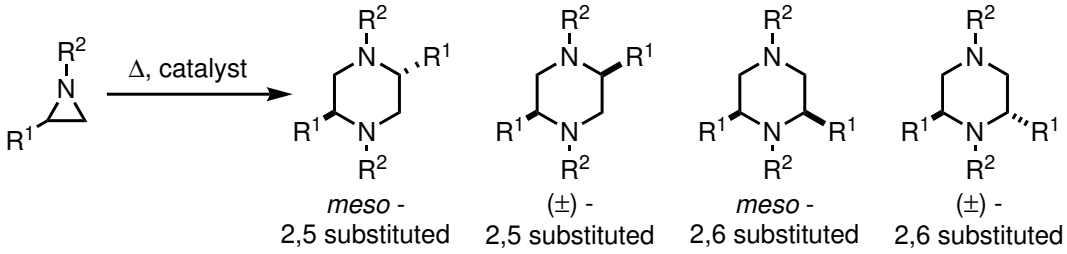

Scheme 2.2.2: *Formation of piperazines from the dimerization of aziridines: possible isomers.*

Optimization. As mentioned above, during the optimization of the reaction conditions for the synthesis of 1,3-oxazolidin-2-ones, I observed that higher temperatures (e.g., 75 °C) favored the homocoupling process, leading to the formation of piperazines. Interestingly, the *meso*-2,5 isomer spontaneously precipitated from the crude reaction mixture and could therefore be easily isolated in pure form, particularly when ammonium zincates were used as catalysts.

Building on these findings, I proceeded to optimize the synthesis of symmetrically substituted piperazines, drawing on the experimental insights gained from the oxazolidinone protocol and employing a series of tetrabutylammonium metallates. The best outcomes were achieved with zincates $[TBA]_2[ZnX_4]$ (2.5 mol%) in acetonitrile. For these studies, 1-methyl-2-phenylaziridine (**S1b**) was selected as the model substrate for two reasons: the first one being that the *N*-methyl substituent could function efficiently as a spectroscopic probe in ^{1}H-NMR spectroscopy, and the second being that it was found more reactive towards dimerization. The reaction temperature was fixed at 75 °C for 16 h. The corresponding data are summarized in Table 2.7.

All ammonium zincates were effective in promoting the dimerization of aziridines, with their activity decreasing in the order $[TBA]_2[ZnI_4]$ (**M1c**) > $[TBA]_2[ZnBr_4]$ (**M1b**) > $[TBA]_2[ZnCl_4]$ (**M1a**). This trend correlates with the leaving-group ability of the anion, rather than its nucleophilicity (Table 2.7, entries 1-3). Independent of the catalyst employed, *meso* - **P2b** and (±) - **P2b** were consistently obtained in an approximately equimolar ratio. When $[TBA][FeBr_4]$ (**M2d**) was used as the catalyst, complete conversion of the starting aziridine was achieved, but the reaction exhibited very poor selectivity (Table 2.7, entry 4).

In addition to the two main products, *meso* - **P2b** and (±) - **P2b**, small amounts of other isomers were consistently detected in the crude reaction mixture. These minor components were tentatively assigned to 2,6-disubstituted *N*,*N*-dialkylpiperazines. When the selectivity dropped below 85%, polymeric or oligomeric byproducts also

Table 2.7: *Synthesis of symmetric piperazines meso -* ***P2b*** *and* (±) - ***P2b*** (*meso-1,4-dimethyl-2,5-diphenylpiperazine and* (±)*-1,4-dimethyl-2,5-diphenylpiperazine, respectively*) *catalyzed by ammonium zincates,* $[TBA]_2[ZnX_4]$.[a]

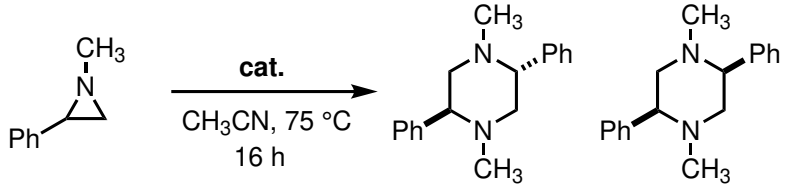

S1b *meso* - **P2b** (±) - **P2b**

Entry	Catalyst	Cat. loading (mol%)	Conversion (%)[b]	Selectivity (%)[c]	TOF (h^{-1})[d]
1	$[TBA]_2[ZnCl_4]$ (**M1a**)	2.5	11	90	0.3
2	$[TBA]_2[ZnBr_4]$ (**M1b**)	2.5	34	90	0.9
3	$[TBA]_2[ZnI_4]$ (**M1c**)	2.5	80	85	2.0
4	$[TBA][FeBr_4]$ (**M2d**)	2.5	>99	27	2.5
5	ZnI_2	2.5	>99	33	2.5
6	TBACl	5	<5	-	-
7	TBAB	5	12	50	0.2
8	TBAI	5	43	62	0.5
9	none	-	<1	-	-

[a]Reaction conditions: 75 °C, 16 h, 1 mmol of 1-methyl-2-phenyl aziridine, **S1b**, in 1 mL of acetonitrile. [b]Conversion was calculated with GC-FID, using dimethyl terephthalate as internal standard. [c]Selectivity determined by ^{1}H-NMR using dimethyl terephthalate as internal standard. Selectivity reported as the sum of *meso* - **P2b** and (±) - **P2b**, obtained as 1:1 mixture. [d]Turnover frequency ($n_{\mathbf{S1b}(\text{converted})} \cdot n_{\text{cat.}}^{-1} \cdot t^{-1}$).

became apparent.

Literature reports indicate that catalytic quantities of Lewis acids promote the dimerization of nonactivated aziridines to give a *cis*/*trans* mixture of symmetrically 2,5-disubstituted piperazines.[91] On this basis, I examined ZnI_2 as a catalyst. Although the starting aziridine **S1b** was almost completely consumed, the reaction predominantly afforded uncharacterized oligomeric and/or polymeric material (Table 2.7, entry 5). When the analogous halide ammonium salts were employed as catalysts (in this case at a 5 mol% loading to maintain the same stoichiometric ratio as for the ammonium zincates) the same qualitative pattern of reactivity and selectivity was observed, but with lower yields of **P2b** (Table 2.7, entries 6-8). Under otherwise identical conditions, omitting any catalyst resulted in no detectable conversion of aziridine **S1b**, thus confirming its stability in dry acetonitrile at 75 °C (Table 2.7, entry 9).

After recognizing that a cooperative interplay between the Lewis acidity of the metal center and the nucleophilic character/leaving group ability of the halide ion favors piperazines formation (and that bromide and iodide are markedly superior to chloride in this respect) I turned to optimizing the catalytic system. To accelerate the reaction, I adopted a more efficient energy input by employing dielectric heating in closed vessels. This approach made it possible to exceed the boiling point of acetonitrile, thereby enabling higher reaction temperatures and significantly shorter reaction times.

Under microwave irradiation, using 2.5 mol% of **M1c**, I obtained 68% conversion in only 20 minutes at 100 °C; increasing the temperature to 120 °C led to a comparable conversion within just 5 minutes, while maintaining good selectivity (Table 2.8, entries 1 and 2). At 120 °C, both **M1b** and **M1c** afforded almost quantitative conversions, although **M1c** delivered superior selectivity and, consequently, a higher yield of piperazines (Table 2.8, entries 4 and 6) within 20 minutes. Extending the reaction time to 1 hour did not significantly compromise selectivity (Table 2.8, entry 5), indicating that piperazines **P2b** are stable at this temperature.

I then examined the effect of catalyst loading. A quantitative conversion was achieved with 1 mol% **M1c** at 120 °C (Table 2.8, entry 7). Even at 0.1 mol% catalyst loading, the starting aziridine **S1b** still underwent almost complete conversion (92%), corresponding to a TOF of 2790 h^{-1}, with an excellent 97% selectivity in only 20 minutes (Table 2.8, entry 8).

Under dielectric heating, ZnI_2 and TBAI also act as effective catalysts, giving very high conversions, although with poorer selectivities; substantial amounts of polymeric material were formed, which account for the rest of the reaction mass balance (Table 2.8, entries 9 and 10). Another advantage associated with the use of ammonium zincates over zinc salts or ammonium halides lies in their easier handling and their markedly lower hydrophilicity.[93] In addition, all metallate salts are recognized as excellent microwave absorbers because of their ionic character.

To assess whether the nature of the ammonium cation could affect the reaction

Table 2.8: *Optimization of the synthesis of symmetric piperazines meso -* ***P2b*** *and* (±) - ***P2b*** (*meso-1,4-dimethyl-2,5-diphenylpiperazine and* (±)*-1,4-dimethyl-2,5-diphenylpiperazine, respectively*) *under microwave heating.*[a]

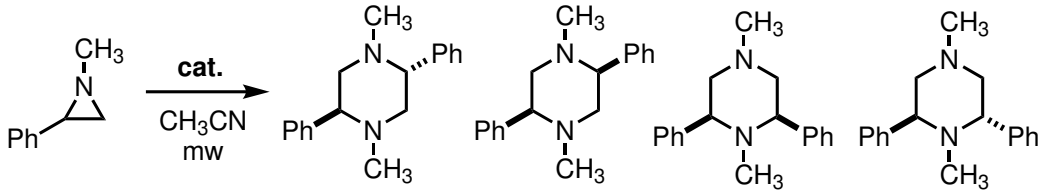

S1b *meso* - **P2b** (±) - **P2b** *meso* - **P2b'** (±) - **P2b'**

Entry	Catalyst	Cat. loading (mol%)	*T* (°C)	*t* (min)	Conv. (%)[b]	Sel. (%)[c]	TOF (h^{-1})[d]
1	**M1c**	2.5	100	20	68	81	82
2	**M1c**	2.5	120	5	68	85	326
3	**M1c**	2.5	120	10	78	88	187
4	**M1c**	2.5	120	20	**96**	**94**	115
5	**M1c**	2.5	120	60	>99	77	40
6	**M1b**	2.5	120	20	>99	75	120
7	**M1c**	1	120	20	>99	82	300
8	**M1c**	0.1	120	20	**93**	**97**	**2790**
9	ZnI_2	1	120	20	94	79	282
10	TBAI	1	120	20	96	73	288
11	$[TMA]_2[ZnI_4]$ (**M1d**)	2.5	120	20	95	80	114
12	none	-	120	20	62	67	-

[a]Reaction conditions: 1 mmol of 1-methyl-2-phenyl aziridine, **S1b**, in 1 mL of acetonitrile. [b]Conversion was calculated with GC-FID, using dimethyl terephthalate as internal standard. [c]Selectivity determined by ^{1}H-NMR using dimethyl terephthalate as internal standard. Selectivity reported as the sum of *meso* - **P2b** and (±) - **P2b**, obtained as 1:1 mixture. [d]Turnover frequency ($n_{\mathbf{S1b}(\text{converted})} \cdot n_{\text{cat.}}^{-1} \cdot t^{-1}$).

outcome, I synthesized and evaluated the catalytic performance of $[TMA]_2[ZnI_4]$ (TMA = tetramethylammonium). As anticipated, the results were essentially identical to those obtained with the original ammonium zincate (Table 2.8, entry 11). It is also noteworthy that, under the same conditions, the coupling of two aziridine molecules proceeds to a certain extent even in the complete absence of any catalyst (Table 2.8, entry 12); however, in this catalyst-free system, polymeric materials again account for part of the mass balance.

Under the conditions used for entry 4 in Table 2.8, piperazine *meso* - **P2b** spontaneously precipitated from the crude reaction mixture. In this case, *meso* - **P2b** was isolated in pure form in 44% yield, while the racemic piperazine (±) - **P2b** was obtained in 27% yield after purification by column chromatography (Table 2.11, entry 1). The proposed structures of both diastereoisomers were elucidated by NMR analysis and corroborated by comparison with reported data (see Chapter 6).

A minor fraction of (±) - **P2b** (approximately 10%) was obtained as a mixture with a closely eluting by-product that could not be isolated in analytically pure form. Nevertheless, its ^{1}H-NMR signals were consistent with a 2,6-disubstituted *N*,*N*-dialkylpiperazine, (±) - **P2b'**. In addition, a third compound with lower R_F was isolated in a 1% yield; based on NMR and MS data, its structure and stereochemistry were assigned to *meso* - **P2b'** (see Chapter 6). These two 2,6-disubstituted piperazines were formed in an approximate 1:1 ratio and, to the best of our knowledge, their formation has not previously been proposed in the literature.

Previous work from my group,[93] along with extensive literature data,[33] has shown that nucleophilic ring opening of non-activated 2-phenyl-substituted aziridines occurs preferentially at the benzylic position. However, in Lewis acid catalysis, nucleophilic attack has also been described at the unsubstituted (terminal) position.[91] In the present case, I propose that products (±) - **P2b'** and *meso* - **P2b'** arise as by-products from the coupling of two aziridine **S1b** molecules: one undergoing the more favorable ring opening at the benzylic site and the other at the terminal carbon (*Vide infra* for mechanistic discussion).

I then examined how changing the reaction scale (from 0.2 mmol/0.2 mL to 2 mmol/2 mL) and the initial aziridine concentration (0.1 M to 2 M) affected the outcome (Table 2.9). Altering the scale had no significant impact, whereas lowering the concentration of aziridine caused a marked drop in selectivity.

Subsequently, I investigated solvent effects on the catalytic process. Solvent polarity is known to strongly influence the nucleophilic ring opening of aziridines,[94] and this influence becomes even more pronounced under microwave irradiation, because more polar media[95] absorb microwave energy more efficiently. Since the catalyst is ionic, it can itself contribute to rapid heating, accelerating the reaction. To disentangle these factors, I selected solvents with differing dielectric constants and dipole moments and compared their performance in terms of conversion and selectivity, under the optimized conditions (1 mmol of aziridine **S1b**, 1 M in the chosen solvent, 2.5 mol% catalyst loading, T = 120 °C, t = 20 min).

Table 2.9: *Effect of aziridine **S1b** concentration and of the scale-up and -down on the catalytic reaction.*[a]

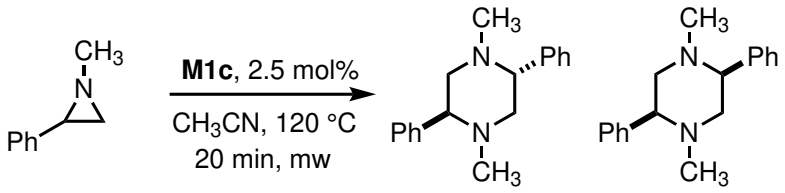

S1b *meso* - **P2b** (±) - **P2b**

Entry	S1b (mmol)	CH_3CN (mL)	Conversion (%)[b]	Selectivity (%)[c]	TOF (h^{-1})[d]
1	1.0	1.0	96	94	116
2	0.2	0.2	83	84	101
3	2.0	2.0	88	79	107
4	0.2	0.2	94	53	114
5	1.0	0.5	99	85	120

[a]Reaction conditions: 120 °C, 20 min, 1 mmol of 1-methyl-2-phenyl aziridine, **S1b**, in 1 mL of acetonitrile, 2.5 mol% of **M1c**. [b]Conversion was calculated with GC-FID, using dimethyl terephthalate as internal standard. [c]Selectivity determined by ^{1}H-NMR using dimethyl terephthalate as internal standard. Selectivity reported as the sum of *meso* - **P2b** and (±) - **P2b**, obtained as 1:1 mixture. [d]Turnover frequency ($n_{\mathbf{S1b}(\text{converted})} \cdot n_{\text{cat.}}^{-1} \cdot t^{-1}$).

With 2.5 mol% of the catalyst (which, as noted, is an excellent microwave absorber) even toluene allowed the system to reach the target temperature. By contrast, in the absence of **M1c** or at much lower catalyst loadings (0.1 mol%), low-dielectric solvents could not reach 120 °C. The results, arranged in order of increasing dielectric constant, are presented in Table 2.10. Although the conversions are uniformly high, preventing a clear-cut correlation, it is evident that the solvent dielectric constant is not the key parameter controlling aziridine ring opening. The selectivity, on the other hand, varies substantially across the solvent series. The best performance is achieved in acetonitrile, which offers the additional practical advantage that the meso aziridine form precipitates quantitatively and spontaneously, simplifying its isolation in pure form at the end of the reaction.

Reaction scope. With the optimal catalyst and reaction conditions established (Table 2.8, entry 4), I then examined the scope and limitations of this methodology. The starting aziridines were prepared following reported procedures. Parallel control experiments were carried out under identical conditions but in the absence of the catalyst; in these cases, homocoupling products were detected only for entries 1, 2, and 8 (Table 2.11), and even then in very low yields. All reported yields refer to isolated products. The *meso* isomer precipitated directly from the crude reaction mixture and was obtained as a pure white solid simply by filtration, whereas the racemic piperazines were isolated and purified by column chromatography (see Chapter 6 for full experimental details). Importantly, NMR analysis of the crude mixtures consistently revealed an equimolar ratio of the two diastereoisomers of

Table 2.10: *Effect of solvent on the catalytic performance.*[a]

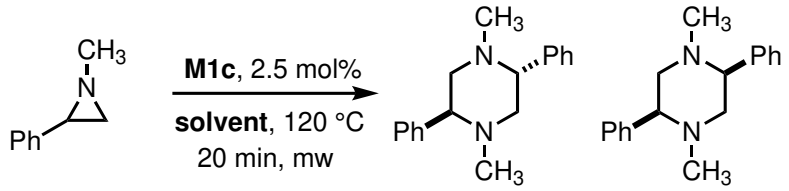

S1b *meso* - **P2b** (±) - **P2b**

Entry	Solvent	Conversion (%)[b]	Selectivity (%)[c]	Dielectric constant
1	toluene	79	22	2.38
2	clorobenzene	97	63	5.62
3	AcOEt	92	66	6.02
4	DME	97	67	7.25
5	THF	99	48	7.58
6	*o*-diclorobenzene	99	71	9.93
7	DCE	99	0	10.36
8	EtOH	99	60	24.55
9	DMF	99	0	36.71
10	acetonitrile	90	94	37.50
11	DMSO	99	0	46.68

[a]Reaction conditions: 120 °C, 20 min, 1 mmol of 1-methyl-2-phenyl aziridine, **S1b**, in 1 mL of solvent, 2.5 mol% of **M1c**. [b]Conversion was calculated with GC-FID, using dimethyl terephthalate as internal standard. [c]Selectivity determined by ^{1}H-NMR using dimethyl terephthalate as internal standard. Selectivity reported as the sum of *meso* - **P2b** and (±) - **P2b**, obtained as 1:1 mixture.

the target piperazines, indicating that chromatographic isolation of the racemate is invariably incomplete. In addition, uncharacterized oligomeric and polymeric byproducts were observed, which account for the remaining mass balance.

Table 2.11: *Reaction scope.*[a]

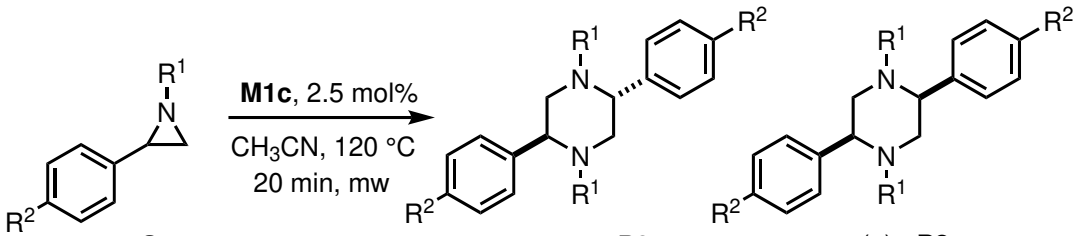

S1 *meso* - **P2** (±) - **P2**

Entry	R^1	R^2	Product	Yield *meso* - **2** (%)[b]	Yield (±) - **2** (%)[c]	Yield *meso* - **2** (%), uncatal.[d]
1	Me	H	**P2b**	44	27	21
2	^{n}Bu	H	**P2a**	27	20	41
3	H	H	**P2d**	n.d.	n.d.	n.d.
4	^{s}Bu	H	**P2e**	n.d.	n.d.	n.d.
5	Bn	H	**P2j**	13	8	n.d.
6	CH_2CHCH_2	H	**P2i**	15	12	n.d.
7	CH_2CH_2NHTs	H	**P2o**	n.d.	n.d.	n.d.
8	Me	Me	**P2p**	46	36	44
9	Me	^{t}Bu	**P2q**	31	21	n.d.
10	Me	Br	**P2r**	20	17	n.d.
11	Me	F	**P2s**	14	6	n.d.
12	^{n}Bu	Me	**P2h**	15	7	n.d.
13	^{n}Bu	Cl	**P2t**	8	4	n.d.
14	^{n}Bu	F	**P2u**	n.d.	n.d.	n.d.

[a]Reaction conditions: 120 °C, 20 min, 1 mmol of substrate, in 1 mL of acetonitrile, 2.5 mol% of **M1c**. [b]The *meso* - **P2** products were collected as white solids after filtration of the reaction crude at the end of the reaction [c]Pure (±) - **P2** fractions were obtained after column cromatography. [d]Yield determined by ^{1}H-NMR using dimethyl terephthalate as internal standard, reported as the sum of *meso* - **P2** and (±) - **P2**, obtained as a 1:1 mixture.

I first examined a range of differently *N*-substituted aziridines. When 1-butyl-2-phenylaziridine **S1a** was used, the overall isolated yields were slightly lower than those obtained with the standard substrate, whereas the more sterically encumbered 1-(1-methylpropyl)-2-phenylaziridine **S1e** did not afford any of the desired coupling products (Table 2.11, entries 2 and 4). In this latter case, about 35% of unreacted aziridine was recovered, together with polymeric byproducts. Somewhat unexpectedly, 2-phenylaziridine **S1d** also failed to give the coupling products (Table 2.11, entry 3). This behavior can be attributed to the presence of the N-H functionality, which appears to promote polymerization. A comparable outcome was observed when starting from commercially available 7-azabicyclo[4.1.0]heptane.

I also investigated benzyl- and allyl-substituted aziridines. For these systems, the isolated yields of the corresponding piperazines were low; however, the pu-

rification of these compounds was particularly challenging, and the actual yields are likely underestimated (Table 2.11, entries 5 and 6). In addition, traces of benzaldehyde were detected, most plausibly arising from hydrolysis of the Schiff base formed upon aziridine ring opening.

Next, I turned to electronic effects by modifying the phenyl ring with *para*-substituents. *Ortho*-substituted and *meta*-substituted 2-phenylaziridines were not pursued: in the *ortho* case, steric and electronic contributions are difficult to disentangle, and in the *meta* case, any electronic influence was expected to be negligible. Electron-withdrawing *para* substituents such as Br, Cl, and F led to a decrease in the observed yields (Table 2.11, entries 10, 11, 13, and 14). By contrast, 1-methyl-2-(4-methylphenyl)aziridine **S1p** provided the best results, with (±) - **P2p** and *meso* - **P2p** isolated in a combined 82% yield (Table 2.11, entry 8), and no additional products were detected.

To probe a practical nitrogen protecting group that could be removed at a later stage, I then focused on deactivated *N*-tosyl aziridines, which are synthetically more accessible and easier to handle. I tested the coupling of 1-tosylaziridine **S1m**, 2-phenyl-1-tosylaziridine **S1v**, and 2-(1,1-dimethylethyl)-1-tosylaziridine **S1w**. Only in the case of the fully unsubstituted *N*-tosyl aziridine did I obtain the desired product 1,4-bis(tosyl)piperazine **P2m**, which precipitated spontaneously from the reaction mixture, and was isolated in 25% yield. In contrast, substitution at the 2-position resulted in complete polymerization of the starting aziridines, presumably due to enhanced steric hindrance.

Mechanistic considerations. From a mechanistic perspective, in $MgBr_2$-catalyzed couplings it has been proposed that the Lewis acid activated aziridine can undergo nucleophilic attack by either a free aziridine molecule or a halide anion. The latter pathway, followed by a second nucleophilic substitution and intramolecular ring opening, together with the first pathway, accounts for the observed 1:1 diastereomeric mixture of piperazines.[91]

My group's earlier work on ammonium metallate salts, supported by DFT calculations, suggests that in solution there is an equilibrium between the *ate* complex and the corresponding metal salt plus free halide anion X^-.[93] More recently, in related ammonium ferrate systems, it was shown that nucleophilic attack by a free bromide ion on the LA-activated aziridine proceeds with almost barrierless; the ring-opening step is overall exothermic, with an enthalpy change of −18.1 kcal/mol.[65] Nucleophilic attack at the terminal carbon atom is less favored. By analogy, it is reasonable to propose that in the present case the initial, fast step involves nucleophilic attack of I^- at the benzylic position of the LA-activated aziridine, generating intermediate **IIa**, as depicted in Scheme 2.2.3, **a**.

Mechanism

a) Pre-equilibrium and nucleophilic attack

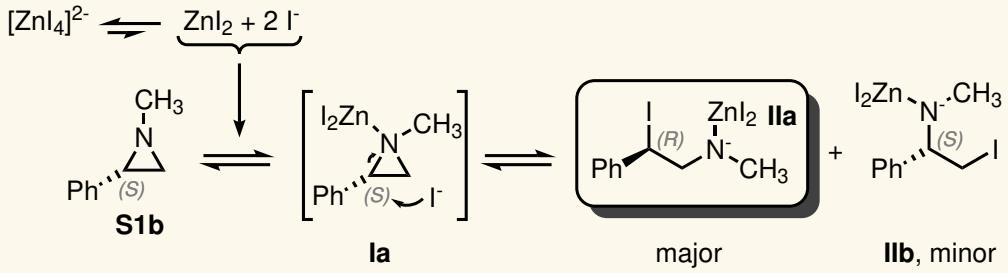

b) Formation of 2,6-disubstituted diastereoisomers P2'

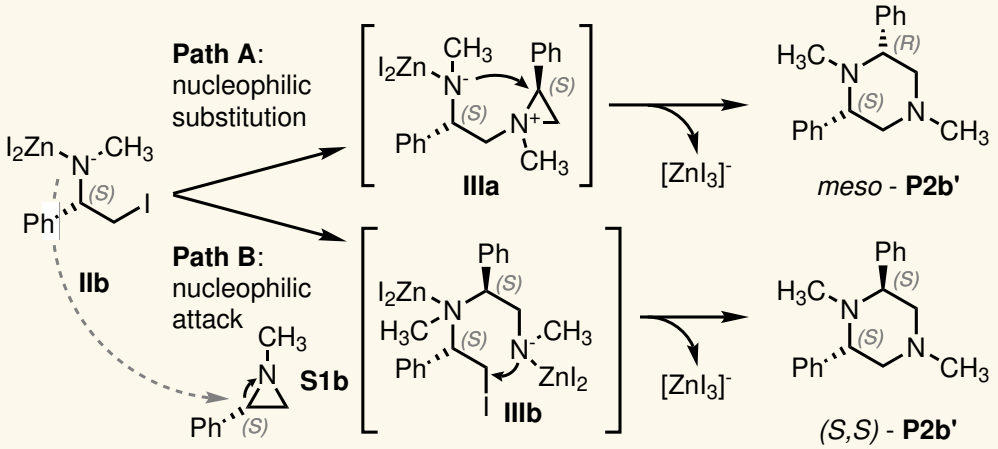

c) Formation of 2,5-disubstituted meso P2 through S_N2 pathways

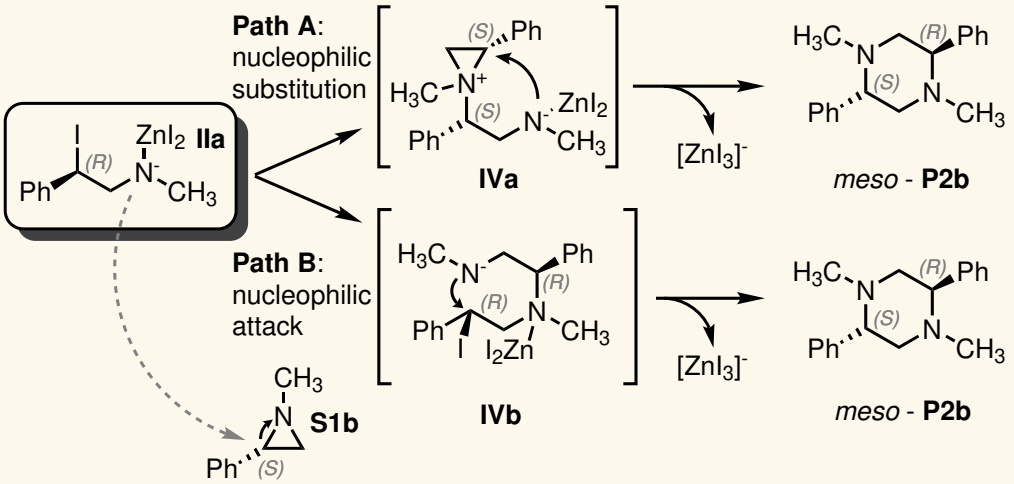

Scheme 2.2.3: *Proposed mechanism for the aziridine dimerization to piperazines catalyzed by **M1c** - S_N2 pathways.*

A minor formation of intermediate **IIb**, arising from nucleophilic attack at the less hindered position, can account for the production of the 2,6-disubstituted di-

astereoisomers **P2'** (Scheme 2.2.3, **b**). From intermediate **IIa**, two competing pathways may then operate (Scheme 2.2.3, **c**). In Path A, **IIa** first undergoes a nucleophilic substitution to give intermediate **IVa**; this species subsequently furnishes piperazine **P2** through attack of the amido anion at the benzylic position of the aziridinium ion. In contrast, Path B involves a direct nucleophilic attack by the amido intermediate **IIa** on a free aziridine molecule at the more substituted carbon atom, yielding intermediate **IVb**, which then undergoes concerted ring closure with elimination of iodine to afford the piperazine. All of these nucleophilic substitutions are thought to proceed via an S_N2 mechanism,[96] a view that is further supported by the weak dependence of the reaction outcome on solvents with markedly different dielectric constants.

Beginning from a racemic mixture, either of the two proposed mechanisms would be expected to produce piperazines as a 1:1 mixture of the meso and racemic diastereoisomers, in agreement with the experimental observations. In order to gain further insight into the reaction pathway, I carried out the transformation using enantiomerically pure (*S*)-1-methyl-2-phenylaziridine, (*S*)-**S1b**, synthesized according to a well-established literature protocol. The outcome was surprising and markedly different from that previously described for the same transformation catalyzed by $MgBr_2$.[91] Under these conditions, the isolated products were again *meso* - **P2b** and the racemic piperazine (±) - **P2b**, but now in a 2.2:1 ratio favoring the meso isomer as the predominant product.

Such a result can only be rationalized by invoking either a competing S_N1 pathway for the nucleophilic substitution, giving rise to intermediate **IVa'** (Scheme 2.2.4 **d**), or a racemization pre-equilibrium of the starting aziridine (intermediate **Ib**, Scheme 2.2.4 **e**). The presence of such a process is supported by the experimentally observed reactivity trend $[ZnI_4]^{2-} > [ZnBr_4]^{2-} > [ZnCl_4]^{2-}$, which mirrors the leaving-group ability within the halide series and is opposite to their nucleophilic character. Either of these scenarios rationalizes the formation of the chiral piperazine as a racemate despite starting from an enantiomerically pure aziridine. This, in turn, implies that the most favorable pathways are those indicated in Scheme 2.2.3 **c** as Path A or Path B, both of which lead predominantly to *meso* - **P2b**. At the current stage, the available data do not allow a clear distinction to be made between these two mechanistic hypotheses.

Because monitoring the reaction in situ was not feasible under microwave heating, I instead ran a series of reactions under identical conditions, quenching them at different times to determine the aziridine conversion. Although experimental limitations prevented drawing a definitive correlation, aziridine conversion over the first 10 minutes of reaction could be reasonably fitted to a second-order dependence, which is in line with the proposed mechanism. It is noteworthy that acceptable fits could also be obtained by assuming even higher-order dependence on aziridine concentration, a behavior that may be attributed to the partial formation of oligomeric and polymeric by-products.

Mechanism

d) Competing S_N1 pathway

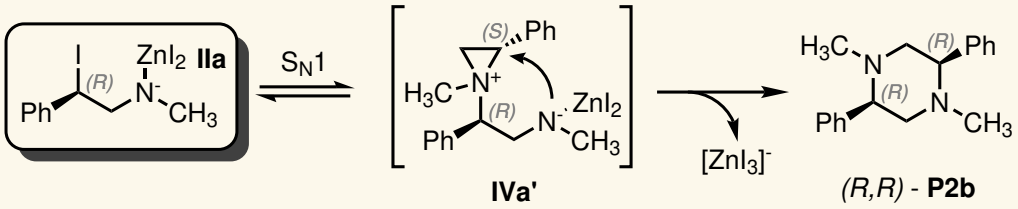

e) Racemization

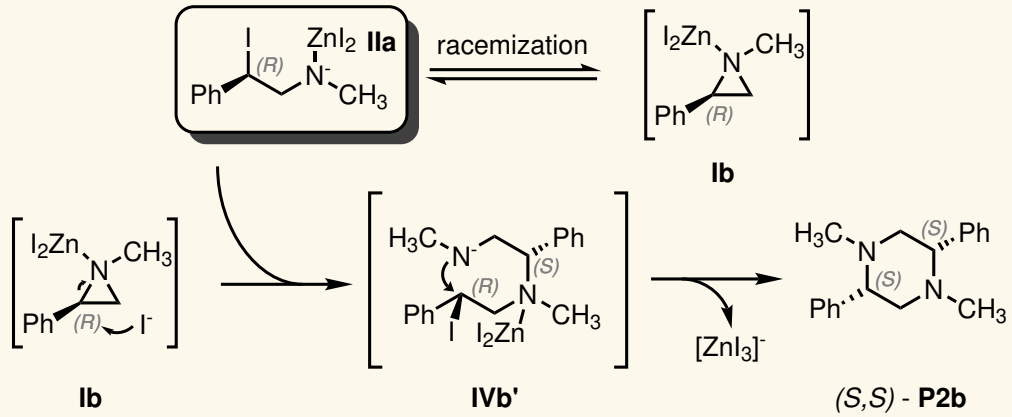

Scheme 2.2.4: *Proposed mechanism for the aziridine dimerization to piperazines catalyzed by* ***M1c*** *- S_N1 and racemization pathways.*

2.2.4 Coupling of CO_2 with epoxides, catalyzed by IER-supported metallates.[97]

Aziridines' ring strain endows them with a remarkable reactivity, which translates into an exceptional synthetic versatility and renders them excellent building blocks for a plethora of applications. In the previous section it was shown how, with a simple change in reaction conditions, aziridines can exhibit two divergent reactivities. However, their limited commercial availability and synthetic accessibility limits the applicability of the process to laboratory synthesis and small scale production.

In contrast, another class of three-membered eterocycles is highly available in commerce and is part of several important industrial processes: epoxides. Indeed, among the non-reductive processes of CO_2 utilization, its coupling with epoxides to form either cyclic carbonates or polycarbonates is one of the few that saw industrial application.[98,99]

In this context, my research group already developed several catalytic systems that catalyzed the formation of cyclic carbonates through the CO_2 coupling to epox-

ides, ranging from Pyclen zinc complexes,[100] to tetrahaloferrates,[93] to ammonium tetrahalozincates.[66] Thus, the development of an IER-supported heterogeneous system seemed the natural evolution of these studies.

To evaluate the catalytic cycloaddition of CO_2 to epoxides, again, I implemented a Design of Experiment (DoE) strategy. Because there were many experimental variables to consider (catalyst type, catalyst loading, reaction time, substrate, pressure, and temperature) the optimization study was organized into two distinct phases.

In the first phase, a screening step was carried out to simplify the system by reducing the number of variables. This involved discarding those factors that appeared to have little influence and narrowing the levels of discrete variables. For instance, catalysts or substrates that consistently performed poorly across the tested conditions were identified and removed from subsequent experiments.

With this streamlined set of variables, the second phase focused on optimization. Here, I aimed to determine the best reaction conditions within the reduced experimental space and to construct a statistical model capable of reliably describing the system's reactivity under a range of conditions. This two-step strategy not only allows a thorough exploration of the experimental space, but also enables the model to propose multiple optimized sets of conditions adapted to specific user priorities, such as minimizing pressure or temperature, adjusting catalyst loading, or tuning other parameters.

Screening phase. Drawing on prior experience, I already knew with reasonable confidence that this catalytic system is highly sensitive to pressure and temperature.[93] With this notion in mind, CO_2 pressure and temperature were initially fixed at $p = 1$ MPa and $T = 100$ °C, and I then focused on evaluating the influence of the remaining variables using a factorial split-plot D-optimal design.[101]

As already stated, the screening aimed to determine which factors significantly affected the reaction yield. Four different resins were treated as a single factor with four levels. In addition, I selected three substrates: propylene oxide (**S2a**), styrene oxide (**S2b**), and cyclohexene oxide (**S2c**). Propylene oxide and styrene oxide served as representative terminal epoxides (aliphatic in the case of **S2a** and aromatic in the case of **S2b**) while cyclohexene oxide was included to investigate the behavior of internal epoxides. Its known propensity to form polymerization products was also viewed as an opportunity to generate possible CO_2 copolymers.[102]

Two further factors were introduced into the design: catalyst loading (ranging from 1 to 20 mg of catalyst per mmol of substrate) and reaction time (from 1 to 16 h). Because all experiments were carried out in a single stainless-steel autoclave, simultaneous runs were necessarily subject to practical restrictions. In particular, the duration of an experiment could not be independently adjusted for each sample within the same run, making time a hard-to-change (HTC) factor. For this reason, a split-plot design was employed: experiments were organized into batches, each

batch corresponding to a fixed level of the HTC factor, while other variables (catalyst type, catalyst loading, and substrate) were varied within each batch.

For the screening itself, a factorial design was selected. A fully randomized full factorial configuration would have required 48 runs ($4^1 \cdot 3^1 \cdot 2^2$). Instead, I adopted a fractional factorial design based on D-optimality, which reduced the total number of runs to 34, arranged in only 8 batches. The complete set of experiments and the corresponding results are provided in Table 6.18 of Chapter 6.

The experiment was initially planned to achieve statistical significance for all factors and their interactions. To prevent overfitting and to obtain a more realistic representation of the reactivity, certain factors were deliberately excluded from the final fit. The model parameters were selected using a simple backwards-elimination algorithm: starting from the full two-factor interaction model, terms with p-values[103] greater than 0.1 were sequentially removed. The final set of parameters is reported in Table 6.19, while the corresponding analysis of variance is summarized in Table 6.20.

Although reaction time did not emerge as a particularly strong parameter, its p-value was close to the 0.05 threshold; for this reason, it was retained in the model and used for the optimization design. A graphical representation of the regression analysis is provided in Figure 2.7, which allows rapid identification of the most influential factors on the yield. In this visualization, the D[1] factor stands out as especially critical, exhibiting the largest coefficient after the intercept. This outcome suggests that styrene oxide and propylene oxide are both far more reactive than cyclohexene oxide. The latter showed very low reactivity with all the catalysts tested, and in most experiments it did not afford the desired product at all.

The screening also revealed that A26 resins performed best, outperforming IRA-400 resins. In addition, Figure 2.8 shows that zinc-based catalysts consistently yielded higher yields than their ferric analogs. Nevertheless, given the high abundance of iron and its promising behavior in combination with the A26 resin, I chose to further explore its catalytic performance in the subsequent optimization stage. Both reaction time and catalyst loading were confirmed as highly influential variables; in particular, a higher catalyst loading was required to obtain satisfactory yields, as decreasing it to 1 mg/mL led to a pronounced drop in performance. Consequently, I proceeded to optimize the reaction using propylene oxide and styrene oxide, with catalysts **R1d** and **R2d**.

Optimization phase. The aim of the optimization experiment is to determine the most favorable reaction conditions by constructing and analyzing a detailed reactivity model within a predefined experimental space. By probing the relevant variables and then refining this model, the most suitable conditions can be found. This approach enables the user to maximize yield while deciding which parameters to minimize or constrain, assigning each a specific level of priority. In addition, the use of DoE reduces the risk of exploring only a small portion of the experimental space;

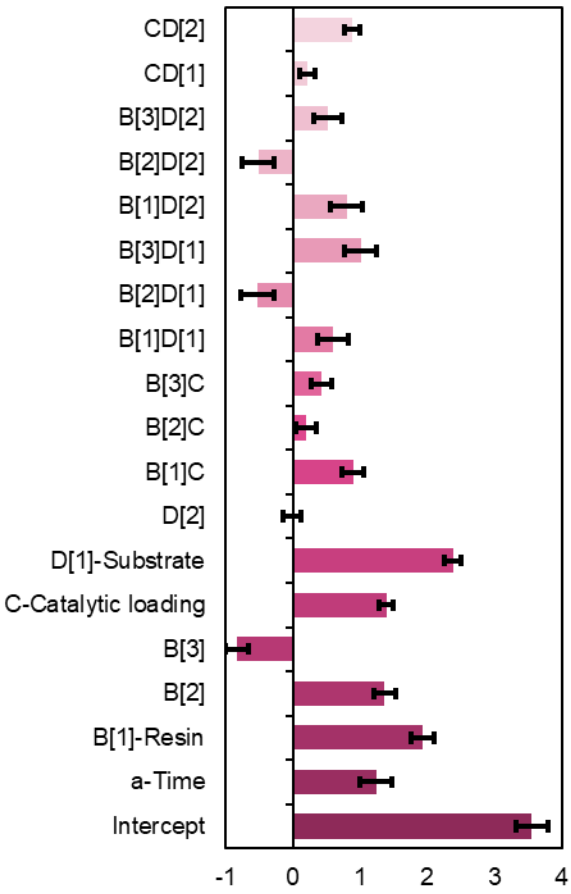

Figure 2.7: *Graphical depiction of the model's coefficient estimates for the screening experiment. Factors are coded, meaning levels are coded as -1/+1 and not as experimental values. The intercept is omitted for better readability.*

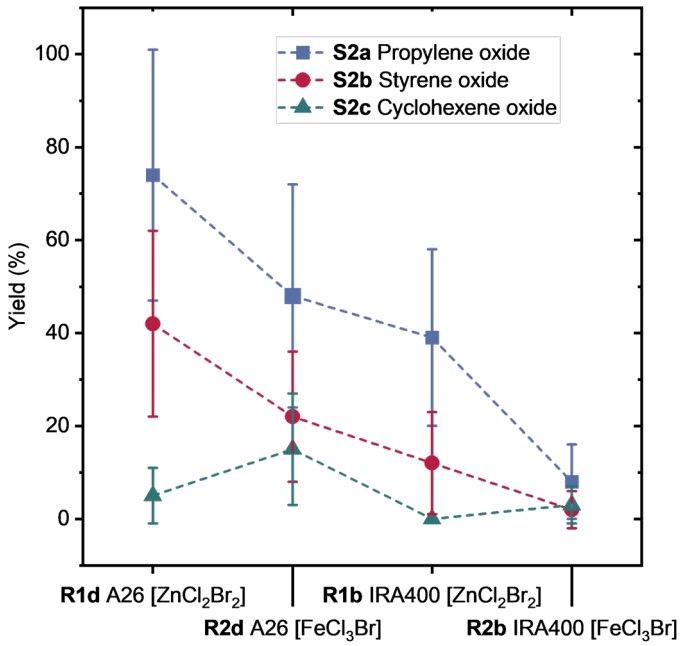

Figure 2.8: *Interaction between catalyst and substrate. The error bars of some points are truncated due to an error (theoretical yield < 0).*

through response surface methods, any non-linearities in the system's response are taken into account.

In this phase, CO_2 pressure (0.2-2.0 MPa), temperature (50-100 °C), and reaction time (0-16 h) were treated as hard-to-change variables. As model substrates, propylene oxide (**S2a**) and styrene oxide (**S2b**) were examined, using catalysts **R2d** and **R1d**, while varying the catalyst loading from 5 to 30 mg per mmol of substrate. Based on these factors, I set up a split-plot I-optimal response surface design. The model was constructed so that all two-factor interactions and the quadratic terms would be statistically significant. This approach yielded a design consisting of 32 unique experiments arranged in 13 batches. In addition, 4 further runs were carried out as replicates to verify selected results (reported in Chapter 6, Table 6.21).

In analogy to the screening experiment, the parameters of the model were selected with great care, with the aim of limiting overfitting and retaining only statistically significant terms. The same selection algorithm used in the screening phase was applied here as well; in this case, however, no parameter with a p-value < 0.05 was obtained. The final set of parameters, together with their coefficients and analysis of variance, is reported in Tables 6.22 and 6.23, and a graphical summary of the coefficients is presented in Figure 2.9.

Figure 2.9 clearly shows that the squared pressure term has the largest coefficient in absolute value. This feature mirrors the sharp rise in reactivity observed as the system runs at increasing pressures (up to about 0.8-1.2 MPa), followed by diminishing returns when pressures above roughly 1.4 MPa are employed. Overall, the model captures the behavior of the system quite accurately; nevertheless, the

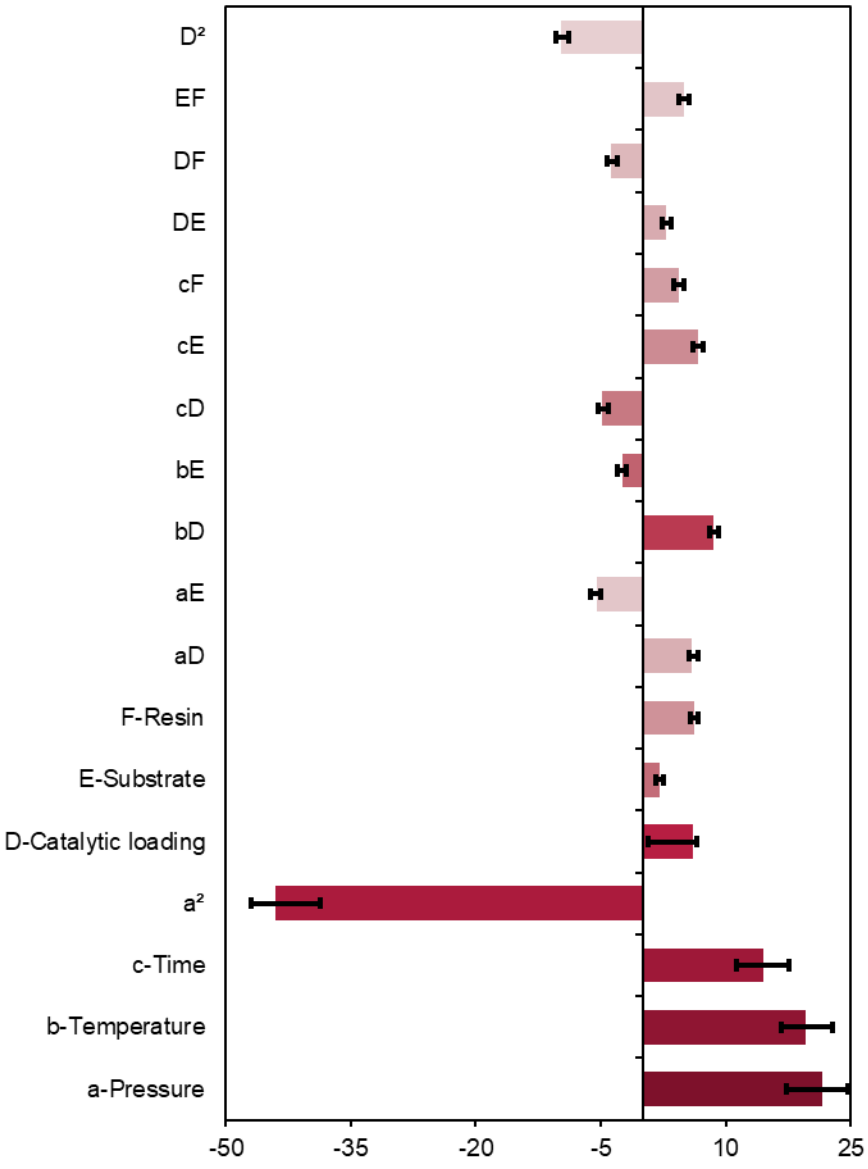

Figure 2.9: *Graphical depiction of the model's coefficient estimates for the optimization experiment. Factors are coded, meaning levels are coded as -1/+1 and not as experimental values. The intercept is omitted for better readability.*

large negative coefficient associated with the a^2 term leads to an underestimation of the yield in the high-pressure region.

Both propylene oxide (**S2a**) and styrene oxide (**S2b**) require sufficiently high pressures to achieve efficient conversion. This requirement is especially pronounced for **S2a**, which exhibits an optimal pressure of around 1.4 MPa when all other factors are kept at their center point. Styrene oxide (**S2b**), by contrast, is converted more readily at comparatively lower pressures. As previously discussed, the extent of activity loss at elevated pressures is probably overemphasized by the model. However, given the very low p-value (0.0018), the a^2 term remains statistically significant and essential for an accurate description of how pressure influences the system.

In the explored temperature range (up to 100 °C), higher temperatures proved advantageous in every case. Under the more forcing conditions, **S2a** consistently outperformed **S2b**. For styrene oxide, the zinc-based resin **R1d** showed superior activity at all reaction times. In contrast, with propylene oxide, the iron-based resin **R2d** initially provided a faster reaction rate and better performance at shorter reaction times, although **R1d** exceeded **R2d** when the reaction was allowed to proceed longer. This difference likely originates from distinct mechanistic pathways, a hypothesis that still requires detailed verification. Overall, while the zinc-based resin is more efficient with **S2b**, A26 [$FeCl_3Br$] emerges as a promising option for propylene epoxide and other terminal alkyl epoxides. It is also generally recognized that styrene oxide requires longer reaction times than propylene oxide.[104]

Both substrates benefit from increased catalyst loading, though a slight loss of selectivity is sometimes observed at higher catalyst amounts. As illustrated for **S2b** in Figure 2.10, the response surface shows a local maximum. A similar pattern is seen for propylene oxide, **S2a**. This shape of the regression surface defines a finite region within the experimental domain where yield optimization can be refined further.

Direct comparison with homogeneous systems based on ammonium zincates[66] and ferrates[93] is not straightforward. However, the optimization data indicate that the polystyrene matrix does more than simply act as a support. A synergistic effect in the activation of CO_2 is apparent, particularly with iron salts, where higher yields are reached at lower metal loadings under otherwise comparable conditions.

On this basis, the final optimization was conducted within the following limits: pressure was maintained in the original interval (0.2-2.0 MPa) and temperature in the range of 50-100 °C. The reaction time was capped at 8 hours. Catalyst loading for styrene oxide **S2b** was kept at 5-30 mg/mmol, whereas for propylene oxide **S2a** it was restricted to 5-20 mg/mmol. Since **R1d** emerged as the most generally effective catalyst, it was selected to derive the optimized conditions for each substrate. The search for optimal parameters was carried out using a minimum yield target of 90%. These conditions, together with the corresponding experimental data, are summarized in Table 2.12. To assess the robustness of the model, several valida-

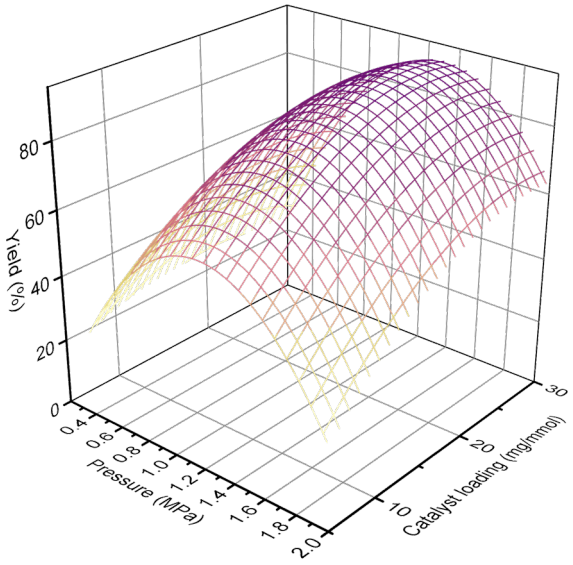

Figure 2.10: *Surface plot of the predicted yield, interaction between catalytic loading and pressure. Yield is represented both as an axis of the graph and as a color of the surface. Conditions: T = 100 °C, t = 2 h, substrate:* ***S2b****, catalyst:* ***R1d****.*

tion experiments were performed, and their outcomes are reported in Table 6.24 for substrate **S2a** and Table 6.25 for substrate **S2b**.

Table 2.12: *Optimized conditions employing* ***R1d*** *as the catalyst and comparison between experimental and model yields.*

Substrate	p (MPa)	T (°C)	t (h)	Catalyst loading (mg/mmol)	Model yield (%)	Experimental yield (%)
S2a	1.35	97.8	6.7(2)[a]	17.5 (2.0 mol%)[b]	93.3	96.3[a]
S2b	1.23	94.1	6.4	21.7 (2.5 mol%)[b]	97.9	>99

[a]The desired yield was obtained already in 2 hours in the scale-up experiments. [b]Estimated from SEM-EDS surface measurements.

Scale up, recycling tests and catalyst stability. To examine the scalability of the process, the reaction was carried out on propylene oxide using a 5 g scale. Under the optimized conditions, equivalent results were already achieved within two hours, so the reaction time was shortened to 2 h. As summarized in Table 3, the catalyst was then subjected to five consecutive runs to evaluate its reusability. It could be efficiently reused for four cycles following the initial run, whereas a clear decline in performance was observed in the fifth cycle.

After the last catalytic cycle, the composition of the spent catalyst was further examined by SEM-EDS. Relative to the starting material, a lower zinc content was detected. The decline in catalytic activity is most likely attributable to passivation

Table 2.13: *Catalyst recycling.*[a]

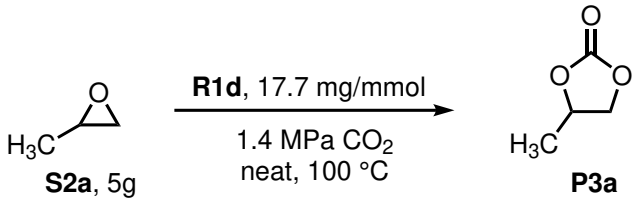

N° recycle	Yield (%)
-	96.3
1	98.0
2	94.1
3	94.9
4	92.9
5	46.7

[a] All reactions were carried out using the **R1d** resin as the catalyst, at 100 °C, 1.4 MPa of CO_2 pressure, for 2 hours and on 5 g of substrate (86 mmol).

of the resin surface through deposition of carbonaceous species.

Substrates scope. After completing the optimization, I moved on to investigate the reaction scope, the results of which are reported in Table 4. In line with expectations, terminal alkyl epoxides emerged as the most suitable substrates. Epichlorohydrin (**S2d**) and butylene oxide (**S2e**), in particular, afforded the corresponding products in almost quantitative yields. By contrast, 1,2-epoxyhexane (**S2f**) showed a significantly lower reactivity, providing only 66% of the desired product (NMR yield), which differs from the performance previously observed for ammonium zincates in homogeneous conditions.[66]

A set of five glycidyl ethers (**S2g-k**) was also examined. Within this series, the *O*-phenyl-substituted derivative **S2h** outperformed the *O*-allyl- and *O*-benzyl-substituted analogues **S2g** and **S2j**. The diglycidyl ether **S2k** gave particularly noteworthy results; this substrate is relevant as a monomer precursor for epoxy thermosets and NIPUs (non-isocyanate polyurethanes).[105] Introduction of an *ortho*-substituted aryl ring, as in **S2i**, led to diminished reactivity, suggesting that the ether moiety may play a significant role in the reaction mechanism for this type of substrate.

In contrast, internal epoxides proved to be largely unreactive. As already mentioned, cyclohexene oxide (**S2c**) behaved poorly under these conditions, and substrate **S2l** failed to undergo reaction at the internal epoxide unit; the only product detected was the terminal cyclic carbonate. Similarly, the 1,1-disubstituted epoxide **S2m** was found to be completely nonreactive.

Whenever the yields were sufficiently high, the corresponding products were obtained in pure form simply by recrystallization.

Table 2.14: *Substrate scope.*[a]

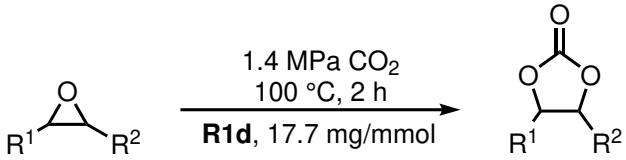

Subs.	Prod.	Scheme	Yield (%)	Subs.	Prod.	Scheme	Yield (%)
S2c	**P3c**	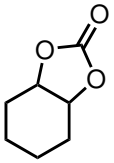	22.9 (GC)[b]	**S2d**	**P3d**	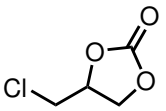	>99 (isolated)
S2e	**P3e**	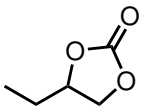	95.5 (isolated)	**S2f**	**P3f**	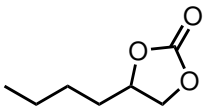	66 (NMR)
S2g	**P3g**	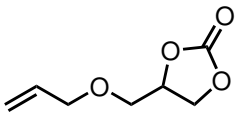	53.8 (NMR)	**S2h**	**P3h**	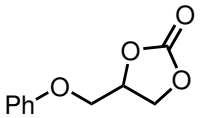	98.7 (isolated)
S2i	**P3i**	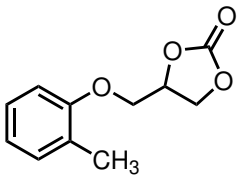	51.3 (isolated)	**S2j**	**P3j**	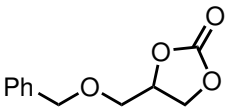	66.8 (NMR)
S2l	**P3l**	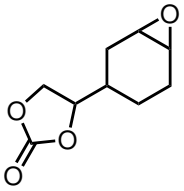	9.7 (NMR)	**S2m**	**P3m**	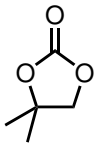	n.d. (NMR)
S2k	**P3k**	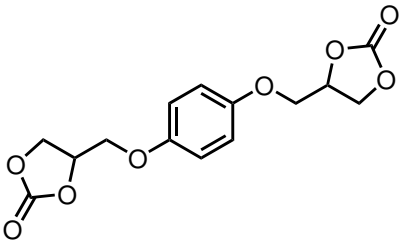	85.7 (NMR) 83.2 (isolated)				

[a]General reaction conditions: 100 °C, 1.4 MPa CO_2, 17.7 mg/mmol **R1d**. The reactions were carried out for 2 h in neat conditions. In the case of solid substrates, propylene carbonate was used as a solvent. When possible, yields were obtained from the mass of the isolated products; otherwise, they were calculated from ^{1}H-NMR analysis, using mesitylene as an internal standard [b]Reaction conditions: 100 °C, 1.0 MPa CO_2, 20 mg/mmol **R2d**, 16 hours.

2.2.5 Coupling of CO_2 with epoxides, catalyzed by Pytren zinc complexes.

Functionalization of ion-exchange resins with tetrahalometallates demonstrated that the coupling of CO_2 with aziridines and epoxides can proceed with excellent results and under mild conditions, even when using easily prepared heterogeneous catalysts. After obtaining these results under heterogeneous conditions, my focus was shifted toward homogeneous systems. My research group had already developed several efficient catalysts for this transformation, particularly based on ammonium metallates.[65,66,93,106] Notably, in 2021 we first entered the field of non-reductive CO_2 utilization through our work on zinc-Pyclen complexes catalyzing the formation of cyclic carbonates.[100] Although the synthesis of macrocyclic ligands is decidedly more demanding than the preparation of ammonium tetrahalometallates or their immobilization on ion-exchange resins, we maintain that the rational design of *tailored* homogeneous catalysts remains highly relevant for processes at any scale.[107,108] With this idea in mind, we we decided to improve upon this concept by introducing a new family of catalysts for the coupling of CO_2 with epoxides. The pyclen framework was modified through the introduction of a pendant arm bearing a primary amine donor, thus generating a *lariat* ligand. We reasoned that embedding this primary amine in the ligand architecture should further lower the energetic requirements of the reaction, in light of the strong affinity of amines for carbon dioxide.[109] In such a configuration, an *ambiguously* coordinated amine could assist in shuttling CO_2 to the metal center, thus assisting its activation.

Synthesis of ligands L1 and L2, preparation of complexes C1a and C1b. The first difficulty encountered was the synthesis of the ligand itself which, although closely related to the preparation of pyclen, nonetheless presented several challenges. The inspiration was drawn from the work of the García-España group,[110] which over recent decades has reported a large number of pyclen-derived lariat ligands for diverse applications. While the contribution of the group are certainly significant, in our hands we found some difficulties in the use of their reported methodologies and consequently we decided to optimize the synthetic protocol.

Azamacrocycles are frequently prepared under Richman-Atkins conditions,[111] which consist in reacting tosyl-protected polyamines with chains bearing suitable terminal leaving groups in dilute solutions and in the presence of heterogeneous bases. Accordingly, the first step in the synthesis of Pytren was the protection of tren (tris(2-aminoethyl)amine). Tosyl protection of polyamines is typically carried out in dichloromethane, by reacting the amine with tosyl chloride (sparingly soluble in DCM) in the presence of triethylamine as base. In the specific case of tren, this procedure gave unsatisfactory results (incomplete conversion, formation of mono- and bis-tosylated species, and several unidentified side products). Significantly improved results were obtained by switching to a biphasic Et_2O/H_2O solvent system (Scheme 2.2.5). Under these conditions, tosyl chloride is fully soluble in diethyl

ether, tren dissolves well in water, and the protected product (**1**) precipitates as a white solid with good purity and yield. It was also found to be essential to carefully remove any residual triethylamine in order to avoid the presence of a homogeneous base in the subsequent step.

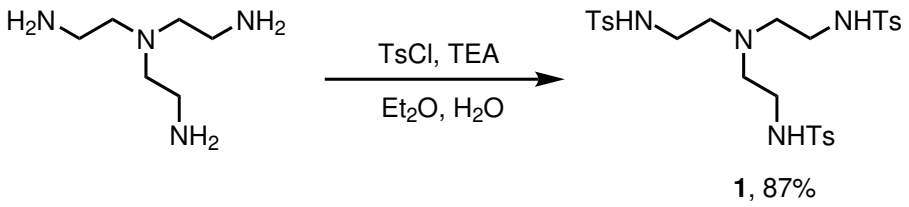

1, 87%

Scheme 2.2.5: *Synthesis of the tritosylamide of tren,* ***1***

Then, the macrocycle was synthesized under Richman-Atkins conditions. Tosyl-protected tren (**1**) was reacted with mesylated 2,6-bismethanolpyridine in dry acetonitrile, using potassium carbonate as base (Scheme 2.2.6). In contrast to pyclen, which typically forms within three hours, this transformation required an extended reaction time of 24 hours. Moreover, the presence of an additional nucleophilic site led to the formation of undesired oligomeric polymerization by-products. These, together with most of the potassium carbonate, were removed at the end of the reaction by simple filtration. Subsequent extraction from water with dichloromethane afforded the product in sufficient purity to proceed to the deprotection step.

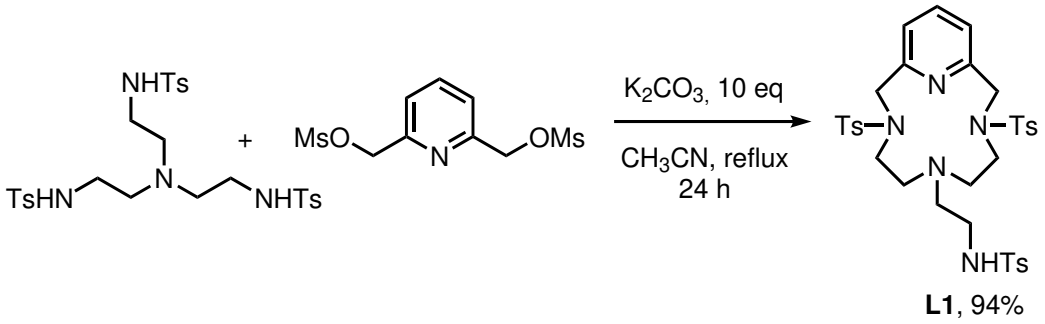

L1, 94%

Scheme 2.2.6: *Synthesis of tosyl protected pytren* (***L1***).

Although most literature protocols describe tosyl deprotection of pyclen-derived macrocycles using a phenol/HBr/acetic acid mixture, in this work the acid hydrolysis was optimized employing neat sulfuric acid, a simpler yet efficient deprotection method previously established for pyclen. The procedure is extremely straightforward: the tosylated intermediate is dissolved in concentrated sulfuric acid and heated under microwave irradiation at 120 °C. In contrast to pyclen, for which an optimal yield is obtained after 35 minutes, significantly longer reaction times are required, with full deprotection reached only after two hours.

The isolation of the final ligand is also simple. First, the hydrogen sulfate salt of the ligand is precipitated by cooling the reaction mixture in an ice bath and slowly adding diethyl ether dropwise. When no further solid forms, the ether/sulfuric acid

phase is discarded and the precipitate is dissolved in water. An excess of sodium hydroxide pellets is then added to the aqueous solution (adjusting the pH to 14), and the free base is extracted repeatedly with dichloromethane; TLC can be used to monitor the presence of product in each organic fraction. For pyclen, these operations typically are sufficient to obtain the pure compound. In the case of pytren, however, an additional acid-base purification step is needed: the crude free base is dissolved in an ether/methanol mixture and treated with ethereal HCl or gaseous HCl to form the corresponding hydrochloride salt, which is collected by filtration and subsequently basified as described above.

The free base is obtained as an off-white solid. Removal of the final traces of solvent is particularly challenging, often requiring several days under reduced pressure. Furthermore, the free base is highly sensitive to atmospheric CO_2 and must therefore be manipulated under anaerobic conditions. Although this sensitivity complicates both the synthesis and handling of the ligand, it was considered an encouraging feature in view of potential CO_2 activation.

Once the ligand synthesis had been optimized, the synthesis of the zinc complexes was undertaken (Scheme 2.2.7). Whereas the zinc chloride complex **C1a** was readily obtained from the hydrochloride salt of pytren, which can be easily isolated, preparation of the zinc bromide complex **C1b** required isolation of the free base in order to prevent the formation of mixed-halide complexes.

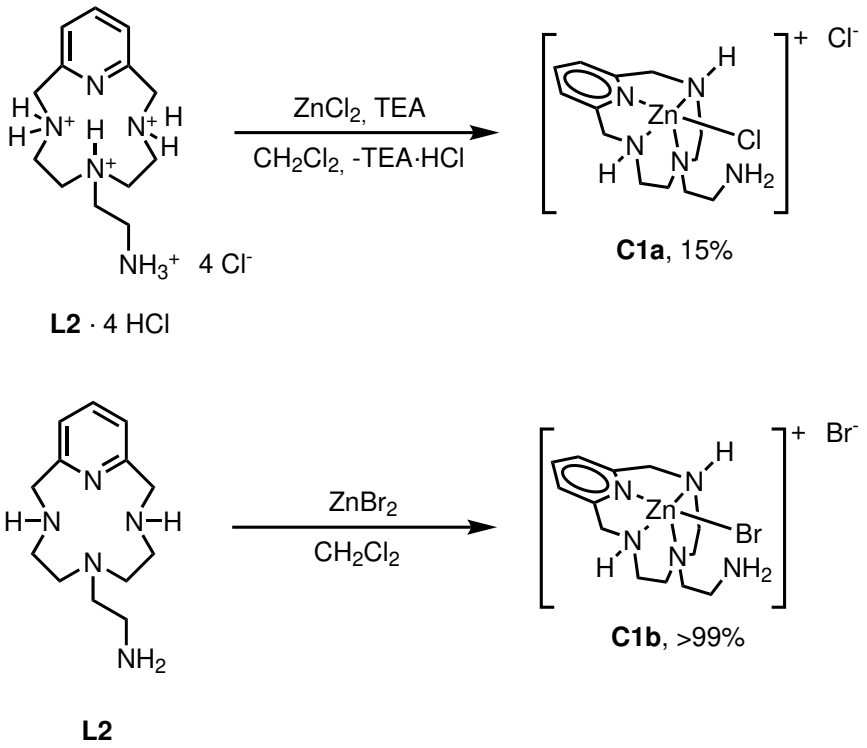

Scheme 2.2.7: *Synthesis of complexes **C1a** and **C1b**.*

The choice of DCM as the reaction medium was particularly suitable for complex **C1a**, as any excess unreacted ligand remained dissolved and could be easily

removed during filtration. Both complexes, however, displayed considerable solubility in DCM, so this approach did not allow for quantitative recovery of the products. For **C1b**, a strictly stoichiometric procedure was therefore employed, and the complex was isolated by precipitation with diethyl ether at the end of the reaction. A more in-depth description of these procedures, along with the analytical data of complexes **C1a-b** , is detailed in the experimental section (Chapter 6).

Comparison of Pyclen and Pytren zinc complexes in CO_2 coupling to epoxides. Once the complexes had been isolated with good reproducibility, the next step was to evaluate their catalytic activity in the cycloaddition of CO_2 to styrene oxide. In a first instance, the catalytic performance of the zinc pytren complexes was compared with that of the zinc pyclen analogues (Table 2.15).

Table 2.15: *Catalyst recycling.*[a]

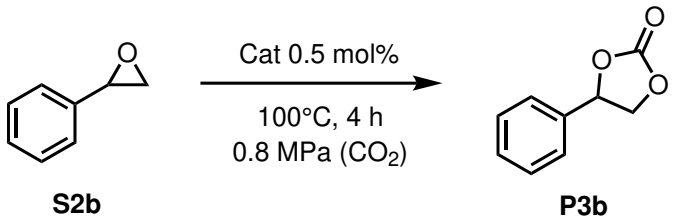

Catalyst	Conversion (%)[a]	Yield (%)[a]	Selectivity (%)
[ZnPytrenCl]Cl (**C1a**)	35	6	16
[ZnPytrenBr]Br (**C1b**)	69	40	58
[ZnPcLH$_3$Cl]Cl	17	2	9
[ZnPcLH$_3$Br]Br	33	32	97

[a]Conversion and yield were determined by GC-FID. Reaction conditions: catalyst loading, 0.5 mol%; temperature, 100 °C; reaction time, 4 h; CO_2 pressure, 0.8 MPa.

As anticipated, the bromide complexes outperformed the chlorides, and an overall enhancement in activity was observed for the zinc pytren complexes relative to their pyclen analogues. At 100 °C, with a catalyst loading of 0.5 mol% and a CO_2 pressure of 0.8 MPa, **C1b** afforded a 69% conversion of styrene oxide with a 58% selectivity. In comparison with the pyclen complex, the conversion was approximately doubled ([ZnPcLH$_3$Br]Br: 33%), although the selectivity was substantially reduced ([ZnPcLH$_3$Br]Br: 97%).

In my view, however, these findings were nevertheless encouraging and corroborated that the pendant arm could promote CO_2 activation. To achieve a more competitive selectivity, the optimization of the system was therefore undertaken.

Optimization. The reaction conditions for both catalysts were optimized (Tables 2.16 and 2.17). The optimization was carried out by varying the temperature between 60 and 120 °C, the pressure between 0 and 1.2 MPa, and the reaction time

from 2 to 16 hours. The catalyst loading was investigated in the range of 0.1-1 mol%. The following effects were observed:

Temperature: analysis of the data from the different reactions indicated that higher temperatures were essential to achieve good conversions and yields. The optimal temperature corresponded to the upper limit of the experimental range (120 °C), whereas at lower temperatures (60 °C and 90 °C) the reaction proceeded with poor performance.

Pressure: it was observed that lower pressures resulted in decreased selectivity, as similar conversions were obtained but with lower yields. The best selectivity was achieved at 0.8 MPa.

Time and Catalyst Loading: as expected, the reaction time was strongly dependent on the catalyst loading. Using 1 mol% catalyst allowed good yields to be obtained even after only two hours. Conversely, when the catalyst loading was reduced to 0.1 mol%, a reaction time of 16 hours was required to reach similarly good yields.

Table 2.16: *Screening of reaction conditions for catalyst **C1b**.*

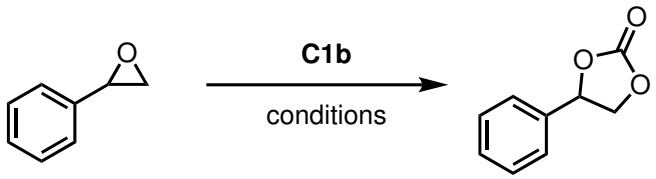

S2b **P3b**

Entry	Temperature (°C)	Pressure (MPa)	Time (h)	Catalyst loading (mol%)	Conversion (%)[a]	Yield (%)[a]
1	120	0	16	0.1	60	22
2		0.4	16	0.1	59	46
3		0.4	2	1	50	37
4		0.8	16	0.1	95	88
5		1.2	16	0.1	98	87
6		1.2	2	0.1	20	17
7		1.2	16	1	99	91
8	60	1.2	16	0.1	9	3
9		1.2	2	1	0	0
10	90	0.6	9	0.5	13	12

[a]Conversion and yield were determined by GC-FID. Reaction conditions: catalyst loading, 0.1-1 mol%; temperature, 60-120 °C; reaction time, 2-16 h; CO_2 pressure, 0-1.2 MPa.

While **C1b** was clearly superior to **C1a**, no distinct benefit could be established in comparison with pyclen complexes. The catalyst is undoubtedly more active at lower pressures, but it exhibits lower selectivity across virtually the entire temperature range. Nonetheless, the higher activity of the catalyst allowed its loading to be reduced to 0.1 mol%. This reduction rendered the catalyst competitive with its predecessor, particularly when the increased synthetic complexity is taken into ac-

Table 2.17: *Screening of reaction conditions for catalyst **C1a**.*

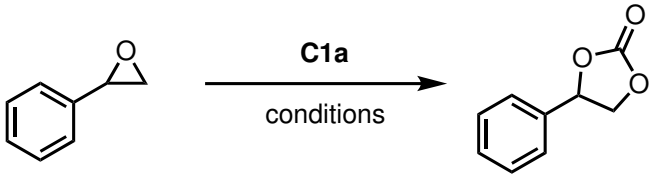

S2b **P3b**

Entry	Temperature (°C)	Pressure (MPa)	Time (h)	Catalyst loading (mol%)	Conversion (%)[a]	Yield (%)[a]
1	120	1.2	16	0.1	24	2
2	60	1.2	16	0.1	2	1
3		1.2	2	1	0	0
4	90	0.6	9	0.5	0	0

[a]Conversion and yield were determined by GC-FID. Reaction conditions: catalyst loading, 0.1-1 mol%; temperature, 60-120 °C; reaction time, 2-16 h; CO_2 pressure, 0-1.2 MPa.

count. Consequently, the scope of the reaction was investigated using **C1b** as the catalyst at a loading of 0.1 mol%, with the CO_2 pressure set to a moderate 0.8 MPa and the temperature maintained at 120 °C.

Substrates scope. As anticipated, terminal epoxides generally reacted smoothly and were efficiently transformed into the corresponding carbonates in good isolated yields (**P3a**, **P3b**, **P3d**, **P3f**, **P3h**, **P3i**, **P3j**, **P3g**, and **P3r**. Particularly significant for potential applications in polycarbonate synthesis are the results obtained with the diglycidyl ethers **S2r** and a fully bio-based analogue of **S2r**, obtained from levulinic acid and not reported here due to pendant patent application, for which high yields of the corresponding carbonate were achieved. The cyclic carbonate derived from the bisphenol-based epoxide **S2r** is widely used as a precursor to industrially relevant polycarbonates.

In contrast, internal (**S2c** and **S2n**) or sterically hindered (**S2m**) epoxides required more forcing conditions and afforded only moderate to low isolated yields of the desired cyclic carbonates. When substrate **S2l**, bearing both a terminal and an internal epoxide, was subjected to milder conditions, selective conversion of the terminal epoxide was observed, although with modest yield. Under harsher conditions, complete consumption of the starting material was achieved, with the terminal carbonate as the major product, accompanied by approximately 30% of the doubly substituted carbonate. Limonene epoxide **S2o** did not undergo conversion even under severe reaction conditions, most likely due to pronounced steric hindrance.

More challenging to interpret is the complete lack of reactivity observed for substrates **S2p** and **S2q**. In the former case, it can be hypothesized that the furan moiety coordinates to the zinc Lewis acid, thereby inhibiting catalysis; in the latter case, the

low reactivity could not be satisfactorily rationalized. An overview of these results is presented in Table 2.18.

Table 2.18: *Substrate scope.*[a]

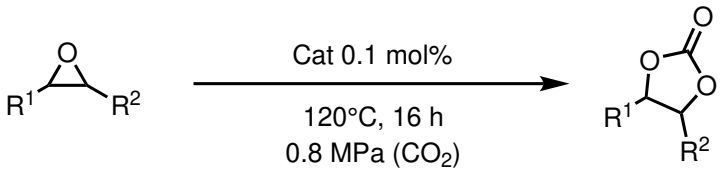

S2 **P3**

Subs.	Prod.	Scheme	Yield (%)[b]	Subs.	Prod.	Scheme	Yield (%)[b]
S2a[c]	**P3a**	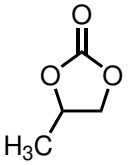	82 99[a]	**S2b**	**P3b**	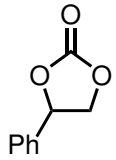	89
S2c	**P3c**	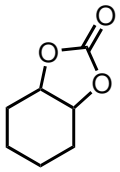	0 35[b]	**S2d**	**P3d**	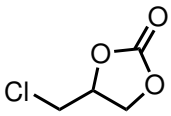	82 99[a]
S2f	**P3f**	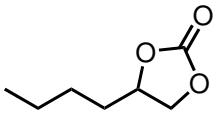	64	**S2g**	**P3g**	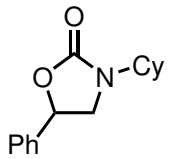	98
S2h	**P3h**	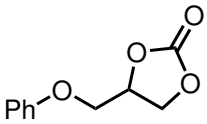	99	**S2i**	**P3i**	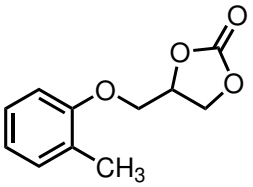	99
S2j	**P3j**	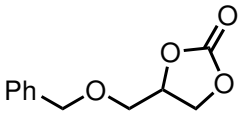	99	**S2l**	**P3l**	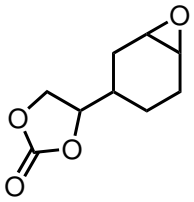	35 99[b]
S2m	**P3m**	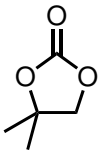	6 54[b]	**S2n**	**P3n**	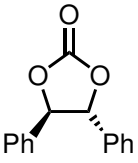	0 7[b]

Continues on next page

Table 2.18 – continued from previous page

Subs.	Prod.	Scheme	Yield (%)[b]	Subs.	Prod.	Scheme	Yield (%)[b]
S2o	**P3o**	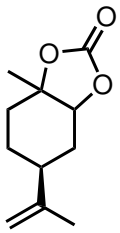	0 0[b]	**S2p**	**P3p**	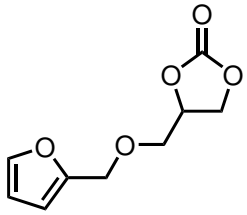	0 10[b]
S2q	**P3q**	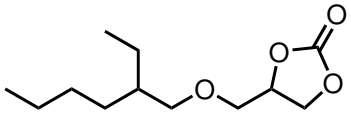	0				
S2r	**P3r**	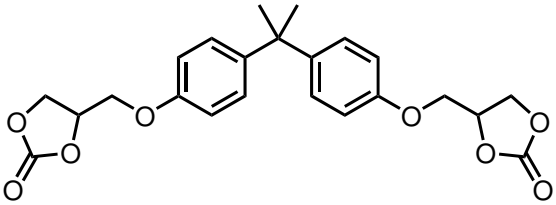	98				

[a]Propylene oxide and epichlorohydrin are volatile. The reaction was repeated without venting the autoclave at its beginning (usually done to prevent air presence during the reaction). This precaution avoided the evaporation of the starting material and improved the yield. [b]The reaction was repeated with harsher conditions: temperature, 140 °C; catalyst loading, 0.5 mol%; CO_2 pressure and reaction time were left unvaried. General reaction conditions: temperature, 120 °C; catalyst loading, 0.5 mol%; CO_2 pressure, 0.8 MPa; reaction time, 16 h. Reported data refers to isolated yields.

Catalyst turnover and control experiments. Lastly, the turnover of the catalyst was assessed over a series of three recycles under the optimized conditions to assess the catalyst's recyclability. It was observed that, after the first cycle, the TOF decreased from 56 h^{-1} to 47 h^{-1}, and by the third cycle it had declined further to 25 h^{-1}. Overall, over these cycles, the total turnover amounted to 2100, demonstrating the robustness of the catalyst. Table 2.19 gathers the recycling tests results. The yield in entry 2 is probably an outlier.

No specific explanation for the catalyst deactivation pathways was elucidated, however, given the clear robustness of the catalyst, the loss of activity can be attributed to the substantial dilution effect observed in the second and third cycles, in comparison with the first cycle, which was carried out under neat conditions.

Then, to demonstrate that the active catalytic species is, in fact, the catalyst, three control experiments were tested (Table 2.20; one without catalyst and two with the two most common impurities found in **C1b**. Satisfyingly, neither **L2** · 4 HCl nor $ZnCl_2$ were able to catalyze the reaction effectively. Although $ZnCl_2$ converted a large amount of substrate (60%), no carbonate was detected as the product, mainly

polyether impurities were found at the end of the reaction. The same was valid for **L2** · 4 HCl, but the conversion was substantially lower (20%). With no catalyst, no product other than the starting material was detected at the end of the reaction.

Table 2.19: *Catalyst recycle.*

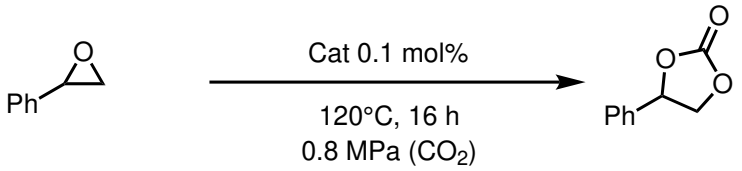

S2b **P3b**

Cycle	Conversion (%)[a]	Yield (%)[a]	Selectivity (%)
1	90	90	99
2	75	40	55
3	45	45	99

[a]Conversion and yield were determined by GC-FID. Reaction conditions: catalyst loading, 0.1 mol%; temperature, 120 °C; reaction time, 16 h; CO_2 pressure, 1.2 MPa.

Table 2.20: *Control experiments.*

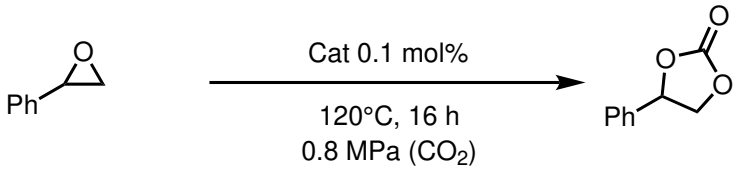

S2b **P3b**

Catalyst	Conversion (%)[a]	Yield (%)[a]	Selectivity (%)
/	26	0	0
$ZnBr_2$	60	0	0
L2 · 4 HCl	20	2	9

[a]Conversion and yield were determined by GC-FID. Reaction conditions: catalyst loading, 0.1 mol% (when possible); temperature, 120 °C; reaction time, 16 h; CO_2 pressure, 1.2 MPa.

2.3 Conclusions

In conclusion, during my doctoral studies, four projects involving zinc and iron catalysts and their reactivity with ring-strained heterocycles were carried out. In all of these cases, the catalysts acted mainly as Lewis acids, though they were fine-tuned to their specific use case. Indeed, all of the catalysts performed remarkably when compared to simple iron and zinc halides, with huge advantages in terms of air-handling and, in the case of heterogeneous catalysts, in terms of recyclability.

More specifically, tetrabutylammonium tetraiodozincate (**M1c**), along with all the other -ate complexes that were used, introduced a nucleophilic functionality that allowed more facile ring opening while still allowing the zinc center to act as

a Lewis acid. Indeed, the catalyst *pre-equilibrium* ($[ZnI_4]^{2-} \rightleftharpoons ZnI_2 + 2I^-$) produced two iodide ions that could function as nucleophiles, while simultaneously enabling ZnI_2 to serve as the Lewis acid.

The support of these catalysts on anion exchange resins made the process even more convenient, allowing catalyst recovery and easier recycling. In the case of CO_2 cycloaddition to aziridines, while recycling the catalyst was not particularly efficient, the addition of a porous support to the active metallate species revealed a synergistic effect between the catalyst and its support.

By contrast, supported tetrahalozincates were easily recycled up to 5 times in the cycloaddition of CO_2 to epoxides. Indeed, this system could represent an interesting solution to an already industrialized process because of its ease of implementation, the use of readily available materials, and efficiency.

The highest complexity was introduced with the last project. A pendant arm was introduced on one of the nitrogens of Pyclen, an already well studied macrocyclic ligand, thus producing a *lariat* aza-macrocycle. Its complexation with zinc chloride and bromide yielded two zinc complexes which were tested in the cycloaddition of CO_2 to epoxides. Although the introduction of the pendant arm did not improve the performance of this class of catalysts as hoped, nonetheless **C1b** proved to be an efficient promoter of this reaction, achieving good performance in catalyst loading as low as 0.1 mol%.

This extended work on CO_2 coupling with ring-strained heterocycles allowed me to gain in-depth knowledge about this reaction. An important lesson I have learned is that complexity does not necessarily mean better catalytic performance. In this specific case, the requirements for the reaction were a nucleophilic moiety and a Lewis-acidic site. Both ammonium and IER-supported metallates were able to efficiently satisfy these two requirements. The added complexity of a well-designed homogeneous catalyst supported by an elaborate macrocyclic ligand synthesized in several steps did not yield the expected results.

For this reason, the following chapter will first address the synthesis and characterization, and subsequently the catalytic applications, of synthetically more elaborate macrocyclic complexes in more demanding reactions, which need a more sofisticated complex dasign.

3

Macrocyclic iron complexes: synthesis, characterization, and application in oxidative reactions

3.1 Introduction

As already stated in the previous chapter, compared to lower-row elements, the metals of the first transition series are more prone to single-electron transfer processes. Although controlling the selectivity of radical processes is not straightforward, the availability of oxidation states renders first-row transition metals strong candidates for oxidative processes. In this sense, iron, endowed with rich redox chemistry and as the most abundant metal on Earth, is one of the best choices.[112] In the simplest form, ferrates(VI) ($[FeO_4]^{2-}$) are stronger oxidants than the more famous yet more hazardous permanganates, and they may serve as an environmentally friendly alternative water treatment chemical, since the byproduct of ferrate oxidation is the relatively benign iron(III).[113]

In Nature, mononuclear nonheme iron enzymes play an essential role in oxidative transformations, efficiently catalyzing a broad spectrum of chemical reactions.[114,115] The design of synthetic model complexes that emulate the strategies of Nature remains an intensely active area of research.[116–122] In both natural enzymes and their synthetic analogs, high-valent iron-oxo intermediates, such as iron(III)-superoxo, iron(III)-peroxo, iron(III)-hydroperoxo, and iron(IV)- or iron(V)-oxo species, are recognized as central intermediates.[114,123]

Iron(III)-superoxo species have been characterised as active oxidants in C–H bond activation and oxygen atom transfer (OAT) processes.[124] Their reactivity, however, tends to be confined to relatively weak, activated C–H bonds in hydrocarbons. By contrast, the role and intrinsic reactivity of nonheme iron(III)-hydroperoxo species remain under debate and continue to motivate extensive experimental and

theoretical studies.[125] Nonheme iron(IV)-oxo species, on the other hand, are well established as potent oxidants that can readily abstract hydrogen atoms in C–H bond activation reactions.[120]

In this context, a careful ligand design is absolutely crucial to control: (a) the oxidation state of the metal center in the intermediate, (b) the charge of the complex, (c) the spin state of the metal center. For instance, in C(sp^3)-H activation reactions, iron(V)-oxo intermediates were shown to be more efficient when compared to an iron(IV)-oxo intermediates.[126] This difference in reactivity is easily explained when considering the first phase of C–H oxidation (Scheme 3.1.1), which is Hydrogen Atom Transfer (HAT). In the case of iron(IV) species, after the HAT event, the iron center is reduced to a stable iron(III)-hydroxo species. Instead, iron(V) intermediates convert to highly reactive iron(IV)-hydroxo species, which can transfer their hydroxyl groups far more rapidly than iron(III) intermediates.

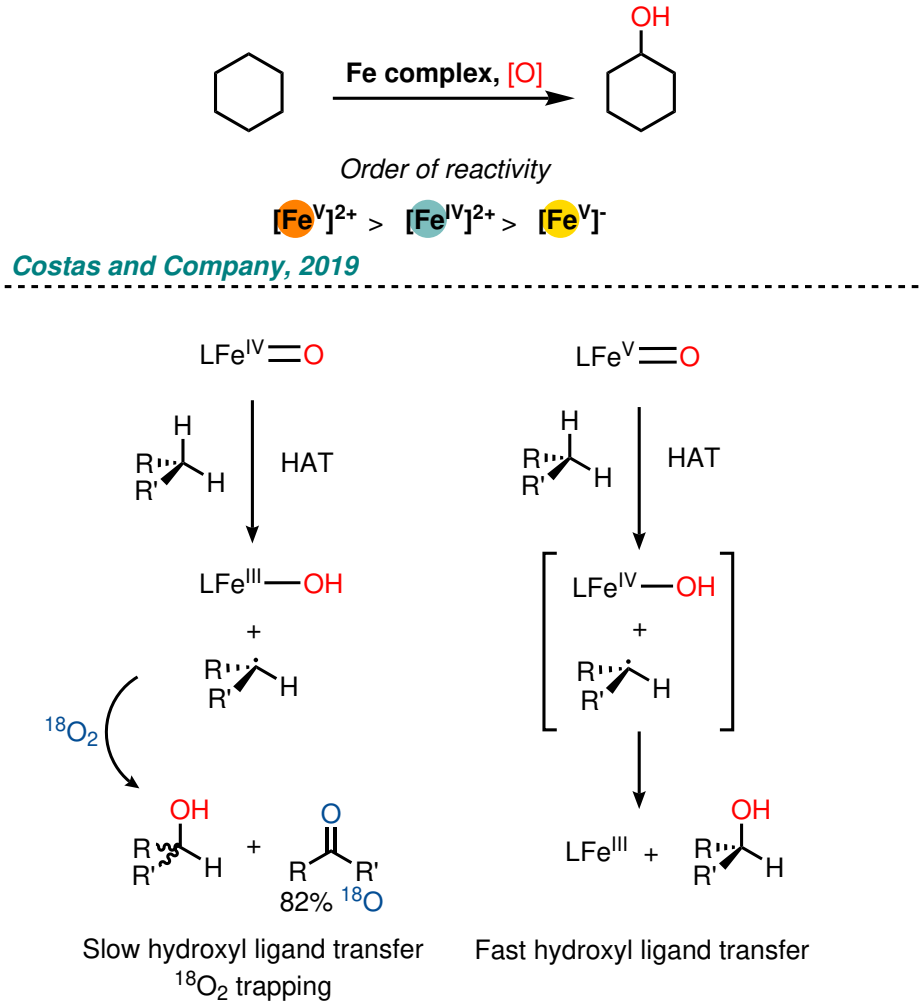

Scheme 3.1.1: *Effect of oxidation state of iron in the intermediate on C–H oxidation, in terms of reaction products selectivity and speed.*[126] *When reacted in $^{18}O_2$ atmosphere, the ketone products showed 82% ^{18}O incorporation in case Fe(IV) active species, while no isotope labelling in case of Fe(V) intermediates, indicating direct and faster Oxigen Atom Transfer (OAT) from the iron center to the carbon radical.*

The second aspect to consider–the charge of the complex–is trivial, easily explained, but often overlooked. Put simply, positively charged complexes have enhanced electrophilicity, thus being more active towards strong C–H bonds. Thus, positively charged complexes in this field are more desirable.

The third aspect (spin state) instead requires a more detailed explanation. In general, high spin states–e.g., $S = 2$ for Fe(IV) and $S = {}^3/_2$ for Fe(V)–show higher reaction rates than Fe(IV) species in the lower spin state.[127] This effect is not easy to rationalize and, in my opinion, the most convincing explanation was reported by Neese & colleagues in 2010 (Figure 3.1).[128] In this theoretical work, the authors mapped four possible C–H abstraction channels: quintet (high spin) *vertical* ($^5TS_\sigma$), quintet *horizontal* ($^5TS_\pi$), triplet *vertical* ($^3TS_\sigma$), and triplet *horizontal* ($^3TS_\pi$). The quintet σ pathway has *by far* the smallest H-abstraction energy barrier, and overall reactivity follows:

$$^5TS_\sigma >^5 TS_\pi >^3 TS_\pi >^3 TS_\sigma$$

Mechanistically, in the quintet σ-mechanism, the substrate electron transfers into the $\sigma(\text{Fe–O})^*$ antibonding orbital, and this channel prefers a nearly linear Fe–O–H geometry (a "vertical/top" approach), which simultaneously gives strong donor-acceptor overlap for the σ interaction, and low Pauli repulsion, as the approach is along the Fe–O axis.

The *vertical/top* approach is thus more efficient than the horizontal *approach*, and the energy barrier to overcome in the triplet state to achieve this interaction is way higher, to the point that $^3TS_\sigma$ is essentially non-competitive. Indeed, due to greatly reduced spin polarization in the triplet state, the $\sigma(\text{Fe–O})^*$ acceptor orbital sits much higher in energy.

Thus, low-spin complexes mostly react through a higher-barrier π pathway that forces a bent approach. This geometry comes with a higher steric/Pauli cost than the axial "σ attack", so even when $^3TS_\pi$ is feasible, it is not as fast as $^5TS_\sigma$.

These requirements dictate a thorough control of ligand design to efficiently support the metal center in its higher, more exotic oxidation states.

Macrocyclic ligands are well known to stabilize high oxidation states of iron,[129] and the stability of the complexes they form is fundamental to withstand the often harsh reaction conditions involved in oxidative processes. Moreover, a proper tuning of the donor groups and their steric hindrance is fundamental to controlling the spin state of the complex. Indeed, although the $\sigma^*_{x^2-y^2}$ orbital is not involved in the bond with the -oxo (or hydroperoxo, etc.) moiety (Figure 3.1), it is involved in the low spin-high spin transition. Thus, controlling the electronic and steric properties of the equatorial plane donors can facilitate the transition to high-spin complexes, consequently lowering the energy of the $\sigma^*_{z^2}$ orbital and allowing a more favorable $^5TS_\sigma$ approach.

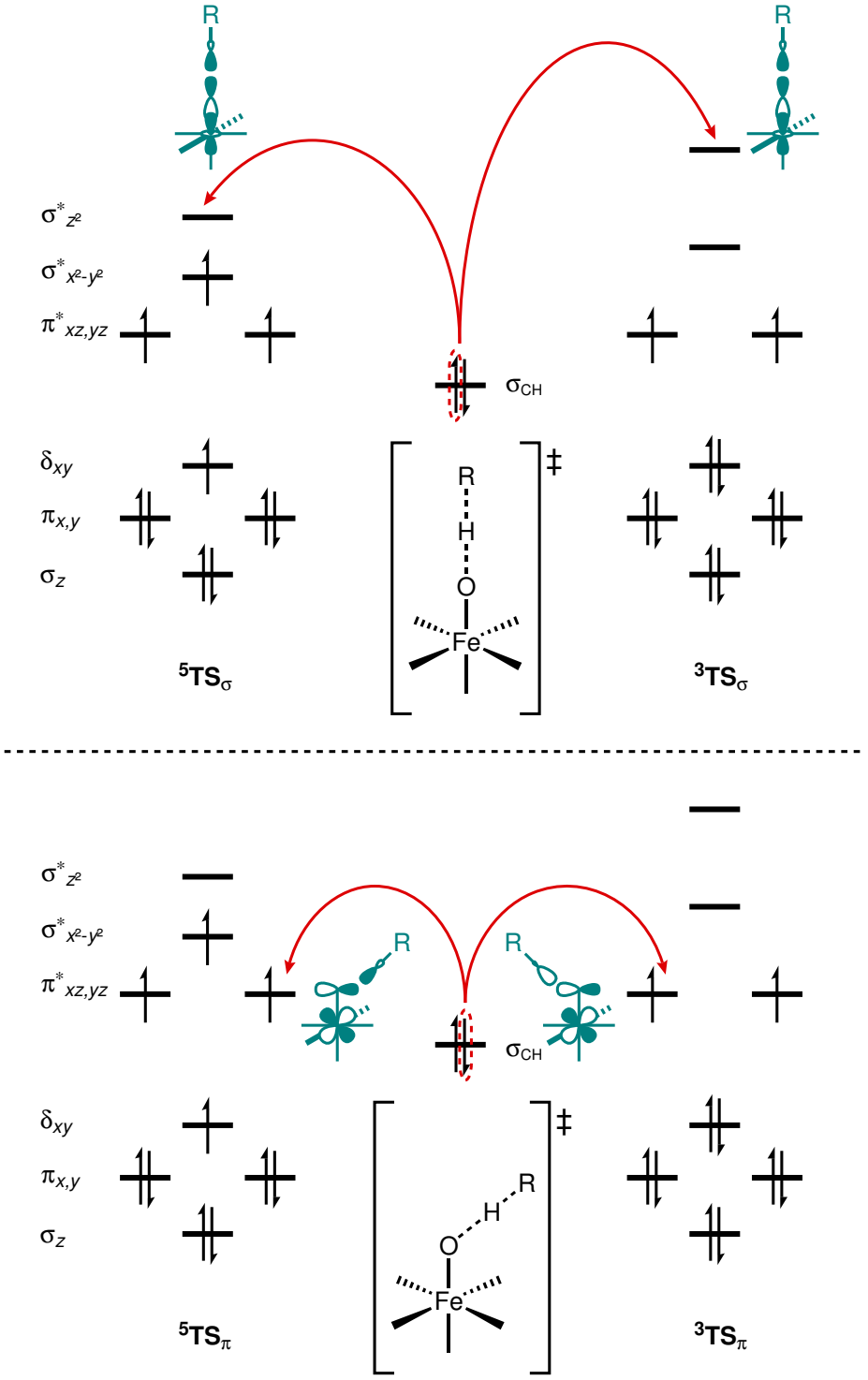

Figure 3.1: *Effect of spin state of iron in the intermediate on C–H oxidation, electron transfer MO diagrams.*[128] *This example is referred to Fe(IV) intermediates.*

Investigating the spin state and oxidation state of iron complexes: *how?* To properly study the oxidation state and the spin state of iron complexes, many analytical methods are possible. Among these, probably the most complete and preferred technique is Mössbauer spectroscopy.

3.1.1 ^{57}Fe Mössbauer spectroscopy

Iron Mössbauer spectroscopy is based on the resonant absorption of gamma rays by ^{57}Fe nuclei present in the sample. Operatively, a radioactive ^{57}Co source decays into an excited state of ^{57}Fe via electron capture: an inner-shell electron is captured by a proton, which is thereby converted into a neutron with the emission of an electron neutrino. The resulting ^{57}Fe nucleus is formed in an excited state with $I = {}^3/_2$, which relaxes to the $I = {}^1/_2$ ground state, emitting an extremely sharp, monochromatic 14.4 keV gamma ray. This radiation can then be resonantly absorbed by ^{57}Fe present in the sample, even at very low concentrations.

Because gamma rays are highly energetic, their emission by an atom would normally impart a significant recoil to the atom. As a consequence, their energy would be modified, and the probability of resonant absorption in another atom would be extremely reduced. However, when the emitting/absorbing atom is fixed in a crystal lattice, and when the gamma-ray energy is insufficient to excite a lattice vibration (*phonon*), the recoil is effectively taken up by the entire lattice and becomes negligible. Under these recoil-free conditions, resonant absorption can be observed.

As in NMR spectroscopy, the resonant response in Mössbauer spectroscopy is very sensitive to the local environment of the nucleus. In addition, in Mössbauer spectra, the presence of external or internal magnetic fields (originating from the sample itself) plays a crucial role: nuclear Zeeman splitting may be observed. This aspect will not be discussed further here; instead, attention will be focused on the other two main parameters:

(a) **Isomer shift** (δ): this parameter describes the position of the center of the absorption line relative to the α-Fe standard. It is analogous to the chemical shift in NMR and depends on the charge density at the nucleus generated by the electrons: the greater the electron density, the smaller the isomer shift. Since the only orbitals for which $|\psi(0)|^2 \neq 0$ (i.e., with non-zero electron density at $r = 0$, directly on the nucleus) are the *s* orbitals, the isomer shift is influenced by the chemical environment only in an indirect way. In a simplified picture, the effect arises from the shielding exerted on the inner *s* orbital by the *d* orbitals involved in bonding. This qualitative description is often sufficient: for example, six *d*-electrons in iron(II) provide stronger shielding and thus permit greater expansion of the *s* orbitals than five *d*-electrons in iron(III). As a consequence, $|\psi(0)|^2$ is expected to be smaller for iron(II) than for iron(III), leading to a larger isomer shift in the former.

In a more rigorous quantum mechanical treatment, the effect is primarily attributed to the partial occupancy of the valence 4*s* orbitals and their participation in molecular orbitals, as well as to the contraction of the radial distribution of the 4*s* and 3*s* orbitals upon chemical coordination of the Mössbauer atom. This contraction modifies the electron density in the vicinity of the nucleus. All these contributions are linked to the oxidation state of the atom, and therefore, a clear correlation between oxidation state and isomer shift is observed, particularly for high-spin species. A summary of typical isomer shift ranges is provided in Figure 3.2A. Note that the isomer shift is expressed in $\mathrm{mm\ s^{-1}}$, a unit of velocity. This is because the energy splittings probed in the experiment are extremely small and are measured via the Doppler effect, by moving the radioactive source at constant acceleration.

(b) **Quadrupole splitting** (ΔE_Q): this phenomenon arises from the electric field gradient surrounding the nucleus. Nuclei with a non-spherical charge distribution (i.e., those with spin quantum number $I \geq {}^1/_2$) possess a quadrupole moment. In such cases, an asymmetric electric field (originating from an uneven electronic charge distribution or a non-symmetric ligand arrangement) causes a splitting of the nuclear energy levels. As a consequence, the Mössbauer spectrum is divided into two distinct lines. Quadrupole splitting is therefore directly connected to the crystal field. It is defined as the separation between these two peaks and is again reported in units of $\mathrm{mm\ s^{-1}}$. Some representative values are shown in Figure 3.2B.

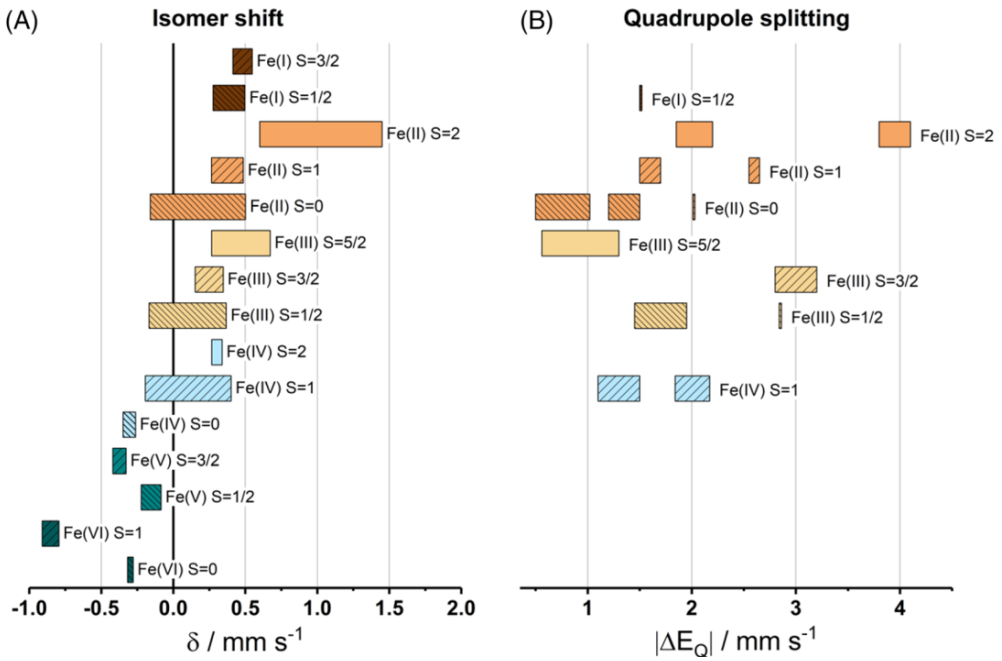

Figure 3.2: *Typical (A) isomer shift and (B) quadrupole splitting values for different iron oxidation and spin states with the FeN_4 environment.*

Mössbauer spectroscopy has been used in several notable studies involving of

high-valent iron species, since the isomer shift and quadrupole splitting make it possible to assign oxidation state, spin state, and local bonding environment at iron sites, even in mixtures and in short-lived intermediates trapped by freeze-quench techniques.

Because it is a non-destructive technique, Mössbauer spectroscopy was successfully employed in several bioinorganic investigations. In fact, most enzymes that activate molecular oxygen contain one or more iron atoms in their active sites. As a first example of the characterization of a biological iron center, the enzyme component BoxB is considered. BoxB catalyzes the key dearomatization step in a specific metabolic pathway for the degradation of aromatic compounds.[130] The enzyme contains two iron centers, and Mössbauer spectra were employed to monitor redox changes at the dinuclear site. Upon reduction, the spectrum could be fitted with two quadrupole doublets exhibiting large δ values, consistent with two nonequivalent high-spin ferrous ions coordinated by hard ligands in approximately octahedral environments.

Another bioinorganic application on which Mössbauer spectroscopy shed light is the investigation of the oxidation state of the heme intermediates in horseradish peroxidase (HRP), a heme enzyme that catalyzes the degradation of peroxides. In the first step of the catalytic cycle, a mononuclear iron-oxo intermediate known as "Compound I" (HRP-I) is generated, which is formally two oxidation equivalents above the initial ferric species. A second intermediate (HRP-II) can be obtained after an additional one-electron reduction. Mössbauer spectroscopy has shown that the transition from HRP to HRP-II involves a fundamental change in the iron electronic configuration, consistent with a net loss of electrons from the *d* shell. Nevertheless, the Fe(V) oxidation state proposed for Compound I is unlikely to be present: the electronic configurations of the iron centers in HRP-I and HRP-II are essentially identical, as noted by Moss in 1969,[131] supporting the view that the second oxidizing equivalent in Compound I is predominantly ligand-centered (porphyrin radical character) rather than corresponding to a genuine Fe(V) state at the metal.

Conversely, in nonheme iron systems, the ligands coordinated to iron are generally regarded as redox-innocent, and high-valent intermediates featuring Fe(IV) or Fe(V) centers have been identified and examined by Mössbauer spectroscopy.[132–135] A particularly robust supporting ligand for the synthesis of such high-valent iron model complexes is the macrocycle 1,4,8,11-tetraazacyclotetradecane (cyclam), which binds iron through four equatorial nitrogen donors in a coordination mode reminiscent of that in porphyrin complexes. In contrast to porphyrins, however, cyclam is *redox-innocent*, meaning that it is not susceptible to oxidation or reduction.

Cyclam, together with its methylated analogues and pendant-arm derivatives, has been widely applied in the preparation of high-valent transition metal complexes, especially mononuclear species with Fe(IV), Fe(V), and Fe(VI).[136–141] Whereas the reactive high-valent iron intermediates in biological systems are typi-

cally stabilized by a strongly electron-donating oxo ligand, iron-nitrido complexes are also of considerable interest and have been exploited in synthetic chemistry, not only owing to their relevance for enzymatic transformations within the biogeochemical nitrogen cycle, but also for fundamental and technological reasons. A particularly appealing route to high-valent iron complexes is the photolytic cleavage of coordinated ferric azide complexes (containing bound N_3^- ions), which generates dinitrogen (N_2) and high-valent Fe=N species.[136–143] In the first reported example, the precursor was a bis-azide iron(III) cyclam complex, $[(\text{cyclam})\text{Fe(III)}(N_3)_2]^+$. This complex can adopt two distinct conformations, in which the two azide ligands occupy either cis or trans positions (see insets of Figure 3.3). The difference between these arrangements has a pronounced influence on the electronic structure, as reflected in the Mössbauer spectra (Figure 3.3A and B). The trans isomer is a typical low-spin ferric species, characterized by a small isomer shift and a large quadrupole splitting ($\delta = 0.29\ \text{mm s}^{-1}$, $\Delta E_Q = 2.26\ \text{mm s}^{-1}$), whereas the more open conformation of the macrocycle in the cis-azide arrangement permits a high-spin configuration, with a moderately increased isomer shift and a small quadrupole splitting, arising from the quasi-cubic symmetry of the half-filled d shell ($\delta = 0.46\ \text{mm s}^{-1}$, $\Delta E_Q = 0.29\ \text{mm s}^{-1}$).[137]

Electrochemical reduction of the ferric compounds leads to distinct ferrous species (Figure 3.3C and D).[137] The Mössbauer parameters of the reduced cis-complex clearly indicate the formation of a high-spin Fe(II) species ($\delta = 1.11\ \text{mm s}^{-1}$, $\Delta E_Q = 2.84\ \text{mm s}^{-1}$), whereas the reduced trans-complex is predominantly present in a low-spin Fe(II) state, characterized by a low isomer shift and small quadrupole splitting. This is attributed to the high symmetry of the filled t_{2g}^6 subshell (subspectrum I, $\delta = 0.55\ \text{mm s}^{-1}$, $\Delta E_Q = 0.72\ \text{mm s}^{-1}$). The trans-configuration of the reduced complex is, however, not stable and gradually isomerizes in solution to the cis-form, as evidenced by the emergence of the same high-spin component observed for the cis-complex (subspectrum II in panel C). The intensity of this component increases with incubation time in solution.

Iron(III) cyclam-azide complexes are photosensitive. Irradiation of trans- and cis-$[(\text{cyclam})\text{Fe(III)}(N_3)_2]^+$ in cold fluid solution at −35 °C with light of approximately 420 nm produces two new species that were identified as mixed-valence dimers containing μ-nitrido-bridged diiron cores of the type $[\text{Fe(III)-N-Fe(IV)}]^{4+}$. In one case, the nitrido and terminal azide ligands at the Fe(IV) center exhibit cis-symmetry, while in the other, they adopt a trans arrangement.[137] The appearance of these products implies that both photooxidation and photoreduction occur as primary photochemical processes, generating Fe(IV) and Fe(II) intermediates that subsequently combine via bimolecular reactions to give the observed Fe(III)/Fe(IV) mixed-valent dimers. In the following, only the properties of the high-valent Fe(IV) sites in these dimers are considered. Applied-field Mössbauer and EPR spectroscopies reveal that these centers are hexacoordinate, low-spin Fe(IV) with spin $S = 1$, consistent with a $3d(t_{2g})^4$ electron configuration (four electrons distributed

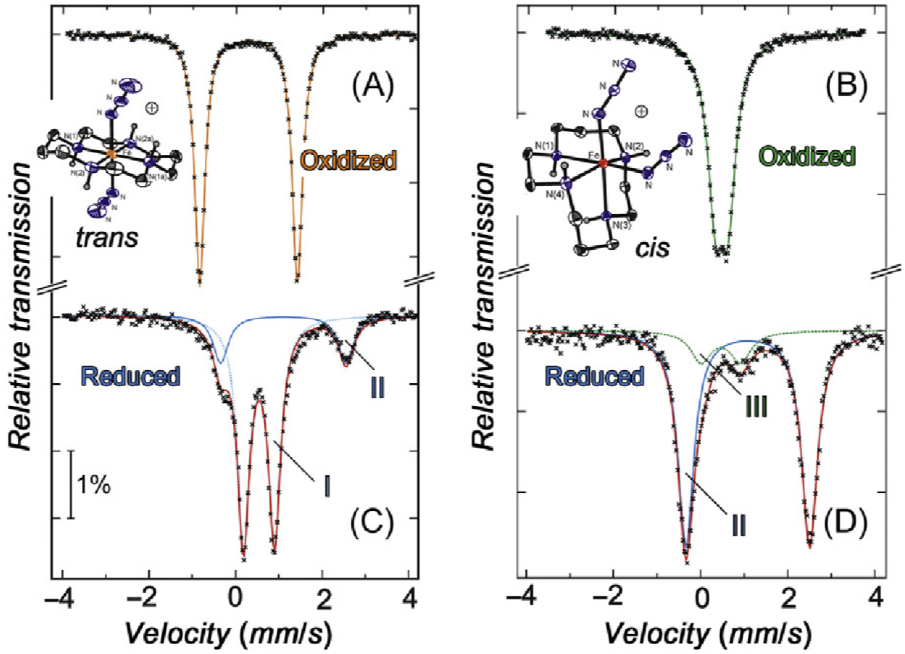

Figure 3.3: *Zero-field Mössbauer spectra of the trans- and cis-*$[(cyclam)Fe(III)(N_3)_2]^+$ *complexes (35%* ^{57}*Fe-enriched, 1.5 mM in acetonitrile, panels A and B)*[137] *and of their electrochemically one-electron-reduced acetonitrile solutions (C and D) recorded at 80 K are shown. The spectra were fitted using Lorentzian doublets. The oxidized complex with trans-orientation of the azide* (N_3^-) *ligands (A) behaves as a typical low-spin Fe(III) system, whereas the chemically identical cis-isomer in (B) exhibits high-spin Fe(III). After coulometric reduction at −30 °C, the reduced trans-species (C) displays a superposition of low-spin Fe(II) (subspectrum I) and high-spin Fe(II) (subspectrum II). Prolonged incubation of the solution at −30 °C leads to a pronounced increase of subspectrum II, accompanied by a corresponding decrease of subspectrum I. In contrast, reduction of the cis-complex (D) affords high-spin Fe(II) exclusively. Subspectrum III in D, characterized by* $\delta = 0.49$ mm s^{-1} *and* $\Delta E_Q = 0.90$ mm s^{-1}*, is most likely attributable to contamination by a* $[Fe(III)\text{-}O\text{-}Fe(III)]^{4+}$ *μ-oxo dimer formed through partial oxidation by trace amounts of air. This spectral component appeared only when a reduced sample was intentionally exposed to air.*

over three orbitals). The Mössbauer isomer shifts and quadrupole splittings are δ = 0.14 mm s^{-1}, ΔE_Q = 0.79 mm s^{-1} for the cis isomer and δ = 0.11 mm s^{-1}, ΔE_Q = 0.97 mm s^{-1} for the corresponding trans complex (measured at 80 K in frozen solution). These parameters are comparable to those reported for Fe(IV)=O porphyrin complexes.[144–147]

Authentic iron(V) remains an exceptionally uncommon oxidation state, and only a small number of rigorously characterized iron(V)-oxo species are known. The majority have been prepared with the redox-innocent, tetranionic tetraamido macrocyclic ligand (TAML),[134] which offers four very strong amide-*N* σ-donor groups, as well as its biuretamide derivative.[148–150] These ligand frameworks are capable of stabilizing iron(V) when an iron(III) precursor complex is treated with an oxygen-atom-transfer reagent. The anticipated $3d^3$ configuration has been confirmed by Mössbauer spectroscopy (δ = −0.42 mm s^{-1} at 4.2 K, ΔE_Q = 4.25 mm s^{-1}), EPR spectroscopy (S = $^1/_2$, g = [1.99, 1.97, 1.74]), and by X-ray absorption spectroscopy (XAS) together with extended X-ray absorption fine structure (EXAFS) measurements (all for the TAML-based complex).[134] Furthermore, one-electron oxidation of a well-defined Fe(IV)=O precursor ligated by tetramethylcyclam (TMC) yields a metastable oxoiron(V) complex that could be interrogated at low temperature using a range of spectroscopic techniques.[151] More recently, pyclen-based ligand platforms developed by the Costas group have enabled the spectroscopic trapping and detailed characterization of highly reactive iron(V)-oxo-carboxylato intermediates, including *in situ* generation, EPR/Mössbauer-based electronic-structure assignment, and direct evaluation of their reactivity.[126,152–155]

Genuine iron(V) nitrido complexes were obtained by low-temperature photolysis of the cyclam iron(III) complexes described above.[136–138,140,141] In frozen solution, where bimolecular reactions are suppressed, the corresponding monomeric Fe(V)≡N species were generated in high yield (Figure 3.4, left). Evidently, photoreduction of the immobilized molecules makes only a negligible contribution, presumably because, in contrast to photooxidation, it is reversible, and any azide radicals formed upon photoreduction can rebind to the immobilized Fe(II) product, thereby regenerating the starting complex. Extensive investigations of [(cyclam-acetato)Fe(V)≡N]$^+$ by XAS and EXAFS, magnetic susceptibility measurements, Mössbauer spectroscopy, nuclear inelastic scattering (NIS), and EPR, in combination with density functional theory (DFT) calculations,[137,138,140,141,156,157] established that this complex is best described as a low-spin $(d_{xy})^2(d_{xz}, d_{yz})^1$ system. The Mössbauer parameters of [(cyclam-acetato)Fe(V)≡N]$^+$ (δ = −0.02 mm s^{-1}, ΔE_Q = 1.60 mm s^{-1}) agree well with those reported for [(cyclam)Fe(V)≡N]$^+$ in CH_3CN solution, which likely bears a sixth ligand at the iron center (δ = −0.04 mm s^{-1}, ΔE_Q = 1.67 mm s^{-1}).

The most appropriate electronic structure was assigned based primarily on the strong correlation between the isomer shifts of the cyclam complexes and the formal oxidation state of iron, as shown in the right panel of Figure 3.4. The observed

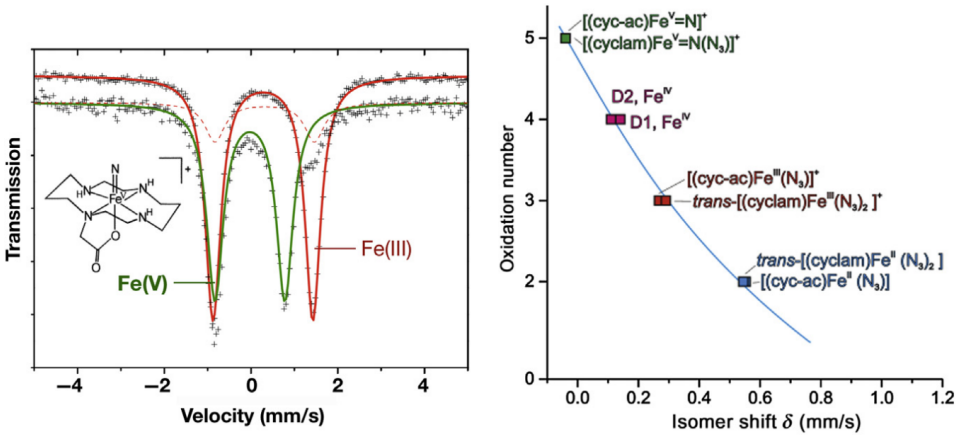

Figure 3.4: *Left: Mössbauer spectra of* $[(cyclam\text{-}acetato)Fe(III)(N_3)]^+$ *(shown in red) and its low-temperature iron(V) photolysis product (shown in green)*[138] *recorded at 80 K. Right: Isomer shift correlation diagram for low-spin iron complexes bearing cyclam and cyclam-acetato supporting ligands, covering iron oxidation states from Fe(II) to Fe(V). The blue line is included merely as a visual guide; it is not derived from any detailed theoretical model beyond the general considerations of* d^n*-electron configurations and isomer shifts. In some cases, straight lines have also been employed for this purpose.*

changes in δ appear to mirror the expected shortening of the apical ligand bond distances with increasing oxidation state. A tight and unambiguous correlation is obtained in this case because, in contrast to the more general scenario in Figure 3.2, a well-defined series of quasi-isomorphous complexes with fixed equatorial ligands is analyzed. All complexes are six-coordinate, and modifications in the valence electron configuration are restricted to the low-spin t_{2g} subshell, together with an increase in the covalency of the axial ligand bonds. A similar correlation is also evident for related complexes bearing axial oxygen or oxo ligands, although the slope of the corresponding isomer shift-oxidation state plot will be different.

Higher oxidation states (VI and VII). Basic ligand field considerations predict relatively high stability for highly oxidized iron complexes with d^2 or d^1 configuration, due to the reduced number of antibonding d-electrons compared to $3d^3$ configuration. As mentioned, iron(VI) ferrates are easily obtained and well-known compounds, while molecular iron(VI) compounds are definitely rarer. Historically, the first example again derives from the work of Berry,[136] whose group was able to isolate a nitrido Fe(VI) complex supported by the bulky $(Me_3cyclam\text{-}acetate)^-$ ligand, by electrochemically oxidizing its iron(IV) azide precursor.

Very recently,[158] the accessible upper limit of molecular iron oxidation-state chemistry has been pushed beyond iron(VI). Meyer and co-workers have described the synthesis and structural and spectroscopic characterization of a stable octahedral Fe(VI) nitrido complex that can undergo a one-electron oxidation to yield an authenticated Fe(VII) species. The highly oxidized Fe(VII) nitride could not be isolated under conventional conditions because it rearranges at temperatures above

approximately −50 °C. Nevertheless, it was unequivocally identified by freeze-quench Mössbauer spectroscopy, showing an exceptionally negative isomer shift ($\delta = -0.72\ \mathrm{mm\,s^{-1}}$), and EPR measurements corroborated its low-spin configuration ($S = {}^1/_2$).

3.1.2 *My take* on this topic

My research group has extensively worked on the synthesis and the application of iron-pyclen complexes in oxidative catalytic processes.[159–161] During my PhD studies, I fine-tuned the synthesis of several of these (specifically, iron(III) complexes), and synthesized their iron(II) counterparts. Then, I moved on to their spectroscopic and magnetic characterization. After studying the oxidation and spin states of the lower valence complexes (II and III), I attempted to characterize their higher oxidation states by freeze-quenching the products of reaction of the iron(III) complexes with hydrogen peroxide, with modest success. Once the spectroscopic, magnetic, and structural studies were concluded, I investigated the photocatalytic capabilities of these compounds in the photooxidation of *p*-xylene and benzyl alcohols.

3.2 Results and discussion

3.2.1 Synthesis of iron-pyclen complexes.

The synthesis of pyclen (**L4**) and pyclen-derived ligands is straightforward and has previously been reported by both my research group and other authors.[152,159–162] It is similar to the synthesis of the previously mentioned **L1**, but simpler. Briefly, a solution of pyridine-2,6-diylbis(methylene)-dimethanesulfonate (**4**) was added dropwise to a suspension of tosyl protected N^1-(2-aminoethyl)ethane-1,2-diamine and *strictly anhydrous* potassium carbonate in acetonitrile, and the reaction mixture is heated for three hours (Scheme 3.2.1).

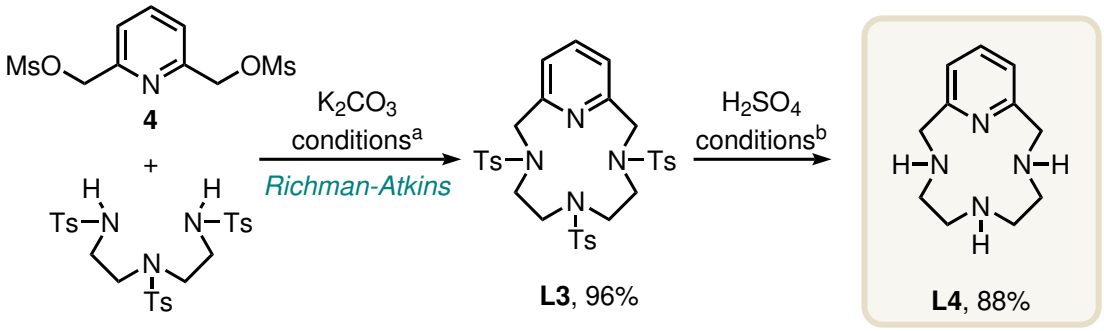

Scheme 3.2.1: *Synthesis of pyclen (**L4**). [a]Reaction conditions for the formation of the macrocycle: 82 °C, 3 h, three equivalents of base, anhydrous acetonitrile. [b]Reaction conditions for the deprotection of the macrocycle: neat sulfuric acid, microwave irradiation at 120 °C for 35 minutes.*

These conditions are known from the work of Richman and Atkins;[111] due to the almost null solubility of potassium carbonate in acetonitrile, tosylamide depro-

tonation occurs in very low concentrations and the formation of polymerization products is drastically reduced, even under moderately diluted conditions.

At the end of the reaction, the product was recovered by evaporating the solvent and separating the base and byproducts via aqueous work-up. The dichloromethane extract of the aqueous phase is usually pure enough to allow the product to be recovered simply by distilling off the solvent.

Compared to previous reports on pyclen deprotection, which often relied on the use of a hydrobromic/acetic acid mixture with phenol and a time-consuming overnight reflux, my group was able to obtain complete deprotection in high yield (88%) in just 35 minutes when aided by microwave irradiation, using simple neat sulfuric acid. In these conditions, the hydrolyzed product was obtained as the hydrogen sulfate salt of pyclen, which precipitated readily from the reaction mixture upon the simple addition of cold diethyl ether. The free base (**L4**) was isolated after the addition of sodium hydroxide and thorough extraction from the aqueous phase with dichloromethane.

Although **L4** was used as the ligand in the formation of complexes **C2a-f** (Scheme 3.2.2), it can be further functionalized by introducing different groups on the donor atoms. Following the expertise of my research group,[159] I decided to focus on benzyl-substituted pyclen (**L5**), obtained by treating **L4** with benzyl bromide and an organic base (in this case, di-isopropylethylamine).

To isolate iron complexes of **L4** and **L5**, the ligands were treated with the appropriate iron source in acetonitrile. Six iron sources were selected; three of them were commercial (ferric chloride; ferric bromide; ferrous bromide), while the other three were lab-made ($[Fe_4Cl_8(THF)_6]$, **C4a**; iron(III) triflate; $Fe(CF_3SO_3)_2 \cdot 2\,CH_3CN$). Attempts to use commercial iron(III) triflate as an iron source were unsuccessful, as the sample we received was heavily contaminated with iron(II) (*Vide infra*.

Complexation usually occurs immediately; however, to ensure full conversion, the reaction mixtures were usually heated gently (60 °C) for one to three hours. In most cases, the complexes precipitated during the addition of the iron source solution or upon cooling, ensuring high purity and crystallinity of the product. In other cases, especially when using triflate sources, the products did not precipitate; removing the solvent under vacuum and triturating the residue in dry diethyl ether was usually sufficient to recover the products in high yield and purity.

Although iron(III) complexes are usually not susceptible to aerobic oxidation, dry solvents and reaction conditions were employed to ensure that no moisture could alter the structure and the properties of the complexes. Iron(II) complexes, on the other hand, required protection from atmospheric oxidation, so the synthesis and handling of the products were carried out under strictly anaerobic conditions.

More experimental information on the synthesis of compounds **C2a-f** and **C3a-f** are detailed in section 6.1.8.

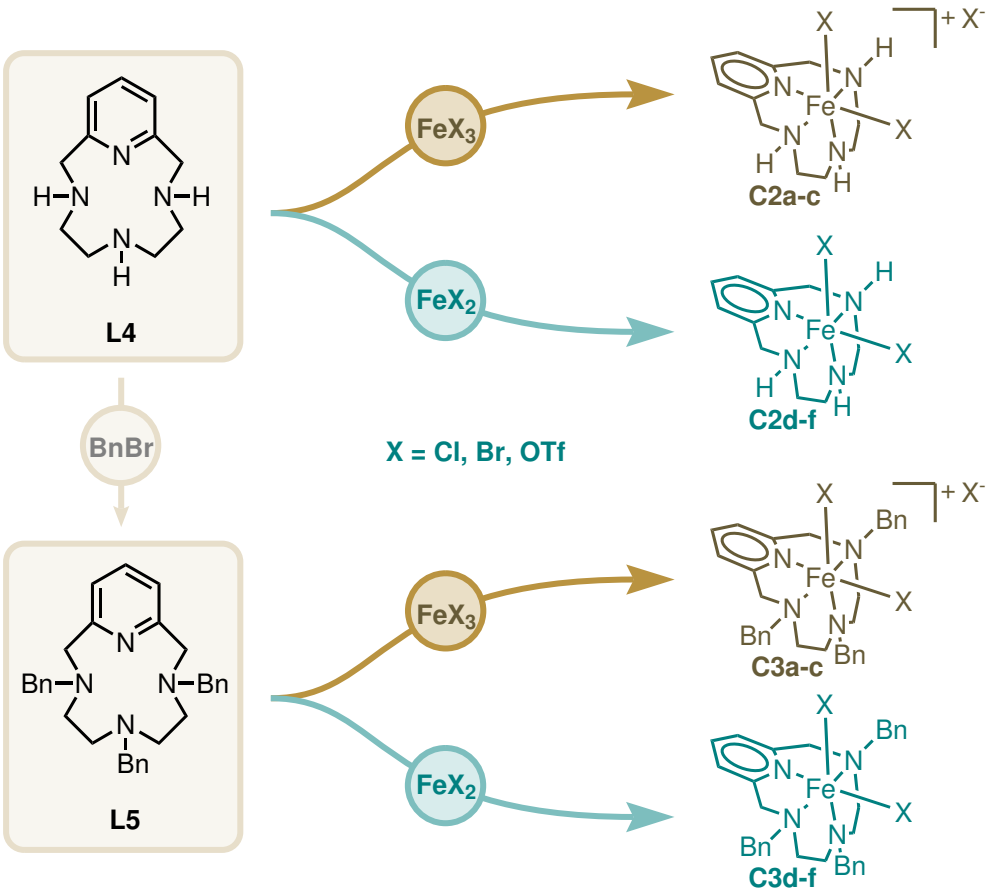

Scheme 3.2.2: *Synthesis of complexes* ***C2a-f*** *(using* ***L4*** *as the ligand) and* ***C3a-f*** *(using* ***L5****).*

3.2.2 Characterization of iron-pyclen complexes (*and a few other interesting species*)

Structural studies, complexes C2. Several crystal structures of $[Fe(PcLH_3)X_2]^+$ cationic complexes, balanced with various counterions, have been reported.[160,162–166] Interestingly, crystallization of compound **C2a** ($[Fe(PcLH_3)Cl_2]Cl$) via solvent diffusion (methanol/diethyl ether, v/v = 1 : 2) led to the concomitant precipitation of two distinct crystal morphologies: clear, yellow, regular blocks (**C2a**) and elongated, dark brown plates (**C2a'**). While structural analysis of the former matched previously published work by Green and co-workers,[165] featuring a chloride counterion, the latter displayed a novel structure, which was determined via X-ray diffraction (Figures 3.5, A.57, A.58 and Table A.20). X-ray diffraction analysis of **C2a'** revealed that although it shares the same molecular geometry and cis-folded tetraazamacrocycle configuration as **C2a**, it incorporates a divalent $[Fe(II)Cl_4]^{2-}$ anion in its second coordination sphere. The presence of $[MCl_4]^{n-}$ species as counterions in analogous cationic coordination compounds has been previously observed by my group[159] and others.[165,167] Auto reduction of Fe(III) to Fe(II) accompanied by oxidation of the halide with concomitant release of X_2 gas has been previously reported.[168] In all these structures, the Fe(III) center adopts a distorted octahedral geometry, coordinated by the four nitrogen atoms of the macrocycle and two monodentate X-type ligands. The pyclen scaffold displays a cis-folded conformation, which has been demonstrated by molecular mechanics calculations to be preferred when M-N bond lengths are greater than 2.0 Å.[169]

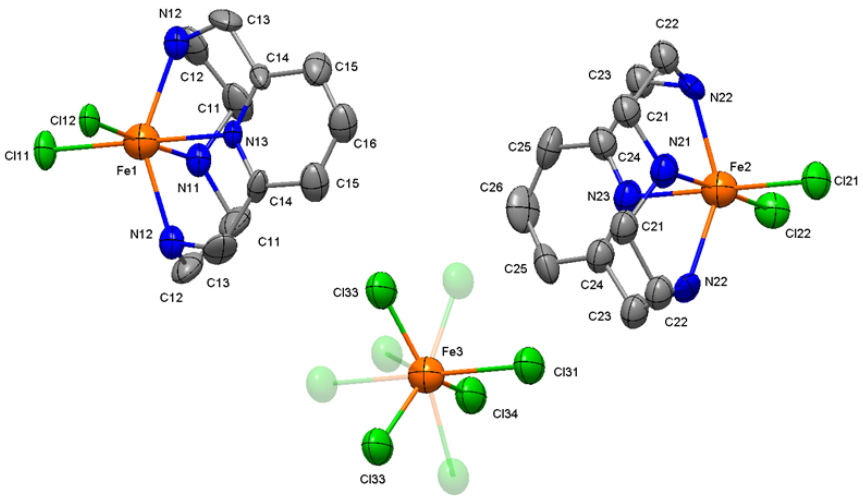

Figure 3.5: *Representation of the crystal structure of* ***C2a'*** *solved in the Cm space group (No. 8), refined with anisotropic displacement parameters. Thermal ellipsoids are drawn at 50% probability. Disordered sites are depicted with lower opacity. Colors: Fe, orange; Cl, green; N, blue; C, grey; H are omitted for clarity. Courtesy of Giulia Taini.*

Attempts to crystallize the Fe(II) equivalent complex (**C2d**, $[Fe(PcLH_3)Cl_2]$)

were met with mixed results: diffraction-quality crystals were obtained from a solution that was inadvertently exposed to the atmosphere, and the complex was oxidized to the Fe(III) μ-oxo dimer (**C2d'**).

Structural studies, complexes C3. Crystallization of complexes bearing the **L5** benzylated ligand were more successful. The structure of cationic $[Fe(PcLBn_3)Cl_2]Cl$ (**C3a**) was already reported from my research group (CCDC-1920775),[159] while attempts at crystallizing the bromo- (**C3b**) and trifluoromethanesulfonic-substituted (**C3c**) iron(III) cationic complexes were not successful.

Conversely, neutral iron(II) complexes **C3d-f** crystals were easily obtained by diffusion of diethyl ether vapors in acetonitrile solutions (**C3d-e**), or by layering dry diethyl ether directly on top of the reaction mixture (**C3f**).

Complex **C3d** crystallizes in the monoclinic space group $C2/c$ (No. 15), as confirmed by systematic absences observed in the diffraction data, forming golden-yellow elongated scalenohedral crystals. The formula unit contains one molecule of $[Fe(PcLBn_3)Cl_2]$ (Figure 3.6, left). **C3e** crystals (triclinic, $P\bar{1}$, no. 2) were lower quality compared to **C3d**. The specimens were rather small and irregularly shaped, with a hemimorphic crystal habit. Also in this case, the formula unit contains one molecule of $[Fe(PcLBn_3)Br_2]$ (Figure 3.6, center).

By far, the highest quality crystals were obtained from the reaction solution of **C3f**. Prism-like colorless crystals were obtained by layering dry diethyl ether on the complexation reaction mixture (acetonitrile, v/v 2 : 1) after cooling overnight and filtering off the unreacted ligand. The compound crystallizes in the monoclinic space group $P2_1/c$. Again, the formula unit contains one molecule of $[Fe(PcLBn_3)(OTf)_2]$ (Figure 3.6, right).

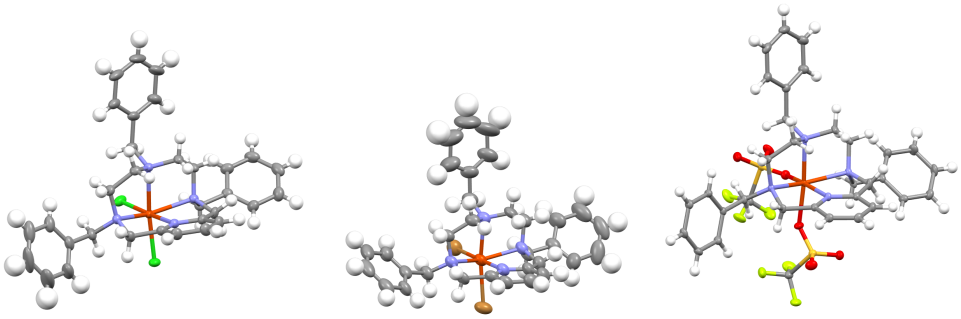

Figure 3.6: *Representation of the crystal structure of **C3d-f**. Thermal ellipsoids are drawn at 50% probability. Colors: Fe, orange; Cl, green; N, blue; O, red; S, yellow; F, green; C, grey; H, white.*

Comparison between structures. To comprehensively represent the molecular geometry and structural distortion in the octahedral coordination complexes, the following parameters have been determined for each species reported in this work (Table 3.1):

(a) Iron center displacement[169] from the macrocyclic cavity, as expressed by its distance (d_{FeN_4}) from the N_4 mean least-square plane.

(b) Folding angle (Ω),[169] which is a measure of the arrangement of the macrocyclic ring along the axis defined by the nitrogen atoms close to the pyridine ring and corresponds to the dihedral angle between the [N_A, N_B, N_D] and [N_B, N_C, N_D] planes illustrated in Figure 3.7a.

(c) Degree of distortion[170] of the coordination sphere from an ideal octahedron (Figure 3.7b), in terms of average Fe–L distances (d_{mean}) and bond stretching (ζ):

$$\zeta = \sum_{i=1}^{6} |d_i - d_{mean}|$$

For reference, an ideal O_h-FeL_6 metal complex would be characterized by $d_{mean} = 1.460$ Å and $\zeta = 0.00$ Å.

(d) Angular Jahn-Teller distortion[171,172] parameter (α), defined as the dihedral angle between the mean least-square plane containing the equatorial and axial ligand (Figure 3.7c). The larger the variation from 90°, the greater the magnitude of the Jahn-Teller effect on the octahedral geometry.

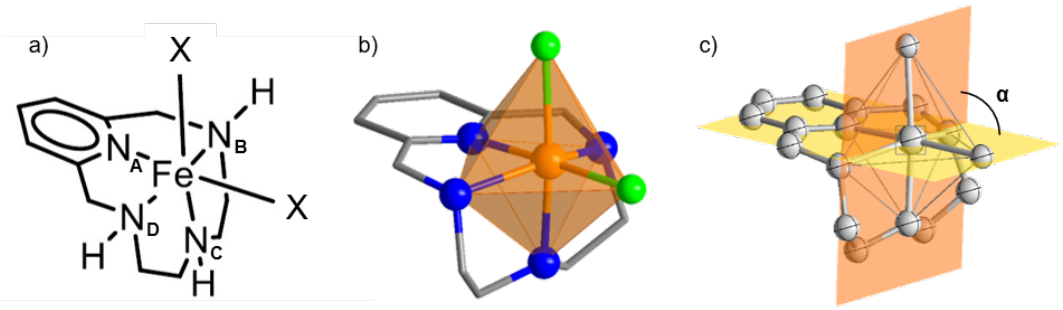

Figure 3.7: *a) Schematic representation, b) octahedral coordination sphere, and c) Jahn-Teller distortion parameter α of complexes of general formula* $[Fe(PcLR_3)]X_2]$.

Table 3.1: *Structural and octahedral distortion parameters or* O_h-$[Fe(PcLR_3)]X_2]$ *complexes.*

Compound	R	X	Fe O.S.	d_{FeN_4} (Å)	Ω (°)	d_{mean} (Å)	ζ (Å)	α (°)
C2a	H	Cl	3+	1.087	65.30	2.198	0.340	87.97
C2a'[a]	H	Cl	3+	1.109	63.95	2.232	0.443	87.67
C3a[b]	Bn	Cl	3+	1.101	69.63	2.226	0.255	88.73
C3d	Bn	Cl	2+	1.179	67.29	2.311	0.391	87.64
C3e	Bn	Br	2+	1.199	66.40	2.379	0.679	86.49
C3f	Bn	OTf	2+	1.057	63.42	2.169	0.435	83.94

[a]The values reported are averaged between the two monomers contained in the asymmetric unit.
[b]The structure was isolated bearing $[FeCl_4]^-$ as the counterion instead of Cl^-. In a first approximation, the structure is considered anyway for comparison purposes.

Comparison between **C2a** and **C2a'** parameters reveal that **C2a'** is generally more distorted (Table 3.1, entries 1 and 2). Instead, surprisingly, complex **C3a** ap-

pears to be less distorted than the *N*-unsubstituted complexes **C2a** and **C2a′** (Table 3.1, entry 3). This was unexpected, as **C3a** was determined to be a low-spin complex ($S = {}^1/_2$),[159] that should be subject to a more pronounced Jahn-Teller distortion compared to high spin $S = {}^5/_2$ complexes with evenly occupied half-filled *d* orbitals.

Conversely, iron(II) complexes are consistently more distorted than their cationic Fe(III) counterparts. Therefore, as expected, **C3d** exhibits higher structural distortion than its Fe(III) counterpart (**C3a**). Complex **C3e** is even more distorted, especially in the ζ parameter, since the long Fe–Br bond distances greatly increase cumulative bond stretching. **C3f** (entry 6) presents a more convoluted scenario. Due to the shorter average bond distances (d_{mean}) also caused by short Fe–O bonds, it exhibits a smaller iron center displacement (d_{FeN_4}) compared to the other compounds; however, all other parameters indicate that the compound is possibly more distorted. These characteristics are fully predicted from high-spin Fe(II) species, which are expected to adopt distorted octahedral geometries due to the Jahn-Teller effect.

Although single crystal X-ray diffraction is extremely useful to rationalize the physical properties of coordination complexes, certain behaviors (i.e., **C3a** lower distortion than **C2a**) require more specialized tools to be elucidated. Mössbauer spectroscopy, in this case, is the most adequate tool, and the next section will demonstrate it.

Mössbauer spectroscopic characterization of selected complexes. As discussed in the introduction, ^{57}Fe Mössbauer spectroscopy is a powerful tool when it comes to determining the oxidation state and the spin state of iron complexes. Unless otherwise noted, all measurements were conducted on solid-state samples at room temperature in a dinitrogen-flushed sample holder.

The first compounds subject to analysis were complexes **C2a-c** (Figure 3.8).

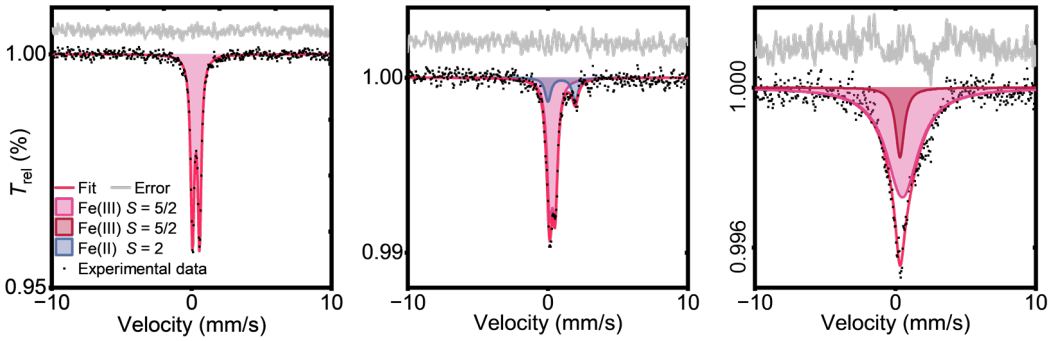

Figure 3.8: *Mössbauer spectra of* ***C2a*** *(left),* ***C2b*** *(center) and* ***C2c*** *(right).*

The spectrum of **C2a** (Figure 3.8, left) is relatively simple, consisting of a single doublet. This signal, characterized by an isomer shift (δ) of 0.31 mm s^{-1} and a quadrupole splitting (ΔE_Q) of 0.51 mm s^{-1}, is unambiguously assigned to a high-

spin Fe(III) species.

A more intricate situation is found in the case of sample **C2b** ($[Fe(PcLH_3]Br_2]Br$, Figure 3.8, center). To achieve an optimal fit, the spectrum was deconvoluted into two subspectra. The primary component ($\geq 80\%$) exhibits an isomer shift of 0.32 $\mathrm{mm\ s^{-1}}$ and a quadrupole splitting of 0.39 $\mathrm{mm\ s^{-1}}$, consistent with a high-spin Fe(III) species. A minor subspectrum ($\leq 20\%$) with an isomer shift of 0.98 $\mathrm{mm\ s^{-1}}$ and a quadrupole splitting of 1.95 $\mathrm{mm\ s^{-1}}$ indicates the presence of an iron(II) high-spin impurity, likely resulting from partial reduction of the starting material.

The presence of Fe(II) was higher in sample **C2c** ($[Fe(PcLH_3)(OTf)_2](OTf)$, Figure A.36), which exhibited three subspectra, one of which corresponds to an iron(II) high-spin species, contributing 32(2)% by weight. Unlike $FeBr_3$, which can easily reduce to $FeBr_2$ under vacuum and heating by evolving bromine, $Fe(OTf)_3$ is not expected to undergo a similar reaction. To confirm this, the commercial $Fe(OTf)_3$ starting material was analyzed using Mössbauer spectroscopy and found to contain up to 46% Fe(II) contamination (Table A.32). Using a pure $Fe(OTf)_3$ source prepared in-house, sample **C2c** did not show any evident sign of the presence of Fe(II) (Figure 3.8, right). However, the material's extreme hygroscopicity posed challenges during analysis. Exposure to atmospheric moisture likely led to ligand exchange, replacing triflate ligands with aquo ligands, resulting in a broad, poorly resolved spectrum. This spectrum was fitted with two broad singlets, but the low resolution precluded reliable quantitative analysis.

Compared to **C2a**, the complex **C3a** produced a dramatically different spectrum (Figure 3.9, Table A.9). As expected from its EPR analysis and its reactivity in alkenes epoxidation,[159] **C3a** is a low-spin iron(III) complex. In this case, the spectrum was deconvoluted into three subspectra. The predominant components are two low-spin octahedral iron(III) species, which together account for 94(6)% of the sample's iron weight. Both signals are characterized by a low isomer shift (0.24 and 0.34 $\mathrm{mm\ s^{-1}}$) and a rather large quadrupole splitting (1.25 and 2.07 $\mathrm{mm\ s^{-1}}$). These values, which vary slightly, are probably due to the presence of two different crystalline forms and are fully compatible with a low-spin iron(III) species. This contrasts with structural data, which showed lower distortion in complex **C3a** than in high-spin **C2a**, but aligns with the reactivity of the complex and EPR spectroscopy, validating the usefulness of the method. A third, minor subspectrum is visible. This signal is characterized by low δ and ΔE_Q, and can be ascribed to the presence of a small quantity of high-spin iron(III), probably $[FeCl_4]^-$.

Complexes **C3d** and **C3f**, being high-spin iron(II) species, exhibit higher structural distortion and thus larger crystal field inhomogeneity. This results in an even larger quadrupole splitting (Figure 3.10). Moreover, due to the higher shielding of the *d* orbitals in iron(II) complexes and the consequent *s*-expansion, the isomer shift increases compared to iron(III) species. Both spectra had to be deconvoluted into two separate contributions. The major components in both samples produce doublets with similar characteristics: large isomer shift (0.98~1.04 $\mathrm{mm\ s^{-1}}$) and

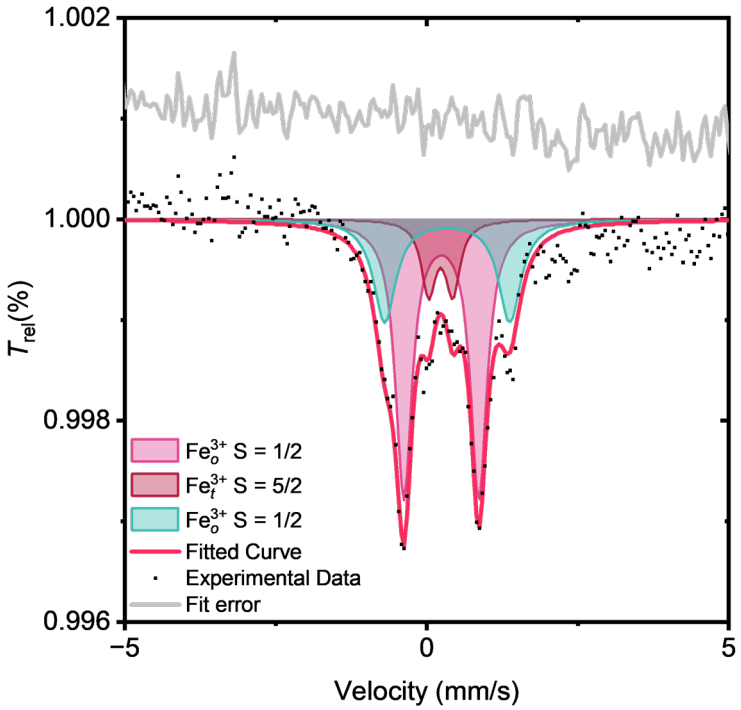

Figure 3.9: *Mössbauer spectrum of **C3a**. Courtesy of prof. Dominika Zákutná.*

quadrupole splitting (0.98~1.04 $\mathrm{mm\,s^{-1}}$, Table A.11 and A.12). These signals are unambiguously assigned to high-spin Fe(II) species. In both cases, a minor impurity was observed, appearing as a doublet with a very small isomer shift and quadrupole splitting ($\delta \approx 0.24\ \mathrm{mm\,s^{-1}}$ $\Delta E_Q \approx 0.29\ \mathrm{mm\,s^{-1}}$). This signal is consistently present in all samples that were measured in a dinitrogen-flushed chamber. This fact raised the suspicion that the sample holder itself could have been responsible for this spurious signal. The sample holder was constructed using common aluminum foil, often produced with alloys such as AA8011, which can contain substantial amounts of iron. The most prominent intermetallic species that form in these materials are Al_6Fe and Al_3Fe, and both show Mössbauer parameters similar to the impurity that was detected here.[173]

After characterizing all the iron complexes that I synthesized, I turned my attention to their possible high-valent derivatives. In a 2020 article, my research group developed a method to catalyze the oxidation of benzyl alcohols using H_2O_2.[160] In this work, it was hypothesized that the oxidation of the substrate could occur through the formation of a high-valent iron species: either a Fe(IV)=O species, generating $^{\bullet}$OH radicals and proceeding through a $1e^-$ pathway, or a Fe(V)=O species, which would then oxidize the substrate in a $2e^-$ process. The system was investigated using a molecular probe, cyclobutanol, which, in the presence of radicals, readily forms ring-opening products. Major formation of cyclobutanone indicated that the iron(V) $2e^-$ mechanism was preferred. To corroborate this theory and to demonstrate the actual formation of iron(V) species, I decided to analyze the frozen

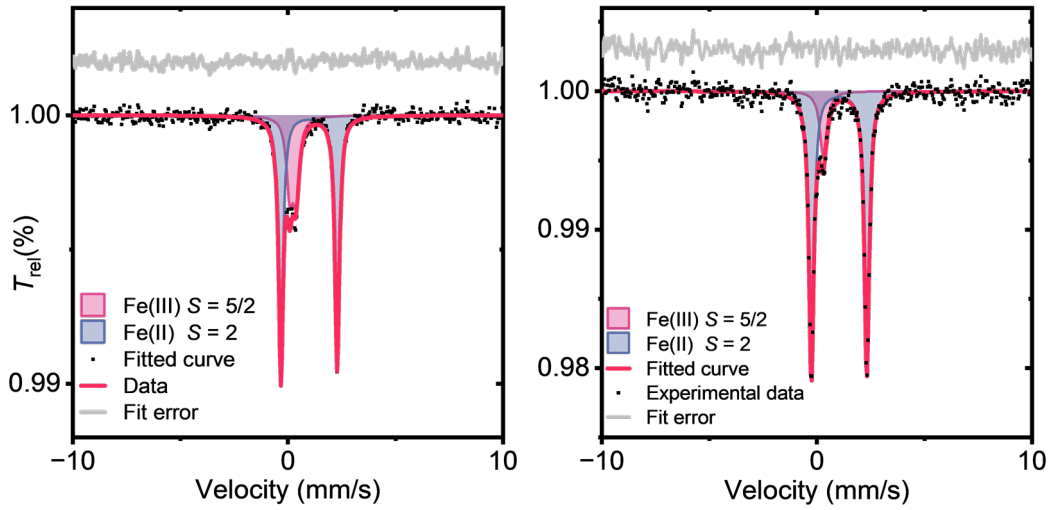

Figure 3.10: *Mössbauer spectra of* ***C3d*** *(left) and* ***C3f*** *(right).*

solution of complex **C2b** ($[Fe(PcLH_3)Br_2]Br$ in the presence of hydrogen peroxide through Mössbauer spectroscopy.

Thus, **C2b** was dissolved in dry acetonitrile, and six equivalents of hydrogen peroxide were slowly added. Experimentally, this procedure posed several problems. The first derives from the fact that ^{57}Fe is the only stable iron isotope on which Mössbauer spectroscopy is feasible; however, its natural occurrence is only about 2%. As I was unable to obtain ^{57}Fe to enrich my sample, the only solution would be to produce rather concentrated solutions of **C2b**. This was detrimental to the success of the experiment for two reasons: first, even though the solutions were concentrated, the time required to obtain a reasonable data quality was very long; second, the high concentration of the solutions favored the *catalase* activity of complex **C2b**, which decomposed hydrogen peroxide to water and oxygen and returned to its Fe(III) pre-catalyst state.

Nevertheless, I decided to proceed with the analysis. The sample was frozen in liquid nitrogen, and its Mössbauer spectrum was measured at 77 K. The resulting spectrum is displayed in Figure 3.11 on the left. The spectrum was deconvoluted into two doublets to account for the asymmetry in the peaks. Each signal contributes about 50% of the total signal, and both are most probably ascribable to conventional iron(III) high-spin species. The peak with a larger ΔE_Q (green) could be attributed to an iron(IV) $S = 1$ species ($\delta = 0.51(0)$ mm s^{-1}, $\Delta E_Q = 1.11(6)$ mm s^{-1}), however, its isomer shift is borderline and the iron(III) $S = {}^5/_2$ assignment is more credible. The other doublet ($\delta = 0.48(0)$ mm s^{-1}, $\Delta E_Q = 0.60(3)$ mm s^{-1}) is solidly ascribed to a high-spin iron(III) species.

Although Mössbauer signals are usually temperature dependent, and direct comparison of two spectra at different temperature is not possible, the latter signal exhibits a striking resemblance to that of the dimer [μ-O(Fe(PcLH$_3$)Br)$_2$]Br (**C2b'**, Figure 3.11, $\delta = 0.35(1)$ mm s^{-1}, $\Delta E_Q = 0.60(1)$ mm s^{-1}). The formation of a μ-oxo

dimer would be justified by the reaction:

$$[\mathrm{LFe(III)}] + \mathrm{H_2O_2} \longrightarrow [\mathrm{LFe(III)-OOH}] \rightleftharpoons [\mathrm{LFe(V)=O}] + \mathrm{OH^-}$$

as the presence of hydroxide, either coordinated or in solution, would ultimately lead to the formation of a dimer. Interestingly, the dimerization of the complex was proposed as a catalyst deactivation pathway in the catalytic benzyl alcohol oxidation, and the necessity of keeping the hydrogen peroxide concentration low by dosing it in small amounts or via syringe pump would support this theory.

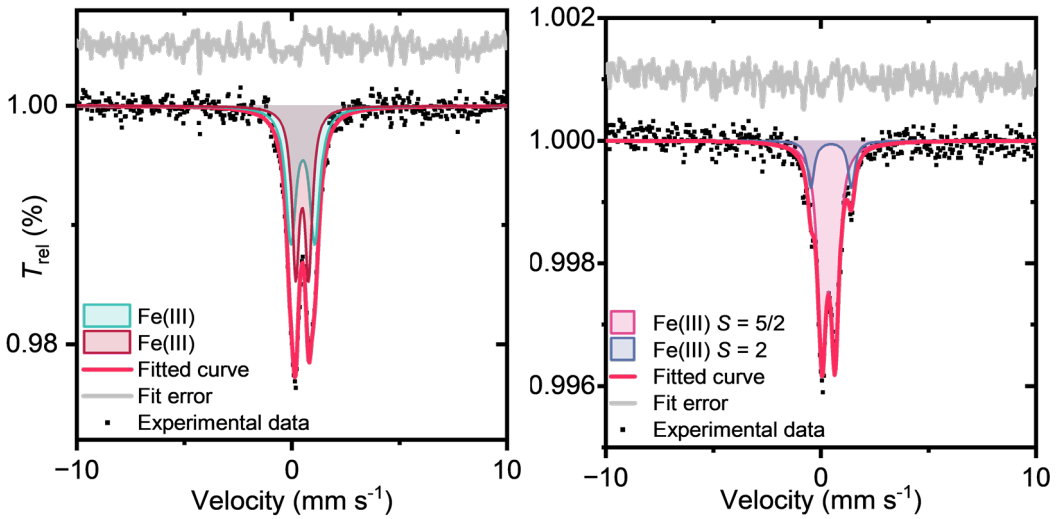

Figure 3.11: *Mössbauer spectrum of **C2b** in the presence of 6 equivalents of H_2O_2, measured at 77 K (left), and **C2b'** ($[\mu\text{-}O(Fe(PcLH_3)Br)_2]Br$, right).*

Although these results are not conclusive and further investigations are needed to determine which active species play a role in the catalytic oxidation of benzyl alcohols, in all other cases Mössbauer spectroscopy was an essential tool to gain a clear view of the oxidation and spin states of iron complexes. Another technique that was often decisive in the characterization of complexes was magnetometry, which is presented in the next section.

Magnetic characterization of selected complexes. The magnetic properties of the synthesized complexes were studied through Zero-Field-Cooled (ZFC), Field-Cooled (FC), and magnetization curves to fully validate the Mössbauer assigned spin states and to gain deeper insights into the bulk magnetic properties of the investigated compounds.

The first samples subjected to magnetic measurements were complexes **C2a** and **C2b**. To obtain magnetization data, a Quantum Design PPMS equipped with a VSM module was used to record ZFC and FC magnetic curves under an applied field of 0.5 T. In both cases, ZFC and FC curves overlapped, indicating the absence of magnetic irreversibility.

The temperature dependence of the molar magnetic susceptibility-temperature product ($\chi_M T$) for compounds **C2a** and **C2b** is shown in Figure 3.12. For compound

C2a, initial analysis using the Curie law yielded an effective magnetic moment (μ_{eff}) of 5.5164(4) μ_{B} (Bohr's magnetons), but clear deviations from ideal paramagnetic behavior were observed at lower temperatures. A subsequent Curie-Weiss law fit revealed antiferromagnetic interactions, with a Weiss temperature (θ) of 5.28 K and a μ_{eff} of 5.7063(7) μ_{B}. As clearly visible from the $\chi_M T$ plot (Figure 3.12 left), the Curie-Weiss law is adequate for fitting the low temperature range, but at higher temperatures, major deviations from paramagnetic behavior cause the fit to be less adequate also in this case. While these divergences could be addressed by adding a simple T-independent diamagnetic term, the fit was still unsatisfactory, and I decided to further investigate the origin of this phenomenon.

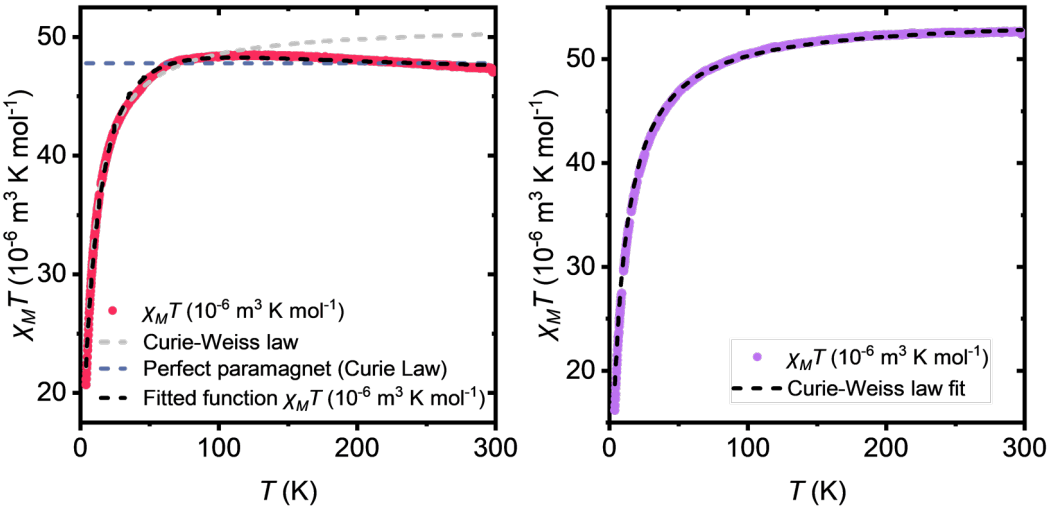

Figure 3.12: *$\chi_M T$ product as a function of temperature, for compound **C2a** (left), and for compound **C2b** (right).*

In systems with an odd number of electrons, such as Fe^{3+} (d^5), the spin multiplicity is even, and the degeneracy cannot be completely lifted in zero field, resulting in zero-field splitting. This effect is well described in O. Kahn's Molecular Magnetism,[174] from which the Van Vleck formalism was adapted to model the magnetic behavior of compound **C2a**, considering axial distortion and zero field splitting.

If the symmetry is low enough, all the components are twofold degenerate and are called Kramers doublets. The zero-field splitting within a $^{2S+1}\Gamma$ state without first-order angular momentum is expressed by the phenomenological Hamiltonian (3.1)

$$\mathbf{H}_{\text{ZFS}} = \mathbf{S} \cdot \mathbf{D} \cdot \mathbf{S} \tag{3.1}$$

where **D** is a symmetric and traceless tensor, and **S** is the polyelectronic spin operator. In matrix notation, the total spin Hamiltonian taking into account the Zeeman perturbation is then (3.2)

$$\mathbf{H} = \mu_{\mathrm{B}} \mathbf{S} \cdot \mathbf{g} \cdot H + \mathbf{S} \cdot \mathbf{D} \cdot \mathbf{S} \tag{3.2}$$

g being the **g**-tensor and H the magnetic field. Assuming that the **D**- and **g**-tensors have the same principal axes, it may be rewritten as (3.3)

$$\mathbf{H} = g_u \mu_{\mathrm{B}} \mathbf{S}_u H_u + D \left(\mathbf{S}_z^2 - \frac{S(S+1)}{3} \right) + E \left(\mathbf{S}_x^2 - \mathbf{S}_y^2 \right) \tag{3.3}$$

where the index u notes the direction of the applied magnetic field; g_u is the value of **g** and $\mathbf{S}_u$ is the component of **S** along this direction. D and E are the axial and rhombic zero-field splitting parameters, respectively. D and E are related to the principal values D_{uu} $(u = x, y, z)$ of the **D**-tensor through

$$D = \frac{3D_{zz}}{2} \tag{3.4}$$

$$E = \frac{|D_{xx} - D_{yy}|}{2} \tag{3.5}$$

In this case, only axial distortion will be considered, thus parameter E will be 0. The energy matrix on the $|M_S\rangle$ (spin quantum number) basis set for a spin sextet, for $H = H_z$ parallel to the unique axis, is the following:

$\left\vert\frac{5}{2}\right\rangle$	$\left\vert\frac{3}{2}\right\rangle$	$\left\vert\frac{1}{2}\right\rangle$	$\left\vert-\frac{1}{2}\right\rangle$	$\left\vert-\frac{3}{2}\right\rangle$	$\left\vert-\frac{5}{2}\right\rangle$
$\frac{5}{2}g_z\mu_{\mathrm{B}}H_z + \frac{25}{4}D$	0	0	0	0	0
	$\frac{3}{2}g_z\mu_{\mathrm{B}}H_z + \frac{9}{4}D$	0	0	0	0
		$\frac{1}{2}g_z\mu_{\mathrm{B}}H_z + \frac{1}{4}D$	0	0	0
			$-\frac{1}{2}g_z\mu_{\mathrm{B}}H_z + \frac{1}{4}D$	0	0
				$-\frac{3}{2}g_z\mu_{\mathrm{B}}H_z + \frac{9}{4}D$	0
					$-\frac{5}{2}g_z\mu_{\mathrm{B}}H_z + \frac{25}{4}D$

The eigenvalues are

$$\begin{aligned} E_{1,2} &= \pm \frac{g_z \mu_{\mathrm{B}} H_z}{2} \\ E_{3,4} &= 2D \pm \frac{3 g_z \mu_{\mathrm{B}} H_z}{2} \\ E_{5,6} &= 6D \pm \frac{5 g_z \mu_{\mathrm{B}} H_z}{2} \end{aligned} \tag{3.6}$$

where μ_{B} is Bohr's magneton and the zero-field energy of the $\left|\pm\frac{1}{2}\right\rangle$ Kramers doublet has been taken as the energy origin.

The energy levels E_n do not contain any quadratic term of H. In this case, the Van Vleck's formula is expressed as (3.7):

$$\chi = \frac{N \sum_n \left(E_n^{(1)}\right)^2 e^{\frac{-E_n^{(0)}}{kT}}}{kT \sum_n e^{\frac{-E_n^{(0)}}{kT}}} \tag{3.7}$$

where k is Boltzmann's constant. The Zeeman coefficients E_n^0 and E_n^1 can be derived from the expansion of the eigenvalues (3.6). This affords:

$$\chi_z = \frac{N g_z^2 \mu_B^2}{4kT} \frac{1 + 9e^{\frac{-2D}{kT}} + 25e^{\frac{-6D}{kT}}}{1 + e^{\frac{-2D}{kT}} + e^{\frac{-6D}{kT}}} \tag{3.8}$$

For $H = H_x$, perpendicular to the unique axis, the elements of the energy matrix are calculated as:

$\left\vert\frac{5}{2}\right\rangle$	$\left\vert-\frac{5}{2}\right\rangle$	$\left\vert\frac{3}{2}\right\rangle$	$\left\vert-\frac{3}{2}\right\rangle$	$\left\vert\frac{1}{2}\right\rangle$	$\left\vert-\frac{1}{2}\right\rangle$
$6D$	0	$\frac{\sqrt{5}}{2} g_x \mu_B H_x$	0	0	0
	$6D$	0	$\frac{\sqrt{5}}{2} g_x \mu_B H_x$	0	0
		$2D$	0	$\sqrt{2} g_x \mu_B H_x$	0
			$2D$	0	$\sqrt{2} g_x \mu_B H_x$
				0	$\frac{3}{2} g_x \mu_B H_x$
					0

Assuming that $|D|$ is much larger than $g_x \mu_B H_x$, the eigenvalues of this matrix may be approximated by (3.9):

$$\begin{aligned} E_{1,2} &= 6D + \frac{5 g_x^2 \mu_B^2 H_x^2}{16D} \\ E_{3,4} &= 2D + \frac{11 g_z^2 \mu_B^2 H_x^2}{16D} \\ E_{5,6} &= \pm \frac{3 g_x \mu_B H_x}{2} - \frac{g_x^2 \mu_B^2 H_x}{D} \end{aligned} \tag{3.9}$$

The Van Vleck's formula for χ_x is derived similarly, however, because the energies E_n contain non-linear terms, the second-order Zeeman coefficient $E_n^{(2)}$ has to be taken into account. Thus, the Van Vleck's formula is (3.10):

$$\chi = \frac{N \sum_n \left(\frac{\left(E_n^{(1)}\right)^2}{kT} - 2E_n^{(2)} \right) e^{\frac{-E_n^{(0)}}{kT}}}{\sum_n e^{\frac{-E_n^{(0)}}{kT}}} \tag{3.10}$$

Again, expanding the E_n functions yields the $E_n^{(0)}$, $E_n^{(1)}$ and $E_n^{(2)}$ Zeeman coefficients, from which the perpendicular magnetic susceptibility can be calculated:

$$\chi_x = \frac{N g_x^2 \mu_B^2}{4} \frac{\frac{9}{kT} + \frac{8}{D} - \frac{11e^{-\frac{2D}{kT}}}{2D} - \frac{5e^{\frac{-6D}{kT}}}{2D}}{1 + e^{\frac{-2D}{kT}} + e^{\frac{-6D}{kT}}} \tag{3.11}$$

Bulk magnetometry cannot distinguish perpendicular from axial susceptibility, thus the averaged susceptibility is calculated as(3.12):

$$\chi_{\perp+\parallel} = \frac{\chi_z + 2\chi_x}{3} \tag{3.12}$$

The first fit was not satisfactory enough, as it did not take into account the intermolecular interactions between the iron centers, which are evident at low temperatures, where an antiferromagnetic interaction produces a fall in effective magnetization. To take this into account, a *pseudo*-Weiss temperature ϑ was introduced. The function was reevaluated exchanging the variable T with $x = T - \vartheta$, and it was fitted to the χT data using the `scipy.optimize.curve_fit` Python function, optimizing the parameters g_z, g_x, D and ϑ.

The final equation, thus, was as follows (3.13):

$$\text{with } \chi_{\perp+\parallel} = \frac{\chi_z + 2\chi_x}{3} \tag{3.13}$$

$$\chi_z = \frac{N g_z^2 \mu_B^2}{4k(T-\vartheta)} \frac{1 + 9e^{\frac{-2D}{k(T-\vartheta)}} + 25e^{\frac{-6D}{k(T-\vartheta)}}}{1 + e^{\frac{-2D}{k(T-\vartheta)}} + e^{\frac{-6D}{k(T-\vartheta)}}} \tag{3.14}$$

$$\chi_x = \frac{N g_x^2 \mu_B^2}{4} \frac{\frac{9}{k(T-\vartheta)} + \frac{8}{D} - \frac{11e^{-\frac{2D}{k(T-\vartheta)}}}{2D} - \frac{5e^{\frac{-6D}{k(T-\vartheta)}}}{2D}}{1 + e^{\frac{-2D}{k(T-\vartheta)}} + e^{\frac{-6D}{k(T-\vartheta)}}} \tag{3.15}$$

Here, $\chi_{\perp+\parallel}$, χ_x, χ_z represent the global magnetic susceptibility and the magnetic susceptibility on the x and the z axis, respectively. N is Avogadro's number, g is the value of the g-tensor, μ_B is the Bohr's magneton, k is Boltzmann's constant. The results of the fit are reported in Table 3.2, while the function is plotted along with experimental data in Figure 3.12.

In contrast, complex **C2b** displays characteristic Curie-Weiss behavior, with antiferromagnetic intermolecular interactions, as evidenced by a gradual decrease in $\chi_M T$ at low temperatures (Figure 3.12, right). Its magnetic response is well described by the Curie-Weiss law over the entire temperature range, consistent with a high-spin Fe(III) center. The effective magnetic moment of 5.87(4) μ_B is in excellent agreement with the spin-only value of 5.91 μ_B, and the Weiss temperature is −7.66 K (Table 3.2).

Next, the χ_M and χ_M^{-1} temperature dependence of compound **C3a** is presented (Figure 3.13). In this case, magnetometry supports the Mössbauer spin state assignment. The compound shows a paramagnetic behavior, with some evident de-

Table 3.2: *Curie and Curie-Weiss laws fits for compounds **C2a** and **C2b**, fitted parameters for the Van Vleck equation of compound **C2a**.*

Parameter	C2a	C2b
μ_{eff} (μ_{B}), Curie Law	5.5164(4)	5.7506(2)
μ_{eff} (μ_{B}), Curie-Weiss Law	5.7063(7)	5.87(4)
θ_W (K)	−5.28	−7.66
g_{tot} [a]	2.041(2)	-
D ($\text{cm}^{-}1$)	20.0(1)	-
ϑ (K)	−2.44(4)	-

[a] $g_{\text{tot}} = \frac{2g_x+g_z}{3}$.

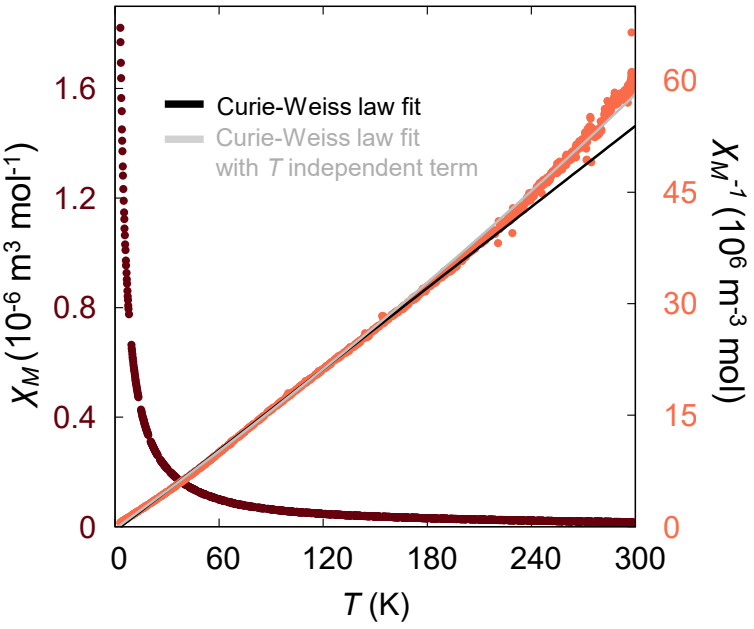

Figure 3.13: *χ_M and χ_M^{-1} as a function of temperature for compound **C3a**. Courtesy of prof. Dominika Zákutná.*

viations from Curie-Weiss law at higher temperatures. In this case, these deviations were assessed by introducing a temperature-independent diamagnetic term (χ_0), such that the Curie-Weiss law becomes (3.16):

$$\chi_M = \frac{C}{T - \theta_W} + \chi_0, \; \chi_M^{-1} = \frac{T - \theta_W}{\chi_0 (T - \theta_W) + C} \tag{3.16}$$

As a result, the compound shows an effective magnetic moment of 1.93(1) μ_B, which is close to the expected value for iron(III) $S = {}^1/_2$ ions (1.73 μ_B). This small deviation is acceptable, since low-spin iron(III) has a $^2T_{2g}$ ground term and a minor orbital angular momentum contribution has to be expected.

A similar case was complex **C2d** ($[Fe(PcLH_3)Cl_2]$, Figure 3.14). **C2d** is a high-spin iron(II) compound ($S = 2$), which shows paramagnetic response across the temperature ranges at which it was measured. Also in this case, a slightly antiferromagnetic behavior is visible at low temperatures, as the quenching of the $\chi_M T$ product below 67 K clearly shows (Figure 3.14, right). As for **C3a**, deviations from Curie-Weiss law were visible at higher temperatures, and also in this case they were well fitted by introducing a temperature-independent diamagnetic term. Fitting equation 3.16 to this data yielded an effective magnetic moment of 5.10(4) μ_B (fitting results are summarized in Table A.47). Again, the result is slightly higher than the spin-only value of 4.9 μ_B, which is totally expected since also high-spin iron(II) has a $^5T_{2g}$ ground term and an orbital angular momentum contribution is present.

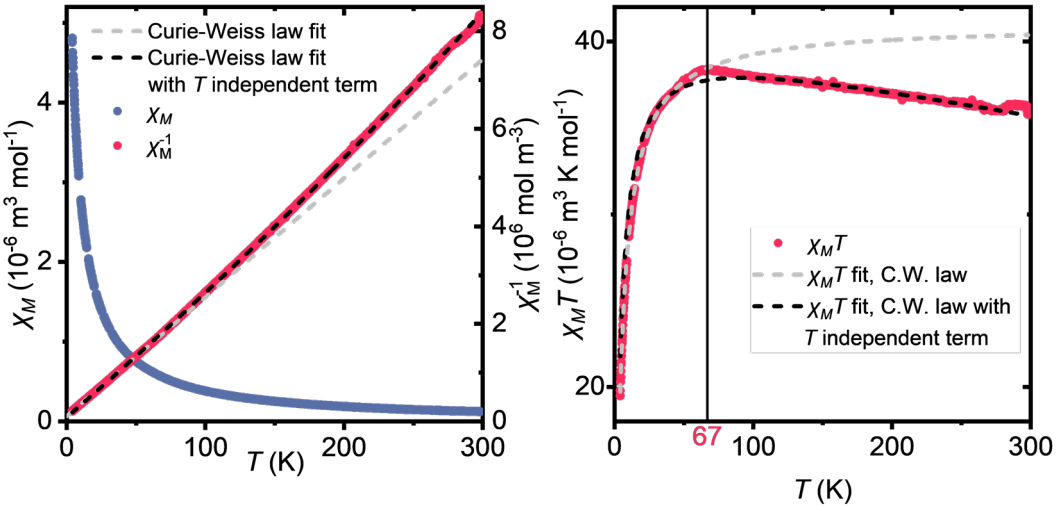

Figure 3.14: *χ_M and χ_M^{-1} as a function of temperature for compound **C2d** (left) and $\chi_M T$ product as a function of temperature, for the same compound (right).*

C2d and **C3d** were synthesized starting from complex **C4a** ($[Fe_4Cl_8(THF)_6]$), which is a common precursor for many applications of iron in organometallic chemistry.[175] Together with other tetrahydrofuran adducts of metallic chlorides (among which $[Co_4Cl_8(THF)_6]$, **C4b**, and $\{(Mn_4Cl_8(THF)_6)(Mn(THF)_2Cl_2)\}_\infty$, **C4c**), **C4a** is regarded as a reliable source for synthesizing iron complexes and for rendering ferrous chloride more synthetically accessible. The synthesis of **C4a** and analogous

cobalt or manganese clusters is referred as *cluster excision*, and involves refluxing the corresponding anhydrous metallic chlorides in THF, a process that cleaves the bridging bonds and stabilizes finite cluster motifs, yielding discrete tetranuclear complexes for Fe and Co, while in the case of manganese it results in a chain-like polymer.[176]

These clusters include two nonequivalent M^{2+} sites, and consequently two different possible superexchange interactions (to be more precise, the manganese polymer has three nonequivalent sites and thus three different superexchange interactions). Consequently, investigating their magnetic behavior was deemed compelling. As I had already synthesized **C4a** as a precursor for $FeCl_2$ derivatives, $[Fe_4Cl_8(THF)_6]$ was the first compound which magnetic properties were measured.

C4a is characterized by a tetrameric structure, where the iron centers are connected together by μ_2-Cl and μ_3-Cl bridges with Fe-Cl-Fe angles of approximately 90° that could mediate ferromagnetic interactions through superexchange (Figure 3.15). Moreover, the iron centers could be involved in antiferromagnetic exchange interactions rising from their close distance. To explore these properties, first ZFC and FC measurements were conducted with a low external magnetic field (0.5 T, Figure 3.17, top left and right). In these conditions, the compound behaves as a paramagnet, with an effective magnetic moment of 5.5483(1) μ_B for each Fe^{2+} ion and a Weiss temperature of 7.40 K. Observing the $\chi_M T$ plot, however, it is immediately clear that this compound is not easily ascribed to the *paramagnetic* state. Above 9 K, the $\chi_M T$ product decreases with temperature, while, below that temperature, there is a clear drop in the $\chi_M T$ product.

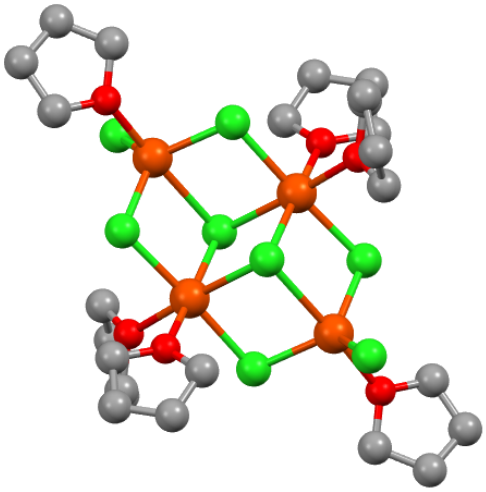

Figure 3.15: $[Fe_4Cl_8(THF)_6]$ (***C4a***) *molecular structure representation.*

This behavior suggests a competition between *ferromagnetic* ($J > 0$) and *antiferromagnetic* ($J < 0$) interactions. For reference, in a simpler dinuclear compound with two d^8 ions, where only one of the two interactions would be visible, the magnetic susceptibility is given by (3.17):[177]

$$\chi = \frac{2Ng^2\mu_B}{kT\left(3 + e^{-J/kT}\right)} \tag{3.17}$$

and the typical χT plot would have the appearance of that in Figure 3.16: upon cooling, for $J > 0$ the χT product should increase (red line, in case of d^8 ions, like in the example, it should tend to $^2/_3$); for $J < 0$, the χT product should continuously decrease, while for $J = 0$ it should be constant throughout the temperature range.

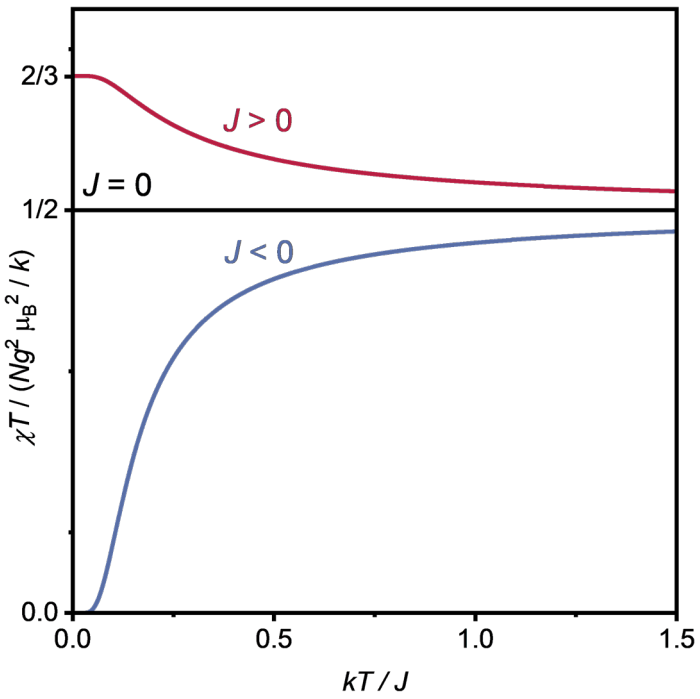

Figure 3.16: *χT (in $Ng^2\mu_B^2/k$ units) versus $kT/|J|$ curves for a model dinuclear d^8 compound with J positive, negative, or zero.*[174]

In **C4a**, since it is tetranuclear and permits two distinct coupling modes, the situation becomes considerably more complex, but qualitatively, both trends are visible, with a switch from a $J > 0$ interaction prevailing above 9 K to a $J < 0$ interaction prevailing below 9 K.

To gain a deeper understanding of these competing interactions, magnetization curves (M versus $\mu_0 H$) were recorded at 10 K and 4 K. While two sligthly open hysteresis loops are already visible at 10 K (Figure 3.17, center left), lowering the temperature to 4 K allowed to discern at least two different magnetic transitions (Figure 3.17, center right).

Between −2.5 and 2.5 T the curve is linear, without any open hysteresis loop. Over |2.5| T, a open hysteresis is observed. Proceeding to higher applied fields, two discontinuities are visible at ±3.8 and ±4.6 T. These points are denoted by grey dotted lines in Figure 3.17 (center, right). These findings may signify a state transition in the material. At low magnetic fields the compound demonstrates antiferromag-

netic properties, while at higher fields, ferromagnetic behavior becomes clearly predominant.

This was confirmed by ZFC and FC measurements at 3.5 T (Figure 3.17, bottom left) and 6 T (Figure 3.17, bottom right). In the first case, a transition to an antiferromagnetic state is clearly visible, with χ_M increasing continuously upon cooling, and then sharply transitioning to antiferromagnetic behavior at $T_N = 22$ K. At 6 T, a similar response is detected over $T_C = 17$ K, while at lower temperatures the compound transitions to a ferromagnetic state.

These results were very intriguing, and suggested that it would be interesting to study the magnetic properties of similar clusters. First, I focused on $\{(Mn_4Cl_8(THF)_6)(Mn(THF)_2Cl_2)\}_\infty$ (**C4c**), which forms a linear polymer of $[Mn_4Cl_8(THF)_6]$ clusters linked by $[MnCl_2(THF)_2]$ bridges. The magnetic measurements of **C4c** are reported in Appendix A (Figures A.55 and A.56); unfortunately neither obvious sign of exchange nor open hysteresis curves were observed, only weak ferromagnetic interactions were observable in the $\chi_M T$ versus temperature plot.

Zhao et al.[175] describe **C4b** as a *canted metamagnet* at low temperatures. It exhibits an intricate behavior, with the $\chi_M T$ product shows a minimum at 12 K and signatures of magnetic ordering emerging below 3.5 K. Because the tetramer contains two distinct Co(II) sites which are probably stabilized by spin frustration effects, the compound exhibits an intermediate spin state.

$[Co_4Cl_8(THF)_6]$ (**C4b**), was not analyzed by magnetometric methods for time reasons. However, given its interesting properties, preliminary Inelastic Neutron Scattering (INS) measurements were conducted to support a proposal for full characterization at Institut Laue-Langevin (ILL) in Grenoble. When measuring the sample at 1.5 K and 3.5 Å, magnetic excitations between 2 and 4.5 meV (Figure 3.18) were detected.

UV-VIS spectroscopy of complexes C2a-c. Turning our attention back to macrocyclic compounds, the last characterization technique that was applied to complexes **C2a-c** is UV-VIS spectroscopy. Moreover, in collaboration with dr. Fausto Cargnoni and dr. Mario Italo Trioni, DFT (Density Functional Theory) calculations were performed to investigate the electronic transitions of complexes **C2a-c**.

Figure 3.19 shows the experimental and calculated UV-Vis spectra of **C2a**, **C2b**, and **C2c** in acetonitrile. The calculated spectra reproduce the experimental profiles well, although the computed absorption bands appear at somewhat different energies compared to the experimental ones, which is expected given the known limitations of the TD-DFT approach.[178] Importantly, for the specific systems investigated here, the discrepancy between computed and measured spectra enables a straightforward, peak-by-peak comparison of the absorption features.

The experimental spectrum of **C2a** displays three main absorption bands, centered at 258, 320, and 377 nm, which are likewise reproduced in the calculated spec-

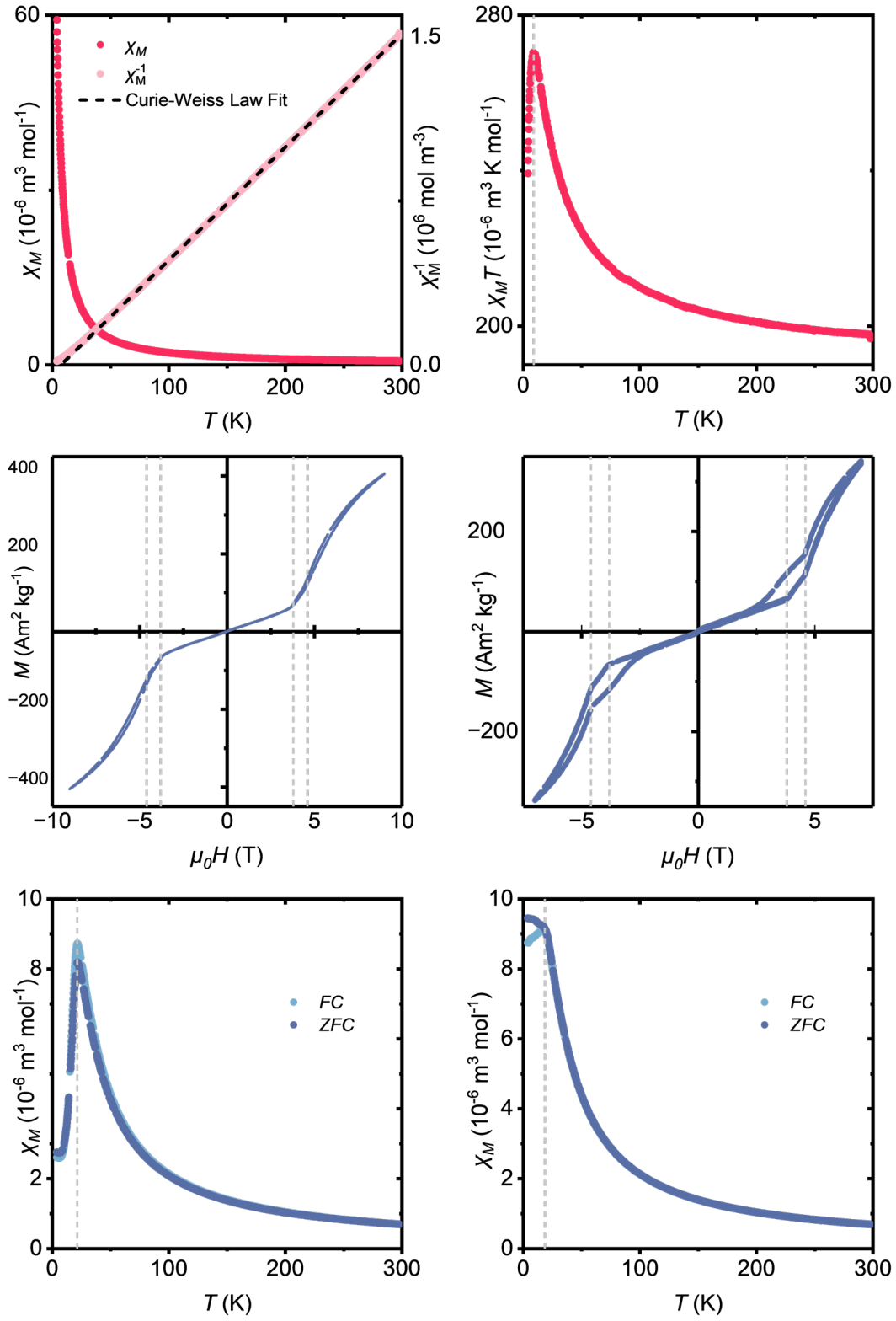

Figure 3.17: *Magnetic data of tetranuclear cluster* ***C4a****:* χ_M *and* χ_M^{-1} *as a function of temperature, measured at 0.5 T (top, left);* $\chi_M T$ *product as a function of temperature, measured at 0.5 T (top, right); magnetization measured as a function of external magnetic field, at 10 K (center, left); magnetization measured as a function of external magnetic field, at 4 K (center, right);* χ_M *as a function of temperature, measured at 3.5 T (bottom, left);* χ_M *as a function of temperature, measured at 6 T (bottom, right).*

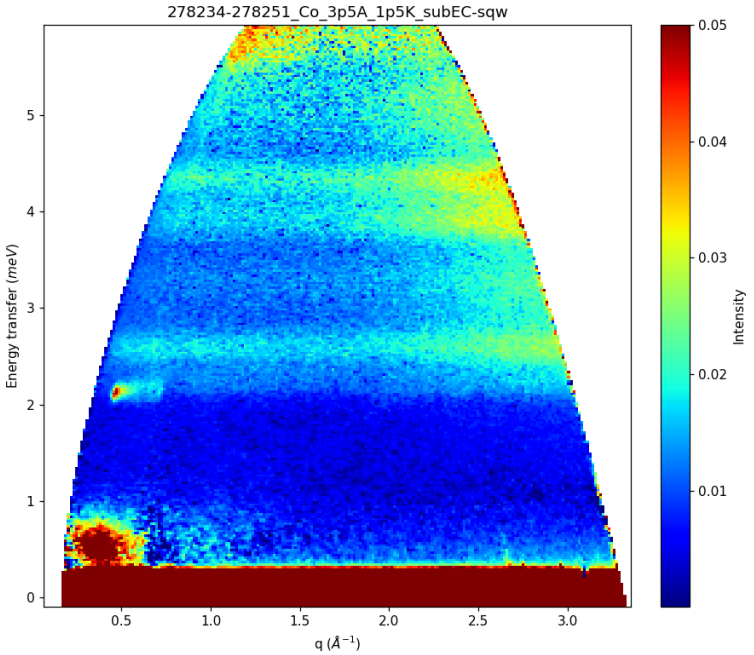

Figure 3.18: *$S(q, \omega)$ map at 1.5 K and 3.5 Å of **C4b**. Courtesy of Ketty Beauvois and Lucile Mangin-Thro.*

tra. As anticipated, each of these peaks does not result from single electronic transitions. Instead, they arise from three groups of pyclen/Cl ligand-to-metal transitions, which progressively lose intensity and become more diffuse as the photon energy decreases. Examination of these data shows the presence of chlorine-to-iron transitions, with the associated photon energies falling within the range probed in the present experiments. This finding motivated a computational study of the potential Fe–Cl homolytic bond cleavage. The calculated energy threshold for homolytic rupture of an Fe–Cl bond is 3.34 eV, corresponding to a wavelength of 371 nm, which lies within the lowest-energy absorption band (green bands in Figure 3.19a and b). As illustrated in Figure 3.20 (left panel), wavefunction analysis of the transitions just above this threshold shows that, upon excitation, a single electron is transferred from the chloride ligands to the metal center, and the complex acquires sufficient energy to release a chlorine radical. Although this does not constitute a rigorous demonstration that homolytic dissociation actually takes place–since alternative relaxation pathways and other limiting factors are not taken into account–it nonetheless provides strong evidence that such a process is plausible, because the excited state lies at higher energy than the species formed upon homolytic bond cleavage.

In **C2b**, the lower-energy absorption bands are red-shifted relative to **C2a** and are centered at 395 and 470 nm, respectively (Figure 3.19c). Apart from this extension of the absorption toward longer wavelengths, the assignment of the electronic transitions follows considerations analogous to those described above for **C2a**. The calculated threshold for homolytic cleavage of the Fe–Br bond in **C2b** is 2.94 eV

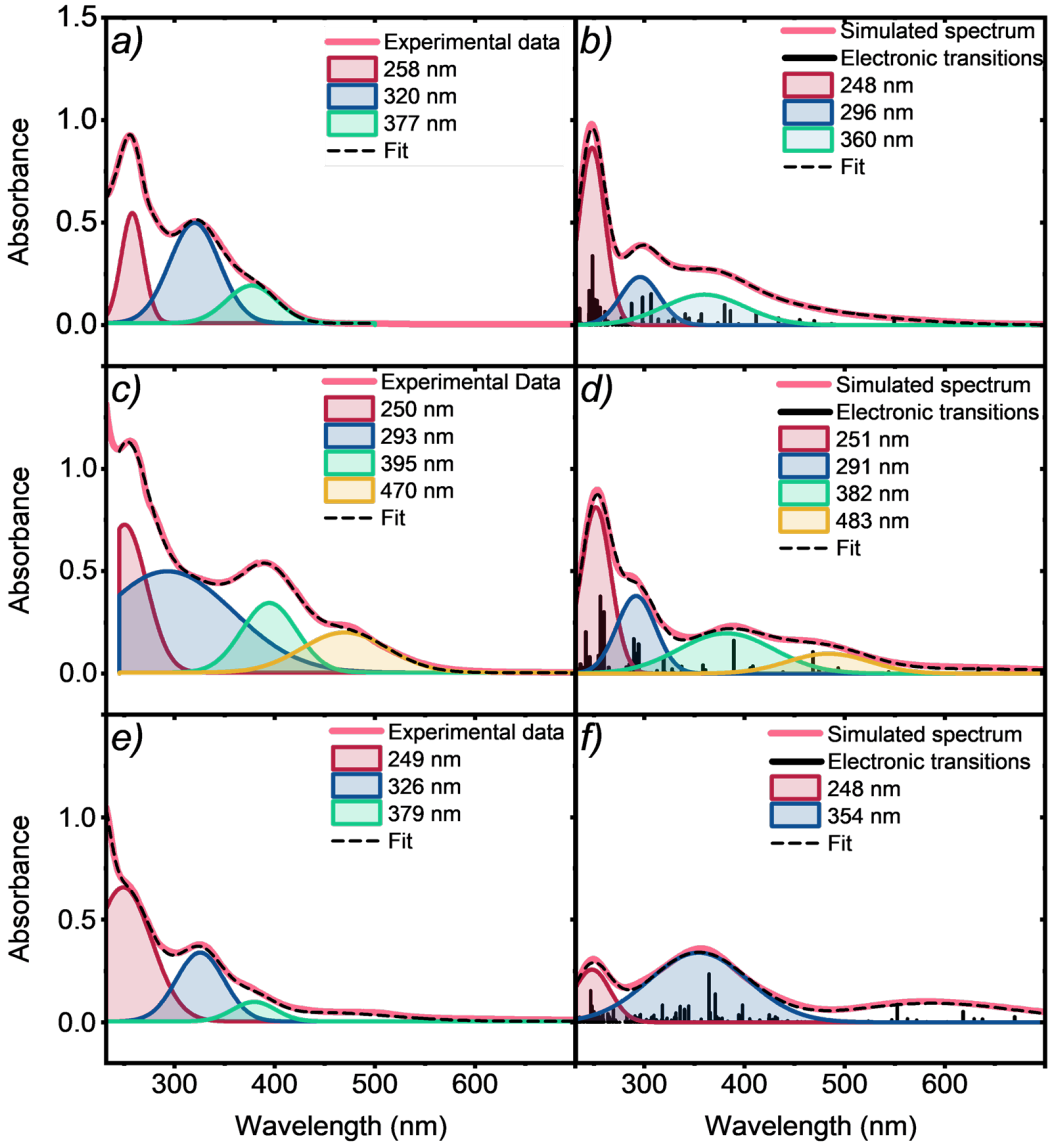

Figure 3.19: *UV-VIS experimental (left) and theoretical (right) spectra of* ***C2a*** *(top) (a and b, respectively),* ***C2b*** *(middle) (c and d), and* ***C2c*** *(bottom) (e and f) complexes. Left panels: the experimental data are reported as a solid red line, while data obtained by Gaussian fitting are depicted as a dashed black line. Right panels: the computed electronic transitions are reported as solid black lines; the solid red line (the simulated spectrum) is obtained by smearing delta-like absorption peaks with a Gaussian function, and the dashed black line is obtained by fitting the simulated spectrum with the same criterion adopted for experimental data. The fitting Gaussian functions encompass several transitions each, and they are reported as a guide to the eye. In Figure A.62 (Appendix A), all the Gaussians that were used to fit the spectra are reported.*

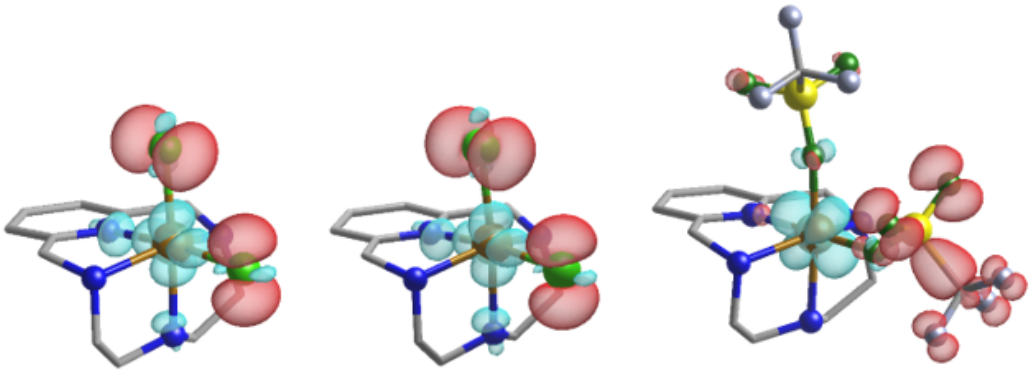

Figure 3.20: *Representative electron density maps for sample electronic transitions above the dissociation threshold of* ***C2a*** *(left),* ***C2b*** *(middle), and* ***C2c*** *(right). Maps are obtained as the difference between the electron density of the excited state and the ground state, and they refer to the main components of transitions at 357 nm (left), 389 nm (middle), and 486 nm (right). Positive values are in light-blue and negative values are in red. In the three reported transitions, electron excitation removes an electron from the ligands (X) and localizes it onto the Fe atom, which is likely to induce homolytic Fe–X dissociation when this is energetically allowed, i.e. in the case of* ***C2a*** *and* ***C2b****. Credits: Fausto Cargnoni and Mario Italo Trioni.*

(corresponding to 421 nm), placing it between the lowest-energy electronic transitions (green and orange bands in Figure 3.19c and d). Notably, the computed band centered at 382 nm (green band in Figure 3.19d) shows a pronounced Br-to-metal charge-transfer character, as depicted in Figure 3.20 (middle). This intense transition is likely the primary contributor to the photoinduced homolytic dissociation of an Fe–Br bond in **C2b** (vide infra).

The experimental spectrum of **C2c** differs somewhat from those of **C2a** and **C2b**. It displays two intense bands centered at 249 and 326 nm, followed by a weak, broad band peaking at 379 nm. The data also reveal an additional smooth, broad shoulder at even longer wavelengths. This feature indicates the presence of several low-intensity transitions distributed over a wide region around 500 nm.

The theoretical simulation of the absorption profile of **C2c** likewise yields two distinct peaks at 248 and 354 nm, in overall agreement with the measurements. However, theory predicts similar intensities for these two bands, whereas experimentally the 249 nm peak is significantly more intense than the one at 326 nm. At longer wavelengths, first-principles calculations foresee a sparse manifold of transitions spanning the 550-650 nm range. This picture is broadly consistent with experiment, even though the calculated spectrum does not reproduce all the fine details of the measured one.

Overall, the allowed electronic transitions of **C2c** extend over a broader energy interval than those of **C2a** and **C2b**. Most transitions possess partial ligand-to-metal charge-transfer character and have comparable intensities, which results in a rather featureless spectrum. The difficulty in capturing the finer aspects of the experimental spectrum of **C2c** most likely reflects the more intricate electronic structure of this complex compared to **C2a** and **C2b**, and is therefore consistent with the overall re-

liability of the adopted computational protocol.[179]

A direct DFT calculation of the energy required for homolytic cleavage of the Fe–OTf bond in **C2c** was hindered by the challenge of accurately describing the $^{\bullet}$OTf radical (Table A.29). Therefore, this energy was estimated as 3.89 eV (corresponding to 319 nm) by comparing the relative stabilities of the Cl$^{\bullet}$ and $^{\bullet}$OTf radicals at the CISD level, using the bond dissociation free energies (BDFEs) of H–Cl and H–OTf (CISD = Configuration Interaction with Single and Double excitations). This relatively high value is consistent with the expected instability of the oxygen-centered $^{\bullet}$OTf radical and effectively rules out its generation from **C2c** under visible-light irradiation.

3.2.3 Photo-oxidation of *p*-xylene to *p*-tolualdehyde[*180*]

With the UV-VIS spectroscopy and DFT calculations suggesting the possibility of promoting the homolytic cleavage of the Fe–X bond by light, the next logical step was to explore the photocatalytic activity of Fe(PcLH$_3$) complexes.

Hydrogen peroxide is an attractive oxidant, as its only byproduct is water; however, the truly ideal oxidant is molecular oxygen, O_2, which aligns with sustainability goals in industrial processes.[181] In this context, the use of visible light together with dioxygen for the photocatalytic oxidation of hydrocarbons represents an atom-economical and greener alternative to conventional methods.[182,183]

Iron complexes have been extensively studied for the chemical activation of oxidants, yet their light-driven reactivity in photocatalytic processes remains comparatively underexplored.[184] They have attracted renewed attention with the recent resurgence of photocatalysis in sustainable chemistry and synthetic organic transformations, while solar-driven reforming is emerging as a promising technology for circular chemical industries.[185] Recent work has focused on the photochemical behavior of FeX_3 (X = Cl, Br) in the upcycling of polystyrene, proceeding via the photogeneration of X$^{\bullet}$ radicals.[186,187]

As a first challenge, my research group, together with the joint effort from Andrea Sartorel group, focused on the photo-oxidation of *p*-xylene. Among its oxidation products, terephthalic acid is particularly relevant to the polymer industry, with an estimated annual production of approximately 90 million tons in 2024 via the Amoco process. This method employs a cobalt-manganese-bromide catalyst in acetic acid as the solvent, under conditions of 175-225 °C and 15-30 bar air pressure.[188–191] In addition to terephthalic acid, several intermediate oxidation products, such as *p*-methylbenzyl alcohol, *p*-tolualdehyde, and *p*-toluic acid, have attracted significant interest. The oxidation of *p*-xylene requires activation of the benzylic C–H bonds, which possess a bond dissociation free energy of 80 kcal mol^{-1}. The oxidative activation of C–H bonds is a highly active research area,[192–197] and there is growing interest in developing photochemical systems capable of oxidizing *p*-xylene under visible light.

Recently, Sun and co-workers employed UV irradiation (Hg lamp, 500 W, 0–2 Sun) to enhance an ozonization process, achieving an 84% yield of terephthalic acid in acetonitrile.[198] In a continuous-flow photoreactor, tetrabutylammonium decatungstate catalysis under 365 nm irradiation produced more than 90% terephthalic acid.[199] Titanium oxide nanoparticles have been activated at the same wavelength to oxidize *p*-xylene to *p*-methylbenzyl alcohol and *p*-tolualdehyde as the primary products.[200] Alternatively, quinone-based organic photocatalysts, capable of promoting hydrogen atom transfer (HAT) reactivity, have been investigated for the visible-light oxidation of *p*-xylene in acetone, yielding *p*-toluic acid as the main product, while overoxidation of *p*-toluic acid led to approximately 27% formation of terephthalic acid.[201]

Thus, the recent advances in photocatalysis, the intriguing light-absorption properties of pyclen complexes, as well as their proven performance in oxidative processes were strong reasons to investigate their photochemical activity. Photoexcitation of ligand-to-metal charge transfer transitions in coordination complexes provides an effective route to generate halogen radicals under low-energy irradiation.[202] These radicals are highly relevant for C–H functionalization chemistry,[203] as their reactivity is dominated by their ability to mediate hydrogen atom transfer (HAT) steps.[204,205] This behavior is governed by the strength of the H–halogen bond, with bond dissociation energies of 102 kcal mol^{-1} for HCl, 87 kcal mol^{-1} for HBr, and 71 kcal mol^{-1} for HI. As a consequence, $Cl^{\bullet}$ is a particularly strong hydrogen atom abstractor, whereas $I^{\bullet}$ is generally ineffective in HAT processes.[206]

The photochemical reactivity of **C2a-c** towards the oxidation of *p*-xylene (80 mM in acetonitrile solution) was therefore evaluated using a home-made photoreactor equipped with inexpensive household lamps emitting white light (33 mW cm^{-2}, corresponding to approximately one third of standard solar irradiation).[207] The emission spectrum of the light source, overlapped with the absorption spectra of the Fe pyclen derivatives, is shown in Figure 6.7 (Chapter 6). After irradiation, the reaction mixtures from the photocatalytic experiments were analyzed by ^{1}H NMR spectroscopy, with mesitylene added as an internal standard. The corresponding results are summarized in Table 3.3 and are discussed below:

(a) Among the investigated iron complexes, **C2b** was the only system displaying significant photocatalytic activity (entries 1–3 in Table 3.3). This complex selectively promoted the formation of *p*-tolualdehyde as the major oxidation product, affording a yield of 31±5%, which corresponds to a turnover number of 9.9±1.6 when calculated per iron center (entry 2 in Table 3.3). These values were derived from six independent experiments, including measurements performed on two separate batches of **C2b**. Control reactions established that irradiation, the iron catalyst, and the presence of an aerobic atmosphere are all required for the photochemical oxidation of *p*-xylene. Performing the reaction under an O_2 atmosphere did not result in any substantial enhancement

Table 3.3: *Photocatalytic oxidation of p-xylene to p-tolualdehyde.*

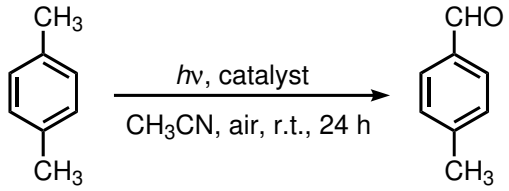

Entry	Catalyst	Deviations from standard conditions	*p*-Tolualdehyde yield (%) / selectivity (%)	Other products, yield (%)
1	**C2a**	–	≈1	–
2	**C2b**	–	31±5/79±5	*p*-Toluic acid, 7.5±3 Terephthalic acid, 1.5±0.5 *p*-Methylbenzyl alcohol, <1
3	**C2c**	–	5	–
4	**C2b**	O_2 instead of air	31/81	*p*-Toluic acid, 6 *p*-Methylbenzyl alcohol, 1
5	**C2b**	Acetone as solvent	20/55	*p*-Toluic acid, 15 *p*-Methylbenzyl alcohol, <1
6	**C2b**	Propylene carbonate as solvent	2/>95	–
7	**C2b**	In *p*-xylene neat	–	–
8	$FeCl_3$	–	24±3/56	*p*-Toluic acid, 13 Terephthalic acid, 1 *p*-Methylbenzyl alcohol, 5
9	$FeBr_3$	–	20/66	*p*-Toluic acid, 6 *p*-Methylbenzyl alcohol, 4
10	$FeCl_3$	Acetone as solvent	4/22	*p*-Toluic acid, 5 Terephthalic acid, 9
11	**C2b**	LED 405 nm[a]	21/87	*p*-Toluic acid, 1 *p*-Methylbenzyl alcohol, 2

Standard conditions: 1 mL of solution containing 80 mM *p*-xylene and 2.5 mM iron catalyst in acetonitrile, irradiation with white light (33 mW cm^{-2}) for 24 h under an air atmosphere. [a]Irradiation with a blue LED (405 nm, 18 mW cm^{-2}) for 2 hours.

of either yield or product selectivity (entry 4 in Table 3.3).

(b) A selectivity of 79±5% toward *p*-tolualdehyde was observed relative to other oxidation products, with *p*-toluic acid detected as a minor component. The enhanced selectivity can be rationalized by considering C–H bond strengths in the relevant substrates. In aromatic aldehydes, the formyl C–H bond is significantly stronger than the benzylic C–H bond of a $-CH_3$ substituent. For instance, benzaldehyde exhibits a C–H bond dissociation free energy of 89 kcal mol^{-1}, whereas the corresponding value for *p*-xylene is 80 kcal mol^{-1}.[194,206] As a consequence, further oxidation of *p*-tolualdehyde is energetically less favorable than the initial oxidation of *p*-xylene, accounting for the high product selectivity observed.

(c) The photocatalytic activity of **C2b** was retained when acetone was employed as the reaction solvent[186] (entry 5 in Table 3.3), albeit with reduced selectivity, affording a *p*-tolualdehyde yield of 20% and a selectivity of 55%. The reaction was also examined in propylene carbonate as a greener solvent; however, only a low conversion was achieved, corresponding to a product yield of 2% (entry 6 in Table 3.3). In contrast, no detectable reactivity was observed when the reaction was carried out in neat *p*-xylene (entry 7 in Table 3.3). Taken together, these observations point to a non-innocent role of the solvent in enabling the desired reactivity.

(d) Photochemical activity was also detected for $FeCl_3$ and $FeBr_3$,[186] although both systems displayed lower overall yields compared to **C2b** (entries 8–10 in Table 3.3). In these cases, a reduction in reaction selectivity was observed, accompanied by increased formation of *p*-methylbenzyl alcohol and *p*-toluic acid as the main by-products.

(e) The reaction mediated by **C2b** was also performed under monochromatic irradiation using a 405 nm LED as the light source, affording a *p*-tolualdehyde yield of 21% after 2 h with a selectivity of 87% (entry 11 in Table 3.3). Quantification of the photon flux absorbed by the system, as determined using a power meter, allowed the quantum yield for *p*-tolualdehyde formation at 405 nm (Φ_{405}) to be estimated at 0.14%.

Taken together, these observations are consistent with the photoinduced generation of bromine radicals, which initiate hydrogen atom transfer (HAT) from *p*-xylene to form H−Br and a *p*-xylene-centered radical. Subsequent reaction of this radical with dioxygen is expected to yield an organic peroxy radical, which can in turn abstract a hydrogen atom from *p*-xylene, thereby sustaining a radical chain process (Scheme 3.2.3).

Support for the involvement of reactive oxygen species was obtained by EPR spectroscopy using 5-*tert*-butoxycarbonyl-5-methyl-1-pyrroline *N*-oxide (BMPO) as a spin trap.[208] Under these conditions, a multi-component EPR signal was detected that is compatible with the formation of BMPO adducts with peroxide-type radi-

cals.[209,210] Due to the low signal intensity, reliable spectral simulation and unambiguous assignment of the individual components were not possible (Figure 3.21). BMPO was selected in preference to DMPO (5,5-dimethyl-1-pyrrolidine-*N*-oxide) due to its greater stability under the experimental conditions;[208,209] indeed, only very weak EPR signals were observed when DMPO was employed as the spin trap.

Mechanism

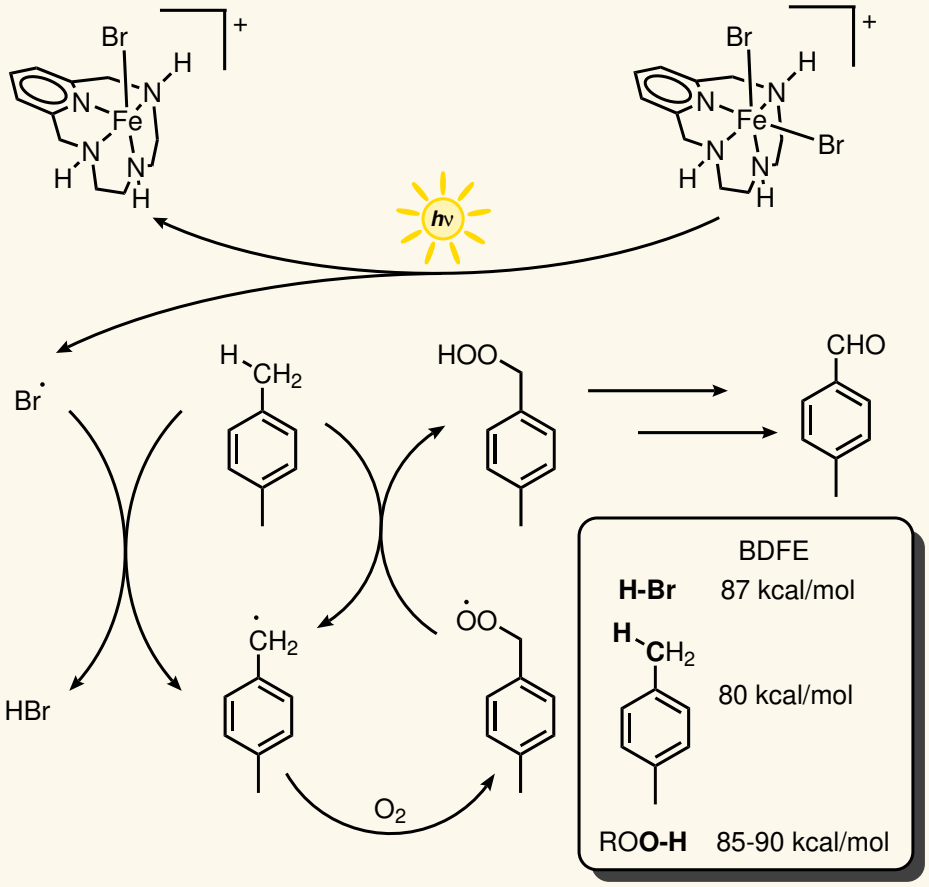

Scheme 3.2.3: *Proposed photochemical mechanism and competent BDFE values*

In contrast, **C2a** displayed almost no detectable reactivity under otherwise identical conditions. From a mechanistic standpoint, photochemical homolysis of the Fe–Cl bond in **C2a** would be expected to generate highly reactive $Cl^{\bullet}$ species; however, this behavior was not observed experimentally. The limited activity of **C2a** is tentatively attributed to rapid deactivation of the photoexcited state, a hypothesis that is currently being examined in greater detail.

The low photocatalytic performance of **C2c** can instead be rationalized by the high energetic barrier associated with homolytic cleavage of the Fe–OTf bond. The stability of **C2b** under photocatalytic conditions was further assessed by UV-VIS spectroscopy, which revealed only minor variations in the absorption profile, consistent with preservation of the Fe(III) $PcLH_3$ motif (Figure 6.8, Chapter 6). By con-

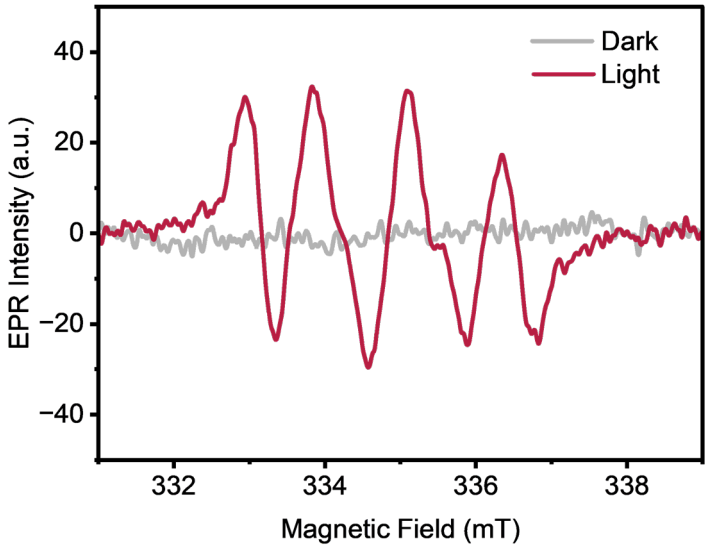

Figure 3.21: *EPR spectra of a solution p-xylene (80 mM) and 2.5 mM* ***C2b*** *in acetonitrile in the presence of BMPO, before and after irradiation with 405 nm LED. Credits: Luka Đorđević.*

trast, pronounced bleaching of the absorption bands was observed for $FeBr_3$ under identical conditions (Figure 6.8).

3.2.4 Photo-oxidation of benzyl alcohols to benzaldehydes

Encouraged by the results obtained with *p*-xylene oxidation, I moved to the oxidation of benzyl alcohols to their carbonyl compounds, a more familiar field to my research group. While this process is already well known and reported,[211] the development of selective and efficient methods is still a challenge. In particular, there is an increasing demand for environmentally sound oxidants and catalysts to substitute highly toxic metal-oxo reagents (e.g. $KMnO_4$) and metal oxide surfaces, which to this day represent the industrial standard.[212] In 2020 my research group reported the catalytic activity of iron pyclen complexes in the oxidation of benzyl alcohol using hydrogen peroxide as the oxidant. Indeed, H_2O_2 is one of the reagents of choice as a green and sustainable oxidant, due to its high oxygen content, low cost and high commercial accessibility.[213,214] Aerobic oxidation is even more desirable, since the cost of the oxidant is essentialy eliminated and the atom economy is usually 100%. Consequently, the recent success with the aerobic oxidation of *p*-xylene provided a strong motivation to extend the scope of this investigation to the oxidation of benzyl alcohols.

Experimental setup: a small note. In the last three years, the design of a new photoreactor has become a requirement for my laboratory. My previous attempt at building a custom-made photoreactor consisted in an extremely trivial but effective design: a short PVC pipe was used as the main body of the reactor, with a 405 nm LED strip glued in a spiral-fashion on the inside wall, while a 12 V fan with a magnet

positioned in its center was used both for stirring and cooling. I decided to build on this concept a more practical, versatile and solid reactor. My new design should have satisfied these requirements:

(a) The ability to run multiple reaction simultaneously.
(b) The ability to select the wavelength of each reaction independently.
(c) The ability to provide efficient cooling and stirring.
(d) The ability to run reaction in standard sized vials.
(e) A small size factor

I decided to design the body of the reactor using CAD software, which would enable to easily 3D print it. As for electronics, I opted for commercially available, off-the-shelf components and wiring. The LED strips, instead, were bought from a specialized supplier (Ledpoint S.R.L.), which was able to provide LED strips with certified emission spectra and power output. The reactor design, thus, was divided into two parts, the main one being the reactor's body, which was intended to accommodate the electronics, the wiring, the power delivery, along with cooling and stirring fans (Figure A.238, Appendix A). The reactions themselves then would run in standard 3 mL scintillation vials, which were supported by four modules (Figure A.239, Appendix A), in which one meter of LED strips was glued in a spiral fashion. Because the reactor was designed to run four reactions simultaneously, possibly at four different wavelengths, to use it at its full potential I made a total of sixteen modules, four for each wavelength. The selected wavelengths were 365 nm (UV), 405 nm (UV, close to violet), 460 nm (blue) and a broadband white LED. The last part that needed printing was a magnet holder, to secure four powerful NIB magnets to the center of the fans.

Once the casing, the magnet holders and the modules were printed, I moved to designing the electric scheme. The circuit is extremely simple (Figure A.240): the power unit, protected by a 1 A fuse, delivers 24 V DC; the four LEDs are directly connected to one of the power unit terminals and switched on and off with four simple push/push buttons. The LED strips are connected to power with a standard DC barrel connector. The fans are powered by a 12 V circuit, originating from a DC/DC converter connected directly to a power unit terminal. The fan motors are voltage-controlled, so four DC/DC converters were equipped with 10 kΩ potentiometers and employed to control the voltage delivered to the fans (0-12 V). To add further protection to the circuit, four 1N4007 diodes were installed, one for each motor. The assembled photoreactor is depicted in Figure 3.22.

Optimization of the reaction. Once the photoreactor was built, I proceeded with testing the oxidation of benzyl alcohol under photocatalytic conditions, using **C2b** as the catalyst and acetonitrile as the solvent. Due to the *fiddly* response to reaction conditions encountered in photocatalytic processes, together with the large number of experimental variables, I again decided to use Design of Experiment (DoE)

Figure 3.22: *Photograph of the finished reactor.*

to optimize this process. Moreover, preliminary experiments showed that, within the tested experimental space, the main response (yield) was strongly non-linear. For this reason, the optimization was conducted directly using a response surface methodology, without any prior screening using factorial methods, which would have been inappropriate in this case. The runs were randomized, and the D-optimal criterion was employed to select the most informative set of experiments. The experimental space was defined as follows:

(A) Concentration: 0.01–1.00 mol L^{-1}
(B) Catalyst loading: 0.1–5 mol%
(C) Reaction time: 1–8 hours
(D) Light source (categorical factor): 365 nm, 405 nm, and white LED

This resulted in 32 experiments, six of which were repeated runs included to improve statistical robustness. The experiments, together with the corresponding results, are collected in Table 6.27.

It is worth noting that the obtained response data were extremely unbalanced, with the few high-yield data points located only in the low-concentration region. For this reason, a data transformation was required, and the data were treated in their logarithmic form.

As in the previous examples of Design of Experiment (Chapter 2), significant factors in the optimization study were identified using the Akaike Information Criterion (AIC) algorithm. The variables retained in the model are shown in Figure 3.23. The model reveals a strong negative correlation between reaction yield and concentration. Indeed, the reaction performs best at very high dilutions, converting even traces of benzyl alcohol to benzaldehyde. Moreover, the reaction reaches completion relatively quickly (under optimal conditions, approximately one hour), as indicated by the positive coefficient associated with reaction time. However, the strongly negative second-order term for reaction time reveals a rapid decline after full conversion of benzyl alcohol is achieved. This behavior arises because, once benzyl alcohol is completely consumed, benzaldehyde begins to oxidize to benzoic acid. Benzyl alcohol is, in fact, a known inhibitor of benzaldehyde oxidation.[215]

This behavior is clearly visible in Figure 3.24, which provides a graphical representation of the model. The wave-like appearance of the response surface indicates the presence of an optimum in reaction time. Higher catalyst loadings allow for shorter reaction times and shift the optimum earlier in the course of the reaction, while also increasing selectivity and, consequently, yield.

At higher catalyst loadings (5 mol%), the reaction is very fast, and the yield decreases rapidly at longer reaction times due to the oxidation of benzaldehyde to benzoic acid. As can be readily observed from Figure 3.24, lower catalyst loadings also shift the selectivity of the reaction toward the formation of benzoic acid. It is therefore crucial to keep reaction times short, operate at relatively high catalyst loadings, and work at low substrate concentrations. Accordingly, the best results

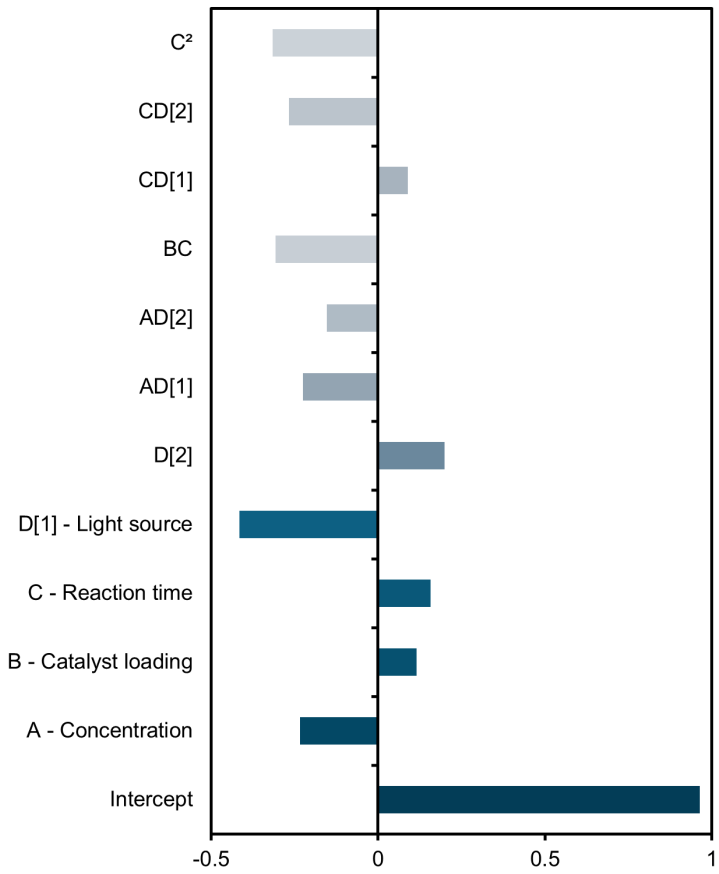

Figure 3.23: *Graphical depiction of the model's coefficient estimates for the optimization experiment. Factors are coded, meaning levels are expressed as $-1/+1$ rather than as experimental values. Upper-case letters represent easy-to-change factors, whereas lower-case letters indicate hard-to-change factors (HTC). The intercept was omitted for improved readability.*

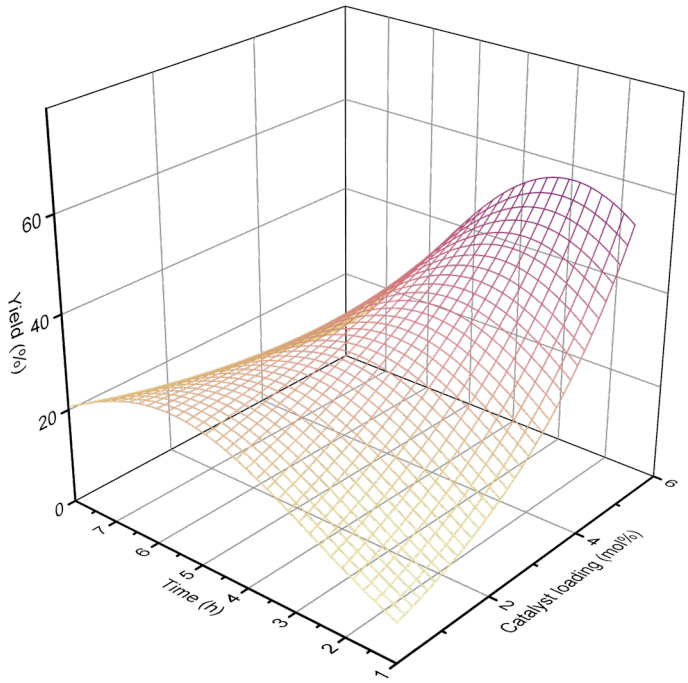

Figure 3.24: *Surface plot of the predicted yield. Reaction conditions: 0.01 mol L^{-1} substrate concentration, 405 nm LED; catalyst loading on the y axis and reaction time on the x axis.*

corresponded to Run 3 in Table 6.27, which was repeated for confirmation (Run 29). After one hour of irradiation at 405 nm, using a substrate concentration of 0.01 mol L^{-1} and a catalyst loading of 5 mol%, almost full conversion was achieved (94% on average), affording benzaldehyde with an average yield of 89%.

Because of the delicate response of the reaction, the results were poorly distributed, with most runs resulting in low-yield despite the small experimental space. To describe the reactivity more accurately, the design was augmented by enriching a more restricted experimental space–the more productive one–with more data. The new experimental space was defined in these limits: 4–5 mol% catalyst loading, 1–4 hours of reaction time, and 0.01–0.1 mol L^{-1} of substrate concentration. These additional results, reported in Table 6.30, did not lead to further optimization of the conditions but allowed a more detailed exploration of the most *productive* area of the experimental space.

3.3 Conclusions

This chapter has explored the synthesis, structural characterization, spectroscopic analysis, and reactivity in photo-oxidative processes of a family of iron-pyclen complexes.

A major outcome of this section is the demonstration that pyclen-based macrocycles provide a versatile and robust platform for stabilizing iron centers across

multiple oxidation and spin states. Structural analysis proved fundamental for characterizing the complexes, but the apparent contradictions with reactivity and other analytical tools highlighted the limitations of relying on crystallographic metrics alone. Notably, cases such as the unexpectedly low distortion observed for low-spin Fe(III) complex **C3a** emphasize the need for complementary probes to achieve reliable assignments.

In this respect, Mössbauer spectroscopy proved indispensable. Across this work, it permitted differentiation between oxidation and spin states, resolved the presence of iron(II) impurities in commercial iron sources (which were, most of all, *sources of frustration*), and clarified ambiguities arising from structural data.

The study of photocatalytic oxidation reactions extended the relevance of these complexes beside coordination studies. The ability of iron-pyclen species to promote aerobic oxidation reactions under visible-light irradiation was corroborated by an in-depth spectroscopical study supported by theoretical insights.

Taken as a whole, this chapter represents to me the most engaging part of the present work, in which synthetic effort, characterization, and reactivity studies converge most directly.

4

Novel pincer ligands

4.1 Introduction

In the earlier part of my PhD, most of my work was devoted to grafting simple metallates on commercially available resins, with the aim of producing a highly applicable catalytic system for waste (CO_2) utilization. In their homogeneous form (for example, as ammonium salts), these catalysts performed remarkably in the dimerization of aziridines. Then, I synthesized a small library of macrocyclic complexes. Of these, zinc complexes of *pytren* were tested in CO_2 cycloaddition to epoxides, yielding moderately satisfying results. Iron pyclen complexes, on the other hand, produced remarkable results in photo-oxidative processes. Although their straightforward synthesis posed as an attractive feature and their high stability allowed for quite harsh oxidative transformations, at times their inertness was disadvantageous. Controlling their catalytic properties through functionalization, moreover, turned out to be rather difficult. These reasons, along with my desire to conduct more basic research, led me to the search for other research lines.

In recent years, PC(sp^3)P pincer ligands, particularly those derived from bis[(2-dialkylphosphino)phenyl]methane (Figure 4.1) have emerged as an increasingly relevant class of ligands in organometallic chemistry.[216] Unlike their more extensively studied aromatic PC(sp^2)P counterparts, these ligands feature a central methylene sp^3 carbon, which allows for unique reactivity patterns inaccessible to rigid aromatic backbones. In particular, their availability for C–H activation at their methylene position attracted my interest, and I decided to delve into this field.

This brief introduction gathers some representative works in this field of the last two decades, demonstrating how the unique features of these ligands have enabled rare C–H activation patterns and the consequent formation of unusual carbene complexes.

The first report of this type of ligand dates back to 1990, when Roper et al.[217] serendipitously obtained a ruthenium bimetallacyclic carbene complex. The ini-

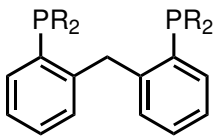

Figure 4.1: *PC(sp^3)P ligands: backbone structure.*

tial aim was to synthesize a ruthenium dibromocarbene complex by reacting excess boron tribromide with a ruthenium trifluoromethyl precursor. Specifically, $[Ru(CF_3)Br(CO)_2(PPh_3)_3]$ was selected as the starting material. Treatment with excess boron tribromide did lead to the formation of the desired dibromocarbene complex; however, due to its instability, the authors were unable to isolate it in crystalline form (the formation of the product was confirmed by IR spectroscopy). Over time, the sample evolved CO and two aryl rings of the phosphine ligands underwent electrophilic aryl substitution with the carbene ligand to produce a bicyclic complex (Scheme 4.1.1). This product is stable, can be purified by column chromatography, and in cationic form the carbenic moiety readily undergoes nucleophilic attack (e.g. by $NaBH_4$ or diethylamine). The synthetic accessibility of these ligands and the relative kinetic stability of their complexes led to a revival in this field, which Manzano and Young defined as a *renaissance* in a 2021 review.

The first deliberate synthesis of this compound as a standalone ligand was reported by Floriani et al.[218] in 1997. The ligand was prepared from commercially available (2-aminophenyl)phenylmethane, which underwent diazotization to introduce an iodide substituent into one of the phenyl rings. The iodide was then oxidized to form an iodonium salt intramolecularly. Subsequent anion exchange with potassium iodide yielded the iodide-iodonium salt, which, upon heating, formed *bis*(2-iodophenyl)methane. Lithiation of this intermediate followed by reaction with chlorodiphenylphosphine afforded bis[(2-diphenylphosphino)phenyl]methane, the target phosphine.

Floriani originally proposed this ligand primarily as an NMR spectroscopic probe to investigate the coordination environment around metals. In fact, when the ligand does not undergo aliphatic metalation, it forms a rather rigid eight-membered metallacycle that forces a proton of the bridging methylene in proximity with the metal, rendering the two benzylic protons diastereotopic, with chemical shifts widely different due to the anagostic interaction. Moreover, the ligand can indeed undergo C–H activation, and such reaction was indeed explored in the cited reference. The electrophilic attack of Rh(III) on the bridging methylene was reported in the same work, where the reaction of $RhCl_3$ with *bis*[(2-diphenylphosphino)phenyl]methane afforded an alkyl complex.

At the beginning of the 2010 decade these ligands saw a resurgence, when Piers and co-workers introduced their dialkyl phosphine variant as β-elimination-immune ligands.[219] In this study, several PC(carbene)P iridium complexes were synthesized through a double C–H activation process. First, the free ligand was co-

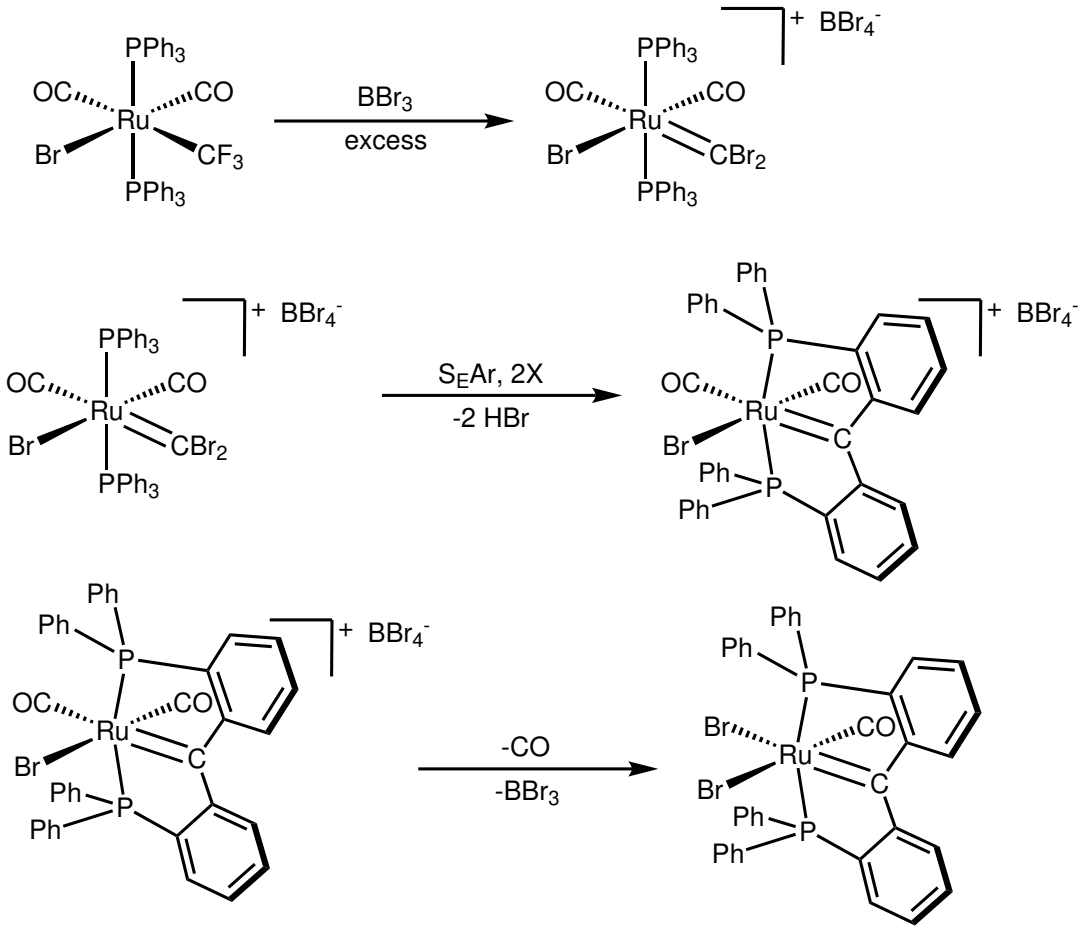

Scheme 4.1.1: *In-situ formation of $PC(sp^3)P$ ligand.*

ordinated to $[Ir(coe)_2Cl]_2$, forming complex **III** (Scheme 4.1.2), which upon heating under vacuum eliminated H_2 to yield the carbene complex **IV**. This carbene species and its derivatives react rapidly and cleanly with dihydrogen gas at atmospheric pressure, inserting H_2 at an extremely fast rate across the Ir−C double bond. Furthermore, direct exposure of complex **III** to dihydrogen led to the formation of a polyhydride complex. The latter could not be crystallized, but spectroscopic data indicated the presence of four hydride ligands bound to the iridium center.

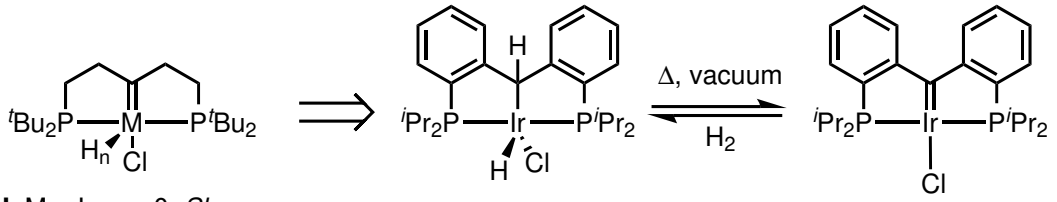

I: M = Ir, n = 0; *Shaw*
II: M = Ru/Os, n = 1; *Gusev*
III: *Piers*
IV

Scheme 4.1.2: *Complex **IV** solves the β-elimination problems that afflicted **I** and **II** by using a fully alkyl backbone.*

4.1.1 Structural and fundamental studies

Iluc and colleagues in 2014 explored the coordination flexibility of a *P*-diisopropyl substituted PCP ligand with palladium (0) and (II), as well as an ethylene bridged *P*-diisopropyl ligand with palladium and rhodium.[220] While the C–H activation capability of the ligands was not tested, the authors showed that the ethylene bridged ligand was able to coordinate Pd(II) in a trans-chelating configuration, with a low energy barrier (~12.4 kcal/mol) for the *cis* configuration. This conformational flexibility allows the ligand to perform quite well in catalysis, and the palladium complexes of these diphosphines performed notably well in Suzuki and Heck couplings.

One year later Arras and colleagues synthesized another methylene-bridged diphosphine bearing tert-butyl groups on the aryl rings.[221] Compared to the Iluc's studies, the authors extensively investigated C–H activation at the methylene bridge. Complexation of this ligand with $RhCl_3 \cdot H_2O$ in isopropanol/toluene yielded an interesting dimeric Rh(III) complex (Scheme 4.1.3, **V**). The PCP ligand coordinated facially to the metal, with two positions occupied by the phosphines and one by the methylene bridge. This coordination mode is quite rare in the PCP family of ligands, and in this case the flexible nature of the ligand allowed for this geometry. Moving to Rh(I) sources, other types of coordination were observed. When the complexation of $[(COD)RhCl]_2$ was performed in pyridine (Scheme 4.1.3, **VII**), an electronically saturated square pyramidal complex was observed, where the PCP ligand acted as a simple *cis*-bidentate phosphine. To obtain the oxidative addition of the methylene C–H bond, the complex was treated with tin(II) chloride. This transformed the coordination mode of the phosphine from a *cis*-bidentate ligand to a meridional tridentate, with the $SnCl_3^-$ anion occupying the *trans* position to the

metalated carbon.

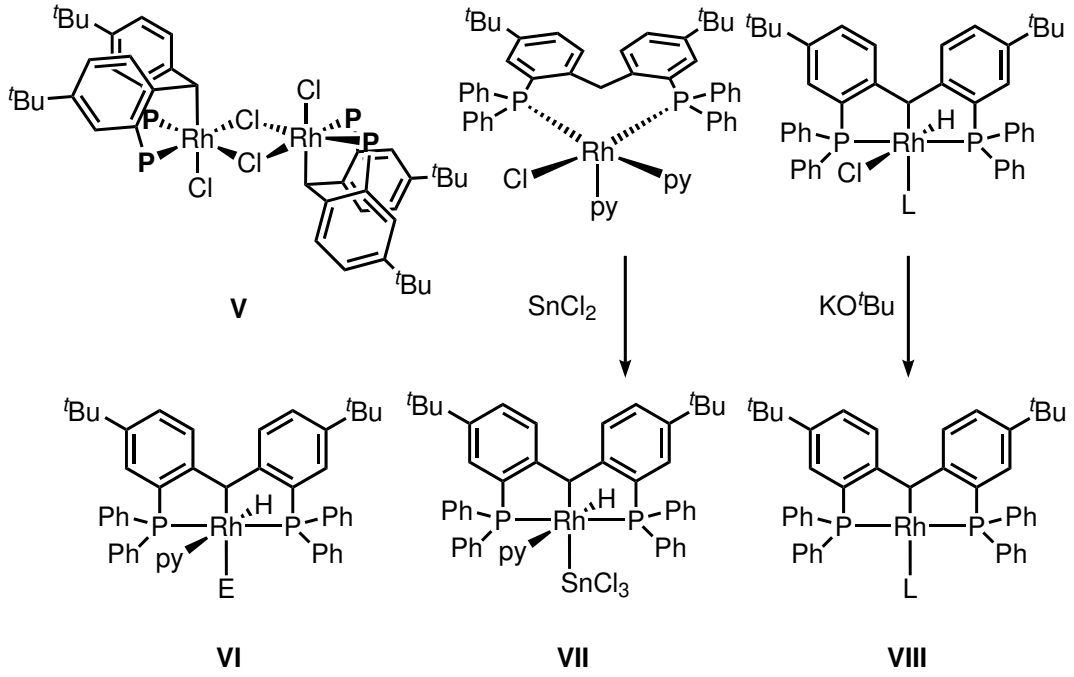

Scheme 4.1.3: *Rhodium PCP complexes, synthetized and characterized by Arras and colleagues. Abbreviations: P = PPh_2. L = HP(Ph)o-$C_6H_4NMe_2$, PPh_2Py, PPh_3. E = $SnB_{11}H_{11}^{2-}$, $GeB_{11}H_{11}^{2-}$.*

This ligand showed quite remarkable flexibility, being able to adopt the facial, *cis*-bidentate, and *mer*-tridentate coordination modes. The authors also attempted to synthesize a rhodium-carbene complex. To do this, $[(COD)RhCl]_2$ was treated with the PCP ligand in the presence of L donor ligands (HP(Ph)*o*-$C_6H_4NMe_2$, PPh_2Py, PPh_3). The obtained product was then exposed to KO^{t}Bu. Interestingly, the carbene was not recovered, but an electron deficient square planar complex was observed (4.1.3, **VIII**). The author also reported the synthesis of alkyl complexes in the presence of stanna- and germa-closo-dodecaborates (4.1.3, **VI**).

In 2016, Logan, Piers et al.[222] demonstrated that the second C–H activation in rhodium PC(sp^3)P complexes to obtain PC(carbene)P complexes is in fact possible and facile, however, the *trans* arrangement of Rh-H and C–H in the initial products hinders H_2 elimination and carbene formation. The *cis* geometry would facilitate this step, but it is disfavored. Additionally, they studied the *P* substituent and its effect on the second C–H activation: they showed that the use of bulkier phosphine substituents (e.g. ^{t}Bu) favors the formation of monomeric unsaturated complexes rather than dimeric complexes (obtained, for example, with ^{i}Pr substituents). As expected, the yield of carbene complexes from the thermolysis of monomeric complexes is significantly higher.

An in-depth study of the effects that the X^- ligand exerts as the leaving group on the C–H activation process was conducted by Iluc and colleagues in 2018.[223] The authors showed that both chloride and triflate substituted complexes are able

to form a Pd–C bond on the backbone upon thermal activation. The chloride complex followed a clear first order kinetic ($k = 0.011$ min^{-1}), suggesting a concerted coordination for the formation of complex **IX** (Scheme 4.1.4). The triflate complex, instead, displayed more complicated kinetics. The authors explained this fact with a multi-step process, which includes first the dissociation of a triflate ligand and the formation of a cationic complex, followed by the deprotonation and formation of the alkyl complex **X**. Treatment of the chloride complex with methyl lithium afforded the dimethyl complex **XI**, which was found to be particularly thermolabile and prone to reductively eliminating ethane to yield dimer **XII**. The authors were also able to obtain the C–H activation of this complex by irradiating at 254 nm, releasing methane and forming complex **XIII**. The same compound could be obtained by treating complex **IX** with methyl lithium. The acetate derivative **XIV**, in contrast, could not be isolated starting from the diacetate complex, and it was synthesized by treating the chloride complex **IX** with silver acetate. Thermolysis of the diacetate complex at 60 °C or photolysis allowed the acetate substituent to deprotonate one of the methine protons of the isopropyl groups and form a quite rare three-membered palladacycle with a very acute C–Pd-P angle (47.35°) (**XV**).

4.1.2 Carbene complexes

As already stated, great effort has been made to synthesize carbene complexes with this class of PCP ligands. In a 2014 study, Iluc and co-workers reported the synthesis and reactivity of a nucleophilic palladium(II) carbene complex.[224] The authors demonstrated that the dehydrohalogenation of complex **IX** in the presence of tertiary phosphines gave rise to square-planar Pd(II) complexes featuring a Pd–C bond that shows a partial double bond character (**XVI**, Scheme 4.1.5a). The reactivity of the complexes revealed that it is unusually nucleophilic, displaying facile methylation at the carbene carbon, protonation-induced reversal to the C–H pincer form, and metal-ligand cooperative activation of small molecules such as methanol and *p*-toluidine. The reactivity of this class of complexes was further explored in the following works by the same research group. In an early 2015 work,[225] they demonstrated that these electron-rich carbene complexes can activate a wide variety of C–H bonds via formal insertion into relatively acidic sp^3 and sp-hybridized positions. Substrates such as acetone, acetonitrile, phenylacetylene, fluorene, and 9,10-dihydroanthracene underwent clean C–H activation to form Pd–C bonds, with reactivity broadly correlated to substrate pKa. In contrast, no reaction occurred with diphenylmethane (pKa ~32), emphasizing the importance of C–H acidity. Furthermore, the activation of 9,10-dihydroanthracene let to the full reduction of the carbene to a Pd(0) complex.

In the same year, the same group investigated the interaction between these nucleophilic palladium compounds and the strong Lewis acid $B(C_5F_6)_3$.[226] The authors identified two distinct zwitterionic products: one via para-attack on the aryl

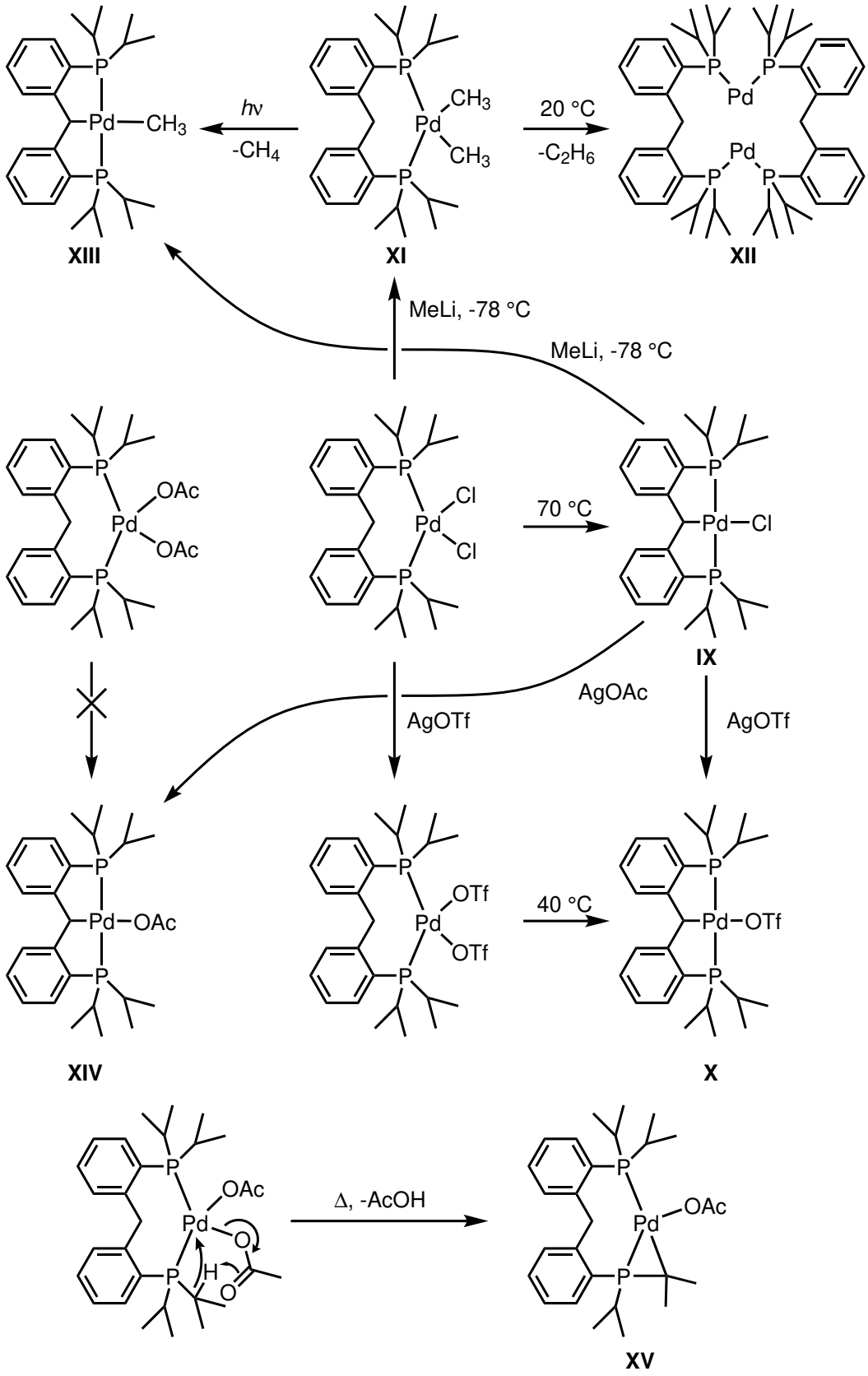

Scheme 4.1.4: *Study on the influence of the leaving group on C–H activation pathways.*

backbone of the pincer ligand and another via C–F bond activation of the borane. These reactions mimic frustrated Lewis pair behavior, enabled by steric hindrance at the carbene center. In a hydrogen atmosphere, both complexes also mediated H_2 activation, yielding hydride-borate ion pairs.

Next, they expanded the scope of these palladium carbene reactivity to include E-H bond activation (E = B, Si, Ge). The study included both the electron richer [Pd(PC(sp^2)P)(PMe_3)] (**XVI**) carbene complex and the electron poorer [Pd(PC(sp^2)P)(PPh_3)] complex. Both complexes activated pinacolboranes, silanes, and germanes, but the authors found that the distribution of the product depended on the electronic nature of the phosphine ligand and the substrate. [Pd(PC(sp^2)P)(PPh_3)] consistently yielded hydride products, while [Pd(PC(sp^2)P)(PMe_3)] (**XVI**) formed hydride or silyl/germyl complexes.

The last work of this series reports the synthesis of a complete series of palladium-bound chalcogenoketones (O, S, Se, Te) from [Pd(PC(sp^2)P)(PMe_3)] (**XVI**).[227] Elemental chalcogens and nitro/nitrosobenzene (for O) were used as atom transfer agents. The resulting complexes featured η^2-bound C=E moieties, with NMR data and structural metrics indicating a partial double bond character. Notably, the telluroketone was the first structurally characterized Pd-Te=C complex. Regarding the formation of the *O*-ketone through the reaction with nitrobenzene, the authors suggested that nitrobenzene was reduced to a nitrosobenzene intermediate. When nitrosobenzene itself was exposed to the complex, it was demonstrated to form a transient nitrone species that evolved to the final ketone product.

The same authors invested a great deal of effort also in the characterization of the redox activity of these compounds, which, as already stated, exhibit interesting properties. In addition to the normally available palladium oxidation states, the non innocence of these ligands allows them to access several coordination modes and very different reactivities depending on the number of electrons present in the system. Remarkably, the authors were able to synthesize, characterize, and study the reactivity of persistent radical carbene palladium complexes. The initial focus lied on the generation of persistent radical carbene derived the already well known [Pd(PC(sp^2)P)(PMe_3)] (**XVI**) complex.[228] Through controlled oxidation using dihalogens or halogen atom transfer from dihalomethanes, the authors isolated three distinct radical species: [Pd(PC$^{\cdot}$(sp^2)P)I], [Pd(PC$^{\cdot}$(sp^2)P)Br], and [Pd(PC$^{\cdot}$(sp^2)P)Cl] (**XVII**, Scheme 4.1.5a). These complexes are characterized by square planar geometries around the palladium center and a planar carbene carbon, as confirmed by X-ray crystallography. Notably, the iodo derivative dimerized in the solid state, forming a structure reminiscent of Gomberg's dimer (**XVIII**), while the bromo and chloro analogs remain monomeric in both the solid and solution phases.

The radical nature of these species is convincingly demonstrated by magnetic susceptibility measurements and EPR spectroscopy. All three complexes exhibit magnetic moments consistent with an $S = 1/2$ ground state and g-factors close to

2.0. The EPR spectrum of the chloro derivative reveals, in particular, well-resolved hyperfine coupling to phenyl protons and the ^{105}Pd nucleus, providing direct evidence of spin delocalization across the ligand framework. DFT calculations support these experimental observations, showing that the unpaired electron is primarily localized on the carbene carbon, with significant delocalization into the ortho and para positions of the phenyl rings. This electronic structure rationalizes the observed reactivity of the radicals, which includes hydrogen atom abstraction from donors such as 9,10-dihydroanthracene and $^{n}Bu_3SnH$. The resulting products are Pd(II) hydrides bearing PC(sp^3)HP ligands, which were independently synthesized to confirm their identity.

Building upon this foundation, the authors explored the redox chemistry of this carbene scaffold.[229] Starting from the nucleophilic carbene **XXI** (Scheme 4.1.5), they demonstrated a reversible redox sequence involving two successive one-electron oxidations. The first oxidation, using 0.5 equivalents of I_2, yielded a monomeric radical carbene (**XXII**). A second oxidation with $[Cp_2Fe][BAr^F{}_4]$ provided the corresponding cationic carbene (**XXIII**). Each member of this redox series was structurally characterized, and the progression is marked by a systematic contraction of the Pd–C bond, from 2.076 Åin the nucleophilic species to 1.968 Å in the cationic complex. This trend was found to be consistent with an increase in bond order, as corroborated by computational analysis. The cationic carbene exhibited a pronounced electrophilic character, reacting readily with a range of nucleophiles including NaH, *p*-TolNHLi, PhONa and PMe_3. Interestingly, the products derived from amide and phenoxide nucleophiles displayed dynamic behavior in solution, attributed to hindered rotation around the Pd–C bond and the flexibility of the ligand framework.

In a further extension of this chemistry, the authors investigated the formation of heterobimetallic Pd-K carbene complexes.[230] These were accessed via substitution of the radical carbene **XXI** with potassium amides or benzyl potassium, followed by reduction with KC_8. The resulting anionic complexes exhibited polymeric structures in the solid state, with potassium ions bridging the carbene and aryl moieties; while in donor solvents like THF, these polymers dissociated into monomeric species. These heterobimetallic complexes retained the nucleophilic character of the carbene, as evidenced by their reactivity with electrophiles such as acetonitrile. The authors proposed that the interaction between the potassium ion and the carbene ligand may have played a role in substrate activation, drawing parallels to Lewis acid co-catalysts in homogeneous systems.

4.1.3 First-row transition metals

Up to this point, most of the discussion has focused on noble-metal systems. However, the coordination behavior of these ligands suggested that they could also support unusual and highly reactive complexes of first-row transition metals, which

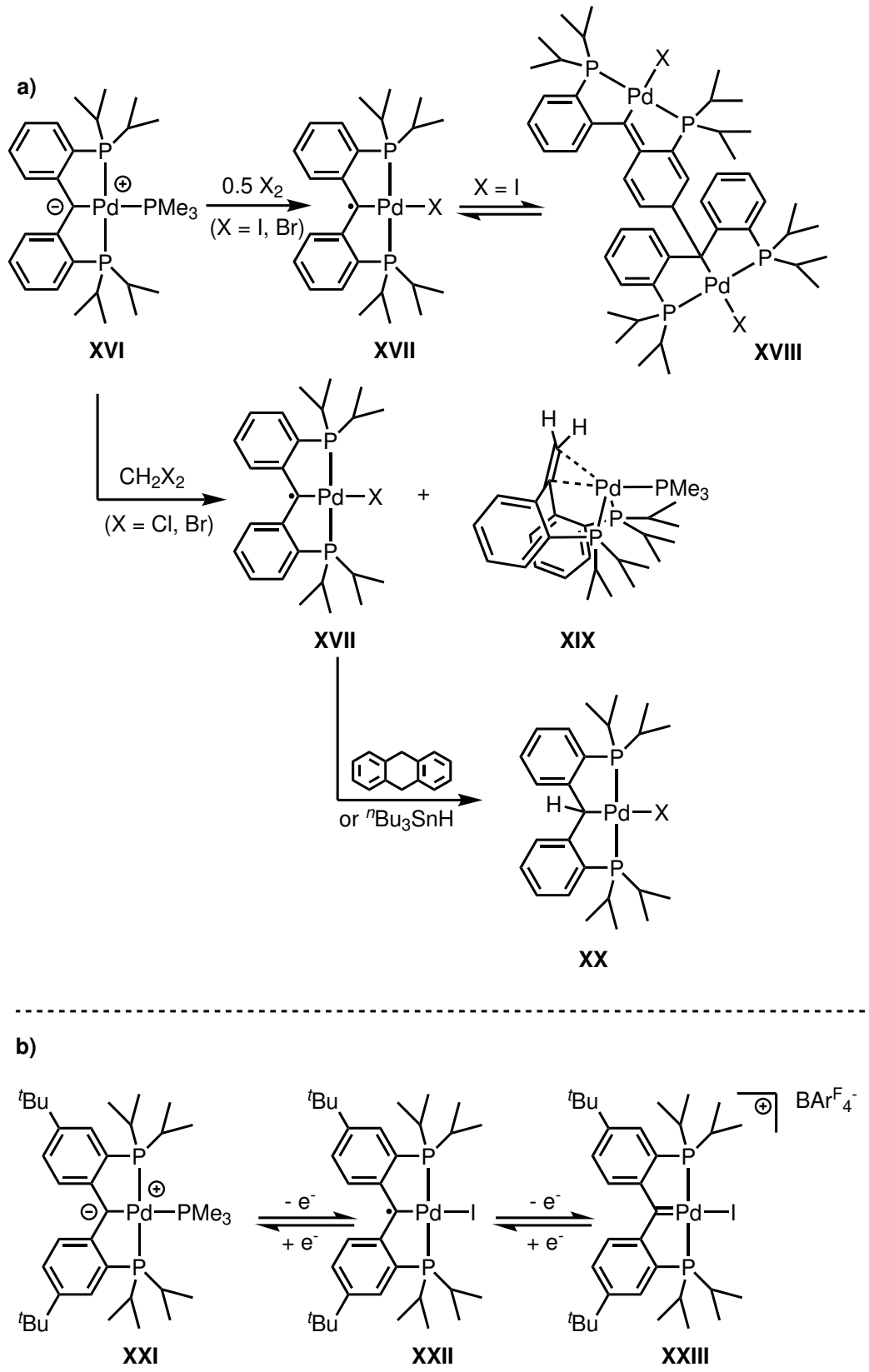

Scheme 4.1.5: *a) Synthesis and properties of persistent radical palladium carbene complexes. b) Redox chemistry of PC(sp^2)P palladium complexes: from nucleophiles to electrophiles.*

form the central subject of this thesis. This possibility was particularly appealing, and several significant literature examples already show how these complexes can support interesting reaction patterns that would be normally unusual for classic first-row transition metal complexes.

In an early study by Gutsulyak, Piers and co-workers,[231] dehydrobromination of a square-planar (PC(sp^3)P)NiBr precursor yielded PC(carbene)P nickel complexes featuring a strongly σ-donating anionic carbene anchor bound to a formally Ni(II) center (Figure 4.2 **a**). These complexes undergo rapid heterolytic addition of various E-H bonds (E = H, C, N, O) across the Ni=C bond, including those of H_2, phenylacetylene, NH_3, H_2O, and MeOH. The corresponding hydride, acetylide, amido, hydroxo, and methoxide complexes were obtained cleanly, and the reappearance of the benzylic C–H signal provided a diagnostic spectroscopic marker for these transformations. In the case of ammonia, the initially formed monomeric amido species underwent dimerization to give a $Ni_2(\mu\text{-}NH_2)_2$ structure. Several E-H additions, including H-H and N-H activation, were found to be reversible, as confirmed by isotopic exchange experiments. The electron-rich carbene donor also renders the site trans to carbon relatively labile, a feature that surely held revelance for later catalytic applications.

In a more recent work, Zhao, Sun and Li reported that treatment of the PCP ligand bis[(2-diphenylphosphino)phenyl]methane with [Fe(PMe_3)$_4$] resulted in C(sp^3)-H activation at room temperature to give the hydride pincer complex (Figure 4.2 **b**).[232] The reaction proceeded through the oxidative addition of the benzylic C–H bond, substituting two of the PMe_3 ligands, yielding a Fe(II) hydride that was isolated. When $FeMe_2(PMe_3)_4$ was employed instead, sequential activation of one Csp^3-H bond and one arylic C(sp^2)-H bond produced a pincer complex in which an ortho-metalated aryl donor completed the chelating framework. Subsequently, both complexes were evaluated in the hydrosilylation of ketones; while catalysis was demonstrated, the reactivity profiles were modest.

Later in 2015, the Piers group expanded their expertise in nickel chemistry with PCP ligands by preparing a series of Ni(II) PCP hydroxo complexes that served as precursors for nitrile hydration catalysis (Figure 4.2 **c**).[233] The synthesis relied on an improved synthetic approach in which the PCP proligands underwent C–H activation with NiX_2 (X = Cl, Br), using triethylamine to subtract the HX byproduct. This modification allowed the (PCP)NiX compounds to be obtained in yields greater than 90%. Subsequent treatment of (PCP)NiX compounds with excess CsOH in wet THF afforded the corresponding hydroxo complexes. Great effort was invested in studying the lability of the hydroxo group which was further supported by ^{17}O exchange experiments, which showed rapid loss of the isotopic label from Ni-^{17}OH species in the presence of water. Although catalysis was not the main focus of the study, the hydroxo complexes were shown to mediate the hydration of a range of nitriles under mild conditions.

The same authors continued their research in this field in 2018 by investigating

the reactivity of cationic nickel PCP complexes to oxygen atom transfer (Figure 4.2 **d**).[234] Their study started from well-defined Ni(II)PCP bromide complexes, which were converted into the corresponding triflate or cationic derivatives using AgOTf or $AgSbF_6$, or by ion exchange with TlOTf when silver salts led to oxidation. Reaction of these electrophilic nickel complexes with various amine *N*-oxides resulted in oxygen atom transfer, giving products in which one or both phosphine arms of the pincer ligand were oxidized to P=O groups. For $ONMe_3$, a single oxygen insertion was observed, whereas the more strongly donating $ONMePh_2$ induced sequential oxidation of both phosphine arms. The transformations occurred under mild conditions and did not provide evidence for the formation of a nickel-oxo intermediate, consistent with the proposed mechanism of direct oxygen insertion into the Ni-P bond.

In the same year, LaPierre and Piers expanded their investigations of PC(carbene)P nickel complexes to describe their reactivity toward CO_2, CO and related heteroallenes (Figure 4.3 **e**).[235] Starting from a well-defined Ni(II)PC(carbene)P precursor, exposure to CO_2 or CO under ambient conditions resulted in immediate formation of complex mixtures that could not be isolated. These findings led the authors to explore the more tractable reactivity of isocyanates and isocyanides. Reaction with tert-butyl isocyanate afforded a clean 2+2 addition across the Ni=C bond. Treatment with aryl isocyanides instead led to a formal group-transfer at the carbene center, giving products in which one isocyanide inserted into the Ni=C bond while the second remained terminally bound. To rationalize the behavior observed with CO_2 and CO, another Ni(II)PC(carbene)P complex with a more rigid PC(carbene)P ligand was prepared. This modified system displayed remarkably cleaner reactivity: exposure to CO_2 yielded a reversible 2+2 addition in the Ni=C unit, while reaction with CO produced a stable product analogous to the isocyanide insertion chemistry.

Cobalt PC(carbene)P systems were first explored by Sung and co-workers in 2018, who showed that reaction of an alcoholic PCP α-hydroxyalkyl proligand with $[Co(PMe_3)_4][BArF_4]$ under heating produced a cationic Co(I) PC(carbene)P complex by ligand dehydration (Figure 4.3 **f**).[236] This route provided direct access to the alkylidene pincer without requiring double C–H activation of the methylene backbone. The resulting PC(carbene)P cobalt complex was then used to study small molecule activation processes involving, among others, H_2, halogens, nitriles and olefins. More recently, Piers and co-workers reported neutral Co(I) PC(carbene)P complexes supported by a family of aryl-linked PCP ligands of different donor strength and rigidity.[237] In this case, addition of the PCP proligands to $CoBr_2$ gave tetrahedral Co(II) PCP complexes, which served as precursors to square-planar PC(alkyl)P and PC(carbene)P species obtained via deprotonation of the benzylic position and subsequent hydrogen atom abstraction with persistent organic radicals or related reactions. Further salt metathesis reactions were performed at cobalt with hydroxide, organolithium, and amide reagents, followed by protonation with

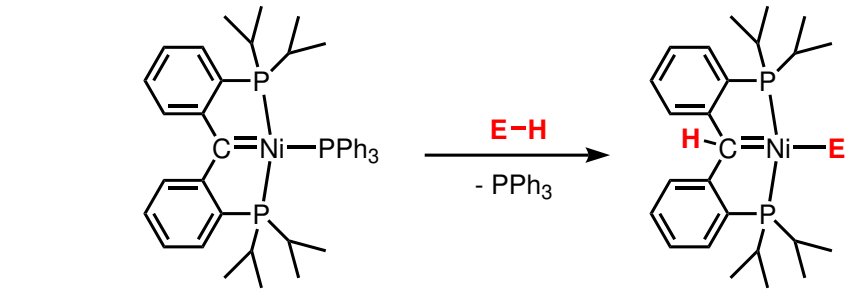

a) *Gutsulyak, 2013*

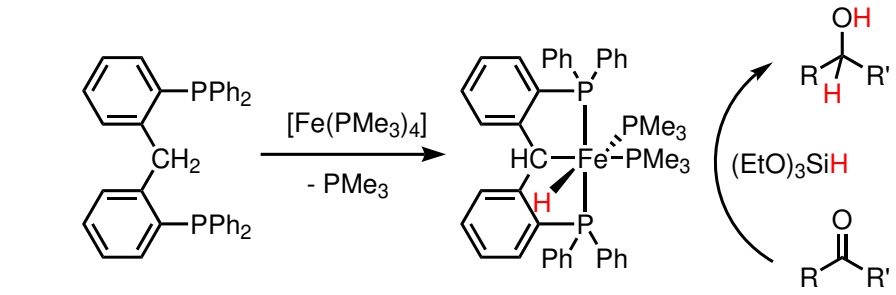

b) *Zhao, 2014*

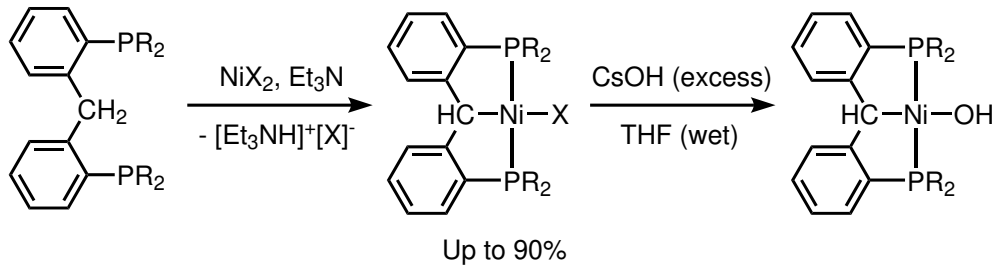

c) *Borau-garcia, 2015*

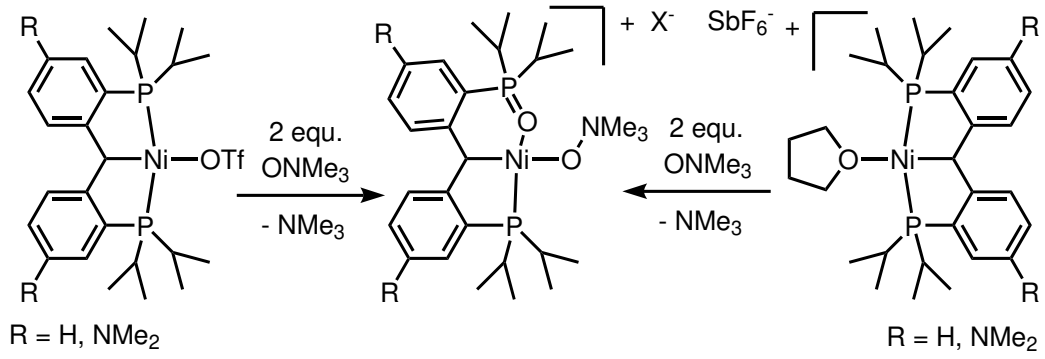

d) *LaPierre, 2018*

Figure 4.2: *$PC(sp^3)P$ complexes of the first transition, part 1.*

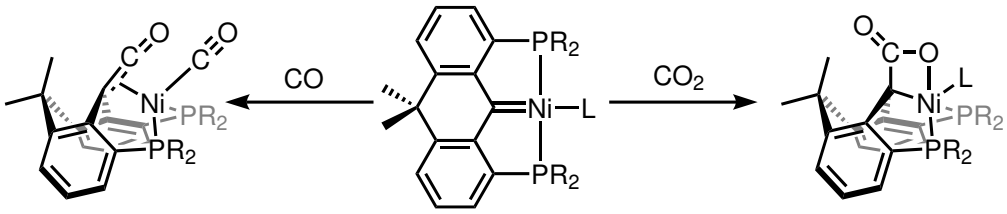

e) **LaPierre, 2018**

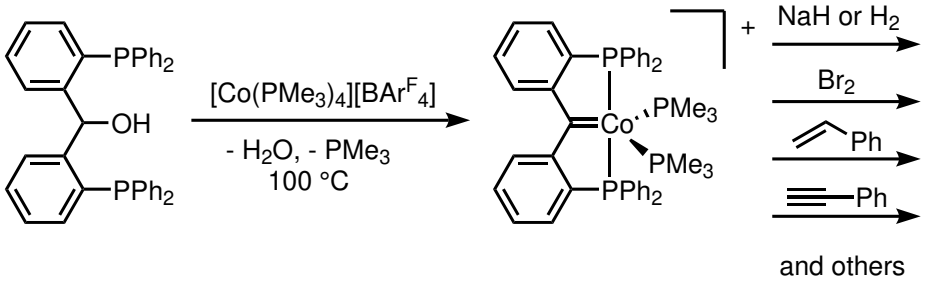

f) **Sung, 2018**

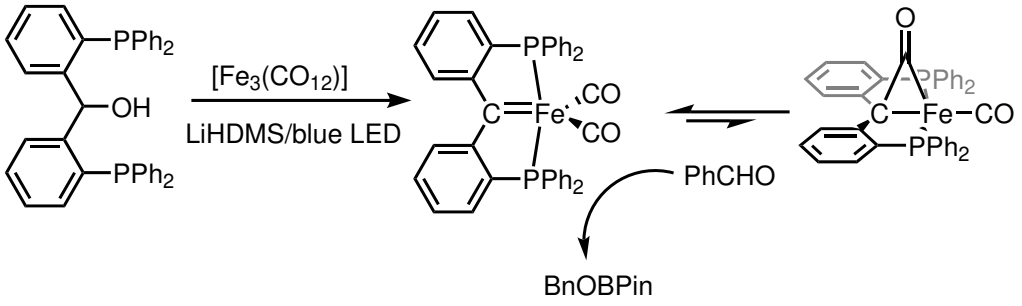

g) **Wang, 2021**

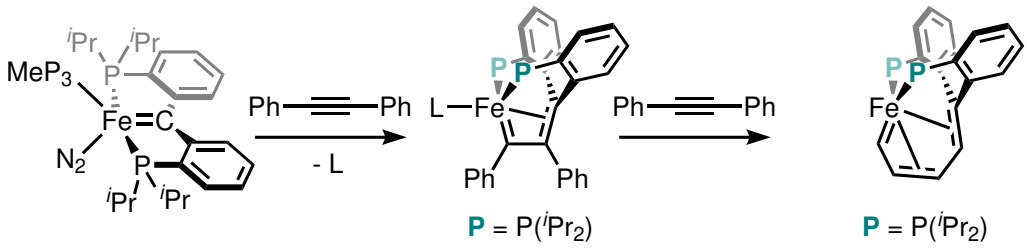

h) **Hoffbauer, 2021**

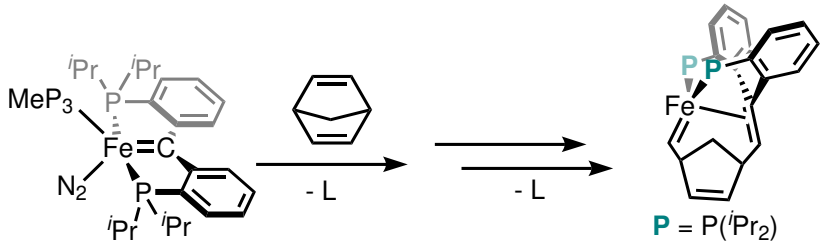

i) **Lincoln, 2024**

Figure 4.3: *$PC(sp^3)P$ complexes of the first transition, part 2.*

benzoic acid furnished hydroxo, alkyl, amido, and carboxylate derivatives.

In this context, a series of studies have shown that PCP ligands bearing an alkylidene donor can allow rich iron chemistry spanning multiple oxidation states and bond activation pathways. Wang and Young reported that an Fe(0) PC(carbene)P pincer complex could be accessed via dehydration of an α-hydroxyalkyl hydrido precursor derived from a bisphosphine Fe carbonyl intermediate (Figure 4.3 **g**).[238] The resulting Fe(0) carbene complex displayed reversible migration of a carbonyl ligand into the Fe=C bond, which enabled coordination of additional ligands and heterolytic addition of E-H bonds (E = H, B, Cl) across the iron carbene to give PC(sp^3)P hydride, boryl, and chlorohydride derivatives. In particular, the boronated PC(sp^3)P complex formed upon reaction with HBpin transfers its {H, Bpin} fragment to benzaldehyde, regenerating the Fe(0) carbene and producing the corresponding benzyl boronate ester, thus illustrating a closed stoichiometric cycle based on metal-ligand cooperativity. The same ligand framework was further shown to stabilize formal Fe(II), Fe(I), and Fe(-I) complexes obtained by halide abstraction and stepwise reduction; the most reduced species was found to abstract hydrogen atoms from aliphatic C–H donors, consistent with significant carbene-centered radical character.

In parallel, Iluc and colleagues developed an iron PC(sp^2)P carbene system specifically aimed at investigating enyne metathesis (Figure 4.3 **h**).[239] Starting from a tetrahedral PC(sp^3)P FeCl complex obtained by metalation of the methylene-bridged proligand with butyllithium first and then transmetalation an $FeCl_2$ precursor, treatment with MeLi afforded a square-planar Fe–Me derivative **XXVII** (Scheme 4.1.6). In the presence of *tert*-butyl nitrile, this intermediate underwent methane elimination to generate a Fe(II) PC(sp^2)P carbene bearing N_2 and ^{t}BuCN ligands (**XXVIII**), from which ligand exchange gave [PC(sp^2)PFe(N_2)(PMe_3)] (**XXIX**). This iron carbene reacted stoichiometrically with internal alkynes such as diphenylacetylene by a formal 2+2 cycloaddition across the Fe=C bond to afford isolable η^3-vinyl carbene complexes, in which the new C_2 fragment remained bound to iron. Further reaction of these η^3-vinyl carbenes with an additional equivalent of alkyne gave extended conjugated carbene products incorporating two alkyne units. Although no catalytic turnover was demonstrated, these transformations represent fundamental steps to achieve enyne metathesis and alkyne polymerization with iron complexes.

Developing directly on this groundwork, Lincoln and Iluc later examined the reactivity of the same PC(sp^2)P iron carbene toward strained olefins in order to approach olefin metathesis with iron (Figure 4.3 **i**).[240] In this study, [PC(sp^2)PFe(PMe_3)(N_2)] (**XXIX**) was used to react with norbornadiene derivatives and related strained substrates. Under these conditions, the iron carbene engaged in $2\pi + 2\pi$ cycloadditions with the C=C bond to form metallacyclobutane complexes that could be isolated and structurally characterized. Upon warming or further reaction, these metallacycles underwent cycloreversion to generate

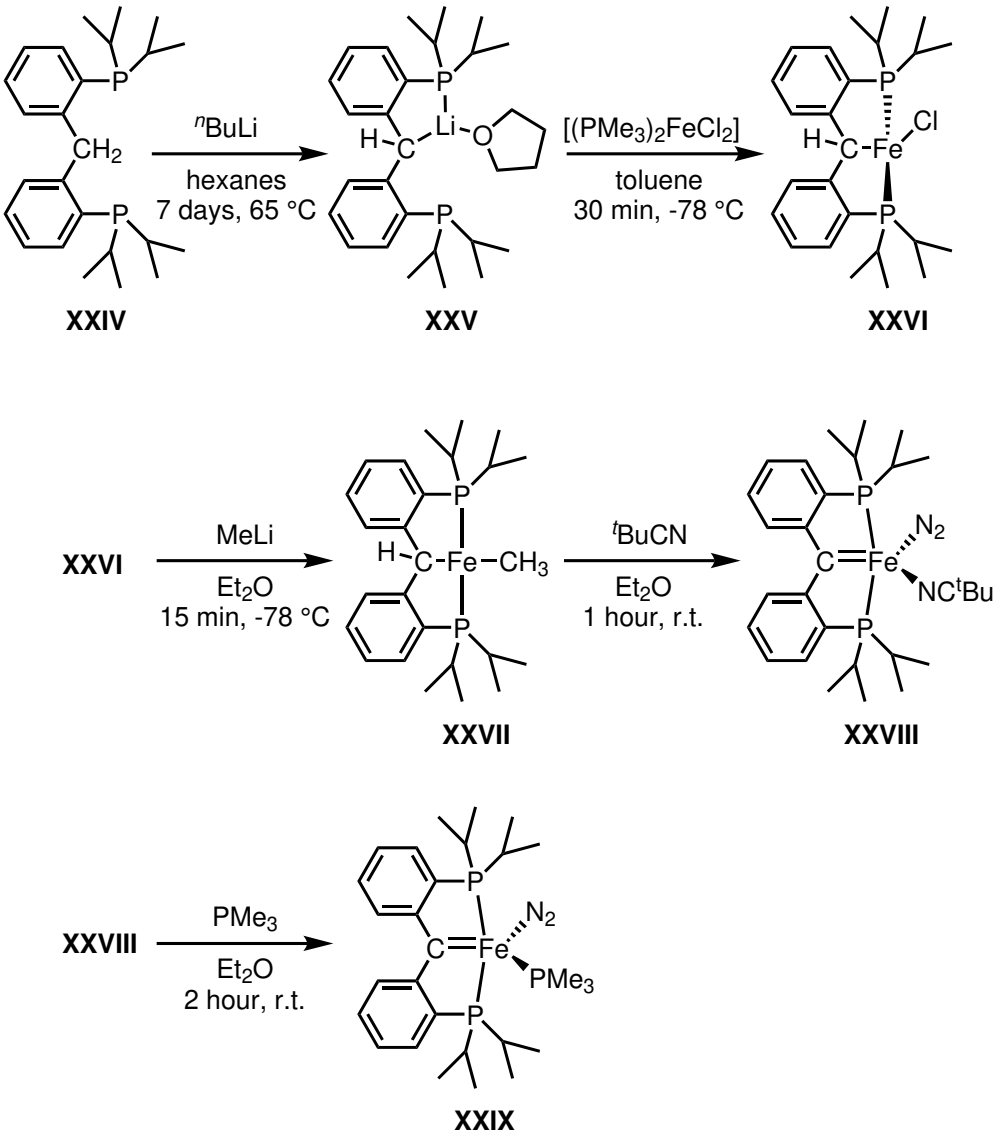

Scheme 4.1.6: *Synthesis of complex XXIX.*

ring-opened iron alkylidene products that were formally related to olefin metathesis outcomes between the starting carbene and the olefin. The sequence of reversible cycloaddition and cycloreversion provided direct stoichiometric evidence for a Chauvin-type olefin metathesis pathway at an iron center, even though sustained catalytic metathesis was not achieved under the reported conditions.

More recently, the same iron PC(sp^2)P carbene scaffold has been used to investigate directed C–H activation with substrates containing coordinating groups.[241] The complexes were treated with imines, ketones, diazenes, 2-vinylpyridine and 8-methylquinoline, leading in each case to cyclometalated PC(sp^3)HP iron species derived from formal 1,2-addition of an aryl, vinyl or benzylic C–H bond across the Fe=C unit. For *N*-benzylideneaniline and aryl ketones, ortho C–H activation of the aryl ring gave five-membered metallacycles in which the benzylic proton on the pincer backbone was reformed and a new Fe–C(aryl) bond formed. Azobenzene behaved analogously with C–H activation directed by the diazene functionality. In the case of 2-vinylpyridine, an apparent anti-addition product was formed.

Intrigued by this rapidly developing field and by the idea of granting iron the *dignity* of *pedigree-emblazoned* noble metals, I decided to design a new NCN pincer ligand (Scheme 4.1.7).

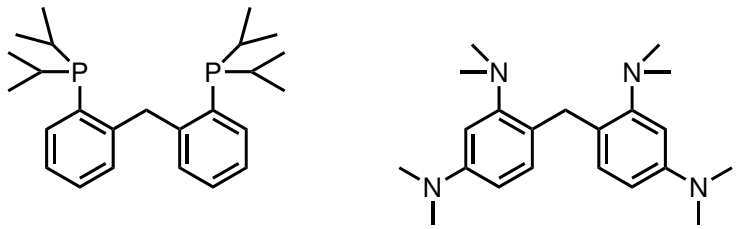

Iluc's ligand **L6**

Scheme 4.1.7: *Iluc's ligand (left) and* ***L6****, the new ligand designed for this thesis project.*

In my vision, the use of nitrogen donor atoms instead of phosphines would offer three principal advantages.

1. Easier synthesis: the ligands could be easily accessed by readily available methylene bridged dianilines
2. Exasperation of the σ-donor properties of the carbene using weaker donors in the lateral positions. This factor is believed to be crucial for achieving a stable metallacycle and thus a sustainable catalytic activity in olefin metathesis.[242]
3. While the literature on PC(sp^3)P ligands is quite extensive, NC(sp^3)N ligands are understudied, and examples are reported only for scandium, yttrium, samarium, alkali and alkaline earth metals.[243–247]

4.2 Results and discussion

The synthesis of **L6** was designed starting from 4,4'-methylenebis(*N*,*N*-dimethylaniline), a commercially available and very common chemical. Following Floriani's procedure,[248] the aniline was first nitrated on the ortho positions (Scheme 4.2.1). Subsequently, the installed nitro groups needed to be reduced to anilines. Here, I decided to diverge from Floriani's procedure, and I attempted the reduction of the nitro groups with a well-known procedure, which involves the use of iron powder and HCl. To my surprise, in every iteration, this procedure resulted in the cyclization of the reduced product to the very fluorescent acridine orange. Thus, I decided to revert to the original procedure, which I originally discarded to avoid the generation of tin byproducts, which are notoriously hard to remove. In this case, the reaction proceeded smoothly and the tin byproducts were removed by precipitating them with H_2S gas. **6** was isolated in a 65% yield.

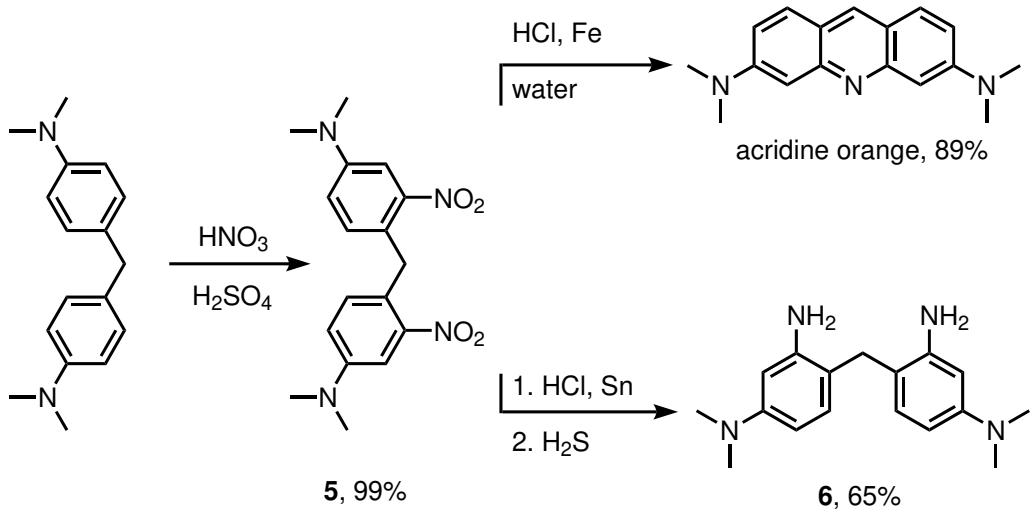

Scheme 4.2.1: *Synthesis of* ***6****.*

The methylation of **6** to obtain **L6** was attempted in several ways (primarily classic Eschweiler-Clarke methylation and catalytic methylation using dimethyl carbonate as the methylating agent),[249] but unfortunately, it was not successful. I did not establish the exact reasons for the reaction's failure; however, I can assume that the vicinity of the methylene bridge caused enough steric hindrance to disfavor the methylation of the anilines, which by itself is a rather thermodynamically challenging reaction. With this hypothesis in mind, I decided to attempt the synthesis of the product by methylating *m*-phenylendiamine before joining the anilines together with a methylene bridge (Scheme 4.2.2). This approach was more successful: the methylation of *m*-phenylendiamine was obtained even with green methylating agents, such as dimethyl carbonate, using tetraethyl phosphonium iodide as a catalyst,[249] while the condensation of the aniline with formaldehyde proceeded smoothly, cleanly and in excellent yields (97%).

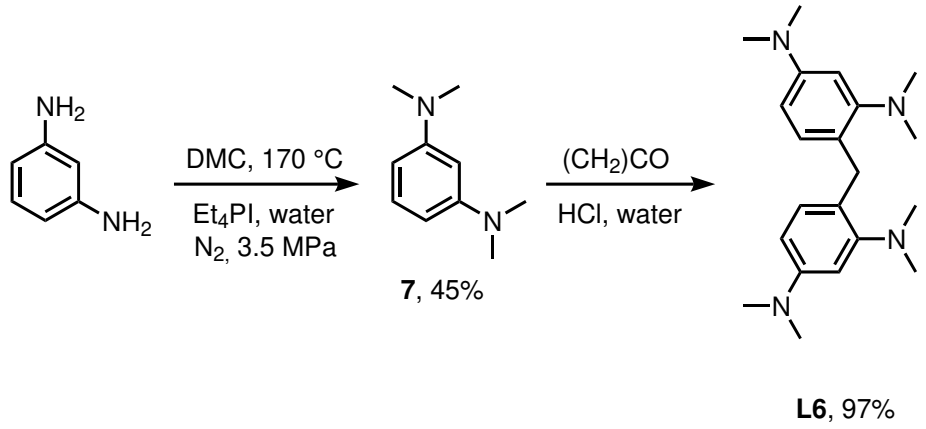

Scheme 4.2.2: *Synthesis of **L6**.*

Because iron is not as prone to C–H activation as second and third-row transition metals, I decided that the preferred method to install an iron atom in the desired position would be through the formation of the alkyl complex as the carbene precursor. As Iluc and colleagues demonstrated, this can be obtained from the transmetallation of the lithium salt of the ligand, that can then be followed by the formation of the iron carbene, which can be achieved with several methods. To obtain the lithium salt, ligand **L6** was dissolved in THF and reacted with *n*-butyllithium at low temperature. As expected, the characterization of the products of the reaction was not trivial. Because a mixture of products was obtained, however, we assumed that the ortho-lithiation product was the major one, and that the desired product was produced only in traces (Scheme 4.2.3). Reaction with a different base (sodium hydride) yielded even more obscure results.

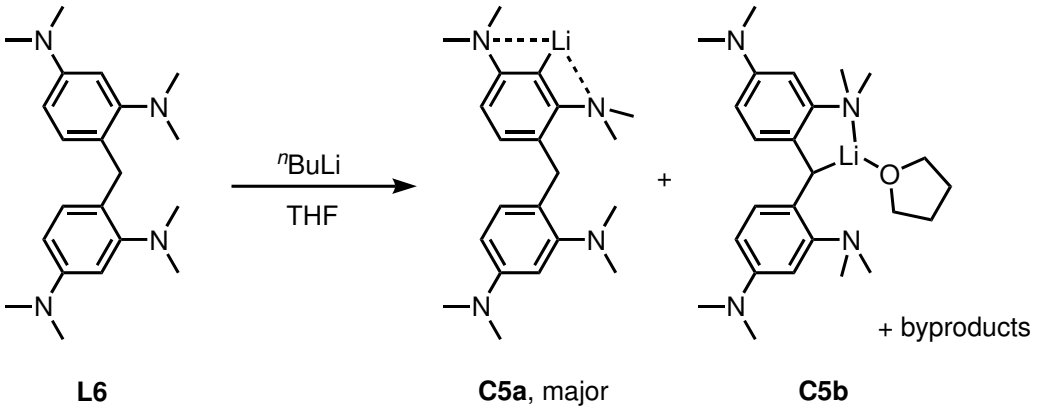

Scheme 4.2.3: *Formation of lithium salts of **L6**.*

The last attempt to tackle this problematic project aimed at functionalizing the methylene bridge of the ligand with a bromine. In this way, the brominated ligand could have reacted with a low-valent iron species, such as $[Fe_3(CO)_9]$, undergoing easy oxidative addition and forming the desired Fe(II) alkyl complex. I decided to take advantage of radicals' selectivity for benzylic positions rather than phenylic

positions, thus opting for a Wohl-Ziegler bromination (Scheme 4.2.4). The reaction was tested first using azobisisobutyronitrile as the radical initiator. The desired product, however, was not observed, but rather disappointingly, the ring bromination occurred, even though in low yield. The second attempt was carried out in milder conditions, with an initiator that did not need thermal activation ($FeBr_2$). Unfortunately, similar results were observed, and, for time reasons, the project was not further investigated.

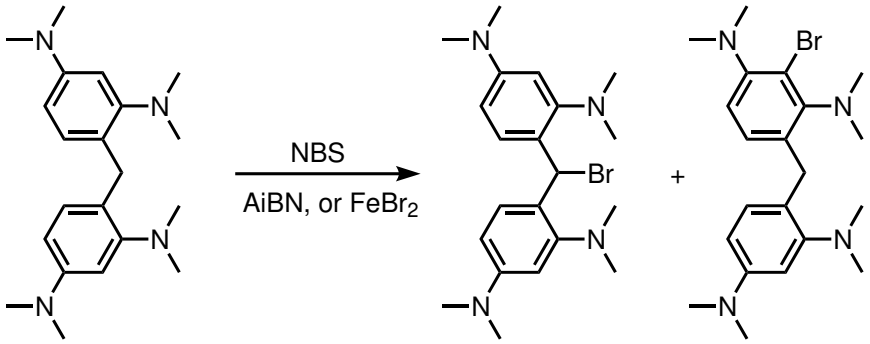

L6 **L7**, not observed 20%

Scheme 4.2.4: *Attempts at bromination of **L6**.*

5
Conclusions

The work presented in this thesis demonstrates that iron and zinc can be a good foundation for building effective and versatile catalysts when their intrinsic properties are matched with appropriate chemical environments. The work presented in this thesis spans three distinct research directions, namely metallate based catalysis, macrocyclic iron photochemistry, and pincer ligand design, each addressing different aspects of reactivity control in first row transition metal systems.

In the study of tetrahalometallate catalysts, it was shown that simple species such as iron and zinc halides can be transformed into highly efficient bifunctional systems that can function both as Lewis acids and nucleophilic species. These systems proved particularly effective for the cycloaddition of carbon dioxide to aziridines and epoxides, reactions that require simultaneous activation of a strained heterocycle and delivery of a nucleophile. Immobilization of these metallates on anion exchange resins provided heterogeneous catalysts that were easily handled and, in some cases, exhibited enhanced activity and selectivity due to cooperative interactions between the resin support and the active metal species. These results suggest that, for carbon dioxide cycloaddition reactions examined in this work, efficient catalysis can be achieved without the need for highly elaborate ligand frameworks.

The macrocyclic iron pyclen complexes investigated in this work addressed a different set of challenges. Here, the aim was to stabilize iron in well defined electronic states capable of engaging in photochemical redox processes. Pyclen ligands proved to be a robust and versatile platform, allowing iron to access multiple oxidation and spin states while remaining sufficiently stable for detailed spectroscopic study. Mössbauer spectroscopy was shown to be indispensable for correctly assigning iron speciation and for revealing limitations in structural characterization based solely on crystallography. The ability of these complexes to mediate visible light driven aerobic oxidations demonstrates that iron can support selective photochemical transformations that are typically associated with precious metals.

The exploration of pincer type ligands extended this work by targeting metal ligand cooperativity as a means to unlock new reactivity at first row metals. The

design and synthesis of a new NCN pincer ligand were motivated by recent advances in PC(sp^3)P systems, which have enabled carbene type reactivity and small molecule activation across a range of metals. Although the targeted iron carbene complexes could not be obtained, the synthetic challenges encountered provide a robust foundation for further development. These results underscore that the transfer of concepts developed for noble metals to first row metals is not straightforward, but requires precise control over both ligand geometry and electronics.

These studies illustrate that no single design strategy is universally optimal for first row transition metal catalysis. Tetrahalometallates excel in reactions driven by Lewis acid-base cooperativity, macrocyclic ligands provide control over redox and photochemical processes, and PC(sp^3)P pincer frameworks offer access to metal ligand cooperative pathways, albeit with significant synthetic challenges. The main conclusion of this thesis is that achieving sustainable catalysis with iron and zinc requires selecting a level of molecular complexity that matches the mechanistic needs of the reaction. When the catalyst design is properly tuned to the demands of the transformation, earth-abundant metals can mediate reactions that are both fundamentally useful and significant.

6
Experimental section

Reading guidance

This chapter includes the experimental details of the work that was presented in the previous chapters, focusing first on the synthesis and characterization of the complexes and their precursors, and later on the catalytic procedures.

General remarks. All chemicals were commercially available and used as received except where specified. All reactions that involved the use of sensitive chemicals were performed under a nitrogen atmosphere using standard Schlenk line techniques. Manipulations of air-sensitive solid samples were performed, when possible, in a nitrogen-flushed glovebox. Acetonitrile, dichloromethane, dichloroethane, and methanol were distilled over calcium hydride. Diethyl ether, tetrahydrofurane, and hexanes were distilled over sodium/benzophenone. $CDCl_3$ for NMR analysis was passed through a basic alumina column and subsequently thoroughly degassed with several freeze-pump-thaw cycles. ^{1}H NMR analyses were performed with 400 MHz spectrometers at room temperature. ^{13}C NMR analyses were performed with the same spectrometers at 101 MHz. The coupling constants (J) are expressed in hertz (Hz), and the chemical shifts (δ) in ppm. Magnetization measurements were performed with a Quantum Design physical property measurement system (PPMS) equipped with a Vibrating Sample Magnetometry (VSM) module. Mössbauer spectroscopy of ^{57}Fe was carried out on a Wissel spectrometer using transmission geometry and a proportional detector at ambient temperature without a magnetic field. An α-Fe foil was used as a standard and the spectra fitting was performed using the Wissel NORMOS routine. UV spectra were recorded at 20 °C. Low resolution mass spectra were acquired with instruments equipped with ESI/ion trap sources. High resolution mass spectra were acquired with a Waters Q-ToF SYNAPT G2-Si HDMS 8K high-resolution mass spectrometer by the Unitech COSPECT laboratory. SEM images and EDX spectra were acquired with a Jeol JSM-5500 LV scanning electron microscope (SEM). The Raman spectra were measured

at several (three) random positions to demonstrate the homogeneity of the sample. The Raman spectra were recorded on a Thermo Scientific DXR Raman Microscope interfaced to an Olympus microscope (objectives 50×) using a depolarized 532 and 780 nm frequency-stabilized single mode laser (0.1-5 mW for 532 nm and 15-24 mW for 780 nm laser power, approx. 30-1874 cm^{-1} and 25-1877 cm^{-1}) spectral range, 1800 and 830 lines/mm gratings, for 532 and 780 nm wavelength, respectively). The spectrometer was calibrated using a software-controlled calibration procedure employing multiple neon emission lines (wavelength calibration), multiple polystyrene Raman bands (laser frequency calibration), and standardized white light sources (intensity calibration). Gaschromatographic analyzes were performed with the GC-FAST technique using a Shimadzu GC-2010 equipped with a Supelco SLB^{TM}-5ms capillary column. Elemental analyzes were performed at the University of Milan. Microwave enhanced reactions were performed on a Biotage® Initiator^{+} microwave synthesizer. All CO_2 cycloaddition reactions were carried out in a 300 mL steel Parr autoclave, with standard autoclave glass vials, capped with a septum. The optimizations of the reactions were designed with Stat-Ease 360 Software.

6.1 Complexes synthesis and characterization

6.1.1 Synthesis, characterization and support on anionic exchange resins of zincates

$TBA_2[ZnCl_4]$ (M1a). To a solution of tetrabutylammonium chloride in ethanol (6.00 mmol, 1.67 g in 15 ml) a solution of zinc chloride (II) in ethanol (3.00 mmol, 0.408 g in 15 ml) was slowly added. After stirring for 1 h at 40 °C, the solution was concentrated under reduced pressure and the residue was dissolved in the minimum amount of methanol and cooled at −20 °C overnight. The precipitated product was filtered and obtained as a white solid. Yield: 1.31 g (63%). The product was fully characterized by ESI-MS (Figures A.1-A.3, page 221) and elemental analysis. **HRMS-ESI(+)**: calculated for $C_{16}H_{36}N$ 242.2848, found 242.2850 (100%, TBA^+). **HRMS-ESI(−)**: calculated for $ZnCl_3^-$ 168.8357, found 168.8357 (100%, $ZnCl_3^-$). **Elemental analysis** calculated for $[C_{32}H_{72}Cl_4ZnN_2]$ C, 55.53%; H, 10.49%; N, 4.05%; found C, 54.89%; H, 9.92%; N, 3.58%.

Note

Despite several different preparations, I never managed to have a better elemental analysis for this compound. The anion $[ZnCl_3^-]$ is the most stable among all synthesized salts and an equilibrium with TBA $[ZnCl_3]$ exists (a ratio $TBA_2[ZnCl_4]$/TBA $[ZnCl_3]$ = 5:1 would explain the observed elemental analysis). Another possibility is the formation of a partially hydrated form, due to the high hydrophilicity of the starting $ZnCl_2$ and TBACl.

TBA_2 $[ZnBr_4]$ (M1b). To a solution of tetrabutylammonium bromide in ethanol (6.00 mmol, 1.93 g in 15 mL) a solution of zinc(II) bromide in ethanol (3.00 mmol, 0.675 g in 15 mL) was slowly added. After stirring for 1 h at 40 °C, the solution was concentrated in vacuum and the residue dissolved in the minimum amount of methanol and cooled at -20 °C overnight. The precipitated product was filtered and obtained as a white solid. Yield: 1.86 g (71%). The product was fully characterized by ESI-MS (Figures A.4 and A.5, page 223) and elemental analysis.
HRMS-ESI(+): calculated for $C_{16}H_{36}N$ 242.2848, found 242.2850 (100%, TBA^+).
HRMS-ESI(−): calculated for $ZnBr_3^-$ 300.6843, found 300.6842 (100%, $ZnBr_3^-$).
Elemental analysis calculated for $[C_{32}H_{72}Br_4ZnN_2]$ C, 44.18%; H, 8.34%; N, 3.22%; found C, 44.60%; H, 8.60%; N, 3.35%.

$TBA_2[ZnI_4]$ (M1c). To a solution of tetrabutylammonium iodide in ethanol (9.20 mmol, 3.40 g in 15 mL) a solution of zinc(II) iodide in ethanol (4.60 mmol, 1.47 g in 5 mL) was slowly added. After stirring for 1 h at 40 °C, the solution was filtered and concentrated to a third of the volume and cooled at −20 °C overnight. The product was obtained as a pale-yellow solid. Yield: 4.28 g (88%). The product was fully characterized by ESI-MS (Figure A.6, page 224) and elemental analysis.
HRMS-ESI(+): calculated for $C_{16}H_{36}N$ 242.2848, found 242.2850 (100%, TBA^+).
HRMS-ESI(−): only I^-, NaI_2^- and I_3^- were found (see Figure A.6).
Elemental analysis calculated for $[C_{32}H_{72}I_4ZnN_2]$ C, 27.91%; H, 5.27%; N, 2.03%; found C, 27.92%; H, 5.23%; N, 1.92%.

$TMA_2[ZnI_4]$ (M1d). To a solution of tetramethylammonium iodide in ethanol (2.0 mmol, 402.1 mg in 5 ml) a solution of zinc(II) iodide in ethanol (1.0 mmol, 319.2 mg in 5 ml) was slowly added. After stirring for 1 h at 40 °C, the solution was filtered and concentrated to a third of the volume and cooled at −20 °C overnight. The product was obtained as a pale-yellow solid. Yield 685.2 mg (95%). The product was characterized by elemental analysis.
Elemental analysis calculated for $[C_8H_{24}I_4ZnN_2]$ C, 13.32%; H, 3.35%; N, 3.88%; found C, 13.72%; H, 3.23%; N, 3.92%.

General procedure for resins conditioning. 50 g of Amberlite™ IRA-400 (**IRA400**) or Amberlyst™ A26 (**A26**) resins, both in Cl^- form, were packed into a Versaflash™ solid sample loading cartridge. 250 mL of a 20% wt KBr aqueous solution were then recirculated for 4 hours at a 50 mL/min rate. 1 L of distilled water was then flushed to remove excess KBr. The resins (**IRA400-Br** and **A26-Br**) were then filtered and the bromide exchange was verified by EDX spectroscopy (Figures A.20 and A.21, page 231. Table 6.1 displays the chlorine and bromine content in the resins). The resins were then used for further functionalization.

Table 6.1: *Bromide exchange in **IRA400-Br** and **A26-Br**, verified by EDX spectroscopy, measuring chlorine and bromine weight percentages.*

Resin	**Chlorine content** (% wt)	**Bromine content** (% wt)
IRA400-Br	3.3	96.7
A26-Br	6.9	93.1

IRA400 [$ZnCl_4$] (R1a). 4 mL of **IRA400** were poured into a test tube containing a 10 mL solution of zinc chloride (anhydrous) in acetone. The necessary zinc chloride mass was calculated on the basis of the maximum theoretical capacity of **IRA400** (1.4 meq/mL), which converts into 95.42 mg/mL of zinc chloride (382 mg). The tube was then placed onto a vibromechanical agitator overnight. The resin was filtered and washed 5 times with 10 mL of acetone and 3 times with 10 mL of dichloromethane. To avoid the collapse of the pores, the resin was not dried under vacuum.

IRA400 [$ZnCl_2Br_2$] (R1b). 4 mL of **IRA400-Br** were poured into a test tube containing a 10 mL solution of zinc chloride (anhydrous) in acetone. The necessary zinc chloride mass was calculated on the basis of the maximum theoretical capacity of **IRA400** (1.4 meq/mL), which converts into 95.42 mg/mL of zinc chloride (382 mg). The tube was then placed onto a vibromechanical agitator overnight. The resin was filtered and washed 5 times with 10 mL of acetone and 3 times with 10 mL of dichloromethane. To avoid the collapse of the pores, the resin was not dried under vacuum. The product was then analyzed with SEM-EDX spectroscopy to evaluate correct metalation. Table 6.2 summarizes the EDX results for the zincate functionalized resins; Figure A.22 is the record of the EDX spectrum, Figure A.23 is a micrograph of the resin.

A26 [$ZnCl_4$] (R1c). 4 mL of **A26** were poured into a test tube containing a 10 mL solution of zinc chloride (anhydrous) in acetone. The necessary zinc chloride mass was calculated on the basis of the maximum theoretical capacity of **A26** (0.8 meq/mL), which converts into 54.53 mg/mL of zinc chloride (218 mg). The tube was then placed onto a vibromechanical agitator overnight. The resin was filtered and

washed 5 times with 10 mL of acetone and 3 times with 10 mL of dichloromethane. To avoid the collapse of the pores, the resin was not dried under vacuum.

A26 [$ZnCl_2Br_2$] (R1d). 4 mL of **A26-Br** were poured into a test tube containing a 10 mL solution of zinc chloride (anhydrous) in acetone. The necessary zinc chloride mass was calculated on the basis of the maximum theoretical capacity of **A26** (0.8 meq/mL), which converts into 54.53 mg/mL of zinc chloride (218 mg). The tube was then placed onto a vibromechanical agitator overnight. The resin was filtered and washed 5 times with 10 mL of acetone and 3 times with 10 mL of dichloromethane. To avoid the collapse of the pores, the resin was not dried under vacuum. The product was then analyzed with SEM-EDX spectroscopy to evaluate correct metalation. Table 6.2 summarizes the EDX results for the zincate functionalized resins; Figure A.24 is the record of the EDX spectrum, Figure A.25 is a micrograph of the resin.

Table 6.2: *EDX spectra integrations for compounds **R1b** and **R1d**.*

Resin	**Zinc content** (% wt)	**Chlorine content** (% wt)	**Bromine content** (% wt)
R1b	1.720	5.071	93.209
R1d	31.223	13.958	54.820

6.1.2 Synthesis, characterization and support on anionic exchange resins of ferrates

TBA [$FeCl_4$] (M2a). A solution of iron(III) chloride in ethanol (0.36 mmol, 100 mg, in 10 mL) was slowly added to a solution of tetrabutylammonium chloride in ethanol (0.36 mmol, 97 mg in 10 mL). With a sufficiently slow addition, the formation of needle-shaped yellow crystals could be observed; otherwise, a yellow powder was formed. Yield: 185 mg (94%). The product was fully characterized by ESI-MS, melting point, and elemental analysis.
Melting point: 113 °C
MS-ESI(+): calculated for $C_{16}H_{36}N$ 242.28, found 242.32 (100%, TBA^+).
HRMS-ESI(−): calculated for $FeCl_4$ 193.8150, found 193.8147 (100%, $FeCl_4^-$), calculated for $FeCl_3$ 158.8462, found 158.8461 (40%, $FeCl_3^-$).
Elemental analysis calculated for [$C_{16}H_{36}Cl_4FeN$]: C, 43.66%; H, 8.25%; N, 3.18%; found: C, 43.82%; H, 8.23%; N, 3.16%.

TBA [$FeCl_3Br$] (M2b). A solution of iron(III) chloride hexahydrate in ethanol (0.31 mmol, 84 mg, in 10 mL) was slowly added to a solution of tetrabutylammonium bromide in ethanol (0.31 mmol, 100 mg, in 10 mL). With a sufficiently slow addition, the formation of needle-shaped orange crystals could be observed; otherwise, an orange powder was formed. Yield: 176 mg (96%). The product was fully characterized by ESI-MS, melting point, and elemental analysis.

Melting point: 132 °C
MS-ESI(+): calculated for $C_{16}H_{36}N$ 242.28, found 242.40 (100%, TBA^+).
HRMS-ESI(−): calculated for $FeCl_3Br$ 237.7645, found 237.7644 (5%, $FeCl_3Br^-$); calculated for $FeCl_4$ 193.8150, found 197.8150 (100%, $FeCl_4^-$); calculated for $FeCl_3$ 158.8462, found 158.8462 (40%, $FeCl_3^-$).
Elemental analysis calculated for $[C_{16}H_{36}BrCl_3FeN]$: C, 39.66%; H, 7.49%; N, 2.89%; found: C, 39.98%; H, 7.51%; N, 2.86%.

TBA $[FeClBr_3]$ (M2c). A solution of iron(III) bromide in ethanol (0.36 mmol, 106 mg, in 10 mL) was slowly added to a solution of tetrabutylammonium chloride in ethanol (0.36 mmol, 100 mg, in 10 mL). With a sufficiently slow addition, the formation of needle-shaped light red crystals could be observed; otherwise, a red powder was formed. Yield: 200 mg (97%). The product was fully characterized by ESI-MS, melting point, and elemental analysis.
Melting point: 129 °C
MS-ESI(+): calculated for $C_{16}H_{36}N$ 242.28, found 242.35 (100%, TBA^+).
HRMS-ESI(−): calculated for $FeClBr_3$ 325.6635, found 325.6632 (5%, $FeClBr_3^-$); calculated for $FeCl_2Br_2$ 281.7140, found 281.7137 (10%, $FeCl_2Br_2^-$); calculated for $FeCl_3Br$ 237.7645, found 237.7645 (40%, $FeCl_3Br^-$); calculated for $FeCl_4$ 193.8150, found 197.8150 (100%, $FeCl_4^-$); calculated for $FeCl_3$ 158.8462, found 158.8463 (50%, $FeCl_3^-$).
Elemental analysis calculated for $[C_{16}H_{36}Br_3ClFeN]$: C, 33.51%; H, 6.33%; N, 2.44%; found: C, 33.68%; H, 6.22%; N, 2.56%.

TBA $[FeBr_4]$ (M2d). A solution of iron(III) bromide in ethanol (0.31 mmol, 91 mg, in 10 mL) was slowly added to a solution of tetrabutylammonium bromide in ethanol (0.31 mmol, 100 mg, in 10 mL). With a sufficiently slow addition, the formation of needle-shaped dark red crystals could be observed; otherwise, a red powder was formed. Yield: 187 mg (98%). The product was fully characterized by ESI-MS, melting point, and elemental analysis.
Melting point: 135 °C
MS-ESI(+): calculated for $C_{16}H_{36}N$ 242.28, found 242.34 (100%, TBA^+).
HRMS-ESI(−): calculated for $FeBr_4$ 369.6130, found 369.6121 (100%, $FeBr_4^-$); calculated for $FeBr_3$ 290.6946, found 290.6942 (10%, $FeBr_3^-$).
Elemental analysis calculated for $[C_{16}H_{36}Br_4FeN]$: C, 31.10%; H, 5.87%; N, 2.27%; found: C, 30.98%; H, 5.86%; N, 2.00%.

> **Tip**
>
> These products can be crystallized from concentrated ethanol solutions at −20 °C.

IRA400 [$FeCl_4$] (R2a). 4 mL of **IRA400** were poured into a test tube containing a 10 mL solution of iron chloride (anhydrous) in acetonitrile. The necessary iron chloride mass was calculated on the basis of the maximum theoretical capacity of **IRA400** (1.4 meq/mL), which converts into 227.08 mg/mL of iron chloride (908 mg). The tube was then placed onto a vibromechanical agitator overnight. The resin was filtered and washed five times with 10 mL of acetonitrile and 3 times with 10 mL of dichloromethane. To avoid the collapse of the pores, the resin was not dried under vacuum.

IRA400 [$FeCl_3Br$] (R2b). 4 mL of **IRA400-Br** were poured into a test tube containing a 10 mL solution of iron chloride (anhydrous) in acetonitrile. The necessary iron chloride mass was calculated on the basis of the maximum theoretical capacity of **IRA400** (1.4 meq/mL), which converts into 227.08 mg/mL of iron chloride (908 mg). The tube was then placed onto a vibromechanical agitator overnight. The resin was filtered and washed five times with 10 mL of acetonitrile and 3 times with 10 mL of dichloromethane. To avoid the collapse of the pores, the resin was not dried under vacuum. The product was then analyzed with SEM-EDX spectroscopy to evaluate correct metalation. Table 6.3 summarizes the EDX results for the ferrate functionalized resins; Figure A.26 is the record of the EDX spectrum, and Figure A.27 is a micrograph of the resin. A preliminary evaluation of iron loading in the resin was performed employing magnetometry. The results are discussed in Section 3, while a graph of magnetometry data is available in the Supporting information (Figure A.45, page 251).

A26 [$FeCl_4$] (R2c). 4 mL of **A26** were poured into a test tube containing a 10 mL solution of iron chloride (anhydrous) in acetonitrile. The necessary iron chloride mass was calculated on the basis of the maximum theoretical capacity of **A26** (0.8 meq/mL), which converts to 129.76 mg/mL of iron chloride (519 mg). The tube was then placed onto a vibromechanical agitator overnight. The resin was filtered and washed five times with 10 mL of acetonitrile and 3 times with 10 mL of dichloromethane. To avoid the collapse of the pores, the resin was not dried under vacuum.

A26 [$FeCl_3Br$] (R2d). 4 mL of **A26-Br** were poured into a test tube containing a 10 mL solution of iron chloride (anhydrous) in acetonitrile. The necessary iron chloride mass was calculated on the basis of the maximum theoretical capacity of **A26** (0.8 meq/mL), which converts to 129.76 mg/mL of iron chloride (519 mg). The tube was then placed onto a vibromechanical agitator overnight. The resin was filtered and washed five times with 10 mL of acetonitrile and 3 times with 10 mL of dichloromethane. To avoid the collapse of the pores, the resin was not dried under vacuum. The product was then analyzed with SEM-EDX spectroscopy to evaluate correct metalation. Table 6.3 summarizes the EDX results for the ferrate functionalized resins; Figure A.28 is the record of the EDX spectrum, and Figure

A.29 is a micrograph of the resin. A preliminary evaluation of iron loading in the resin was performed employing magnetometry. The results are discussed in Section 3, while a graph of magnetometry data is available in the Supporting information (Figure A.46, page 251).

Table 6.3: *EDX spectra integrations for compounds* ***R2b*** *and* ***R2d****.*

Resin	**Iron content** (% wt)	**Chlorine content** (% wt)	**Bromine content** (% wt)
R2b	12.348	37.935	49.717
R2d	17.633	40.314	42.053

6.1.3 Chemical schemes of ligands and their precursors

Reading guidance

The next table summarizes the structure of the compounds that are described in section 6.1.4.

Table 6.4: *Schemes of the compounds of section 6.1.4.*

Comp.	**Scheme**	**Comp.**	**Scheme**
1	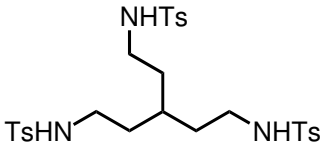	**2**	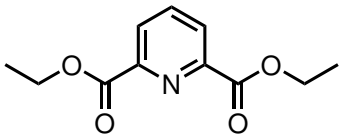
3	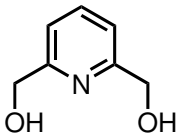	**4**	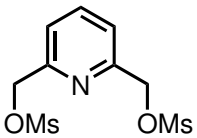
5	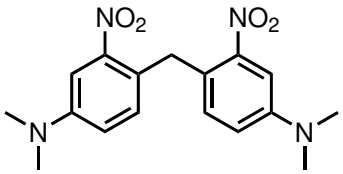	**6**	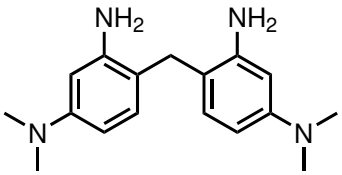
7	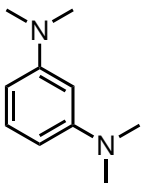	**L1**	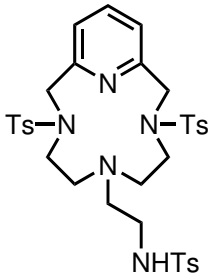

Continues on next page

Table 6.4 – continued from previous page

Comp.	Scheme	Comp.	Scheme
L2	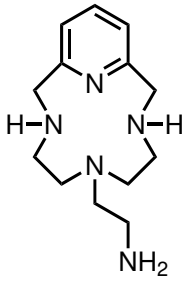	**L3**	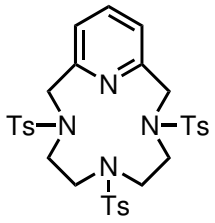
L4	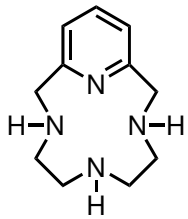	**L5**	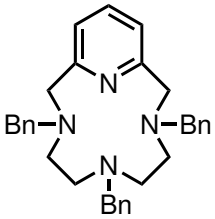
L6	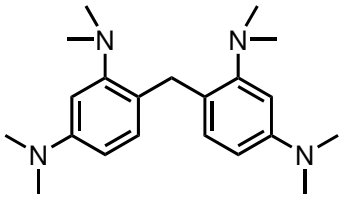	**L7**	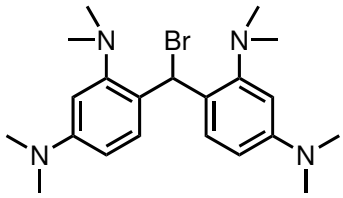

6.1.4 Synthesis and characterization of ligands and their precursors

***N,N′,N″*-(nitrilotris(ethane-2,1-diyl))tris(4-methylbenzenesulfonamide) (1).** A solution of tosyl chloride (11.64 g, 0.061 mol) dissolved in 100 mL of diethyl ether was added to a solution of distilled triethylamine and tren (N^1,N^1-bis(2-aminoethyl)ethane-1,2-diamine, 2.9 mL, 0.019 mmol) in 80 mL of deionized water. After about five minutes, a white precipitate formed. The reaction mixture was stirred vigorously for 14 hours. The solid then was filtered, washed two times with water and three times with diethyl ether. Drying under vacuum produced the pure product as a white powder (yield: 96%). Characterization data were consistent with published material.[250] ^{1}H NMR (400 MHz, $CDCl_3$) δ 7.79 (d, J = 8.3 Hz, 4H), 7.30 (d, J = 8.3 Hz, 2H), 5.89 (bs, 3H), 2.91 (m, 6H), 2.47 (m, 6H), 2.40 (s, 9H) (Figure A.63, page 277).

> **Note**
>
> Triethylamine is very difficult to remove from the product. Make sure to remove it completely by washing the product thoroughly at the end of the reaction. It is very important for the synthesis of the macrocycle to use a triethylamine-free product.

Diethyl pyridine-2,6-dicarboxylate (2). In a round bottom flask, pyridine-2,6-dicarboxylic acid (10.03 g, 60 mmol) was dissolved in ethanol (300 mL) and 2.5 mL of concentrated sulfuric acid were carefully added under stirring. The resulting solution was refluxed for 24 h. Subsequently, the solvent was removed under reduced pressure and the residue was dissolved in a mixture of ethyl acetate and an aqueous sodium hydrogen carbonate solution (100 mL each). The product was extracted with ethyl acetate (2 × 100 mL). The combined organic extracts were washed with brine (100 mL), dried over anhydrous sodium sulfate, filtered, and concentrated under reduced pressure to afford the crude product as a white powder with a yield of 76%. Characterization data were consistent with published material.[251] ^{1}H NMR (400 MHz, $CDCl_3$) δ 8.27 (d, J = 7.8 Hz, 2H), 7.99 (t, J = 7.8 Hz, 1H), 4.48 (q, J = 7.1 Hz, 4H), 1.45 (t, J = 7.1 Hz, 6H) (Figure A.64, page 277).

2,6-dimethanolpyridine (3). In a round-bottom flask, diethyl pyridine-2,6-dicarboxylate (**2**, 10.15 g, 45.5 mmol) was dissolved in ethanol (230 mL), and 2.07 g of sodium borohydride (54.6 mmol) were added portionwise under stirring. Subsequently, calcium chloride (6.06 g, 54.6 mmol)) was added gradually, and a drying tube was fitted to the flask to maintain anhydrous conditions. After several minutes, the suspension turned pink; multiple color changes were observed during the course of the reaction. The mixture was stirred for 4 h at room temperature, after which the solvent was removed under reduced pressure. A saturated aqueous solution of potassium carbonate (60 mL) was then added, and the resulting suspension was briefly stirred. The solvent was again evaporated under reduced pressure, and the resulting residue was subjected to continuous extraction in a Soxhlet apparatus for 24 h using chloroform as the solvent. The product, which precipitated as a crystalline white solid from the extract, was collected by filtration and dried under vacuum (yield: 70%). Characterization data agreed with published material.[252] ^{1}H NMR (400 MHz, $CDCl_3$) δ 7.69 (t, J = 7.7 Hz, 1H), 7.19 (d, J = 7.7 Hz, 2H), 4.78 (s, 4H), 3.32 (bs, 2H) (Figure A.65, page 278).

> **Tip**
>
> It might be tempting to try a liquid/liquid extraction instead of the aforementioned Soxhlet extraction. Liquid/liquid extraction is not recommended because the product is sparingly soluble in chlorinated solvents or apolar organic solvents and tends to stay in the aqueous phase even after many washings; moreover, the product is prone to emulsions.

Pyridine-2,6-diylbis(methylene)-dimethanesulfonate (4).
In a round bottom flask, 5 g of 2,6-dimethanolpyridine (**3**; 36 mmol) were dissolved in 100 mL of ethyl acetate, and triethylamine was added under stirring (25 mL,

180 mmol). The reaction mixture was cooled to 0 °C in an ice bath and methanesulfonyl chloride (8.52 mL, 108 mmol) was added dropwise. The solution was stirred for 15 minutes and then quenched with a saturated aqueous solution of sodium hydrogen carbonate (100 mL). The mixture was extracted three times with ethyl acetate (3 × 100 mL). The combined organic layers were washed with brine (100 mL), dried over anhydrous sodium sulfate, filtered and concentrated under reduced pressure to produce a yellow solid (in some cases, depending on the source of methanesulfonyl chloride, a pink coloration was observed). The crude product was recrystallized from hot methanol, yielding white needle-shaped crystals upon cooling (yield: 71%). Characterization data agreed with published material.[253] ^{1}H NMR (400 MHz, $CDCl_3$) δ 7.83 (t, J = 8.0 Hz, 1H), 7.47 (d, J = 8.0 Hz, 2H), 5.32 (s, 4H), 3.10 (s, 6H) (Figure A.66, page 278).

4,4′-methylenebis(*N*,*N*-dimethyl-3-nitroaniline) (5).
15 g (59 mmol) of 4,4′-methylenebis(*N*,*N*-dimethylaniline) were dissolved in 70 mL of concentrated sulfuric acid. The solution was cooled to 0 °C, and a solution of nitric acid (60%, 8.5 mL) in sulfuric acid (8.5 mL) was added dropwise over the course of 3 hours. At the end of the addition, the reaction mixture was poured into an ice-filled beaker and carefully basified with a cold ammonia solution. The orange precipitate was collected by filtration and washed abundantly with distilled water. Subsequently, the collected solid was refluxed for one hour in 150 mL of ethanol, filtered and dried under vacuum (yield: 99%). Characterization data agreed with published material.[248] ^{1}H NMR (400 MHz, $CDCl_3$) δ 7.24 (d, J = 2.8 Hz, 2H), 6.95 (d, J = 8.6 Hz, 2H), 6.79 (dd, J = 8.6, 2.8 Hz, 2H), 4.37 (s, 2H), 2.98 (s, 12H) (Figure A.67, page 279).

4,4′-methylenebis(N^1,N^1-dimethylbenzene-1,3-diamine) (6).
5 g of **5** (14.5 mmol) were dissolved in a solution of HCl (37%, 120 mL) and distilled water (30 mL). The solution was cooled to 0 °C, and 10 g of powdered tin (84 mmol) were slowly added, resulting in the evolution of gas. Afterward, the mixture was allowed to warm to ambient temperature and it was allowed to react until the full dissolution of the tin. The pH of the solution was adjusted to *ca*. 6 with sodium hydroxide and the tin by-products were precipitated by bubbling H_2S. The precipitate was filtered off and the solution was completely basified with sodium hydroxide, allowing the product to precipitate. The solid was filtered, washed thoroughly with water and cold ethanol, and dried under vacuum (yield: 65%). Characterization data agreed with published material.[248] ^{1}H NMR (400 MHz, $CDCl_3$) δ 6.88 (d, J = 8.3 Hz, 2H), 6.18 (dd, J = 8.3, 2.5 Hz, 2H), 6.09 (d, J = 2.5 Hz, 1H), 3.63 (bs, 4H), 3.61 (s, 2H), 2.88 (s, 12H) (Figure A.68, page 279).

Warning

Hydrogen sulfide is extremely toxic and fatal if inhaled.

Tip

1. A safer alternative to H_2S gas is Na_2S. Because it is a strong base, if added in a large excess, it can precipitate the product as well. Thus, it is advised to monitor the pH and keep it slightly acidic while adding it. Bare in mind that H_2S gas is still produced from the reaction of Na_2S with HCl, thus also this procedure should be conducted with every precaution.
2. The product is slightly soluble in ethanol. Use small amounts of ethanol when washing the products, and try to keep it as cold as possible.
3. Other methods of reduction were attempted to avoid the generation of dangerous tin byproducts and especially the use of hydrogen sulfide, with little success. In particular, reduction with iron and HCl was tested, which is a well-known method for nitro group reduction; however, it resulted in the formation of acridine orange. This reactivity has already been reported.[254]

***N,N,N′,N′*-tetramethyl-*m*-phenylendiamine (7).**
This procedure was adapted from Shivarkar's anilines methylation.[249] In a stainless steel autoclave, 3.482 g of *m*-phenylenediamine (32.2 mmol), 32 mL of dimethyl carbonate (0.38 mol), 1.836 g of tetraethylammonium iodide (7.14 mmol) and 4 mL of distilled water were added. The reactor was charged with 3.4 MPa of dinitrogen gas and heated at 170 °C for two hours under stirring. Subsequently, the autoclave was cooled to room temperature, degassed, and its contents were transferred to a round bottom flask. Most of the unreacted dimethyl carbonate was removed by distillation under reduced pressure, and the product was isolated by column cromatography, using a hexane/ethyl acetate solution (8:2) as the eluent. The product appears as a colorless oil (yield: 45%). *N,N,N′,N′*-tetramethyl-*m*-phenylendiamine is rather sensitive to air exposure and degrades quite quickly; it is suggested to store it at 4 °C in a well-sealed vial. Characterization data agreed with published material.[255] ^{1}H NMR (400 MHz, $CDCl_3$) δ 7.13 (t, J = 8.2 Hz, 1H), 6.22 (dd, J = 8.2, 2.3 Hz, 2H), 6.13 (d, J = 2.3 Hz, 1H), 2.96 (s, 12H) (Figure A.69, page 280).

***N*-(2-(3,9-ditosyl-3,6,9-triaza-1(2,6)-pyridinacyclodecaphane-6-yl)ethyl)-4-methylbenzenesulfonamide (L1).** In an oven-dried round bottom flask, 4.56 g of anhydrous potassium carbonate (33 mmol) were kept under vacuum for one hour at 120 °C. Subsequently, the flask was cooled to 30 °C and 2 g of **1** (3.3 mmol) were

added along with 120 mL of distilled acetonitrile. The suspension was brought to boiling point and a solution of pyridine-2,6-diylbis(methylene) dimethanesulfonate (**4**, 0.975 g, 3.3 mmol) was added dropwise to it. The mixture was refluxed for 20 hours with vigorous agitation. In the end, the solution was filtered, the volatiles were removed in vacuo, and the solid residue was dissolved in dichloromethane/water (50 + 50 mL). The product was extracted three times with DCM (50 mL). The organic phases were washed once with brine (50 mL), gathered and dried with sodium sulfate. The solution was filtered, and the solvent was removed under vacuum. The product was recovered with a yield of 94%. Characterization data agreed with published material.[110] ^{1}H NMR (400 MHz, $CDCl_3$) δ 7.75-7.69 (m, 7H), 7.36-7.32 (m, 6H), 7.28 (d, J = 7.7 Hz, 2H), 5.03 (t, J = 5.6 Hz, 1H), 4.32 (s, 4H), 3.07 (m, 4H), 2.85 (psq,J = 5.6, 5.6 Hz, 2H), 2.46 (s, 6H), 2.41 (s, 3H), 2.39-2.36 (m, 2H), 2.32 (m, 4H) (Figure A.70, page 280).

2-(3,6,9-triaza-1(2,6)-pyridinacyclodecaphane-6-yl)ethan-1-amine (L2).
850 mg of **L1** (1.2 mmol) were suspended in 6 mL of concentrated sulfuric acid in a microwave vial. The vial was sealed and then heated to 120 °C with microwave radiation. After two hours, the solution was cooled and transferred to a 250 mL round bottom flask. The flask was cooled to 0 °C and 50 mL of diethyl ether were added dropwise under gentle stirring. The product precipitated first as a white powder and then as a gum-like agglomerate. During this process, the stirring speed was progressively raised to ensure complete dissolution of sulfuric acid in the solvent. The product was decanted and the supernatant was discarded. The obtained solid was dissolved in 10 mL of distilled water and basified with NaOH pellets. The free base was then extracted (up to twelve times) with dichloromethane until no trace of the product was detected in the organic phase (a TLC plate was used to check its presence in each fraction). The organic phases were collected, dried with sodium sulfate, and concentrated in vacuo. The product was purified by dissolving the residue in 15 ml of diethyl ether and 5 mL of methanol, and the hydrochloride salt was precipitated either by bubbling dry gaseous HCl or by adding a solution of HCl in diethyl ether until no more precipitate formed. The final product can be isolated as the hydrochloride salt or basified as previously described. The hydrochloride salt was isolated in a yield of 64%, while the free base (**L2**) yield was 30%. ^{1}H NMR (**L2** · 4 HCl) (400 MHz, D_2O) δ 7.88 (t, J = 7.8 Hz, 1H), 7.38 (d, J = 7.8 Hz, 2H), 4.56 (bs, 4H, overlapping with water, partially suppressed), (m), 3.22-3.19 (m, 4H), 3.16 (t, J = 7.5 Hz, 2H), 2.94 (t, J = 7.5 Hz, 2H), 2.86-2.83 (m, 4H) (Figure A.71, page 281). ^{1}H NMR (free base, **L2**) (101 MHz, $CDCl_3$) δ 7.53 (t, J = 7.6 Hz, 1H), 6.98 (d, J = 7.6 Hz, 2H), 3.91 (m, 4H), 2.85 (m, 2H), 2.67-2.51 (m, 6H), 2.41 (m, 4H) (Figure A.73, page 282). ^{13}C NMR (hydrochloride salt) (101 MHz, D_2O) δ 148.90, 139.77, 122.19, 51.97, 50.50, 49.52, 45.88, 35.36 (Figure A.72, page 281). ^{13}C NMR (free base, **L2**) (101 MHz, $CDCl_3$) δ 158.87, 136.46, 120.29, 58.99, 55.95, 53.31, 47.58, 40.17 (Figure A.74, page 282). **MS-ESI(+)**: calculated for $C_{13}H_{24}N_5$ 250.20, found

250.26 (MH^+). **Elemental analysis** calculated for $[C_{13}H_{27}Cl_4N_5]$ (**L2** · 4 HCl): C, 39.51%; H, 6.89%; N, 17.72%; found: C, 38.72%; H, 7.29%; N, 16.56%.

3,6,9-tritosyl-3,6,9-triaza-1(2,6)-pyridinacyclodecaphane (L3). In an oven-dried round bottom flask, 2 g of anhydrous potassium carbonate (14.5 mmol) were kept under vacuum for 1 h at a temperature of 120 °C. Subsequently, the solid was cooled to 30 °C, and 2.72 g of 1,4,7-tritosyl-1,4,7-triazaheptane (4.81 mmol) were added along with 140 mL of dry acetonitrile. A solution containing 1.42 g of mesyl-protected pyridine-2,6-diyldimethanol (**4**, 4.81 mmol) in 60 mL of dry acetonitrile was added dropwise. The suspension was then brought to the boiling point and refluxed for 3 hours with vigorous agitation. In the end, the solvent was removed in vacuo and the solid residue was dissolved in DCM/H_2O (60 + 60 mL). The product was extracted three times with DCM (60 mL). The organic phases were washed once with brine, gathered, and dried with sodium sulfate. The solution was filtered, and the solvent was removed in vacuo. The product was recovered pure with a yield of 96%. Characterization data agreed with published material.[253] ^{1}H NMR (400 MHz, $CDCl_3$) δ 7.75 (t, J = 7.7 Hz, 1H. Overlapped with the next doublet), 7.72 (d, J = 8.4 Hz, 4H), 7.65 (d, J = 8.4 Hz, 2H), 7.43 (d, J = 7.7 Hz, 2H), 7.34 (d, J = 8.4 Hz, 4H), 7.27 (d, J = 8.4 Hz, 2H), 4.29 (bs, 4H), 3.33 (t, J = 7.7 Hz, 4H), 2.75 (bs, 4H), 2.45 (s, 6H), 2.41 (s, 3H) (Figure A.75, page 283).

3,6,9-triaza-1(2,6)-pyridinacyclodecaphane (pyclen, L4). In a microwave vial, 2 g of 3,6,9-tritosyl-3,6,9-triaza-1(2,6)-pyridinacyclodecaphane (**L3**, 3 mmol) were suspended in 8 mL of concentrated sulfuric acid. The vial was sealed and then heated to 120 °C with microwave radiation. After 35 minutes, the solution was cooled to 0 °C and 100 mL of diethyl ether was added with slow stirring. The gum-like precipitate was decanted and the supernatant was removed. The solid was dissolved in 20 mL of water and basified with NaOH pellets until pH 14 was reached. The product was then extracted with DCM until the organic phases contained no product (it can be checked with a TLC plate). The organic phases were then collected, quickly dried with sodium sulfate, and the solvent was evaporated. The product was recovered pure with a yield of 88%. Characterization data agreed with published material.[159] ^{1}H NMR (400 MHz, $CDCl_3$) δ 7.51 (t, J = 7.6 Hz, 1H), 6.99 (d, J = 7.6 Hz, 2H), 3.96 (s, 4H), 2.93 (bs, 3H), 2.74-2.66 (m, 4H), 2.27-2.20 (m, 4H) .

Purification of L4. Product **L4** can be easily purified by precipitating the hydrochloride salt and regenerating the freebase. 369 mg of the crude ligand were suspended in 20 mL of diethyl ether. In the suspension, methanol was added until a complete dissolution of the product was obtained (approximately 5 mL). Afterward, a diethyl ether solution of HCl was added dropwise (alternatively, gaseous HCl can be bubbled in the solution). A white precipitate started to form and HCl was added until precipitation stopped. The suspension was then fractionated in four separate

centrifuge vials and centrifuged for five minutes at 4000 RPM. The supernatant was removed and fresh Et_2O was added. The solid was dispersed in the solvent and centrifuged again. This procedure was repeated two other times. Subsequently, the four solid fractions were dissolved in 5 mL of distilled water each and collected. At this point, the product was basified and extracted as previously reported.

Tip

1. Before starting the reaction, be sure to properly clean the walls of the microwave vial as the solvent will not be heated to reflux and residuals of the starting material will contaminate the product if some sticks to the walls.
2. It is important to control wisely the stirring when precipitating the hydrogen sulfate salt. Too vigorous stirring will lead to an excessively fine precipitate, while too shy stirring will result in ether being layered over the acid. If ether does not mix properly, the product will not precipitate quantitatively and, even worse, the sulfuric acid and the side products will not be separated from the product. This could result in a very difficult basification.
3. Try to use a precise amount of water when dissolving the precipitate before basification.

3,6,9-tribenzyl-3,6,9-triaza-1(2,6)-pyridinacyclodecaphane (L5).
L2 was dissolved in anhydrous acetonitrile (30 mL). 0.62 mL of DiPEA were then added along with 424 μL of benzyl bromide. The reaction mixture was left stirring at room temperature overnight. The solvent was then evaporated and the crude was purified by silica column chromatography, using toluene/isopropanol/TEA as eluent (gradient: 96:2:2, 200 mL; 94:4:2, 100 mL; 92:6:2, 100 mL; 90:8:2, 200 mL). The product was eluted last, with a yield of 78%. Characterization data agreed with published material.[159] ^{1}H NMR (400 MHz; $CDCl_3$) δ 7.61 (t, J = 7.6 Hz, 1H), 7.36-7.27 (m, 10H), 7.19-7.10 (m, 5H), 7.08 (d, J = 7.6 Hz, 2H), 3.79 (s, 4H), 3.74 (s, 4H), 3.40 (s, 2H), 2.75-2.65 (m, 4H), 2.50-2.42 (m, 4H) (Figure A.77, page 284). **Elemental analysis** calculated for $[C_{32}H_{40}N_4O_2]$ (**L5** · 2 H_2O): C, 74.97%; H, 7.86%; N, 10.93%; found: C, 75.66%; H, 7.33%; N, 10.35%. Single crystals of **L5** suitable for X-ray diffraction were isolated by slow evaporation of a solution of **L5** in diethyl ether.

Tip

1. Always deactivate the column and the TLCs with TEA, as the product is extremely basic.
2. Do not wash the crude with basic solutions before the column, as it will basify the DiPEA·HBr salt and make its separation more difficult.
3. When dissolving the crude in toluene, the DiPEA·HBr salt precipitates as a white flaky crystalline powder. It can be discarded (avoiding its presence in the column will make the column easier; it is suggested to dissolve the crude in toluene without adding TEA and to filter it later).

4,4′-methylenebis(N^1,N^1,N^3,N^3-tetramethylbenzene-1,3-diamine) (L6).
In a round bottom flask 1.00 g of **7** (6.09 mmol) was added along with 2.5 mL of water and 0.51 mL of 37% HCl. The solution was stirred until the starting material was fully dissolved. Afterward, 3 mL of a 4% aqueous formaldehyde solution were added dropwise over the course of 15 minutes. The reaction mixture was left stirring at room temperature overnight. The product was then basified with 292 mg of NaOH and extracted with dichloromethane (3 × 10 mL). The organic phases were collected, dried with sodium sulfate, and the volatiles were removed under reduced pressure. The crude product was purified by silica column cromatography, using hexane/ethyl acetate/TEA as eluent (gradient: 95:5:1; 80:20:1). The product was isolated with a yield of 97%. ^{1}H-NMR 400 MHz; $CDCl_3$) δ 6.87 (d, J = 8.4 Hz, 2H), 6.52 (d, J = 2.6 Hz, 2H), 6.38 (dd, J = 8.4, 2.6 Hz, 2), 3.97 (s, 2H), 2.92 (s, 12H). 2.70 (s, 12H) (Figure A.78, page 284). ^{13}C-NMR (101 MHz, $CDCl_3$) δ 153.50, 149.66, 131.34, 125.02, 107.83, 104.03, 44.85, 40.97, 30.02 (Figure A.82, page 286). 2D NMR spectra are available at pages 285-286.

6.1.5 Chemical schemes of macrocyclic complexes and $[M_4Cl_8(THF)_6]$ clusters

Reading guidance

The next table summarizes the structure of the compounds that are described in sections 6.1.6-6.1.9

Table 6.5: *Schemes of the compounds of section 6.1.6-6.1.9.*

Comp.	Scheme	Comp.	Scheme
C1a	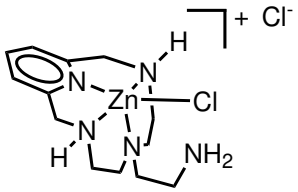	**C1b**	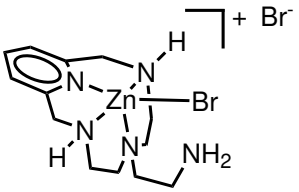
C2a	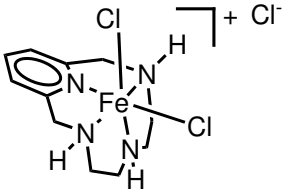	**C2b**	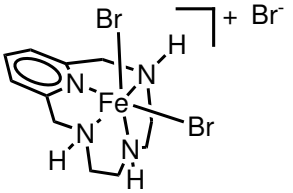
C2c	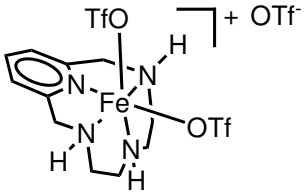	**C2d**	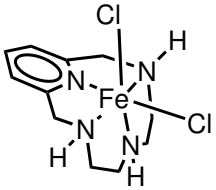
C2e	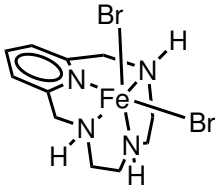	**C2f**	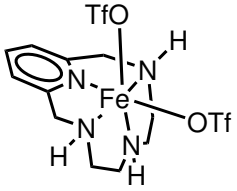
C2a′	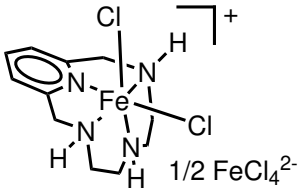	**C3a**	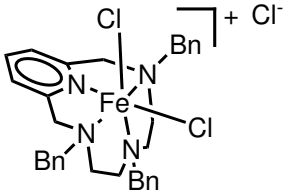
C3b	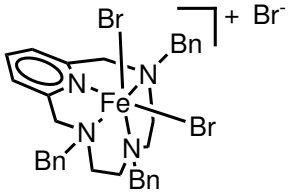	**C3c**	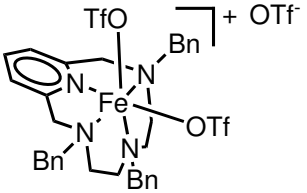
C3d	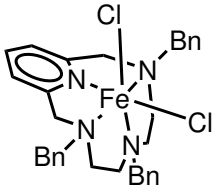	**C3e**	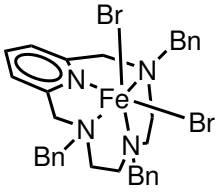

Continues on next page

Table 6.5 – continued from previous page

Comp.	Scheme	Comp.	Scheme
C3f	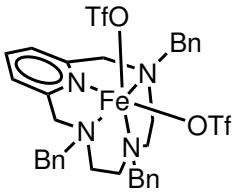	**C4a**	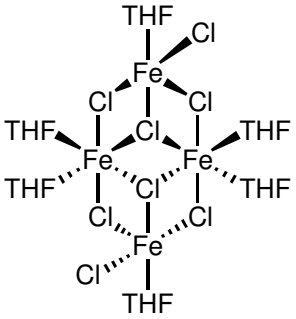
C4b	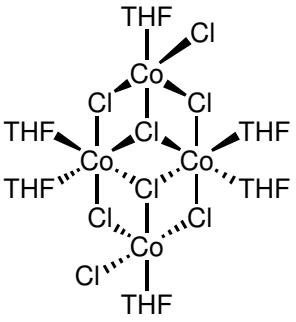	**C4c**	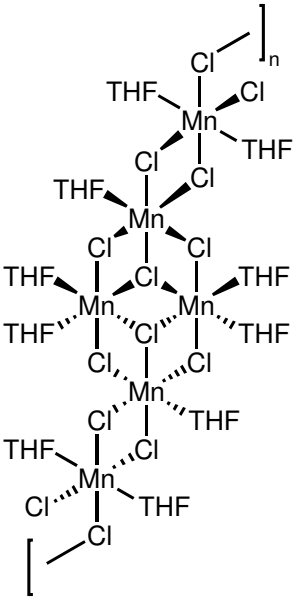
C5a	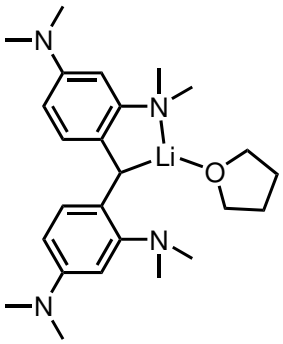	**C5b**	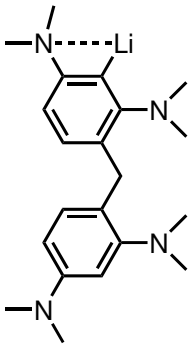
C2b′	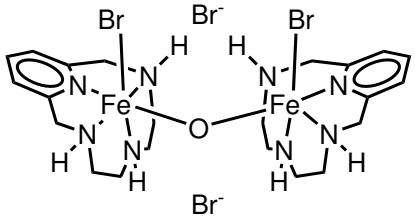		

Continues on next page

Table 6.5 – continued from previous page

Comp.	Scheme	Comp.	Scheme
C2d′	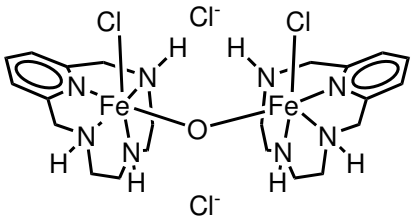		

6.1.6 Synthesis and characterization of zinc complexes

[Zn(Pytren)Cl]Cl (C1a). All procedures were performed in an inert atmosphere of pure dinitrogen gas. 95 mg of **L2 · HCl** (0.375 mmol) were dispersed in 10 mL of freshly distilled DCM, then 170 μL of triethylamine (1.22 mmol) were added. The solution was stirred until the complete dissolution of the ligand. Subsequently, 50 mg of $ZnCl_2$ (0.375 mmol) were added portion wise. As the zinc salt slowly dissolved, the temperature was gradually increased until reflux was reached. The mixture was left to react for two hours, and upon cooling, the product precipitated as a white fine powder. The solid was filtered under dinitrogen pressure, washed two times with distilled DCM (5 mL each time) and dried under vacuum (yield: 15%). ^{1}H-NMR (400 MHz; DMSO-d_6) δ 7.99 (t, J = 7.7 Hz, 1H), 7.41 (d, J = 7.7 Hz, 2H), 4.37-4.33 (m, 2H), 4.30 (dd, J = 16.1, 8.3 Hz, 2H), 3.82 (d, J = 16.1 Hz, 2H), 3.40-3.35 (m, 2H), 3.26-3.13 (m, 2H), 2.82-2.72 (m, 2H), 2.67-2.63 (m, 2H), 2.55-2.46 (m, 2H, superimposed with DMSO signal), 1.71 (td, J = 13.0, 3.9 Hz, 2H) (Figure A.83, page 287). ^{13}C-NMR (101 MHz; DMSO-d_6) δ 154.68, 140.61, 121.48, 55.93, 52.55, 52.45, 48.47, 45.87 (Figure A.84, page 287). **HRMS-ESI(+)**: calculated for $C_{13}H_{23}ClN_5Zn$ 348.09, found 348.0923 (100%, M^+ −Cl) (Figure A.7, page 224).

> **Tip**
>
> The product does not precipitate completely because it is partially soluble in chlorinated solvents. Avoid precipitation with diethyl ether, as it will cause the TEA · HCl salt to precipitate along with the product.

[Zn(Pytren)Br]Br (C1b). All procedures were performed in an inert atmosphere of pure dinitrogen gas. In a Schlenk flask, 150 mg of **L2** (0.602 mmol) were dissolved in 15 mL of distilled DCE. Afterward, 108 mg of zinc bromide (0.480 mmol) were added portion wise. The solution was refluxed for 24 hours, at which point the solution was concentrated under vacuum and transferred to a centrifuge vial. The product was precipitated by adding distilled diethyl ether, centrifuged, and washed three times with fresh diethyl ether. The product was dried in vacuum and

recovered as a white powder (yield: 99%). ^{1}H-NMR (400 MHz; DMSO-d_6) δ 8.03 (t, J = 7.7 Hz, 1H), 7.45 (d, J = 7.7 Hz, 2H), 4.46-4.40 (m, 2H), 4.33 (dd, J = 17.0, 7.0 Hz, 2H), 3.86 (d, J = 17.0, 2H), 3.57-3.54 (m, 2H), 3.24-3.18 (m, 2H), 2.81-2.78 (m, 2H), 2.69-2.66 (m, 2H), 2.61-2.58 (m, 2H), 1.79 (td, J = 12.9, 4.0 Hz, 2H) (Figure A.85, page 288). ^{13}C-NMR (101 MHz; DMSO-d_6) δ 154.77, 141.05, 121.78, 55.68, 52.47, 52.24, 48.52, 45.57 (Figure A.86, page 288). **HRMS-ESI(+)**: calculated for $C_{13}H_{23}BrN_5Zn$ 394.04, found 394.0409 (40%, M^+ −Br) (Figure A.8, page 225). **Elemental analysis** calculated for $C_{13}H_{23}Br_2N_5Zn$: C, 32.90%; H, 4.89%; N, 14.76%; found: C, 32.93%; H, 4.90%; N, 13.78%.

> **Note**
>
> Unlike **C1a**, this complex cannot be synthesized starting from the hydrochloride salt of pytren, as it will result in an admixture of chloride and bromide substituted complexes.

6.1.7 Synthesis of iron precursors

> **Warning**
>
> These syntheses involve the use of trifluoromethanesulfonic acid, which is a very strong and toxic acid. It causes severe burns and it is fatal if inhaled.

Iron(III) triflate. Iron(III) trifluoromethanesulfonate was prepared following a slightly modified literature reported method,[256] working under anaerobic and anhydrous conditions using typical Schlenk techniques. Briefly, two grams of anhydrous iron(III) chloride were transferred to an oven-dried Schlenk flask and 5 mL of thionyl chloride were carefully added. The solid was stirred under reflux overnight to ensure total elimination of water. Then, it was filtered under dinitrogen atmosphere and washed with two 5 mL portions of distilled hexanes. The solid was then collected in a 50 mL Schlenk flask equipped with a stirring bar and a distilling bridge. In another flask, 40 mL of trifluoromethanesulfonic acid were stirred with 1 mL of trifluoromethanesulfonic anhydride for 30 minutes. The acid was then distilled under static vacuum onto the anhydrous iron(III) chloride. The mixture was then stirred at 150 °C for 8 hours and under reflux conditions for 32 hours. The temperature was gradually raised to avoid disproportionation of iron(III) chloride with iron(II) chloride and elemental chlorine.[257] The product is insoluble in acid; therefore, it was filtered and washed with freshly distilled trifluoromethanesulfonic acid. The solid was then dried by heating under vacuum at 50 °C. Yield: 76%. **Elemental analysis** calculated for $FeC_3F_9S_3O_9$: C, 7.16%; H, 0.00%; N, 0.00%; S, 19.12%; found: C, 9.72%; H, 1.06%; N, 0.00%; S, 17.54%.

Iron(II) triflate-acetonitrile complex. $Fe(CF_3SO_3)_2 \cdot 2\,CH_3CN$ was prepared following a literature reported method.[258] Briefly, finely divided iron powder (5.00 g, 89.5 mmol) was added to a Schlenk flask, along with 100 mL of dry acetonitrile. Subsequently, 30 g of trifluoromethane sulfonic acid (0.20 mol) were carefully added to the mixture, resulting in a green solution. The suspension was stirred at 60 °C for 24 hours. The unreacted iron powder was then filtered and the volume of the solution was reduced to half under vacuum. The solution was kept at −25 °C overnight, which afforded very pale turquoise crystals ($[Fe(CH_3CN)_4(CF_3SO_3)_2]$). This first batch of product was filtered (keeping the filtrate), washed with dry diethyl ether, and dried under vacuum. Upon drying, the product loses two coordinated acetonitrile molecules and becomes a free-flowing white powder ($Fe(CF_3SO_3)_2 \cdot 2\,CH_3CN$). The rest of the product was isolated by adding diethyl ether to the filtrate of the first batch and applying the same treatment as that of the first batch (global yield: 77%). The purity of the product was assessed by Mössbauer spectroscopy (Figure A.33, page 239).

6.1.8 Synthesis and characterization of iron complexes

$[Fe(PcLH_3)Cl_2]Cl$ (C2a). All procedures were performed in an inert atmosphere of pure dinitrogen gas. In a Schlenk flask, 202 mg of **L4** (0.979 mmol) were dissolved in 15 mL of dry acetonitrile, gently heating the flask to facilitate ligand dissolution. In another Schlenk flask, a solution containing 265 mg of $FeCl_3 \cdot 6\,H_2O$ (0.979 mmol) was prepared in 5 mL of dry acetonitrile. The iron chloride solution was transferred dropwise to the ligand solution via cannula transfer. A red precipitate formed, which turned yellow with time. The reaction was refluxed for two hours. The solution was filtered under inert conditions and the product was washed with dry diethyl ether first and hexane subsequently. The product was recovered pure with a yield of 60%. Diffraction-quality crystals were grown by diffusion of diethyl ether vapors in a solution of **C2a** in acetonitrile. **HRMS-ESI(+)**: calculated for $C_{11}H_{18}Cl_2N_4Fe$ 332.03, found 297.0579 (100%, M^+ −Cl, Figure A.9, page 225). **Elemental analysis** calculated for $C_{11}H_{18}Cl_3FeN_4$: C, 35.85%; H, 4.92%; N, 15.20%; found: C, 34.86%; H, 4.93%; N, 14.28%. The compound was characterized using Mössbauer spectroscopy (Figure A.34, page 240) and magnetometric analysis (Figure A.47, page 252).

$[Fe(PcLH_3)Cl_2]_2[FeCl_4]$ (C2a'). Single crystals of **C2a'** suitable for X-ray diffraction were isolated by slow diffusion of diethyl ether, layered on top of a methanolic solution of compound **C2a** (v/v 2:1).

$[Fe(PcLH_3)Br_2]Br$ (C2b). All procedures were performed in an inert atmosphere of pure dinitrogen gas. In a Schlenk flask, 260 mg of **L4** (1.26 mmol) were kept under vacuum for an hour. Subsequently, 15 mL of dry acetonitrile were added and

the suspension was gently heated to favor the solid dissolution. Similarly, a solution of iron(III) bromide (373 mg, 1.26 mmol) in 6 mL of acetonitrile was prepared. The iron bromide solution was transferred dropwise to the ligand solution via cannula transfer. Immediately, the solution turned deep red and during the addition a brick red solid started precipitating. The solution was refluxed for two hours. Once the solution returned to room temperature, the solid was filtered and washed with dry diethyl ether and hexane. The product was recovered pure with a yield of 75%. **HRMS-ESI(+)**: calculated for $C_{11}H_{18}Br_2N_4Fe$ 421.92, found 421.9221 (5%, M^+), 341.0040 (90%, M^+ −Br, Figure A.10, page 226). The enlargement of the M^+−Br fragment is depicted on page 226, together with the simulated isotope model. **Elemental analysis** calculated for $C_{11}H_{18}Br_3FeN_4$: C, 26.33%; H, 3.62%; N, 11.16%; found: C, 26.05%; H, 3.58%; N, 10.33%. The compound was characterized using Mössbauer spectroscopy (Figure A.35, page 241) and magnetometric analysis (Figure A.48, page 253).

[μ-O(Fe(PcLH$_3$)Br)$_2$]Br$_2$ (C2b'). 200 mg (0.399 mmol) of **C2b** were dissolved in 44 mL of acetonitrile and 111 μL (0.796 mmol) of triethylamine were added. The reaction mixture was stirred overnight. Then, most of the solvent was evaporated under vacuum, halving the volume of the reaction mixture. The solid was filtered and washed with anhydrous diethyl ether (5 mL). The final product appears as a brown powder (yield: 75%).

[Fe(PcLH$_3$)(OTf)$_2$](OTf) (C2c). All procedures were performed in an inert atmosphere of pure dinitrogen gas. 76 mg of **L4** (0.37 mmol) were stirred under vacuum for one hour, then 5 mL of anhydrous acetonitrile were added. In another Schlenk flask, 176 mg of Fe(OTf)$_3$ (0.349 mmol) were treated similarly and dissolved in 5 mL of dry acetonitrile. The iron triflate solution was then added dropwise to the ligand solution by cannula transfer. Immediately, a sharp color change was observed, from yellow to deep red. The reaction was left stirring at 50 °C for 2 h. Subsequently, the volume of the solution was halved by evaporating the solvent under vacuum, and the flask was left at −20°C overnight. The solution was then filtered to remove the excess ligand, which precipitated upon cooling. The solvent was then removed under vacuum; the oily residue was treated with dry diethyl ether and frozen under inert conditions. The frozen dispersion was left to thaw while being agitated and the process was repeated until the compound was recovered as a powder (yield: 99%). **HRMS-ESI(+)**: calculated for $C_{12}H_{18}F_3FeN_4O_3S$ 411.04, found 411.0419 (30%, M^+ −OTf). **Elemental analysis** calculated for $C_{14}H_{18}F_9FeN_4O_9S_3$: C, 23.71%; H, 2.56%; N, 7.90%; found: C, 23.40%; H, 3.11%; N, 7.51%. The compound was characterized using Mössbauer spectroscopy (Figure A.36, synthesized from commercial Fe(OTf)$_3$ and Figure A.37, synthesized from lab-made Fe(OTf)$_3$, page A.37). The difference in the proposed spectra highlights the importance of a clean iron source.

> **Note**
>
> This compound is very hygroscopic, and must be handled in strictly inert conditions.

[Fe(PcLH$_3$)Cl$_2$] (C2d). All procedures were performed in an inert atmosphere of pure dinitrogen gas. 296 mg of [Fe$_4$Cl$_8$(THF)$_6$] (**C4a**, 1.260 mmol, synthesis in section 6.1.9, page 150) were dissolved in 10 mL of dry acetonitrile. Then, 373 mg of **L4** (1.81 mmol) were dissolved in 21 mL of dry acetonitrile. The two solutions were gently heated to promote the dissolution of the solids. The iron chloride solution was then transferred dropwise to the ligand solution via cannula transfer. The solution turned immediately deep orange, and during the addition, a bright orange precipitate started to form. The suspension was stirred for one hour at 45 °C, then the reaction volume was halved by evaporating part of the solvent under vacuum. To precipitate a larger amount of product, 10 mL of dry diethyl ether were added. The product was filtered and washed two times with dry diethyl ether (2×5 mL). The product appears as a bright orange powder (yield: 83%). ^{1}H-NMR (400 MHz; $CDCl_3$) δ 13.36 (bs, 1H), 10.34 (bs, 2H), 7.26 (t, J = 7.5 Hz, 1H), 7.07 (d, J = 7.5 Hz, 2H), 4.14 (bs, 4H), 3.32 (bs, 4H), 2.85 (bs, 4H) (Figure A.87, page 289). **HRMS-ESI(+)**: calculated for $C_{11}H_{18}Cl_1N_4Fe$ 297.0560, found 297.0570 (20%, M^+–Cl, Figure A.13, page 227). Enlargements of the M^+ and M^+–Cl fragments are depicted on page 228, along with the simulated isotope models for each ion. **Elemental analysis** calculated for $C_{11}H_{18}Cl_2FeN_4$: C, 39.67%; H, 5.45%; N, 16.82%; found: C, 40.29%; H, 5.54%, N, 16.19%. The compound was characterized using Mössbauer spectroscopy (Figure A.38, page 244) and magnetometric analysis (Figure A.49, page 254).

[μ-O(Fe(PcLH$_3$)Cl)$_2$]Cl$_2$ (C2d'). Single crystals of **C2d'** suitable for X-ray diffraction were isolated by diffusion of diethyl ether vapors in an acetonitrile solution of **C2d** that was previously exposed to the atmosphere.

[Fe(PcLH$_3$)Br$_2$] (C2e). All procedures were carried out in an inert atmosphere of dinitrogen gas. 372.9 mg of **L4** (1.808 mmol) were stirred under vacuum for one hour. In another Schlenk flask containing 10 mL of dry acetonitrile, 272 mg of $FeBr_2$ (1.26 mmol) were suspended. The ligand was then dissolved in anhydrous acetonitrile (21 mL); to promote its dissolution, the flask was gently heated to 50 °C. The ligand solution was then slowly transferred to the $FeBr_2$ suspension by cannula filtration. The reaction mixture was stirred under reflux conditions overnight. Then, part of the solvent was evaporated under vacuum, halving the volume of the mixture. The solid was filtered and washed with anhydrous diethyl ether (2×5 mL) in an inert atmosphere. The final product appears as an orange powder (yield: 47%). **HRMS-ESI(+)**: calculated for $C_{11}H_{18}Br_2N_4Fe$ 421.92, found 341.0047 (70%,

M^+-Br, Figure A.16, page 229). The enlargement of the M^+-Br fragment is depicted on page 229, together with the simulated isotope model. **Elemental analysis** calculated for $C_{11}H_{18}Br_2FeN_4$: C, 31.31%; H, 4.30%; N, 13.28%; found: C, 31.77%; H, 4.37%; N, 12.96%.

$[Fe(PcLH_3)(OTf)_2]$ (C2f). All procedures were carried out in an inert atmosphere of dinitrogen gas. 258 mg of **L4** (1.25 mmol) and 545 mg of $Fe(CF_3SO_3)_2 \cdot 2\,CH_3CN$ (1.25 mmol) were kept under vacuum for one hour in two separate flasks. Following this, the ligand was dissolved in 22 mL and the iron source in 7 mL of dry acetonitrile. Using a metal cannula, the iron triflate solution was transferred dropwise to the ligand solution, which was kept warm to facilitate the full dissolution of the solid. The reaction mixture quickly turned deep purple and was stirred at 50 °C for one hour. Most of the solvent was then removed by vacuum distillation and dry diethyl ether (20 mL) was added to promote precipitation of the product. The solid was left stirring in diethyl ether overnight, filtered, and washed with dry diethyl ether. The isolated product (yield: 43%) appears as a brownish powder. **HRMS-ESI(+)**: calculated for $C_{12}H_{18}F_3N_4FeO_9S$ 411.04, found 411.0395 (90%, M^+, Figure A.18, page 230). **Elemental analysis** calculated for $C_{13}H_{18}F_6FeN_4O_6S_2$: C, 27.87%; H, 3.24%; N, 10.00%; found: C, 28.22%; H, 3.47%; N, 10.04%.

$[Fe(PcLBn_3)Cl_2]Cl$ (C3a). All procedures were carried out in an inert atmosphere of dinitrogen gas. 202 mg of **L5** (0.42 mmol) were stirred under vacuum for one hour. Subsequently, the ligand was dissolved in 4.6 mL of dry acetonitrile and the mixture was gently heated to aid in dissolution. Subsequently, a solution of anhydrous iron chloride (68 mg, 0.42 mmol) in dry acetonitrile (4.6 mL) was added dropwise by cannula transfer. The reaction mixture was left stirring at room temperature for one hour. Afterward, the solvent was evaporated under vacuum; the oily residue was treated with dry diethyl ether and frozen under inert conditions. The frozen dispersion was left to thaw while being agitated and the process was repeated until the compound was recovered as a powder (yield: 83%). **Elemental analysis** calculated for $C_{32}H_{38}Cl_3FeN_4O$ (**C3a** $\cdot$ H_2O): C, 58.51%; H, 5.83%; N, 8.53%; found: C, 58.42%; H, 5.99%, N, 8.78%. The compound was characterized using Mössbauer spectroscopy (Figure A.40, page 246) and magnetometric analysis (Figure A.50, page 255).

$[Fe(PcLBn_3)(OTf)_2](OTf)$ (C3c). All procedures were carried out in an inert atmosphere of dinitrogen gas. 101 mg of **L5** (0.21 mmol) were stirred under vacuum for one hour. Subsequently, the ligand was dissolved in 2.3 mL of dry acetonitrile and the mixture was gently heated to aid in dissolution. Subsequently, a solution of anhydrous iron chloride (106.58 mg, 0.21 mmol) in dry acetonitrile (2.3 mL) was added dropwise by cannula transfer. The reaction mixture was left stirring at room temperature for one hour. Afterward, the solvent was evaporated under vacuum;

the oily residue was treated with dry diethyl ether and frozen under inert conditions. The frozen dispersion was left to thaw while being agitated and the process was repeated until the compound was recovered as a powder (yield: 72%). **Elemental analysis** calculated for $C_{35}H_{36}F_9FeN_4O_9S_3$: C, 42.91%; H, 4.34%; N, 5.58%; found: C, 42.13%; H, 3.84%, N, 5.62%. The compound was characterized using Mössbauer spectroscopy (Figure A.41, page 247) and magnetometric analysis (Figure A.51, page 256).

[Fe(PcLBn$_3$)Cl$_2$] (C3d). All procedures were carried out in an inert atmosphere of dinitrogen gas. 200 mg of **L5** (0.420 mmol) were transferred to an oven dried Schlenk flask and dissolved in 10 mL of dry acetonitrile. In another flask, 89 mg of **C4a** (0.381 mmol, synthesis in section 6.1.9, page 150) were dissolved in 5 mL of dry acetonitrile. The second solution was then transferred to the first one dropwise by cannula addition. Immediately a change in color to amber was noticed. The reaction mixture was heated to 60 °C and left stirring for one hour. As the reaction returned to room temperature, the formation of some precipitate was observed. The flask was cooled to −20 °C and the complex was allowed to precipitate over night. The next day, the solid was collected on a frit under nitrogen atmosphere, while the filtrate was transferred to a test tube and used for crystallization. The global yield (powder and crystals amount to 63%. **HRMS-ESI(+)**: calculated for $C_{32}H_{36}ClFeN_4$ 567.1979, found 567.1979 (100%, M^+−Cl, Figure A.19, page 230). **Elemental analysis** calculated for $C_{32}H_{36}Cl_2FeN_4$: C, 63.70%; H, 6.01%; N, 9.29%; found: C, 60.75%; H, 6.23%, N, 9.36%. The compound was characterized using Mössbauer spectroscopy (Figure A.42, page 248). Single crystals of **C3d** suitable for X-ray diffraction were isolated by diffusion of diethyl ether vapors in the reaction filtrate.

[Fe(PcLBn$_3$)Br$_2$] (C3e). All procedures were carried out in an inert atmosphere of dinitrogen gas. 148.7 mg (0.3120 mmol) of **L5** were dissolved in 5 mL of anhydrous acetonitrile. Gentle heating was applied to aid in the dissolution. At the same time, 61.2 mg (0.284 mmol) of anhydrous iron(II) bromide were kept under vacuum to remove residual moisture. After being treated for two hours, they were suspended in 2 mL of dry acetonitrile, and the ligand solution was added dropwise to the iron bromide dispersion. The color of the suspension gradually changed from dark brown to orange and the mixture was refluxed for 16 h. The light brown precipitate was then filtered under inert conditions and washed with 4 mL of diethyl ether. Subsequently, the filtrate was transferred through a cannula filter to an oven dried test tube kept under an inert atmosphere for crystallization. The yield (filtered powder) amounts to 45%. **Elemental analysis** calculated for $C_{32}H_{36}Br_2FeN_4$: C, 55.52%; H, 5.24%; N, 8.09%; found: C, 52.40%; H, 5.21%, N, 7.56%. Single crystals of **C3e** suitable for X-ray diffraction were isolated by diffusion of diethyl ether vapors in the reaction filtrate.

[Fe(PcLBn$_3$)(OTf)$_2$] (C3f). All procedures were carried out in an inert atmosphere of dinitrogen gas. 422.4 mg of **L5** (0.8861 mmol) were dissolved in 10 mL of purified and thoroughly degassed acetonitrile. The solution, which was heated gently to favor full dissolution of the ligand, was then transferred to a 100 mL Schlenk flask, where it was frozen, pumped and thawed two more times. Meanwhile, in a nitrogen filled glovebox, 348 mg of $Fe(CF_3SO_3)2 \cdot 2\ CH_3CN$ were transferred to an RBF, which was then fitted with a septum and transferred to the Schlenk line. The salt was dissolved in 10 mL of dry acetonitrile. The resulting solution was added dropwise to the ligand solution via cannula transfer. A sharp color change during the addition was noticed, with the solution of the ligand turning from pale yellow to orange to deep brown. The solution was stirred under gentle heating (approximately 50°C) for one hour. Afterward, the volume of the solution was halved by evaporating the solvent under vacuum, and the flask was left at −20 °C for one night. The solution was then filtered to remove the excess ligand, which precipitated upon cooling. The flask was then transferred to a nitrogen filled glovebox, and dry diethyl ether was layered on top of the reaction solution. After one week, pale-yellow prism shaped crystals formed and were collected for structural determination. 0.254 g of crystals are collected (38%) by filtration. The solvent was then removed under vacuum from the filtrate, and the obtained tar was taken up in distilled ether and freeze-dried 2 times. The solid was collected on a frit under nitrogen atmosphere. The obtained product is a brown powder (0.273 g, 41%). The total yield amounts to 79%. A ^{1}H-NMR of **C3f** in deuterated acetonitrile was recorded; however, the compound is too paramagnetic and its interpretation is not feasible (Figure A.88, page 289). **Elemental analysis** calculated for $C_{34}H_{36}F_6FeN_4O_6S_2$: C, 49.16%; H, 4.37%; N, 6.75%; S, 7.72; found: C, 48.98%; H, 4.45%, N, 6.63%; S, 7.85. The compound was characterized using Mössbauer spectroscopy (Figure A.42, page 248).

[Fe(PcLBn$_3$)](PF$_6$)$_2$ (C3g). All procedures were carried out in an inert atmosphere of dinitrogen gas. 60 mg of **C3d** (0.10 mmol) were dissolved in 10 mL of deionized and thoroughly degassed water. Because the complex is not very soluble in water, the dissolution was aided with heating and sonication. After the solid was almost completely dissolved and only minor opalescence was left, the solution was filtered. Subsequently, a solution of NH_4PF_6 (162 mg, 1 mmol) in 2 mL of deionized and degassed water was added dropwise through cannula transfer to the ferrous complex solution. Immediately, a white precipitate formed. The suspension was transferred to a Falcon centrifuge tube, which was previously filled with nitrogen atmosphere and fitted with a measure 29 septum. The dispersion was centrifuged for five minutes and the supernatant was discarded. The solid was redispersed in fresh distilled and degassed water to remove any residual starting material and centrifuged again. The supernatant was again discarded and the product was dried under vacuum and gentle heating (45 °C). The recovered yield was 99%.

6.1.9 Synthesis and characterization of $[M_4Cl_8(THF)_6]$ clusters

$[Fe_4Cl_8(THF)_6]$ (C4a.) 5.0 g of $FeCl_2 \cdot 4\,H_2O$ (25 mmol) were heated at 160 °C under vacuum for 48 hours. In these conditions, anhydrous ferrous chloride is formed, and any trace of ferric chloride is reduced to $FeCl_2$. The solid was transferred to a 250 mL Schlenk flask and suspended in 150 mL of dry THF (distilled twice over sodium/benzophenone). The mixture was refluxed for a week, after which the solid was filtered and transferred to a continuous solid-liquid extractor fitted with a frit. The solid was extracted for one week with fresh THF (150 mL). The product precipitated in the THF still as an off-white crystalline solid. It was collected on a frit and dried under vacuum (yield: 90%). The product was characterized with PXRD, which confirmed the presence of a single phase consisting of the desired one. Moreover, Mössbauer spectroscopy was performed on the sample (Figure A.44, page 250) and extensive magnetic measurements were carried out on the sample (Figures A.52-A.54, pag. 257-259).

$[Co_4Cl_8(THF)_6]$ (C4b). 5.0 g of anhydrous cobalt(II) chloride (39 mmol) were heated at 100 °C under vacuum for 8 hours in 250 mL Schlenk. Subsequently, the solid was suspended in 100 mL of dry THF (distilled twice over sodium/benzophenone). The mixture was refluxed for a week, after which the solid was filtered and transferred to a continuous solid-liquid extractor fitted with a frit. The solid was extracted for one week with fresh THF (100 mL). The product precipitated in the THF still as a bright blue crystalline solid. It was collected on a frit and dried under vacuum (yield: 81%).

$\{(Mn_4Cl_8(THF)_6)(Mn(THF)_2Cl_2)\}_\infty$ (C4c). $MnCl_2 \cdot 4\,H_2O$ (10 g, 50 mmol) was refluxed for two days in degassed thionyl chloride (excess, 15 mL), until gas evolution stopped. The solid was suspended in dry *n-hexane*, filtered, and washed with fresh *n*-hexane until the black pitch was eliminated and then suspended in THF (50 mL). The suspension was refluxed for two days. The solid was then filtered, transferred to a continuous solid-liquid extractor fitted with a frit, and extracted for one week with fresh THF (50 mL). The product precipitated in the THF still as a white microcrystalline solid. It was collected on a frit and dried under vacuum (82.5%). Magnetic measurements were carried out on the sample (Figures A.55 and A.56).

6.2 Catalysis: procedures and supplementary data.

6.2.1 Synthesis of oxazolidinones from aziridines and CO_2, catalyzed by IER supported iron(III) halides

General catalytic procedure. The catalyst (**R1d**, **R2b**, **R2d**, 1-60 mg), dichloroethane (1 mL) and substrate (**S1a-n**, 0.2-1 mmol) were added to oven-dried autoclave vials. The vials were equipped with magnetic stirring bars, sealed with adequate caps, and secured in a 300 mL stainless steel Parr autoclave reactor. The autoclave was then charged with CO_2 at half of the desired pressure and vented off. After charging the autoclave to the final pressure (0.1-3.5 MPa), it was placed in a pre-heated bath for 1 to 8 hours. At the end of the reaction, the autoclave was cooled to room temperature (if necessary) and slowly vented off. The internal standard (decane) was added directly to the reaction vial and thoroughly mixed. A known aliquot of the reaction mix was then diluted in 10 mL of acetate for GC-FID analysis. The isolated products were purified by flash chromatographic column (silica gel, 60 μm, *n*-hexane/ethyl acetate solutions were used as eluent in various proportions. Triethylamine (1%) was added).

Scale up of the reaction. The catalyst (**R2d**, 245 mg), dichloroethane (5.7 mL) and 1-butyl-2-phenylaziridine (**S1a**, 1 g, 5.7 mmol) were added to an oven dried autoclave vial, which was then equipped with a magnetic stirring bar, sealed with an adequate cap, and secured in a 200 mL stainless steel Parr autoclave reactor. The autoclave was then charged with 0.4 MPa of CO_2, vented off and recharged with 0.8 MPa of CO_2. The reactor was placed in a pre-heated bath at 25 °C for two hours. At the end of the reaction, the product was recovered by filtering off the catalyst. The catalyst was washed with ethyl acetate to recover the residual product. Soluble iron residues were removed by washing the solution three times with brine. The product was recovered pure and analyzed with ^{1}H-NMR.

Solvent selection and leaching effect on various solvents. Table 6.6 shows the impact of solvent choice on reaction performance and the amount of iron leached from the catalyst, both in weight and as a percentage of the original iron content.

Screening experiment. Table 6.7 collects the results of the screening experiment. Only yield was analyzed as a response. The results of the regression analysis are presented in Table 6.8 in the form of coded coefficients, which means that in the factors the high levels are coded as +1 and the low levels are coded as -1, instead of using actual values. Table 6.9 presents the analysis of variance (ANOVA) for the selected model, highlighting the significance of each factor.

Optimization experiment. Table 6.10 collects the results of the optimization experiment. Only yield was analyzed as a response. The results of the regression analysis, shown in Table 6.11, use coded coefficients (+1 for high levels, -1 for low levels), allowing for a direct comparison of the effects of factors rather than relying on the actual experimental values. In this way, the effect of each factor can be directly compared. In Table 6.12, the analysis of variance for the selected model is presented.

Table 6.6: *Catalyst screening: leaching and solvent effect.*[a]

Entry	Solvent	Conversion (%)[b]	Yield $(\%)_b$	Selectivity (%)	Fe (mg) in the residue[c]	% of Fe lost[d]
1	CH_3CN	99	71	71	0.52	26%
2	*n*-hexane	22	4	18	0.29	14%
3	AcOEt	18	12	66	0.82	40%
4	Acetone	51	50	98	0.94	46%
5	DCE	82	76	93	0.42	21%

[a]Reaction conditions: 30 °C, 1.6 MPa CO_2, 30 mg of resin (corresponding to 3.4 mol% and 3.6 mol% for **R2a** and **R2b**, respectively, 1 h, 1 mmol of **R2a** in 1 mL of acetonitrile. [b]Conversion and yield were calculated with GC-FID, using decane as internal standard. [c]The amount (mg) of iron content in the solid residue was calculated at the end of the reaction by filtering the reaction mixture, evaporating the volatiles in the filtrates, and performing ICP-OES analyses after mineralization. [d]Iron lost from the fresh catalyst (%) was calculated by dividing the iron total weight (mg) found in solution by the iron total weight (mg) in the fresh catalyst.

Table 6.7: *Screening experiment: performed tests*

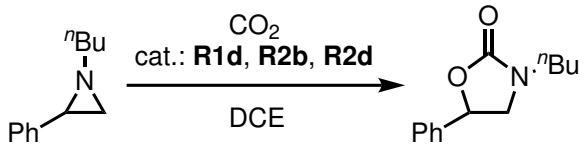

S1a **P1a**

Entry	Cat.	*p* (MPa)	*T* (°C)	Cat. load. (mg/ mmol)	[S1a] (mmol/ mL)	*t* (h)	Conv. (%)[a]	Yield (%)[a]
1	**R2b**	0	60	30	0.2	1	10	0
2	**R2d**	1.6	30	30	1	1	85	76
3	**R2b**	0	60	30	0.2	1	4	3
4	**R1d**	1.6	30	30	0.2	8	16	2
5	**R2d**	0	60	30	1	8	40	17
6	**R2b**	0	30	5	1	8	5	1
7	**R1d**	1.6	60	5	1	1	0	0
8	**R2b**	0	30	5	0.2	8	0	0
9	**R2d**	1.6	30	30	0.2	8	99	85
10	**R2d**	0	30	5	1	1	1	1
11	**R1d**	0	30	5	0.2	1	0	0
12	**R1d**	0	30	5	0.2	1	1	1
13	**R1d**	0	60	5	0.2	8	12	8
14	**R2d**	0	60	30	0.2	1	13	1
15	**R2b**	1.6	60	5	1	8	23	21
16	**R2b**	1.6	60	5	1	8	25	23
17	**R1d**	1.6	60	5	1	1	0	0
18	**R2b**	1.6	30	5	0.2	1	12	2
19	**R1d**	0	30	30	1	8	1	1
20	**R2b**	1.6	60	30	1	1	6	6
21	**R2d**	1.6	60	5	0.2	8	32	17
22	**R2d**	0	30	5	1	1	1	1
23[b]	**R2d**	1.6	60	5	0.2	8	29	17
24[c]	**R2d**	1.6	30	30	1	1	80	72

[a]Conversion and yield were determined with GC-FID, using decane as the internal standard. [b]Replicate point for run 21. [c]Replicate point for run 2

Table 6.8: *Coefficient estimate for the screening experiment. Factors are coded, meaning levels are coded as -1/+1 and not as experimental values.*

Term	Coefficient Estimate	Standard Error
Intercept	10.64	0.5132
A[1] - Catalyst	15.97	0.6607
A[2]	−5.49	0.8217
B - Pressure	8.02	0.5405
C - Temperature	−3.87	0.7959
D - Catalyst loading	3.63	0.6008
F - Time	5.29	0.7991
A[1]B	10.94	0.8326
A[2]B	−3.87	0.7729
A[1]C	−12.39	0.7329
A[2]C	9.84	0.8962
A[1]D	13.98	0.7314
A[2]D	−5.07	1.37

Table 6.9: *ANOVA of the model selected for the screening experiment.*

Factor	Degrees of freedom	Mean Square	F-value	p-value	
Model	12	1236.98	271.21	<0.0001	significant
A - Catalyst	2	1154.89	253.21	<0.0001	
B - Pressure	1	2169.16	475.59	<0.0001	
C - Temperature	1	638.37	139.96	<0.0001	
D - Catalyst loading	1	1093.83	239.82	<0.0001	
F - Time	1	200.14	43.88	<0.0001	
AB	2	399.2	87.52	<0.0001	
AC	2	701.98	153.91	<0.0001	
AD	2	833.55	182.76	<0.0001	
Residual	11	4.56			
Lack of Fit	4	8.79	4.1	0.0505	not significant
Pure Error	7	2.14			

Table 6.10: *Optimization: performed experiments.*

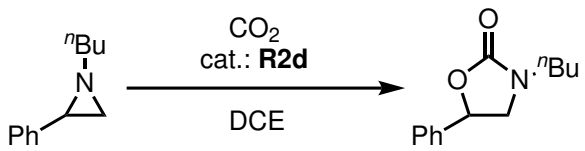

S1a **P1a**

Batch	Entry	p (MPa)	T (°C)	Cat. load. (mg/ mmol)	t (h)	Conv. (%)[a]	Yield (%)[a]
1	1	3.5	57	5	0.67	14	10
	2	3.5	57	49	0.67	97	92
2	3	3.5	32	60	5.18	97	94
	4	3.5	32	12	5.18	99	98
3	5	2	63	34	3.44	99	97
	6	2	63	5	3.44	46	43
4	7[b]	2.2	25	23	0.5	53	50
	8	2.2	25	60	0.5	89	81
5	9	2	63	34	3.25	100	96
	10	2	63	34	3.25	100	98
6	11	0.4	100	12	5.09	24	15
	12	0.4	100	60	5.09	93	51
7	13	0.4	69	23	0.5	15	12
	14	0.4	69	60	0.5	45	31
8	15	3.5	100	27	2.32	91	83
	16	3.5	100	60	2.32	99	93
9	17	0.4	25	5	6	25	22
	18	0.4	25	45	6	97	82
10	19	2	63	34	3.25	99	98
	20	2	63	34	3.25	99	94
11	21	0.4	25	60	2.34	91	75
	22	0.4	25	5	2.34	11	10
12	23	2	63	60	6	99	94
	24	2	63	27	6	100	97
13	25	1.7	100	47	0.5	84	69
	26	1.7	100	5	0.5	10	8
14	27	3.5	100	53	6	100	93
	28	3.5	100	5	6	37	30
15	29[c]	1.7	100	47	0.5	72	68
16	30[d]	3.5	32	60	5.18	99	98

[a]Conversion and yield were determined with GC-FID, using decane as the internal standard. [b]This run achieved the highest TOF of all the experiments: 37.9 h^{-1}. [b]Replicate point for run 25. [c]Replicate point for run 3.

Table 6.11: *Coefficient estimate for the optimization experiment. Fac-tors are coded, meaning levels are coded as -1/+1 and not as experimental values. Upper case letters represent easy-to-change factors, lower case letters hard-to-change factors.*

Source	Coefficient Estimate	Standard Error
Intercept	96.79	3.16
Whole-plot Terms:		
a - Pressure	19.32	2.01
b - Temperature	−8.23	2.01
d - Time	14.49	2.03
bd	−5.56	2.44
$\mathbf{a^2}$	−15.07	3.43
$\mathbf{d^2}$	−15.94	3.61
Subplot Terms:		
C - Catalyst loading	27.11	1.99
Cd	−6.37	2.5
$\mathbf{C^2}$	−27.33	3.93

Table 6.12: *ANOVA of the model selected for the optimization experiment.*

Source	Degrees of freedom	F-value	p-value	
Whole-plot	6	33.6	<0.0001	significant
a - Pressure	1	92.05	<0.0001	
b - Temperature	1	16.8	0.0006	
d - Time	1	51.05	<0.0001	
bd	1	5.18	0.034	
$\mathbf{a^2}$	1	19.35	0.0003	
$\mathbf{d^2}$	1	19.49	0.0003	
Subplot	3	76.82	<0.0001	significant
C - Catalyst loading	1	185.72	<0.0001	
Cd	1	6.51	0.019	
$\mathbf{C^2}$	1	48.39	<0.0001	

General GC method. The yield and conversion of the substrate used for the screening and optimization of the reaction (1-butyl-2-phenylaziridine, **S1a**) were calculated by fast GC-FID analysis, with an external calibration method. The calibration curve was determined using decane as the internal standard. The instrumental parameters are presented in Table 6.13. The column temperature was programmed as shown in Table 6.14. The purpose of the program was to match the retention time of the analytes with its isothermal sections of the program. As a result, retention times are as shown in Table 6.15.

Table 6.13: *GC-FID instrumental parameters for aziridines and oxazolidinones.*

Parameter	Value
Column	Supelco SLB-5ms
Detector	FID
Carrier pressure	0.274 MPa
Total flow	11.7 mL/min
Helium flow	0.35 mL/min
Hydrogen flow	40.0 mL/min
Air flow	400.0 mL/min
Split ratio	30.0

Table 6.14: *GC column program*

Rate (°C/min)	Temperature (°C)	Hold time (min)
-	90.0	1.30
45.00	110.0	0.50
100.00	180.0	1.00
100.00	265.0	1.00
100.00	280.0	1.00

Table 6.15: *Retention times of the analyzed compounds.*

Compound	Retention time (min)
Decane	1.908
1-butyl-2-phenylaziridine	3.698
3-butyl-5-phenyloxazolidin-2-one	5.539

Calibration curves The calibration curves were determined using five standard solutions of the substrate (1-butyl-2-phenylaziridine, **S1a**), which was made and purified in-house, and the product (3-butyl-5-phenyloxazolidinone **P1a**), in a concentration range of 0.035-0.35 mg/mL, each containing decane as internal standard in a concentration of 0.073 mg/mL. The calibration curves are shown in Figures 6.1 and 6.1.

ICP-OES analyses: Mineralization and determination of Fe content in the samples. All determinations were performed using a microwave assisted " *vessel-inside*

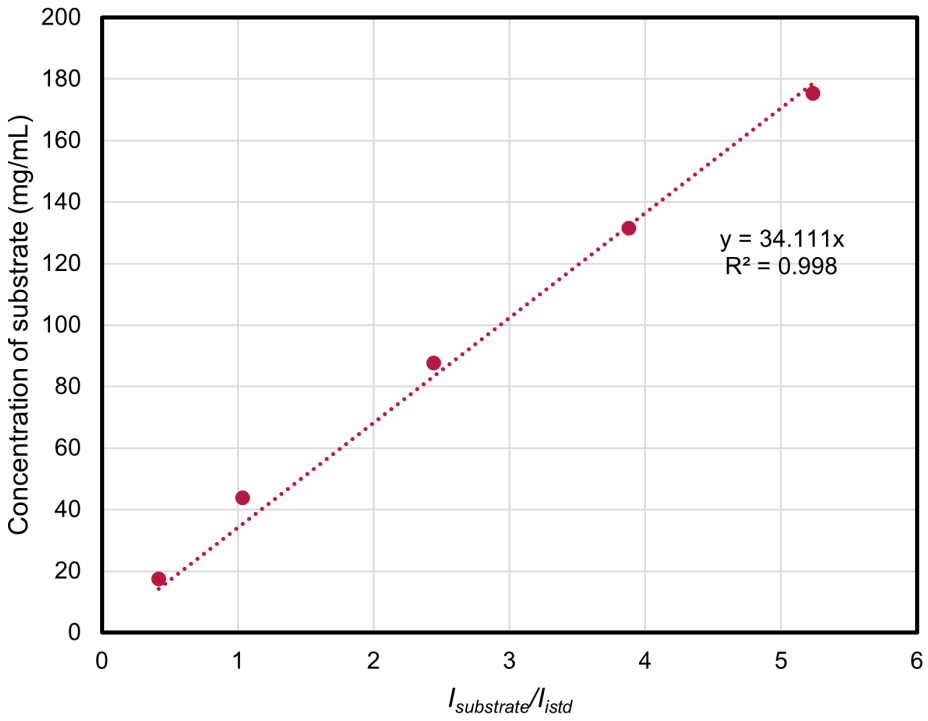

Figure 6.1: *Calibration curve of 1-butyl-2-phenylaziridine. On the y axis, the concentration is referred to the reaction solution. On the x axis, I stands for integral of the relative peak.*

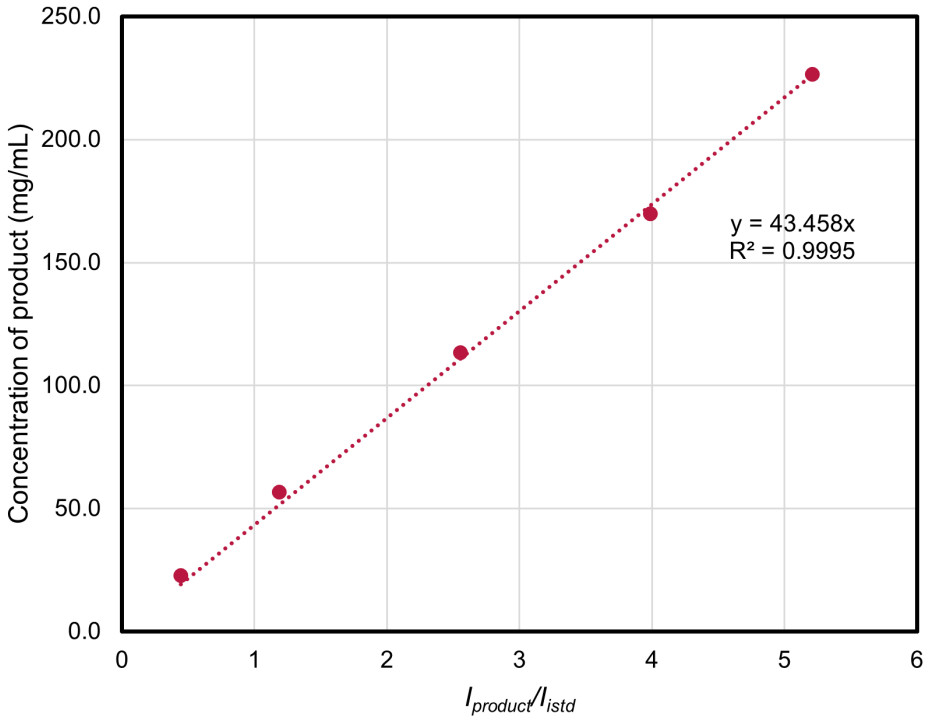

Figure 6.2: *Calibration curve of 3-butyl-5-phenyloxazolidinone. On the y axis, the concentration is referred to the reaction solution. On the x axis, I stands for integral of the relative peak.*

vessel strategy, reported elsewhere.[259] Briefly, the optimized sample digestion was conducted as follows:

1. Approximately 10 mg of catalyst were accurately weighed on a 5 digit analytical balance and transferred to a 7 mL PFA vessel with 1 mL of HCl. The vessel was sealed and heated at 180 °C (2 h) using a hot plate, under a laminar flow hood.
2. 0.4 mL of HNO_3 and 2.0 mL of H_2O_2 were added and the microwave strategy mentioned above was carried out using an ETHOS One (Milestone MLS) MW digestion system, with the following power program: 250 W (2 min), 0 W (1 min), 400 W (2 min), 0 W (1 min), 500 W (10 min).
3. After microwave digestion, the PFA vessel was opened and posed over a hot plate (under a laminar flow hood) to evaporate the digestion solution to a low volume. 0.6 mL of HNO_3 were added before transferring the digested solution to a 30 mL LDPE container: dilution to 20 g was performed using ultrapure water. An additional 1:20 dilution was necessary before instrumental determination.

An Agilent ICP-OES (mod. 5800 VDV) was used for the final determination. Radial and axial calibrations were performed at three different wavelengths (238.204, 258.588, and 259.940 nm): as a result, the measurements were consistent with each other at each wavelength. Ultrapure hydrochloric acid (Sigma-Aldrich, 36% in water) and ultrapure nitric acid produced by sub-boiling distillation from commercial HNO_3 (Carlo Erba, 65% pure)[260] were used for sample digestion. Hydrogen peroxide (for trace analysis, ≥ 30%, Sigma Aldrich) was employed. Ultrapure water was used for the preparation of each solution. Ultrapure water was produced with a Sartorius Arium mini plus UV Lab Water System. Table 6.16 reports the iron content of **R2d**, as freshly synthetized, after catalysis and after stirring it for 24 hours in DCE, in a solution of **S1a** in DCE and in a solution of **P1a** in DCE. The iron content of the starting material, **A26-Br**, was also measured.

Table 6.16: *Determination of Iron content in solid samples.*

Entry	Sample	Weight (mg)	Made up to (g)	With-drawn (g)	Made up to (g)	Fe con-centration (µg/kg)	%Fe
1	**R1d** (43 mg), after 24 h in DCE (1 mL)	9.04	20.06	0.9936	20.01	1396.05	6.55
2	**R1d** (43 mg), after 24 h in DCE (1 mL) and **S1a** (1 mmol)	7.52	20.18	0.9608	19.95	1192.82	6.97
3	**R1d** (43 mg), after 24 h in DCE (1 mL) and **P1a** (1 mmol)	6.99	20.04	0.9708	20.06	1008.90	6.27[a]
4	**R1d** after one catalytic cycle in DCE	12.53	20	0.9865	19.98	1593.45	5.41
5	**R1d** after one catalytic cycle in CH_3CN	7.9	20.27	0.9772	20.06	939.88	5.19
6	Freshly synthesized **R1d**	13.42	20	0.98	20.03	2122.82	6.79
7	**A26-Br**	8.33	20.01	0.9637	20.00	1.00	<0.005

[a] A repeated analysis resulted in an iron concentration of 6.24%.

Table 6.17: *Determination of Iron content in liquid samples.*

Entry	Sample	Made up to (g)	Fe con-centration (µg/kg)	Absolute weight of Fe (µg
1	Commercial DCE	10	13.83	0.145
2	Commercial CH_3CN	10	7.99	0.084
3	Filtrate of entry 1, Table 6.16	10	210.97	2.21
4	Filtrate of entry 2, Table 6.16	10	504.88	5.30
5	Filtrate of entry 3, Table 6.16	10	41271	433
6	Filtrate of entry 4, Table 6.16	10	57951	608
7	Filtrate of entry 5, Table 6.16	10	71373	749
8	DCE washing of entry 1, Table 6.16	10	10.54	0.111
9	DCE washing of entry 2, Table 6.16	10	66.35	0.696
10	DCE washing of entry 3, Table 6.16	10	1503	15.8
11	DCE washing of entry 4, Table 6.16	10	393	4.12

6.2.2 Dimerization of aziridines, catalyzed by ammonium tetrahalozincates

General catalytic procedure, method A. The catalyst (0.025 mmol), acetonitrile (1 mL), and substrate (1 mmol) were added in this order in a round bottom pressure tube. Each piece of glassware was previously dried in an oven at 120 °C. The reaction mixture was stirred for 16 hours at 75 °C in a preheated hot bath.

Method B. The catalyst (0.025 mmol), acetonitrile (1 mL) and the substrate (1 mmol) were added in this order in a microwave vial. The reaction was stirred for 20 minutes - 80 minutes (according to the specific experiment) at 100 - 140 °C.

GC analysis. At the end of the reaction the reaction mixture was diluted with ethyl acetate in a 10 mL volumetric flask. 0.5 mL were taken and further diluted in a volumetric flask to obtain a concentration of analytes in the range of 0.1-0.3 mg/mL. Before completing dilution, 0.5 mL of a solution of DMT (dimethyl terephthalate) was added as IS, to obtain a final IS concentration of 0.1 mg/mL.

NMR yield with IS. At the end of the reaction, the solvent was evaporated with reduced pressure. To the residue, 24.3 mg (0.125 mmol) of DMT were added as IS. The solvent was evaporated under reduced pressure, and about 750 μL of $CDCl_3$ was added for ^{1}H-NMR analysis.

6.2.3 Synthesis of cyclic carbonates from epoxides and CO_2, catalyzed by IER supported iron(III) and zinc(II) halides

General catalytic procedure. The catalyst (1-30 mg/mmol) and the epoxide (500 mg) were mixed together in an oven-dried autoclave vial. The vial was equipped with a magnetic stirring bar, sealed with an adequate cap, and secured in a stainless steel 300 mL Parr autoclave reactor. The autoclave was then loaded with CO_2 at the desired pressure (0.2-2 MPa) and placed in a pre-heated bath at 50-100 °C for the desired reaction time (0.5-16 hours). The autoclave was then cooled at 0 °C to quench the reaction and slowly vented off. The reaction mixture was either dissolved in an appropriate solvent and filtered to remove the resin or directly filtered when the product was in the liquid form. Yield was calculated with GC analysis or ^{1}H-NMR using an appropriate internal standard. Isolated products were purified either by precipitation with hexanes or by flash chromatographic column (silica gel, 60 μm, *n*-hexane/ethyl acetate solutions were used as eluent in various proportions).

Screening experiment conditions: propylene oxide (S2a, R^1 = Me, R^2 = H). The catalyst (loading = 1-20 mg/mmol) and propylene oxide (500 mg, 8.6 mmol) were added in an auto-clave vial capped with a septum. The vial was transferred to a

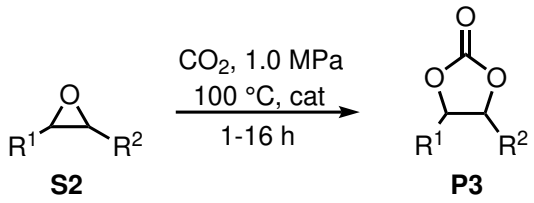

Scheme 6.2.1: *Screening experiment reaction conditions.*

Parr steel autoclave, which was loaded with 1.0 MPa of CO_2 and heated at 100 °C. After a reaction time of 1-16 hours, the autoclave was cooled at 0 °C. The reaction mixture was diluted with ethyl acetate and filtered to remove the resin. Yield was calculated via fast GC-FID analysis.

Styrene oxide (S2b, R^1 = Ph, R^2 = H). The catalyst (loading = 1-20 mg/mmol) and styrene oxide (500 mg, 4.16 mmol) were added in an auto-clave vial capped with a septum. The vial was transferred to a Parr steel autoclave, which was loaded with 1.0 MPa of CO_2 and heated at 100 °C. After 1-16 hours the autoclave was cooled at 0 °C. When the reaction did not proceed to completion, the carbonate was solubilized in epoxide, and the procedure for yield determination was the same as for propylene oxide. When the epoxide was completely converted to styrene carbonate, conversely, the solid product needed to be dissolved in dichloromethane. The resin was then removed by filtration and the solvent was evaporated under reduced pressure. Yield was calculated by fast GC-FID analysis.

Cyclohexene oxide (S2c, $R^1 = R^2 = CH_2CH_2CH_2CH_2$). The catalyst (loading = 1-20 mg/mmol) and cyclohexene oxide (500 mg, 8.6 mmol) were added in an autoclave vial capped with a septum. The vial was transferred to a Parr steel autoclave, which was loaded with 1.0 MPa of CO_2 and heated at 100 °C. After 1-16 hours, the autoclave was cooled at 0 °C. The reaction mixture is diluted with ethyl acetate and filtered to remove the resin. Yield was calculated by fast GC-FID analysis.

Scale up of the reaction and recycling - procedure. The resin (1.5 g) and 5 g of propylene oxide (86 mmol) were mixed together in an steel Parr autoclave. The autoclave was loaded with 1.4 MPa of CO_2 and heated to 100 °C. After 2 hours, the autoclave was cooled to 0 °. The resin was recovered by filtration and washed 3 times with 5 mL of dichloromethane. Yield was calculated via fast GC-FID analysis.

Screening experiment results Table 6.18 collects the results of the screening experiment. Only yield was analyzed as a response. Unlike in the previous Design of Experiment, these data required a power transform. Indeed, reduce the non-normality of the errors in the linear model, and often to improve linearity itself, a power transform can be applied to the model. In a linear model:

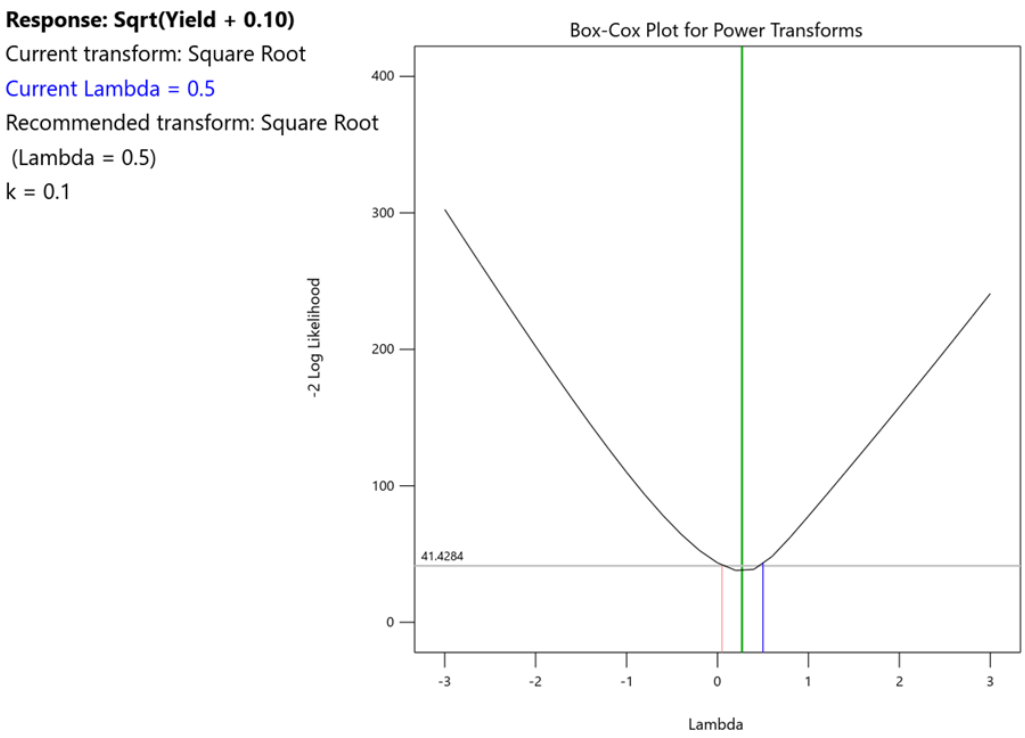

Figure 6.3: *Box-Cox plot of the screening experiment*

$$Y_i = \beta_0 + \beta \mathbf{X} + \varepsilon_i, \quad \varepsilon_i \sim \mathcal{N}\left(0, \sigma^2\right) \tag{6.1}$$

Where Y_i is the response variable (in our case, the yield), β_0 is the intercept, β are the coefficients for the variables $\mathbf{X}$, and ε_i are the errors, which follow a normal distribution centered around 0. The simple Box-Cox transform is:

$$Y_i^\lambda = \begin{cases} \frac{Y_i^\lambda - 1}{\lambda} & \text{for } (0) \\ \log Y_i & \text{for } (\lambda = 0) \end{cases} \tag{6.2}$$

The λ parameter is determined by maximum likelihood, i.e., which value of λ is most likely to have given rise to the observed distribution of the model residuals. When plotting the negative double logarithm of the likelihood function $\mathcal{L}$ for $\lambda = [-3 \ldots 3]$ (Figure 6.3), the minimum of the function can be assumed to be the correct λ value. In this case, the minimum was near $\lambda = 0.5$, which corresponds to a square root transform. Because the response needs to be greater than zero, an arbitrary constant was added. Thus the transform applied to the data is:

$$Y_i^\lambda = \sqrt{Y_i + 0.1} \tag{6.3}$$

The results of the regression analysis are presented in Table 6.19 in the form of coded coefficients, which means that in the factors the high levels are coded as +1 and the low levels are coded as -1, instead of using actual values. Table 6.20

presents the analysis of variance (ANOVA) for the selected model, highlighting the significance of each factor.

Optimization experiment. Table 6.21 collects the results of the optimization experiment. Only yield was analyzed as a response. The results of the regression analysis, shown in Table 6.22, use coded coefficients (+1 for high levels, -1 for low levels), allowing for a direct comparison of the effects of factors rather than relying on the actual experimental values. In this way, the effect of each factor can be directly compared. In Table 6.23, the analysis of variance for the selected model is presented.

Validation of the model and control experiments. To validate the optimization model, experiments were carried out varying the parameters and comparing the experimental yield to the theorical yield calculated by the model. The reactions were carried out ac-cording to general procedure. Yield and conversion were calculated via fast GC-FID analysis.

Table 6.18: *Screening results. Conditions: p = 1.0 MPa, T = 100 °C. Yield determined with GC-FAST analysis, using dodecane as IS.*

Batch	Entry	*t* (h)	Catalyst	Cat. load. (mg/ mmol)	Substrate	Yield (%)[a]
1	1	16	**R1b**	1	**S2a**	37.2
	2	16	**R1d**	1	**S2c**	0
	3	16	**R2d**	20	**S2a**	88.9
	4	16	**R1b**	1	**S2b**	0
2	5	1	**R2d**	1	**S2b**	0
	6	1	**R1b**	1	**S2a**	1.6
	7	1	**R2b**	1	**S2c**	0
	8	1	**R1d**	20	**S2b**	57.3
3	9	1	**R1d**	20	**S2a**	100
	10	1	**R1d**	1	**S2b**	5.4
	11	1	**R1d**	1	**S2c**	0
	12	1	**R2b**	1	**S2a**	2.7
	13	1	**R2d**	20	**S2b**	23.9
4	14	16	**R2b**	20	**S2a**	11.1
	15	16	**R2d**	20	**S2c**	22.9
	16	16	**R2d**	1	**S2a**	29.2
	17	16	**R1d**	20	**S2b**	100
5	18	1	**R1d**	20	**S2c**	0
	19	1	**R1b**	20	**S2a**	23.2
	20	1	**R1d**	1	**S2a**	7.1
	21	1	**R2d**	1	**S2c**	0
6	22	16	**R2b**	20	**S2c**	0
	23	16	**R2d**	20	**S2b**	79
	24	16	**R1b**	20	**S2a**	90.2
	25	16	**R2b**	1	**S2a**	9.1
7	26	16	**R1b**	1	**S2c**	0
	27	16	**R2b**	1	**S2b**	2.6
	28	16	**R1b**	20	**S2b**	73.4
	29	16	**R2d**	1	**S2b**	17.8
	30	16	**R1d**	1	**S2a**	76.8
8	31	1	**R1b**	1	**S2b**	2.98
	32	1	**R2b**	20	**S2b**	3.08
	33	1	**R1b**	20	**S2c**	0
	34	1	**R2d**	20	**S2a**	87

Table 6.19: *Coefficient estimate for the screening experiment. Factors are coded, meaning levels are coded as -1/+1 and not as experimental values.*

Term	Coefficient Estimate	Standard Error
Intercept	3.56	0.4857
Whole-plot Terms:		
a - Time	1.24	0.4866
Subplot Terms:		
B[1] - Resin	1.93	0.3324
B[2]	1.37	0.3098
B[3]	−0.8215	0.3456
C - Catalytic loading	1.39	0.2001
D[1] - Substrate	2.38	0.2419
D[2]	−0.0168	0.2701
B[1]C	0.8965	0.3147
B[2]C	0.1986	0.3203
B[3]C	0.4274	0.3091
B[1]D[1]	0.5965	0.4599
B[2]D[1]	−0.5184	0.4923
B[3]D[1]	1.01	0.486
B[1]D[2]	0.806	0.4757
B[2]D[2]	−0.5131	0.4821
B[3]D[2]	0.5253	0.4159
CD[1]	0.2159	0.2386
CD[2]	0.8904	0.2361

Table 6.20: *ANOVA of the model selected for the screening experiment.*

Source	Degrees of freedom	F-value	p-value	
Whole-plot	1	6.51	0.0566	not significant
a - Time	1	6.51	0.0566	
Subplot	17	24.27	<0.0001	significant
B - Resin	3	25.59	<0.0001	
C - Catalyst loading	1	48.33	<0.0001	
D - Substrate	2	64.49	<0.0001	
BC	3	7.36	0.0088	
BD	6	4.88	0.0167	
CD	2	10.74	0.0048	

Table 6.21: *Optimization: performed experiments.*

Batch	Entry	p (MPa)	T (°C)	t (h)	Cat. load. (mg/mmol)	Subst.	Cat.	Yield (%)
1	1	1.1	50	16	26	**S2b**	**R2d**	32.2
	2	1.1	50	16	5	**S2a**	**R1d**	40.4
2	3	1	100	13	22	**S2a**	**R1d**	99.8
	4	1	100	13	5	**S2b**	**R2d**	61.8
3	5	1.4	76	7.79	30	**S2a**	**R2d**	75.2
	6[a]	1.4	76	7.79	20	**S2b**	**R1d**	24.7
4	7	2	50	0.5	8	**S2b**	**R1d**	0
	8	2	50	0.5	30	**S2a**	**R1d**	7
	9	2	50	0.5	5	**S2a**	**R2d**	3.7
5	10	2	100	16	5	**S2b**	**R1d**	93.5
	11	2	100	16	15	**S2a**	**R2d**	92.2
	12	2	100	16	30	**S2b**	**R2d**	99
6	13	2	63	14	28	**S2a**	**R1d**	41.2
	14	2	63	14	8	**S2b**	**R2d**	25.8
7	15	1.2	76	6.78	13	**S2a**	**R1d**	95
	16	1.2	76	6.78	11	**S2a**	**R2d**	90.6
8	17	0.2	76	16	11	**S2b**	**R2d**	24.6
	18	0.2	76	16	6	**S2a**	**R2d**	0
	19	0.2	76	16	30	**S2a**	**R1d**	0
9	20	0.2	50	7.24	5	**S2b**	**R2d**	5.7
	21	0.2	50	7.24	30	**S2b**	**R1d**	18.4
	22	0.2	50	7.24	22	**S2a**	**R2d**	4.4
10	23	0.6	68	0.5	20	**S2a**	**R1d**	9.1
	24	0.6	68	0.5	30	**S2b**	**R2d**	6.35
11	25	0.2	100	0.5	5	**S2b**	**R1d**	0
	26	0.2	100	0.5	6	**S2a**	**R2d**	0
12	27	2	100	0.5	30	**S2b**	**R1d**	51.7
	28	2	100	0.5	17	**S2b**	**R2d**	18.4
	29	2	100	0.5	5	**S2a**	**R1d**	20.1
13	30	0.2	100	9.03	5	**S2a**	**R1d**	0
	31	0.2	100	9.03	24	**S2b**	**R2d**	12.9
	32	0.2	100	9.03	30	**S2a**	**R2d**	1
14	33[b]	2	50	0.5	8	**S2b**	**R1d**	1.2
15	34[c]	1.4	76	7.79	20	**S2b**	**R1d**	92.7
	35[b]	1.4	76	7.79	30	**S2a**	**R2d**	85.3
16	36[d]	0.2	76	16	11	**S2b**	**R1d**	32.6

[a]Run 6 was found to be an outlier and thus was repeated. [b]Run 33 and 35 are repetitions of run 7 and run 5, respectively. They were repeated to improve statistics, as these points were found to have high leverage (>1). [c]Run 34 is the repetition of run 6. [d]Run 36 was added because run 17 was supposed to be done with catalyst **R1d**, but it was erroneously performed with **R2d**.

Table 6.22: *Coefficient estimate for the optimixation experiment. Factors are coded, meaning levels are coded as -1/+1 and not as experimental values.*

Term	Coefficient Estimate	Standard Error
Intercept	72.36	8.57
Whole-plot Terms:		
a - Pressure	21.62	5.96
b - Temperature	19.64	6.26
c - Time	14.45	6.12
$\mathbf{a^2}$	−43.94	10.75
Subplot Terms:		
D - Catalyst loading	6.08	0.9755
E - Substrate	2.12	0.7911
F - Resin	6.21	0.7784
aD	5.95	1.42
aE	−5.48	0.9182
bD	8.45	1.22
bE	−2.38	0.9687
cD	−4.84	1.44
cE	6.71	1.18
cF	4.36	1.15
DE	2.9	1.05
DF	−3.72	1.4
EF	5.04	1.27
$\mathbf{D^2}$	−9.79	1.99

Table 6.23: *ANOVA of the model selected for the optimization experiment.*

Source	Degrees of freedom	F-value	p-value
Whole-plot	4	10.92	0.0008
a - Pressure	1	10.88	0.004
b - Temperature	1	10.81	0.0097
c- Time	1	10.89	0.0379
$\mathbf{a^2}$	1	11.04	0.0018
Subplot	14	5.31	0.0055
D - Catalyst loading	1	5.35	0.0012
E - Substrate	1	5.37	0.041
F - Resin	1	5.37	0.0004
aD	1	5.81	0.0062
aE	1	5.46	0.0014
bD	1	5.3	0.0007
bE	1	5.28	0.055
cD	1	5.47	0.0176
cE	1	5.69	0.0015
cF	1	5.64	0.01
DE	1	5.43	0.0366
DF	1	5.72	0.0394
EF	1	6.15	0.0069
$\mathbf{D^2}$	1	5.35	0.0036

Table 6.24: *Validation runs carried out on propylene oxide. The first run refers to the control experiment, using the unfunctionalized resin in its bromide form. Red-colored runs are highlighted as possible outliers. All runs but the ones reported in red are inside the error range of the model.*

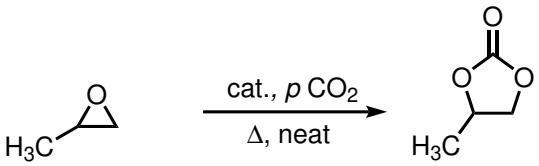

S2a **P3a**

Time (h)	T (°C)	p CO_2 (MPa)	Catalyst	Loading (mg/mmol)	Experimental Yield (%)	Calculated Yield (%)
3.16	99	1.9	**A26-Br**	22	76.9	-
3.16	99	1.9	**R2d**	22	12.7	84.5
3.16	99	1.9	**R1d**	22	100.0	78.5
0.5	98	1.9	**R2d**	24	75.0	85.6
0.5	98	1.9	**R1d**	24	81.2	75.3
15.6	99	0.9	**R2d**	17.7	85.9	85.3
15.6	99	0.9	**R1d**	17.7	97.3	95.8
1	100	1.4	**R1d**	28	96.4	91.5
2	100	1.4	**R1d**	28	44.1	92.5
2	100	1.6	**R1d**	28	100.0	91.0
2	100	1.6	**R1d**	17.7	100.0	85.4

Table 6.25: *Validation runs carried out on styrene oxide. The penultimate run is in optimized conditions. The last run is the control experiment. Results are comprised inside the model error.*

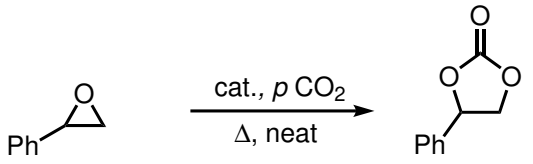

S2b **P3b**

Time (h)	T (°C)	p CO_2 (MPa)	Catalyst	Loading (mg/mmol)	Exper. yield (%)	Calc. Yield (%)
15.6	99	0.9	**R1d**	10	91.9	>100
15.6	99	0.9	**R2d**	10	81.7	77.5
6.5	94	1.2	**R1d**	21.6	100	97.9
6.5	94	1.2	**A26-Br**	21.6	58	-

General GC method. The yield and conversion of the substrates used for the screening and optimization of the reaction were calculated by fast GC-FID analysis, with an external calibration method. The calibration curve was determined using decane as the internal standard. The instrumental parameters are presented in Table 6.26.

Table 6.26: *GC-FID instrumental parameters for epoxides and cyclic carbonates.*

Parameter	Value
Column	Supelco SLB-5ms
Detector	FID
Carrier pressure	0.264 MPa
Total flow	11.6 mL/min
Helium flow	0.34 mL/min
Hydrogen flow	40.0 mL/min
Air flow	400.0 mL/min
Split ratio	30.0

Propylene oxide and propylene carbonate. In the case of propylene oxide (Figure 6.4), conversion could not be determined because the substrate is quite volatile (T_{eb} = 34 °C) and part of the substrate was inevitably lost by heating and while degassing the autoclave; for the same reason propylene oxide has similar a retention time when compared with the solvents used to dilute the samples and could not be measured by GC analysis. The calibration curve was determined using 4 standard solutions of commercial propylene carbonate (rt = 1.3 min), in a concentration range of 0.35-1 mg/mL, each containing dodecane (rt = 2.03 min) as the internal standard in a concentration of 0.1 mg/mL.

Styrene oxide and styrene carbonate. The calibration curve was determined using 5 standard solutions of commercial styrene oxide, in a concentration range of 0.05-0.33 mg/mL, and 5 standard solutions of styrene carbonate, in a concentration range of 0.05-0.30 mg/mL, each containing dodecane (rt = 2.03 min) as the internal standard in a concentration of 0.1 mg/mL (Figure 6.5).

Cyclohexene oxide and cyclohexene carbonate. The calibration curve was determined using 4 standard solutions of commercial cyclohexene oxide, in a concentration range of 0.05-0.26 mg/mL, and 4 standard solution of cyclohexene carbonate, in a concentration range of 0.05-0.26 mg/mL, each containing dodecane as the internal standard in a concentration of 0.1 mg/mL (Figure 6.6).

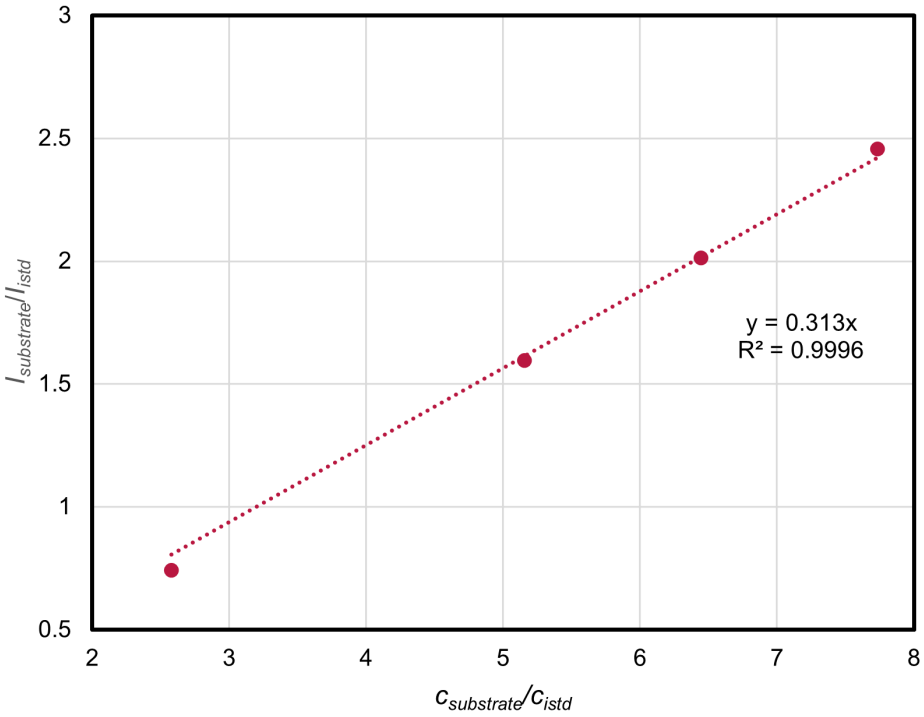

Figure 6.4: *Calibration curve for propylene carbonate. PC concentration = 0.37-0.72-0.92-1.1 mg/mL (rt = 1.3 min), internal standard concentration = 0.1 mg/mL (rt = 2.09 min).*

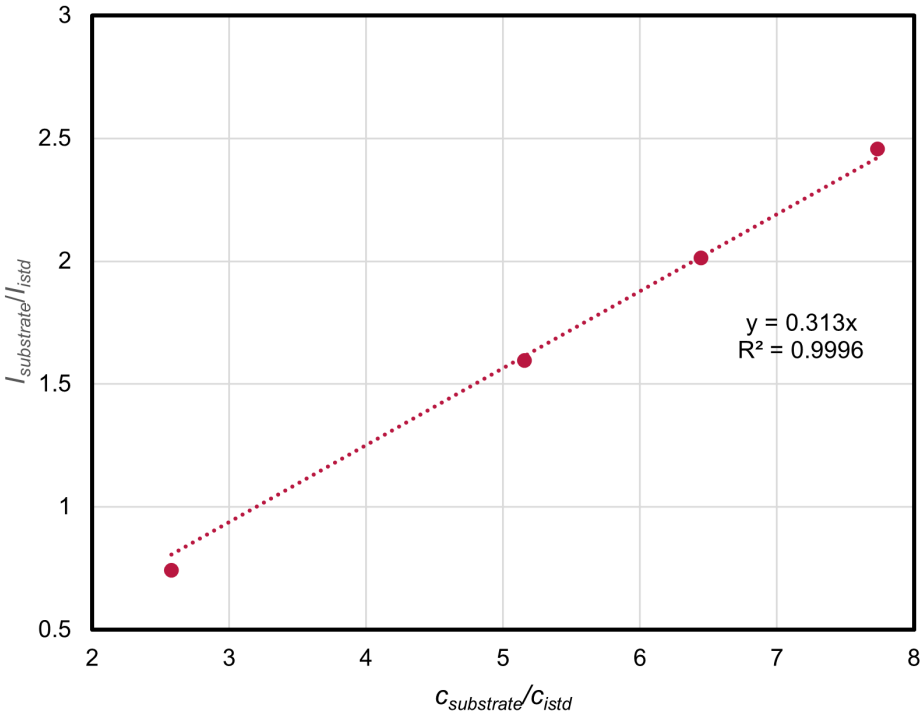

Figure 6.5: *Calibration curves for styrene oxide and styrene carbonate. SO concentration = 0.05-0.11-0.22-0.27-0.33 mg/mL, SC concentration = 0.05-0.10-0.20-0.25-0.30 mg/mL, istd concentration = 0.1 mg/mL.*

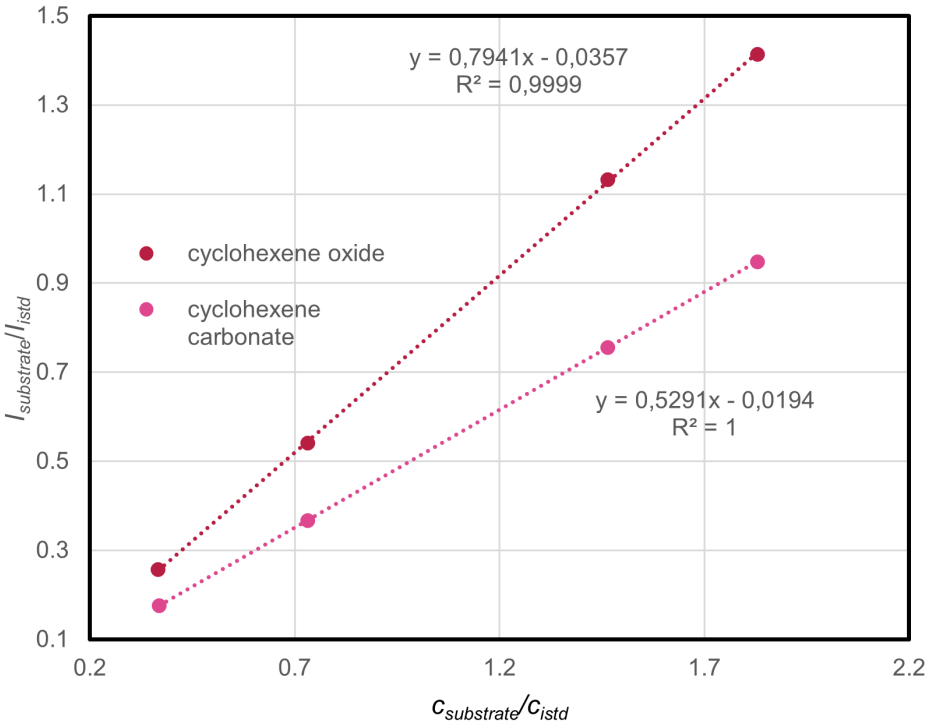

Figure 6.6: *GC-FID calibration curves for cyclohexene oxide and cyclohexene carbonate. CO concentration = 0.05-0.10-0.21-0.26 mg/mL (rt = 1.58 min), CC concentration = 0.05-0.10-0.21-0.26 mg/mL (rt = 4.31 min), istd concentration = 0.1 mg/mL (rt = 3.49 min).*

6.2.4 Synthesis of cyclic carbonates from epoxides and CO_2, catalyzed by [Zn(pytren)] complexes

General catalytic procedure. In a vial sealed with a septum and fitted with a needle to allow gas exchange, the substrate and catalyst were combined. The vial was then placed in the autoclave and subjected to the desired CO_2 pressure. The reaction mixture was heated at the specified temperature for the designated time, after which the product was transferred to a 10 mL volumetric flask and diluted to volume with EtOAc. A 200 μL aliquot of this solution was then transferred to another 10 mL volumetric flask and again diluted to volume with EtOAc. Conversion and yield were determined by GC-FID, using dodecane as the internal standard.

6.2.5 Photo-oxidation of *p*-xylene to *p*-tolualdehyde

General catalytic procedure. Photochemical experiments for the oxidation of *p*-xylene were conducted in 8 mL commercial glass vials, using a homemade photoreactor with 16 positions irradiating from the bottom of the vial with white light (33 mW/cm^2 corresponding to 0.33 sun intensity), or with blue LED at 405 nm. Typical conditions employed 1 mL of a solution of 80 mM *p*-xylene and 2.5 mM iron catalyst under stirring (400 rpm). For quantum yield determination, a blue LED emitting at 405 nm was employed, and the fraction of absorbed photons was estimated with a power meter, by subtracting the emission intensity in the absence and in the presence of the reaction solution. Identification and quantification of the products was performed by ^{1}H-NMR by comparison with commercial chemicals and by adding mesitylene as internal standard.

Electron Paramagnetic resonance (EPR) spectra were acquired on a Bruker ESR5000 operating at a microwave frequency of 9.4 GHz. 25 μL of solution samples containing BMPO spin trap (50 mM) were introduced into capillaries. The spectra were recorded using ESRStudio at room temperature with 20 mT microwave power, 0.1 mT modulation and 360 seconds sweep time. The sample was irradiated in situ using 405 nm LED for 60 seconds.

Emission spectrum of white lamp

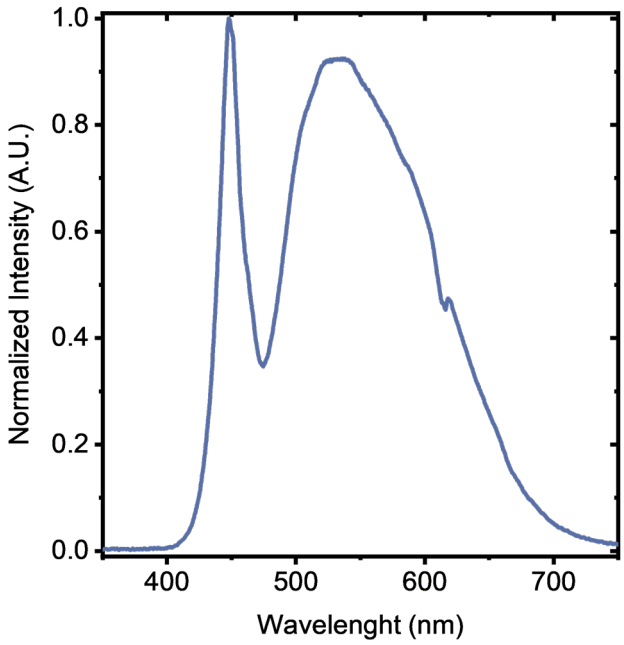

Figure 6.7: *Emission spectrum of white lamp used as light source in the photocatalytic oxidation of p-toluene.*

UV-VIS degradation studies

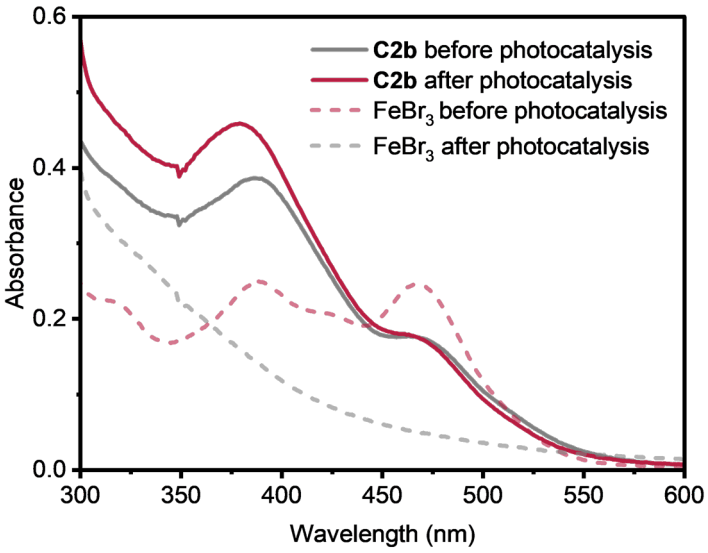

Figure 6.8: *UV-VIS spectra of* ***C2b*** *(solid lines) and of $FeBr_3$ (dashed lines) before and after photocatalysis with white light (2.5 mM in acetonitrile, 80 mM p-xylene, 24 h irradiation under air atmosphere, 33 mW cm^{-2}).*

6.2.6 Photo-oxidation of benzylic alcohols to benzaldehydes

General catalytic procedure. In a 3 mL scintillation vial sealed with a septum and fitted with a needle to allow gas exchange a solution of the substrate was combined with a solution of the catalyst. The vial was placed in the photoreactor, exposed to irradiation of the required wavelenght and allowed to react for the required reaction time. At the end of the reaction, the whole content of the vial was transferred to a volumetric flask, the internal standard (dodecane) was added and the solution was brought up to volume with ethyl acetate. Conversion and yield were determined by GC-FID.

Optimization experiment. Table 6.27 collects the results of the optimization experiment. Only yield was analyzed as a response. The results of the regression analysis, shown in Table 6.28, use coded coefficients (+1 for high levels, -1 for low levels), allowing for a direct comparison of the effects of factors rather than relying on the actual experimental values. In this way, the effect of each factor can be directly compared. In Table 6.29, the analysis of variance for the selected model is presented.

Extension of the optimization experiment. Due to the poor distribution of the results, the optimization experiment was augmented by introducing new runs in a more restricted design space. More specifically, the concentration was restricted between 0.01 and 0.1 mol L^{-1}, the catalyst loading between 4.0 and 5.0 mol%, and the reaction time between 1 and 4 hours. Again, Table 6.30 collects the results of the optimization experiment. Only yield was analyzed as a response. The results contributed to a better understanding of the experimental space, but no improvements were obtained over the already optimized conditions.

Table 6.27: *Optimization experiments for the photooxidation of benzyl alcohol catalyzed by* ***C2b****.*

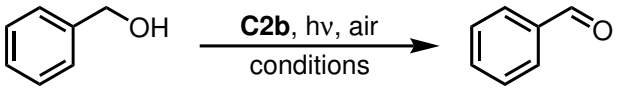

Run	Conc. (mol L^{-1})	Cat. load. (mol %)	t (h)	LED	Conversion (%)	Aldehyde yield (%)[a]
1	1	5.0	1.0	365 nm	0	0
2	0.75	4.8	5.1	405 nm	9	10
3	0.01	0.1	1.0	White	9	0
4	0.59	3.7	1.3	White	7	7
5	0.05	2.9	2.8	365 nm	6	5
6	0.01	5.0	1.0	405 nm	92	90
7	1	0.1	3.7	White	15	12
8	1	0.1	8.0	405 nm	6	4
9	0.37	5.0	8.0	365 nm	8	2
10	0.27	0.3	3.9	405 nm	35	10
11	0.75	4.8	5.1	405 nm	11	6
12	0.01	0.1	8.0	365 nm	25	12
13	0.27	0.3	3.9	405 nm	14	9
14	1	1.9	1.0	405 nm	7	2
15	1	5.0	6.0	365 nm	1	1
16	0.01	0.1	3.1	365 nm	20	4
17	0.43	1.4	7.8	White	21	12
18	0.64	0.1	1.0	365 nm	0	0
19	0.51	0.1	5.7	365 nm	2	3
20	0.43	1.4	7.8	White	17	11
21	0.05	2.9	2.8	365 nm	18	6
22	0.59	3.7	1.3	White	7	5
23	0.62	2.8	8.0	405 nm	6	8
24	0.96	2.2	6.2	365 nm	7	1
25	1	5.0	8.0	White	24	19
26	0.01	3.2	8.0	405 nm	100	8
27	0.01	5.0	5.4	White	100	6
28	0.01	1.7	4.6	White	100	23
29	0.01	5.0	1.0	405 nm	96	88
30	0.59	3.7	1.3	White	7	6
31	1	5.0	6.0	365 nm	1	1
32	0.01	1.7	4.6	White	100	29

[a] Aldehyde yields were determined by GC-FID using dodecane as an internal standard.

Table 6.28: *Coefficient estimates for the optimization experiment. Factors are coded, meaning levels are expressed as −1/+1 rather than experimental values.*

Term	Coefficient Estimate	Standard Error
Intercept	0.9634	0.0705
A - Concentration	−0.2331	0.0552
B - Catalyst loading	0.1155	0.0574
C - Time	0.1566	0.0565
D[1]	−0.4160	0.0591
D[2]	0.1997	0.0608
AD[1]	−0.2256	0.0760
AD[2]	−0.1529	0.0822
BC	−0.3073	0.0741
CD[1]	0.0899	0.0816
CD[2]	−0.2668	0.0808
$\mathbf{C^2}$	−0.3149	0.1007

Table 6.29: *ANOVA of the model used for the benzyl alcohol photooxidation optimization.*

Source	Degrees of freedom	F-value	p-value	
Model	7	13.88	<0.0001	significant
A - Concentration	1	21.25	0.0002	
B - Catalyst loading	1	3.81	0.0651	
C - Time	1	6.53	0.0189	
D - LED	1	21.21	<0.0001	
AD	2	11.81	0.0004	
BC	1	17.19	0.0005	
CD	2	5.78	0.0105	
$\mathbf{C^2}$	1	9.78	0.0053	
Residual	20			
Lack of Fit	11	21.50	<0.0001	significant
Pure Error	9			
Cor Total	31			

Table 6.30: *Extension of the optimization experiments for the photooxidation of benzyl alcohol catalyzed by **C2b**.*

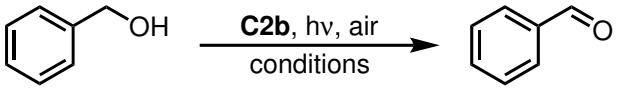

Run	Conc. (mol L^{-1})	Cat. load. (mol %)	t (h)	LED	Conversion (%)	Aldehyde yield (%)[a]
5	0.05	2.9	2.8	365 nm	6	5
6	0.01	5.0	1.0	405 nm	92	90
21	0.05	2.9	2.8	365 nm	18	6
26	0.01	3.2	8.0	405 nm	100	8
27	0.01	5.0	5.4	White	100	6
29	0.01	5.0	1.0	405 nm	96	88
33[b]	0.06	4.5	2.5	White	57	44
34	0.06	4.5	2.5	405 nm	53	41
35	0.06	4.5	2.5	365 nm	7	4
36	0.01	5.0	1.0	White	99	77
37	0.01	4.0	4.0	365 nm	32	22
38	0.01	5.0	1.0	White	99	81
39	0.10	4.0	1.0	365 nm	5	1
40	0.06	4.5	2.5	405 nm	55	41
41	0.01	5.0	1.0	365 nm	13	4
42	0.10	4.9	1.1	365 nm	2	2

[a]Aldehyde yields were determined by GC-FID using dodecane as an internal standard. [b]Starting from this run, these experiments were conducted on top of the previous optimization.

6.3 Catalysis: substrates and products synthesis and characterization

6.3.1 Aziridines

Reading guidance

The next table summarizes the structure of the compounds that are described in section 6.3.1.

Table 6.31: *Schemes of the compounds of section 6.3.1.*

Comp.	Scheme	Comp.	Scheme
S1a	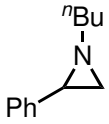	**S1b**	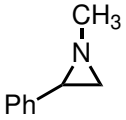
S1c	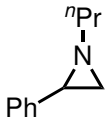	**S1d**	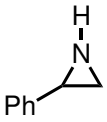
S1e	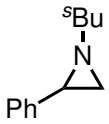	**S1f**	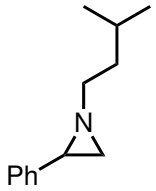
S1g	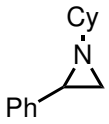	**S1h**	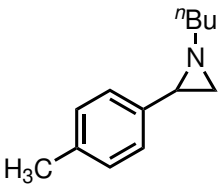
S1i	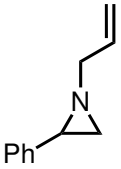	**S1j**	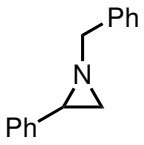
S1k	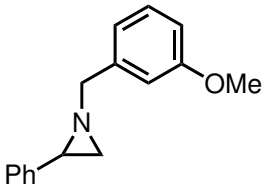	**S1l**	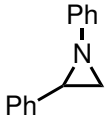
S1m		**S1n**	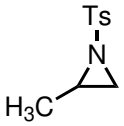

Continues on next page

Table 6.31 – continued from previous page

Comp.	Scheme	Comp.	Scheme
S1o	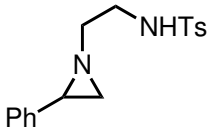	**S1p**	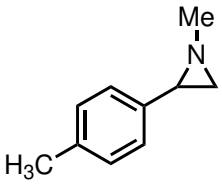
S1q	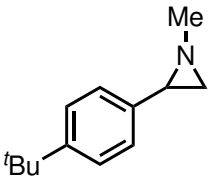	**S1r**	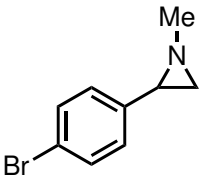
S1s	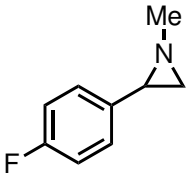	**S1t**	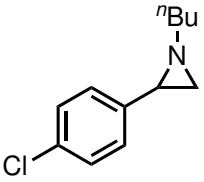
S1u	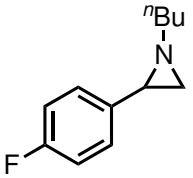		

Aziridines **S1c**, **S1a**, **S1e**, **S1f**, **S1h**, **S1i**, and **S1j**;[75] **S1d** and **S1b**;[261] **S1g**,[262] **S1k**,[31] **S1n**,[263] **S1s**,[264] **S1t** and[28] **S1u**[265] were synthetized according to published procedures. **S1m** is commercially available. Substrate **S1l** was prepared from the reaction of styrene oxide with *N*-phenyl-diethylphosphoramidate.[266] The latter was prepared according to literature.[267]

The syntheses of unreported aziridines are reported next.

General procedure.

Step one. Dimethyl sulfide (14.7 mL, 200 mmol) was dissolved in dichloromethane (40 mL) and the solution was cooled to 0 °C; then a bromine solution (10 mL, 200 mmol) in DCM (40 mL) was added dropwise over 30 minutes; the temperature was maintained at 0 °C during the addition. The precipitation of yellow-orange bromodimethylsulfonium bromide crystals was noticeable since the beginning of the addition. The precipitate was then collected on a septum and washed with cold diethyl ether to remove residual bromine traces.

Step two. Styrene (200 mmol) was added dropwise at 0 °C to a solution of bromodimethylsulfonium bromide (200 mmol) in acetonitrile (80 mL); the mixture was allowed to react at 0 °C for a different time, which depended on the nature of the employed styrene. The starting orange solution turned white or yellow during the reaction. At the end of the reaction, the brominated salt was precipitated by

the addition of diethyl ether (70-100 mL); the precipitate was then collected on a septum and washed with diethyl ether and dried *in vacuo*.
Step three. The white crystals of 1-(dimethylsulfonium)-1-aryl-2-bromoethyl bromide (1 eq, amount depending on step 2) were suspended in water (6 mL per each gram of styrene sulphonium bromide) and a solution of the desired amine (5 eq) in water (10 M) was added dropwise. The resulting mixture was stirred overnight. Then 20.0 mL of brine and 20.0 mL of diethyl ether were added and the phases were separated. The aqueous phase was washed twice with 20.0 mL of diethyl ether and the combined organic phases were dried over Na_2SO_4. The solid was filtered off, and the solvent was evaporated under reduced pressure. The obtained crude was purified by flash chromatography.

1-(ethyl-2-tosyl)-2-phenylaziridine (S1o). The general procedure was followed by using styrene and *N*-(2-aminoethyl)-4-methylbenzenesulfonamide. In this case, due to the low solubility of the amine in water, it was added directly dropwise during Step 3. Workup was carried out using distilled DCM instead of diethyl ether, and the crude product was purified through column chromatography (eluent DCM:EtOAc:TEA = 5:5:0.1) to obtain a greenish oil (yield: 60%). ^{1}H-NMR (400 MHz; 25 °C; $CDCl_3$) δ 7.67 (dd, 2H, J = 8.3, 1.5 Hz), 7.42-7.05 (m, 7H), 5.14 (s, 1H), 3.30-2.95 (m, 2H), 2.63 (dddd, 1H, J = 11.8, 7.3, 4.5, 1.4 Hz), 2.45-2.39 (tdd, 1H, J = 5.9, 4.5, 1.6 Hz), 2.38 (s, 3H), 2.32 (ddd, J = 6.6, 3.4, 1.4 Hz), 1.92-1.88 (m, 1H), 1.71 (dd, 1H, J = 6.6, 1.4 Hz) (Figure A.89, page 290). ^{13}C-NMR (101 MHz; 25 °C; $CDCl_3$) δ 143.2, 139.5, 136.6, 129.6, 128.4, 127.1, 127.1, 126.0, 59.11, 42.9, 40.9, 37.7, 21.5 (Figure A.90, page 290). **Elemental analysis** calculated for $C_{17}H_{20}N_2O_2S$: C, 64.53%; H, 6.37%; N, 8.85%; found: C, 64.10%; H, 6.55%; N, 8.51%. **MS-ESI(+)**: m/z ($C_{17}H_{20}N_2O_2S$) calculated 316.12, found $[MH]^+$ 317.25 (100%).

1-methyl-2-(4-methylphenyl)aziridine (S1p). The general procedure was followed by using *p*-methyl styrene and methylamine to obtain a light pink oil (yield: 97%). ^{1}H-NMR (400 MHz; 25 °C; $CDCl_3$) δ 7.14 (s, 4H), 2.51 (s, 3H), 2.35 (s, 3H), 2.26 (dd, 1H, J = 6.5, 3.4 Hz), 1.91 (d, 1H, J = 3.4 Hz), 1.62 (d, 1H, J = 6.5 Hz) (Figure A.91, page 291). ^{13}C-NMR (101 MHz; 25 °C; $CDCl_3$) δ 137.24, 136.41, 129.00, 125.89, 48.00, 42.21, 39.23, 21.08 (Figure A.92, page 291). **Elemental analysis** calculated for $C_{10}H_{13}N$: C, 81.58%; H, 8.90%; N, 9.51%; found: C, 81.62%; H, 8.96%; N, 9.42%. **MS-ESI(+)**: m/z ($C_{10}H_{13}N$) calculated 147.10, found $[MH]^+$ 148.21 (100%).

1-methyl-2-(4-(1',1'-dimethyl)ethylphenyl)aziridine (S1q). The general procedure was followed by using *p*-tertbutyl styrene and methylamine to obtain a light pink oil (yield: 78%). ^{1}H-NMR (400 MHz; 25 °C; $CDCl_3$) δ 7.36 (d, 2H, J = 8.3 Hz), 7.19 (d, 2H, J = 8.3 Hz), 2.50 (s, 3H), 2.27 (dd, 1H, J = 6.5, 3.4 Hz), 1.93 (dd, 1H, J = 3.4, 0.8 Hz), 1.63 (d, 1H, J = 6.5 Hz), 1.33 (s, 9H) (Figure A.93, page 292). ^{13}C-NMR (101 MHz; 25 °C; $CDCl_3$) δ 149.83, 137.25, 125.68, 125.24, 48.01, 42.14,

39.22, 31.38 (Figure A.94, page 292). **Elemental analysis** calculated for $C_{13}H_{19}N$: C, 82.48%; H, 10.12%; N, 7.40%; found: C, 82.66%; H, 10.01%; N, 7.52%. **MS-ESI(+)**: m/z ($C_{13}H_{19}N$) calculated 189.15, found $[MH]^+$ 190.18 (100%).

(S)-1-methyl-2-phenylaziridine (*S*-S1b). **Step 1.** (*S*)-2-amino-2-phenylethan-1-ol (100 mg, 66 mmol) was dissolved in 2.5 mL of toluene and cooled to 0 °C. To the cold solution, chlorosulfonic acid (44 µL, 0.66 mmol) was added slowly. Immediately, a white crystalline precipitate formed. The mixture was then filtered and the obtained solid was washed with diethyl ether (yield: 90%).

Step 2. The chiral salt was dissolved in a 6.0 molar solution of NaOH (1 mL for each 10 mg of reagent); then an equal volume of toluene was added to the mixture. The reaction was heated for 18 h under reflux, leading to the formation of an orange organic phase. The two phases were separated, and the aqueous phase was extracted with ethyl acetate. The unified organic phase was then washed with brine, dried over $MgSO_4$, and concentrated under vacuum. The pure product was isolated by column chromatography, using as eluent hexane/ethyl acetate 8:2 + 1% TEA initially, and hexane/ethyl acetate 3:7 after elution of the by-product. A yellowish liquid was obtained (yield: 65%). ^{1}H-NMR (400 MHz; 25 °C; $CDCl_3$) δ 7.37-7.24 (m, 5H), 3.03 (dd, 1H, J = 6.3, 3.4 Hz), 2.22 (d, 1H, J = 6.3 Hz), 1.81 (s, 1H), 0.76 (bs, 1H). Data are in agreement with literature.[91]

Step 3. One equivalent of the N-H aziridine was dissolved in THF (20 mL for each mmol of aziridine), and a 2.0 molar solution of *n*-butyllithium (1 eq) in hexane was added dropwise. The mixture was allowed to react under nitrogen atmosphere for about 30 min, until a bright orange color was observed. Once the lithiated salt was formed, 1 eq of methyl iodide was added dropwise, and the reaction was stirred for 1 h. At the end of the reaction time, the residual basicity was quenched with a saturated NH_4Cl solution. The product was extracted with diethyl ether, dried over $MgSO_4$, concentrated under reduced pressure, and purified by column chromatography using hexane/ethyl acetate 9:1 + 5% TEA as eluent. A colorless liquid was obtained (yield: 30%). ^{1}H-NMR (400 MHz; 25 °C; $CDCl_3$) δ 7.34-7.22 (m, 5H), 2.51 (s, 3H), 2.29 (dd, 1H, J = 6.5, 3.3 Hz), 1.93 (d, 1H, J = 3.3 Hz), 1.65 (d, 1H, J = 6.5 Hz). Data are in agreement with literature.[91]

Optical purity. The compound was injected in a chiral HPLC system (Chiralpak IB, 25 °C, flow rate 0.5 mL/min) using hexane/isopropanol 9:1 as eluent; only one peak was detected, with a retention time of 11.5 min.

6.3.2 Oxazolidinones

Reading guidance

The next table summarizes the structure of the compounds that are described in section 6.3.2. The general catalytic procedure is reported in section 6.2.1, at page 151.

Table 6.32: *Schemes of the compounds of section 6.3.2.*

Comp.	Scheme	Comp.	Scheme
P1a	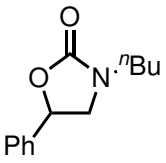	**P1b**	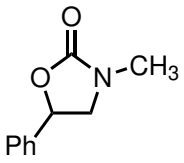
P1c	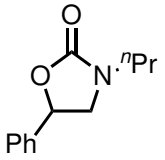	**P1d**	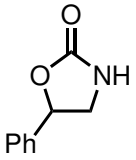
P1e	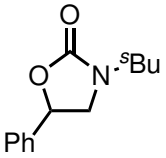	**P1f**	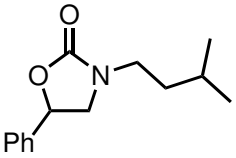
P1g	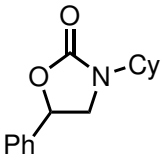	**P1h**	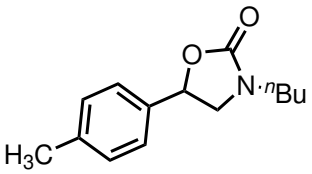
P1i	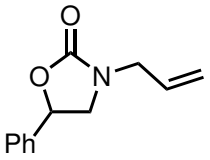	**P1j**	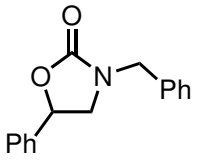
P1k	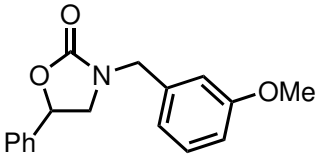	**P1l**	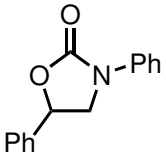
P1m	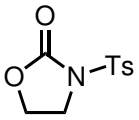	**P1n**	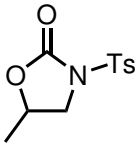
P1n'	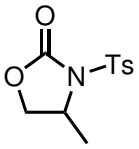		

3-butyl-5-phenyloxazolidin-2-one (P1a). The general catalytic procedure was followed using **S1a** as the substrate. The product was isolated by filtering the crude, washing the catalysts with DCM, diluting the filtrate with ethyl acetate and washing it with water. The organic phase was then dried with sodium sulfate and the solvents were evaporated. The product was isolated as a pale yellow oil (yield:

>99%). ^{1}H-NMR (400 MHz, 25 °C, $CDCl_3$): δ 7.45-7.31 (m, 5H), 5.48 (dd, J = 8.8, 7.4 Hz, 1H), 3.91 (pst, J = 8.7 Hz, 1H), 3.42 (dd, J = 8.7, 7.4 Hz, 1H), 3.39-3.22 (m, 2H), 1.60-1.48 (m, 2H), 1.43-1.29 (m, 2H), 0.94 (t, J = 7.3 Hz, 1H) (Figure A.95, page 293). ^{13}C-NMR (101 MHz, 25 °C, $CDCl_3$): δ 157.91, 138.94, 129.29, 128.81, 125.49, 74.30, 52.19, 43.94, 29.43, 19.84, 13.68 (Figure A.96, page 293). Data are in agreement with literature.[31]

3-methyl-5-phenyloxazolidin-2-one (P1b). The general catalytic procedure was followed using **S1b** as the substrate. The product was isolated by column chromatography, using a hexane/ethyl acetate/triethylamine solution (6:4:0.1) as the eluent (yield: 78%). ^{1}H-NMR (400 MHz, 25 °C, $CDCl_3$): δ 7.43-7.29 (m, 5H), 5.45 (dd, J = 8.7, 7.4 Hz, 1H), 3.90 (pst, J = 8.7 Hz, 1H), 3.42 (dd, J = 8.7, 7.4 Hz, 1H), 2.90 (s, 3H) (Figure A.97, page 294). ^{13}C-NMR (101 MHz, 25 °C, $CDCl_3$): δ 157.17, 137.69, 127.85, 127.76, 124.52, 73.14, 73.12, 53.43, 30.05 (Figure A.98, page 294). Data are in agreement with literature.[261]

5-phenyl-3-propyloxazolidin-2-one (P1c). The general catalytic procedure was followed using **S1c** as the substrate. The product was isolated by filtering the crude, washing the catalysts with DCM, diluting the filtrate with ethyl acetate and washing it with water. The organic phase was then dried with sodium sulfate and the solvents were evaporated. The product was isolated as a pale yellow oil (yield: >99%). ^{1}H-NMR (400 MHz, 25 °C, $CDCl_3$): δ 7.43-7.29 (m, 5H), 5.46 (dd, J = 8.8, 7.3 Hz, 1 H), 3.90 (pst, J = 8.8 Hz, 1H), 3.40 (dd, J = 8.8, 7.4 Hz, 1H), 3.33-3.15 (m, 2H), 1.56 (m, 2H), 0.91 (t, J = 7.4 Hz, 3H) (Figure A.99, page 295). ^{13}C-NMR (101 MHz, 25 °C, $CDCl_3$): δ 157.99, 138.96, 128.89, 128.75, 125.51, 74.31, 52.13, 45.80, 20.65, 11.09 (Figure A.100, page 295). Data are in agreement with literature.[75]

5-phenyloxazolin-2-one (P1d). The general catalytic procedure was followed using **S1d** as the substrate. The product was isolated by column chromatography, using a hexane/ethyl acetate/triethylamine solution in a polarity gradient (starting from 6:4:0.1 and ending with 2:8:0.1) as the eluent (yield: 55%). ^{1}H-NMR (400 MHz, 25 °C, $CDCl_3$): δ 7.43-7.29 (m, 5H), 6.57 (bs, 1H - NH), 5.60 (pst, J = 8.2 Hz, 1H), 3.97 (pst, 8.7 Hz), 3.54 (pst, J = 8.7, 1H) (Figure A.101, page 296). ^{13}C-NMR (101 MHz, 25 °C, $CDCl_3$): δ 160.23, 138.49, 128.91, 125.72, 77.96, 48.36 (Figure A.105, page 298). Two peaks in the aromatic zone coincide. Data are in agreement with literature.[261]

3-(sec-butyl)-5-phenyloxazolidin-2-one (P1e). The general catalytic procedure was followed using **S1e** as the substrate. The product was isolated by column chromatography, using a hexane/ethyl acetate/triethylamine solution in a polarity gradient (starting from 9:1:0.1 and ending with 5:5:0.1) as the eluent (yield: 21%). In

harsher conditions (120 °C, 1.2 MPa of CO_2, 16 hours of reaction time) the yield increased to 80%. ^{1}H-NMR (400 MHz, 25 °C, $CDCl_3$): δ 7.45-7.31 (m, 5H), 5.48 (dd, J = 8.8, 7.3 Hz, 1H), 3.98-3.85 (m, 1H), 3.86 and 3.78 (pst, J = 8.8 Hz and J = 8.7 Hz, respectively, 1H), 3.35 and 3.30 (dd, J = 8.7, 7.7 Hz and J = 8.7, 6.9 Hz, respectively, 1H), 1.60-1.40 (m, 2H), 1.19 and 1.14 (d, J = 6.8 Hz and J = 6.7 Hz, 3H), 0.95 and 0.86 (t, both J = 7.4 Hz, 3H) (Figure A.106, page 298). ^{13}C-NMR (101 MHz, 25 °C, $CDCl_3$): δ 157.61, 139.30 and 138.97, 128.90, 128.75 and 128.70, 125.50 and 125.37, 74.59 and 74.41, 50.70 and 50.61, 47.44 and 47.41, 27.25 and 27.01, 18.00 and 17.61, 10.98 and 10.86 (Figure A.110, page 300). Data are in agreement with literature.[75]

3-isopentyl-5-phenyloxazolidin-2-one (P1f). The general catalytic procedure was followed using **S1f** as the substrate. The product was isolated by column chromatography, using a hexane/ethyl acetate/triethylamine solution in a polarity gradient (starting from 9:1:0.1 and ending with 5:5:0.1) as the eluent (yield: 95%). ^{1}H-NMR (400 MHz, 25 °C, $CDCl_3$): δ 7.41-7.23 (m, 5H), 5.44 (dd, J = 8.8, 7.4 Hz, 1H), 3.88 (pst, J = 8.7 Hz, 1H), 3.39, (dd, J = 8.7, 7.4 Hz, 1H), 3.38-3.21 (m, 2H), 1.66-1.51 (m, 1H), 1.48-1.37 (m, 2H), 0.92 (d, J = 6.6 Hz, 3H), 0.90 (d, J = 6.6 Hz, 3H) (Figure A.111, page 301). ^{13}C-NMR (101 MHz, 25 °C, $CDCl_3$): δ 157.84, 138.94, 128.88, 128.74, 125.51, 74.31, 52.03, 42.58, 36.08, 25.73, 22.46, 22.40 (Figure A.112, page 301). Data are in agreement with literature.[31]

3-cyclopentyl-5-phenyloxazolidin-2-one (P1g). The general catalytic procedure was followed using **S1g** as the substrate. The product was isolated by column chromatography, using a hexane/ethyl acetate/triethylamine solution (9:1:0.1) as the eluent (yield: 11%). In harsher conditions (120 °C, 1.2 MPa of CO_2, 16 hours of reaction time) the yield increased to 92%. ^{1}H-NMR (400 MHz, 25 °C, $CDCl_3$): δ 7.44-7.32 (m, 5H), 5.47 (dd, J = 8.7, 7.5 Hz, 1H), 4.30 (p, J = 7.9 Hz, 1 H), 3.88 (pst, J = 8.7 Hz, 1 H), 3.39 (dd, J = 8.6, 7.5 Hz, 1H), 2.00-1.87(m, 2H), 1.76-1.46 (m, 6H) (Figure A.113, page 302). ^{13}C-NMR (101 MHz, 25 °C, $CDCl_3$): δ 157.54, 139.00, 128.91, 128.76, 125.50, 74.47, 54.67, 48.60, 29.17, 28.64, 23.98 (Figure A.117, page 304). Data are in agreement with literature.[31]

3-butyl-5-(p-tolyl)oxazolidin-2-one (P1h). The general catalytic procedure was followed using **S1h** as the substrate. The product was isolated by column chromatography, using a hexane/ethyl acetate/triethylamine solution (9:1:0.1) as the eluent (yield: 91%).^{1}H-NMR (400 MHz, 25 °C, $CDCl_3$): δ 7.22 (d, J = 8.2 Hz, 2H), 7.17 (d, J = 8.1 Hz, 2H), 5.44 (dd, J = 8.7, 7.5 Hz, 1H), 3.89 (pst, J = 8.7 Hz, 1H), 3.41 (dd, J = 8.7, 7.5 Hz, 1H), 3.38-3.20 (m, 2H), 2.36 (s, 3H), 1.59-1.47 (m, 2H), 1.41-1.30 (m, 2H), 0.94 (t, J = 7.3 Hz, 3H) (Figure A.118, page 304). ^{13}C-NMR (101 MHz, 25 °C, $CDCl_3$): δ 158.00, 138.64, 135.91, 129.52, 125.58, 74.36, 52.18, 43.89, 29.41, 21.17, 19.84, 13.70 (Figure A.119, page 305). Data are in agreement with literature.[75]

3-allyl-5-phenyloxazolidin-2-one (P1i). The general catalytic procedure was followed using **S1i** as the substrate. The product was isolated by column chromatography, using a hexane/ethyl acetate/triethylamine solution in a polarity gradient (starting from 9:1:0.1 and ending with 7:3:0.1) as the eluent (yield: 61%).^{1}H-NMR (400 MHz, 25 °C, $CDCl_3$): δ 7.42-7.30 (m, 5H), 5.81 (ddt, J = 10.8, 9.9, 6.2 Hz, 1H), 5.51 (pst, J = 8.1 Hz, 1H), 5.30-5.21 (m, 2H), 4.01-3.84 (m, 2H), 3.90 (pst, J = 8.7 Hz, 1H), 3.42 (dd, J = 8.6, 7.7 Hz, 1H) (Figure A.120, page 305). ^{13}C-NMR (101 MHz, 25 °C, $CDCl_3$): δ 157.69, 138.99, 138.72, 131.90, 128.90, 128.80, 125.51, 118.83, 74.48, 51.80, 46.95 (Figure A.124, page 307). Data are in agreement with literature.[75]

3-benzyl-5-phenyloxazolidin-2-one (P1j). The general catalytic procedure was followed using **S1j** as the substrate. The crude was analyzed by diluting it in ethyl acetate and washing the obtained solution with water. The organic phase was then dried with sodium sulfate; the volatiles were evaporated in vacuo and the internal standard (dibromomethane) was added and measured by weight (yield: 85%). ^{1}H-NMR (400 MHz, 25 °C, $CDCl_3$): δ 7.39-7.26 (m, 10H), 5.45 (dd, J = 8.7, 7.5 Hz, 1H), 4.53 (d, J = 14.8 Hz, 1H), 4.41 (d, J = 14.9 Hz, 1H), 3.76 (pst, J = 8.8 Hz, 1H), 3.30 (dd, J = 8.8, 7.5 Hz, 1H) (Figure A.125, page 308). Data are in agreement with literature.[31]

3-(3-methoxybenzyl)-5-phenyloxazolidin-2-one (P1k). The general catalytic procedure was followed using **S1k** as the substrate. The crude was analyzed by diluting it in ethyl acetate and washing the obtained solution with water. The organic phase was then dried with sodium sulfate; the volatiles were evaporated in vacuo and the internal standard (dibromomethane) was added and measured by weight (yield: 80%). ^{1}H-NMR (400 MHz, 25 °C, $CDCl_3$): δ 7.37-7.25 (m, 9H), 6.97-6.82 (m, 3H), 5.42 (dd, J = 8.9, 7.5 Hz, 1H), 4.55 (d, J = 14.7 Hz, 1H), 4.49 (d, J = 14.9 Hz, 1H), 3.81 (s, 3H), 3.32 (dd, J = 8.9, 7.5 Hz, 1H) (Figure A.126, page 308). Data are in agreement with literature.[31]

3-phenyl-5-phenyloxazolidin-2-one (P1l). The general catalytic procedure was followed using **S1l** as the substrate. The crude was analyzed by diluting it in ethyl acetate and washing the obtained solution with water. The organic phase was then dried with sodium sulfate; the volatiles were evaporated in vacuo and the internal standard (dibromomethane) was added and measured by weight. The product was observed only when employing harsher reaction conditions (120 °C, 1.2 MPa of CO_2, 16 hours of reaction time, yield: 6%).^{1}H-NMR (400 MHz, 25 °C, $CDCl_3$): δ 7.56 (dd, J = 8.7, 1.1 Hz, 2H), 7.45-7.39 (m, 7H), 5.65 (dd, J = 8.7, 7.5 Hz, 1H), 4.39 (pst, J = 8.8 Hz, 1H), 3.98 (dd, J = 8.9, 7.5 Hz, 1H) (Figure A.127, page 309). One aromatic signal is missing, as in our case it is superimposed with the broad signal of an oligomeric compound that I was not able to separate. Otherwise, the data are in agreement with literature.[268]

3-tosyloxazolidin-2-one (P1m). Following the general catalytic procedure using **S1m** as the substrate did not yield the desired product. In harsher conditions (120 °C, 1.2 MPa of CO_2, 16 hours of reaction time) the observed yield was 68%. The product was isolated by column chromatography, using a hexane/ethyl acetate/triethylamine solution in a polarity gradient (starting from 6:4:0.1 and ending with 3:7:0.1) as the eluent. ^{1}H-NMR (400 MHz, 25 °C, $CDCl_3$): δ 7.95 (d, J = 8.3 Hz, 2H), 7.37 (d, J = 8.1 Hz, 2H), 4.36 (t, J = 8.2 Hz, 2H), 4.05 (t, J = 8.2 Hz, 2H), 2.46 (s, 3H) (Figure A.128, page 309). ^{13}C-NMR (101 MHz, 25 °C, $CDCl_3$): δ 151.99, 145.82, 133.88, 129.92, 128.35, 62.23, 44.60, 21.71 (Figure A.132, page 311). Data are in agreement with literature.[29]

3-tosyl-4-methyloxazolidin-2-one (P1n'). The general catalytic procedure was followed using **S1n** as the substrate. The crude was analyzed by diluting it in ethyl acetate and washing the obtained solution with water. The organic phase was then dried with sodium sulfate; the volatiles were evaporated in vacuo and the internal standard (dibromomethane) was added and measured by weight. The product was observed only when employing harsher reaction conditions (120 °C, 1.2 MPa of CO_2, 16 hours of reaction time, yield: 8%).^{1}H-NMR (400 MHz, 25 °C, $CDCl_3$): δ 7.94 (d, J = 8.3 Hz, 2H), 7.36 (d, J = 8.3 Hz, 2 H), 4.59-4.52 (m, 1H), 4.42 (pst, J = 8.3 Hz, 1H), 3.92 (dd, J = 8.4, 4.1 Hz, 1H), 2.45 (s, 3H), 1.52 (d, J = 6.2 Hz, 3H). Data are in agreement with literature.[269]

6.3.3 Piperazines

Reading guidance

The next table summarizes the structure of the compounds that are described in section 6.3.3.

Table 6.33: *Schemes of the compounds of section 6.3.3.*

Comp.	Scheme	Comp.	Scheme
***meso* - P2a**	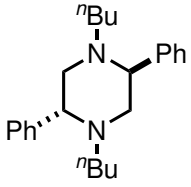	(±) - **P2a**	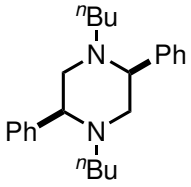
***meso* - P2b**	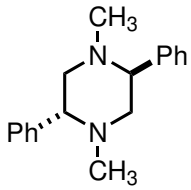	(±) - **P2b**	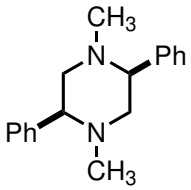

Continues on next page

Table 6.33 – continued from previous page

Comp.	Scheme	Comp.	Scheme
***meso* - P2b′**	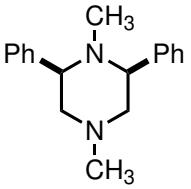	(±) - **P2b′**	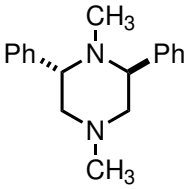
***meso* - P2h**	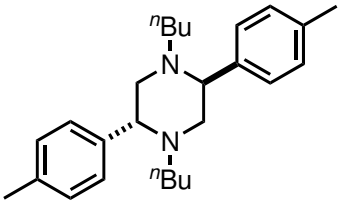	(±) - **P2h**	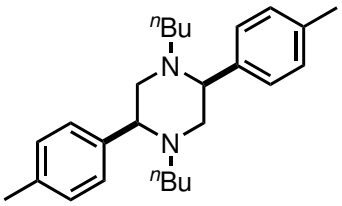
***meso* - P2i**	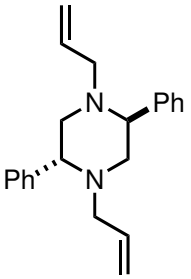	(±) - **P2i**	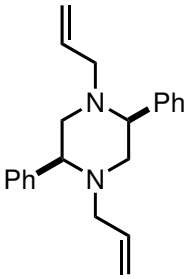
***meso* - P2j**	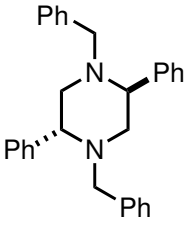	(±) - **P2j**	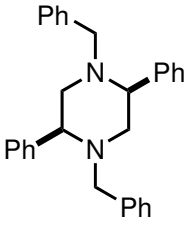
P2m	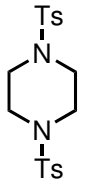		
***meso* - P2p**	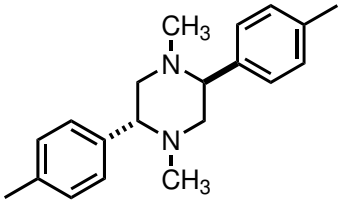	(±) - **P2p**	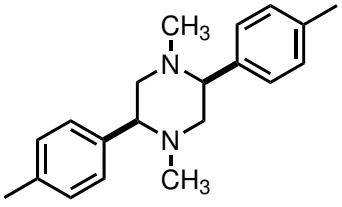
***meso* - P2q**	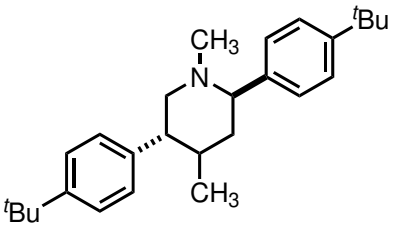	(±) - **P2q**	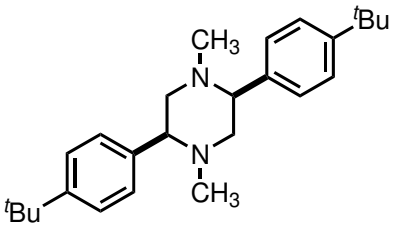

Continues on next page

Table 6.33 – continued from previous page

Comp.	Scheme	Comp.	Scheme
***meso* - P2r**	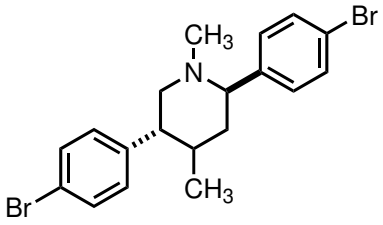	**(±) - P2r**	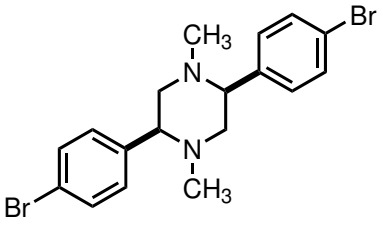
***meso* - P2s**	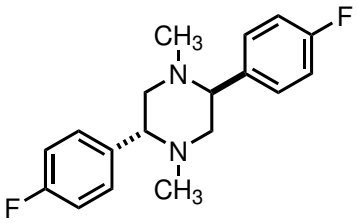	**(±) - P2s**	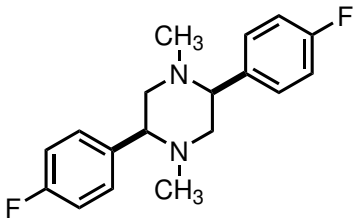
***meso* - P2t**	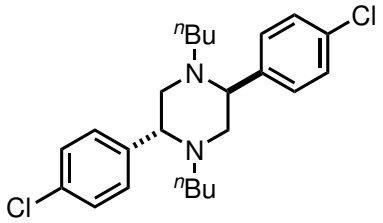	**(±) - P2t**	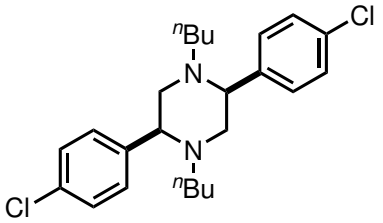

1,4-dibutyl-2,5-phenylpiperazine (P2a). At the end of the reaction, *meso* - **P2a** spontaneously precipitated as a white powder and was collected by filtration (yield: 27%). The solution was evaporated to dryness then separated by column chromatography (eluent *n*-hexane/EtOAc = 9:1). (±) - **P2a** was isolated as a viscous yellowish oil (yield: 20%).

meso - **P2a**: ^{1}H-NMR (400 MHz, 25 °C, $CDCl_3$) δ 7.45 (m, 4H), 7.36 (m, 4H), 7.30 (m, 2H), 3.42 (dd, 2H, J = 10.6, 2.6 Hz), 3.09 (dd, 2H, J = 11.6, 2.8 Hz), 2.48 (m, 2H), 2.27 (pst, 2H, J = 11.0 Hz), 1.92 (m, 2H), 1.41-1.29 (m, 4H), 1.25-1.02 (m, 4H), 0.95 (t, 6H, J = 7.2 Hz) (Figure A.133, page 312). ^{13}C-NMR (101 MHz, 25 °C, $CDCl_3$) δ 142.9 (C), 128.4 (CH), 128.1 (CH), 127.3 (CH), 67.8 (CH), 60.9 (CH_2), 54.4 (CH_2), 28.9 (CH_2), 19.6 (CH_2), 14.0 (CH_3) (Figure A.134, page 312). **Elemental analysis** calculated for $C_{24}H_{34}N_2$: C, 82.23%; H, 9.78%; N, 7.99%; found: C, 82.44%; H, 10.01%; N, 7.78%. **MS-ESI(+)**: m/z ($C_{24}H_{34}N_2$) calculated 350.27, found $[M+H]^+$ 351.36 (100%). **M.p.** = 103-105 °C.

(±) - **P2a**: ^{1}H-NMR (400 MHz, 25 °C, $CDCl_3$) δ 7.70 (d, 4H, J = 7.3 Hz), 7.44-7.19 (m, 6H), 3.70 (m, 2H), 3.02 (dd, 2H, J = 11.8, 6.2 Hz), 2.64 (dd, 2H, J = 11.8, 3.4 Hz), 2.34 (m, 2H), 2.17 (m, 2H), 1.52-1.36 (m, 4H), 1.36-1.12 (m, 4H), 0.85 (t, 6H, J = 7.4 Hz) (Figure A.135, page 313). ^{13}C-NMR (101 MHz, 25 °C, $CDCl_3$) δ 140.6 (C), 129.3 (CH), 128.0 (CH), 127.1 (CH), 64.4 (CH), 61.6 (CH_2), 54.9 (CH_2), 29.2 (CH_2), 20.6 (CH_2), 14.1 (CH_3) (Figure A.136, page 313). **Elemental analysis** calculated for $C_{24}H_{34}N_2$: C, 82.23%; H, 9.78%; N, 7.99%; found: C, 81.97%; H, 10.11%; N, 7.67%.

MS-ESI(+): m/z ($C_{24}H_{34}N_2$) calculated 350.27, found $[M+H]^+$ 351.26 (100%).

1,4-dimethyl-2,5-phenylpiperazine (P2b). At the end of the reaction, *meso* - **P2b** spontaneously precipitated as a white crystalline powder and was collected by filtration (yield: 44%). The solution was evaporated to dryness and then separated by column chromatography (eluent gradient *n*-hexane/EtOAc/TEA from 9:0.5:0.5 to 6:3.5:0.5). (±) - **P2b** was isolated as a viscous yellowish oil (yield: 27%). A further fraction of (±) - **P2b** was also isolated, but mixed with (±) - **P2b'**. Any attempts to separate the two compounds failed, also due to the small amount obtained.

meso - **P2b**: ^{1}H-NMR (400 MHz, 25 °C, $CDCl_3$) δ 7.44 (m, 4H), 7.37 (m, 4H), 7.31 (m, 2H), 3.28 (dd, 2H, J = 10.6, 3.0 Hz), 2.99 (dd, 2H, J = 11.7, 3.0 Hz), 2.40 (dd, 2H, J = 11.7, 10.6 Hz), 2.08 (s, 6H) (Figure A.137, page 314). ^{13}C-NMR (101 MHz, 25 °C, $CDCl_3$) δ 141.3, 128.5, 127.9, 127.6, 69.4, 64.2, 43.3 (A.142, page 316). **Elemental analysis** calculated for $C_{18}H_{22}N_2$: C, 81.16%; H, 8.32%; N, 10.52%; found: C, 81.25%; H, 8.58%; N, 10.41%. **MS-ESI(+)**: m/z ($C_{18}H_{22}N_2$) calculated 266.18, found $[M+H]^+$ 267.33 (100%).

(±) - **P2b**: ^{1}H-NMR (400 MHz, 25 °C, $CDCl_3$) δ 7.71 (d, 4H, J = 8.3 Hz), 7.41 (m, 4H), 7.33 (m, 2H), 3.57 (dd, 2H, J = 6.3, 3.9 Hz), 2.96 (dd, 2H, J = 11.9, 6.2 Hz), 2.68 (dd, 2H, J = 11.9, 3.9 Hz), 2.16 (s, 6H) (Figure A.143, page 317). ^{13}C-NMR (101 MHz, 25° C, $CDCl_3$) δ 141.7, 129.4, 128.0, 127.3, 65.9, 57.9, 43.3 (Figure A.148, page 319). **Elemental analysis** calculated for $C_{18}H_{22}N_2$: C, 81.16%; H, 8.32%; N, 10.52%; found: C, 81.35%; H, 8.45%; N, 10.32%. **MS-ESI(+)**: m/z ($C_{18}H_{22}N_2$) calculated 266.18, found $[M+H]^+$ 267.56 (100%).

1,4-dimethyl-2,6-phenylpiperazine (P2b'). *Meso* - **P2b'** was separated as a yellowish oil (yield: 1%). (±) - **P2b'** could not be isolated in pure form, but it was detected as a minor component in the spectra of (±) - **P2b**.

meso - **P2b'**: ^{1}H-NMR (400 MHz, 25 °C, $CDCl_3$) δ 7.62 (m, 4H), 7.37-7.29 (m, 6H), 3.88 (dd, 2H, J = 6.2, 3.8 Hz), 2.84 (dd, 2H, J = 11.1, 3.8 Hz), 2.64 (m, 2H), 2.28 (s, 3H), 1.87 (s, 3H) (Figure A.149, page 320). ^{13}C-NMR (101 MHz, 25 °C, $CDCl_3$) δ 141.1, 129.4, 128.0, 127.2, 62.8, 62.0, 46.3, 39.9 (Figure A.153, page 322). **Elemental analysis** calculated for $C_{18}H_{22}N_2$: C, 81.16%; H, 8.32%; N, 10.52%; found: C, 81.35%; H, 8.21%; N, 10.23%. **MS-ESI(+)**: m/z ($C_{18}H_{22}N_2$) calculated 266.18, found $[M+H]^+$ 267.28 (100%).

(±) - **P2b'**: as stated above, this isomer was not isolated in pure form, but detected in the spectra of (±) - **P2b** as a minor by-product. ^{1}H-NMR (400 MHz, 25 °C, $CDCl_3$) δ 3.43 (dd, 2H, J = 10.7, 3.0 Hz), 2.87 (m, 2H), 2.30 (s, 3H), 2.21 (m, 2H, overlapping with CH_3 of (±) - **P2b**), 1.88 (s, 3H) (Figure A.154, page 322). Ten aromatic protons were not identified due to overlap with (±) - **P2b**. ^{13}C-NMR (101 MHz, 25 °C, $CDCl_3$) δ 69.9 (CH), 64.1 (CH_2), 45.7 (CH_3), 41.0 (CH_3); aromatic carbons overlapped with (±) - **P2b** (Figure A.156, page 323).

1,4-dibutyl-2,5-(4-methylphenyl)piperazine (P2h). At the end of the reaction, *meso* - **P2h** spontaneously precipitated as a white powder and was collected by filtration (yield: 15%). The solution was evaporated to dryness then separated by column chromatography (eluent *n*-hexane/EtOAc = 8:2). (±) - **P2h** was isolated as a yellow oil (yield: 7%).

meso - **P2h**: ^{1}H-NMR (400 MHz, 25 °C, $CDCl_3$) δ 7.34 (d, 4H, J = 8.0 Hz), 7.18 (d, 4H, J = 8.0 Hz), 3.39 (dd, 2H, J = 10.6, 3.0 Hz), 3.07 (dd, 2H, J = 11.5, 3.0 Hz), 2.50 (m, 2H), 2.39 (s, 6H), 2.26 (pst, 2H, J = 11.1 Hz), 1.93 (m, 2H), 1.44-1.30 (m, 4H), 1.35-0.94 (m, 4H), 0.79 (t, 6H, J = 7.3 Hz) (Figure A.157, page 324). ^{13}C-NMR (101 MHz, 25 °C, $CDCl_3$) δ 139.2, 136.9, 129.1, 127.9, 67.5, 61.0, 54.4, 28.3, 21.2, 20.5, 14.0 (Figure A.161, page 326). **Elemental analysis** calculated for $C_{26}H_{38}N_2$: C, 82.48%; H, 10.12%; N, 7.40%; found: C, 82.11%; H, 9.99%; N, 7.32%. **MS-ESI(+)**: m/z ($C_{26}H_{38}N_2$) calculated 378.30, found $[M+H]^+$ 379.44 (100%).

(±) - **P2h**: ^{1}H-NMR (400 MHz, 25 °C, $CDCl_3$) δ 7.60 (d, 4H, J = 7.8 Hz), 7.20 (d, 4H, J = 7.8 Hz), 3.66 (dd, 2H, J = 6.4, 3.8 Hz), 2.99 (dd, 2H, J = 11.8, 6.3 Hz), 2.62 (dd, 2H, J = 12.0, 3.8 Hz), 2.57-2.48 (m, 2H), 2.39 (s, 6H), 2.18-2.11 (m, 2H), 1.68-1.63 (m, 4H), 1.32-1.20 (m, 4H), 0.85 (t, 6H, J = 7.3 Hz) (Figure A.162, page 326). The purity of the recovered product was not sufficient for Elemental Analysis. **MS-ESI(+)**: m/z ($C_{26}H_{38}N_2$) calculated 378.30, found $[M+H]^+$ 379.42 (100%).

1,4-diallyl-2,5-phenylpiperazine (P2i). At the end of the reaction, *meso* - **P2i** spontaneously precipitated as a white powder and was collected by filtration (yield: 15%). The solution was evaporated to dryness then separated by column chromatography (eluent *n*-hexane/EtOAc = 8:2). (±) - **P2i** was isolated as a yellow oil (yield: 12%).

meso - **P2i**: ^{1}H-NMR (400 MHz, 25 °C, $CDCl_3$) δ 7.46 (d, 4H, J = 7.0 Hz), 7.37 (td, 4H, J = 7.3, 1.4 Hz), 7.32 (dt, 2H, J = 7.5, 1.4 Hz), 5.79 (dddd, 2H, J = 16.9, 10.4, 8.3, 4.8 Hz), 5.05 (dd, 2H, J = 4.8, 1.4 Hz), 5.02 (dt, 2H, J = 16.9, 3.0 Hz), 3.49 (dd, 2H, J = 10.4, 3.0 Hz), 3.23 (ddt, 2H, J = 13.8, 4.8, 1.8 Hz), 3.09 (dd, 2H, J = 11.8, 3.0 Hz), 2.53 (dd, 2H, J = 13.8, 8.3 Hz), 2.32 (dd, 2H, J = 11.7, 10.6 Hz) (Figure A.163, page 327). ^{13}C-NMR (101 MHz, 25 °C, $CDCl_3$) δ 141.6, 134.8, 128.5, 128.1, 127.5, 117.7, 67.2, 60.7, 57.6 (Figure A.166, page 328). **Elemental analysis** calculated for $C_{22}H_{26}N_2$: C, 82.97%; H, 8.23%; N, 8.80%; found: C, 82.88%; H, 8.24%; N, 8.65%. **MS-ESI(+)**: m/z ($C_{22}H_{26}N_2$) calculated 318.21, found $[M+H]^+$ 319.82 (100%).

(±) - **P2i**: ^{1}H-NMR (400 MHz, 25 °C, $CDCl_3$) δ 7.74 (d, 4H, J = 7.0 Hz), 7.42 (t, 4H, J = 7.4 Hz), 7.24 (m, 2H) overlapping with signals due to polymeric materials, 5.88 (dddd, 2H, J = 17.3, 10.3, 7.0, 5.7 Hz), 5.20-5.07 (m, 6H), 3.77 (dd, 2H, J = 6.3, 3.8 Hz), 3.04 (d, 2H, J = 6.1 Hz), 2.87 (dd, 2H, J = 13.9, 7.0 Hz), 2.72 (dd, 2H, J = 12.1, 3.8 Hz) (Figure A.167, page 329). Unfortunately, complete purification from traces of polymeric materials was unsuccessful; therefore, no further analyses were carried out.

1,4-dibenzyl-2,5-phenylpiperazine (P2j). At the end of the reaction, *meso* - **P2j** spontaneously precipitated as a white powder and was collected by filtration (yield: 13%). The solution was evaporated to dryness then separated by column chromatography (eluent gradient *n*-hexane/EtOAc from 9:1 to 6:4). (±) - **P2j** was isolated as a yellowish powder (yield: 8%).

meso - **P2j**: ^{1}H-NMR (400 MHz, 25 °C, $CDCl_3$) δ 7.43-7.22 (m, 20H), 3.81 (d, 2H, J = 13.6 Hz), 3.50 (dd, 2H, J = 10.5, 3.0 Hz), 2.95 (dd, 2H, J = 11.6, 3.0 Hz), 2.88 (d, 2H, J = 13.5 Hz), 2.31 (dd, 2H, J = 11.7, 10.5 Hz) (Figure A.168, page 329). ^{13}C-NMR (101 MHz, 25 °C, $CDCl_3$) δ 141.9, 138.8, 128.7, 128.5, 128.1, 127.5, 127.1, 126.7, 67.6, 60.7, 58.9 (Figure A.172, page 331). **Elemental analysis** calculated for $C_{30}H_{30}N_2$: C, 86.08%; H, 7.22%; N, 6.69%; found: C, 85.94%; H, 7.37%; N, 6.56%. **MS-ESI(+)**: m/z ($C_{30}H_{30}N_2$) calculated 418.24, found $[M+H]^+$ 419.26 (100%).

(±) - **P2j**: ^{1}H-NMR (400 MHz, 25 °C, $CDCl_3$) δ 7.43-7.07 (m, 20H), 3.80 (d, 2H, J = 13.5 Hz), 3.50 (dd, 2H, J = 10.5, 3.1 Hz), 2.95 (dd, 2H, J = 11.7, 3.0 Hz), 2.88 (d, 2H, J = 13.5 Hz), 2.31 (pst, 2H, J = 11.1 Hz) (Figure A.173, page 332). ^{13}C-NMR (101 MHz, 25 °C, $CDCl_3$) δ 141.9, 138.8, 132.9, 128.7, 128.5, 128.1, 127.5, 127.3, 67.6, 60.7, 58.9 (Figure A.177, page 334). **Elemental analysis** calculated for $C_{30}H_{30}N_2$: C, 86.08%; H, 7.22%; N, 6.69%; found: C, 85.94%; H, 7.37%; N, 6.56%. **MS-ESI(+)**: m/z ($C_{30}H_{30}N_2$) calculated 418.24, found $[M+H]^+$ 419.96 (100%).

1,4-ditosylpiperazine (P2m). At the end of the reaction, **P2m** spontaneously precipitated as a white powder and was collected by filtration (yield: 25%).

P2m: ^{1}H-NMR (400 MHz, 25 °C, $CDCl_3$) δ 7.62 (d, 4H, J = 8.3 Hz), 7.35 (d, 4H, J = 8.2 Hz), 3.10 (s, 8H), 2.47 (s, 6H) (Figure A.178, page 334). ^{13}C-NMR (101 MHz, 25 °C, $CDCl_3$) δ 144.2, 132.2, 129.9, 127.7, 45.5, 21.5 (Figure A.182, page 336). **Elemental analysis** calculated for $C_{18}H_{22}N_2O_4S_2$: C, 54.80%; H, 5.62%; N, 7.10%; found: C, 55.01%; H, 5.25%; N, 6.92%. **MS-ESI(+)**: m/z ($C_{18}H_{20}Br_2N_2$) calculated 394.10, found $[M+Na]^+$ 417.38 (100%).

1,4-dimethyl-2,5-(4-methylphenyl)piperazine (P2p). At the end of the reaction, *meso* - **P2p** spontaneously precipitated as a white powder and was collected by filtration (yield: 46%). The solution was evaporated to dryness and then separated by column chromatography (eluent *n-hexane* /EtOAc = 8:2). (±) - **P2p** was isolated as a yellow oil (yield: 36%).

meso - **P2p**: ^{1}H-NMR (400 MHz, 25 °C, $CDCl_3$) δ 7.32 (m, 4H), 7.19 (d, 4H, J = 8.1 Hz), 3.27 (m, 2H), 2.97 (m, 2H), 2.40 (m, 2H) overlapping with 2.38 (s, 6H), 2.08 (s, 6H) (Figure A.183, page 337). ^{13}C-NMR (101 MHz, 25 °C, $CDCl_3$) δ 138.2 (C), 137.3 (C), 129.2 (CH), 127.8 (CH), 69.1 (CH), 64.2 (CH_2), 43.1 (CH_3), 21.1 (CH_3) (Figure A.187, page 339). **Elemental analysis** calculated for $C_{20}H_{26}N_2$: C, 81.58%; H, 8.90%; N, 9.51%; found: C, 81.23%; H, 8.77%; N, 9.41%. **MS-ESI(+)**: m/z ($C_{20}H_{26}N_2$) calculated 294.21, found $[M+H]^+$ 295.33 (100%).

(±) - **P2p**: ^{1}H-NMR (400 MHz, 25 °C, $CDCl_3$) δ 7.60 (d, 4H, J = 7.1 Hz), 7.22

(d, 4H, J = 7.1 Hz), 3.54 (m, 2H), 2.94 (m, 2H), 2.65 (m, 2H), 2.41 (s, 6H), 2.15 (s, 6H) (Figure A.188, page 339). ^{13}C-NMR (101 MHz, 25 °C, $CDCl_3$) δ 137.1 (C), 136.8 (C), 129.3 (CH), 128.7 (CH), 65.7 (CH), 58.0 (CH_2), 43.3 (CH_3), 21.2 (CH_3) (Figure A.190, page 340). **Elemental analysis** calculated for $C_{20}H_{26}N_2$: C, 81.58%; H, 8.90%; N, 9.51%; found: C, 81.67%; H, 8.57%; N, 9.42%. **MS-ESI(+)**: m/z ($C_{20}H_{26}N_2$) calculated 294.21, found $[M+H]^+$ 295.35 (100%).

1,4-dimethyl-2,5-(4-(1',1'-dimethyl)ethylphenyl)piperazine (P2q). At the end of the reaction, *meso* - **P2q** spontaneously precipitated as a white powder and was collected by filtration (yield: 31%). The solution was evaporated to dryness then separated by column chromatography (eluent *n*-hexane/EtOAc = 7:3). (±) - **P2q** was isolated as a yellow powder (yield: 21%).

meso - **P2q**: ^{1}H-NMR (400 MHz, 25 °C, $CDCl_3$) δ 7.41-7.34 (m, 8H), 3.29 (m, 2H), 3.00 (m, 2H), 2.41 (m, 2H), 2.09 (s, 6H), 1.35 (s, 18H) (Figure A.191, page 341). ^{13}C-NMR (101 MHz, 25 °C, $CDCl_3$) δ 150.5, 127.5, 125.4, 69.0, 64.1, 43.2, 34.8, 31.4; one quaternary aromatic carbon was not detected (Figure A.192, page 341). **Elemental analysis** calculated for $C_{26}H_{38}N_2$: C, 82.48%; H, 10.12%; N, 7.40%; found: C, 82.16%; H, 10.33%; N, 7.21%. **MS-ESI(+)**: m/z ($C_{26}H_{38}N_2$) calculated 378.30, found $[M+H]^+$ 379.38 (100%).

(±) - **P2q**: ^{1}H-NMR (400 MHz, 25 °C, $CDCl_3$) δ 7.64 (d, 4H, J = 8.2 Hz), 7.42 (d, 4H, J = 8.3 Hz), 3.54 (dd, 2H, J = 5.7, 4.0 Hz), 2.95 (dd, 2H, J = 11.6, 5.7 Hz), 2.66 (dd, 2H, J = 11.6, 4.0 Hz), 2.15 (s, 6H), 1.38 (s, 18H) (Figure A.193, page 342). ^{13}C-NMR (101 MHz, 25 °C, $CDCl_3$) δ 150.0, 137.1, 129.1, 124.8, 65.6, 58.0, 43.3, 34.5, 31.5 (Figure A.197, page 344). **Elemental analysis** calculated for $C_{26}H_{38}N_2$: C, 82.48%; H, 10.12%; N, 7.40%; found: C, 82.22%; H, 10.01%; N, 7.14%. **MS-ESI(+)**: m/z ($C_{26}H_{38}N_2$) calculated 378.30, found $[M+H]^+$ 379.51 (100%).

1,4-dimethyl-2,5-(4-bromophenyl)piperazine (P2r). At the end of the reaction, *meso* - **P2r** spontaneously precipitated as a white powder and was collected by filtration (yield: 20%). The solution was evaporated to dryness then separated by column chromatography (eluent *n*-hexane/EtOAc = 6:4). (±) - **P2r** was isolated as a yellow powder (yield: 17%).

meso - **P2r**: ^{1}H-NMR (400 MHz, 25 °C, $CDCl_3$) δ 7.50 (d, 4H, J = 8.3 Hz), 7.30 (d, 4H, J = 8.1 Hz), 3.21 (dd, 2H, J = 10.6, 3.0 Hz), 2.91 (dd, 2H, J = 11.7, 3.0 Hz), 2.30 (dd, 2H, J = 11.6, 10.6 Hz), 2.04 (s, 6H) (Figure A.198, page 344). ^{13}C-NMR (101 MHz, 25 °C, $CDCl_3$) δ 140.2, 131.7, 129.6, 121.3, 68.6, 63.9, 43.1 (Figure A.202, page 346). **Elemental analysis** calculated for $C_{18}H_{20}Br_2N_2$: C, 50.97%; H, 4.75%; N, 6.60%; found: C, 51.23%; H, 4.68%; N, 6.45%. **MS-ESI(+)**: m/z ($C_{18}H_{20}Br_2N_2$) calculated 424.00, found $[M+H]^+$ 425.27 (100%).

(±) - **P2r**: ^{1}H-NMR (400 MHz, 25 °C, $CDCl_3$) δ 7.52 (m, 8H), 3.51 (m, 2H), 2.83 (m, 2H), 2.63 (dd, 2H, J = 12.0, 4.1 Hz), 2.12 (s, 6H) (Figure A.203, page 347). ^{13}C-NMR (101 MHz, 25 °C, $CDCl_3$) δ 138.9, 131.2, 131.0, 121.3, 65.0, 57.4,

43.2 (Figure A.207, page 349). **Elemental analysis** calculated for $C_{18}H_{20}Br_2N_2$: C, 50.97%; H, 4.75%; N, 6.60%; found: C, 50.87%; H, 4.63%; N, 6.21%. **MS-ESI(+)**: m/z ($C_{18}H_{20}Br_2N_2$) calculated 424.00, found $[M+H]^+$ 425.32 (100%).

1,4-dimethyl-2,5-(4-fluorophenyl)piperazine (P2s). At the end of the reaction, *meso* - **P2s** spontaneously precipitated as a white powder and was collected by filtration (yield: 14%). The solution was evaporated to dryness then separated by column chromatography (eluent *n*-hexane/EtOAc = 6:4). (±) - **P2s** was isolated as a yellow powder (yield: 6%).

meso - **P2s**: ^{1}H-NMR (400 MHz, 25 °C, $CDCl_3$) δ 7.38 (dd, 4H, J = 8.0, 3.9 Hz), 7.05 (pst, 4H, J = 8.0 Hz), 3.23 (dd, 2H, J = 10.6, 3.0 Hz), 2.92 (dd, 2H, J = 11.7, 3.0 Hz), 2.32 (dd, 2H, J = 11.7, 10.6 Hz), 2.04 (s, 6H) (Figure A.208, page 349). ^{13}C-NMR (101 MHz, 25 °C, $CDCl_3$) δ 162.2 (J = 244 Hz), 136.9 (J = 3 Hz), 129.3 (J = 7 Hz), 115.3 (J = 21 Hz), 68.53, 64.17, 43.13 (Figure A.212, page 351). **Elemental analysis** calculated for $C_{18}H_{20}F_2N_2$: C, 71.50%; H, 6.67%; N, 9.26%; found: C, 71.22%; H, 6.79%; N, 9.00%. **MS-ESI(+)**: m/z ($C_{18}H_{20}F_2N_2$) calculated 302.16, found $[M+H]^+$ 303.44 (100%).

(±) - **P2s**: ^{1}H-NMR (400 MHz, 25 °C, $CDCl_3$) δ 7.75-7.51 (m, 4H), 7.07 (pst, 4H, J = 8.8 Hz), 3.54 (m, 2H), 2.86 (dd, 2H, J = 11.9, 6.2 Hz), 2.64 (dd, 2H, J = 11.9, 3.9 Hz), 2.12 (s, 6H) (Figure A.213, page 352). ^{13}C-NMR (101 MHz, 25 °C, $CDCl_3$) δ 162.1 (J = 244 Hz), 135.7, 130.7 (J = 8 Hz), 114.8 (J = 21 Hz), 65.0, 57.7, 43.1 (Figure A.215, page 353). **Elemental analysis** calculated for $C_{18}H_{20}F_2N_2$: C, 71.50%; H, 6.67%; N, 9.26%; found: C, 71.48%; H, 6.59%; N, 8.92%. **MS-ESI(+)**: m/z ($C_{18}H_{20}F_2N_2$) calculated 302.16, found $[M+H]^+$ 303.39 (100%).

1,4-dibutyl-2,5-(4-chlorophenyl)piperazine (P2t). At the end of the reaction, *meso* - **P2t** spontaneously precipitated as a white powder and was collected by filtration (yield: 8%). The solution was evaporated to dryness then separated by column chromatography (eluent gradient *n*-hexane/EtOAc from 9:1 to 5:5). (±) - **P2t** was isolated as a yellow oil (yield: 4%).

meso - **P2t**: ^{1}H-NMR (400 MHz, 25 °C, $CDCl_3$) δ 7.39-7.30 (m, 8H), 3.37 (dd, 2H, J = 10.6, 3.1 Hz), 3.02 (dd, 2H, J = 11.6, 3.1 Hz), 2.43 (m, 2H), 2.18 (pst, 2H, J = 11.1 Hz), 1.90 (m, 2H), 1.42-1.26 (m, 4H), 1.25-1.00 (m, 4H), 0.79 (t, 6H, J = 7.3 Hz) (Figure A.216, page 353). ^{13}C-NMR (101 MHz, 25 °C, $CDCl_3$) δ 140.6, 133.0, 129.3, 128.6, 67.0, 60.7, 54.4, 28.3, 20.5, 14.0 (Figure A.220, page 355). **Elemental analysis** calculated for $C_{24}H_{32}Cl_2N_2$: C, 71.50%; H, 6.67%; N, 9.26%; found: C, 71.48%; H, 6.59%; N, 8.92%. **MS-ESI(+)**: m/z ($C_{24}H_{32}Cl_2N_2$) calculated 418.19, found $[M+H]^+$ 419.30 (100%).

(±) - **P2t**: ^{1}H-NMR (400 MHz, 25 °C, $CDCl_3$) δ 7.60 (m, 4H), 7.37 (m, 4H), 3.67 (m, 2H), 2.92 (m, 2H), 2.62 (m, 2H), 2.40-2.00 (m, 4H), 1.58-1.43 (m, 4H), 1.34-1.20 (m, 4H), 0.85 (t, 6H, J = 7.3 Hz) (Figure A.221, page 356). The purity of the recovered product was not sufficient for other analyses.

6.3.4 Cyclic carbonates

Reading guidance

The next table summarizes the structure of the compounds that are described in section 6.3.4.

Table 6.34: *Schemes of the compounds of section 6.3.4.*

Comp.	Scheme	Comp.	Scheme
P3a	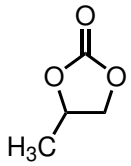	**P3b**	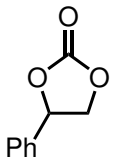
P3c	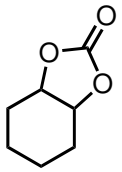	**P3d**	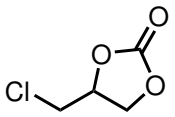
P3e	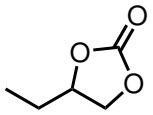	**P3f**	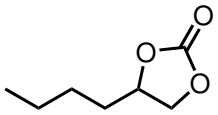
P3g	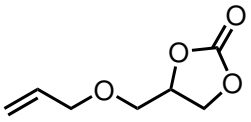	**P3h**	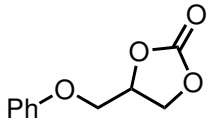
P3i	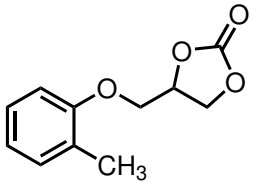	**P3j**	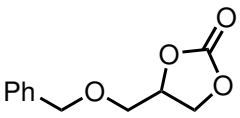
P3k	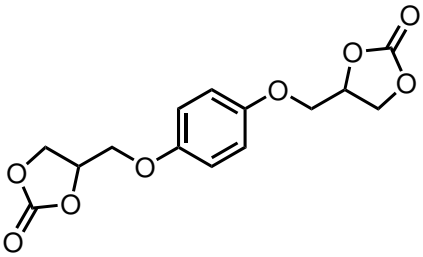	**P3l**	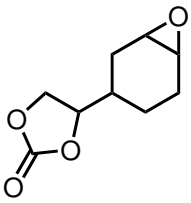
P3l′	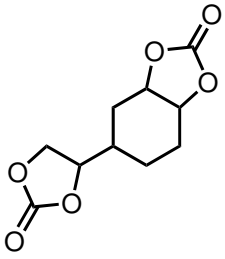	**P3m**	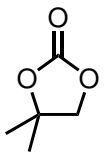

Continues on next page

Table 6.34 – continued from previous page

Comp.	Scheme	Comp.	Scheme
P3n	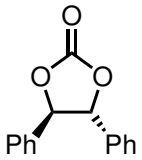	**P3o**	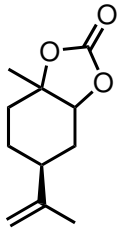
P3p	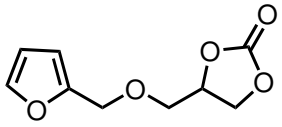	**P3q**	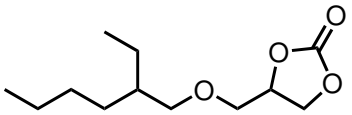
P3r	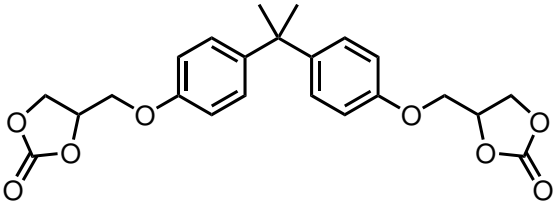		

Propylene carbonate (P3a). ^{1}H-NMR: δ 4.91-4.83 (m, 1H), 4.59-4.55 (t, J = 8 Hz, 1H), 4.06-4.02 (t, J = 8 Hz, 1H), 1.52-1.51 (t, J = 4 Hz, 3H) (Figure A.222, page 356). Data are in agreement with the literature.[270]

Styrene carbonate (P3b). ^{1}H-NMR (400 MHz, 25 °C, $CDCl_3$) δ 7.50-7.37 (m, 5H), 5.72-5.68 (t, J = 8 Hz, 1H), 4.84-4.80 (t, J = 8 Hz, 1H), 4.39-4.35 (t, J = 4 Hz, 1H) (Figure A.223, page 357). Data are in agreement with the literature.[270]

Cyclohexene carbonate (P3c). ^{1}H-NMR (400 MHz, 25 °C, $CDCl_3$) δ 4.72-4.67 (m, 5H), 1.94-1.63 (t, J = 8 Hz, 4H), 1.61-1.58 (m, 2H), 1.50-1.40 (m, 2H) (Figure A.224, page 357). Data are in agreement with the literature.[270]

4-chloromethyl-[1,3]-dioxolan-2-one (P3d). The procedure is reported for the IER-catalyzed reaction. The resin (catalyst loading = 17.7 mg/mmol) and 500 mg of epichlorohydrin (5.4 mmol) were mixed together in an autoclave vial capped with a septum. The autoclave was loaded with 1.4 MPa of CO_2 and heated at 100 °C. After 2 hours, the autoclave was cooled at 0 °C to quench the reaction. The reaction mixture was filtered to remove the resin. No further purification was needed. ^{1}H-NMR (400 MHz, 25 °C, $CDCl_3$) δ 5.00-4.94 (m, 1H), 4.63-4.59 (t, J = 8 Hz, 1H), 4.45-4.41 (m, 1H), 3.78-3.76 (m, 2H) (Figure A.225, page 358). ^{13}C-NMR: δ 154.03 (s, 1C), 74.19 (s, 1C), 66.98 (s, 1C), 43.49 (s, 1C) (Figure A.226, page 358). Data are in agreement with the literature.[270]

Butylene carbonate (P3e). The procedure is reported for the IER-catalyzed reaction. The resin (catalyst loading = 17.7 mg/mmol) and 500 mg of 1,2-epoxybutane (6.93 mmol) were mixed together in an autoclave vial capped with a septum. The autoclave was loaded with 1.4 MPa of CO_2 and heated at 100 °C. After 2 hours, the autoclave was cooled at 0 °C to quench the reaction. The reaction mixture was filtered to remove the resin. No further purification was needed. ^{1}H-NMR (400 MHz, 25 °C, $CDCl_3$) δ 4.71-4.64 (m, 1H), 4.56-4.52 (t, J = 8 Hz, 1H), 4.12-4.08 (t, J = 8 Hz, 1H), 3.88-3.77 (m, 2H; partially overlapping with epoxide's signals), 1.07-1.03 (t, J = 8 Hz, 3H; partially overlapping with epoxide's signals) (Figure A.227, page 359). Data are in agreement with the literature.[270]

Hexylene carbonate (P3f). The procedure is reported for the IER-catalyzed reaction. The resin (catalyst loading = 17.7 mg/mmol) and 500 mg of 1,2-epoxyhexane (4.99 mmol) were mixed together in an autoclave vial capped with a septum. The autoclave was loaded with 1.4 MPa of CO_2 and heated at 100 °C. After 2 hours, the autoclave was cooled at 0 °C to quench the reaction. The product was purified by chromatographic column (hexane:ethyl acetate = 8:2). ^{1}H-NMR (400 MHz, 25 °C, $CDCl_3$) δ 4.76-4.69 (m, 1H), 4.57-4.52 (t, J = 8 Hz, 1H), 4.11-4.07 (m, 1H), 1.89-1.80 (m, 1H), 1.76-1.67 (m, 1H), 1.60-1.38 (m, 4H; overlapping with the epoxide's signals) (Figure A.228, page 359). Data are in agreement with the literature.[270]

4-allyloxymethyl-[1,3]-dioxolan-2-one (P3g). The procedure is reported for the IER-catalyzed reaction. The resin (catalyst loading = 17.7 mg/mmol) and 500 mg of allyl glycidyl ether (4.38 mmol) were mixed together in an autoclave vial capped with a septum. The autoclave was loaded with 1.4 MPa of CO_2 and heated at 100 °C for 2 hours. After 2 hours, the autoclave was cooled at 0 °C to quench the reaction. The product was purified by chromatographic column (hexane:ethyl acetate = 6:4). ^{1}H-NMR (400 MHz, 25 °C, $CDCl_3$) δ 5.86 (ddt, J = 17.1, 10.2, 5.6 Hz, 1H), 5.27 (dd, J = 17.1, 1.6 Hz, 1H), 5.20 (m, 1H), 4.83-4.75 (m, 1H), 4.50-4.42 (m, 1H), 4.38-4.32 (m, 1H), 4.06-4.01 (m, 2H), 3.67 (dd, J = 11.1, 3.5 Hz 1H), 3.57 (dd, J = 11.1, 3.5 Hz 1H) (Figure A.229, page 360). Data are in agreement with the literature.[270]

4-phenyloxymethyl-[1,3]-oxolan-2-one (P3h). The procedure is reported for the IER-catalyzed reaction. The resin (catalyst loading = 17.7 mg/mmol) and 500 mg of phenyl glycidyl ether (3.33 mmol) were mixed together in an autoclave vial capped with a septum. The autoclave was loaded with 1.4 MPa of CO_2 and heated at 100 °C. After 2 hours, the autoclave was cooled at 0 °C to quench the reaction. The product at the end of the reaction precipitated as white crystals. The resin was filtered after dissolving the product in DCM. The solvent was evaporated under reduced pressure and the product was recovered as white powder. ^{1}H-NMR (400 MHz, 25 °C, $CDCl_3$) δ 7.31 (dd, J = 8.8, 7.4 Hz, 2H), 7.02 (tt, J = 7.4, 1.0 Hz, 1H), 6.91 (dd, J = 8.8, 1.0 Hz, 2H), 5.02 (dddd, J = 8.4, 5.9, 4.2, 3.6 Hz, 1H), 4.61 (t, J = 8.4 Hz, 1H), 4.53

(dd, J = 8.4, 5.9 Hz, 1H), 4.24 (dd, J = 10.6, 4.2 Hz, 1H), 4.14 (dd, J = 10.6, 3.6 Hz, 1H) (Figure A.230, page 360). Data are in agreement with the literature.[270]

4-((*o*-tolyloxy)methyl)-[1,3]-dioxolan-2-one (P3i). The procedure is reported for the IER-catalyzed reaction. The resin (catalyst loading = 17.7 mg/mmol) and 500 mg of 2-methyl phenyl glycidyl ether (3.04 mmol) were mixed together in an autoclave vial capped with a septum. The autoclave was loaded with 1.4 MPa of CO_2 and heated at 100 °C. After 2 hours, the autoclave was cooled at 0 °C to quench the reaction. The product was purified by chromatographic column (*n*-hexane/ethyl acetate 7:3). ^{1}H-NMR (400 MHz, 25 °C, $CDCl_3$) δ 7.21-7.16 (m, 2H), 6.97-6.93 (m, 1H), 6.82-6.79 (m, 1H), 5.07 (dddd, J = 8.5, 5.5, 3.7, 3.1 Hz, 1H), 4.66 (t, J = 8.5 Hz, 1H), 4.60 (dd, J = 8.5, 5.5 Hz, 1H), 4.29 (dd, J = 10.6, 3.7 Hz, 1H), 4.16 (dd, J = 10.6, 3.1 Hz, 1H), 2.25 (s, 3H) (Figure A.231, page 361). Data are in agreement with the literature.[271]

4-benzyloxymethyl-[1,3]-oxolan-2-one (P3j). The procedure is reported for the IER-catalyzed reaction. The resin (catalyst loading = 17.7 mg/mmol) and 500 mg of benzyl glycidyl ether (3.05 mmol) were mixed together in an autoclave vial capped with a septum. The autoclave was loaded with 1.4 MPa of CO_2 and heated at 100 °C. After 2 hours, the autoclave was cooled at 0 °C to quench the reaction. The product was purified by chromatographic column (*n*-hexane/ethyl acetate 6:4). ^{1}H-NMR (400 MHz, 25 °C, $CDCl_3$) δ 7.40-7.32 (m, 5H), 4.79-4.75 (m, 1H), 4.62-4.55 (m, 2H), 4.44-4-41 (m, 1H), 4.364.34 (m, 1H), 3.72-3.78 (m, 1H), 3.61-3.57 (m, 1H) (Figure A.232, page 361). Data are in agreement with the literature.[271]

4,4'-((1,4-phenylenebis(oxy))bis(methylene))bis([1,3]-dioxolan-2-one) (P3k). The procedure is reported for the IER-catalyzed reaction. The resin (catalyst loading = 17.7 mg/mmol) and 131 mg of benzyl glycidyl ether (0.59 mmol) were dissolved in 1 mL of propylene carbonate and then mixed together in an autoclave vial capped with a septum. The autoclave was loaded with 1.4 MPa of CO_2 and heated at 100 °C. After 2 hours, the autoclave was cooled at 0 °C to quench the reaction. The resin was filtered away, and after adding mesitylene as the internal standard to calculate NMR yield, the product precipitated as a white solid. The carbonate was filtered to remove mesitylene and propylene carbonate and washed three times with 2 mL of hexane. ^{1}H-NMR (400 MHz, 25 °C, $CDCl_3$) δ 6.92 (s, 4H), 5.15-5.10 (m, 2H), 4.65-4.60 (m, 2H), 4.40-4.36 (m, 2H), 4.25-4.13 (m, 4H) (Figure A.233, page 362). Data are in agreement with the literature.[272]

4-(7-oxabicyclo[4.1.0]heptan-3-yl)-[1,3]-dioxolan-2-one (P3l). The procedure is reported for the IER-catalyzed reaction. The resin (catalyst loading = 17.7 mg/mmol) and 500 mg of vinylcyclohexene dioxide (3.57 mmol) were mixed together in an autoclave vial capped with a septum. The autoclave was loaded with 1.4 MPa

of CO_2 and heated at 100 °C. After 2 hours, the autoclave was cooled at 0 °C to quench the reaction. Since the NMR yield was very low, the product was not further purified. ^{1}H-NMR (400 MHz, 25 °C, $CDCl_3$) δ 4.52-4.47 (m, 2H), 4.20-4.14 (m, 1H), 3.23-3.16 (m, 2H; overlapped with epoxide's signals), 2.7-1 (cyclohexane ring, overlapped with the bis-epoxide's signals) (Figure A.234, page 362). Data are in agreement with the literature.[270]

4,4-dimethyl-1,3-dioxolan-2-one (P3m).
The procedure is reported for the [Zn(pytren)]-catalyzed reaction. The complex (catalyst loading = 0.5 mol%) and 420 mg of 1,2-epoxy-2-methylpropane were mixed together in an autoclave vial capped with a septum. The autoclave was loaded with 0.8 MPa of CO_2 and heated at 140 °C. After 16 hours, the autoclave was cooled at 0 °C to quench the reaction. The product was purified by chromatographic column (*n*-hexane/ethyl acetate 7:3). ^{1}H-NMR (400 MHz, 25 °C, $CDCl_3$) δ 4.15 (s, 2H), 1.54 (s, 6H) (Figure A.235, page 363). Data are in agreement with the literature.[270]

4,5-diphenyl-1,3-dioxolan-2-one (P3n).
The procedure is reported for the [Zn(pytren)]-catalyzed reaction. The complex (catalyst loading = 0.5 mol%), 420 mg of stylbene oxide and 2.1 mL of acetonitrile were mixed together in an autoclave vial capped with a septum. The autoclave was loaded with 0.8 MPa of CO_2 and heated at 140 °C. After 16 hours, the autoclave was cooled at 0 °C to quench the reaction. Since the NMR yield was very low, the product was not further purified.

4,5-diphenyl-1,3-dioxolan-2-one (P3p).
The procedure is reported for the [Zn(pytren)]-catalyzed reaction. The complex (catalyst loading = 0.5 mol%) and 420 mg of 1,2-epoxy-2-methylpropane were mixed together in an autoclave vial capped with a septum. The autoclave was loaded with 0.8 MPa of CO_2 and heated at 140 °C. After 16 hours, the autoclave was cooled at 0 °C to quench the reaction. Since the NMR yield was very low, the product was not further purified. ^{1}H-NMR (400 MHz, 25 °C, $CDCl_3$) δ 7.35 (m, 1H), 6.29 (m, 2H), 4.74 (m, 1H), 4.42 (m, 3H), 4.21 (m, 1H), 3.62-3.52 (m, 2H). Data are in agreement with the literature.[270]

4,4'-(((propane-2,2-diylbis(4,1-phenylene))bis(oxy))bis(methylene))bis(1,3-dioxolan-2-one) (P3r). The procedure is reported for the [Zn(pytren)]-catalyzed reaction. The complex (catalyst loading = 0.1 mol%), 500 mg of bisphenol-A diglycidyl ether and 1.20 mL of acetonitrile were mixed together in an autoclave vial capped with a septum. The autoclave was loaded with 0.8 MPa of CO_2 and heated at 120 °C. After 16 hours, the autoclave was cooled at 0 °C to quench the reaction. The solvent was removed in vacuo, then the residue was taken up in DCM and washed three times to water. The solution was dried with sodium sulfate, and

upon removal of the solvent, the product was recovered pure. ^{1}H-NMR (400 MHz, 25 °C, $CDCl_3$) δ 7.16 (d, J = 8.6 Hz 4H), 6.81 (d, J = 8.6 Hz 4H), 4.98 (m, 2H), 4.56 (m, 2H), 4.47 (m, 2H), 4.20 (ddd, J = 10.8, 3.6, 1.2 Hz, 2H), 4.07 (m, 2H), 1.97 (m, 8H, H16,17,18,19), 1.64 (s, 6H) (Figure A.236, page 363). Data are in agreement with the literature.[273]

This page intentionally left blank.

Bibliography

[1] R. G. Pearson, *Journal of the American Chemical Society* **1963**, *85*, 3533–3539.

[2] K. M. Smith, *Organometallics* **2005**, *24*, 778–784.

[3] R. Dalpozzo, N. Della Ca', B. Gabriele, R. Mancuso, *Catalysts* **2019**, *9*, 511.

[4] T. Sakakura, J.-C. Choi, H. Yasuda, *Chemical Reviews* **2007**, *107*, 2365–2387.

[5] C. Damiano, M. Cavalleri, L. Invernizzi, E. Gallo, *European Journal of Organic Chemistry* **2024**, *27*, e202400616.

[6] A. Bhushan, N. J. Martucci, O. B. Usta, M. L. Yarmush, *Expert Opinion on Drug Metabolism & Toxicology* **2016**, *12*, 475–477.

[7] C. Roger, J. A. Roberts, L. Muller, *Clinical Pharmacokinetics 2017 57:5* **2017**, *57*, 559–575.

[8] T. Niemi, T. Repo, *European Journal of Organic Chemistry* **2019**, *2019*, 1180–1188.

[9] D. McBride, T. Krekel, K. Hsueh, M. J. Durkin, *Expert Opinion on Drug Metabolism & Toxicology* **2017**, *13*, 331–337.

[10] S. D. Burdette, R. Trotman, *Clinical Infectious Diseases* **2015**, *61*, 1315–1321.

[11] S. Lemaire, P. M. Tulkens, F. Van Bambeke, *Antimicrobial Agents and Chemotherapy* **2010**, *54*, 2540–2548.

[12] K. Michalska, I. Karpiuk, M. Król, S. Tyski, *Bioorganic & Medicinal Chemistry* **2013**, *21*, 577–591.

[13] M. Nasibullah, F. Hassan, N. Ahmad, A. R. Khan, M. Rahman, *Advanced Science Engineering and Medicine* **2015**, *7*, 91–111.

[14] A. Wookey, P. J. Turner, J. M. Greenhalgh, M. Eastwood, J. Clarke, C. Sefton, *Clinical Microbiology and Infection* **2004**, *10*, 247–254.

[15] A. Z. Bialvaei, M. Rahbar, M. Yousefi, M. Asgharzadeh, H. S. Kafil, *Journal of Antimicrobial Chemotherapy* **2017**, *72*, 354–364.

[16] E. Perzborn, J. Strassburger, A. Wilmen, J. Pohlmann, S. Roehrig, K. H. Schlemmer, A. Straub, *Journal of Thrombosis and Haemostasis* **2005**, *3*, 514–521.

[17] M. Da Prada, H. H. Keller, R. Kettler, *Psychiatr Prax* **1989**, *16*, 18–24.

[18] F. Sun, E. V. Van der Eycken, H. Feng, *Advanced Synthesis & Catalysis* **2021**, *363*, 5168–5195.

[19] A. Nazari, M. M. Heravi, V. Zadsirjan, *Journal of Organometallic Chemistry* **2021**, *932*, 121629.

[20] L.-Y. Chen, P.-Q. Huang, *European Journal of Organic Chemistry* **2024**, *27*, e2023–01131.

[21] G. F. S. Fernandes, C. B. Scarim, S.-H. Kim, J. Wu, D. Castagnolo, *RSC Medicinal Chemistry* **2023**, *14*, 823–847.

[22] C. C. Truong, D. K. Mishra, *Environmental Chemistry Letters* **2021**, *19*, 911–940.

[23] G. Bresciani, E. Antico, G. Ciancaleoni, S. Zacchini, G. Pampaloni, F. Marchetti, *ChemSusChem* **2020**, *13*, 5586–5594.

[24] X. Y. Dou, L. N. He, Z. Z. Yang, J. L. Wang, *Synlett* **2010**, 2159–2163.

[25] C. Phung, D. J. Tantillo, J. E. Hein, A. R. Pinhas, *Journal of Physical Organic Chemistry* **2018**, *31*, 1–7.

[26] F. Zhou, S. L. Xie, X. T. Gao, R. Zhang, C. H. Wang, G. Q. Yin, J. Zhou, *Green Chemistry* **2017**, *19*, 3908–3915.

[27] D. Adhikari, A. W. Miller, M. H. Baik, S. T. Nguyen, *Chemical Science* **2015**, *6*, 1293–1300.

[28] M. Sengoden, M. North, A. C. Whitwood, *ChemSusChem* **2019**, *12*, 3296–3303.

[29] P. Nayak, A. Chandrasekar Murali, V. Rao Velpuri, V. Chandrasekhar, K. Venkatasubbaiah, *Advanced Synthesis & Catalysis* **2023**, *365*, 230–237.

[30] P. Sonzini, C. Damiano, D. Intrieri, G. Manca, E. Gallo, *Advanced Synthesis and Catalysis* **2020**, *362*, 2961–2969.

[31] C. Damiano, A. Fata, M. Cavalleri, G. Manca, E. Gallo, *Catalysis Science & Technology* **2024**, *14*, 3996–4006.

[32] G. Bresciani, S. Zacchini, F. Marchetti, G. Pampaloni, *Dalton Transactions* **2021**, *50*, 5351–5359.

[33] Y. Xie, C. Lu, B. Zhao, Q. Wang, Y. Yao, *Journal of Organic Chemistry* **2019**, *84*, 35.

[34] C.-S. Cao, Y. Shi, H. Xu, B. Zhao, *Chemical Communications* **2021**, *57*, 7537–7540.

[35] N. Qiao, X.-Y. Xin, W.-M. Wang, Z.-L. Wu, J.-Z. Cui, *Dalton Transactions* **2023**, *52*, 10725–10736.

[36] X.-R. Tian, X.-L. Jiang, S.-L. Hou, Z.-H. Jiao, J. Han, B. Zhao, *Angewandte Chemie* **2022**, *134*, e202200123.

[37] X.-R. Tian, Y. Shi, S.-L. Hou, Y. Ma, B. Zhao, *Inorganic Chemistry* **2021**, *60*, 15383–15389.

[38] A. Sudo, Y. Morioka, E. Koizumi, F. Sanda, T. Endo, *Tetrahedron Letters* **2003**, *44*, 7889–7891.

[39] M. T. Hancock, A. R. Pinhas, *Tetrahedron Letters* **2003**, *44*, 5457–5460.

[40] C. Phung, A. R. Pinhas, *Tetrahedron Letters* **2010**, *51*, 4552–4554.

[41] W.-M. Ren, Y. Liu, X.-B. Lu, *The Journal of Organic Chemistry* **2014**, *79*, 9771–9777.

[42] Y. Chen, R. Luo, Z. Yang, X. Zhou, H. Ji, *Sustainable Energy and Fuels* **2018**, *2*, 125–132.

[43] H. Zhang, W. Zhang, F. Liu, Z.-H. Luo, K. Gao, M. Liu, *AIChE Journal* **2024**, *70*, e18488.

[44] Y. Chen, Y. Wang, J. Nong, D. Yuan, Y. Yao, *Chinese Journal of Chemistry* **2024**, *42*, 1571–1581.

[45] M. Zhou, Z. Qu, J. Zhang, H. Jiang, Z. Tang, R. Chen, *Chemical Communications* **2024**, *60*, 3170–3173.

[46] M. N. Khan, Y. v. Ingen, T. Boruah, A. McLauchlan, T. Wirth, R. L. Melen, *Chemical Science* **2023**, *14*, 13661–13695.

[47] W. Zhang, R. Ping, X. Lu, H. Shi, F. Liu, J. Ma, M. Liu, *Chemical Engineering Journal* **2023**, *451*, 138715.

[48] J. Li, S. Tao, F. Chen, M. Li, N. Liu, *Journal of CO2 Utilization* **2023**, *69*, 102384.

[49] Y. Fu, Y. Xu, Z. Zeng, A.-R. Ibrahim, J. Yang, S. Yang, Y. Xie, Y. Hong, Y. Su, H. Wang, Y. Wang, L. Peng, J. Li, W. L. Queen, *Green Energy & Environment* **2023**, *8*, 478–486.

[50] F. Gao, C. Ji, S. Wang, J. Dong, C. Guo, Y. Gao, G. Chen, *Colloids and Surfaces A: Physicochemical and Engineering Aspects* **2023**, *666*, 131304.

[51] H.-Q. Yin, M.-Y. Cui, H. Wang, Y.-Z. Peng, J. Chen, T.-B. Lu, Z.-M. Zhang, *Inorganic Chemistry* **2023**, *62*, 13722–13730.

[52] T. Zhao, G. Long, H. Liang, W. Xiong, X. Hu, *Microporous and Mesoporous Materials* **2023**, *356*, 112576.

[53] F. Wang, C. Xie, H. Song, X. Jin, *Green Chemistry* **2023**, *25*, 8134–8144.

[54] Y. Liu, S. Li, Y. Chen, M. Li, Z. Chen, T. Hu, L. Shi, M. Pudukudy, S. Shan, Y. Zhi, *Chemical Engineering Journal* **2023**, *474*, 145918.

[55] C. Li, W. Xiong, T. Zhao, F. Liu, H. Cai, P. Chen, X. Hu, *Applied Catalysis B: Environmental* **2023**, *324*, 122217.

[56] H. Lyu, X. Wang, W. Sun, E. Xu, Y. She, A. Liu, D. Gao, M. Hu, J. Guo, K. Hu, J. Cheng, Z. Long, Y. Liu, P. Zhang, *Green Chemistry* **2023**, *25*, 3592–3605.

[57] K. Cai, P. Liu, Z. Chen, P. Chen, F. Liu, T. Zhao, D.-J. Tao, *Chemical Engineering Journal* **2023**, *451*, 138946.

[58] B. Zhao, C. Li, T. Hu, Y. Gao, L. Fan, X. Zhang, *Inorganic Chemistry* **2024**, *63*, 14183–14192.

[59] X. Zhang, X. Wang, C. Li, T. Hu, L. Fan, *Journal of Colloid and Interface Science* **2024**, *656*, 127–136.

[60] B. Zhao, C. Li, T. Hu, X. Zhang, *ACS Applied Nano Materials* **2023**, *6*, 23196–23206.

[61] X. Zhang, C. Li, T. Hu, *ACS Sustainable Chemistry & Engineering* **2023**, *11*, 17837–17848.

[62] A. Rehman, F. Saleem, F. Javed, A. Ikhlaq, S. W. Ahmad, A. Harvey, *Journal of Environmental Chemical Engineering* **2021**, *9*, 105113.

[63] K. Motokura, S. Itagaki, Y. Iwasawa, A. Miyaji, T. Baba, *Green Chemistry* **2009**, *11*, 1876–1880.

[64] S. H. Cho, D. Dahnum, S. H. Cheong, H. W. Lee, U. Lee, J. M. Ha, H. Lee, *Journal of CO2 Utilization* **2020**, *42*, 101324.

[65] N. Panza, M. Alberti, S. Galiè, C. Damiano, F. Cargnoni, M. Italo Trioni, A. Caselli, *European Journal of Organic Chemistry* **2022**, *2022*, DOI 10.1002/ejoc.202200908.

[66] N. Panza, M. Alberti, C. Damiano, A. Caselli, *Frontiers in Catalysis* **2022**, *2*, 19.

[67] T. Wang, K. S. Lackner, A. Wright, *Environmental Science & Technology* **2011**, *45*, 6670–6675.

[68] X. Shi, H. Xiao, X. Liao, M. Armstrong, X. Chen, K. S. Lackner, *The Journal of Chemical Physics* **2018**, *149*, 164708.

[69] Y. Zhang, J. N. Pedersen, B. E. Eser, Z. Guo, *Biotechnology Advances* **2022**, *60*, 107991.

[70] M. Zahorodna, R. Bogoczek, E. Oliveros, A. M. Braun, *Catalysis Today*, Selected Contributions of the 4th European Meeting on Solar Chemistry and Photocatalysis: Environmental Applications (SPEA 4) **2007**, *129*, 200–206.

[71] A. Zafar, Imtiaz-ud-Din, R. G. Palgrave, H. Muhammad, S. Yousuf, T. Evans, *ChemistryOpen* **2023**, *12*, e202200229.

[72] K. Kinugawa, K. Kadono, H. Tanaka, *Journal of Non-Crystalline Solids* **1989**, *110*, 265–272.

[73] M. Alberti, M. Gianelli, D. Boucherabine, S. Recchia, A. Caselli, *ChemCatChem* **2025**, *17*, e00710.

[74] M. Alberti, A. Dariol, N. Panza, G. Abbiati, A. Caselli, *Chemistry – An Asian Journal* **2024**, *19*, e202400688.

[75] D. Carminati, E. Gallo, C. Damiano, A. Caselli, D. Intrieri, *European Journal of Inorganic Chemistry* **2018**, *2018*, 5258–5262.

[76] H. Akaike, *Information Theory and an Extension of the Maximum Likelihood Principle, from Breakthroughs in Statistics*, Springer, **1992**, pp. 610–624.

[77] C. Damiano, P. Sonzini, G. Manca, E. Gallo, *European Journal of Organic Chemistry* **2021**, *2021*, 2807–2814.

[78] S. Arayachukiat, P. Yingcharoen, S. V. C. Vummaleti, L. Cavallo, A. Poater, V. D'Elia, *Molecular Catalysis* **2017**, *443*, 280–285.

[79] A. Jendoubi, Y. Arfaoui, J. Palaudoux, M. M. Al-Mogren, M. Hochlaf, *Journal of Computational Chemistry* **2024**, *45*, 563–573.

[80] E. Vitaku, D. T. Smith, J. T. Njardarson, *Journal of Medicinal Chemistry* **2014**, *57*, 10257–10274.

[81] Y. Zhang, X. Liu, Y. Zou, S. Wang, H. Song, Q. Cai, J. Peng, C. Yi, J. Chen, *Journal of Heterocyclic Chemistry* **2023**, *60*, 1826–1837.

[82] S. Shao, F. Zeng, L. Long, X. Zhu, L. E. Peng, F. Wang, Z. Yang, C. Y. Tang, *Environmental Science & Technology* **2022**, *56*, 12811–12827.

[83] K. J. McCullough, *Rodd's Chemistry of Carbon Compounds*, *Vol. II*, Eds. M .F. Ansell, Elsevier B.V, Amsterdam, **1975**.

[84] R. Kant, S. Maji, *Dalton Transactions* **2021**, *50*, 785–800.

[85] N. C. Johnstone, E. S. Aazam, P. B. Hitchcock, J. R. Fulton, *Journal of Organometallic Chemistry* **2010**, *695*, 170–176.

[86] K. Soai, S. Niwa, Y. Yamada, H. Inoue, *Tetrahedron Letters* **1987**, *28*, 4841–4842.

[87] M. T. Barros, A. M. Faísca Phillips, *European Journal of Organic Chemistry* **2007**, *2007*, 178–185.

[88] M. Chen, J. Hu, X. Tang, Q. Zhu, *Current Organic Synthesis*, *16*, 173–180.

[89] I. Castillo, V. Pérez, I. Monsalvo, P. Demare, I. Regla, *Inorganic Chemistry Communications* **2013**, *38*, 1–4.

[90] J. L. Fiorio, E. C. M. Barbosa, D. K. Kikuchi, P. H. C. Camargo, M. Rudolph, A. S. K. Hashmi, L. M. Rossi, *Catalysis Science & Technology* **2020**, *10*, 1996–2003.

[91] P. Trinchera, B. Musio, L. Degennaro, A. Moliterni, A. Falcicchio, R. Luisi, *Organic and Biomolecular Chemistry* **2012**, *10*, 1962–1965.

[92] W. Chamchaang, A. R. Pinhas, *The Journal of Organic Chemistry* **1990**, *55*, 2943–2950.

[93] N. Panza, R. Soave, F. Cargnoni, M. I. Trioni, A. Caselli, *Journal of CO2 Utilization* **2022**, *62*, 102062.

[94] T. Qadir, A. Amin, D. Sarkar, P. K. Sharma, *Current Organic Chemistry* **2021**, *25*, 1868–1893.

[95] A. M. Rodríguez, P. Prieto, A. de la Hoz, Á. Díaz-Ortiz, D. R. Martín, J. I. García, *ChemistryOpen* **2015**, *4*, 308–317.

[96] N. Chauhan, S. Pradhan, M. K. Ghorai, *The Journal of Organic Chemistry* **2019**, *84*, 1757–1765.

[97] M. Alberti, M. Gianelli, N. Panza, D. Zákutná, I. Matulková, A. Caselli, *European Journal of Inorganic Chemistry* **2024**, *27*, e202400494.

[98] S. Ghorai, D. Nanda, A. Ghosh, P. S. Dash, *Molecular Catalysis* **2024**, *553*, 113720.

[99] Q. Liu, L. Wu, R. Jackstell, M. Beller, *Nature Communications* **2015**, *6*, 5933.

[100] M. Cavalleri, N. Panza, A. Biase, G. Tseberlidis, S. Rizzato, G. Abbiati, A. Caselli, *European Journal of Organic Chemistry* **2021**, *2021*, 2764–2771.

[101] R. Carlson, *Journal of Chemometrics* **2001**, *15*, 495–496.

[102] F. Della Monica, A. Buonerba, C. Capacchione, *Advanced Synthesis & Catalysis* **2019**, *361*, 265–282.

[103] R. L. Wasserstein, N. A. Lazar, *The American Statistician* **2016**, *70*, 129–133.

[104] K. Qiao, F. Ono, Q. Bao, D. Tomida, C. Yokoyama, *Journal of Molecular Catalysis A: Chemical* **2009**, *303*, 30–34.

[105] E. Rix, E. Grau, G. Chollet, H. Cramail, *European Polymer Journal* **2016**, *84*, 863–872.

[106] N. Panza, A. di Biase, E. Gallo, A. Caselli, *Journal of CO2 Utilization* **2021**, *51*, 101635.

[107] Y. G. Shelke, A. Yashmeen, A. V. A. Gholap, S. J. Gharpure, A. R. Kapdi, *Chemistry – An Asian Journal* **2018**, *13*, 2991–3013.

[108] B. Cornils, W. A. Herrmann, *Journal of Catalysis*, 40th Anniversary Commemorative Issue **2003**, *216*, 23–31.

[109] S. Deo, T. Ludwig, M. L. Jue, N. C. Ellebracht, M. J. Rasmussen, J. M. Crawford, M. M. Yung, S. A. Akhade, S. H. Pang, *The Journal of Physical Chemistry C* **2025**, *129*, 8061–8074.

[110] C. Marín, M. P. Clares, I. Ramírez-Macías, S. Blasco, F. Olmo, C. Soriano, B. Verdejo, M. J. Rosales, D. Gomez-Herrera, E. García-España, M. Sánchez-Moreno, *European Journal of Medicinal Chemistry* **2013**, *62*, 466–477.

[111] J. E. Richman, T. J. Atkins, *Journal of the American Chemical Society* **1974**, *96*, 2268–2270.

[112] A. Fürstner, *ACS Central Science* **2016**, *2*, 778–789.

[113] V. K. Sharma, R. Zboril, R. S. Varma, *Accounts of Chemical Research* **2015**, *48*, 182–191.

[114] M. Guo, T. Corona, K. Ray, W. Nam, *ACS Central Science* **2019**, *5*, 13–28.

[115] M. L. Neidig, E. I. Solomon, *Chemical Communications* **2005**, 5843–5863.

[116] L. Vicens, M. Costas, *Dalton Transactions* **2018**, *47*, 1755–1763.

[117] O. Cussó, M. W. Giuliano, X. Ribas, S. J. Miller, M. Costas, *Chemical Science* **2017**, *8*, 3660–3667.

[118] G. Olivo, O. Cussó, M. Borrell, M. Costas, *JBIC Journal of Biological Inorganic Chemistry* **2017**, *22*, 425–452.

[119] G. Olivo, O. Cussó, M. Costas, *Chemistry – An Asian Journal* **2016**, *11*, 3148–3158.

[120] W. Nam, Y.-M. Lee, S. Fukuzumi, *Accounts of Chemical Research* **2014**, *47*, 1146–1154.

[121] J. Yoon, S. A. Wilson, Y. K. Jang, M. S. Seo, K. Nehru, B. Hedman, K. O. Hodgson, E. Bill, E. I. Solomon, W. Nam, *Angewandte Chemie* **2009**, *121*, 1283–1286.

[122] M. Costas, M. P. Mehn, M. P. Jensen, L. Que, *Chemical Reviews* **2004**, *104*, 939–986.

[123] S. H. Bae, X.-X. Li, M. S. Seo, Y.-M. Lee, S. Fukuzumi, W. Nam, *Journal of the American Chemical Society* **2019**, *141*, 7675–7679.

[124] E. Tacchi, E. Anxolabéhère-Mallart, A. Aukauloo, C. Fave, M. Robert, A. Sartorel, *Angewandte Chemie Novit* **2025**, *1*, e70007.

[125] W. Nam, *Accounts of Chemical Research* **2015**, *48*, 2415–2423.

[126] V. Dantignana, J. Serrano-Plana, A. Draksharapu, C. Magallón, S. Banerjee, R. Fan, I. Gamba, Y. Guo, L. Que, M. Costas, A. Company, *Journal of the American Chemical Society* **2019**, *141*, 15078–15091.

[127] G. Xue, R. De Hont, E. Münck, L. Que, *Nature Chemistry* **2010**, *2*, 400–405.

[128] C. Geng, S. Ye, F. Neese, *Angewandte Chemie International Edition* **2010**, *49*, 5717–5720.

[129] J. Hohenberger, K. Ray, K. Meyer, *Nature Communications* **2012**, *3*, 720.

[130] L. J. Rather, T. Weinert, U. Demmer, E. Bill, W. Ismail, G. Fuchs, U. Ermler, *Journal of Biological Chemistry* **2011**, *286*, 29241–29248.

[131] T. H. Moss, A. Ehrenberg, A. J. Bearden, *Biochemistry* **1969**, *8*, 4159–4162.

[132] J. C. Price, E. W. Barr, B. Tirupati, J. M. Bollinger, C. Krebs, *Biochemistry* **2003**, *42*, 7497–7508.

[133] O. Pestovsky, S. Stoian, E. L. Bominaar, X. Shan, E. Münck, L. Que Jr., A. Bakac, *Angewandte Chemie International Edition* **2005**, *44*, 6871–6874.

[134] F. T. de Oliveira, A. Chanda, D. Banerjee, X. Shan, S. Mondal, L. Que, E. L. Bominaar, E. Münck, T. J. Collins, *Science* **2007**, *315*, 835–838.

[135] R. F. De Hont, G. Xue, M. P. Hendrich, J. Que, Lawrence, E. L. Bominaar, E. Münck, *Inorganic Chemistry* **2010**, *49*, 8310–8322.

[136] J. F. Berry, E. Bill, E. Bothe, S. D. George, B. Mienert, F. Neese, K. Wieghardt, *Science* **2006**, *312*, 1937–1941.

[137] K. Meyer, E. Bill, B. Mienert, T. Weyhermüller, K. Wieghardt, *Journal of the American Chemical Society* **1999**, *121*, 4859–4876.

[138] C. A. Grapperhaus, B. Mienert, E. Bill, T. Weyhermüller, K. Wieghardt, *Inorganic Chemistry* **2000**, *39*, 5306–5317.

[139] J.-U. Rohde, J.-H. In, M. H. Lim, W. W. Brennessel, M. R. Bukowski, A. Stubna, E. Münck, W. Nam, L. Que, *Science* **2003**, *299*, 1037–1039.

[140] N. Aliaga-Alcalde, S. DeBeer George, B. Mienert, E. Bill, K. Wieghardt, F. Neese, *Angewandte Chemie International Edition* **2005**, *44*, 2908–2912.

[141] T. Petrenko, S. DeBeer George, N. Aliaga-Alcalde, E. Bill, B. Mienert, Y. Xiao, Y. Guo, W. Sturhahn, S. P. Cramer, K. Wieghardt, F. Neese, *Journal of the American Chemical Society* **2007**, *129*, 11053–11060.

[142] T. A. Betley, J. C. Peters, *Journal of the American Chemical Society* **2004**, *126*, 6252–6254.

[143] S. D. Brown, J. C. Peters, *Journal of the American Chemical Society* **2005**, *127*, 1913–1923.

[144] P. Debrunner, *Iron porphyrins. Part III. VCH Publishers New York* **1989**, 140–234.

[145] J. Rittle, M. T. Green, *Science* **2010**, *330*, 933–937.

[146] S. Shaik, S. Cohen, Y. Wang, H. Chen, D. Kumar, W. Thiel, *Chemical Reviews* **2010**, *110*, 949–1017.

[147] C. Jung, *Biochimica et Biophysica Acta (BBA) - Proteins and Proteomics*, Cytochrome P450: Structure, biodiversity and potential for application **2011**, *1814*, 46–57.

[148] M. Ghosh, K. K. Singh, C. Panda, A. Weitz, M. P. Hendrich, T. J. Collins, B. B. Dhar, S. Sen Gupta, *Journal of the American Chemical Society* **2014**, *136*, 9524–9527.

[149] M. R. Mills, A. C. Weitz, M. P. Hendrich, A. D. Ryabov, T. J. Collins, *Journal of the American Chemical Society* **2016**, *138*, 13866–13869.

[150] S. Pattanayak, A. J. Jasniewski, A. Rana, A. Draksharapu, K. K. Singh, A. Weitz, M. Hendrich, L. J. Que, A. Dey, S. Sen Gupta, *Inorganic Chemistry* **2017**, *56*, 6352–6361.

[151] K. M. Van Heuvelen, A. T. Fiedler, X. Shan, R. F. De Hont, K. K. Meier, E. L. Bominaar, E. Münck, L. Que, *Proceedings of the National Academy of Sciences* **2012**, *109*, 11933–11938.

[152] J. Serrano-Plana, W. N. Oloo, L. Acosta-Rueda, K. K. Meier, B. Verdejo, E. García-España, M. G. Basallote, E. Münck, L. Que, A. Company, M. Costas, *Journal of the American Chemical Society* **2015**, *137*, 15833–15842.

[153] J. Serrano-Plana, A. Aguinaco, R. Belda, E. García-España, M. G. Basallote, A. Company, M. Costas, *Angewandte Chemie International Edition* **2016**, *55*, 6310–6314.

[154] R. Fan, J. Serrano-Plana, W. N. Oloo, A. Draksharapu, E. Delgado-Pinar, A. Company, V. Martin-Diaconescu, M. Borrell, J. Lloret-Fillol, E. García-

España, Y. Guo, E. L. Bominaar, L. Que, M. Costas, E. Münck, *Journal of the American Chemical Society* **2018**, *140*, 3916–3928.

[155] A. Álvarez-Núñez, R. Sarkar, V. Dantignana, J. Xiong, Y. Guo, J. M. Luis, M. Costas, A. Company, *ACS Catalysis* **2024**, *14*, 14183–14194.

[156] J. F. Berry, *Comments on Inorganic Chemistry* **2009**, *30*, 28–66.

[157] H.-C. Chang, B. Mondal, H. Fang, F. Neese, E. Bill, S. Ye, *Journal of the American Chemical Society* **2019**, *141*, 2421–2434.

[158] M. Keilwerth, W. Mao, M. Malischewski, S. A. V. Jannuzzi, K. Breitwieser, F. W. Heinemann, A. Scheurer, S. DeBeer, D. Munz, E. Bill, K. Meyer, *Nature Chemistry* **2024**, *16*, 514–520.

[159] G. Tseberlidis, L. Demonti, V. Pirovano, M. Scavini, S. Cappelli, S. Rizzato, R. Vicente, A. Caselli, *ChemCatChem* **2019**, *11*, 4907–4915.

[160] N. Panza, A. di Biase, S. Rizzato, E. Gallo, G. Tseberlidis, A. Caselli, *European Journal of Organic Chemistry* **2020**, *2020*, 6635–6644.

[161] N. Panza, A. di Biase, A. Caselli, *Inorganica Chimica Acta* **2022**, *541*, DOI 10.1016/j.ica.2022.121091.

[162] M. A. Mekhail, K. Pota, T. M. Schwartz, K. N. Green, *RSC Advances* **2020**, *10*, 31165–31170.

[163] N. Alcock, D. Busch, C. Y. Liu, CCDC 639154: Experimental Crystal Structure Determination, en, **2007**.

[164] S. M. Brewer, P. M. Palacios, H. M. Johnston, B. S. Pierce, K. N. Green, *Inorganica Chimica Acta* **2018**, *478*, 139–147.

[165] S. M. Brewer, K. R. Wilson, D. G. Jones, E. W. Reinheimer, S. J. Archibald, T. J. Prior, M. A. Ayala, A. L. Foster, T. J. Hubin, K. N. Green, *Inorganic Chemistry* **2018**, *57*, 8890–8902.

[166] S. M. Brewer, T. M. Schwartz, M. A. Mekhail, L. S. Turan, T. J. Prior, T. J. Hubin, B. G. Janesko, K. N. Green, *Organometallics* **2021**, *40*, 2467–2477.

[167] N. Alcock, D. Busch, C. Y. Liu, CCDC 639153: Experimental Crystal Structure Determination, en, **2007**.

[168] A. Abedi, N. Safari, V. Amani, H. R. Khavasi, *Dalton Transactions* **2011**, *40*, 6877–6885.

[169] V. Félix, J. Costa, R. Delgado, M. G. Drew, M. T. Duarte, C. Resende, *Journal of the Chemical Society Dalton Transactions* **2001**, 1462–1471.

[170] R. Ketkaew, Y. Tantirungrotechai, P. Harding, G. Chastanet, P. Guionneau, M. Marchivie, D. J. Harding, *Dalton Transactions* **2021**, *50*, 1086–1096.

[171] J. M. Holland, J. A. McAllister, Z. Lu, C. A. Kilner, M. Thornton-Pett, M. A. Halcrow, *Chemical Communications* **2001**, 577–578.

[172] J. Elhaïk, C. A. Kilner, M. A. Halcrow, *CrystEngComm* **2005**, *7*, 151–157.

[173] A. J. Reeder, PhD thesis, Sheffield Hallam University (United Kingdom), Sheffield, **2000**.

[174] Oliver Kahn, *Molecular magnetism*, VCH, **1993**.

[175] H. Zhao, R. Clérac, J.-S. Sun, X. Ouyang, J. Clemente-Juan, C. Gómez-García, E. Coronado, K. Dunbar, *Journal of Solid State Chemistry* **2001**, *159*, 281–292.

[176] C. E. Runyan, T. Hughbanks, *Journal of the American Chemical Society* **1994**, *116*, 7909–7910.

[177] B. Bleaney, K. D. Bowers, *Proceedings of the Royal Society of London. A. Mathematical and Physical Sciences* **1952**, *214*, 451–465.

[178] M. Cazzaniga, F. Cargnoni, M. Penconi, A. Bossi, D. Ceresoli, *Journal of Chemical Theory and Computation* **2020**, *16*, 1188–1199.

[179] A. Prlj, B. F. E. Curchod, A. Fabrizio, L. Floryan, C. Corminboeuf, *The Journal of Physical Chemistry Letters* **2015**, *6*, 13–21.

[180] M. Alberti, G. Rossi, D. Boucherabine, F. Cargnoni, M. I. Trioni, G. Taini, D. Zakutna, A. Gentilin, L. Đorđević, A. Sartorel, A. Caselli, *Dalton Transactions* **2025**, DOI 10.1039/D5DT02534F.

[181] A. N. Campbell, S. S. Stahl, *Accounts of Chemical Research* **2012**, *45*, 851–863.

[182] S. Fukuzumi, K. Ohkubo, *Chemical Science* **2013**, *4*, 561–574.

[183] S. Fukuzumi, *Dalton Transactions* **2015**, *44*, 6696–6705.

[184] W.-J. Zhou, X.-D. Wu, M. Miao, Z.-H. Wang, L. Chen, S.-Y. Shan, G.-M. Cao, D.-G. Yu, *Chemistry – A European Journal* **2020**, *26*, 15052–15064.

[185] S. Bhattacharjee, S. Linley, E. Reisner, *Nature Reviews Chemistry* **2024**, *8*, 87–105.

[186] S. Oh, E. E. Stache, *Journal of the American Chemical Society* **2022**, *144*, 5745–5749.

[187] S. Oh, E. E. Stache, *ACS Catalysis* **2023**, *13*, 10968–10975.

[188] R. A. Tomás, J. C. Bordado, J. F. Gomes, R. J. Sheehan in *Ullmann's Encyclopedia of Industrial Chemistry*, John Wiley & Sons, Ltd, **2024**, pp. 1–17.

[189] R. A. F. Tomás, J. C. M. Bordado, J. F. P. Gomes, *Chemical Reviews* **2013**, *113*, 7421–7469.

[190] N. A. M. Fadzil, M. H. A. Rahim, G. P. Maniam, *Chinese Journal of Catalysis* **2014**, *35*, 1641–1652.

[191] H. M. Lapa, L. M. D. R. S. Martins, H. M. Lapa, L. M. D. R. S. Martins, *Molecules* **2023**, *28*, DOI 10.3390/molecules28041922.

[192] T. Newhouse, P. S. Baran, *Angewandte Chemie International Edition* **2011**, *50*, 3362–3374.

[193] Y. Yang, G. A. Volpato, E. Rossin, N. Peruffo, F. Tumbarello, C. Nicoletti, R. Bonetto, L. Paoloni, P. Umari, E. Colusso, L. Dell'Amico, S. Berardi, E. Collini, S. Caramori, S. Agnoli, A. Sartorel, *ChemSusChem* **2023**, *16*, e202201980.

[194] R. G. Agarwal, S. C. Coste, B. D. Groff, A. M. Heuer, H. Noh, G. A. Parada, C. F. Wise, E. M. Nichols, J. J. Warren, J. M. Mayer, *Chemical Reviews* **2022**, *122*, 1–49.

[195] M. Galeotti, M. Salamone, M. Bietti, *Chemical Society Reviews* **2022**, *51*, 2171–2223.

[196] M. Salamone, M. Galeotti, E. Romero-Montalvo, J. A. van Santen, B. D. Groff, J. M. Mayer, G. A. DiLabio, M. Bietti, *Journal of the American Chemical Society* **2021**, *143*, 11759–11776.

[197] N. Holmberg-Douglas, D. A. Nicewicz, *Chemical Reviews* **2022**, *122*, 1925–2016.

[198] F. Yuan, P. Cao, W. Sun, L. Zhao, *Industrial & Engineering Chemistry Research* **2024**, *63*, 8208–8215.

[199] Z. Li, Y. Dong, Y. Zeng, M. Zhang, H. Lv, G.-Y. Yang, *Chinese Journal of Catalysis* **2024**, *66*, 282–291.

[200] X. Sun, Z. Feng, S. Wang, Q.-N. Wang, P. Zhang, R. Li, C. Li, *ACS Catalysis* **2024**, *14*, 5356–5365.

[201] D. Jiang, Q. Zhang, L. Yang, Y. Deng, B. Yang, Y. Liu, C. Zhang, Z. Fu, *Renewable Energy* **2021**, *174*, 928–938.

[202] S. M. Treacy, T. Rovis, *Journal of the American Chemical Society* **2021**, *143*, 2729–2735.

[203] Q. Yang, Y.-H. Wang, Y. Qiao, M. Gau, P. J. Carroll, P. J. Walsh, E. J. Schelter, *Science* **2021**, *372*, 847–852.

[204] E. Skolia, O. G. Mountanea, C. G. Kokotos, *ChemSusChem* **2024**, *17*, e202400174.

[205] S. Rohe, A. O. Morris, T. McCallum, L. Barriault, *Angewandte Chemie International Edition* **2018**, *57*, 15664–15669.

[206] B. Saxena, R. I. Patel, A. Sharma, *RSC Sustainability* **2024**, *2*, 2169–2189.

[207] Y. Yang, M. Nalesso, A. Basagni, R. Bonetto, R. Signorini, S. Agnoli, L. Đorđević, A. Sartorel, *Journal of Materials Chemistry A* **2025**, *13*, 18436–18444.

[208] H. Zhao, J. Joseph, H. Zhang, H. Karoui, B. Kalyanaraman, *Free Radical Biology and Medicine* **2001**, *31*, 599–606.

[209] S. S. Ranade, D. F. Zamudio Díaz, M. C. Meinke, S. B. Lohan, *Chemico-Biological Interactions* **2025**, *421*, 111744.

[210] L. Gerritz, J. Wei, T. Fang, C. Wong, A. L. Klodt, S. A. Nizkorodov, M. Shiraiwa, *Environmental Science & Technology* **2024**, *58*, 4716–4726.

[211] *Modern Oxidation Methods*, 1st ed., (Ed.: J.-E. Bäckvall), Wiley, **2010**.

[212] *Organic Syntheses by Oxidation with Metal Compounds*, (Eds.: W. J. Mijs, C. R. H. I. De Jonge), Springer US, Boston, MA, **1986**.

[213] E. Mousset, W. H. Loh, W. S. Lim, L. Jarry, Z. Wang, O. Lefebvre, *Water Research* **2021**, *200*, 117234.

[214] J. Piera, J.-E. Bäckvall, *Angewandte Chemie International Edition* **2008**, *47*, 3506–3523.

[215] M. Sankar, E. Nowicka, E. Carter, D. M. Murphy, D. W. Knight, D. Bethell, G. J. Hutchings, *Nature Communications* **2014**, *5*, 3332.

[216] R. A. Manzano, R. D. Young, *Coordination Chemistry Reviews* **2021**, *449*, 214215.

[217] L. Boyd, G. Clark, W. Roper, *Journal of Organometallic Chemistry* **1990**, *397*, 209–218.

[218] W. Lesueur, E. Solari, C. Floriani, A. Chiesi-Villa, C. Rizzoli, *Inorganic Chemistry* **1997**, *36*, 3354–3362.

[219] R. J. Burford, W. E. Piers, M. Parvez, *Organometallics* **2012**, *31*, 2949–2952.

[220] C. C. Comanescu, V. M. Iluc, *Inorganic Chemistry* **2014**, *53*, 8517–8528.

[221] J. Arras, H. Speth, H. A. Mayer, L. Wesemann, *Organometallics* **2015**, *34*, 3629–3636.

[222] J. R. Logan, W. E. Piers, J. Borau-Garcia, D. M. Spasyuk, *Organometallics* **2016**, *35*, 1279–1286.

[223] M. R. Hoffbauer, C. C. Comanescu, B. J. Dymm, V. M. Iluc, *Organometallics* **2018**, *37*, 2086–2094.

[224] C. C. Comanescu, V. M. Iluc, *Organometallics* **2014**, *33*, 6059–6064.

[225] C. C. Comanescu, V. M. Iluc, *Organometallics* **2015**, *34*, 4684–4692.

[226] P. Cui, C. C. Comanescu, V. M. Iluc, *Chemical Communications* **2015**, *51*, 6206–6209.

[227] P. E. Rothstein, C. C. Comanescu, V. M. Iluc, *Chemistry – A European Journal* **2017**, *23*, 16948–16952.

[228] C. C. Comanescu, M. Vyushkova, V. M. Iluc, *Chemical Science* **2015**, *6*, 4570–4579.

[229] P. Cui, V. M. Iluc, *Chemical Science* **2015**, *6*, 7343–7354.

[230] P. Cui, M. R. Hoffbauer, M. Vyushkova, V. M. Iluc, *Chemical Science* **2016**, *7*, 4444–4452.

[231] D. V. Gutsulyak, W. E. Piers, J. Borau-Garcia, M. Parvez, *Journal of the American Chemical Society* **2013**, *135*, 11776–11779.

[232] H. Zhao, H. Sun, X. Li, *Organometallics* **2014**, *33*, 3535–3539.

[233] J. Borau-Garcia, D. V. Gutsulyak, R. J. Burford, W. E. Piers, *Dalton Transactions* **2015**, *44*, 12082–12085.

[234] E. A. LaPierre, M. L. Clapson, W. E. Piers, L. Maron, D. M. Spasyuk, C. Gendy, *Inorganic Chemistry* **2018**, *57*, 495–506.

[235] E. A. LaPierre, W. E. Piers, C. Gendy, *Organometallics* **2018**, *37*, 3394–3398.

[236] S. Sung, Q. Wang, T. Krämer, R. D. Young, *Chemical Science* **2018**, *9*, 8234–8241.

[237] M. L. Clapson, J. K. Kirkland, W. E. Piers, D. H. Ess, B. Gelfand, J.-B. Lin, *Organometallics* **2022**, *41*, 235–245.

[238] Q. Wang, R. A. Manzano, H. Tinnermann, S. Sung, B. Leforestier, T. Krämer, R. D. Young, *Angewandte Chemie International Edition* **2021**, *60*, 18168–18177.

[239] M. R. Hoffbauer, V. M. Iluc, *Journal of the American Chemical Society* **2021**, *143*, 5592–5597.

[240] Z. S. Lincoln, V. M. Iluc, *Journal of the American Chemical Society* **2024**, *146*, 17595–17599.

[241] Z. S. Lincoln, M. R. Hoffbauer, V. M. Iluc, *Inorganic Chemistry Frontiers* **2024**, *11*, 5579–5586.

[242] É. De Brito Sá, L. Rodríguez-Santiago, M. Sodupe, X. Solans-Monfort, *Organometallics* **2016**, *35*, 3914–3923.

[243] D. O. Khristolyubov, D. M. Lyubov, A. V. Cherkasov, G. K. Fukin, A. S. Shavyrin, A. A. Trifonov, *Organometallics* **2018**, *37*, 1627–1634.

[244] A. Fayoumi, D. M. Lyubov, A. O. Tolpygin, A. S. Shavyrin, A. V. Cherkasov, A. M. Ob'edkov, A. A. Trifonov, *European Journal of Inorganic Chemistry* **2020**, *2020*, 3259–3267.

[245] D. O. Khristolyubov, D. M. Lyubov, A. S. Shavyrin, A. V. Cherkasov, G. K. Fukin, A. A. Trifonov, *Inorganic Chemistry Frontiers* **2020**, *7*, 2459–2477.

[246] D. O. Khristolyubov, D. M. Lyubov, A. V. Cherkasov, G. K. Fukin, A. A. Trifonov, *Mendeleev Communications* **2021**, *31*, 54–57.

[247] D. M. Lyubov, D. O. Khristolyubov, A. V. Cherkasov, A. A. Trifonov, *Organometallics* **2023**, *42*, 1300–1309.

[248] W. Lesueur, A. J. Rogers, C. Floriani, A. Chiesi-Villa, C. Rizzoli, *Inorganic Chemistry* **1998**, *37*, 44–49.

[249] A. B. Shivarkar, S. P. Gupte, R. V. Chaudhari, *Journal of Molecular Catalysis A: Chemical* **2005**, *226*, 49–56.

[250] C. A. Ilioudis, D. A. Tocher, J. W. Steed, *Journal of the American Chemical Society* **2004**, *126*, 12395–12402.

[251] P. Weingart, W. R. Thiel, *ChemCatChem* **2018**, *10*, 4844–4848.

[252] T. Shimoda, T. Morishima, K. Kodama, T. Hirose, D. E. Polyansky, G. F. Manbeck, J. T. Muckerman, E. Fujita, *Inorganic Chemistry* **2018**, *57*, 5486–5498.

[253] M. Dellacqua, B. Castano, C. Cecchini, T. Pedrazzini, V. Pirovano, E. Rossi, A. Caselli, G. Abbiati, *Journal of Organic Chemistry* **2014**, *79*, 3494–3505.

[254] K. L. Moudgill, *J. Chem. Soc. Trans.* **1922**, *121*, 1506–1509.

[255] K.-F. Zhang, F. Christoffel, O. Baudoin, *Angewandte Chemie International Edition* **2018**, *57*, 1982–1986.

[256] J. S. Haynes, J. R. Sams, R. C. Thompson, *Canadian Journal of Chemistry* **1981**, *59*, 669–678.

[257] G. Brauer, *Handbook of Preparative Inorganic Chemistry*, **1963**.

[258] K. S. Hagen, *Inorganic Chemistry* **2000**, *39*, 5867–5869.

[259] M. Pinna, A. Signorelli, G. Binda, C. Dossi, L. Rampazzi, D. Spanu, S. Recchia, *Methods and Protocols* **2022**, *5*, 30.

[260] D. Monticelli, A. Castelletti, D. Civati, S. Recchia, C. Dossi, *International Journal of Analytical Chemistry* **2019**, *2019*, 1–5.

[261] G. Bresciani, M. Bortoluzzi, G. Pampaloni, F. Marchetti, *Organic & Biomolecular Chemistry* **2021**, *19*, 4152–4161.

[262] Z. Z. Yang, Y. N. Li, Y. Y. Wei, L. N. He, *Green Chemistry* **2011**, *13*, 2351–2353.

[263] J. Davies, D. Janssen-Müller, D. P. Zimin, C. S. Day, T. Yanagi, J. Elfert, R. Martin, *Journal of the American Chemical Society* **2021**, *143*, 4949–4954.

[264] F. Sebest, L. Casarrubios, H. S. Rzepa, A. J. P. White, S. Díez-González, *Green Chemistry* **2018**, *20*, 4023–4035.

[265] M. Prieschl, D. Cantillo, C. O. Kappe, *Journal of Flow Chemistry 2020 11:2* **2020**, *11*, 117–125.

[266] F. Minicone, W. J. Rogers, J. F. Green, M. Khan, G. M. Smith, C. D. Bray, *Tetrahedron Letters* **2014**, *55*, 5890–5891.

[267] R. Serwa, L. Wakening, G. D. Signore, M. Mühlberg, I. Claußnitzer, C. Weise, M. Gerrits, C. P. Hackenberger, *Angewandte Chemie International Edition* **2009**, *48*, 8234–8239.

[268] M. Lv, P. Wang, D. Yuan, Y. Yao, *ChemCatChem* **2017**, *9*, 4451–4455.

[269] Z. Shen, X. Lu, A. Lei, *Tetrahedron* **2006**, *62*, 9237–9246.

[270] J. Steinbauer, A. Spannenberg, T. Werner, *Green Chemistry* **2017**, *19*, 3769–3779.

[271] H. Ma, S. Liu, H. Wang, G. Li, K. Zhao, X. Cui, F. Shi, *Green Chemistry* **2023**, *25*, 2293–2298.

[272] E. A. Elgohary, Y. M. A. Mohamed, S. T. Rabie, S. A. Salih, A. M. Fekry, H. A. E. Nazer, *New Journal of Chemistry* **2021**, *45*, 17301–17312.

[273] O. Coulembier, S. Moins, V. Lemaur, R. Lazzaroni, P. Dubois, *Journal of CO2 Utilization* **2015**, *10*, 7–11.

[274] G. M. Sheldrick, *urn:issn:2053-2733* **2015**, *71*, 3–8.

[275] L. J. Farrugia, *Journal of Applied Crystallography* **2012**, *45*, 849–854.

[276] Diamond - Crystal and Molecular Structure Visualization, Crystal Impact - Dr. H. Putz & Dr. K. Brandenburg GbR, Kreuzherrenstr. 102, 53227 Bonn, Germany, https://www.crystalimpact.de/diamond.

This page intentionally left blank.

Appendices

This page intentionally left blank.

A

Supporting information

Reading guidance

This appendix contains supporting information, i.e. NMR spectra, mass spectra and other routine analyses.

A.1 Mass spectra

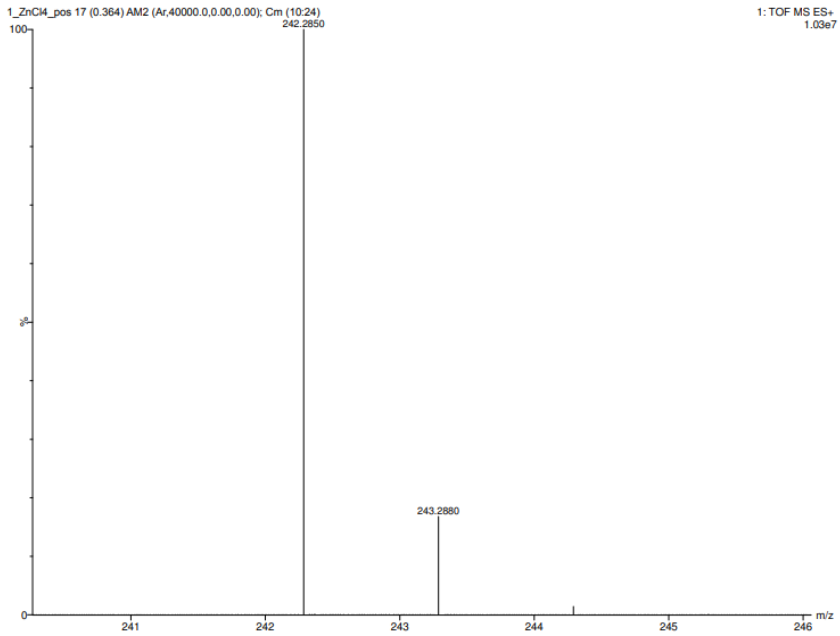

Figure A.1: *HRMS spectra (ESI positive mode) of* ***M1a*** *(40-600 m/z range). The peak at 242.2850 m/z (100%) is assigned to* TBA^+ *(calculated 242.2848).*

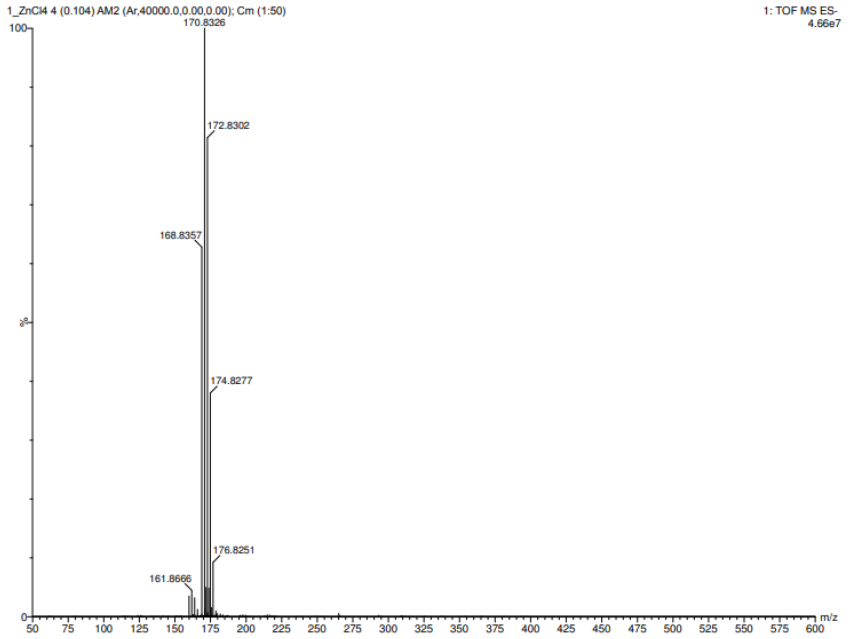

Figure A.2: *HRMS spectra (ESI negative mode) of* ***M1a*** *(50-600 m/z range). The peak at 168.8357 m/z (100%) is assigned to* $[ZnCl_3]^-$ *(calculated 168.8357).*

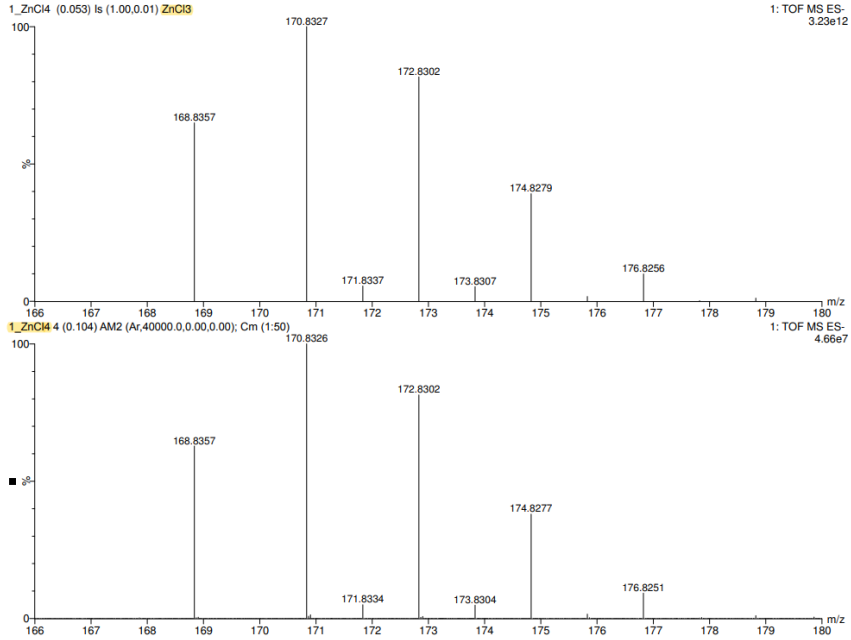

Figure A.3: *Comparison between the found spectra of* ***M1a*** *(below) and the isotope model (above) for the ion* $[ZnCl_3]^-$.

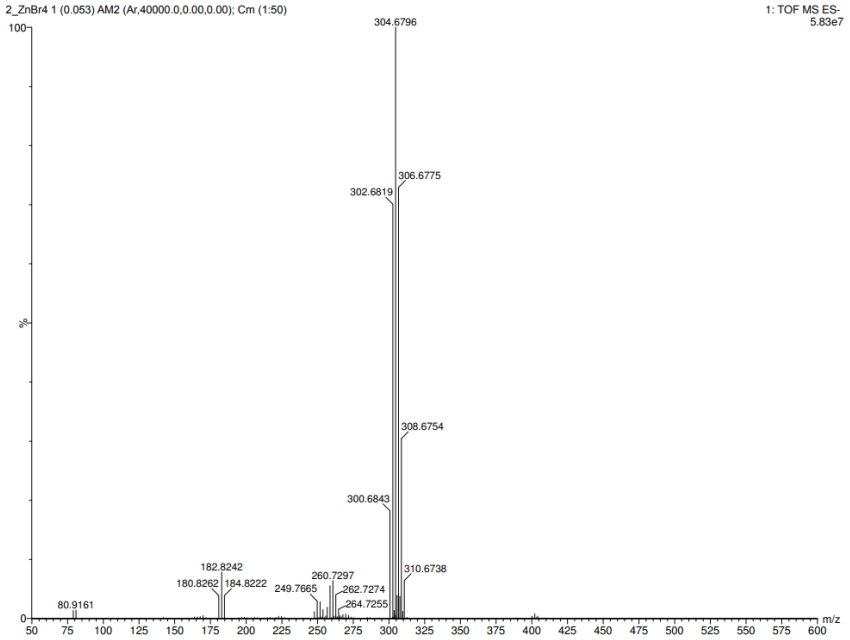

Figure A.4: *HRMS spectra (ESI negative mode) of* ***M1b*** *(50-400 m/z range). The peak at 300.6843 m/z (100%) is assigned to* $[ZnBr_3]^-$ *(calculated 300.6842). The comparison between the found spectra (lower line) and the isotope model is reported below.*

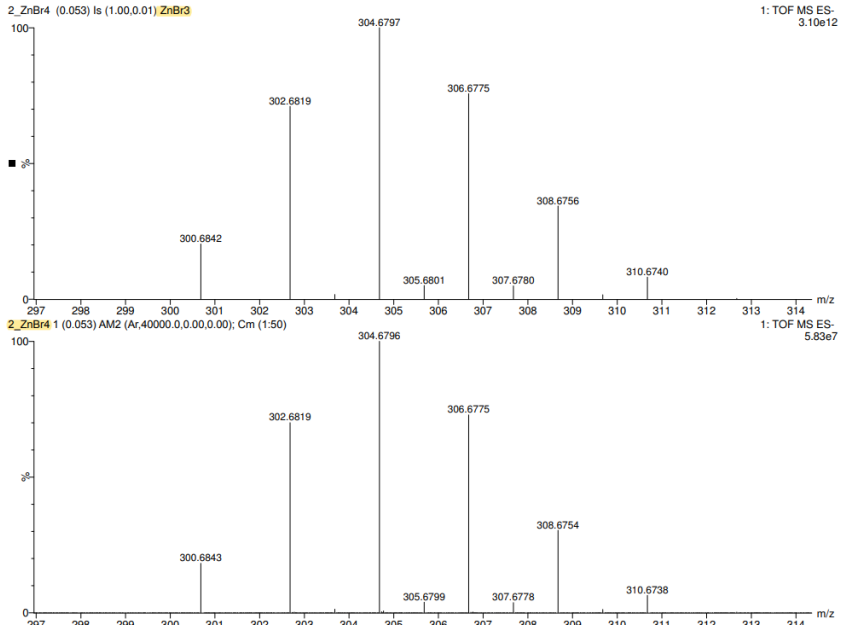

Figure A.5: *Comparison between the found spectra of* ***M1b*** *(below) and the isotope model (above) for the ion* $[ZnBr_3]^-$.

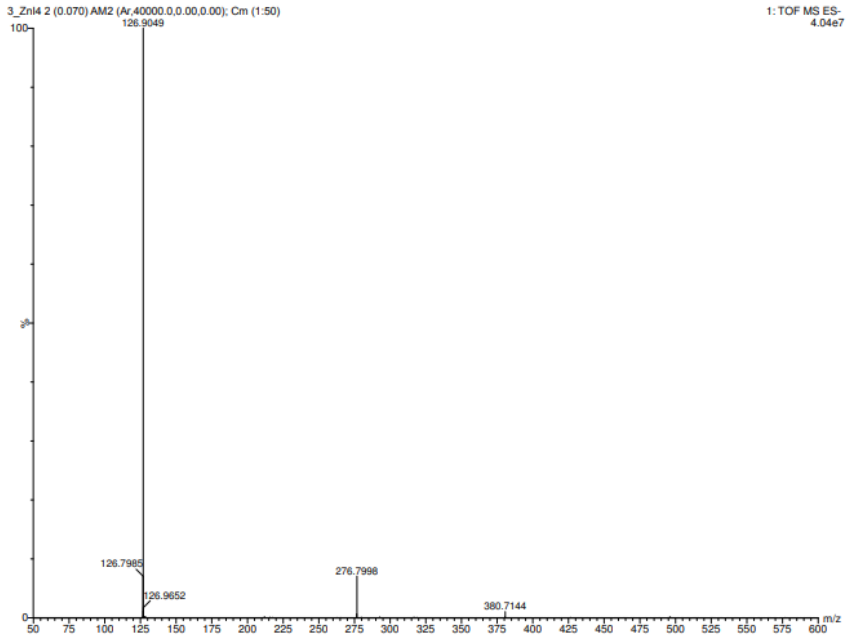

Figure A.6: *HRMS spectra (ESI negative mode) of* ***M1c*** *(50-600 m/z range). The peak at 126.9049 m/z is attributed to I^-, 276.7998 is attributed to NaI_2^- and 380.7144 is I_3^-.*

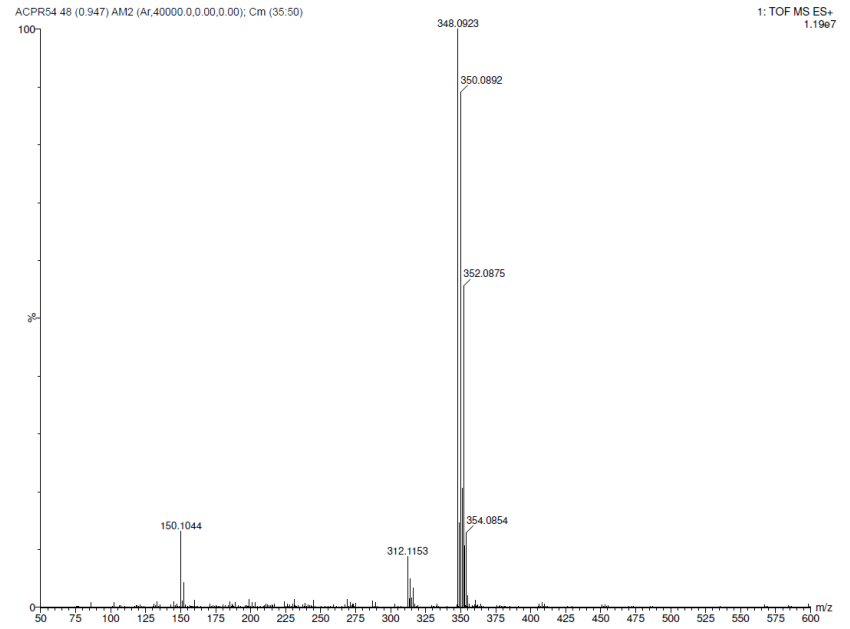

Figure A.7: *HRMS spectra (ESI positive mode) of* ***C1a*** *(50-600 m/z range).*

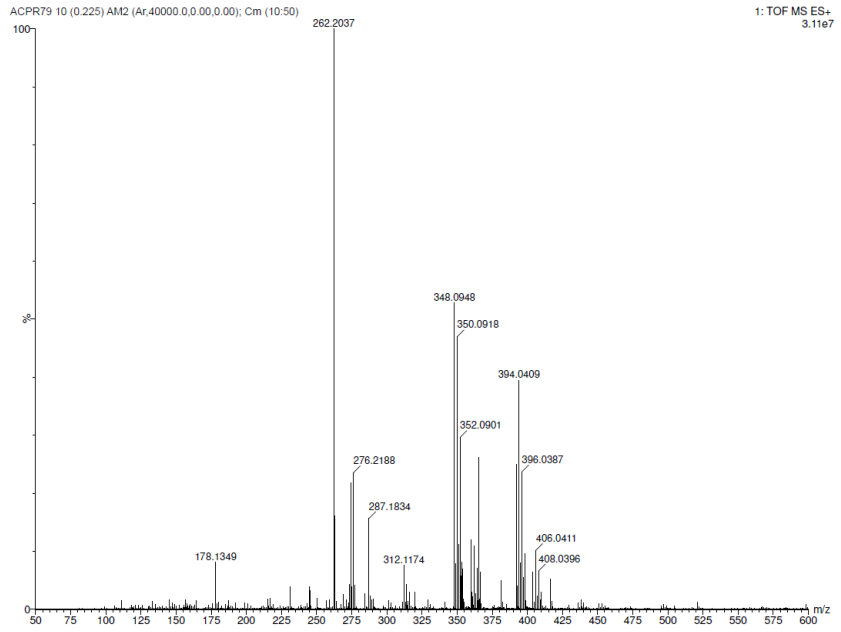

Figure A.8: *HRMS spectra (ESI positive mode) of* ***C1b*** *(50-600 m/z range).*

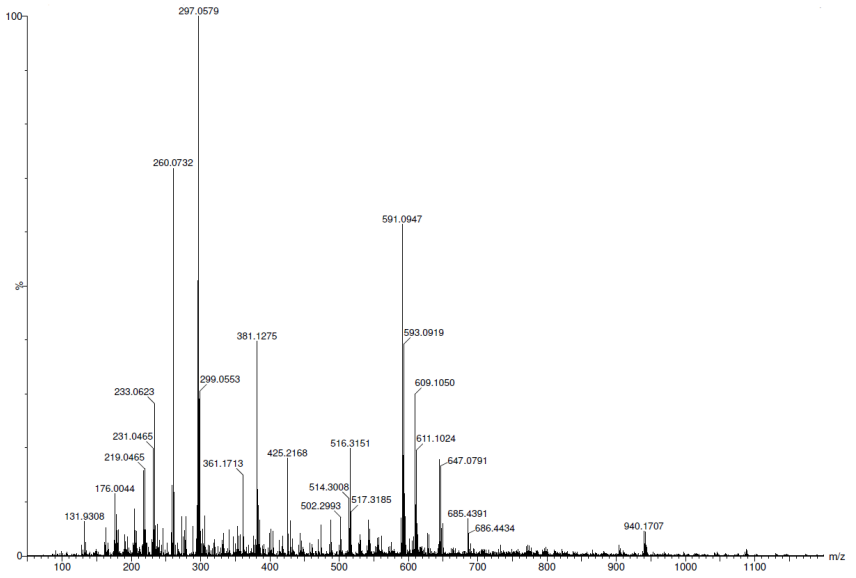

Figure A.9: *HRMS spectra (ESI positive mode) of* ***C2a*** *(50-1200 m/z range).*

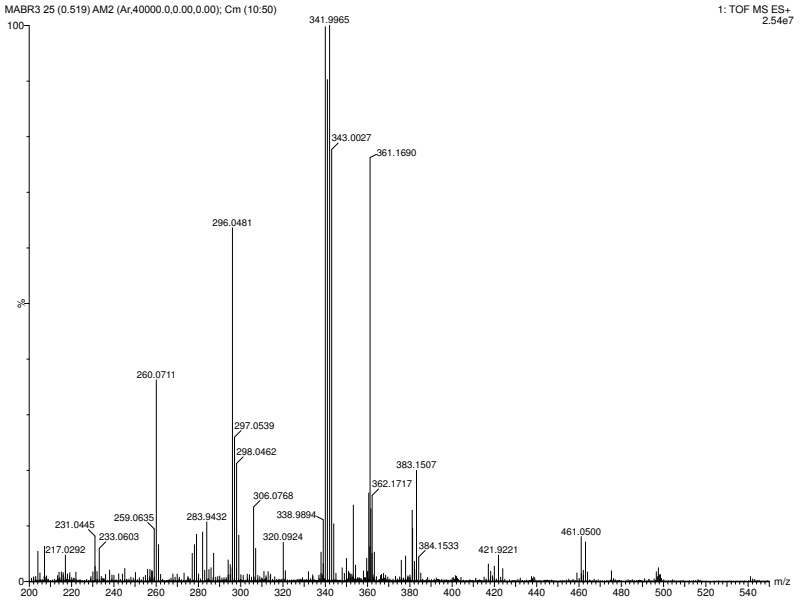

Figure A.10: *HRMS spectra (ESI positive mode) of* ***C2b*** *(200-550 m/z range).*

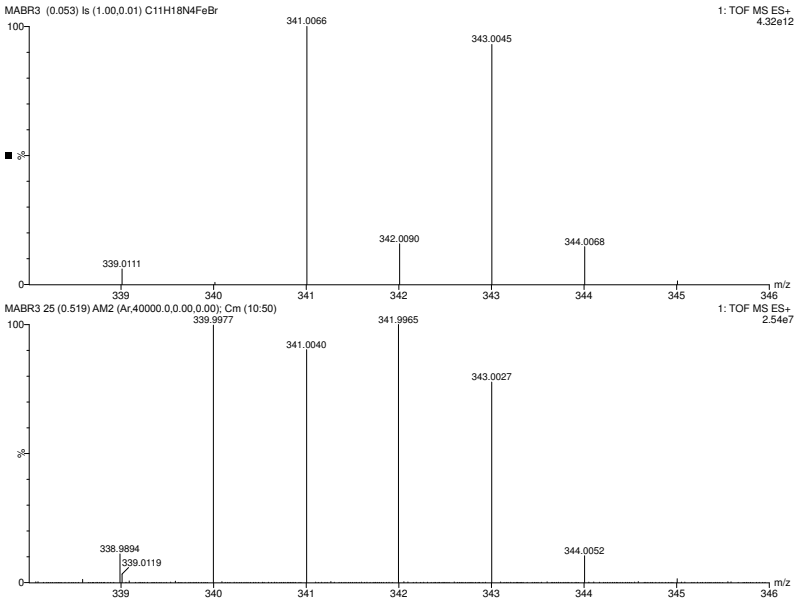

Figure A.11: *HRMS spectra (ESI positive mode) of* ***C2b****, M^+, simulated isotope model (above) experimental data (below).*

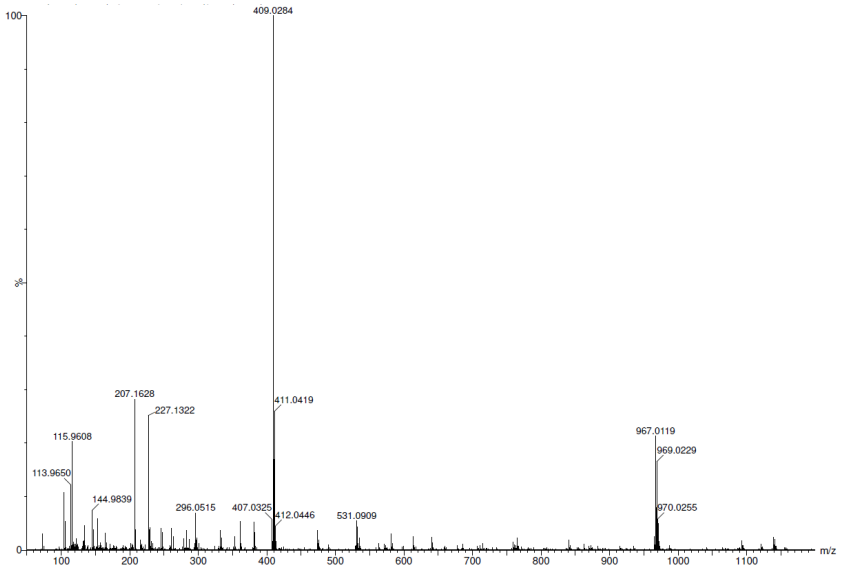

Figure A.12: *HRMS spectra (ESI positive mode) of* ***C2c*** *(50-1200 m/z range).*

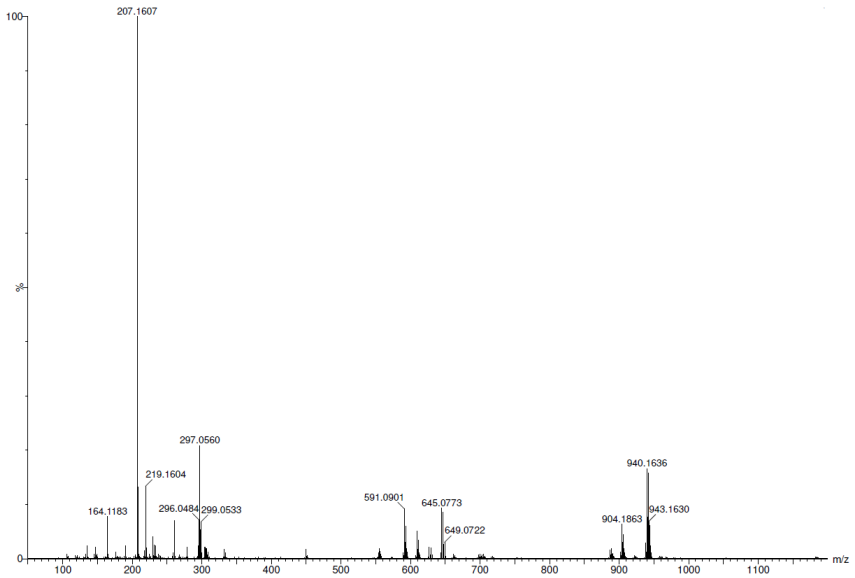

Figure A.13: *HRMS spectra (ESI positive mode) of* ***C2d*** *(50-1200 m/z range).*

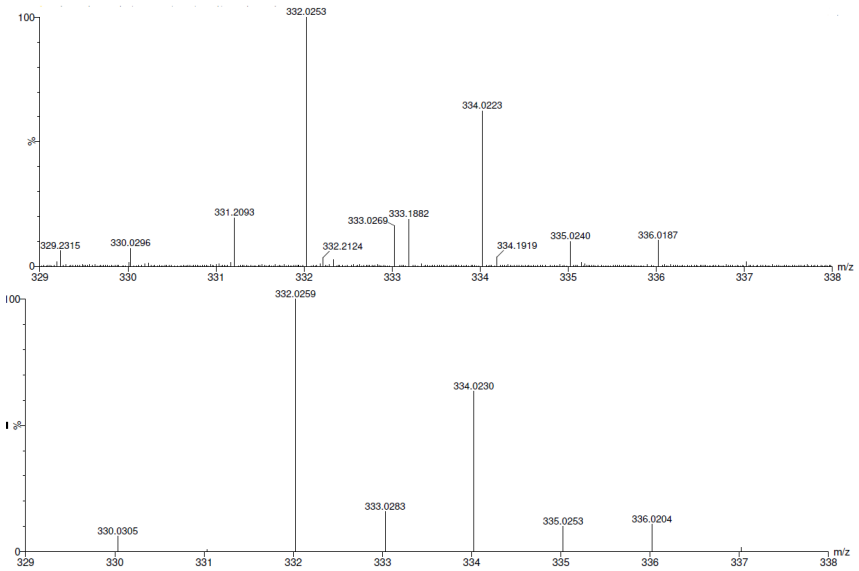

Figure A.14: *HRMS spectra (ESI positive mode) of* ***C2d****, M^+, experimental data (above) and simulated isotope model (below).*

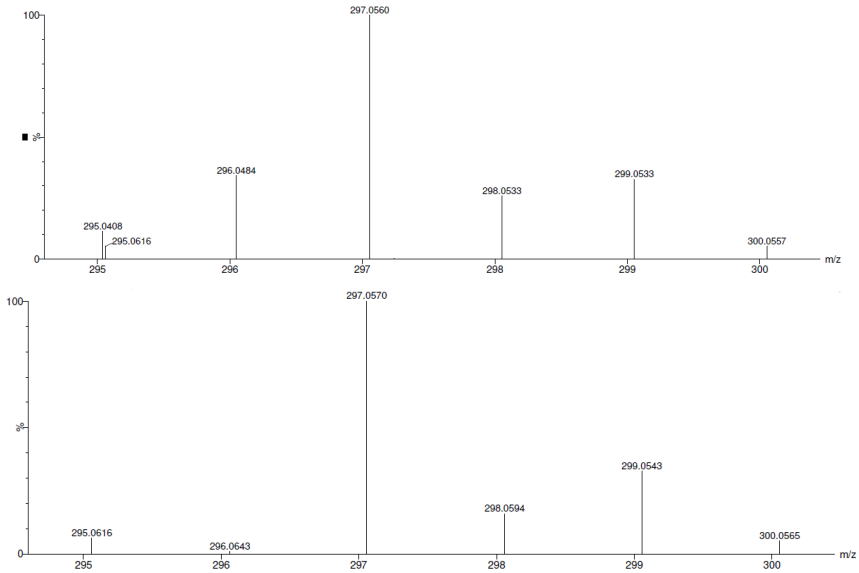

Figure A.15: *HRMS spectra (ESI positive mode) of* ***C2d****, M^+-Cl, experimental data (above) and simulated isotope model (below).*

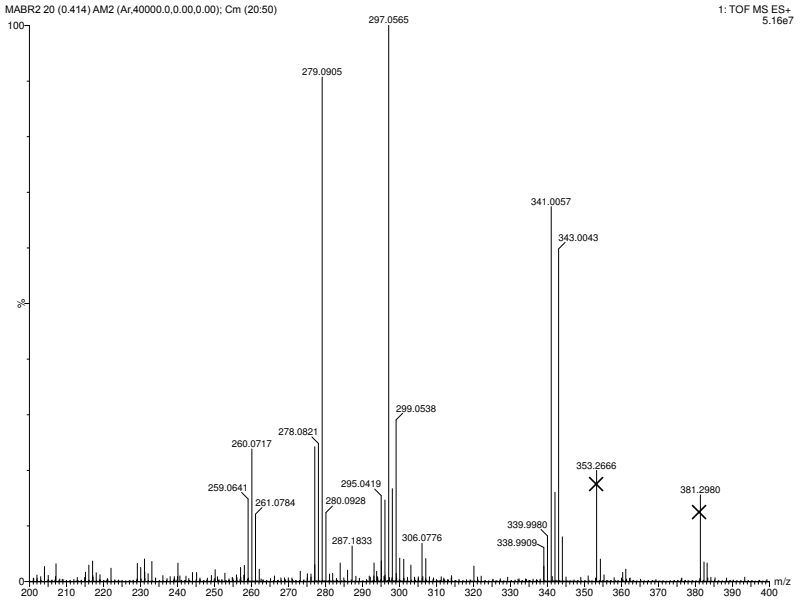

Figure A.16: *HRMS spectra (ESI positive mode) of* ***C2e*** *(200-400 m/z range).*

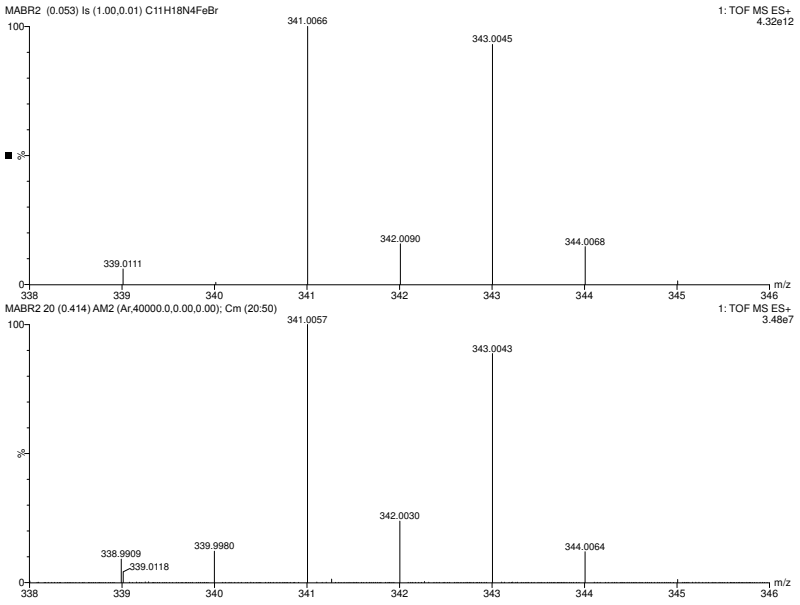

Figure A.17: *HRMS spectra (ESI positive mode) of* ***C2e****, M^+, simulated isotope model (above) experimental data (below).*

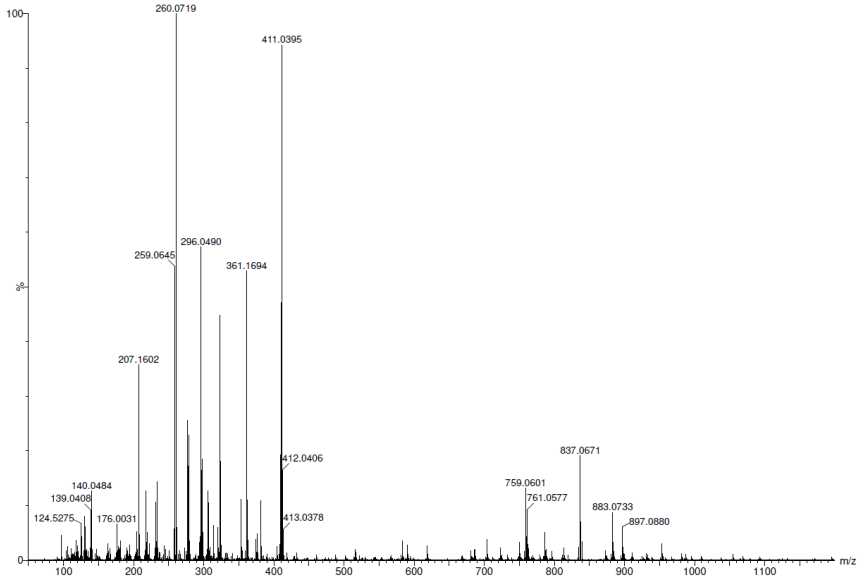

Figure A.18: *HRMS spectra (ESI positive mode) of* ***C2f*** *(50-1200 m/z range).*

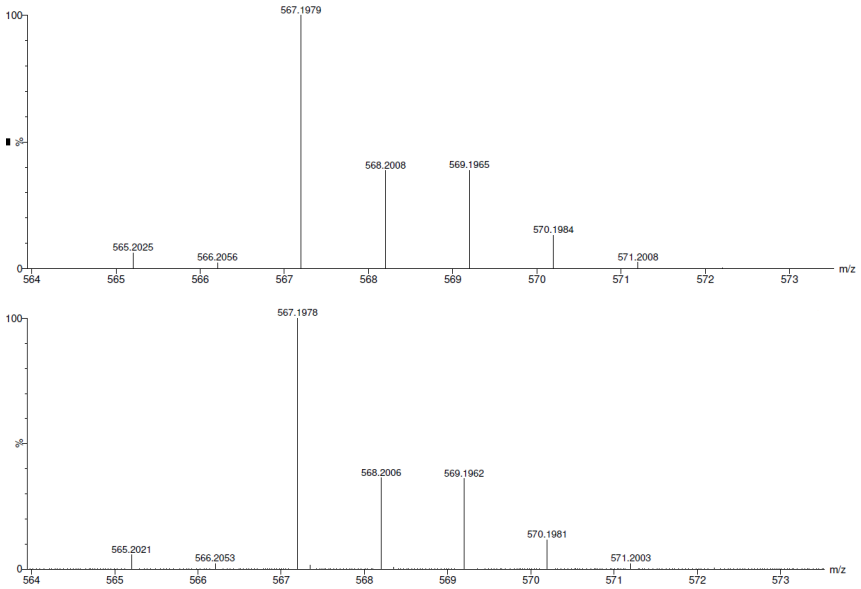

Figure A.19: *HRMS spectra (ESI positive mode) of* ***C3d****, M^+, simulated isotope model (above) experimental data (below).*

A.2 SEM-EDX data

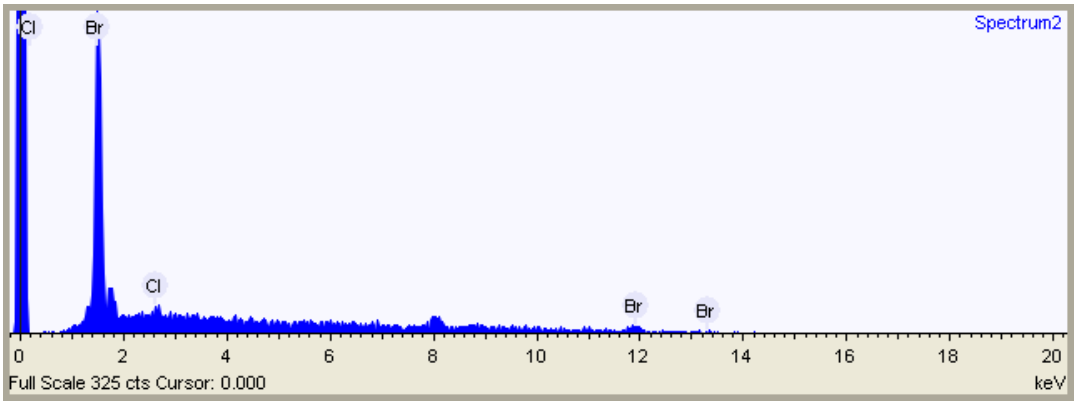

Figure A.20: *EDX spectrum of **IRA400-Br**.*

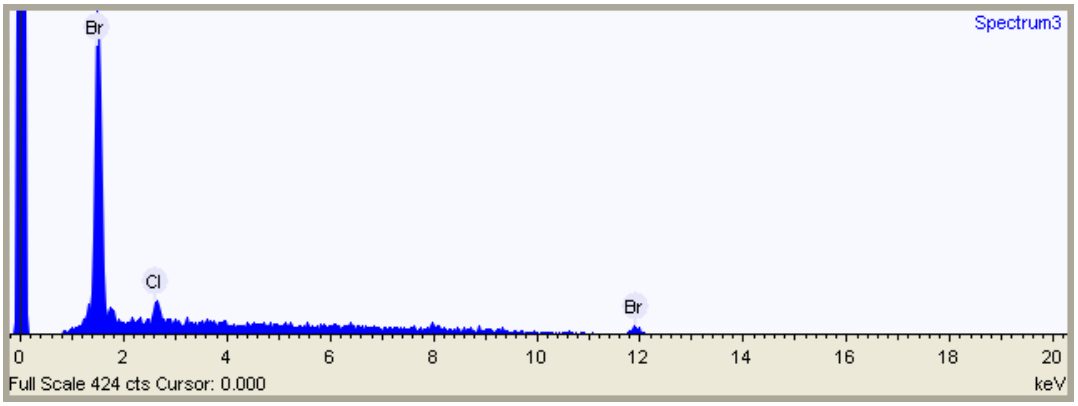

Figure A.21: *EDX spectrum of **A26-Br**.*

Table A.1: *EDX acquisition conditions*

Parameter	Value
Acquisition time (s)	90.0
Process time	4
Accelerating voltage (kV)	15.0

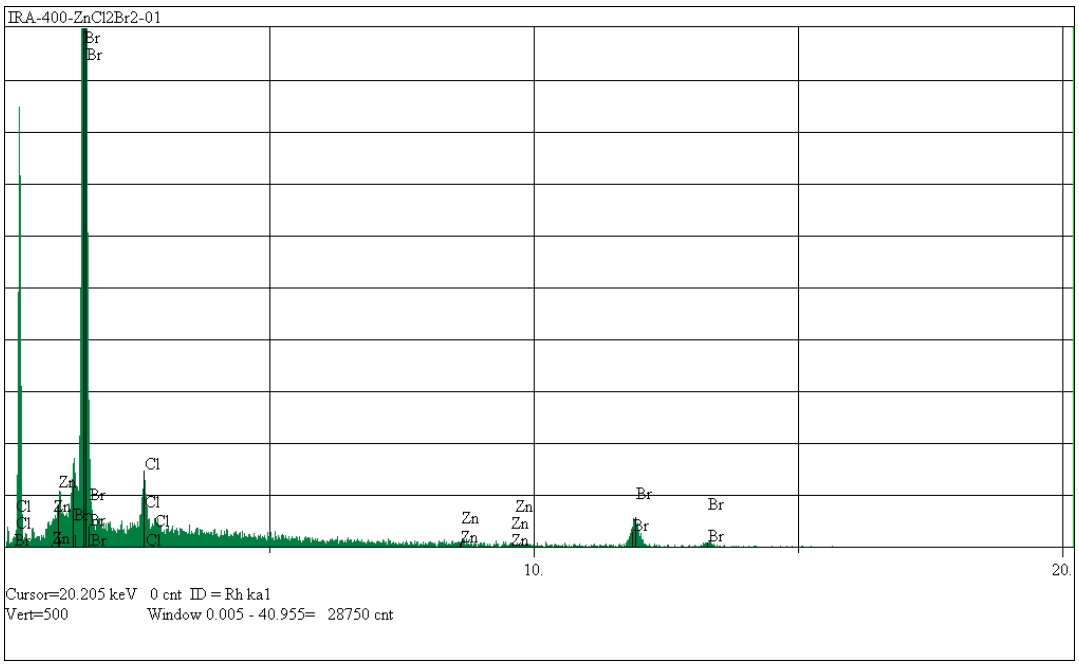

Figure A.22: *EDX spectrum of* ***R1b***

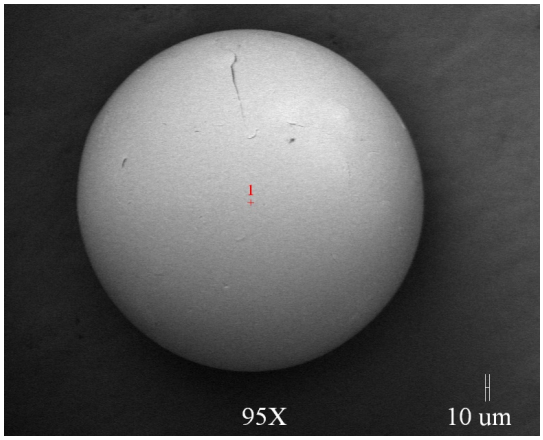

Figure A.23: *Micrograph of* ***R1b****, acquired with SEM.*

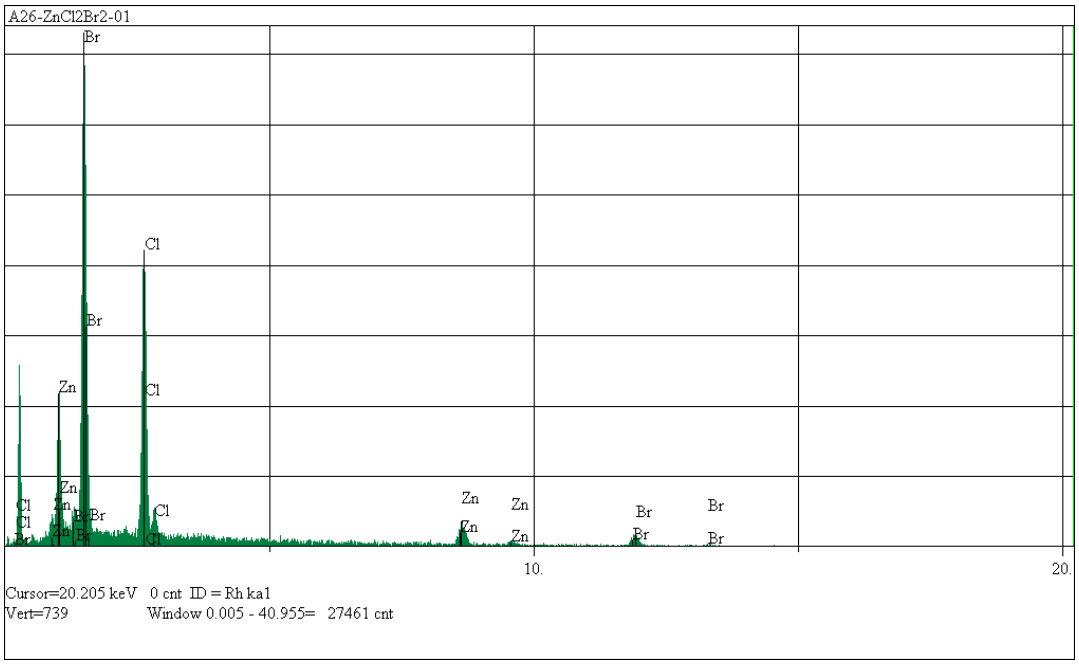

Figure A.24: *EDX spectrum of* ***R1d***

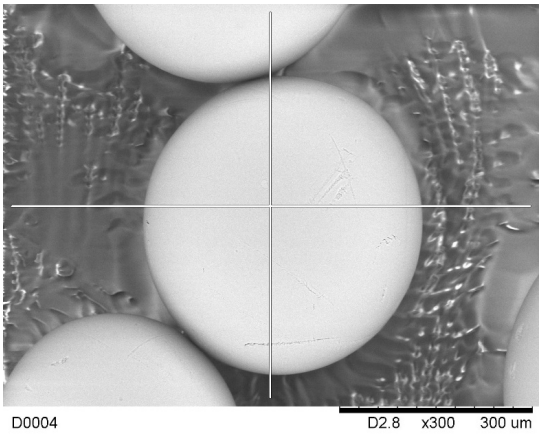

Figure A.25: *Micrograph of* ***R1d****, acquired with SEM.*

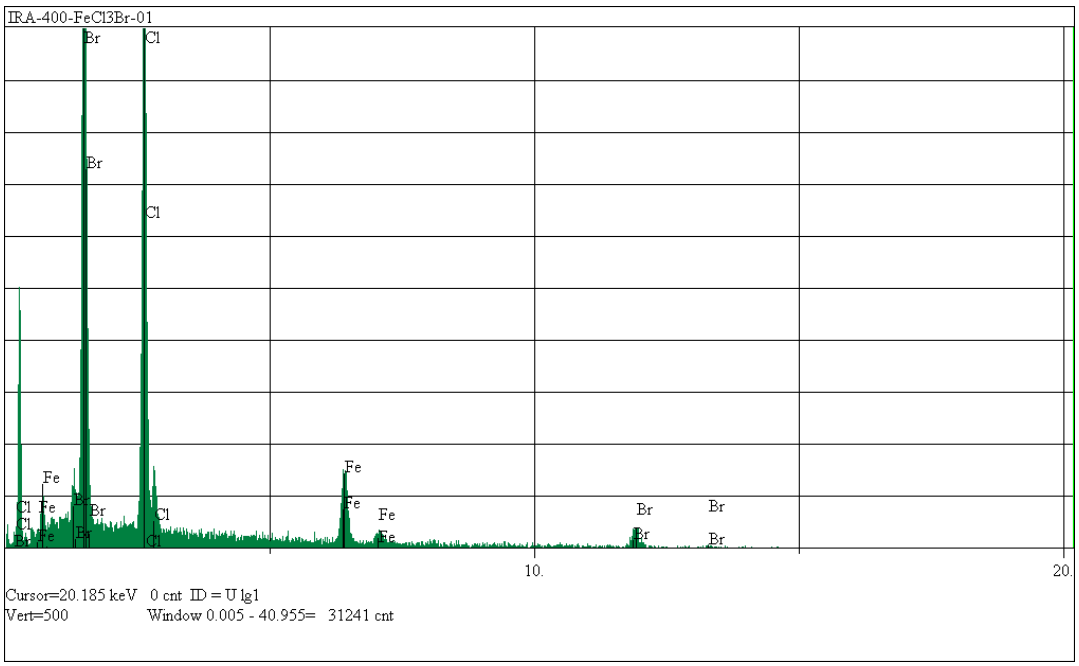

Figure A.26: *EDX spectrum of* ***R1b***

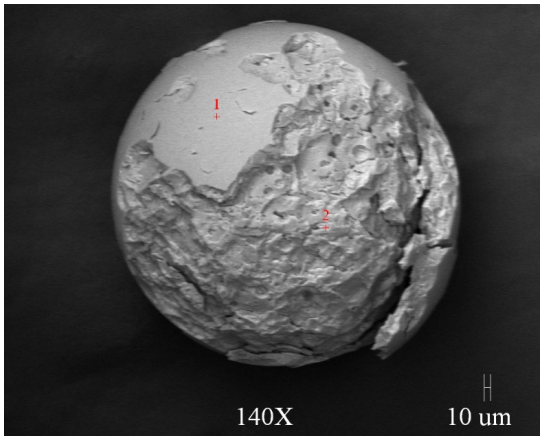

Figure A.27: *Micrograph of* ***R1b****, acquired with SEM.*

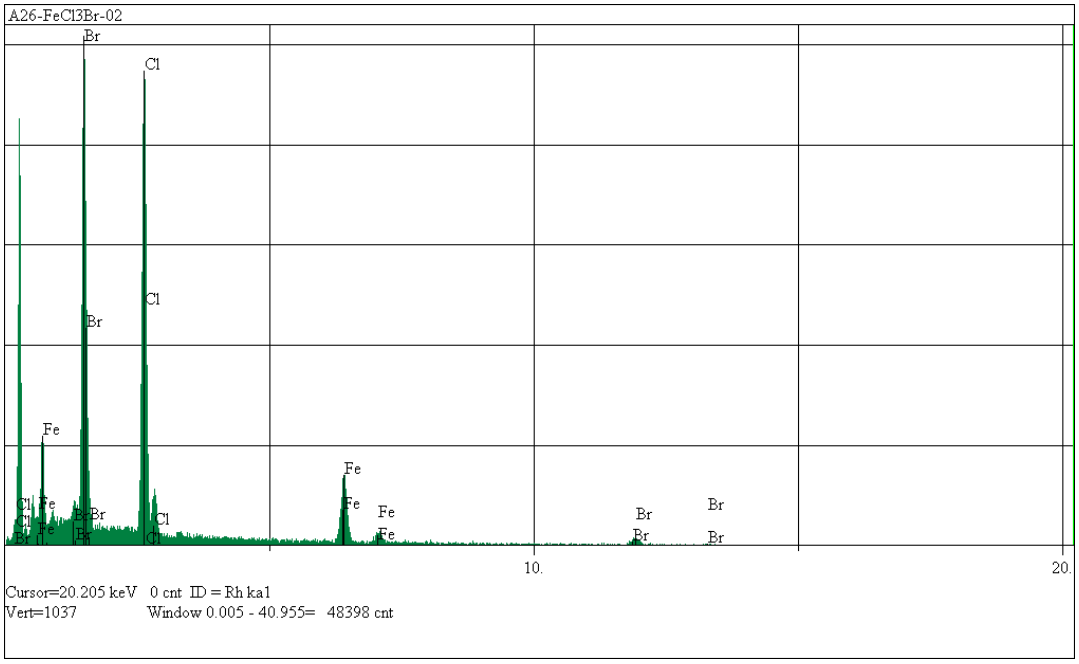

Figure A.28: *EDX spectrum of* ***R1b***

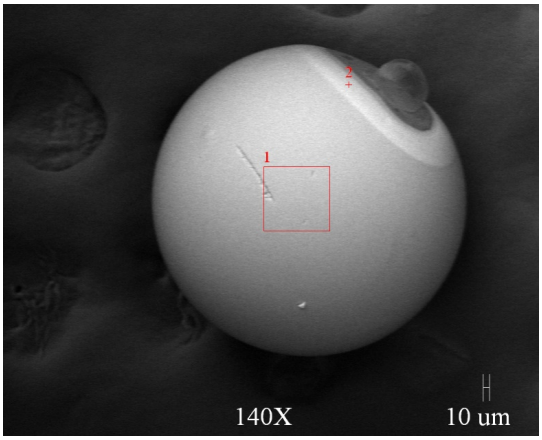

Figure A.29: *Micrograph of* ***R1b****, acquired with SEM.*

A.3 Raman spectra

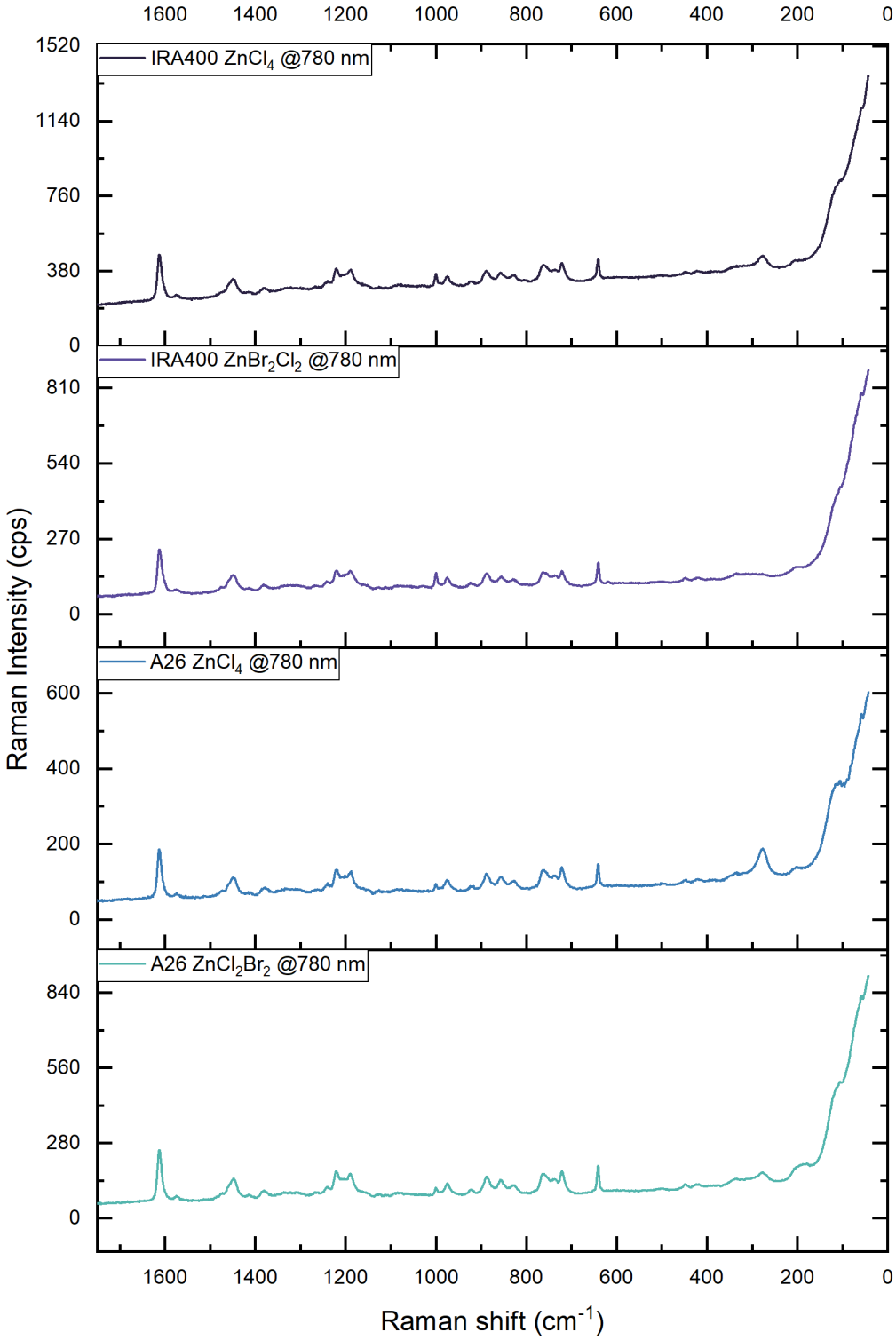

Figure A.30: *Raman spectra of resins **R1a-d**, using a 780 nm light source.*

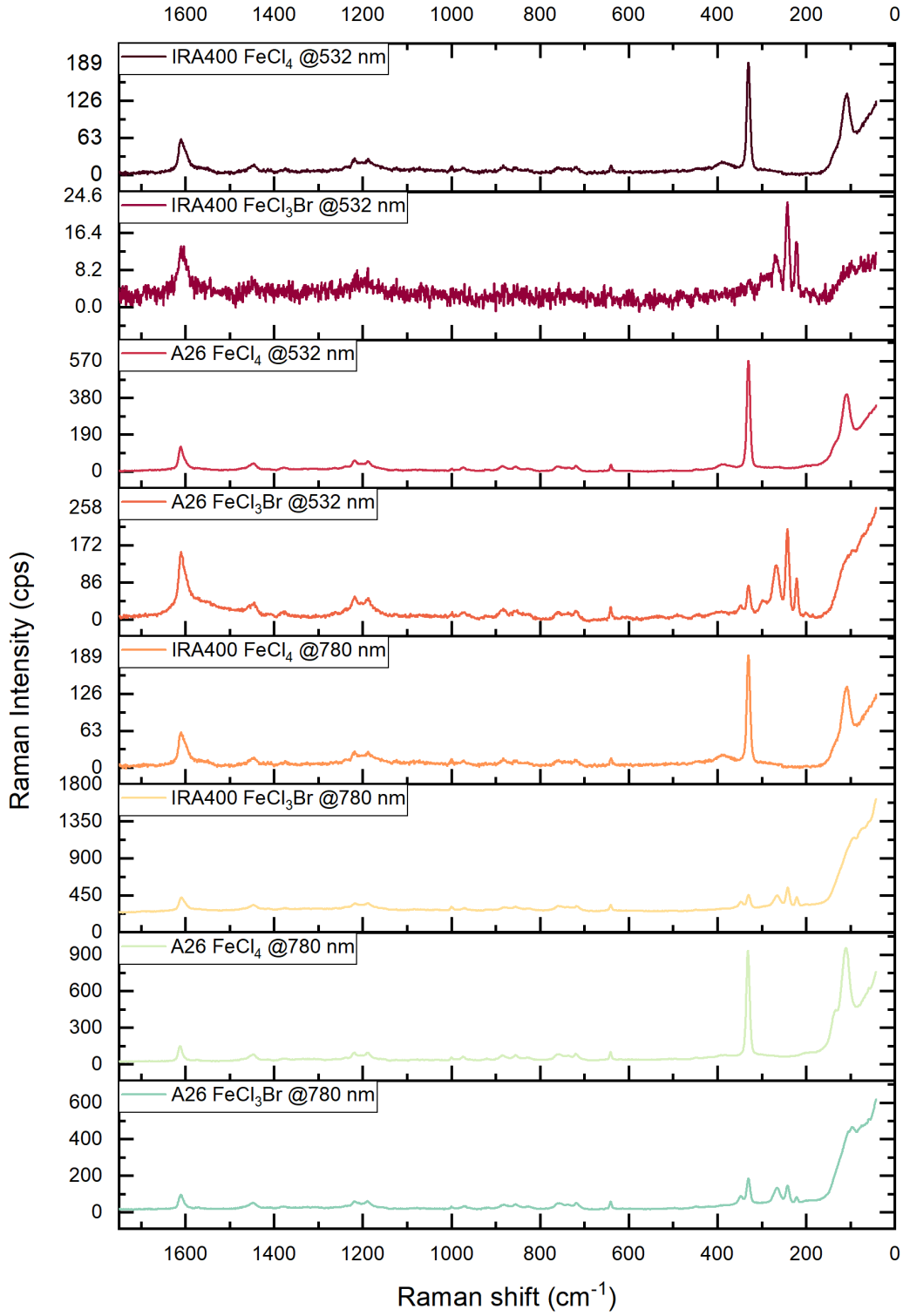

Figure A.31: *Raman spectra of resins **R2a-d**, using a 780 nm and a 532 nm light source.*

A.4 Mössbauer spectra and data

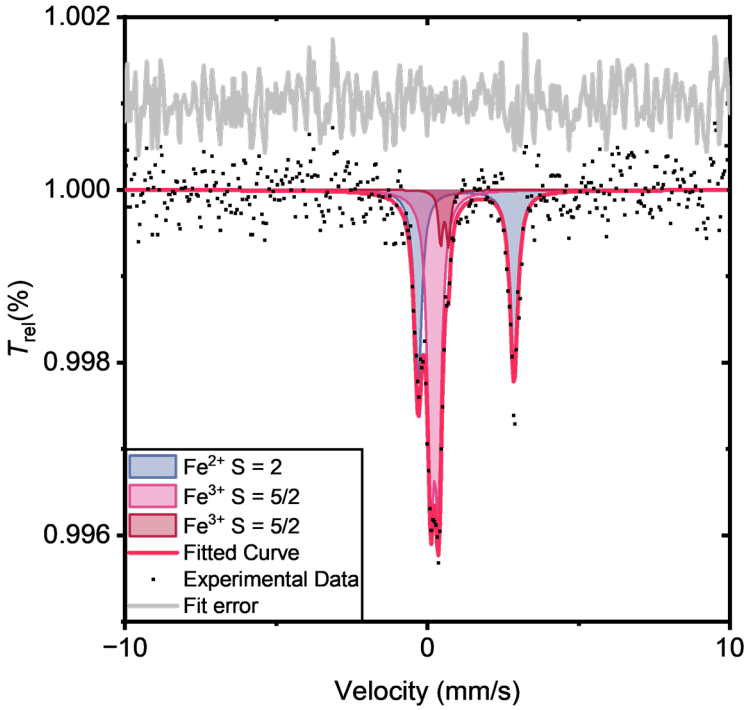

Figure A.32: *Mössbauer spectrum of commercial* $Fe(CF_3SO_3)_3$

Table A.2: *Mössbauer fitting parameters for commercial* $Fe(CF_3SO_3)_3$

Species	Parameter	Value
Fe^{3+} $S = {}^5/_2$	δ $(mm \cdot s^{-1})$	0.23(1)
	ΔE_Q $(mm \cdot s^{-1})$	0.24(1)
	$\%_{wt}$	51(4)%
Fe^{2+} $S = 2$ impurity	δ $(mm \cdot s^{-1})$	0.56(3)
	ΔE_Q $(mm \cdot s^{-1})$	0.26(5)
	$\%_{wt}$	42(4)%
Fe^{2+} $S = 2$ impurity	δ $(mm \cdot s^{-1})$	1.28(1)
	ΔE_Q $(mm \cdot s^{-1})$	3.17(2)
	$\%_{wt}$	6(3)%

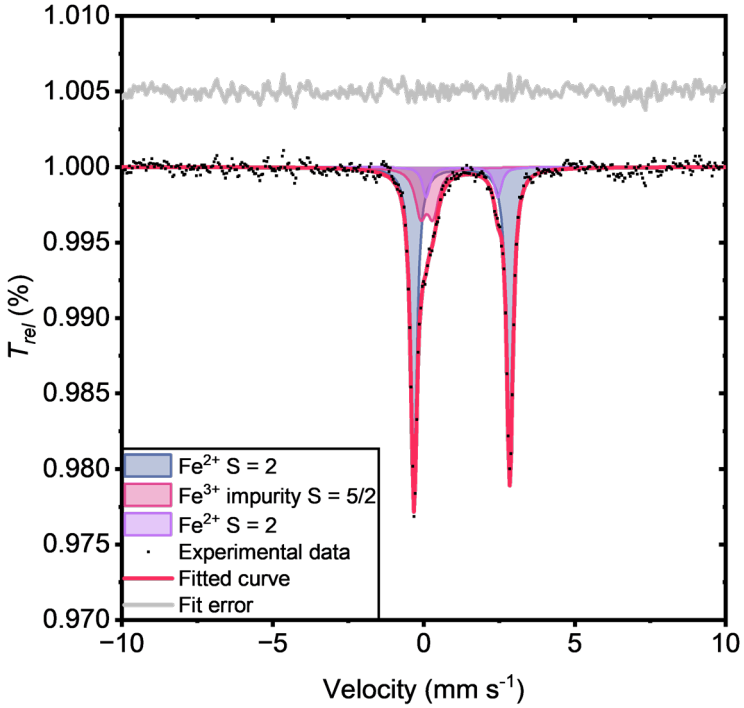

Figure A.33: *Mössbauer spectrum of* $Fe(CF_3SO_3)_2 \cdot 2\ CH_3CN$.

Table A.3: *Mössbauer fitting parameters for* $Fe(CF_3SO_3)_2 \cdot 2\ CH_3CN$.

Species	Parameter	Value
Fe^{2+} $S = 2$	δ (mm · s^{-1})	1.26(1)
	ΔE_Q (mm · s^{-1})	3.18(1)
	$\%_{wt}$	73(2)%
Fe^{2+} $S = 2$ impurity	δ (mm · s^{-1})	1.27(1)
	ΔE_Q (mm · s^{-1})	2.37(4)
	$\%_{wt}$	8(2)%
Fe^{3+} $S = 5/2$ impurity	δ (mm · s^{-1})	0.10(2)
	ΔE_Q (mm · s^{-1})	0.41(2)
	$\%_{wt}$	18(1)%

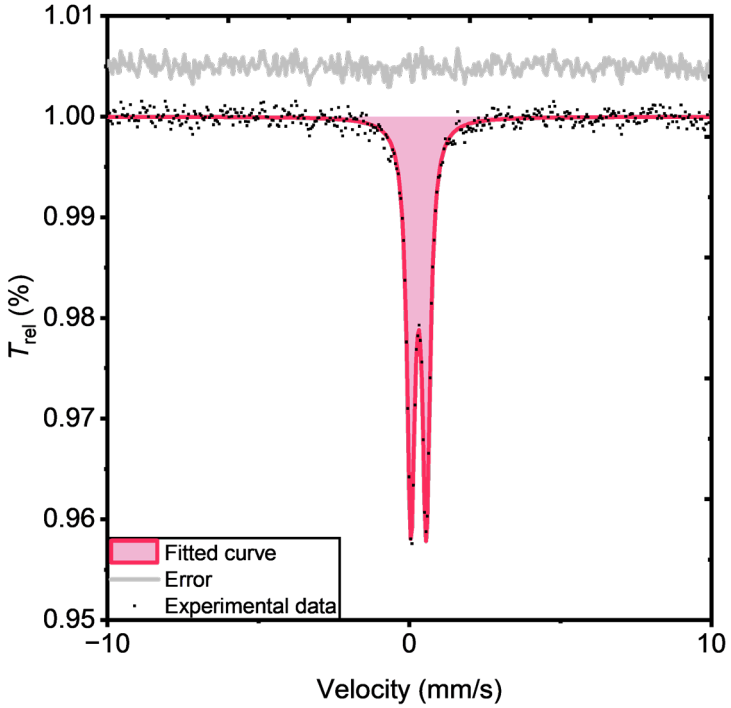

Figure A.34: *Mössbauer spectrum of* ***C2a****.*

Table A.4: *Mössbauer fitting parameters for* ***C2a****.*

Species	Parameter	Value
Fe^{3+} $S = 5/2$	δ $(mm \cdot s^{-1})$	0.31(1)
	ΔE_Q $(mm \cdot s^{-1})$	0.51(1)
	$\%_{wt}$	100%

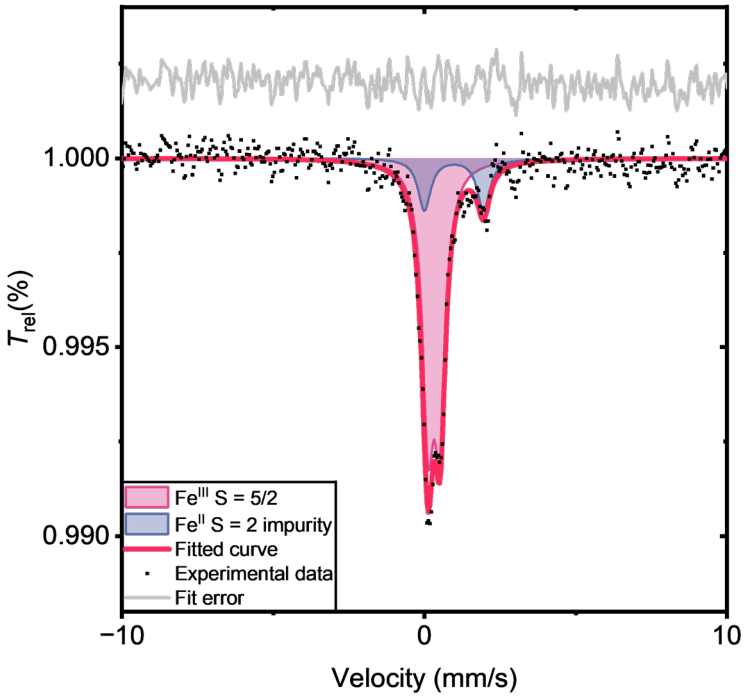

Figure A.35: *Mössbauer spectrum of* ***C2b****.*

Table A.5: *Mössbauer fitting parameters for* ***C2b****.*

Species	Parameter	Value
Fe^{3+} $S = 5/2$	δ $(mm \cdot s^{-1})$	0.32(1)
	ΔE_Q $(mm \cdot s^{-1})$	0.39(1)
	$\%_{wt}$	81(2)%
Fe^{2+} $S = 2$ impurity	δ $(mm \cdot s^{-1})$	0.98(4)
	ΔE_Q $(mm \cdot s^{-1})$	1.95(7)
	$\%_{wt}$	19(3)%

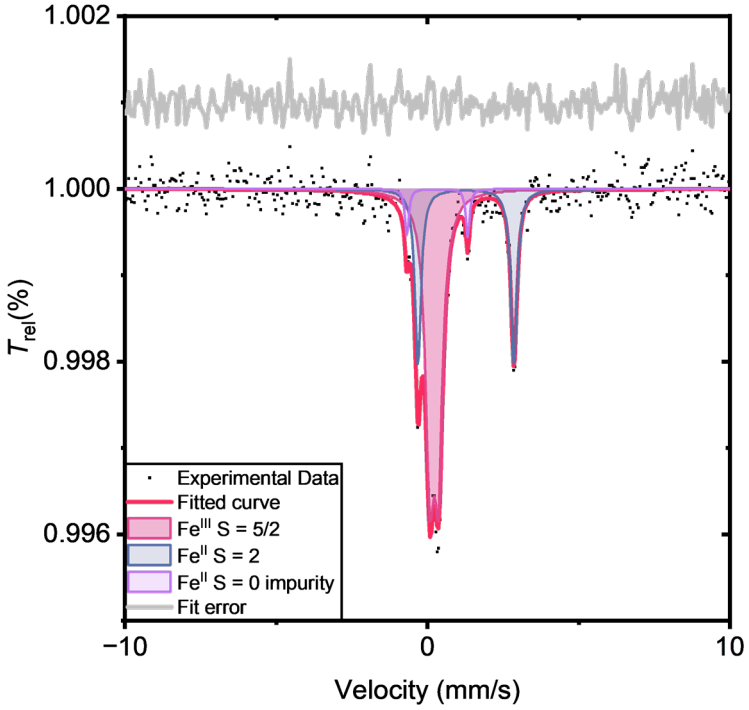

Figure A.36: *Mössbauer spectrum of* ***C2c****, obtained from commercial* $Fe(OTf)_3$.

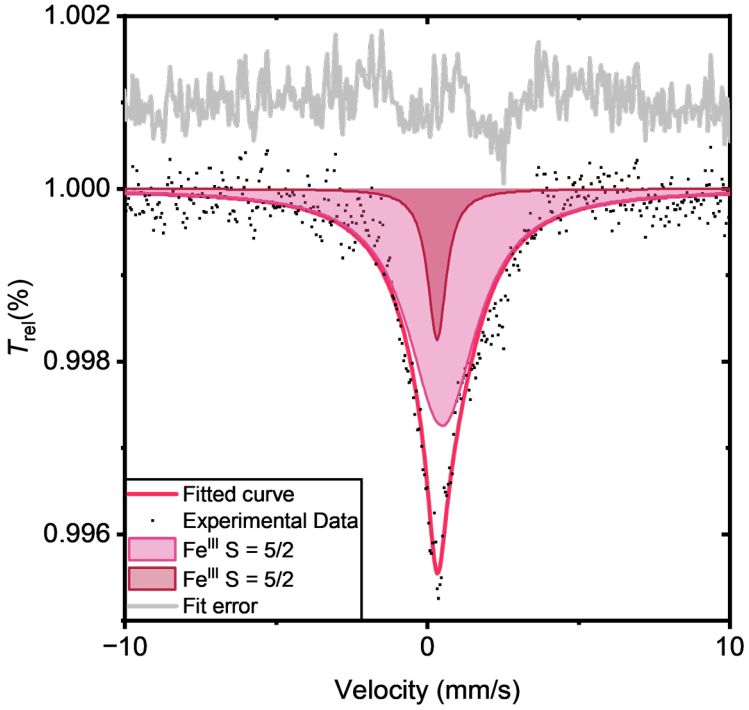

Figure A.37: *Mössbauer spectrum of* ***C2c****.*

Table A.6: *Mössbauer fitting parameters for **C2c**.*

$Fe(OTf)_3$ source	Species	Parameter	Value
Commercial	Fe^{3+} $S = 5/2$	δ $(mm \cdot s^{-1})$	0.23(1)
		ΔE_Q $(mm \cdot s^{-1})$	0.29(1)
		$\%_{wt}$	81(2)%
	Fe^{2+} $S = 2$	δ $(mm \cdot s^{-1})$	1.27(1)
		ΔE_Q $(mm \cdot s^{-1})$	3.17(1)
		$\%_{wt}$	31(1)%
	Fe^{2+} $S = 0$ impurity	δ $(mm \cdot s^{-1})$	0.32(1)
		ΔE_Q $(mm \cdot s^{-1})$	2.01(3)
		$\%_{wt}$	5(1)%
Lab-made	Fe^{3+} $S = 5/2$	δ $(mm \cdot s^{-1})$	0.32
		$\%_{wt}$	15(6)%
	Fe^{3+} $S = 5/2$	δ $(mm \cdot s^{-1})$	0.49
		$\%_{wt}$	85(4)%

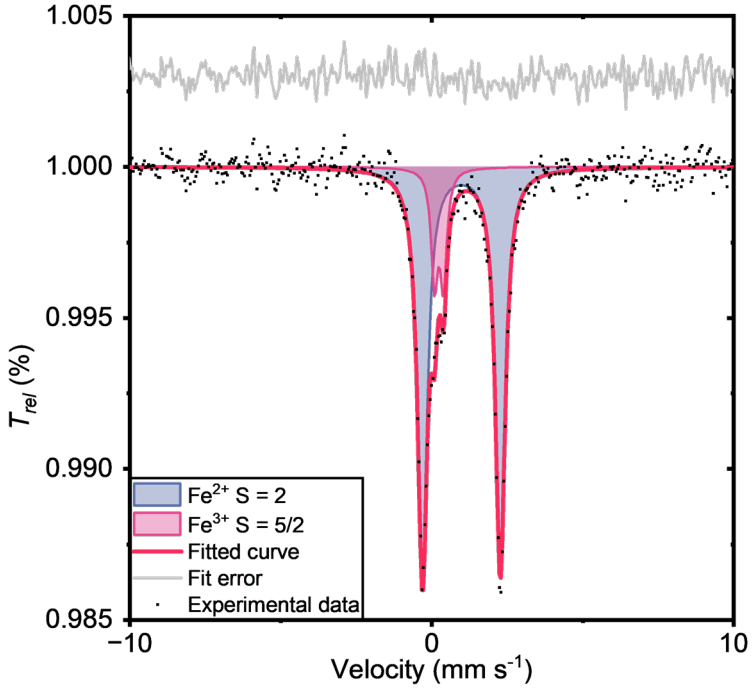

Figure A.38: *Mössbauer spectrum of* ***C2d****.*

Table A.7: *Mössbauer fitting parameters for* ***C2d***

Species	Parameter	Value
Fe^{2+} $S = 2$	δ (mm · s^{-1})	0.98(1)
	ΔE_Q (mm · s^{-1})	2.58(1)
	$\%_{wt}$	84(2)%
Al_6Fe	δ (mm · s^{-1})	0.24(1)
	ΔE_Q (mm · s^{-1})	0.29(2)
	$\%_{wt}$	16(1)%

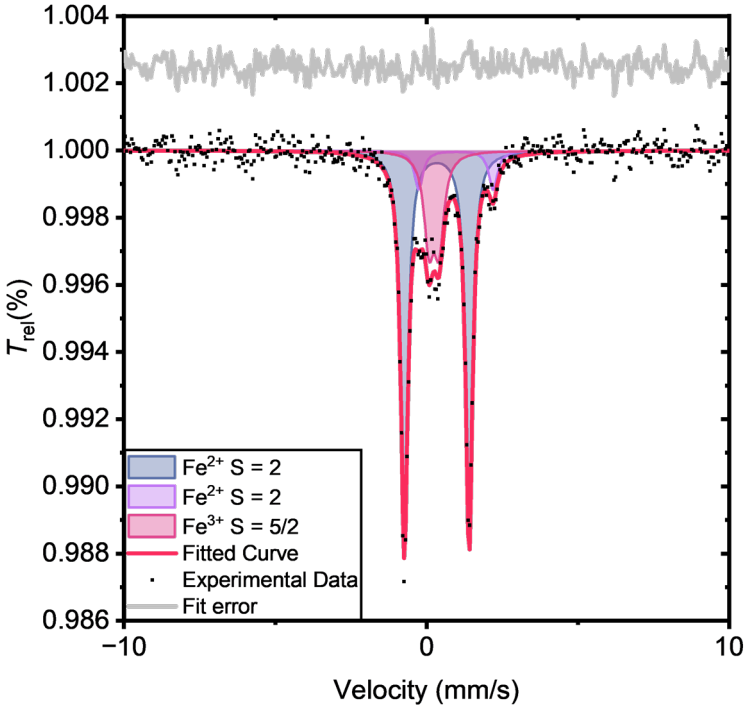

Figure A.39: *Mössbauer spectrum of **C2f**.*

Table A.8: *Mössbauer fitting parameters for **C2f***

Species	Parameter	Value
Fe^{2+a}	δ $(mm \cdot s^{-1})$	0.33(1)
	ΔE_Q $(mm \cdot s^{-1})$	2.14(1)
	$\%_{wt}$	69(2)%
Fe^{2+} $S = 2$	δ $(mm \cdot s^{-1})$	0.97(2)
	ΔE_Q $(mm \cdot s^{-1})$	2.46(5)
	$\%_{wt}$	9(2)%
Al_6Fe	δ $(mm \cdot s^{-1})$	0.24(1)
	ΔE_Q $(mm \cdot s^{-1})$	0.33(1)
	$\%_{wt}$	22(1)%

[a] Ambiguous interpretation, magnetometry is necessary to establish whether $S = 2$ or $S = 0$.

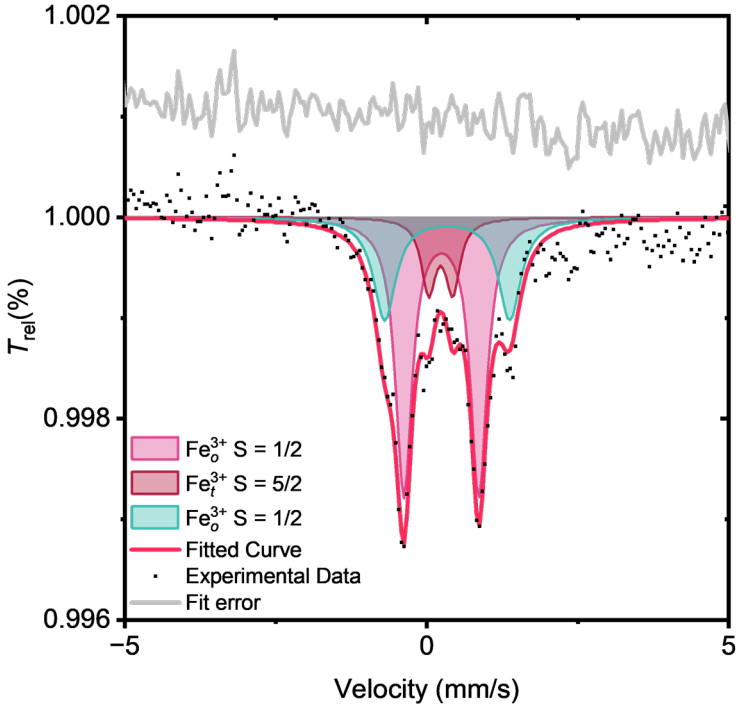

Figure A.40: *Mössbauer spectrum of **C3a**. Courtesy of prof. Dominika Zákutná.*

Table A.9: *Mössbauer fitting parameters for **C3a***

Species	Parameter	Value
Fe_o^{3+} $S = 1/2$	δ (mm · s^{-1})	0.24(1)
	ΔE_Q (mm · s^{-1})	1.25(1)
	$\%_{wt}$	64(4)%
Fe_t^{3+} $S = 5/2$	δ (mm · s^{-1})	0.23(2)
	ΔE_Q (mm · s^{-1})	0.40(4)
	$\%_{wt}$	6(2)%
Fe^{3+} $S = 1/2$	δ (mm · s^{-1})	0.34(2)
	ΔE_Q (mm · s^{-1})	2.07(4)
	$\%_{wt}$	30(2)%

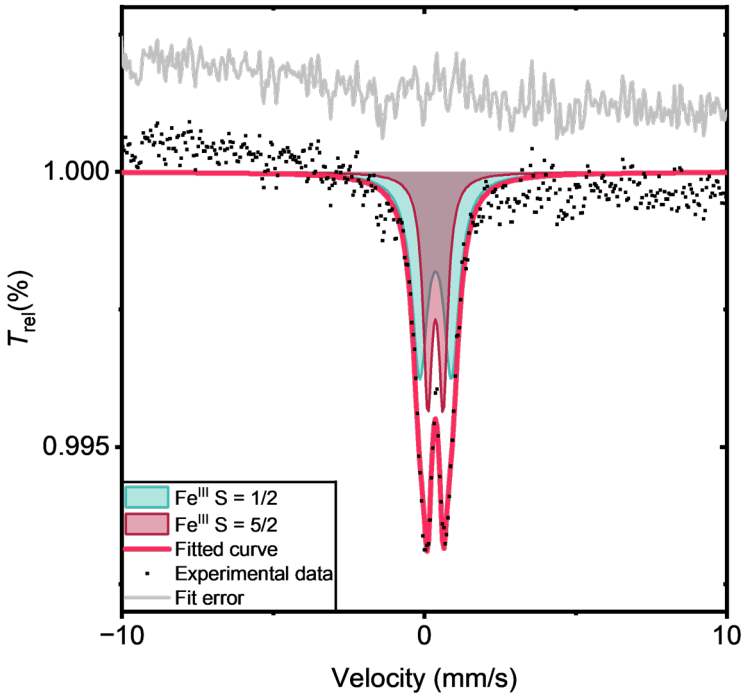

Figure A.41: *Mössbauer spectrum of **C3c**. Courtesy of prof. Dominika Zákutná.*

Table A.10: *Mössbauer fitting parameters for **C3c***

Species	Parameter	Value
Fe_o^{3+} $S = 5/2$	δ (mm · s^{-1})	0.36(1)
	ΔE_Q (mm · s^{-1})	0.54(1)
	$\%_{wt}$	25%
Fe_o^{3+} $S = 1/2$	δ (mm · s^{-1})	0.37(1)
	ΔE_Q (mm · s^{-1})	1.01(1)
	$\%_{wt}$	75%

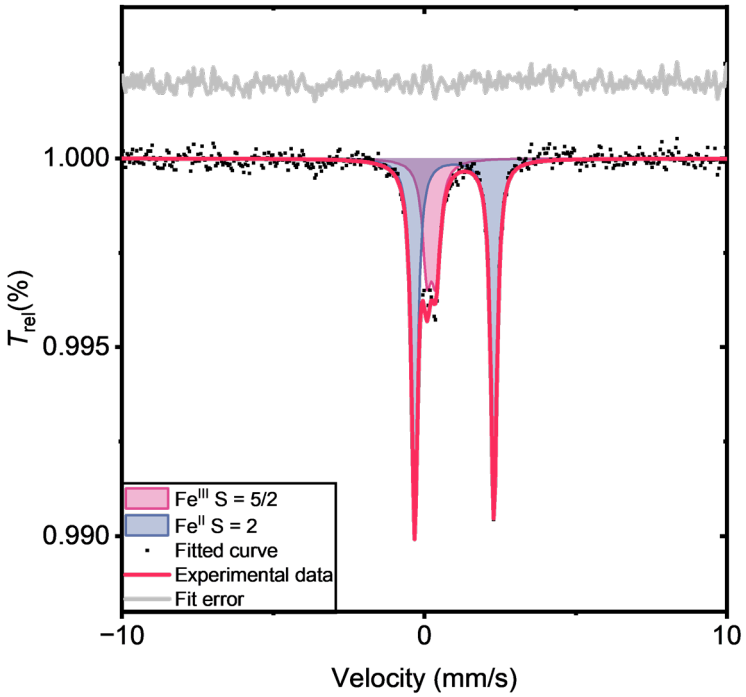

Figure A.42: *Mössbauer spectrum of* ***C3d****.*

Table A.11: *Mössbauer fitting parameters for* ***C3d***

Species	Parameter	Value
Al_6Fe	δ $(mm \cdot s^{-1})$	0.23(1)
	ΔE_Q $(mm \cdot s^{-1})$	0.29(1)
	$\%_{wt}$	21(1)%
Fe^{2+} $S = 2$	δ $(mm \cdot s^{-1})$	0.98(1)
	ΔE_Q $(mm \cdot s^{-1})$	2.62(1)
	$\%_{wt}$	79(1)%

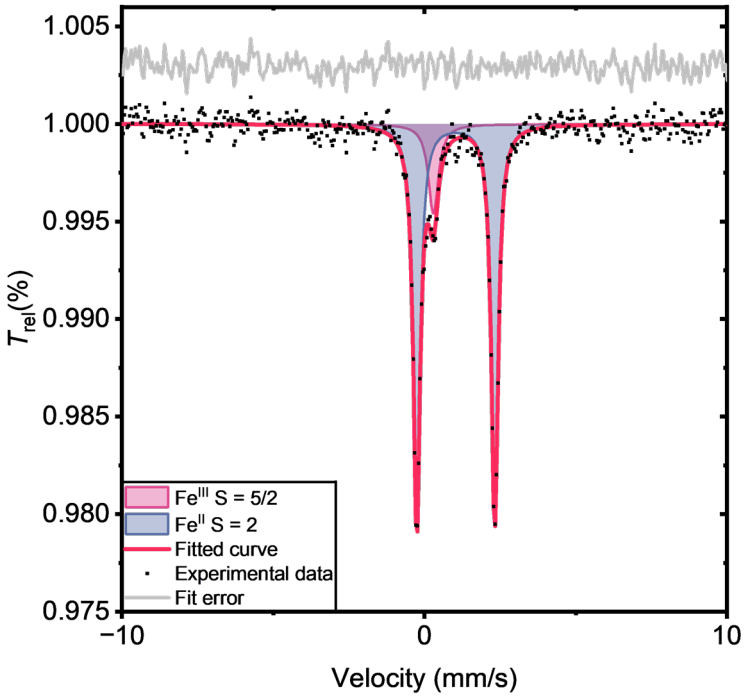

Figure A.43: *Mössbauer spectrum of **C3f**.*

Table A.12: *Mössbauer fitting parameters for **C3f***

Species	Parameter	Value
Al_6Fe	δ (mm · s^{-1})	0.29(1)
	ΔE_Q (mm · s^{-1})	-
	$\%_{wt}$	14.0(5)%
Fe^{2+} $S = 2$	δ (mm · s^{-1})	1.04(1)
	ΔE_Q (mm · s^{-1})	2.58(1)
	$\%_{wt}$	86.0(5)%

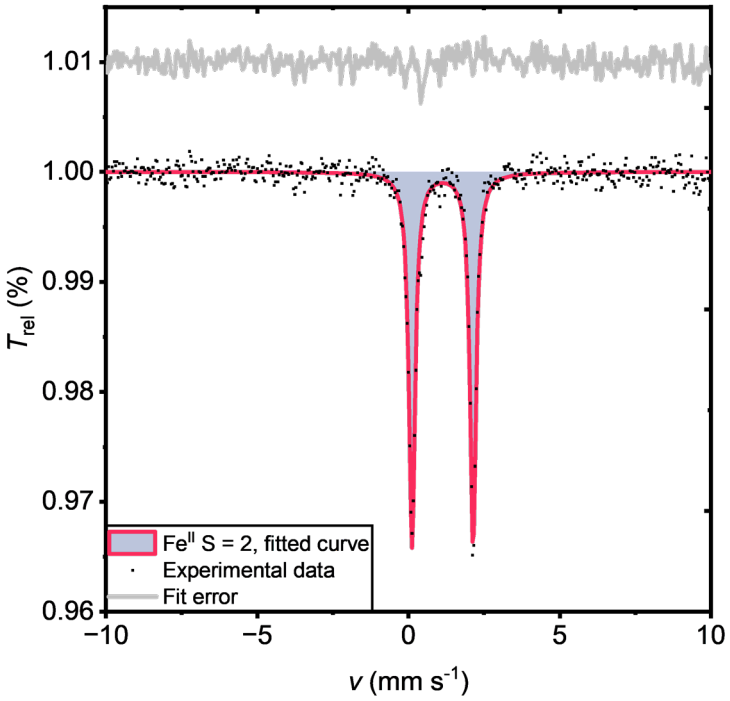

Figure A.44: *Mössbauer spectrum of* ***C4a****.*

Table A.13: *Mössbauer fitting parameters for* ***C4a****.*

Species	Parameter	Value
Fe^{2+} $S = 2$	δ (mm $\cdot$ s^{-1})	1.12(1)
	ΔE_Q (mm $\cdot$ s^{-1})	2.02(1)
	$\%_{wt}$	100%

A.5 Magnetometry data

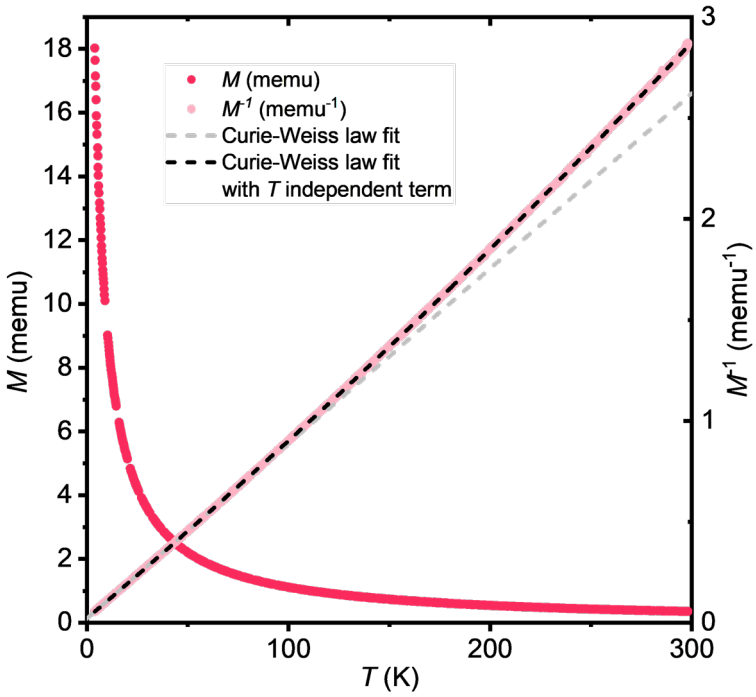

Figure A.45: *M and M^{-1} as a function of temperature, for compound* ***R2b****.*

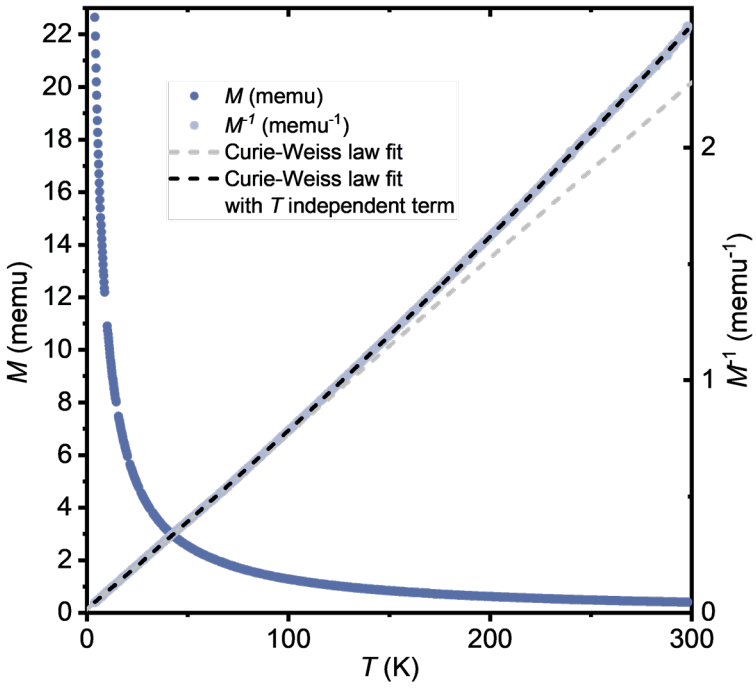

Figure A.46: *M and M^{-1} as a function of temperature, for compound* ***R2d****.*

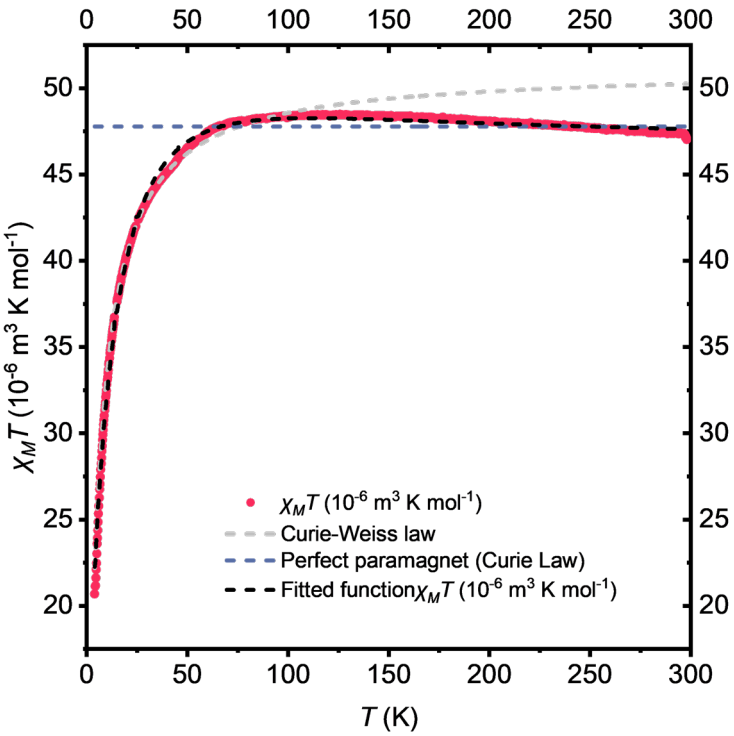

Figure A.47: *$\chi_M T$ product as a function of temperature, for compound **C2a**.*

Table A.14: *Van Vleck formula parameters fit for **C2a**.*

Parameter	Value
g_{tot}[a]	2.041(2)
D	20.0(1) cm^{-1}
ϑ	−2.44(4) K

[a] $g_{tot} = (2g_{xy} + g_z)/3$

Table A.15: *Curie and Curie-Weiss law fit parameters for **C2a**.*

Parameter	Value
μ_{eff} (μ_B, Curie)	5.5164(4)
μ_{eff} (μ_B, Curie-Weiss)	5.7063(7)
θ_{CW} (K)	−5.28

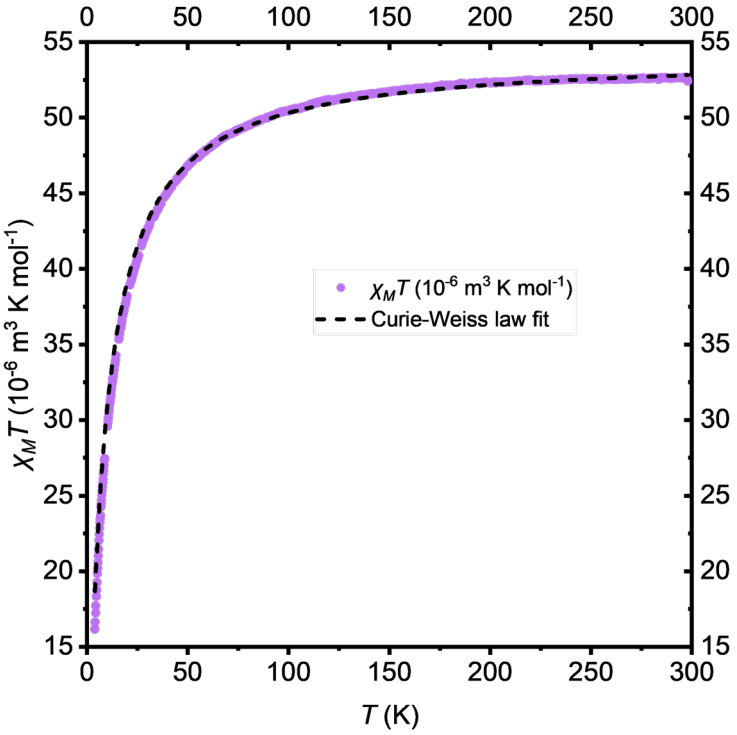

Figure A.48: *$\chi_M T$ product as a function of temperature, for compound **C2b**.*

Table A.16: *Curie and Curie-Weiss law fit parameters for **C2b**.*

Parameter	Value
μ_{eff} (μ_B, Curie)	5.7506(2)
μ_{eff} (μ_B, Curie-Weiss)	5.87(4)
θ_{CW} (K)	−7.66

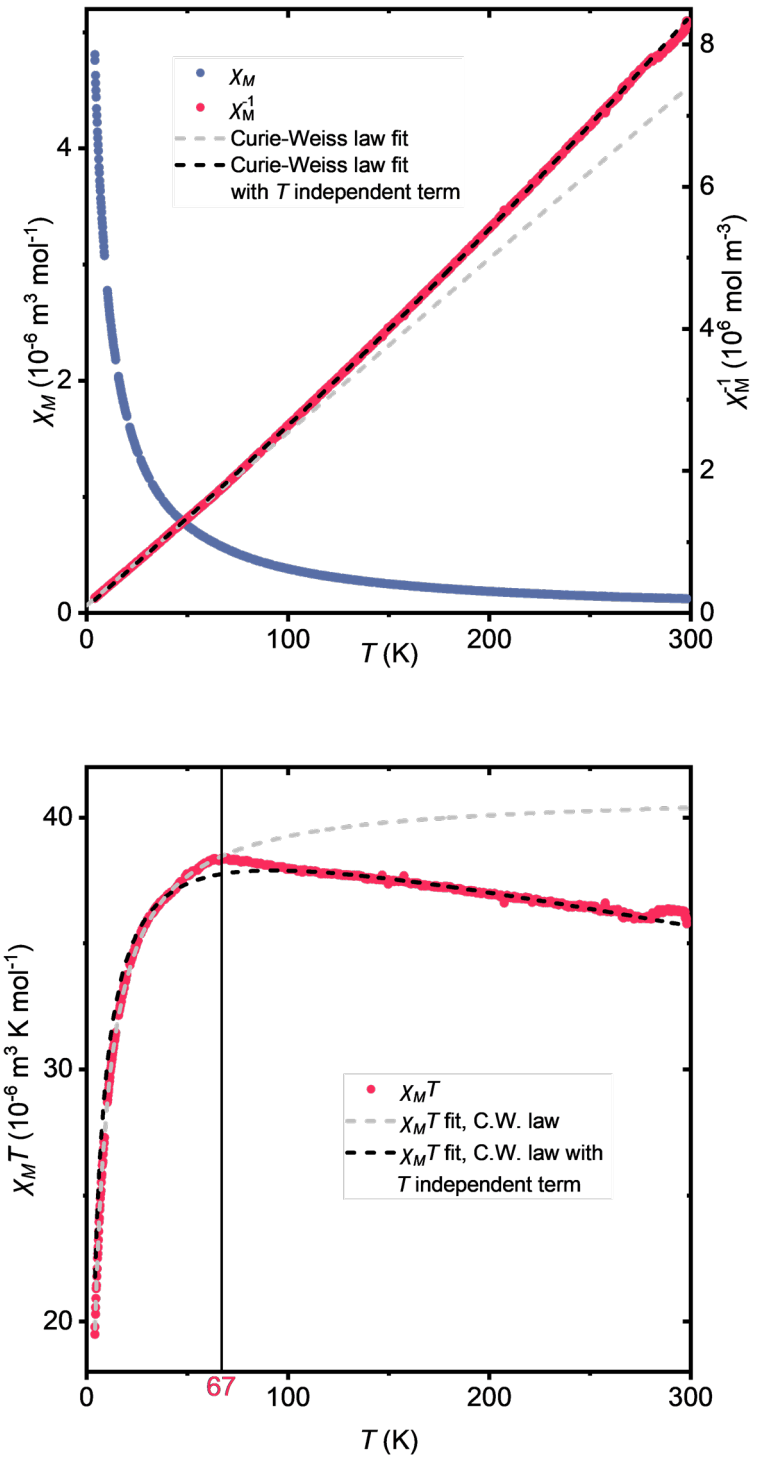

Figure A.49: *Above:* χ_M *and* χ_M^{-1} *as a function of temperature. Below:* $\chi_M T$ *product as a function of temperature, for compound* ***C2d****.*

Table A.17: *Curie and Curie-Weiss law fit parameters for* ***C2a****.*

Technique	Parameter	Value
Curie Law	μ_{eff} (μ_B)	4.8319(8)
Curie-Weiss Law	μ_{eff} (μ_B)	5.1081(5)
	θ_{CW} (K)	−4.37
Curie-Weiss Law, with T independent term	μ_{eff} (μ_B)	5.10(4)
	θ_{CW} (K)	−3.53(4)
	χ_0 (10^{-6}m^{3}mol^{-1})	−0.01561(9)

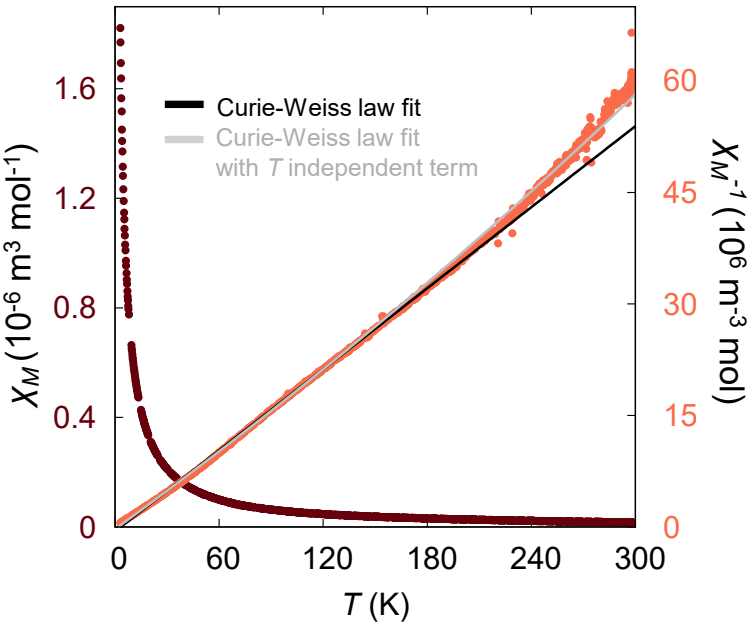

Figure A.50: χ_M *and* χ_M^{-1} *as a function of temperature for compound* ***C3a****. Courtesy of prof. Dominika Zákutná.*

Table A.18: *Curie and Curie-Weiss law fit parameters for* ***C3a****.*

Technique	Parameter	Value
Curie Law	μ_{eff} (μ_B)	1.87(1)
Curie-Weiss Law	μ_{eff} (μ_B)	1.93(1)

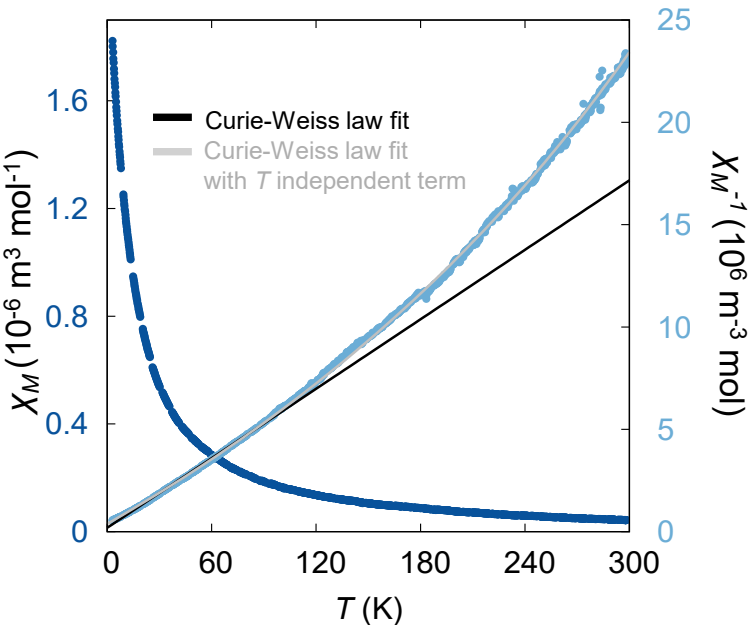

Figure A.51: *χ_M and χ_M^{-1} as a function of temperature for compound **C3c**. Courtesy of prof. Dominika Zákutná.*

Table A.19: *Curie and Curie-Weiss law fit parameters for **C3c**.*

Technique	Parameter	Value
Curie Law	μ_{eff} (μ_B)	3.35(1)
Curie-Weiss Law	μ_{eff} (μ_B)	3.65(1)

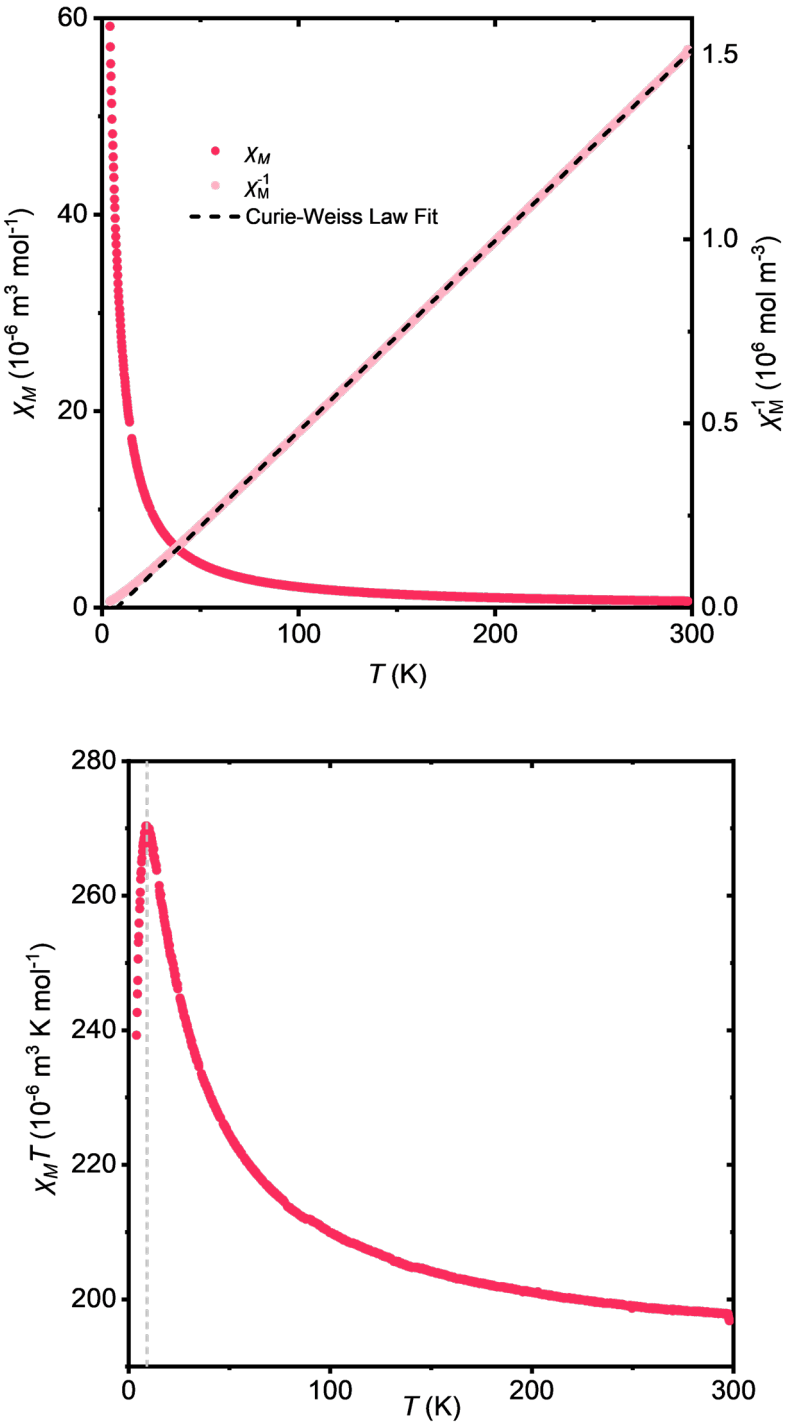

Figure A.52: *Above:* χ_M *and* χ_M^{-1} *as a function of temperature. Below:* $\chi_M T$ *product as a function of temperature, for compound* ***C4a****.* $H = 0.5$ T.

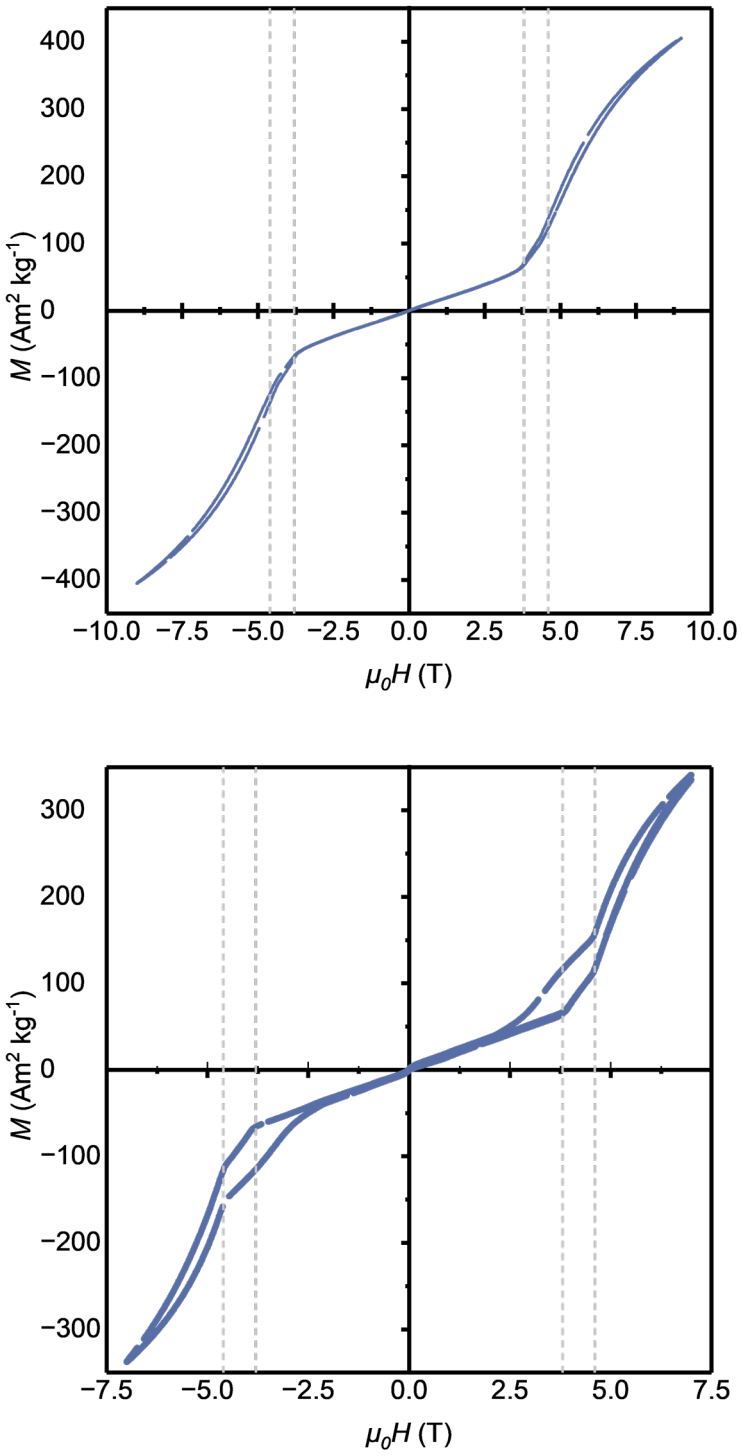

Figure A.53: *Magnetization curves of **C4a**, recorded at 10 K (above) and 4 K (below).*

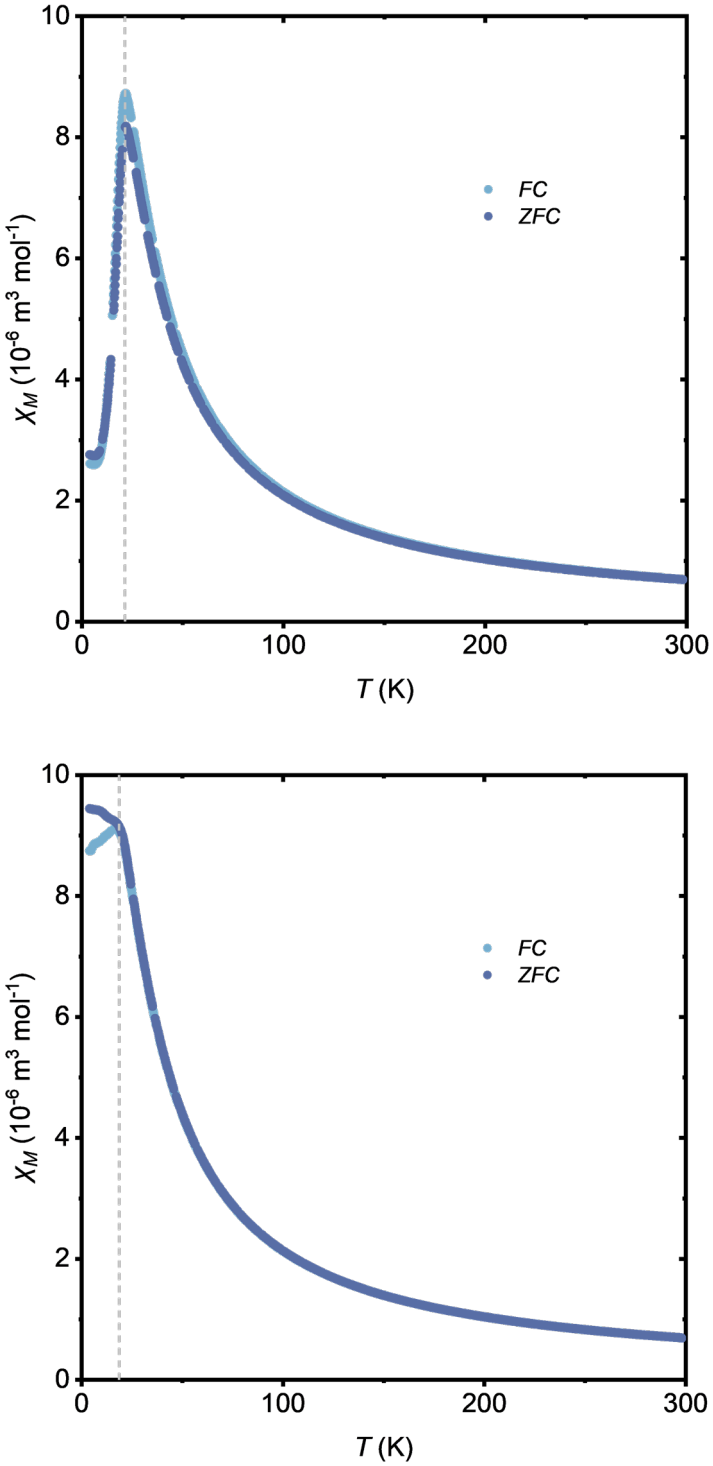

Figure A.54: *ZFC and FC curves of* ***C4a****, recorded at 3.5 T (above) and 6 T (below).*

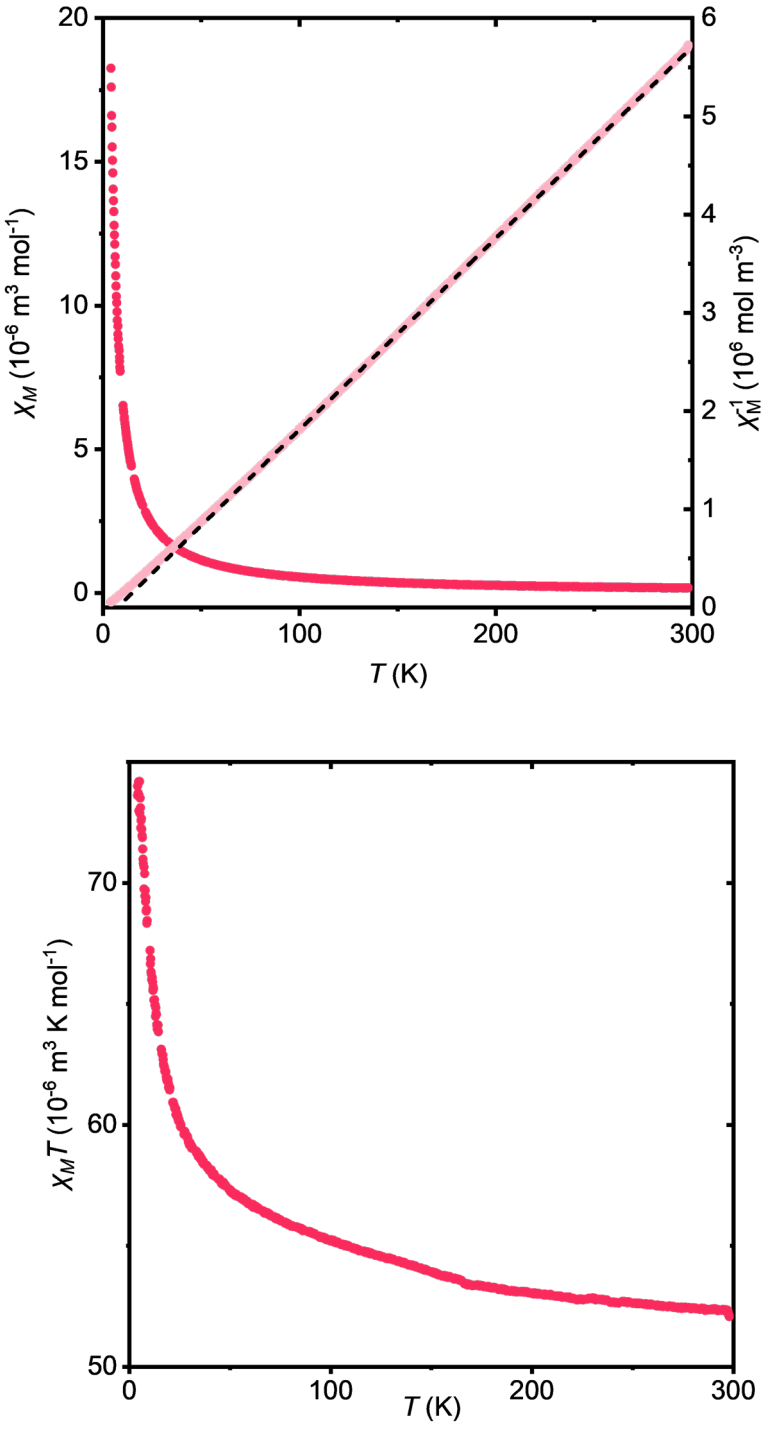

Figure A.55: *Above:* χ_M *and* χ_M^{-1} *as a function of temperature. Below:* $\chi_M T$ *product as a function of temperature, for compound* ***C4c****.* $H = 0.5$ T.

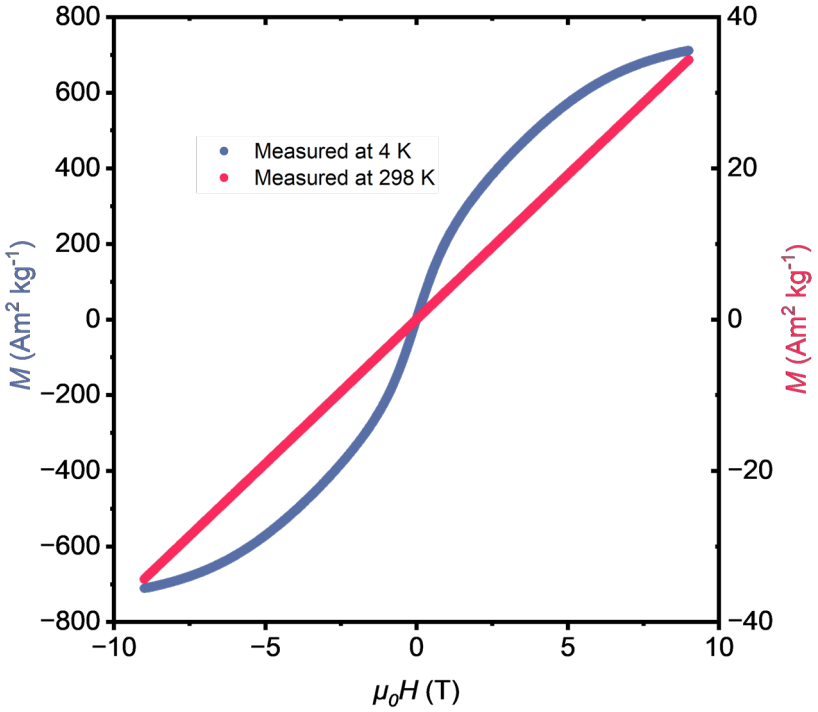

Figure A.56: *Magnetization curves of* ***C4c****, recorded at 298 K (red) and 4 K (blue).*

A.6 SCXRD data

A.6.1 C2a'

Single crystals of **C2a'** suitable for X-ray diffraction were isolated by slow diffusion of diethyl ether, layered on top of a methanolic solution of compound **C2a** (v/v 2:1). A dark brown, elongated plate-like crystal of **C2a'** ($0.380 \times 0.089 \times 0.066$ mm^3) was mounted on a MiTeGen Microloop and measured at 150 K. Data were collected on a XtaLAB Synergy S diffractometer (Rigaku), equipped with Oxford Cryostream 1000 and a micro-focus sealed X-ray tube with copper radiation (Cu-Kα, $\lambda = 1.54184$ Å), with the generator working at 50 kV and 1 mA. Data collection, frame integration, and data reduction were carried out with *CrysAlis Pro7* version 1.171.42.54a, using an empirical absorption correction with spherical harmonics (SCALE3 ABSPACK). The structure was solved by dual space methods with *SHELXT-2015*[274] and refined by iterative cycles of full-matrix least-square routines against F^2 with *SHELXL-2018*[274] within the *WinGX* program suite.[275] All non-hydrogen atoms were refined using anisotropic thermal parameters, while the hydrogen atoms were modelled on idealized positions with $U_{iso} = 1.2\ U_{eq}$. The ORTEP molecular plots (50%) and structural representations were generated with *DIAMOND*[276] version 4.0.

Compound **C2a'** crystallizes in the monoclinic space group $C2/m$ (No. 12), as confirmed by systematic absences observed in the diffraction data. The formula unit contains two positively charged $[Fe(PcLH_3)Cl_2]^+$ monomers, which are balanced by a $[FeCl_4]^{2-}$ counterion (Figure A.57a). The Fe(II) anion is highly disordered, which is reflected by a relatively high R_{int} value on the collected data (10.2%), exhibiting a double tetrahedral geometry (Figure A.57b) with its atoms generated by symmetry. In the first few cycles of refinement, the Fe(II) center of the $[FeCl_4]^{2-}$ moiety occupied a special crystallographic position (coinciding with both a center of inversion and a 2-fold axis), resulting in positional disorder of the four coordinated chlorines. To accurately assess this disorder, the structural refinement was initially tested in the lower symmetry space group Cm (No. 18), derived from the initial space group by removing the 2-fold axis and inversion center. This approach allows for independent treatment of the two opposite $[FeCl_4]^{2-}$ fragments with variable occupancy, confirming a nearly equal probability (0.555:0.445) for the two orientations and indicating that the disorder does not lead to a total disruption of the average crystal symmetry.

Based on this, the final refinement was performed in the higher symmetry space group $C2/m$ (Table A.20, Figure A.58) and allowing the Fe(II) center of the anion to be slightly displaced from the inversion center. This displacement results in the doubling of the Fe(II) site by symmetry, which is better able to account for the larger distribution of electron density in the unit cell caused by the disorder ($R_1 = 6.76\%$, $wR_2 = 0.1715$). The $[FeCl_4]^{2-}$ anion exhibits Fe–Cl bond distances between 1.93–

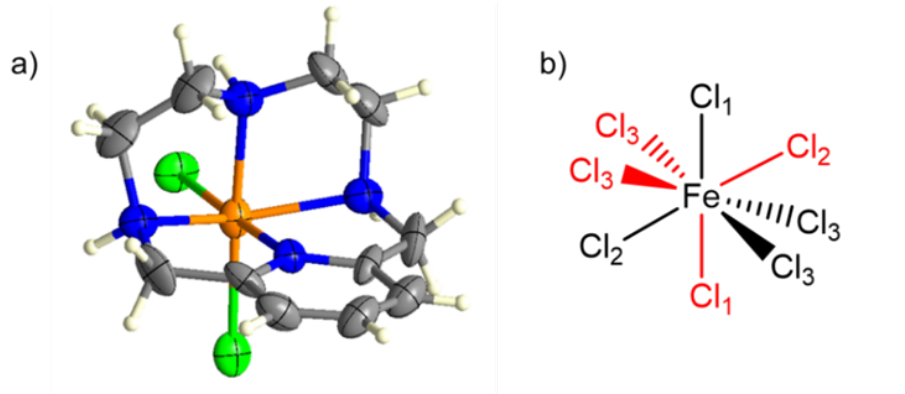

Figure A.57: *a) Molecular structure of the* $[Fe(PcLH_3)Cl_2]^+$ *complex in* ***C2a'****. Thermal ellipsoids are drawn at 50% probability. Colors: Fe, orange; Cl, green; N, blue; C, grey; H, white. b) Schematic representation of the symmetry-generated double tetrahedral geometry of the disordered* $[FeCl_4]^{2-}$ *counterion. Subscripts denote crystallographically equivalent chloride positions.*

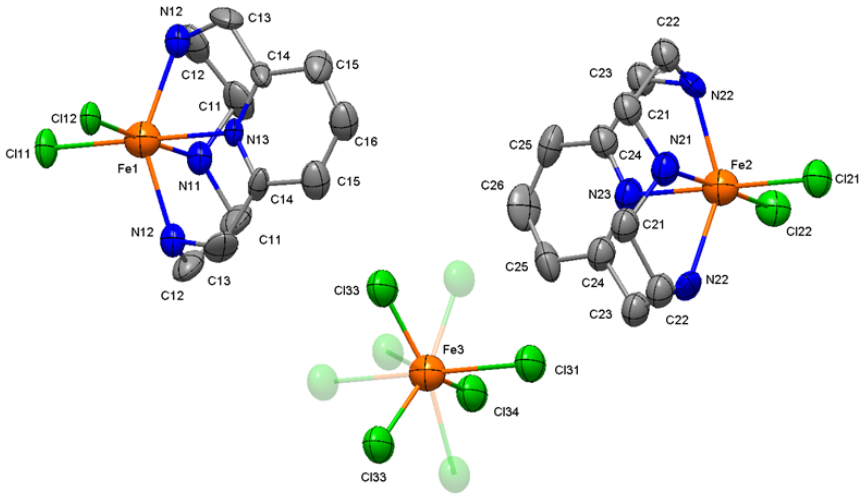

Figure A.58: *Representation of the crystal structure of* ***C2a'*** *solved in the* Cm *space group (No. 8), refined with anisotropic displacement parameters. Thermal ellipsoids are drawn at 50% probability. Disordered sites are depicted with lower opacity. Colors: Fe, orange; Cl, green; N, blue; C, grey; H are omitted for clarity.*

2.42 Å and Cl–Fe–Cl angles between 108.8°–110.8°, compared to the 2.13–2.44 Å and 101.1°–122.4° ranges observed for entries in the Cambridge Structural Database containing the same species. The $[Fe(PcLH_3)Cl_2]^+$ complex structure obtained in the high-symmetry $C2/m$ space group is consistent with the observed features of the Cm model, although with lower standard uncertainties due to the reduced number of parameters.

Full crystallographic data have been deposited with the Cambridge Crystallographic Data Centre (CCDC No. 2404719) and can be obtained free of charge via `www.ccdc.cam.ac.uk/data_request/cif`, by emailing data_request@ccdc.cam.ac.uk, or by contacting The Cambridge Crystallographic Data Centre, 12 Union Road, Cambridge CB2 1EZ, UK; fax: +44 1223 336033. Credit: Giulia Taini.

Table A.20: *Summary of crystallographic data and refinement details for compound **C2a′**.*

CCDC No.	**2404719**
Formula	$C_{22}H_{36}Cl_8Fe_3N_8$
Formula weight	863.74
Crystal system	Monoclinic
Space group	$C2/m$
a [Å]	27.7537(10)
b [Å]	8.7587(4)
c [Å]	7.0757(3)
α [°]	90.00
β [°]	90.105(4)
γ [°]	90.00
V [Å^3]	1720.00(12)
Z	2
Radiation type	Cu-Kα ($\lambda = 1.54184$)
Temp. [K]	150(2)
ρ_{calc} [g cm^{-3}]	1.668
μ [mm^{-1}]	15.966
$F(000)$	527.5
Cryst. size [mm^3]	$0.38 \times 0.09 \times 0.07$
θ range [°]	3.1847–80.6721
Limiting indices	$-35 \leq h \leq 34$; $-8 \leq k \leq 10$; $-9 \leq l \leq 9$
Reflections collected/unique[a]	15600 / 1977 [$R_{\mathrm{int}} = 0.1024$, $R_\sigma = 0.0473$]
Data/restraints/parameters	1977 / 0 / 118
Completeness [%]	99.7
Final R indices ($I > 2\sigma(I)$)[b]	$R_1 = 0.0676$, $wR_2 = 0.1715$
R indices (all data)	$R_1 = 0.0839$, $wR_2 = 0.1914$
Goodness of fit[c] on F^2	1.032
Largest diff. peak and hole [Å^{-3}]	0.92 and −0.63

[a] $R_{\mathrm{int}} = \frac{\sum |F_0^2 - F_{0,\mathrm{mean}}^2|}{\sum F_0^2}$

[b] $R_1 = \frac{\sum ||F_0| - |F_c||}{\sum |F_0|}$, $wR_2 = \sqrt{\frac{\sum w(F_0^2 - F_c^2)^2}{\sum w(F_0^2)^2}}$

[c] $\mathrm{GooF} = \sqrt{\frac{S}{n-p}} = \sqrt{\frac{\sum w(F_0^2 - F_c^2)^2}{n-p}}$

A.6.2 C3 complexes

C3d ([Fe(PcLBn$_3$)Cl$_2$]. Single crystals of **C3d** suitable for X-ray diffraction were isolated by diffusion of diethyl ether vapors, in an acetonitrile solution of compound **C3d** (v/v 2:1). A golden-yellow, elongated scalenohedral crystal of **C3d** was mounted on a MiTeGen Microloop and measured at 150 K. Data were collected on a XtaLAB Synergy S diffractometer (Rigaku), equipped with Oxford Cryostream 1000 and a micro-focus sealed X-ray tube with copper radiation (Cu-Kα, $\lambda = 1.54184$ Å), with the generator working at 50 kV and 1 mA. Data collection, frame integration, and data reduction were carried out with *CrysAlis Pro7* version 1.171.42.54a, using an empirical absorption correction with spherical harmonics (SCALE3 ABSPACK). The structure was solved by dual space methods with *SHELXT-2015*[274] and refined by iterative cycles of full-matrix least-square routines against F^2 with *SHELXL-2018*[274] within the *WinGX* program suite.[275] All non-hydrogen atoms were refined using anisotropic thermal parameters, while the hydrogen atoms were modelled on idealized positions with $U_{iso} = 1.2\, U_{eq}$.

Compound **C3d** crystallizes in the monoclinic space group $C2/c$ (No. 15), as confirmed by systematic absences observed in the diffraction data. The formula unit contains one molecule of [Fe(PcLBn$_3$)Cl$_2$] (Figure A.59, Table A.21).

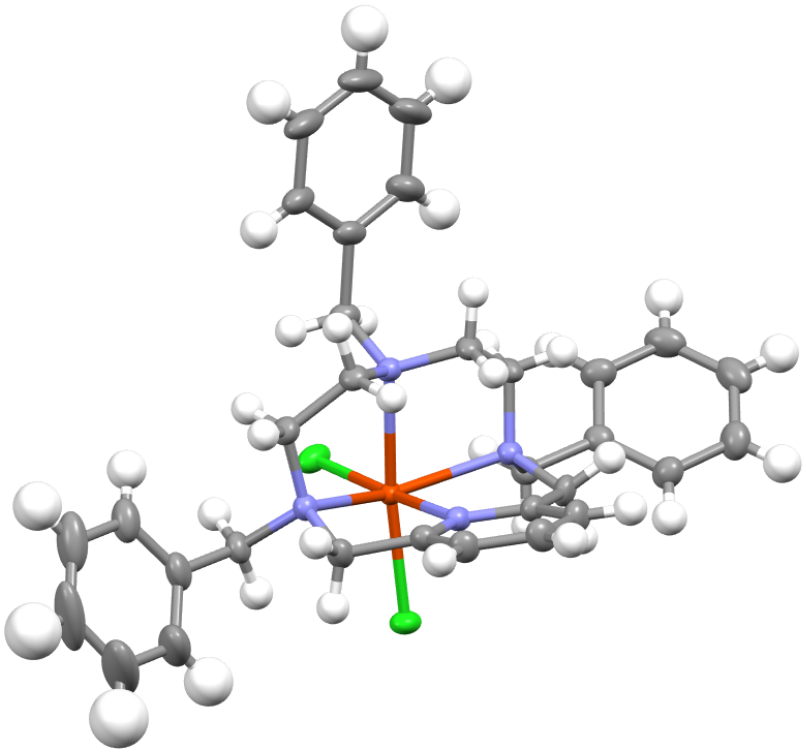

Figure A.59: *Molecular structure of [Fe(PcLBn$_3$)Cl$_2$] (**C3d**). Thermal ellipsoid are drawn at 50% probability. Colors: Fe, orange; Cl, green; N, blue; C, grey; H, white.*

Table A.21: *Summary of crystallographic data and refinement details for compound **C3d**.*

Parameter	**Value**
Formula	$C_{32}H_{36}Cl_2FeN_4$
Formula weight	603.40
Crystal system	Monoclinic
Space group	$C2/c$
a [Å]	17.19570(10)
b [Å]	23.74360(10)
c [Å]	16.08560(10)
α [°]	90.00
β [°]	99.7020(10)
γ [°]	90.00
V [Å^3]	6473.62(6)
Z	5
Radiation type	Cu-Kα ($\lambda = 1.54184$)
Temp. [K]	150(2)
ρ_{calc} [g cm^{-3}]	0.774
μ [mm^{-1}]	3.404
$F(000)$	1580
θ range [°]	3.204–80.061
Limiting indices	$-21 \leq h \leq 21$; $-26 \leq k \leq 30$; $-20 \leq l \leq 20$
Reflections collected/unique[a]	66435 / 7037 [$R_{\mathrm{int}} = 0.0511$, $R_\sigma = 0.0215$]
Data/restraints/parameters	7037 / 0 / 353
Completeness [%]	99.2
Final R indices ($I > 2\sigma(I)$)[b]	$R_1 = 0.0692$, $wR_2 = 0.2317$
R indices (all data)	$R_1 = 0.0704$, $wR_2 = 0.2335$
Goodness of fit[c] on F^2	1.082
Largest diff. peak and hole [Å^{-3}]	2.82 and −0.63

[a] $R_{\mathrm{int}} = \frac{\sum |F_0^2 - F_{0,\mathrm{mean}}^2|}{\sum F_0^2}$

[b] $R_1 = \frac{\sum ||F_0| - |F_c||}{\sum |F_0|}$, $wR_2 = \sqrt{\frac{\sum w(F_0^2 - F_c^2)^2}{\sum w(F_0^2)^2}}$

[c] GooF $= \sqrt{\frac{S}{n-p}} = \sqrt{\frac{\sum w(F_0^2 - F_c^2)^2}{n-p}}$

C3e ($[Fe(PcLBn_3)Br_2]$). Single crystals of **C3e** suitable for X-ray diffraction were isolated by diffusion of diethyl ether vapors, in an acetonitrile solution of compound **C3e** (v/v 2:1). A reddish, hemimorphic crystal of **C3e** was mounted on a glass fiber and measured at 293 K. Data were collected on a XtaLAB Synergy S diffractometer (Rigaku), equipped with Oxford Cryostream 1000 and a micro-focus sealed X-ray tube with copper radiation (Cu-Kα, λ = 1.54184 Å), with the generator working at 50 kV and 1 mA. Data collection, frame integration, and data reduction were carried out with *CrysAlis Pro7* version 1.171.42.54a, using an empirical absorption correction with spherical harmonics (SCALE3 ABSPACK). The structure was solved by dual space methods with *SHELXT-2015*[274] and refined by iterative cycles of full-matrix least-square routines against F^2 with *SHELXL-2018*[274] within the *WinGX* program suite.[275] All non-hydrogen atoms were refined using anisotropic thermal parameters, while the hydrogen atoms were modelled on idealized positions with $U_{iso} = 1.2\ U_{eq}$.

Compound **C3e** crystallizes in the triclinic space group $P\bar{1}$ (No. 2). The formula unit contains one molecule of $[Fe(PcLBn_3)Br_2]$ (Figure A.60, Table A.22).

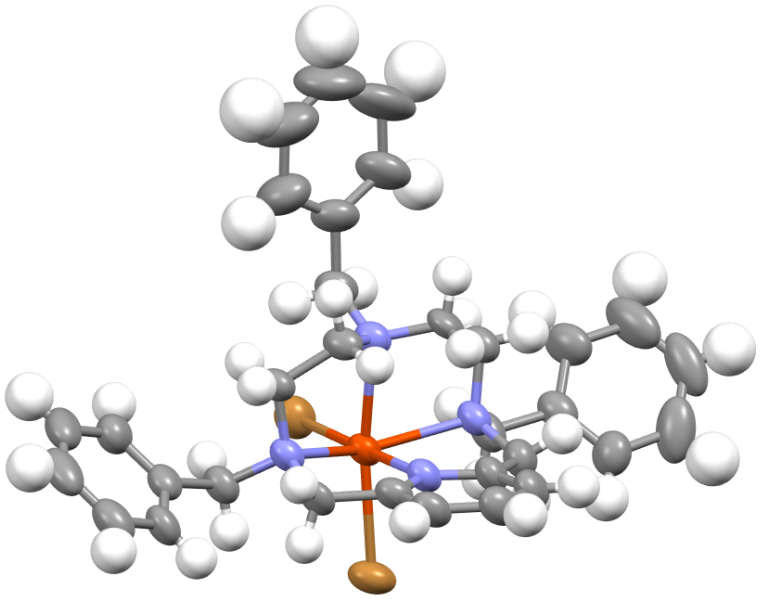

Figure A.60: *Molecular structure of $[Fe(PcLBn_3)Br_2]$ (**C3e**). Thermal ellipsoid are drawn at 50% probability. Colors: Fe, orange; Br, brown; N, blue; C, grey; H, white.*

C3f ($[Fe(PcLBn_3)(OTf)_2]$). A colorless, prism-like specimen of approximate dimensions 0.108 mm × 0.134 mm × 0.194 mm, was used for the X-ray crystallographic analysis. The X-ray intensity data were measured at 120 K (λ = 0.71073 Å).

A total of 307 frames were collected. The total exposure time was 1.28 hours. The frames were integrated with the Bruker SAINT software package using a narrow-frame algorithm. The integration of the data using a monoclinic unit cell yielded a total of 125260 reflections to a maximum θ angle of 27.48° (0.77 Åresolution), of

Table A.22: *Summary of crystallographic data and refinement details for compound **C3e**.*

Parameter	**Value**
Formula	$C_{32}H_{36}Br_2FeN_4$
Formula weight	692.32
Crystal system	Triclinic
Space group	$P\bar{1}$
a [Å]	9.1651(3)
b [Å]	11.2037(4)
c [Å]	17.9554(5)
α [°]	75.045(3)
β [°]	77.698(3)
γ [°]	69.295(3)
V [Å^3]	1651.01(10)
Z	4
Radiation type	Cu-Kα ($\lambda = 1.54184$)
Temp. [K]	293(2)
ρ_{calc} [g cm^{-3}]	0.693
μ [mm^{-1}]	0.357
$F(000)$	364
θ range [°]	4.306–76.972
Limiting indices	$-11 \leq h \leq 11$; $-14 \leq k \leq 14$; $-22 \leq l \leq 21$
Reflections collected/unique[a]	29691 / 6214 [$R_{\mathrm{int}} = 0.0945$, $R_\sigma = 0.0660$]
Data/restraints/parameters	6214 / 0 / 352
Completeness [%]	88.9
Final R indices ($I > 2\sigma(I)$)[b]	$R_1 = 0.0678$, $wR_2 = 0.2103$
R indices (all data)	$R_1 = 0.0925$, $wR_2 = 0.2323$
Goodness of fit[c] on F^2	1.048
Largest diff. peak and hole [Å^{-3}]	1.38 and −0.90

[a] $R_{\mathrm{int}} = \frac{\sum |F_0^2 - F_{0,\mathrm{mean}}^2|}{\sum F_0^2}$

[b] $R_1 = \frac{\sum ||F_0| - |F_c||}{\sum |F_0|}$, $wR_2 = \sqrt{\frac{\sum w(F_0^2 - F_c^2)^2}{\sum w(F_0^2)^2}}$

[c] GooF $= \sqrt{\frac{S}{n-p}} = \sqrt{\frac{\sum w(F_0^2 - F_c^2)^2}{n-p}}$

which 7963 were independent (average redundancy 15.730, completeness = 100.0%, R_{int} = 4.28%, R_{sig} = 1.52%) and 7408 (93.03%) were greater than $2\sigma(F^2)$. The final cell constants of a = 11.8621(5) Å, b = 15.6143(6) Å, c = 19.2733(8) Å, β = 103.448(2)°, volume = 3471.9(2) Å^3, are based upon the refinement of the XYZ-centroids of 9558 reflections above 20 $\sigma(I)$ with 4.519° < 2θ < 56.47°. Data were corrected for absorption effects using the Multi-Scan method (SADABS). The ratio of minimum to maximum apparent transmission was 0.957. The calculated minimum and maximum transmission coefficients (based on crystal size) are 0.8860 and 0.9340.

The structure was solved and refined using the Bruker SHELXTL Software Package, using the space group $P2_1/c$, with Z = 4 for the formula unit, $C_{34}H_{36}F_6FeN_4O_6S_2$. The final anisotropic full-matrix least-squares refinement on F^2 with 478 variables converged at R_1 = 2.61%, for the observed data and wR_2 = 7.79% for all data. The goodness-of-fit was 1.117. The largest peak in the final difference electron density synthesis was 0.530 e$^-$ Å^{-3} and the largest hole was −0.483 e$^-$ Å^{-3} with an RMS deviation of 0.121 e$^-$ Å^{-3}. On the basis of the final model, the calculated density was 1.589 g cm^{-3} and F(000), 1712 e$^-$ (credit: Martin Zábranský, Figure A.61, Table A.23).

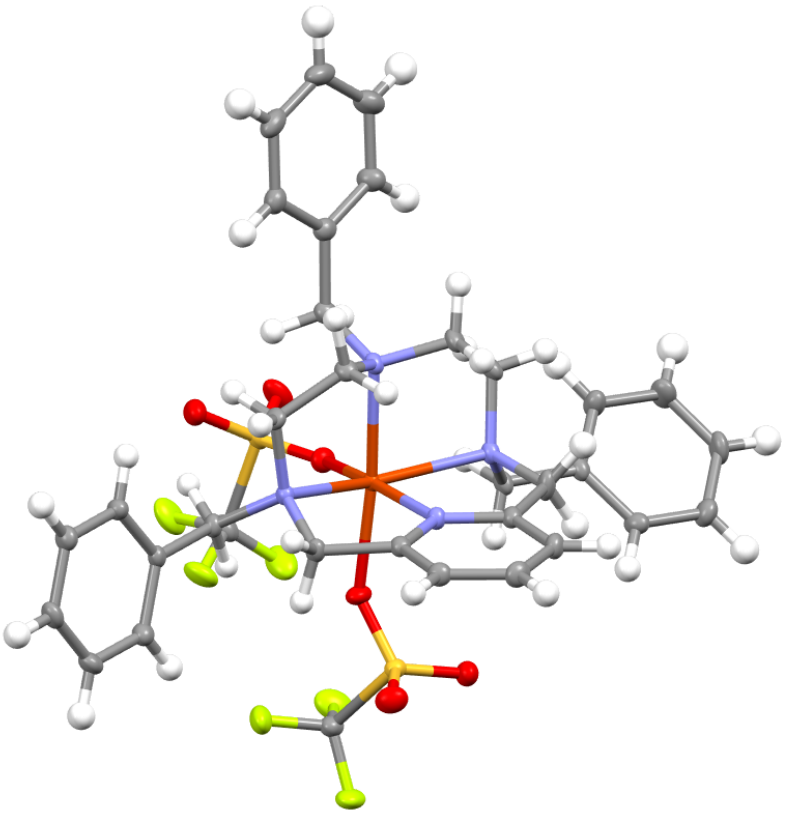

Figure A.61: *Molecular structure of* $[Fe(PcLBn_3)(OTf)_2]$ (***C3f***). *Thermal ellipsoid are drawn at 50% probability. Colors: Fe, orange; O, red; S, yellow; F, green; N, blue; C, grey; H, white.*

Table A.23: *Summary of crystallographic data and refinement details for compound **C3f**.*

Parameter	**Value**
Formula	$C_{34}H_{36}F_6FeN_4O_6S_2$
Formula weight	830.64
Crystal system	Monoclinic
Space group	$P2_1/c$
a [Å]	11.8621(5)
b [Å]	15.6143(6)
c [Å]	19.2733(8)
α [°]	90.00
β [°]	103.448(2)
γ [°]	90.00
V [Å^3]	3471.9(2)
Z	4
Radiation type	Mo-Kα ($\lambda = 0.71073$)
Temp. [K]	120(2)
ρ_{calc} [g cm^{-3}]	1.589
μ [mm^{-1}]	0.639
$F(000)$	1712
Cryst. size [mm^3]	$0.108 \times 0.134 \times 0.194$
θ range [°]	2.17–27.48
Limiting indices	$-15 \leq h \leq 15$; $-20 \leq k \leq 19$; $-25 \leq l \leq 25$
Reflections collected/unique[a]	125260 / 7963 [$R_{\mathrm{int}} = 0.0428$]
Data/restraints/parameters	7963 / 0 / 478
Completeness [%]	100.0
Final R indices ($I > 2\sigma(I)$)[b]	$R_1 = 0.0261$, $wR_2 = 0.0706$
R indices (all data)	$R_1 = 0.0293$, $wR_2 = 0.0779$
Goodness of fit[c] on F^2	1.117
Largest diff. peak and hole [Å^{-3}]	0.53 and −0.483

[a] $R_{\mathrm{int}} = \frac{\sum |F_0^2 - F_{0,\mathrm{mean}}^2|}{\sum F_0^2}$

[b] $R_1 = \frac{\sum ||F_0| - |F_c||}{\sum |F_0|}$, $wR_2 = \sqrt{\frac{\sum w(F_0^2 - F_c^2)^2}{\sum w(F_0^2)^2}}$

[c] $\mathrm{GooF} = \sqrt{\frac{S}{n-p}} = \sqrt{\frac{\sum w(F_0^2 - F_c^2)^2}{n-p}}$

A.7 UV-VIS spectra of complexes C2a-c

The next graph (Figure A.62) includes all the Gaussian curves that were used to fit the experimental data of the UV-VIS spectra of complexes **C2a-c**.

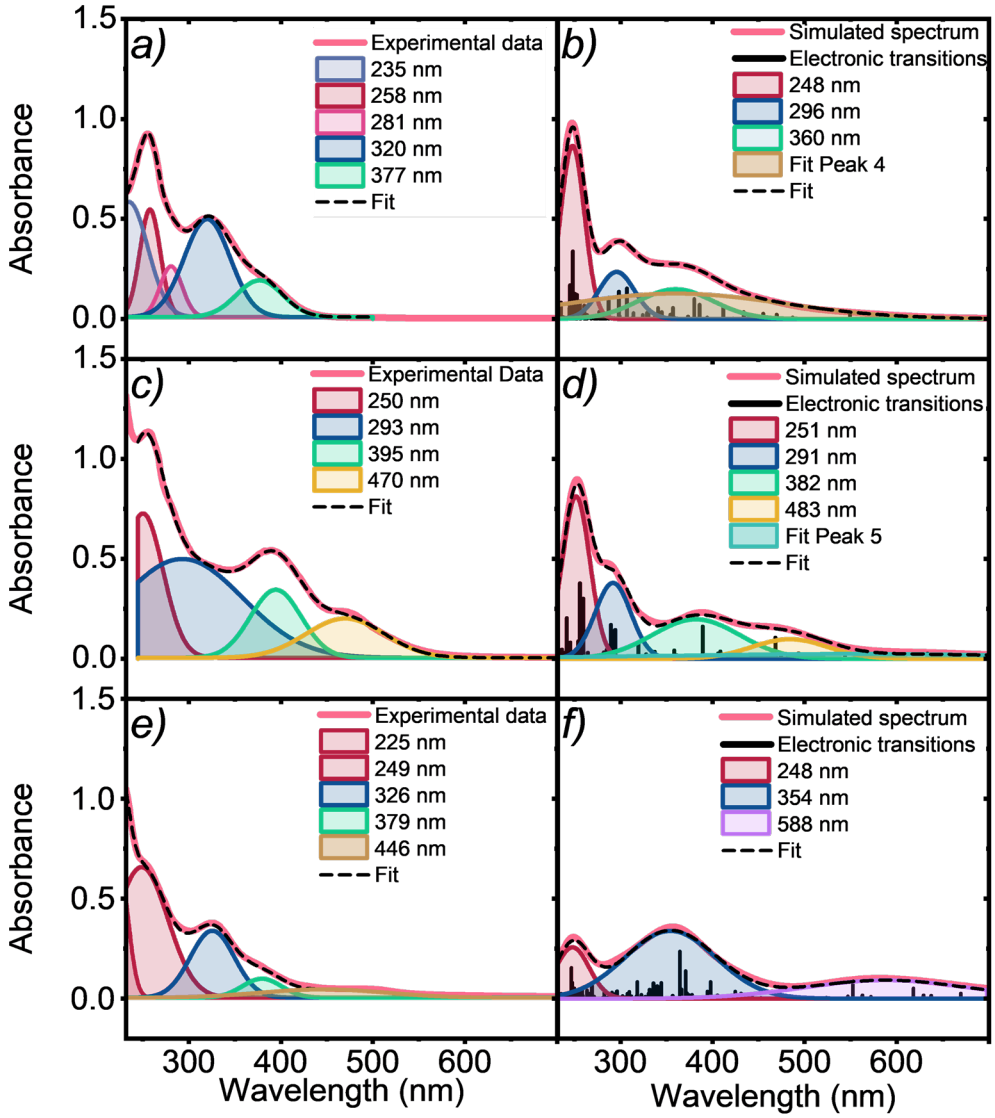

Figure A.62: *UV-VIS experimental (left) and theoretical (right) spectra for* ***C2a*** *(top) (a and b, respectively),* ***C2b*** *(middle) (c and d), and* ***C2c*** *(bottom) (e and f) complexes. These plots display all the Gaussian curves that were used to fit the experimental data are displayed.*

A.8 Energies, spin, DFT functionals and basis set for calculations involving compounds C2a-c.

Energies in kcal/mol. Credits: Fausto Cargnoni and Mario Italo Trioni.

Table A.24

1a	
Functional	OPBE
Basis set	6-31G(d,p)
Calculation	Gas phase / opt
Spin	**Energy (kcal/mol)**
5/2	0.0
3/2	13.1
1/2	13.2
Functional	OPBE
Basis set	6-31G(d,p)
Calculation	Solvent / opt
Spin	**Energy (kcal/mol)**
5/2	0.0
3/2	13.2
1/2	10.2
Functional	OPBE
Basis set	6-31G(d,p)
Calculation	Gas phase / opt + ZPE
Spin	**Energy (kcal/mol)**
5/2	0.0
3/2	13.2
1/2	14.1
Functional	OPBE
Basis set	6-31G(d,p)
Calculation	Solvent / opt + ZPE
Spin	**Energy (kcal/mol)**
5/2	0.0
3/2	13.6
1/2	11.7

Continues on next page

Table A.24 – continued from previous page

Functional	OPBE
Basis set	cc-pVTZ
Calculation	Gas phase / opt
Spin	**Energy (kcal/mol)**
5/2	0.0
3/2	10.3
1/2	9.5
Functional	OPBE
Basis set	cc-pVTZ
Calculation	Solvent / opt
Spin	**Energy (kcal/mol)**
5/2	0.0
3/2	9.7
1/2	6.1
Functional	OPBE
Basis set	cc-pVTZ
Calculation	Gas phase / opt + ZPE
Spin	**Energy (kcal/mol)**
5/2	0.0
3/2	10.5
1/2	10.5
Functional	OPBE
Basis set	cc-pVTZ
Calculation	Solvent / opt + ZPE
Spin	**Energy (kcal/mol)**
5/2	0.0
3/2	9.9
1/2	7.4
Functional	ωB97X
Basis set	cc-pVTZ
Calculation	Gas phase / geom(OPBE)
Spin	**Energy (kcal/mol)**
5/2	0.0
3/2	11.5
1/2	13.4

Continues on next page

Table A.24 – continued from previous page

Functional	ωB97X
Basis set	cc-pVTZ
Calculation	Gas phase / opt
Spin	**Energy (kcal/mol)**
5/2	0.0
3/2	11.5
1/2	12.2

Table A.25

C2b	
Functional	OPBE
Basis set	6-31G(d,p)
Calculation	Gas phase / opt
Spin	**Energy (kcal/mol)**
5/2	0.0
3/2	10.5
1/2	11.1
Functional	ωB97X
Basis set	cc-pVTZ
Calculation	Gas phase / geom(OPBE)
Spin	**Energy (kcal/mol)**
5/2	0.0
3/2	10.6
1/2	14.4
Functional	ωB97X
Basis set	cc-pVTZ
Calculation	Gas phase / opt
Spin	**Energy (kcal/mol)**
5/2	0.0
3/2	9.4
1/2	11.4

Table A.26

C2c	
Functional	OPBE
Basis set	6-31G(d,p)
Calculation	Gas phase / opt
Spin	**Energy (kcal/mol)**
5/2	0.0
3/2	13.9
1/2	26.0
Functional	ωB97X
Basis set	cc-pVTZ
Calculation	Gas phase / geom(OPBE)
Spin	**Energy (kcal/mol)**
5/2	0.0
3/2	11.1
1/2	17.2
Functional	ωB97X
Basis set	cc-pVTZ
Calculation	Gas phase / opt
Spin	**Energy (kcal/mol)**
5/2	0.0
3/2	11.7
1/2	16.8

A.9 Stability of radicals involved in the homolytic Fe–X bond dissociation in C2a, C2b and C2c

Energies in kcal/mole. Data obtained with the 6-31G(d,p) basis set. OPBE data affected by high instability in the convergence procedure is reported in italic. CCSD: coupled Cluster with Singles and Doubles. CISD: Configurations Interaction with Single and Double excitations. Credits: Fausto Cargnoni and Mario Italo Trioni.

Table A.27: $H^{\bullet} + Cl^{\bullet} \longrightarrow HCl$

Method	Gas phase	Gas + ZPE	Solvent	Solvent + ZPE
DFT/OPBE	−106.8	−102.5	−108.5	−104.2
CCSD	−97.4		−98.7	
CISD	−95.5	−91.1	−96.9	−92.5

Table A.28: $H^{\bullet} + Br^{\bullet} \longrightarrow HBr$

Method	Gas phase	Gas + ZPE	Solvent	Solvent + ZPE
DFT/OPBE	−96.0	−92.1	−97.0	−93.1
CCSD	−88.1		−89.0	
CISD	−80.5	−76.6	−81.5	−77.6

Table A.29: $H^{\bullet} + {}^{\bullet}OTf \longrightarrow HOTf$

Method	Gas phase	Gas + ZPE	Solvent	Solvent + ZPE
DFT/OPBE	*−103.6*	*−95.3*	*−107.8*	*−99.7*
CCSD	−113.9		−118.6	
CISD	−108.9	−100.6	−113.5	−105.2

A.10 NMR spectra

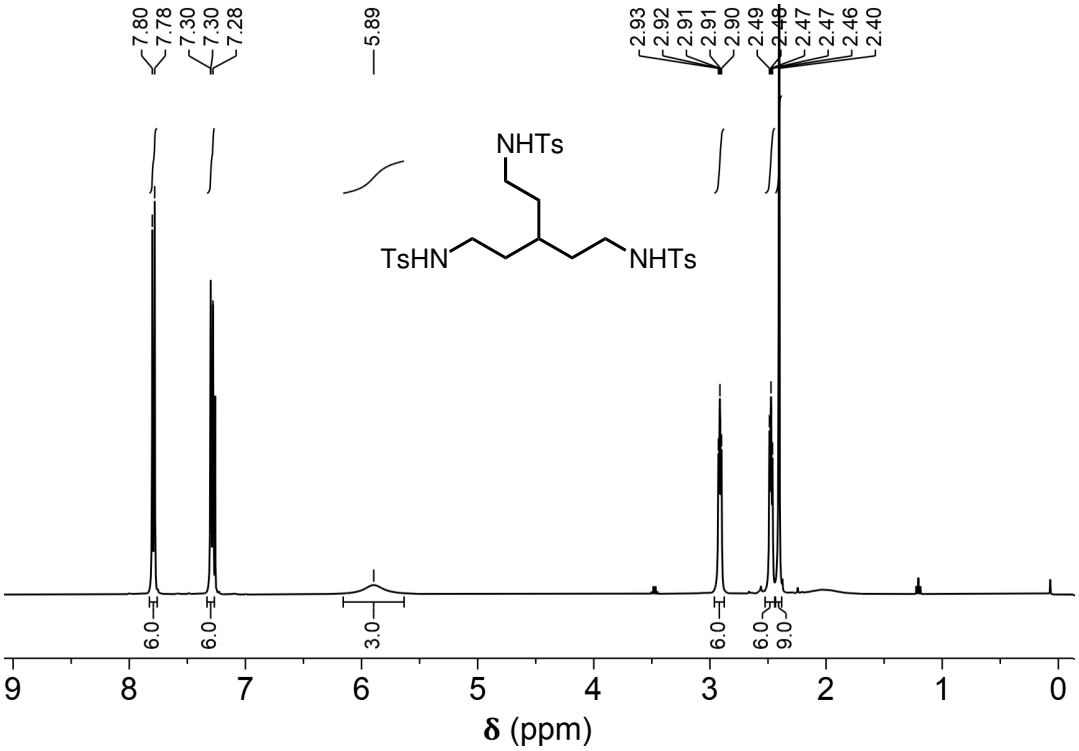

Figure A.63: *^{1}H-NMR spectrum of **1**.*

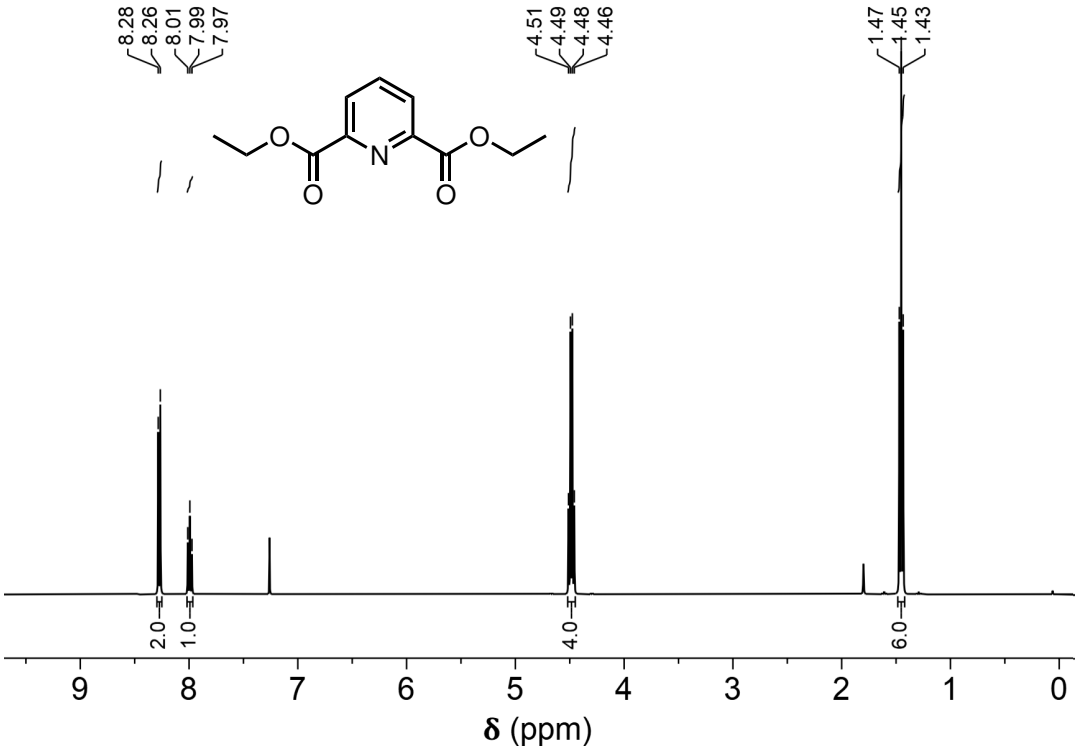

Figure A.64: *^{1}H-NMR spectrum of **2**.*

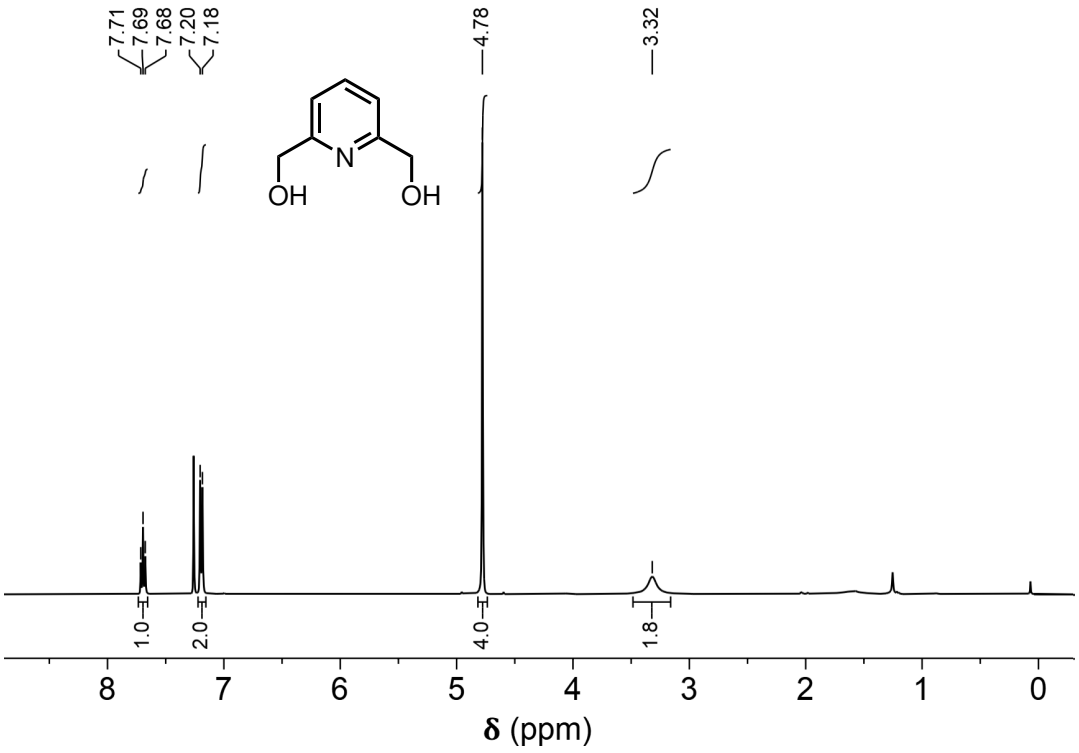

Figure A.65: *^{1}H-NMR spectrum of **3**.*

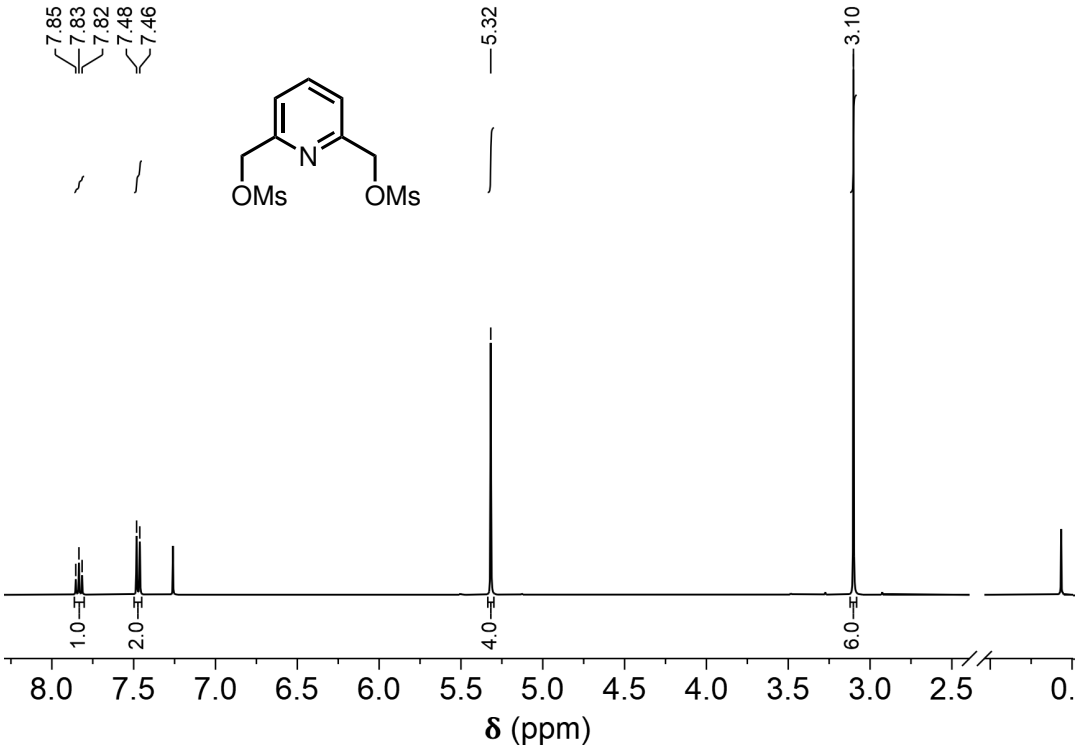

Figure A.66: *^{1}H-NMR spectrum of **4**.*

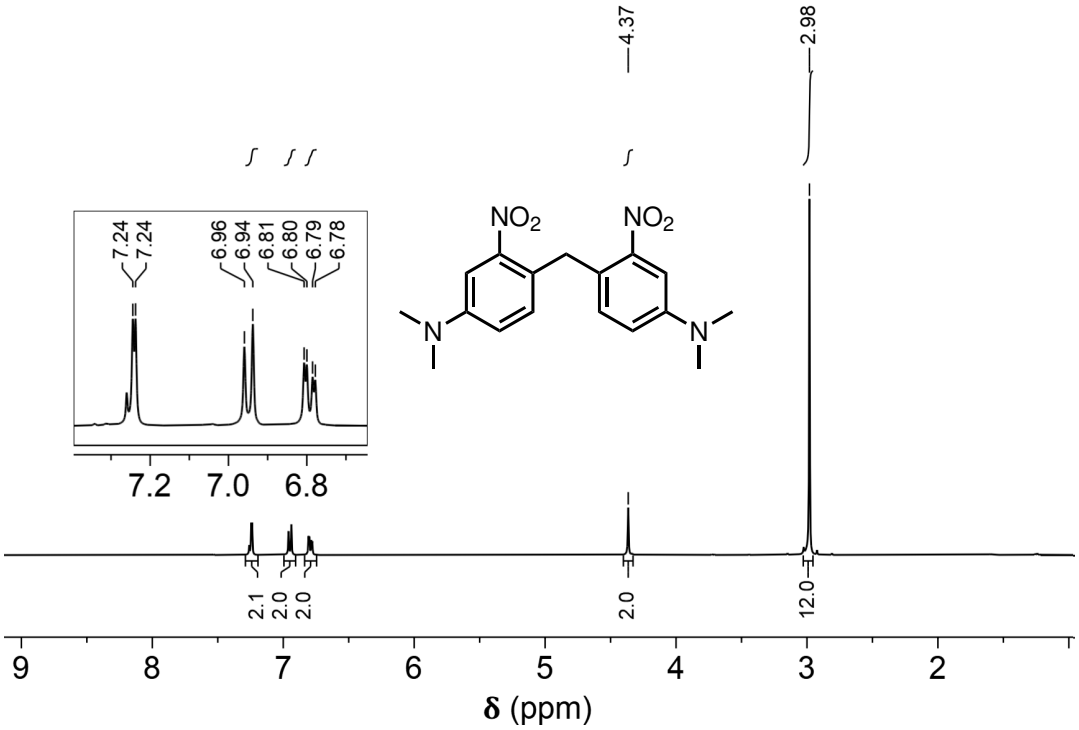

Figure A.67: *^{1}H-NMR spectrum of **5**.*

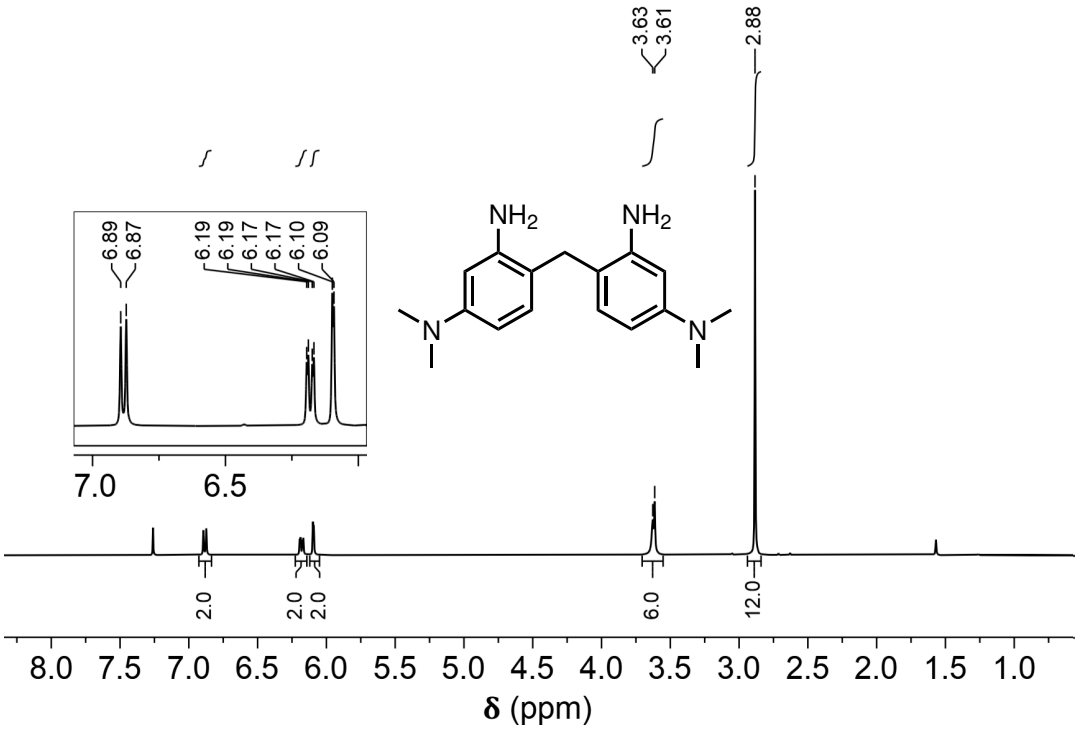

Figure A.68: *^{1}H-NMR spectrum of **6**.*

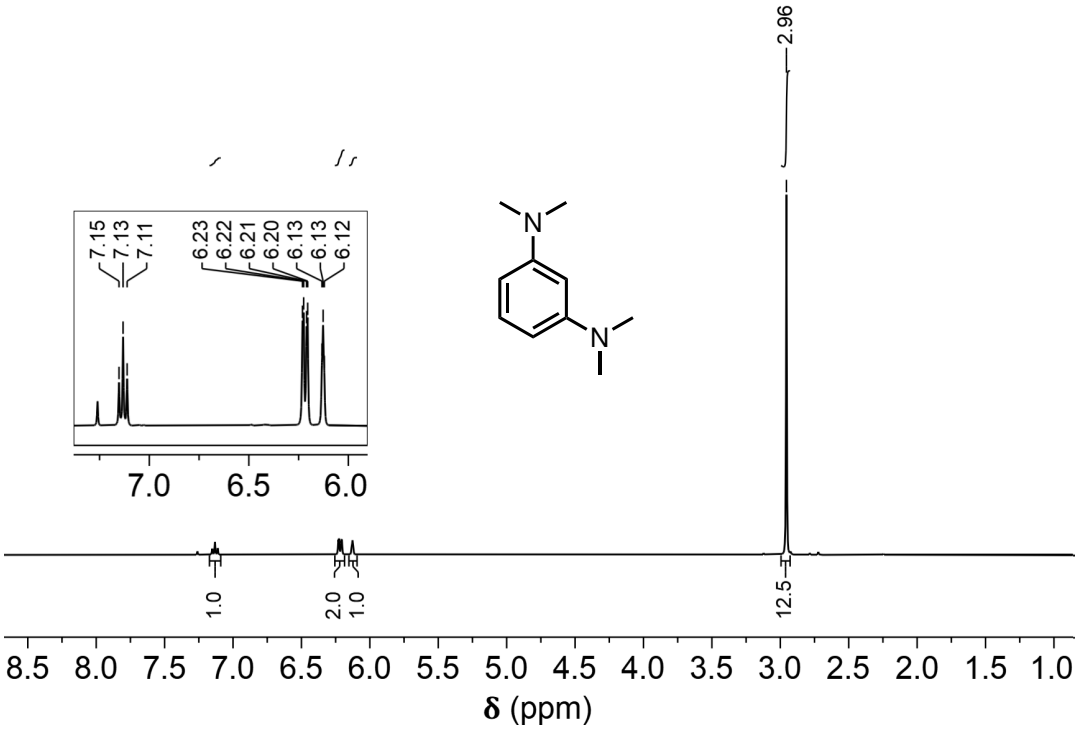

Figure A.69: *^{1}H-NMR spectrum of* ***7****.*

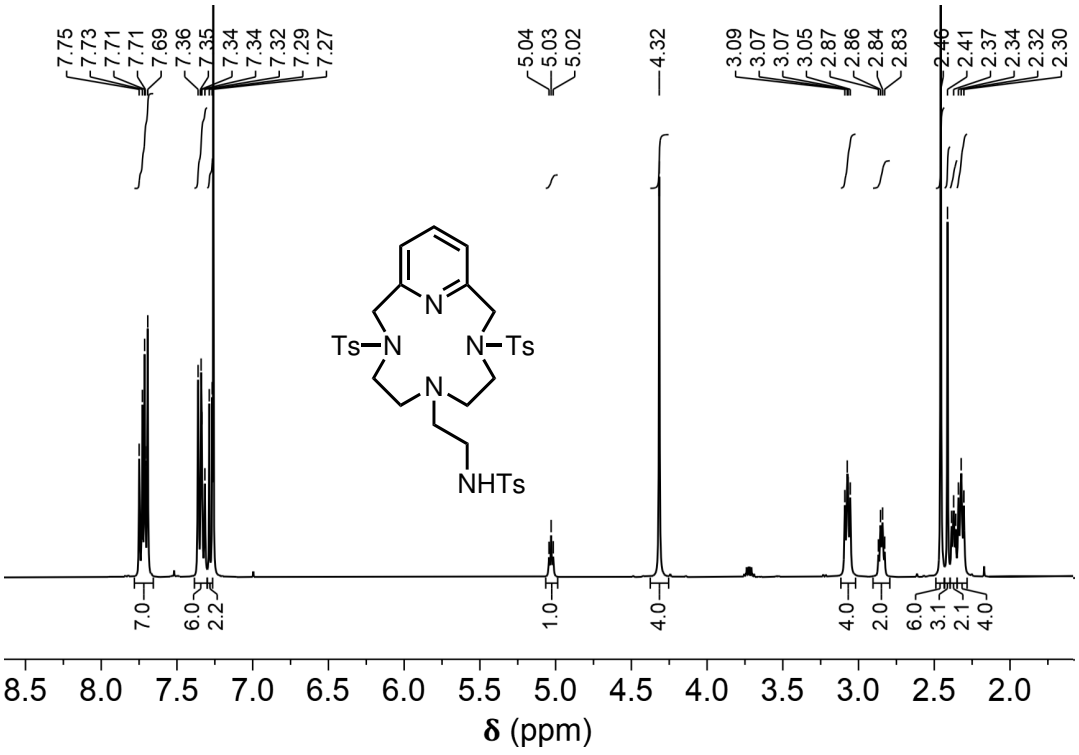

Figure A.70: *^{1}H-NMR spectrum of* ***L1****.*

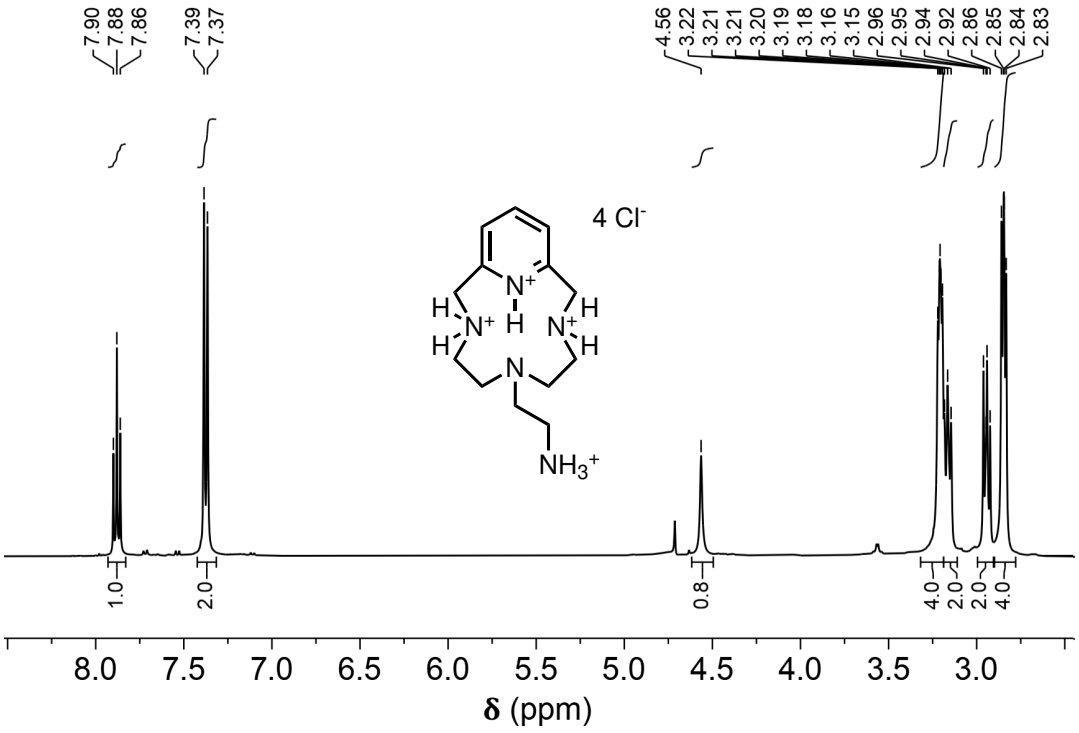

Figure A.71: *^{1}H-NMR spectrum of **L2 · 4 HCl**.*

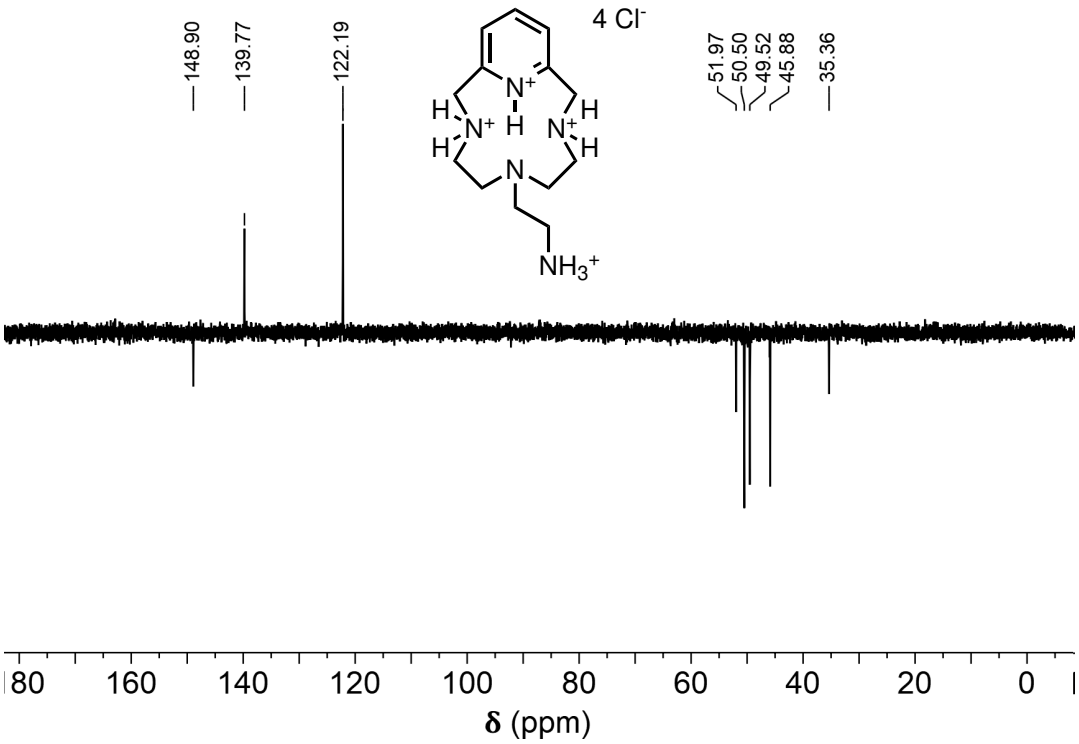

Figure A.72: *^{13}C APT NMR spectrum of **L2 · 4 HCl** (primary and tertiary carbons are positive peaks, secondary and quaternary carbons are negative peaks).*

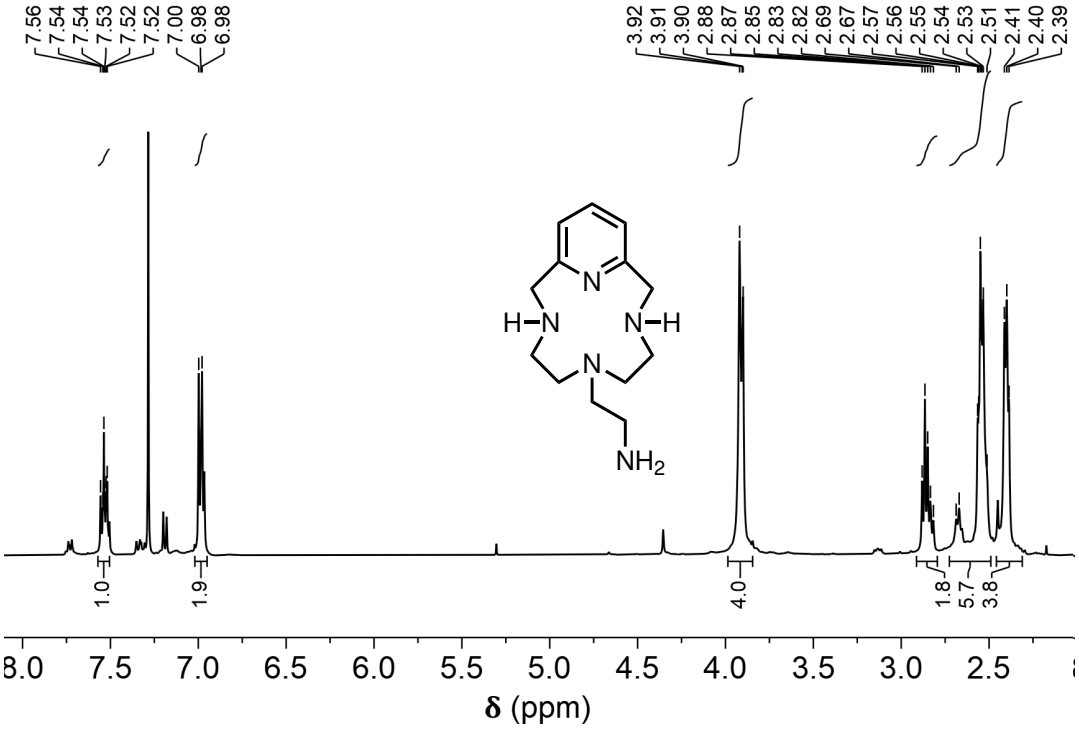

Figure A.73: *^{1}H-NMR spectrum of **L2**.*

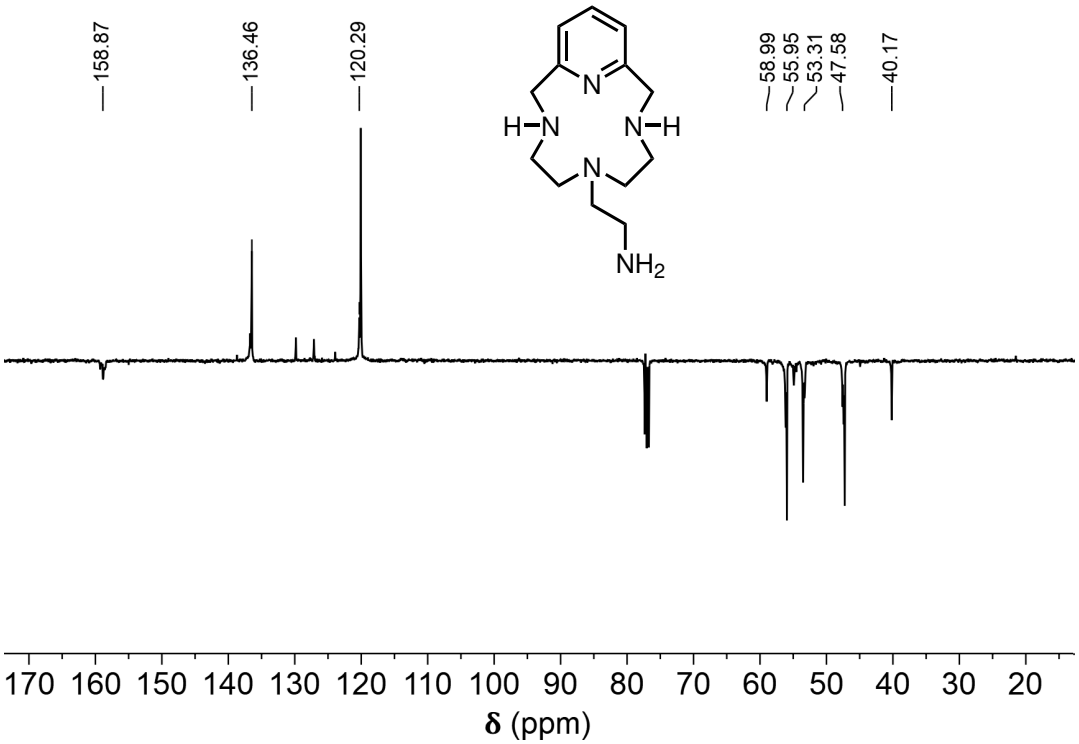

Figure A.74: *^{13}C APT NMR spectrum of **L2** (primary and tertiary carbons produce positive peaks, secondary and quaternary carbons produce negative peaks).*

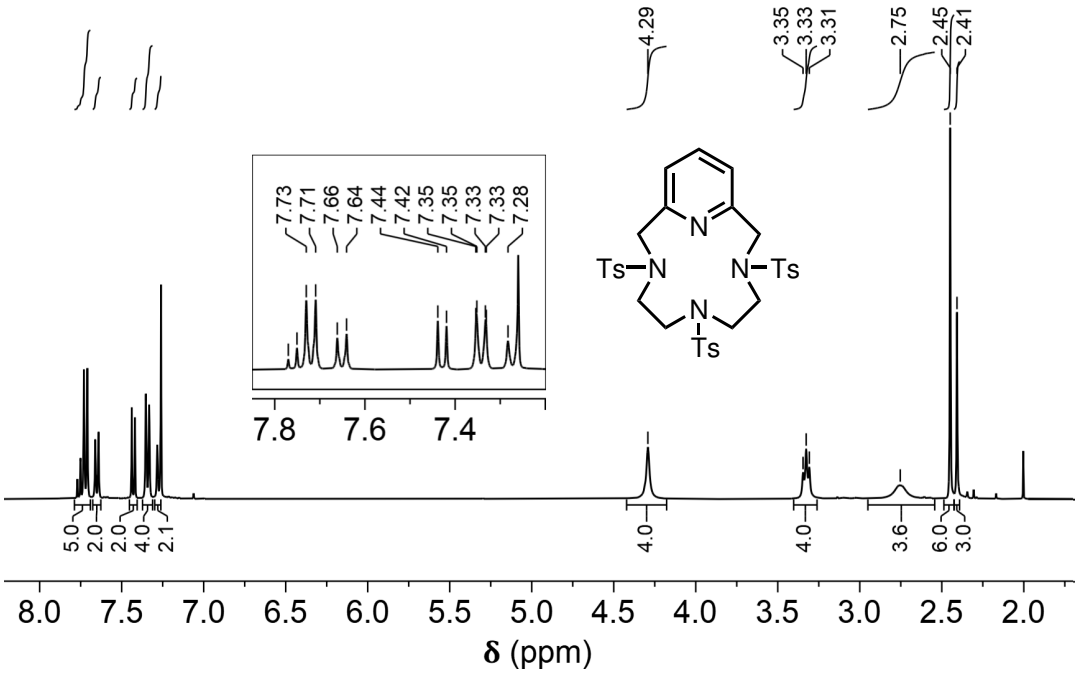

Figure A.75: *^{1}H-NMR spectrum of **L3**.*

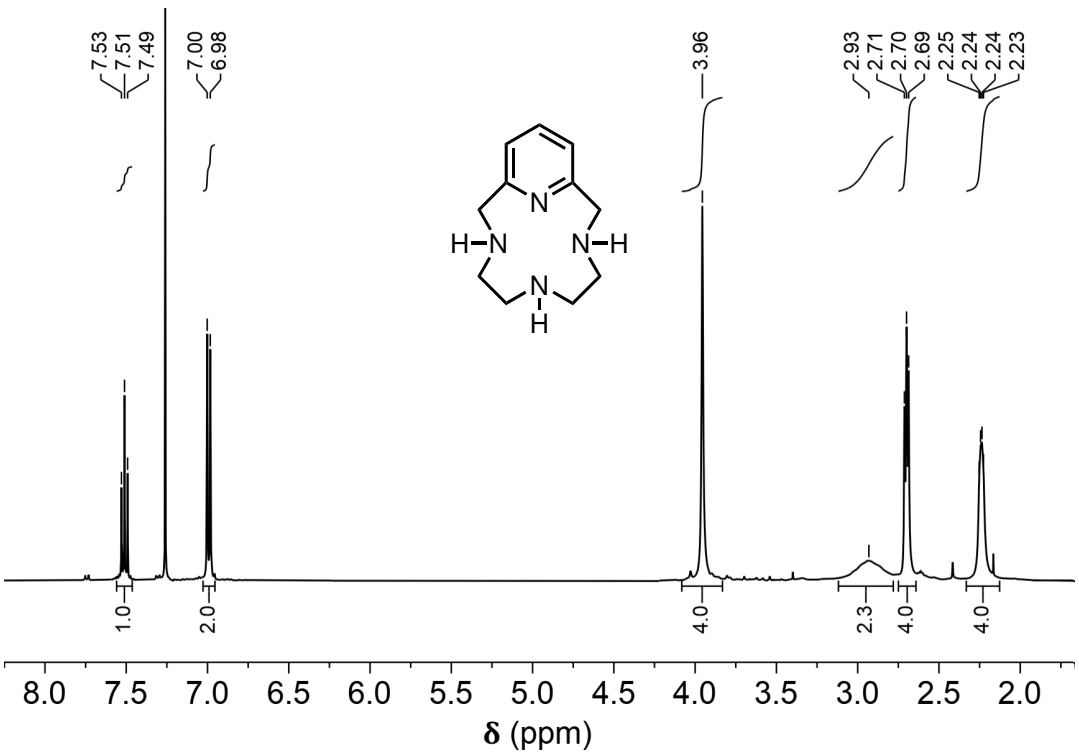

Figure A.76: *^{1}H-NMR spectrum of **L4**.*

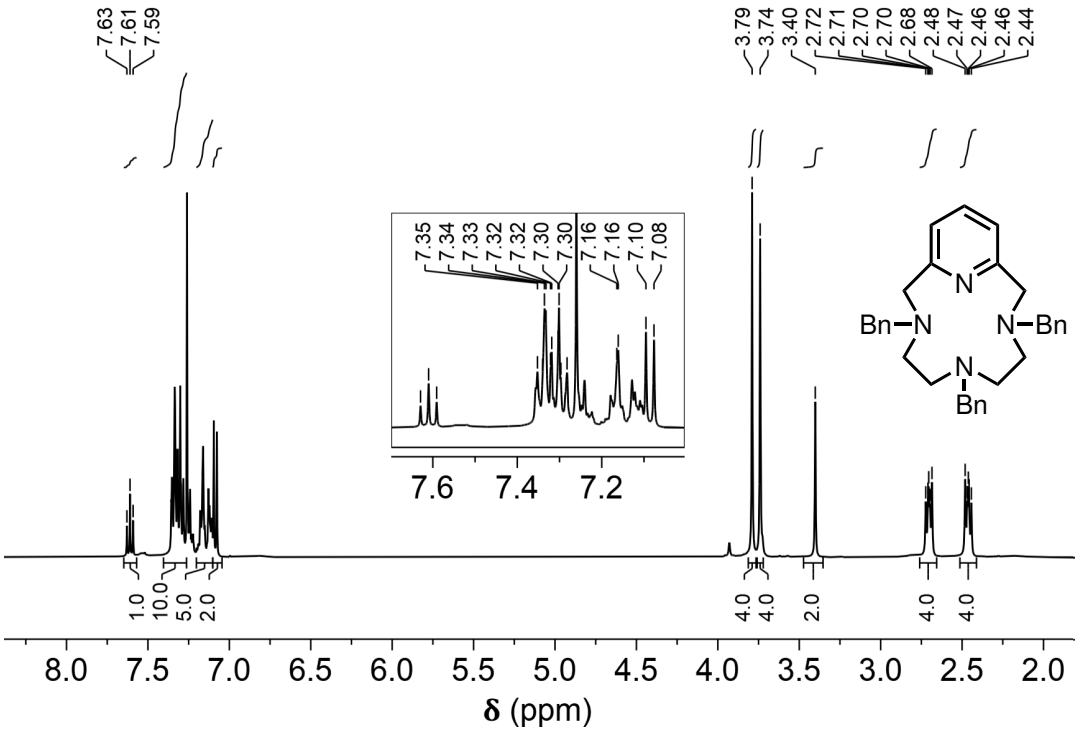

Figure A.77: *^{1}H-NMR spectrum of **L5**.*

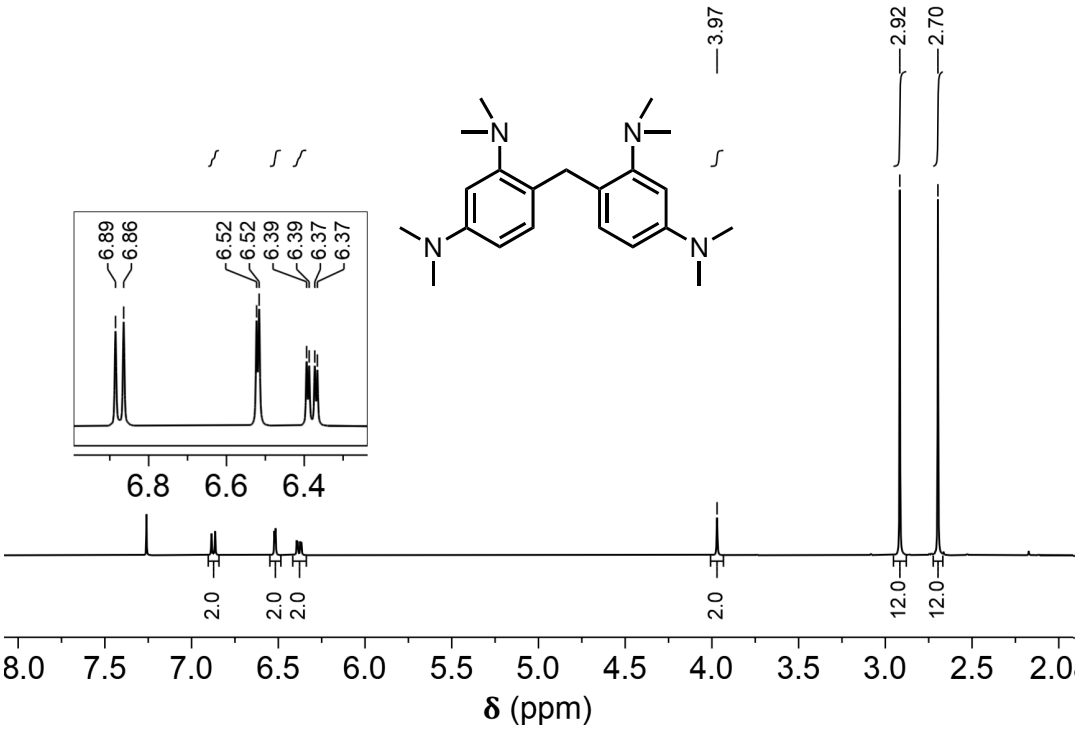

Figure A.78: *^{1}H-NMR spectrum of **L6**.*

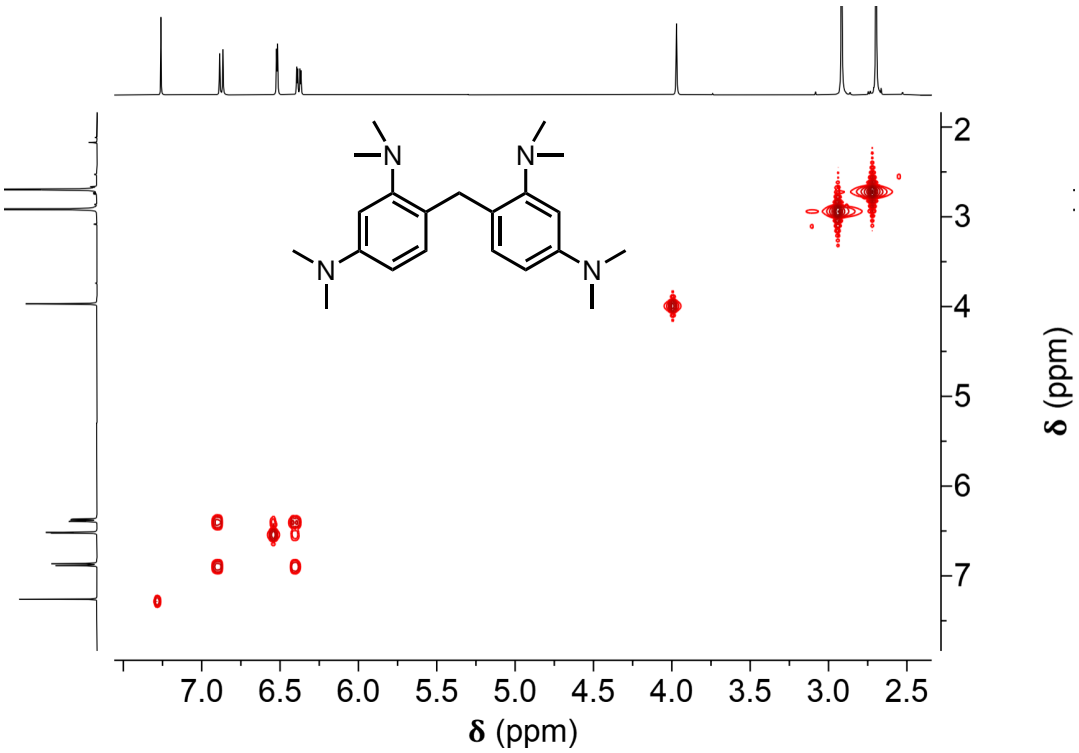

Figure A.79: *^{1}H COSY NMR spectrum of **L6**.*

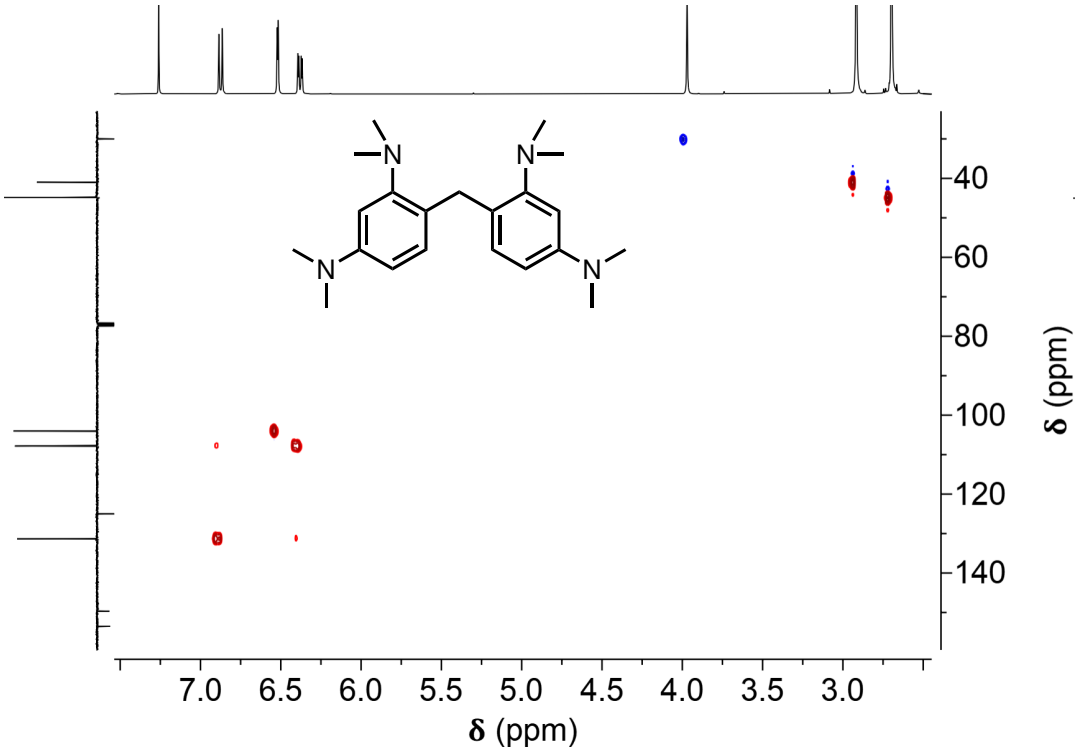

Figure A.80: *^{1}H-^{13}C HSQC NMR spectrum of **L6** (short range, primary and tertiary carbons produce red peaks, while secondary carbons produce blue peaks).*

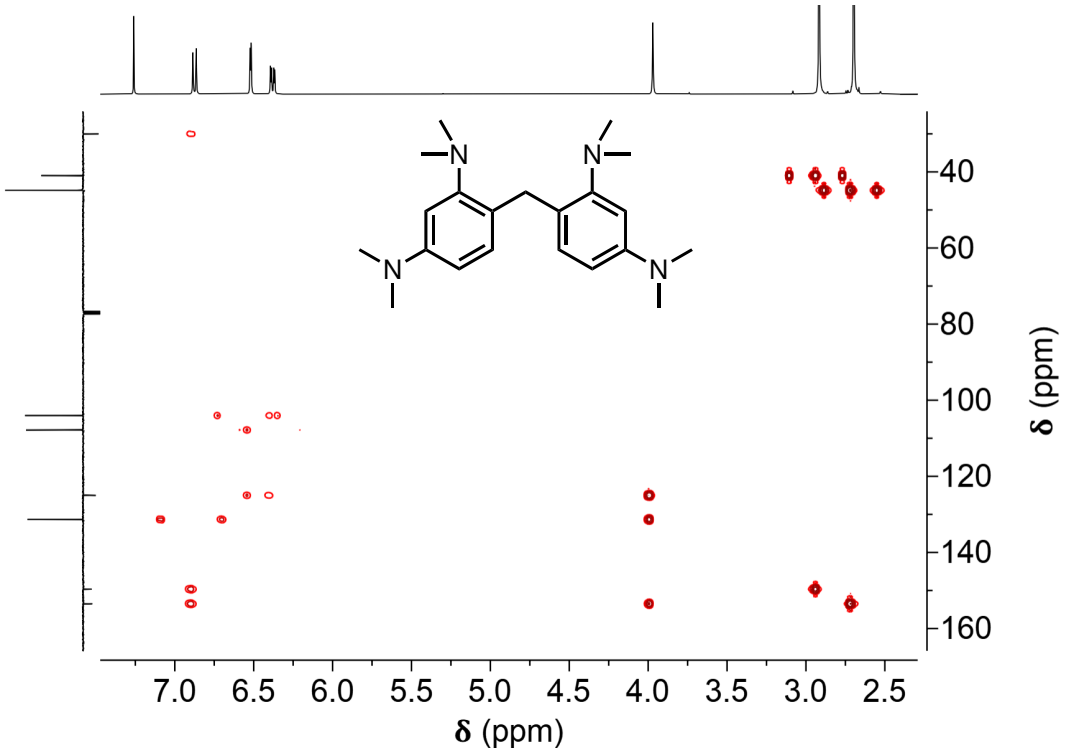

Figure A.81: *^{1}H-^{13}C HMBC NMR spectrum of **L6** (long range).*

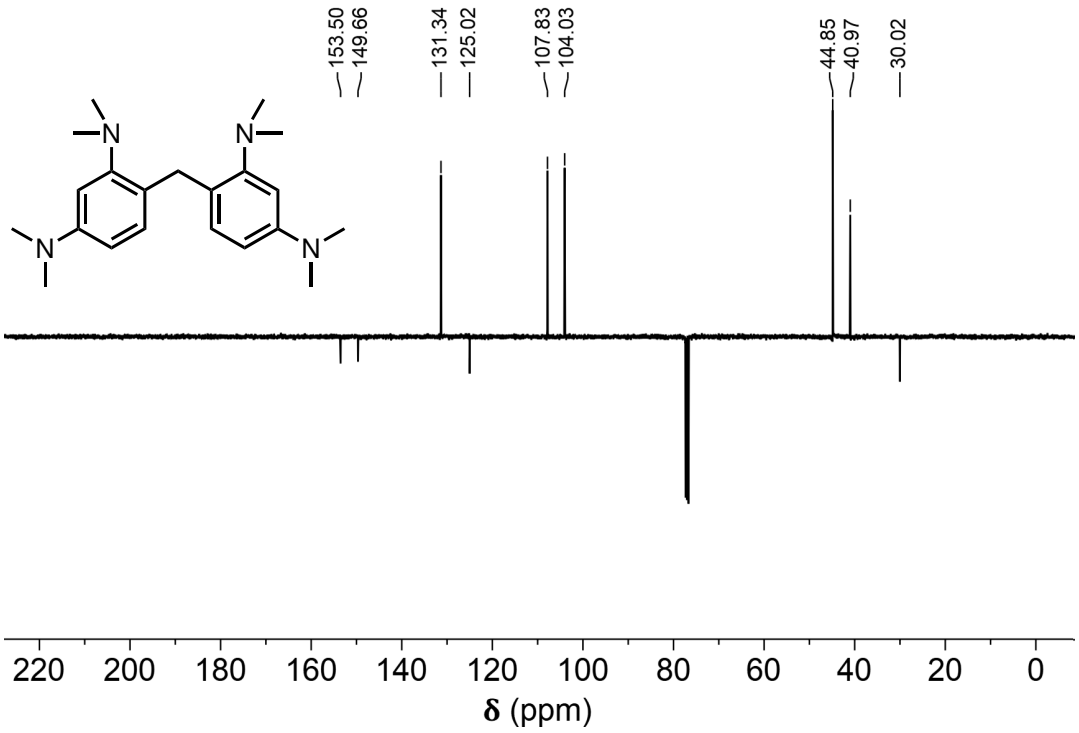

Figure A.82: *^{13}C APT NMR spectrum of **L6** (primary and tertiary carbons produce positive peaks, secondary and quaternary carbons produce negative peaks).*

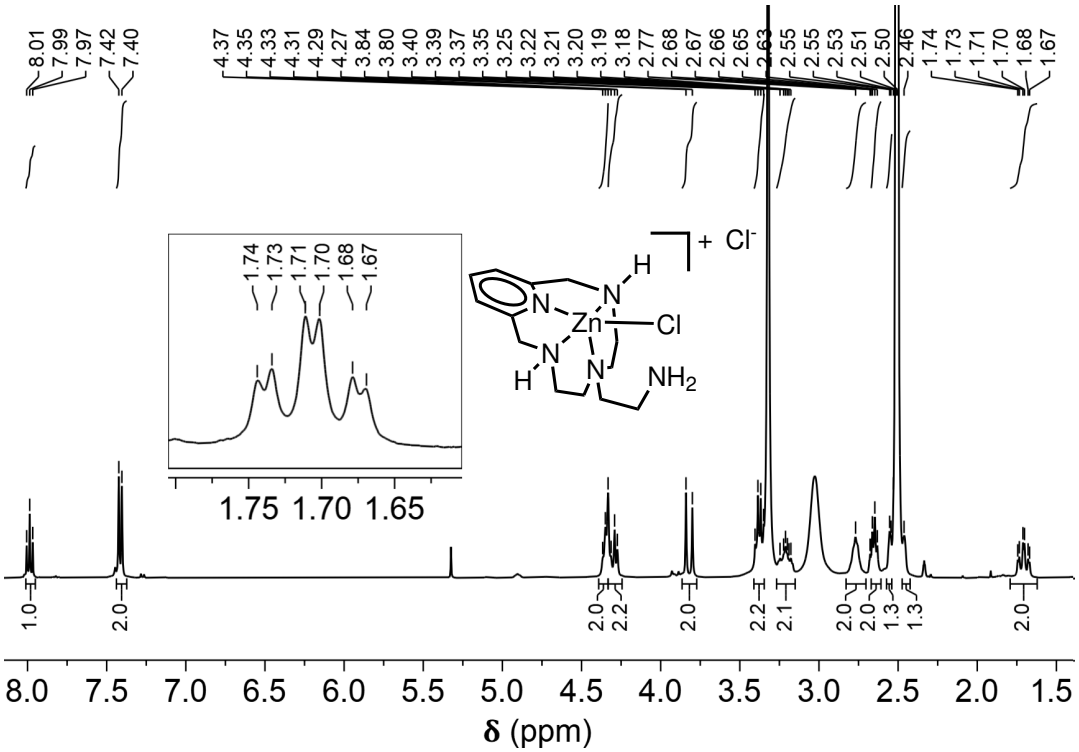

Figure A.83: *^{1}H-NMR spectrum of **C1a**.*

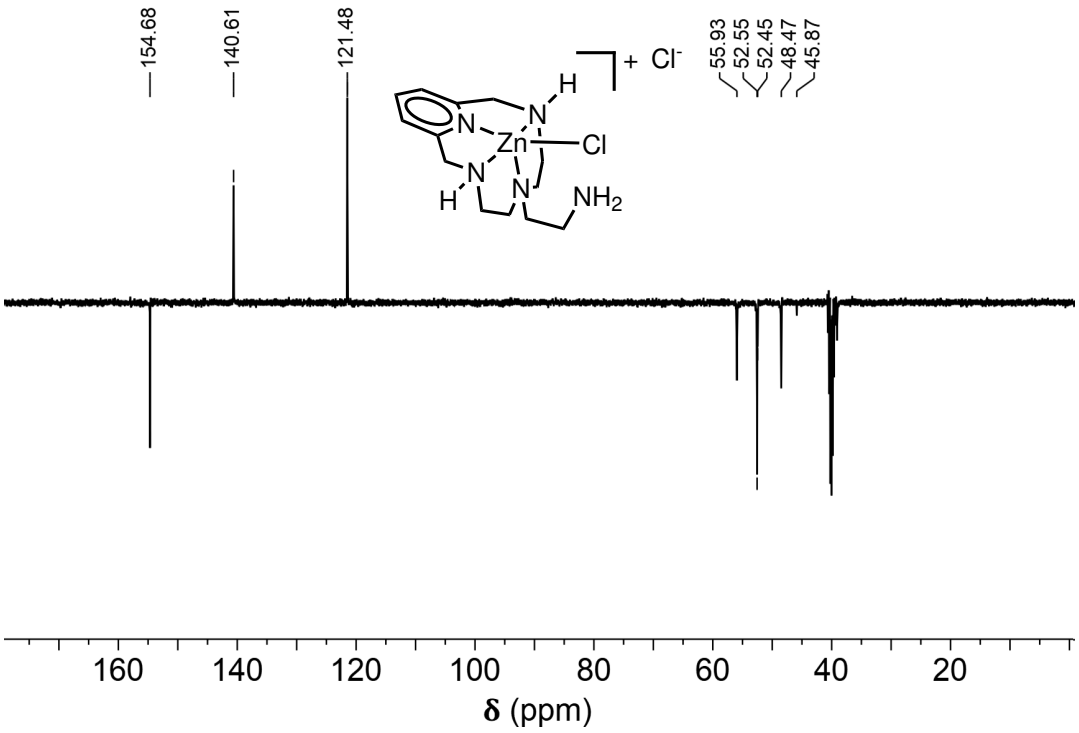

Figure A.84: *^{13}C APT NMR spectrum of **C1a** (primary and tertiary carbons produce positive peaks, secondary and quaternary carbons produce negative peaks).*

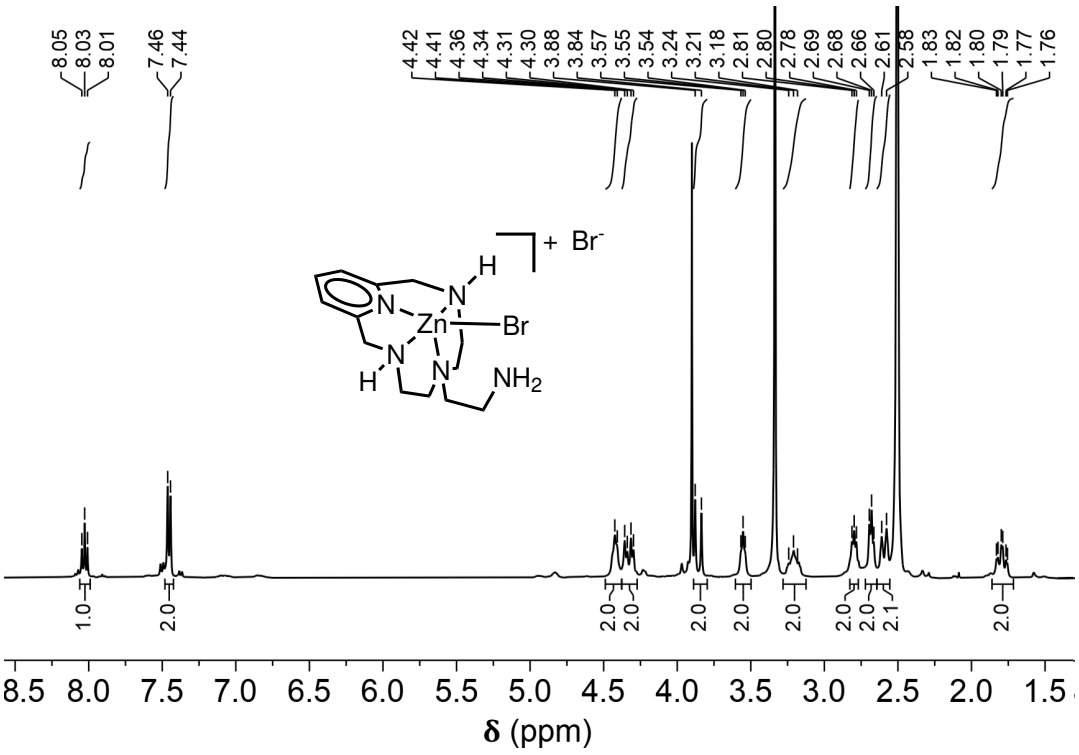

Figure A.85: *^{1}H-NMR spectrum of **C1b**.*

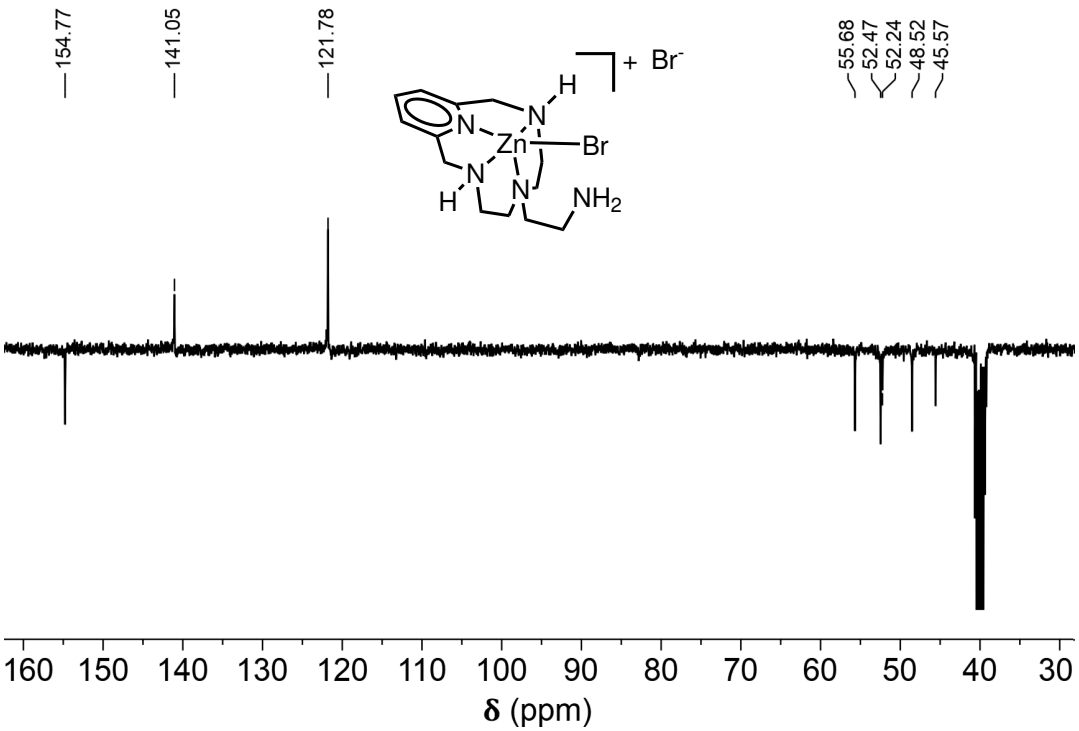

Figure A.86: *^{13}C APT NMR spectrum of **C1b*** (*primary and tertiary carbons produce positive peaks, secondary and quaternary carbons produce negative peaks*).

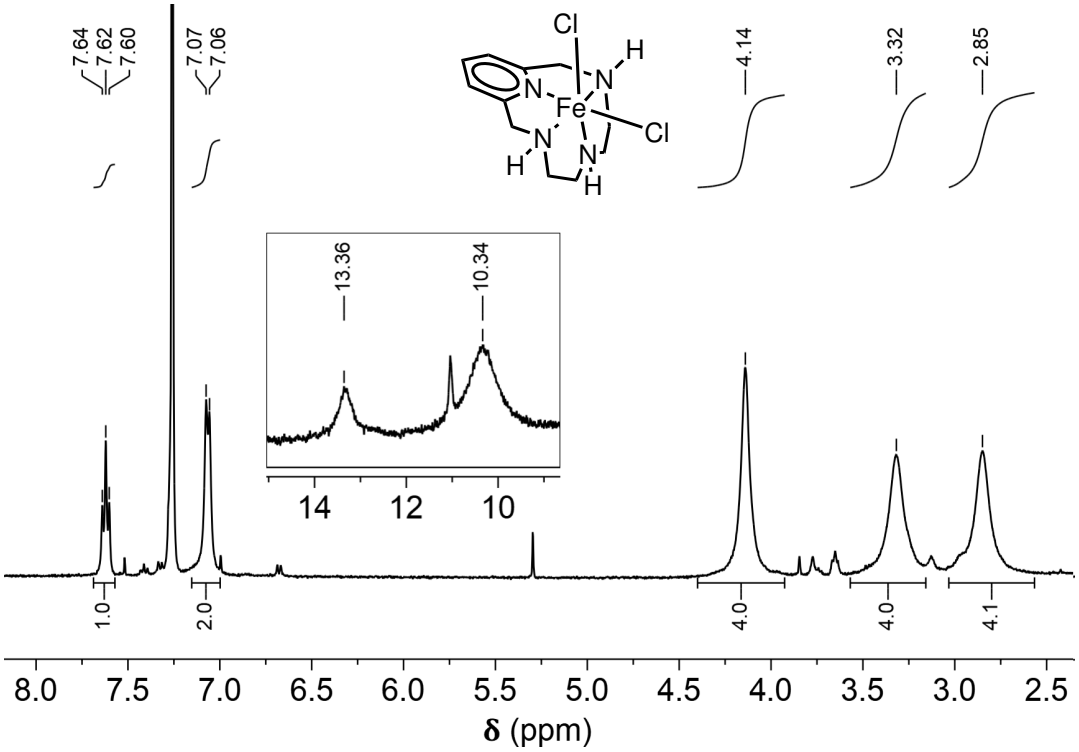

Figure A.87: *^{1}H-NMR spectrum of **C2d**.*

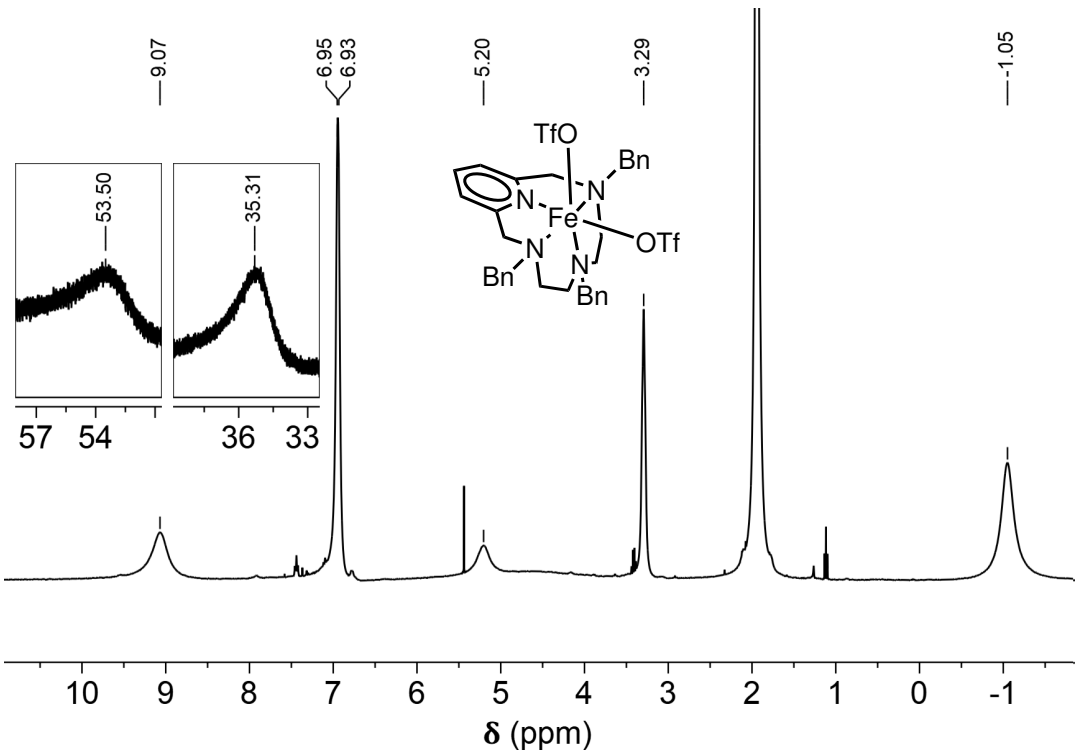

Figure A.88: *^{1}H-NMR spectrum of **C3f**.*

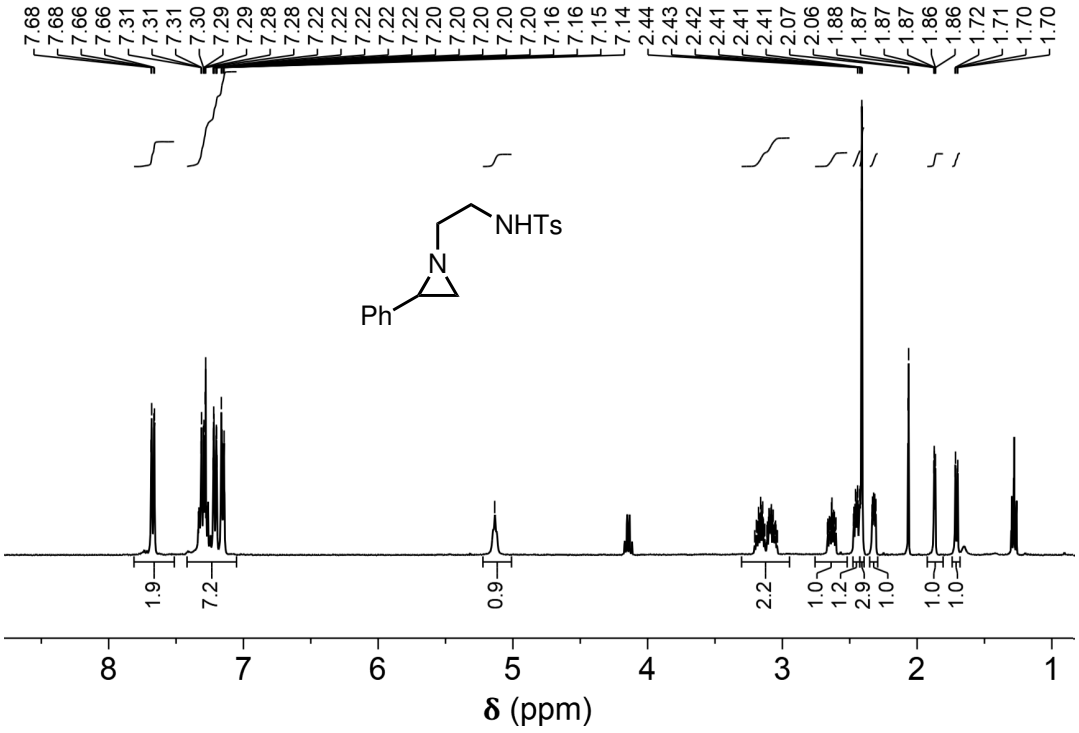

Figure A.89: *^{1}H-NMR spectrum of **S1o**.*

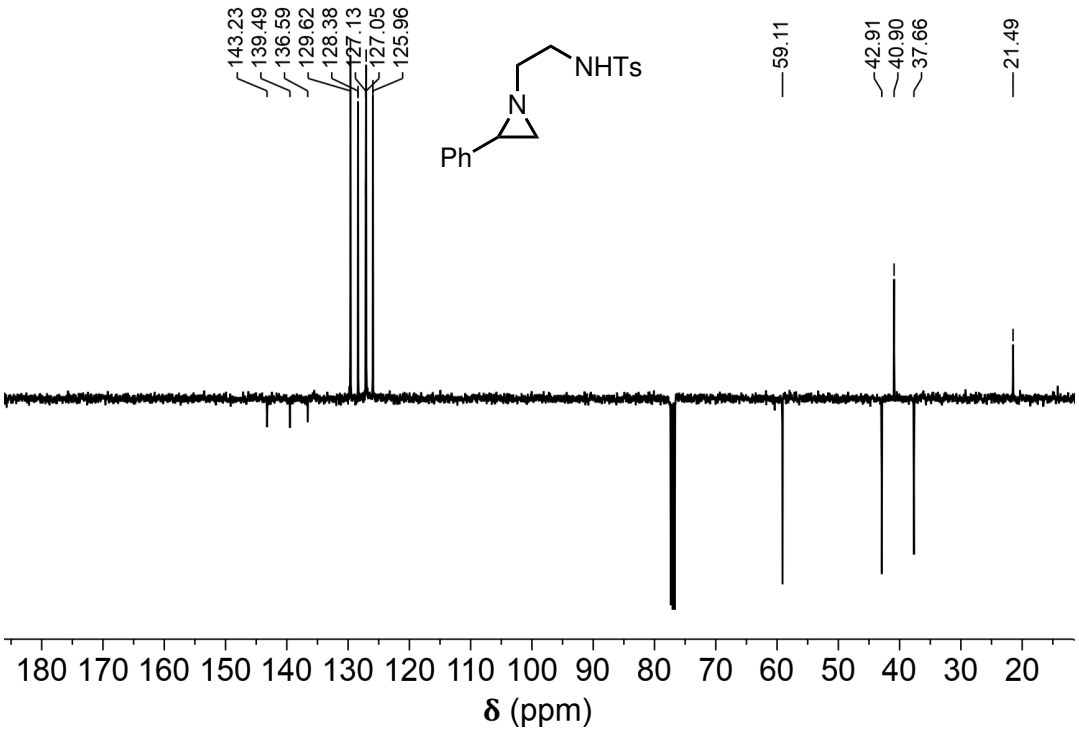

Figure A.90: *^{13}C APT NMR spectrum of **S1o*** (*primary and tertiary carbons produce positive peaks, secondary and quaternary carbons produce negative peaks*).

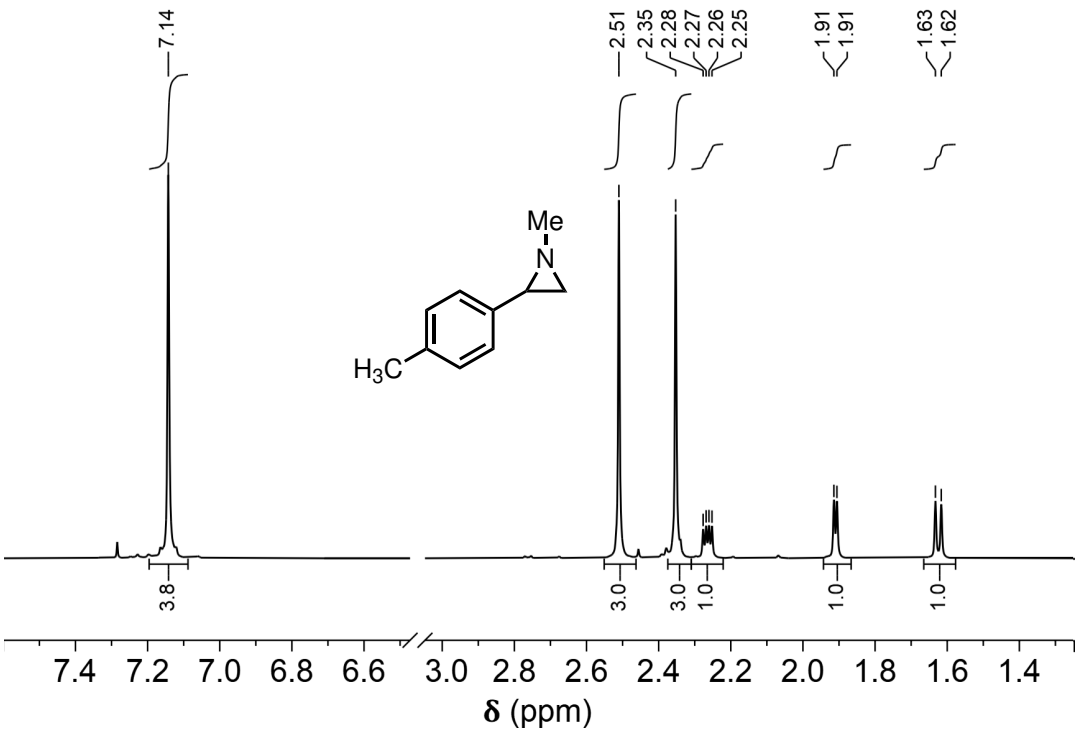

Figure A.91: *^{1}H-NMR spectrum of **S1p**.*

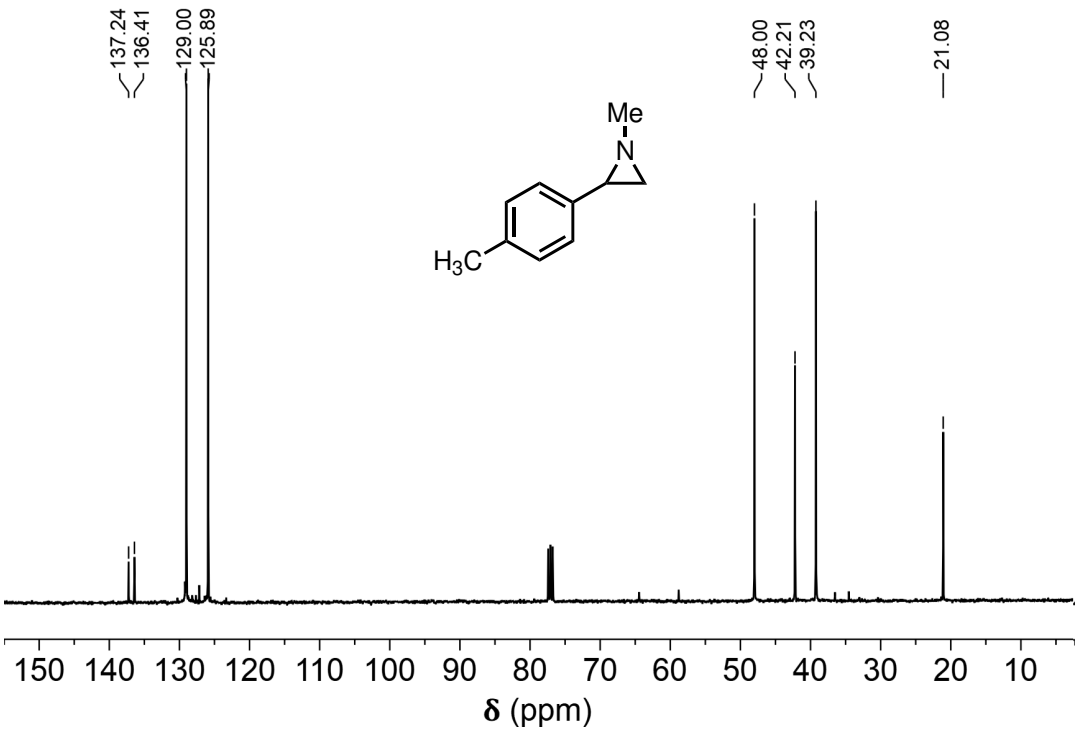

Figure A.92: *^{13}C-NMR spectrum of **S1p**.*

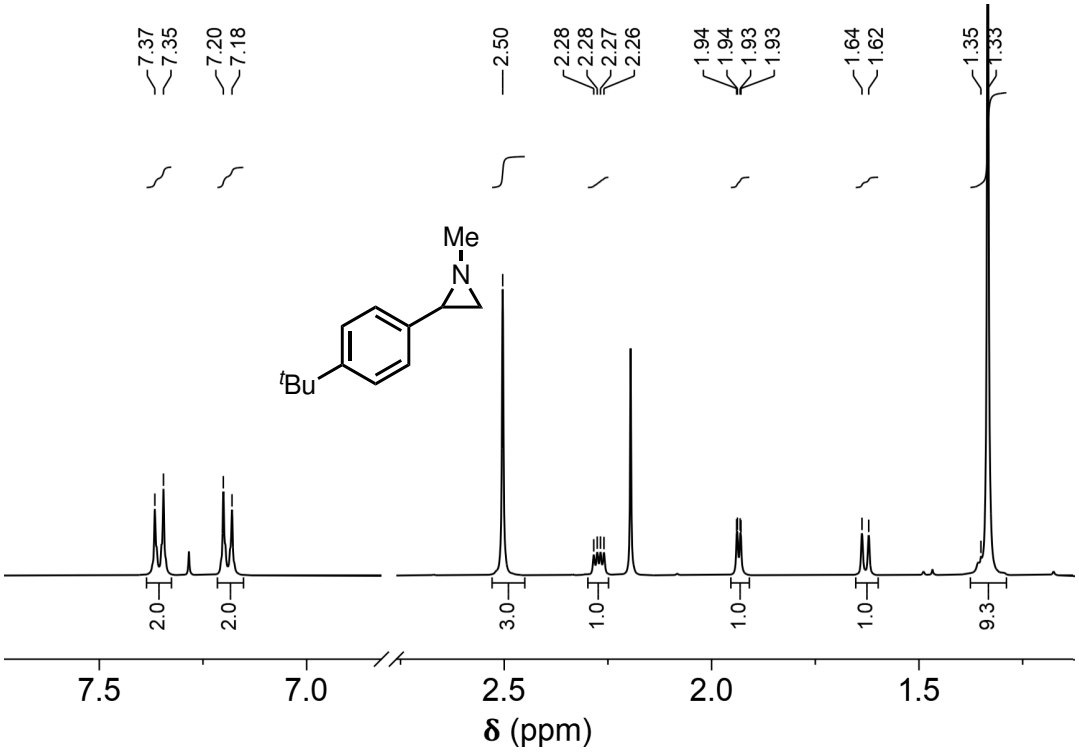

Figure A.93: *^{1}H-NMR spectrum of **S1q**.*

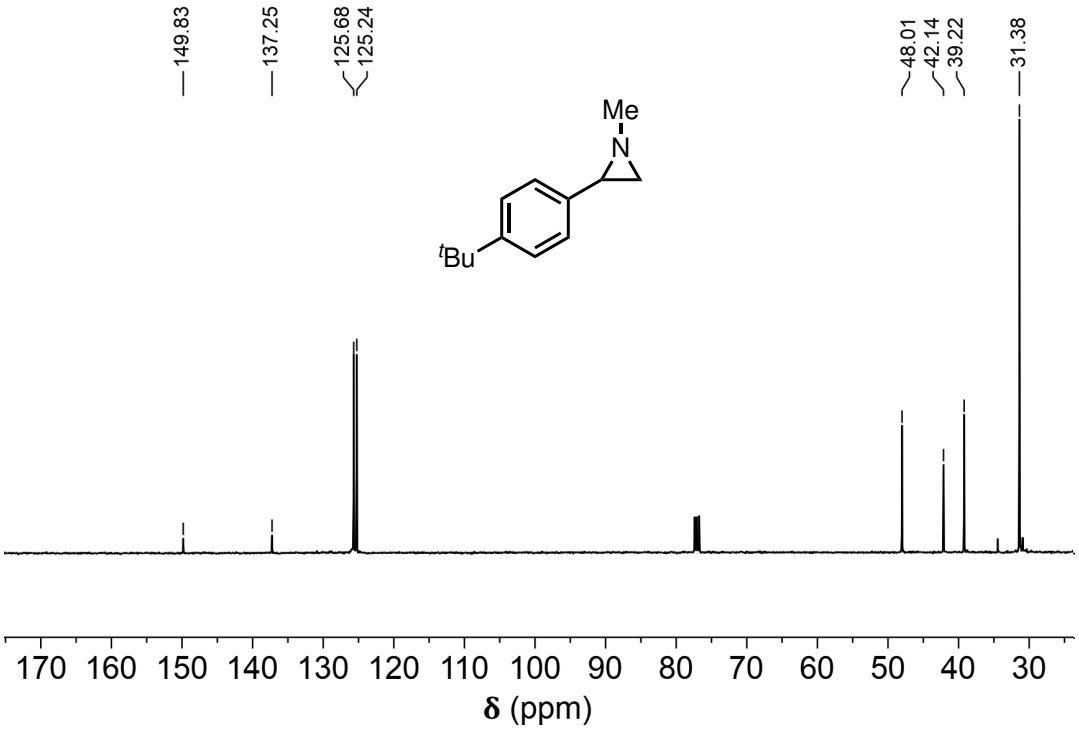

Figure A.94: *^{13}C-NMR spectrum of **S1q**.*

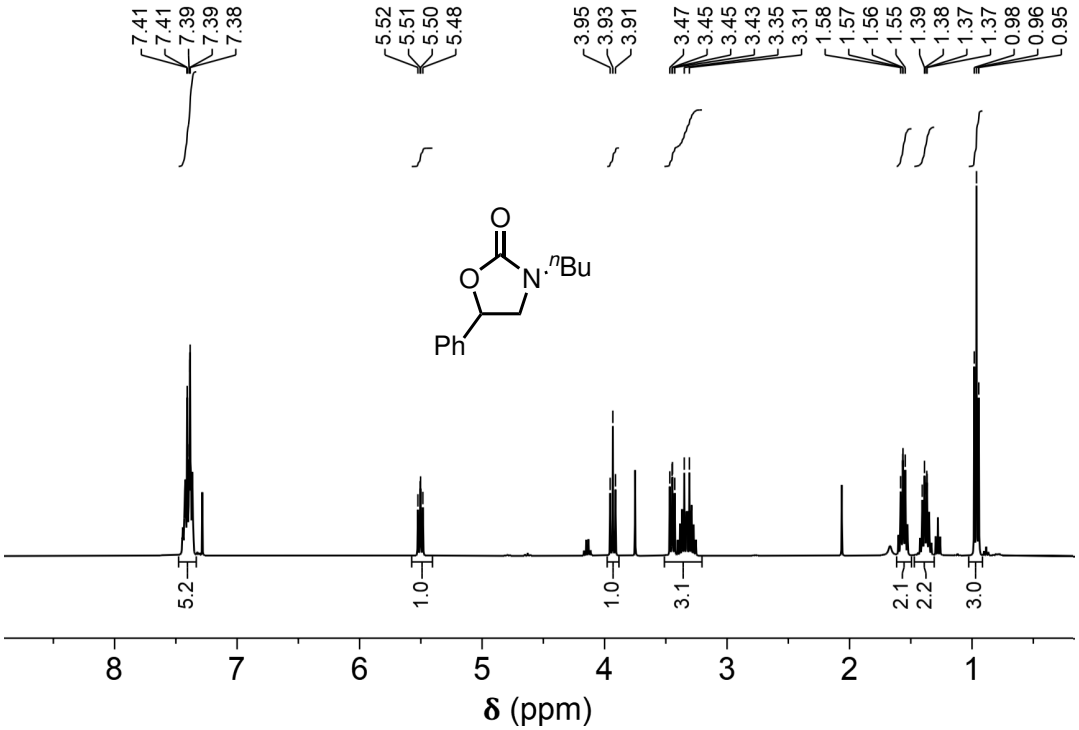

Figure A.95: *^{1}H-NMR spectrum of **P1a**, reaction crude.*

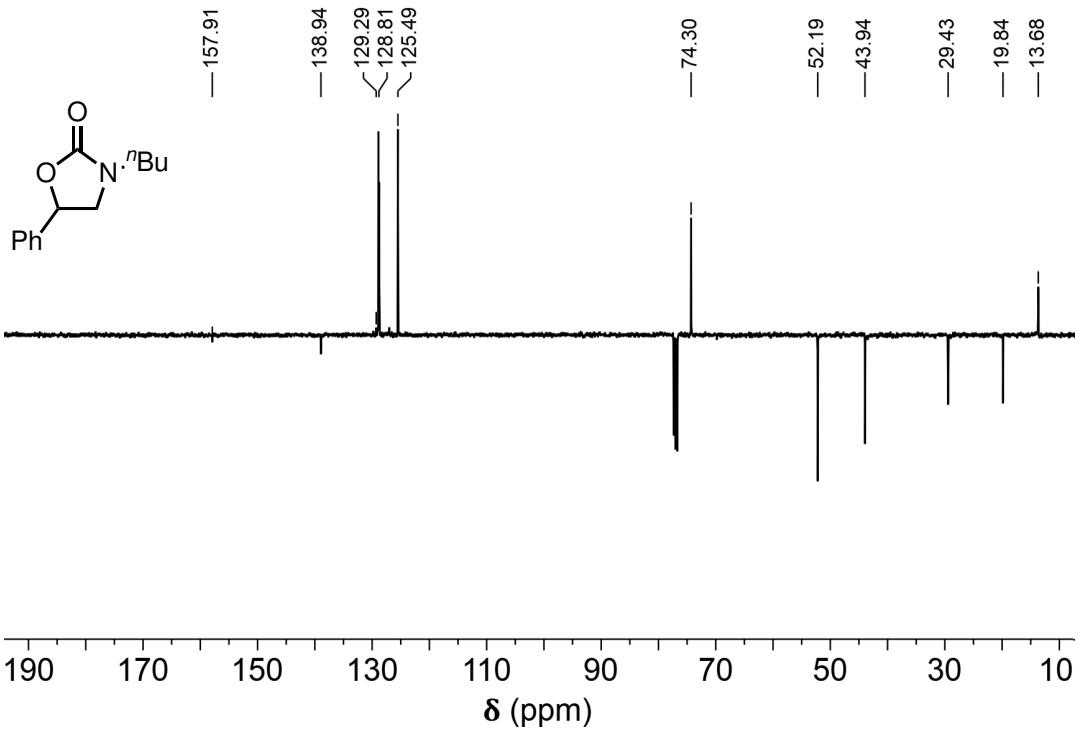

Figure A.96: *^{13}C APT NMR spectrum of **P1a** (reaction crude; primary and tertiary carbons produce positive peaks, secondary and quaternary carbons produce negative peaks).*

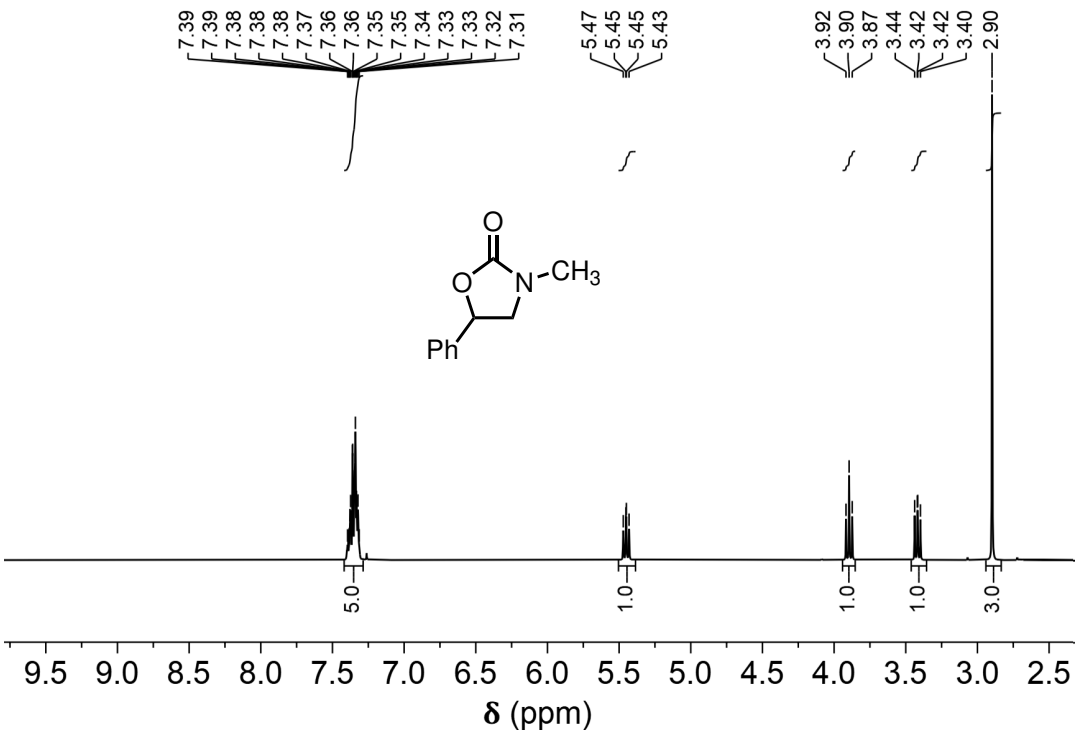

Figure A.97: *^{1}H-NMR spectrum of **P1b**.*

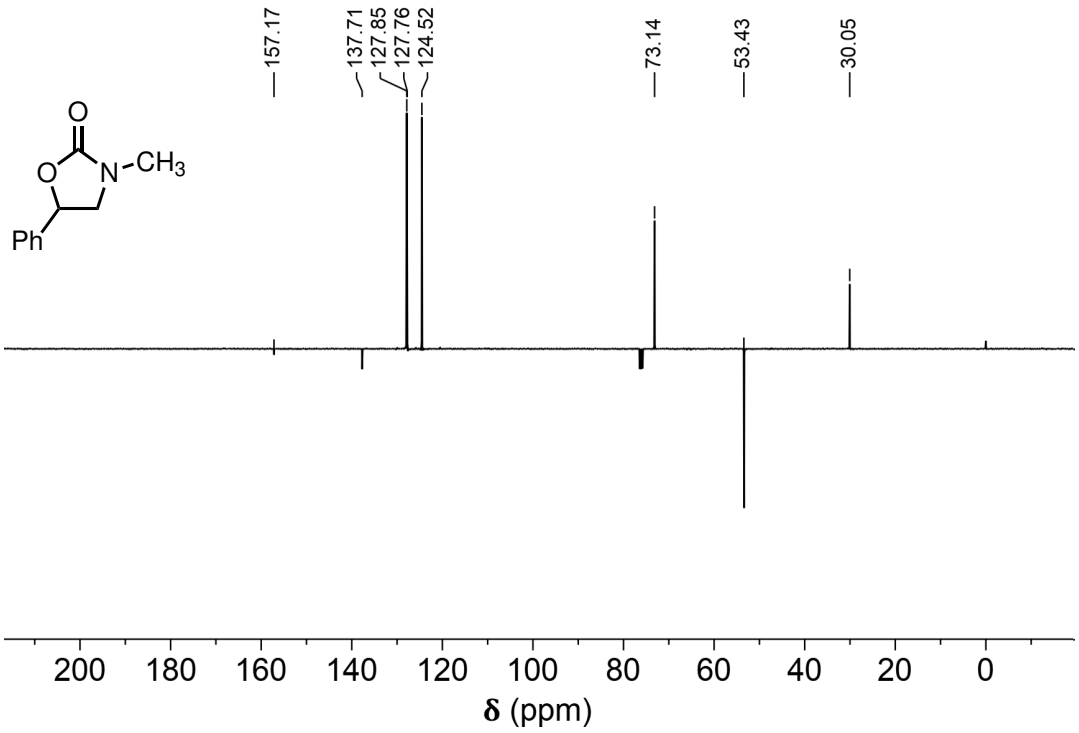

Figure A.98: *^{13}C APT NMR spectrum of **P1b*** (*primary and tertiary carbons produce positive peaks, secondary and quaternary carbons produce negative peaks*).

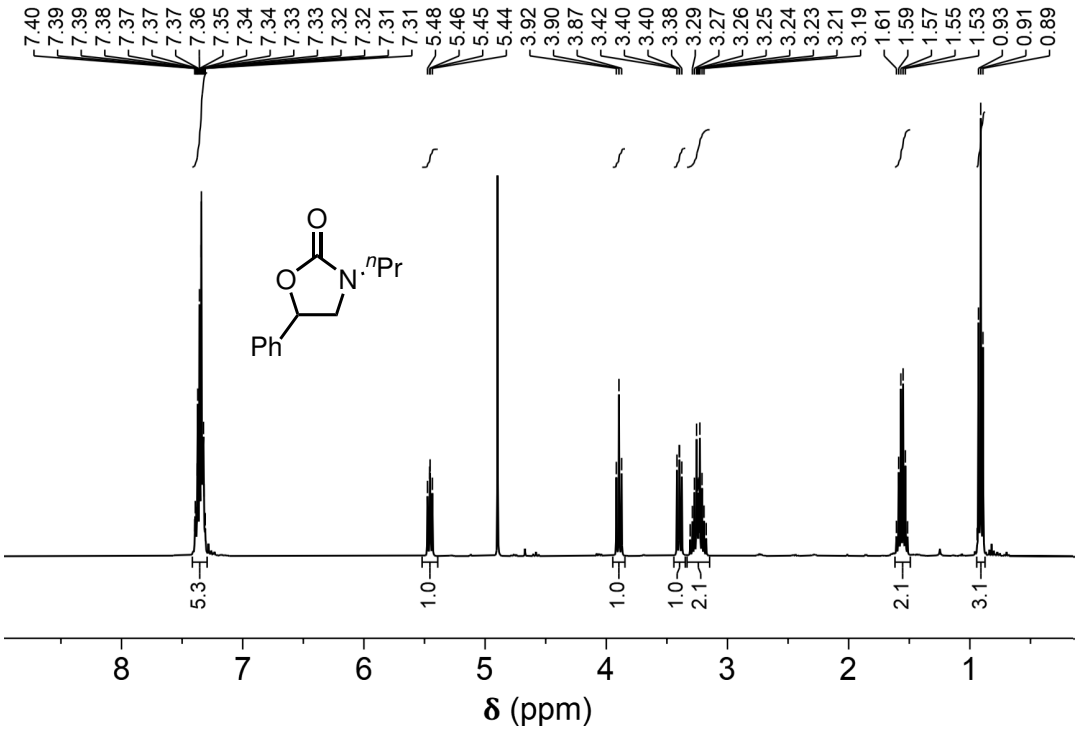

Figure A.99: *^{1}H-NMR spectrum of **P1c**, reaction crude.*

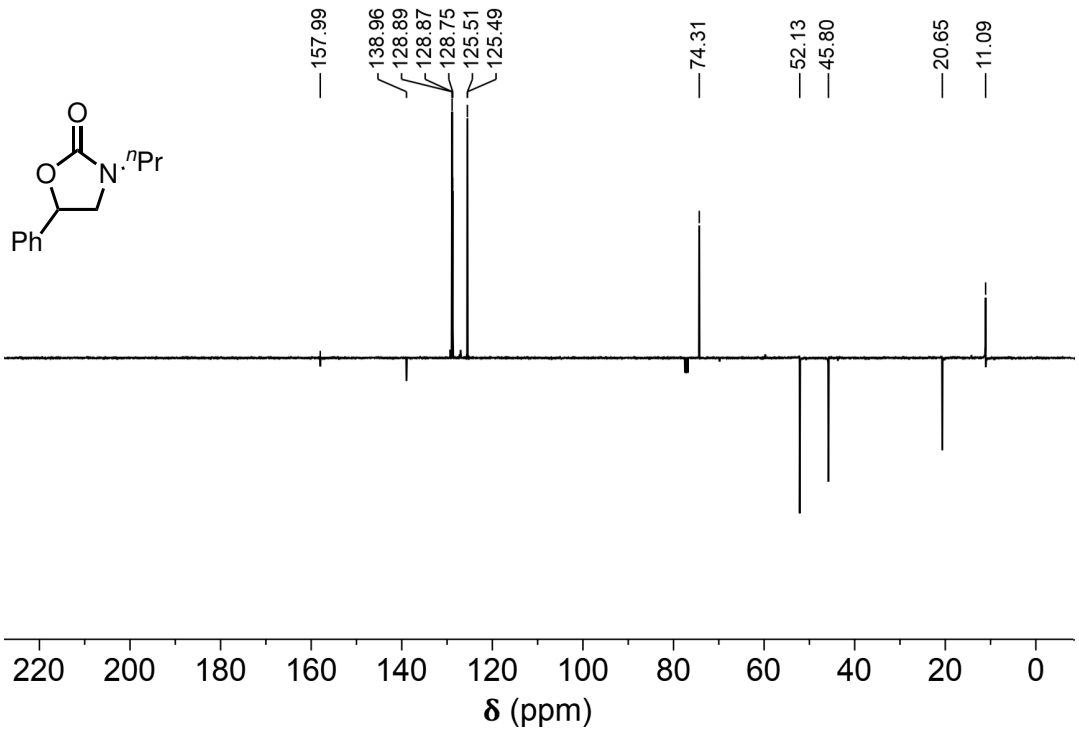

Figure A.100: *^{13}C APT NMR spectrum of **P1c*** (*reaction crude; primary and tertiary carbons produce positive peaks, secondary and quaternary carbons produce negative peaks*).

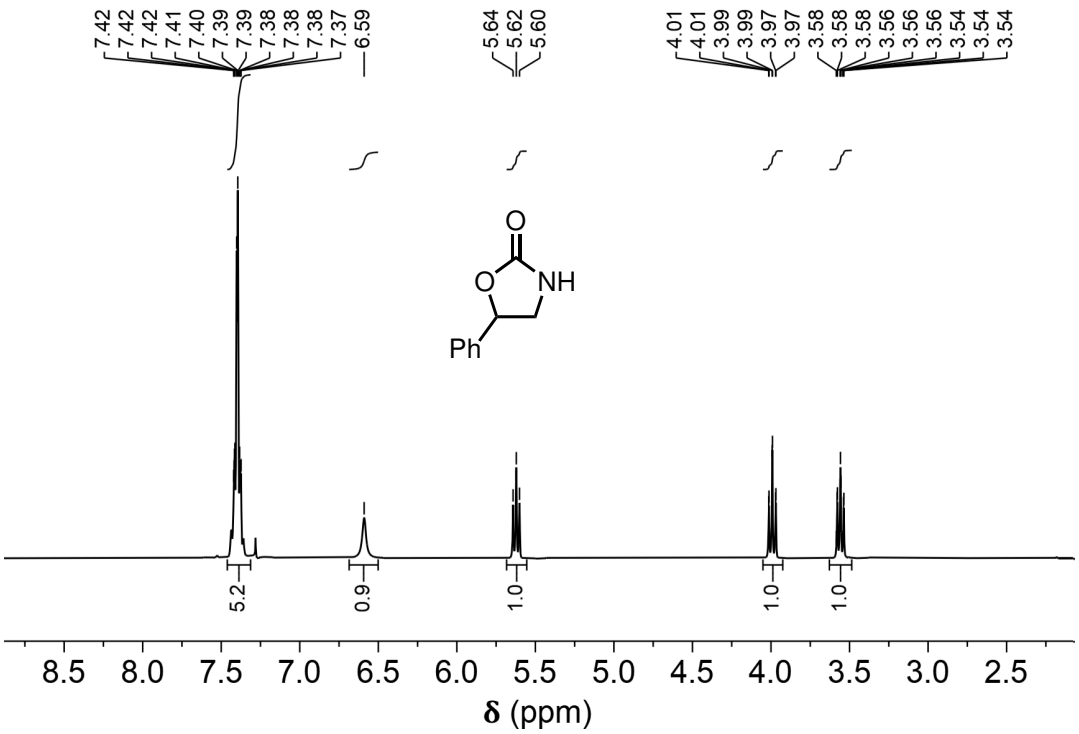

Figure A.101: *^{1}H-NMR spectrum of **P1d**.*

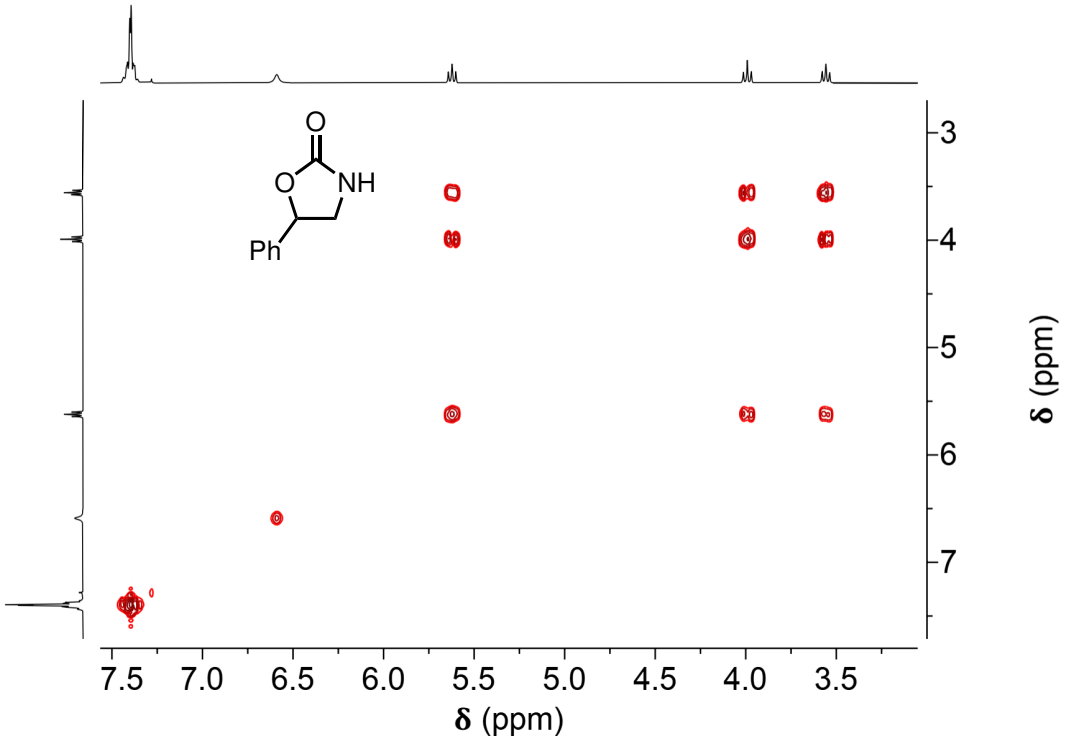

Figure A.102: *^{1}H COSY NMR spectrum of **P1d**.*

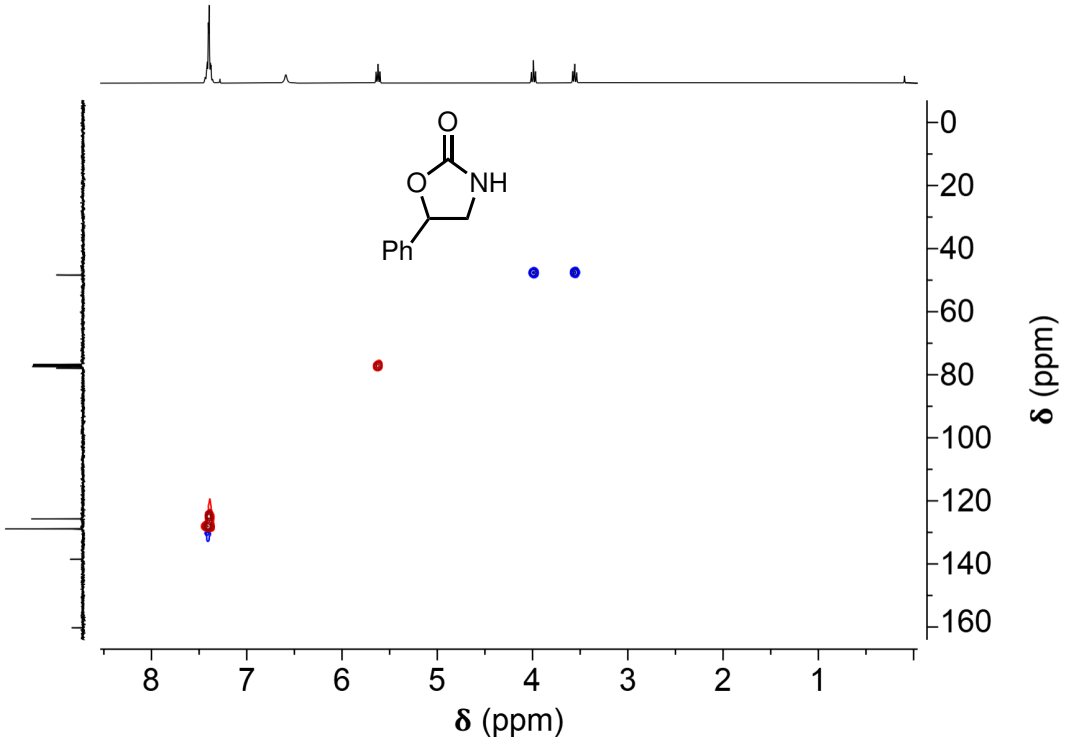

Figure A.103: *^{1}H-^{13}C HSQC NMR spectrum of **P1d** (short range, primary and tertiary carbons produce red peaks, while secondary carbons produce blue peaks).*

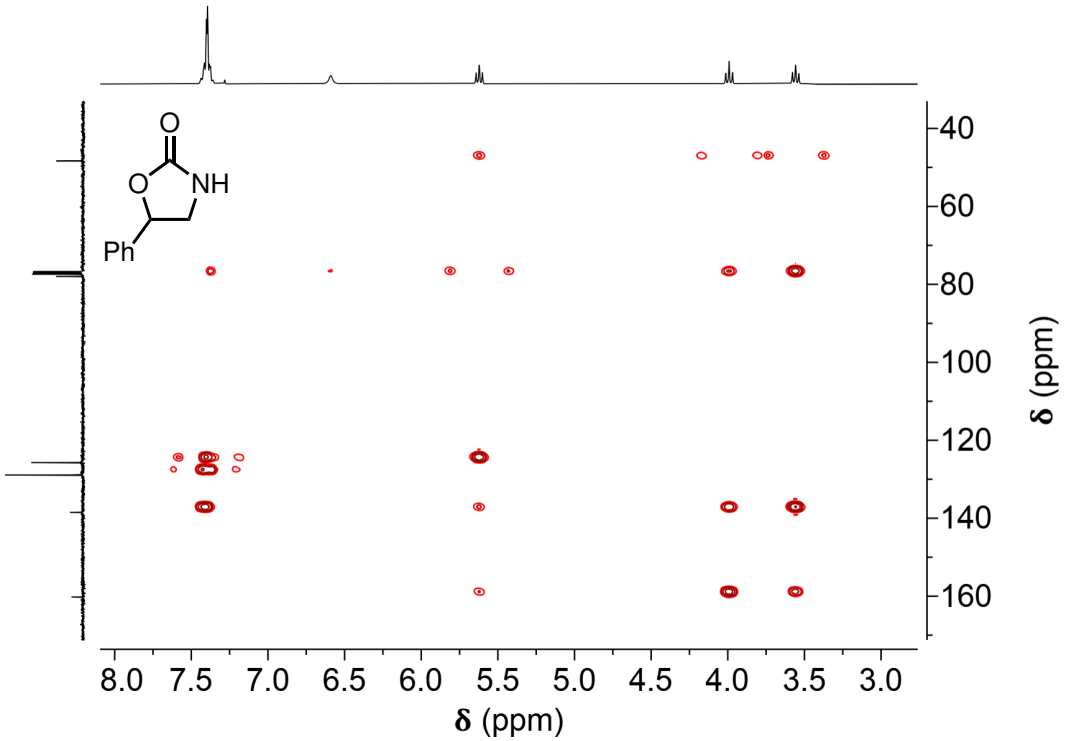

Figure A.104: *^{1}H-^{13}C HMBC NMR spectrum of **P1d** (long range).*

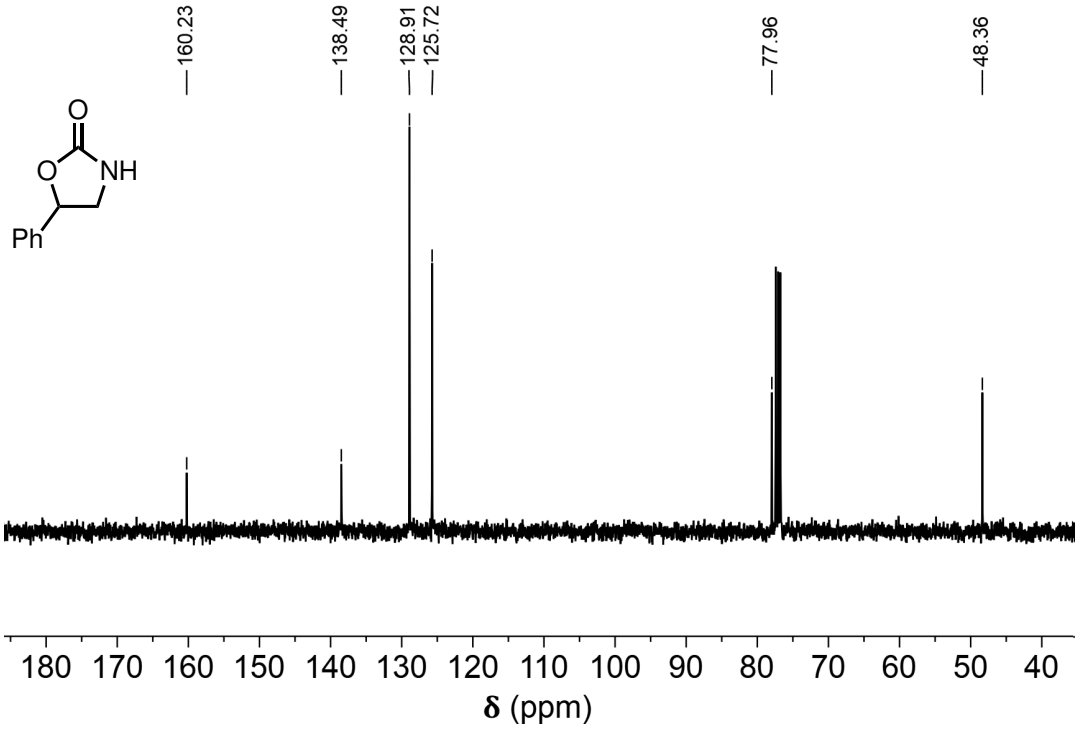

Figure A.105: *^{13}C-NMR spectrum of **P1d**.*

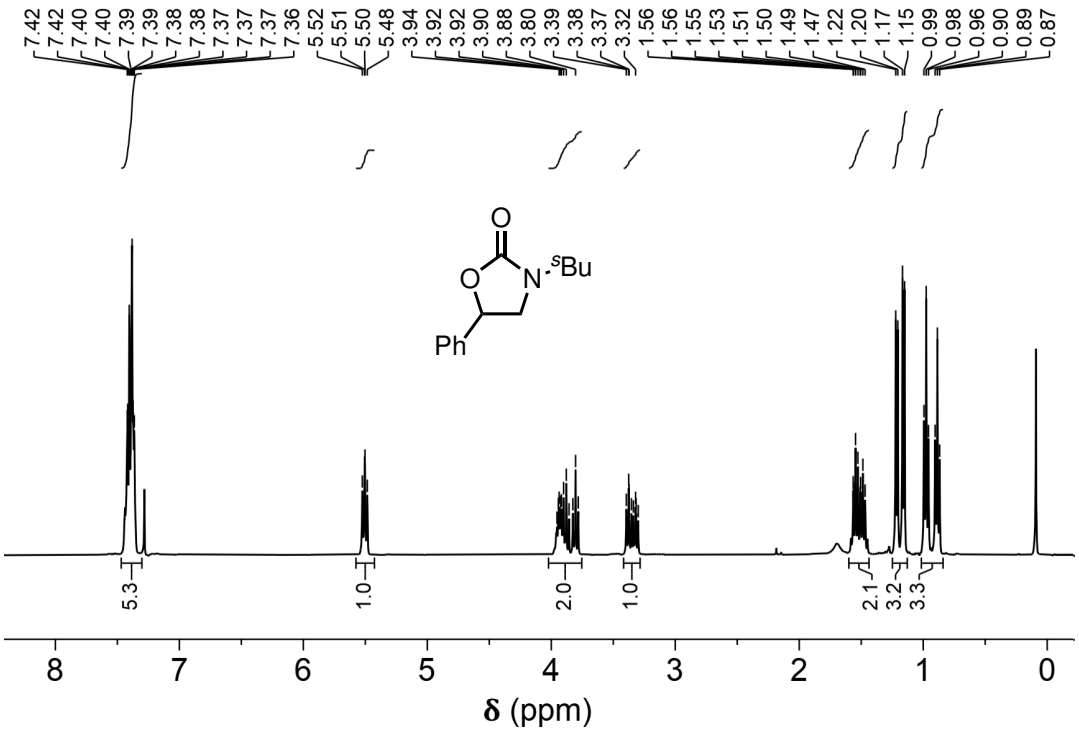

Figure A.106: *^{1}H-NMR spectrum of **P1e**.*

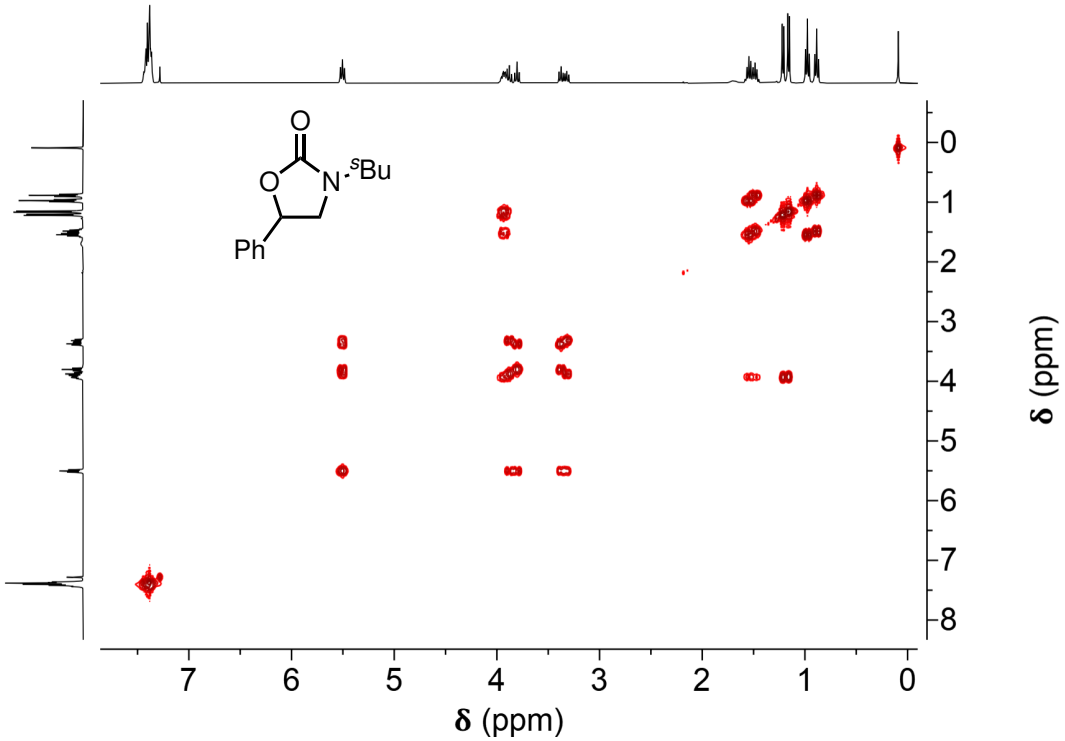

Figure A.107: *^{1}H COSY NMR spectrum of **P1e**.*

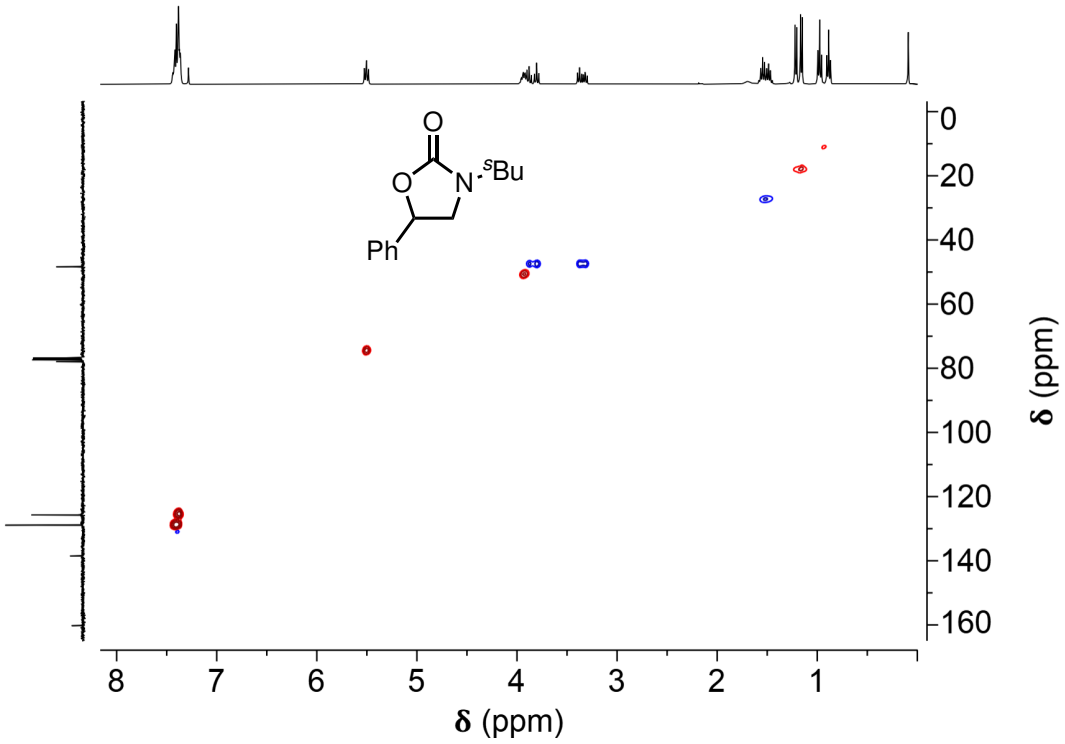

Figure A.108: *^{1}H-^{13}C HSQC NMR spectrum of **P1e** (short range, primary and tertiary carbons produce red peaks, while secondary carbons produce blue peaks).*

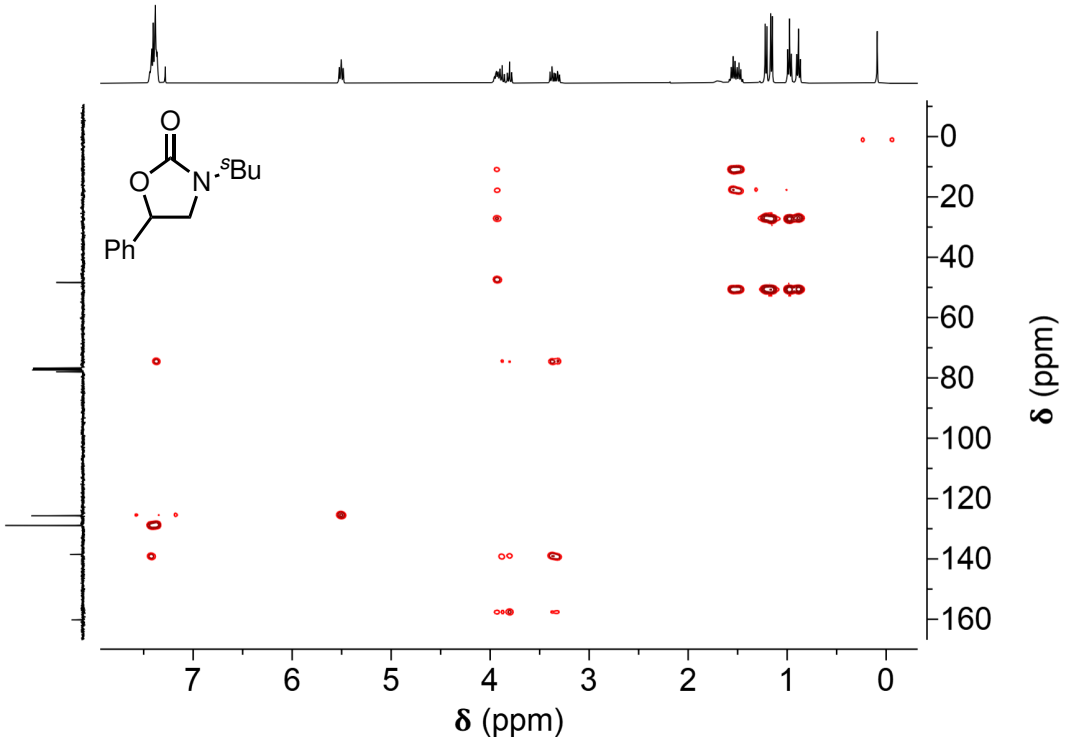

Figure A.109: *^{1}H-^{13}C HMBC NMR spectrum of **P1e** (long range).*

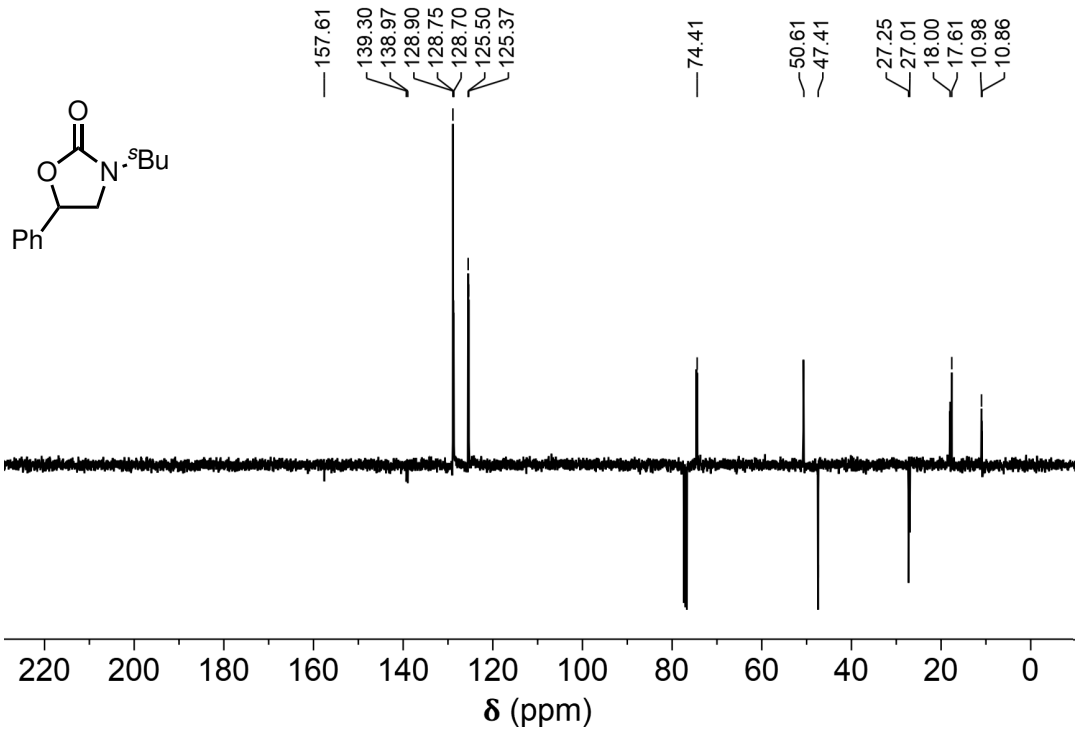

Figure A.110: *^{13}C APT NMR spectrum of **P1e** (primary and tertiary carbons produce positive peaks, secondary and quaternary carbons produce negative peaks).*

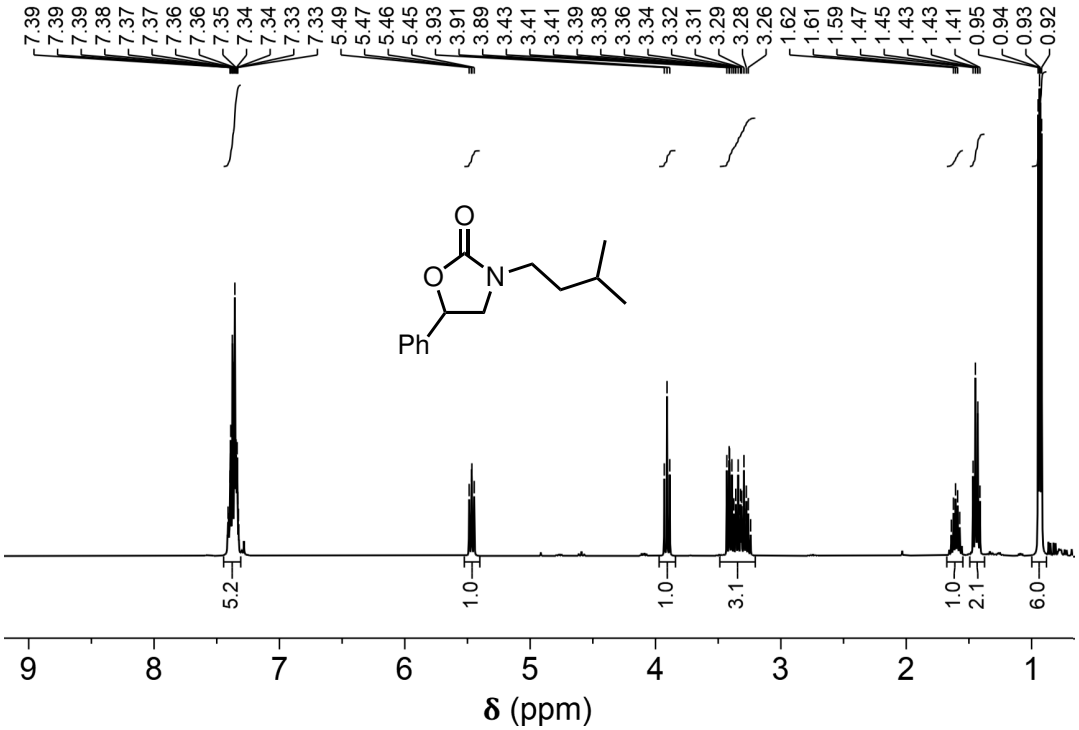

Figure A.111: *^{1}H-NMR spectrum of **P1f**.*

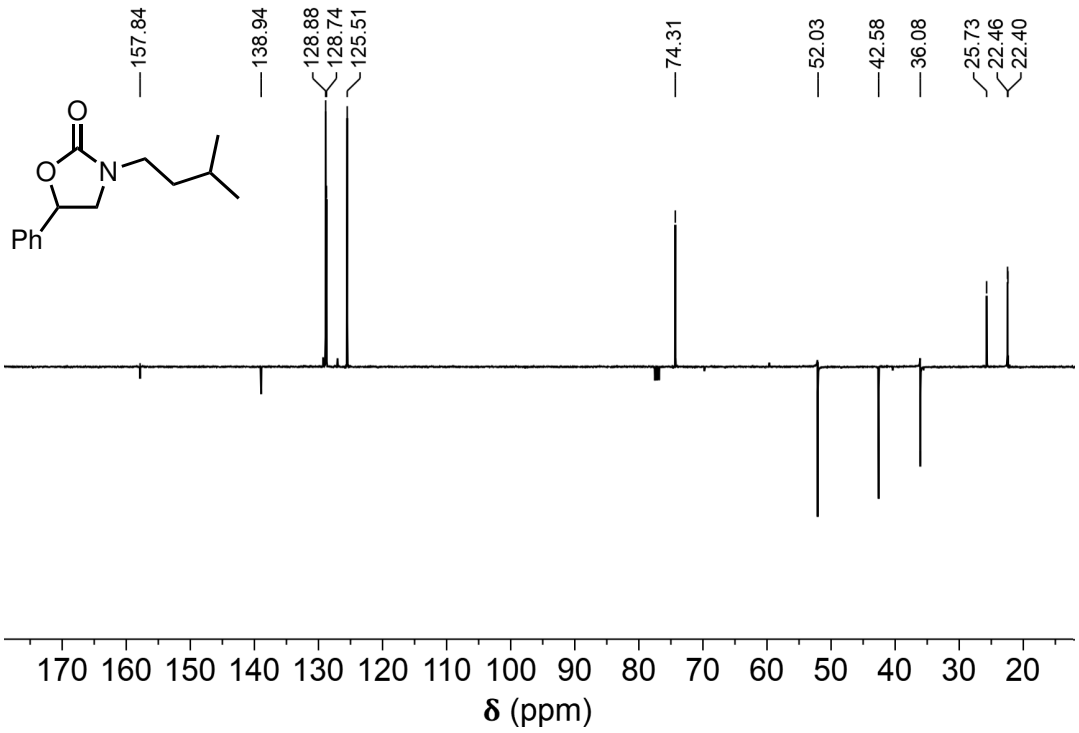

Figure A.112: *^{13}C APT NMR spectrum of **P1f** (primary and tertiary carbons produce positive peaks, secondary and quaternary carbons produce negative peaks).*

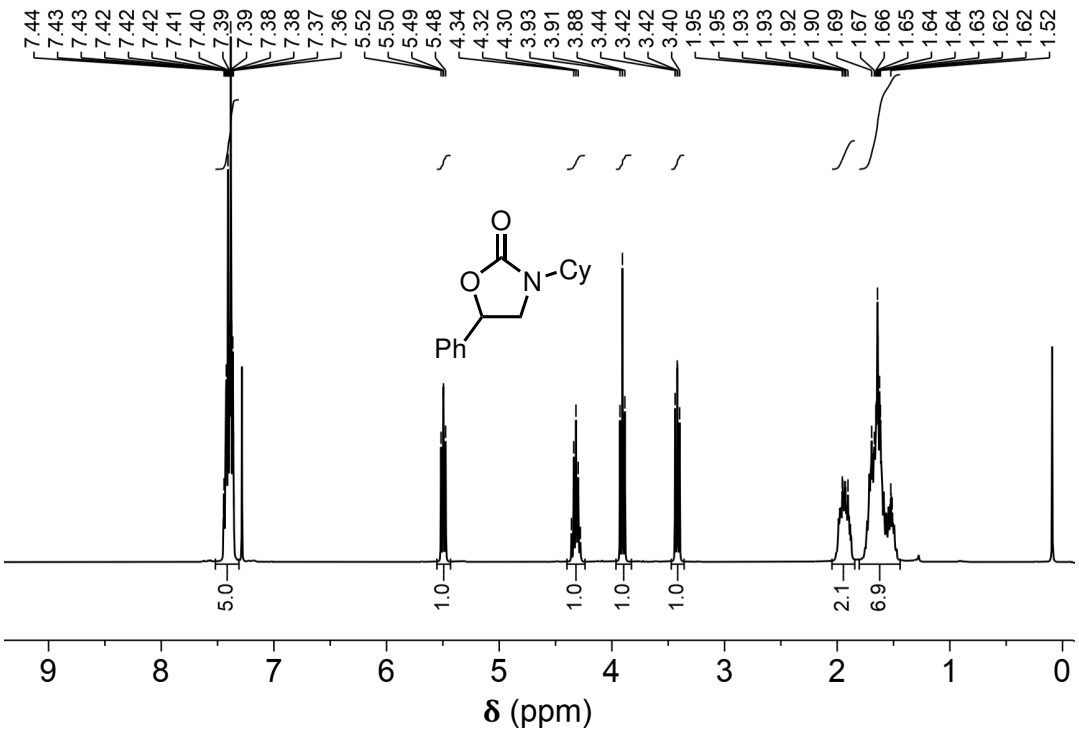

Figure A.113: *^{1}H-NMR spectrum of **P1g**.*

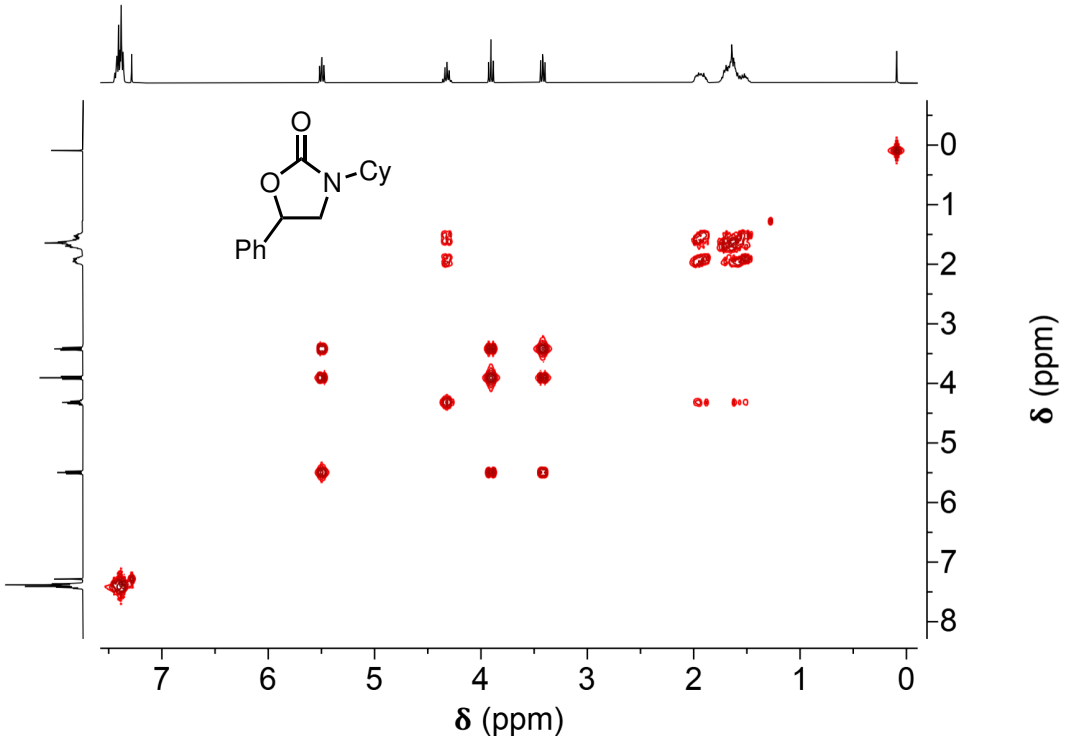

Figure A.114: *^{1}H COSY NMR spectrum of **P1g**.*

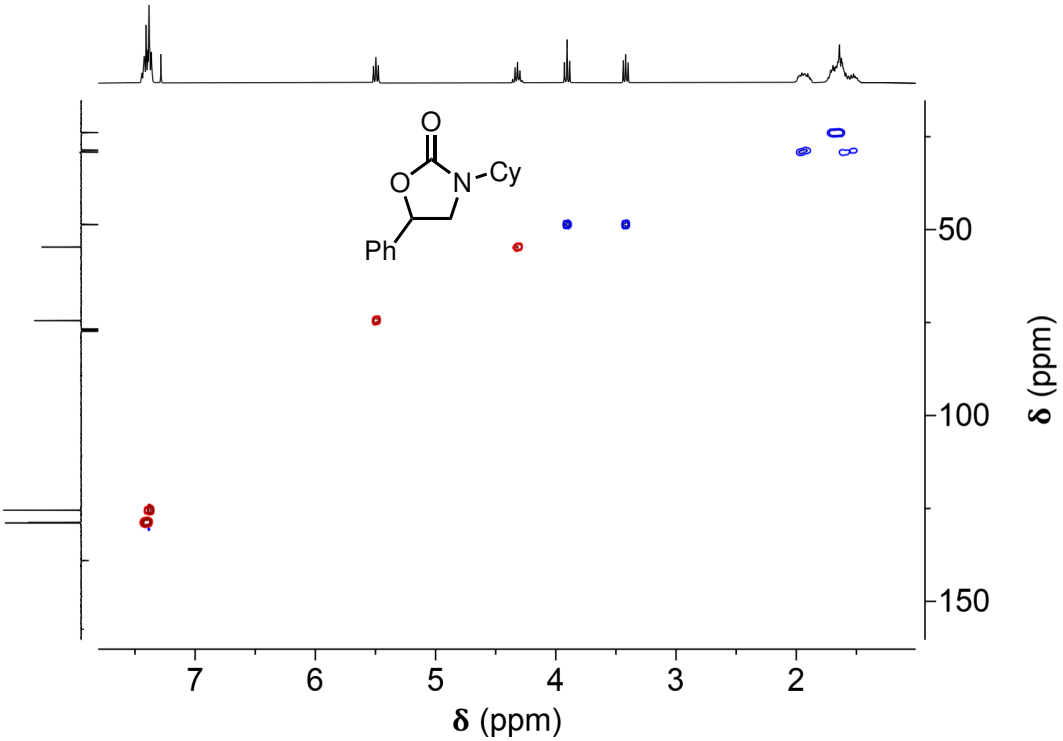

Figure A.115: *^{1}H-^{13}C HSQC NMR spectrum of **P1g** (short range, primary and tertiary carbons produce red peaks, while secondary carbons produce blue peaks).*

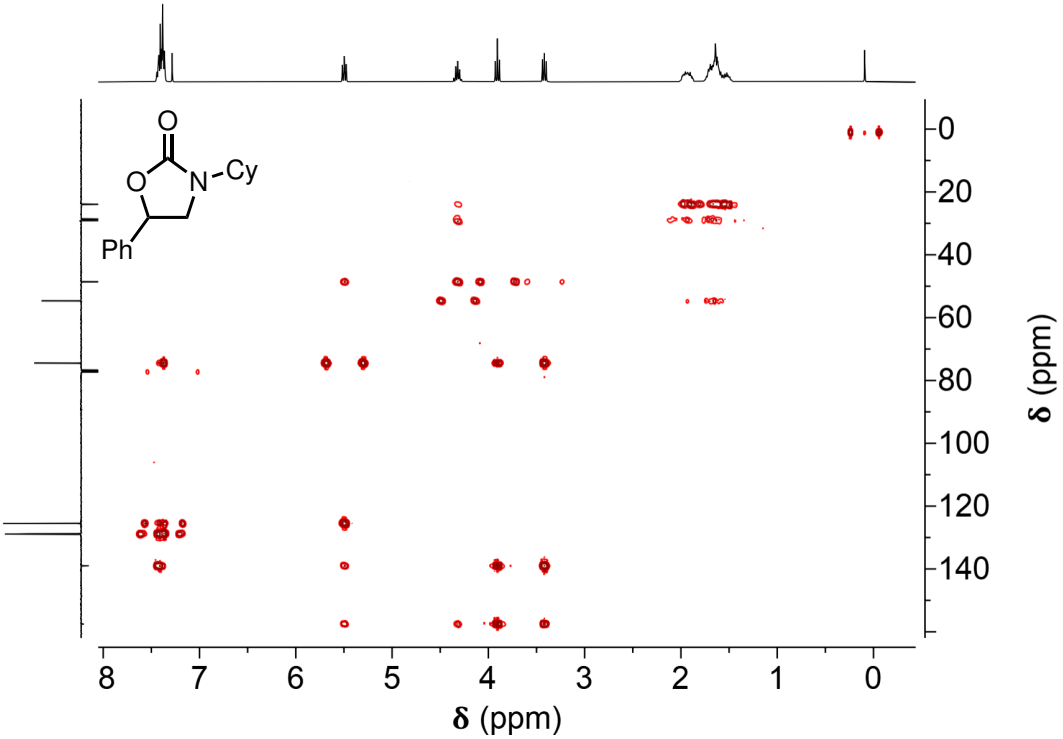

Figure A.116: *^{1}H-^{13}C HMBC NMR spectrum of **P1g** (long range).*

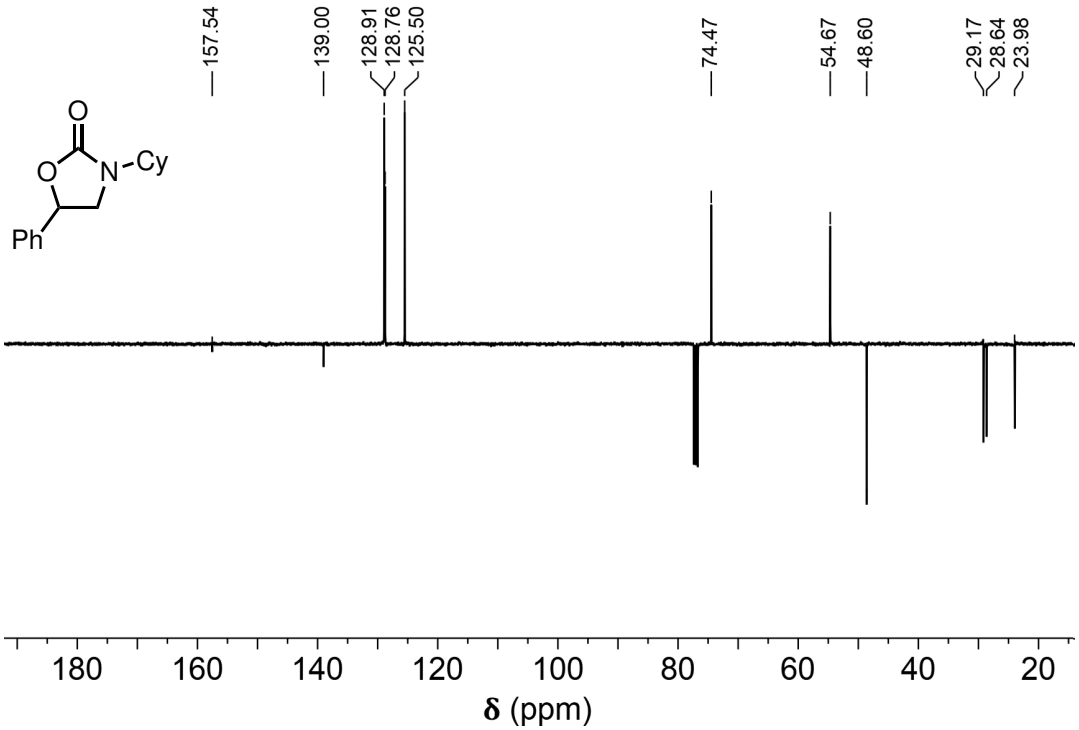

Figure A.117: *^{13}C APT NMR spectrum of **P1g** (primary and tertiary carbons produce positive peaks, secondary and quaternary carbons produce negative peaks).*

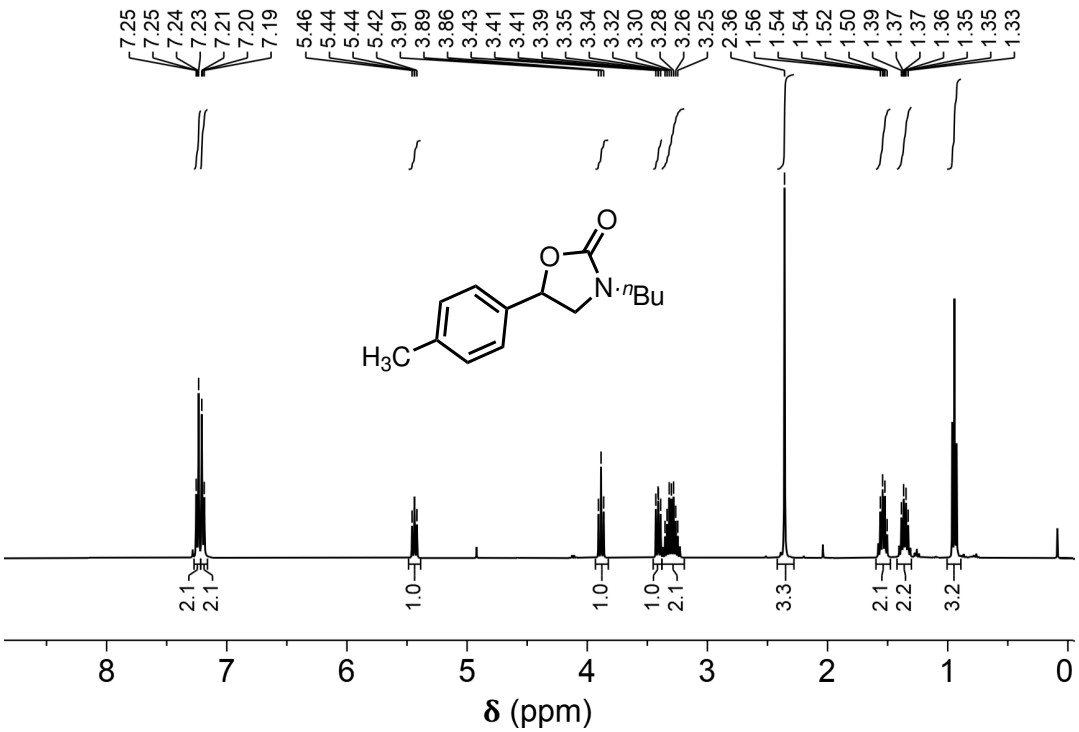

Figure A.118: *^{1}H-NMR spectrum of **P1h**.*

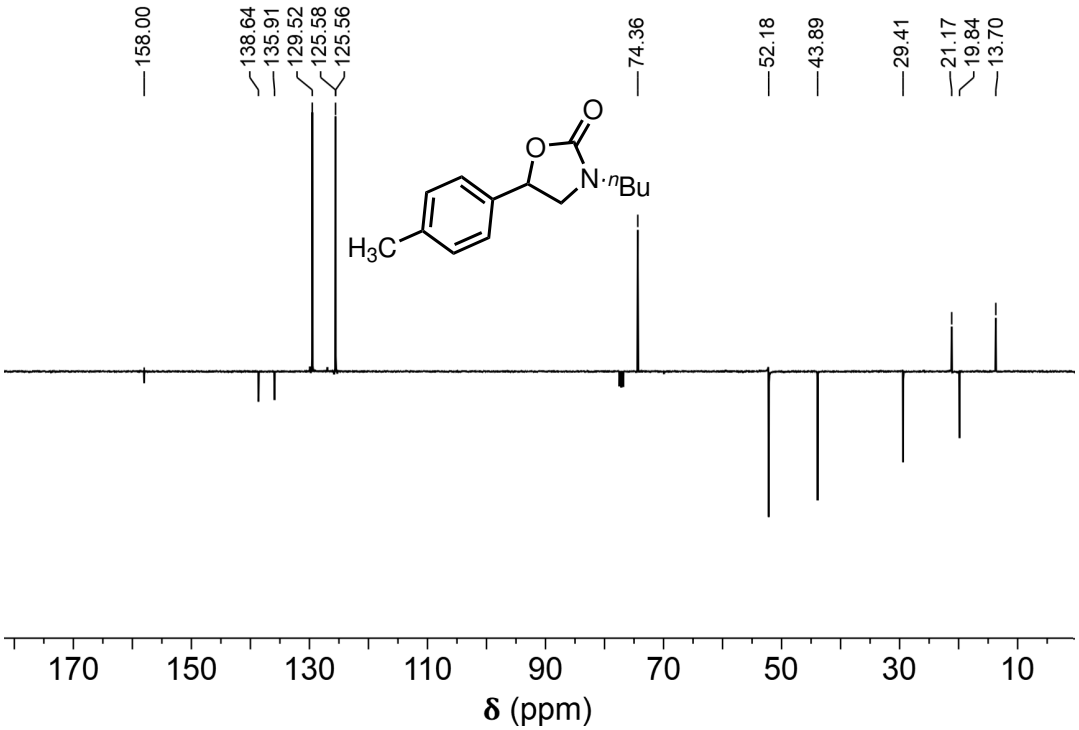

Figure A.119: *^{13}C APT NMR spectrum of **P1h** (primary and tertiary carbons produce positive peaks, secondary and quaternary carbons produce negative peaks).*

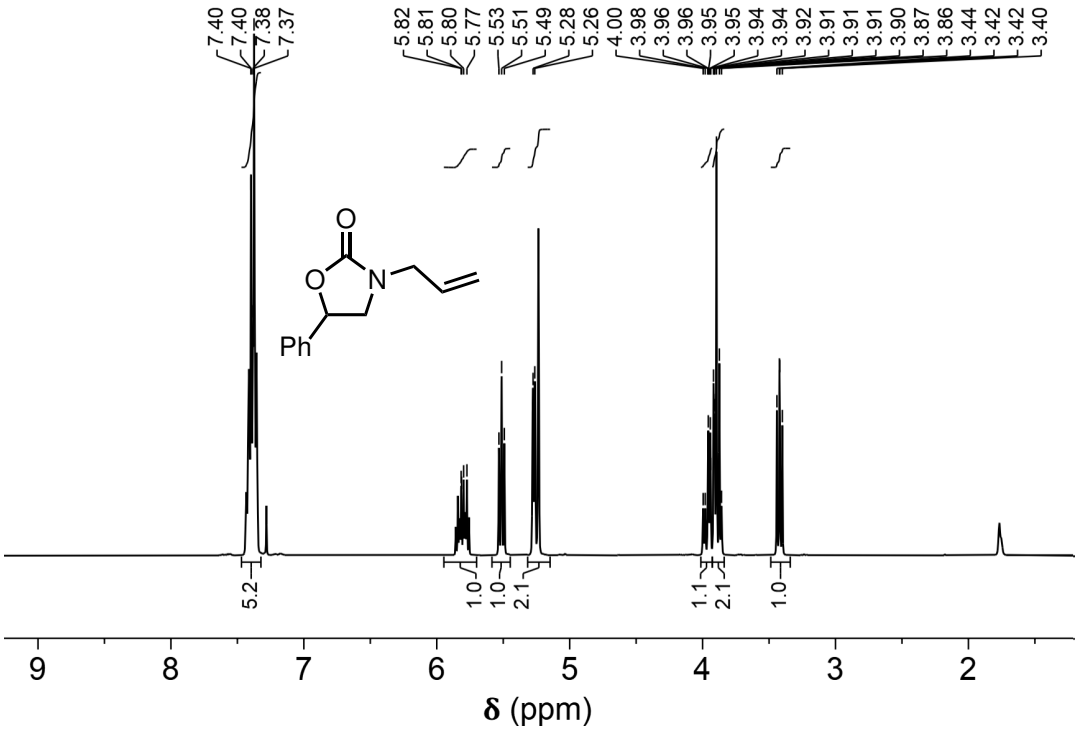

Figure A.120: *^{1}H-NMR spectrum of **P1i**.*

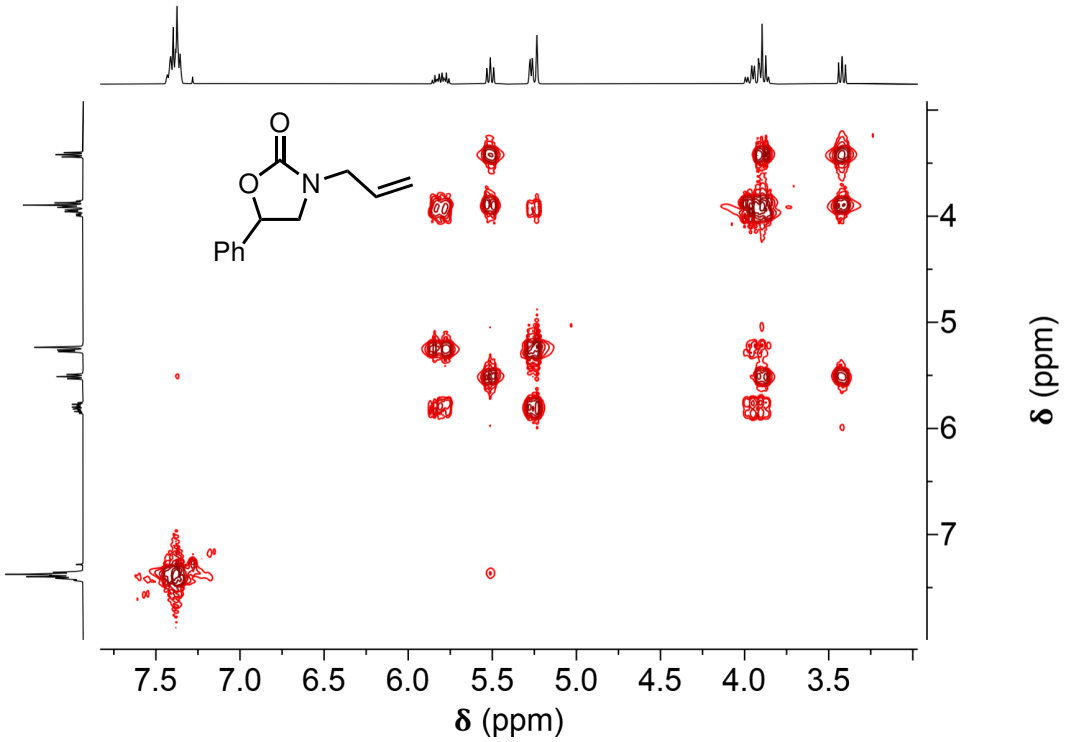

Figure A.121: *^{1}H COSY NMR spectrum of **P1i**.*

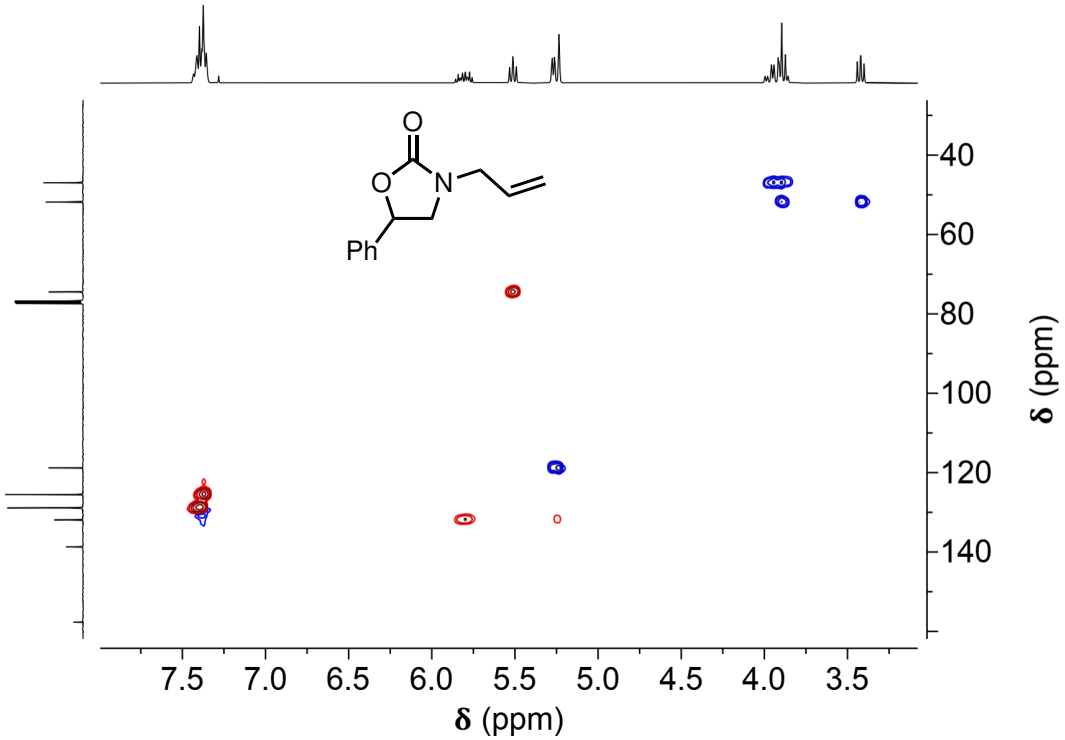

Figure A.122: *^{1}H-^{13}C HSQC NMR spectrum of **P1i** (short range, primary and tertiary carbons produce red peaks, while secondary carbons produce blue peaks).*

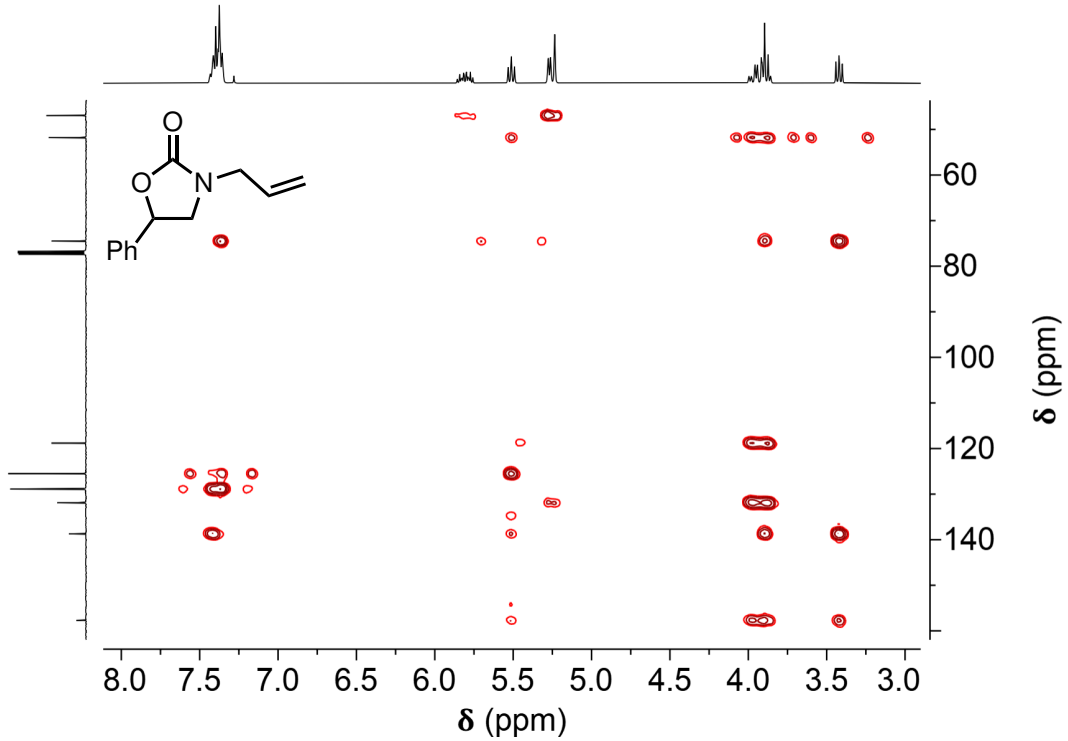

Figure A.123: *^{1}H-^{13}C HMBC NMR spectrum of **P1i** (long range).*

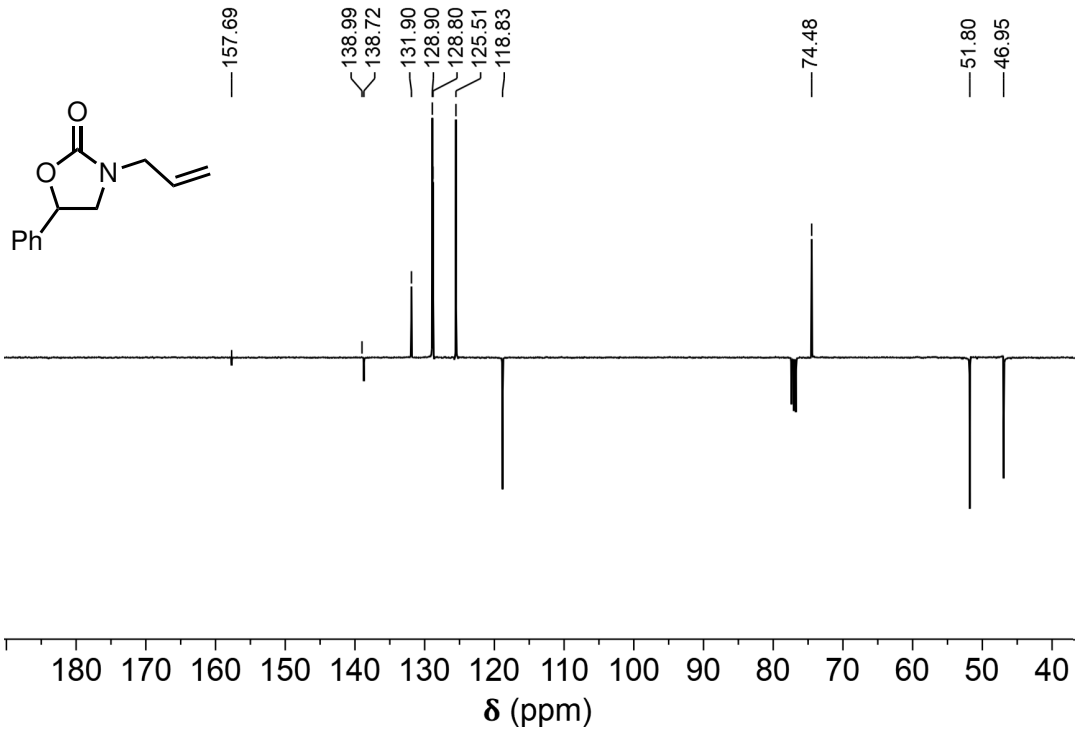

Figure A.124: *^{13}C APT NMR spectrum of **P1i** (primary and tertiary carbons produce positive peaks, secondary and quaternary carbons produce negative peaks).*

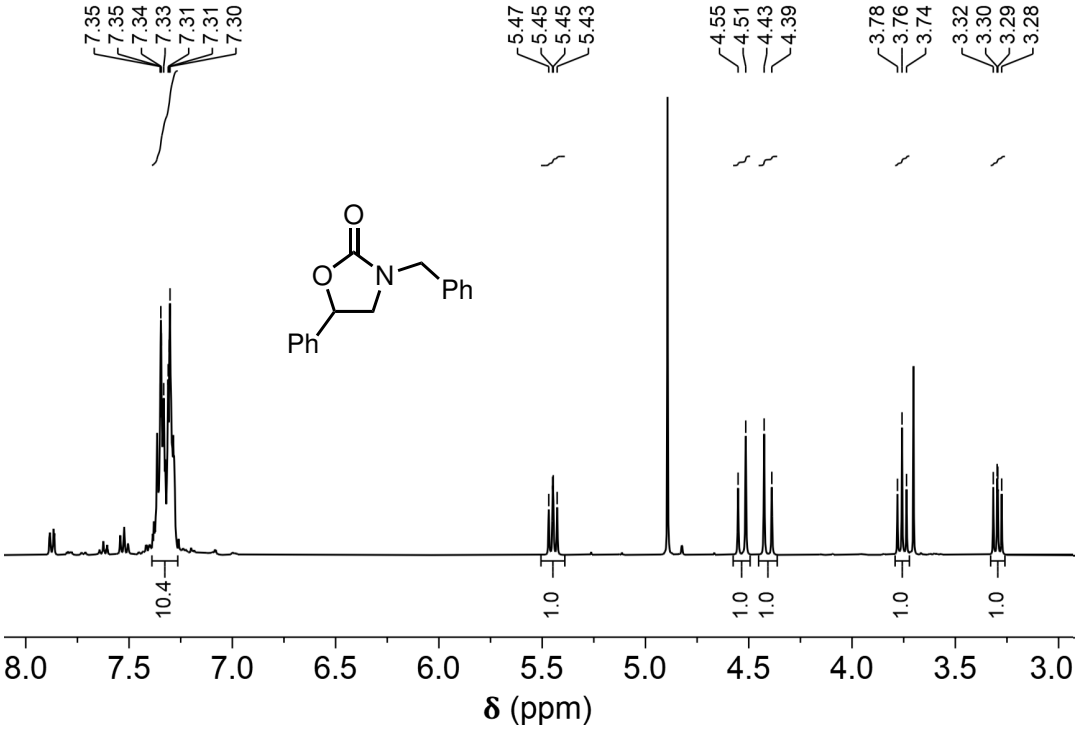

Figure A.125: *^{1}H-NMR spectrum of **P1j**, reaction crude.*

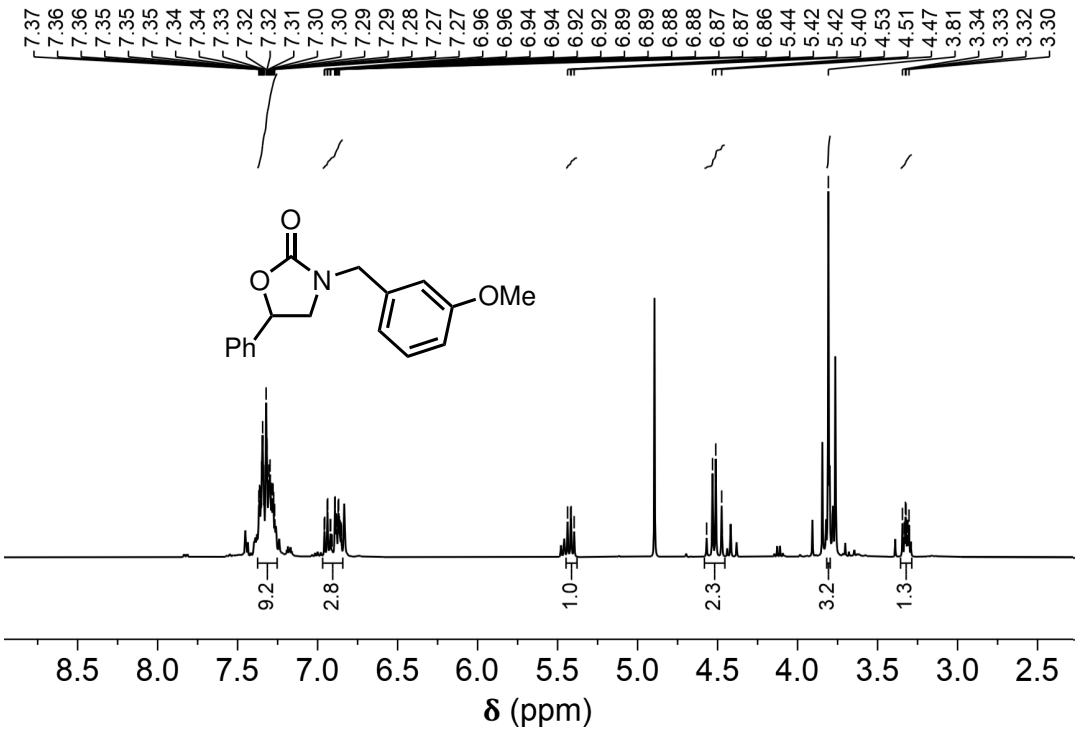

Figure A.126: *^{1}H-NMR spectrum of **P1k**, reaction crude.*

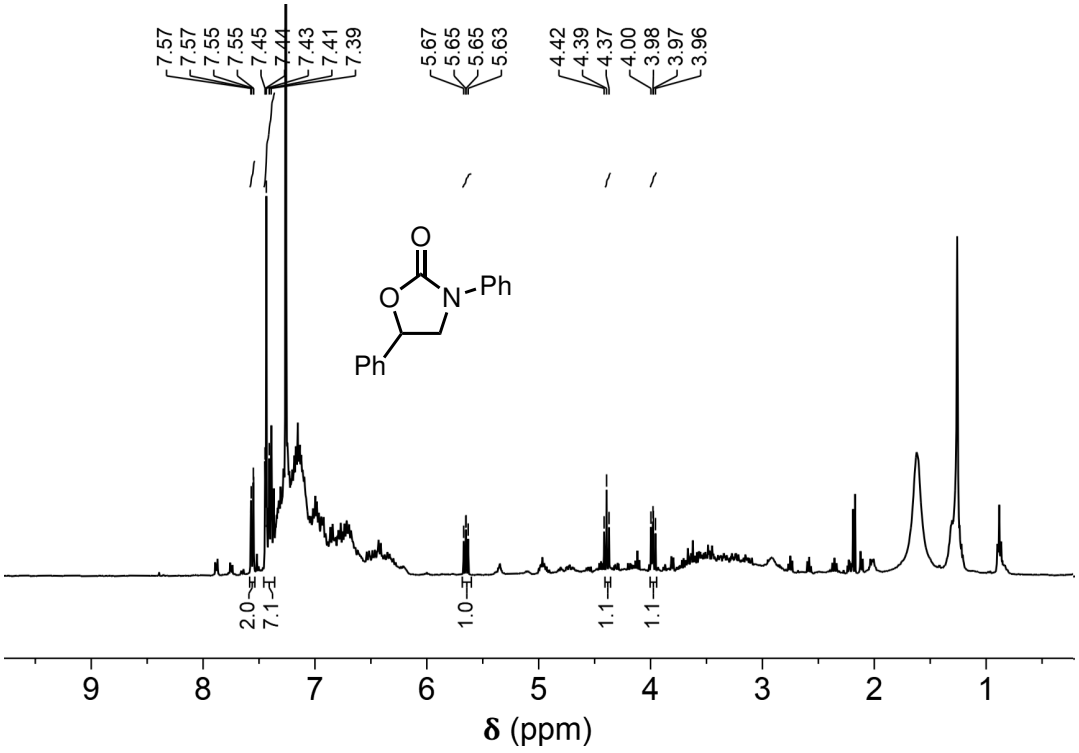

Figure A.127: *^{1}H-NMR spectrum of **P1l**, reaction crude.*

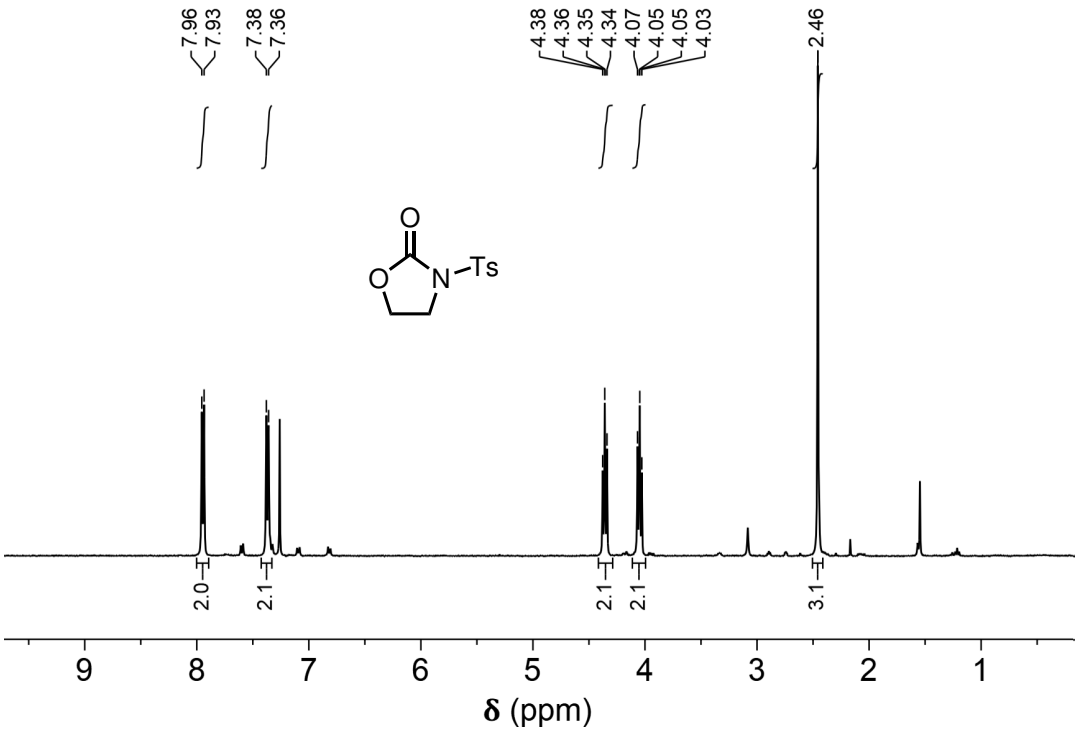

Figure A.128: *^{1}H-NMR spectrum of **P1m**.*

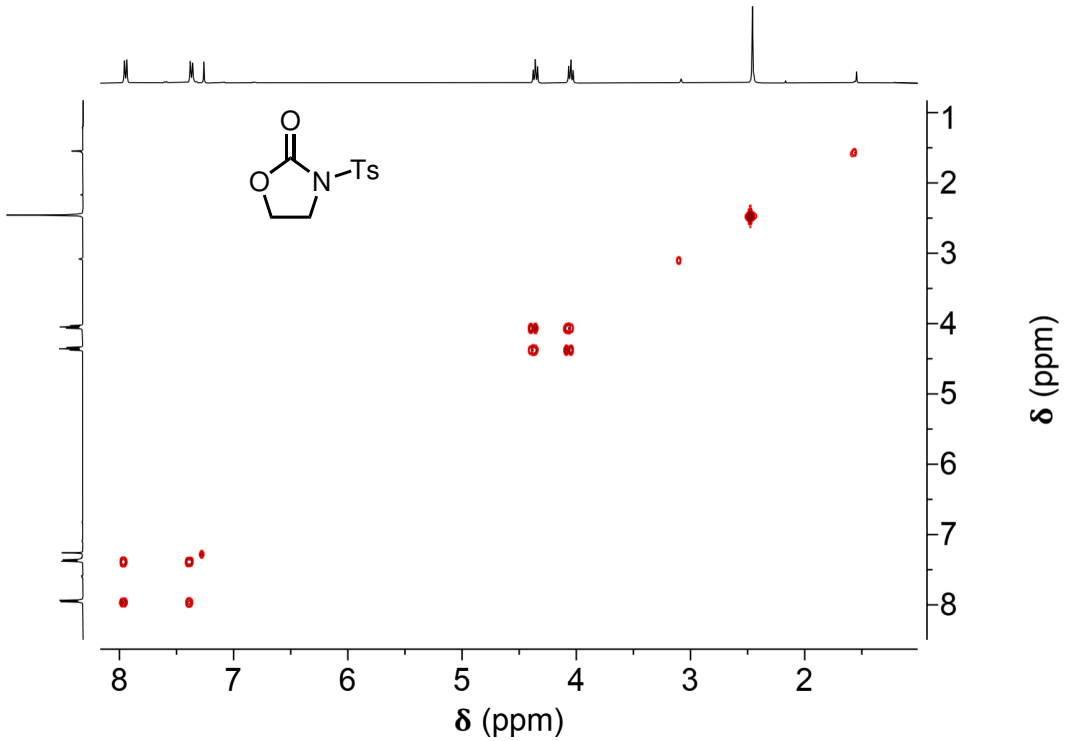

Figure A.129: *^{1}H COSY NMR spectrum of **P1m**.*

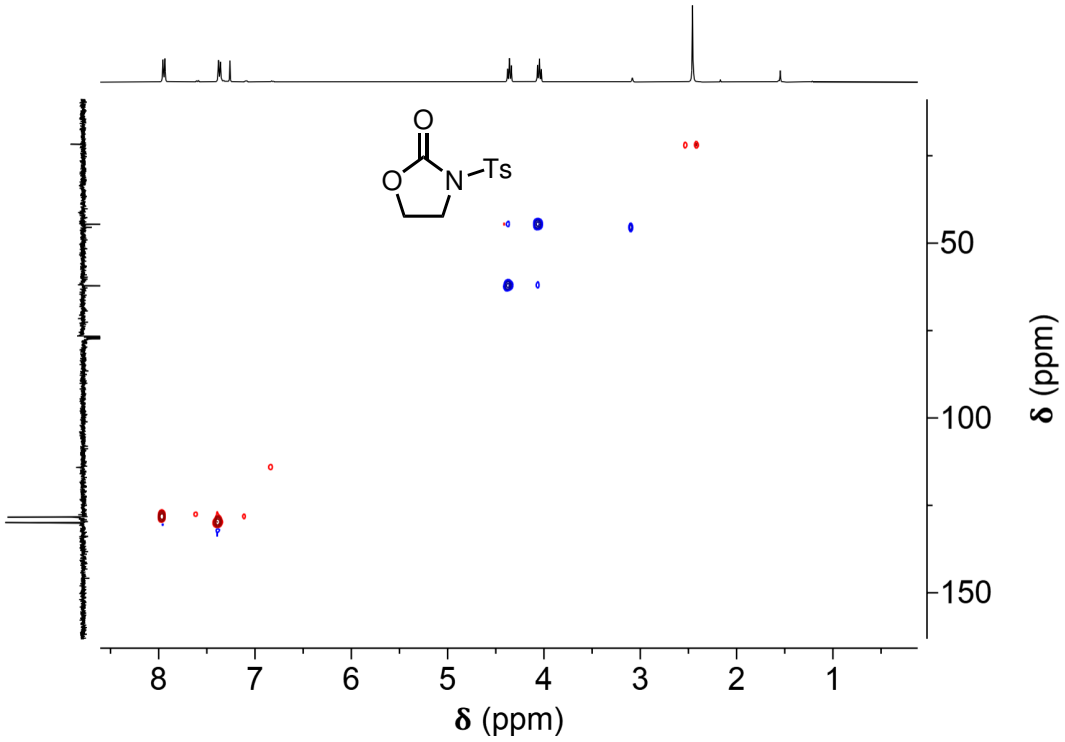

Figure A.130: *^{1}H-^{13}C HSQC NMR spectrum of **P1m** (short range, primary and tertiary carbons produce red peaks, while secondary carbons produce blue peaks).*

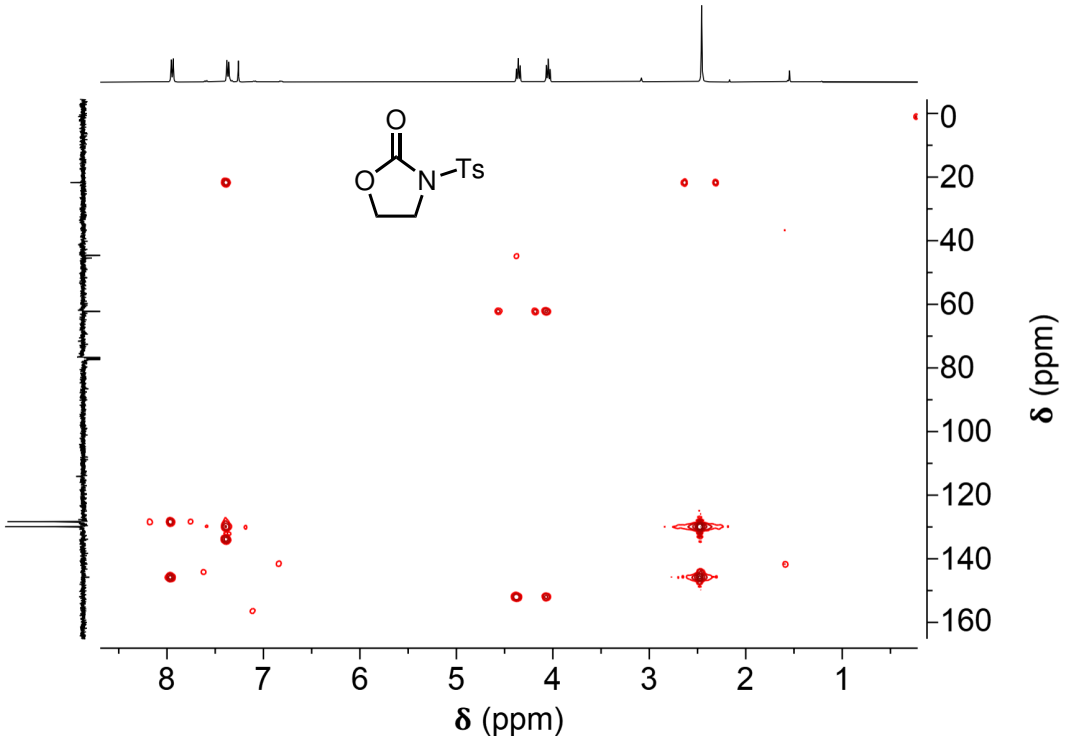

Figure A.131: *^{1}H-^{13}C HMBC NMR spectrum of **P1m** (long range).*

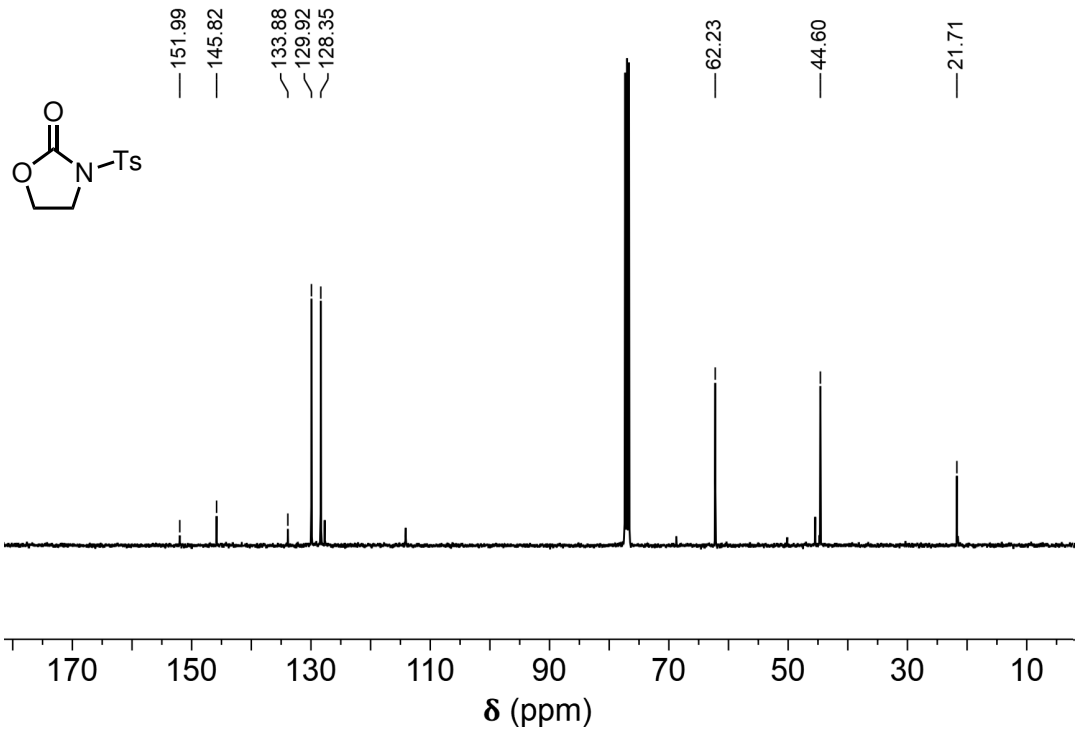

Figure A.132: *^{13}C-NMR spectrum of **P1m**.*

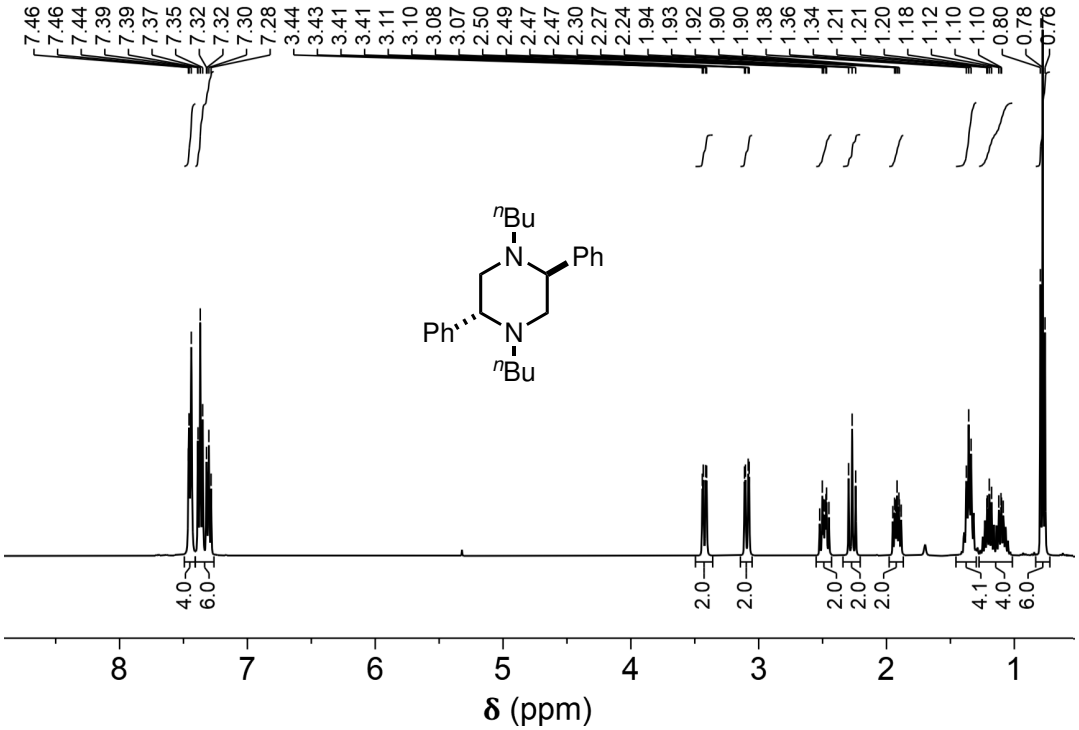

Figure A.133: *^{1}H-NMR spectrum of meso -* ***P2a****.*

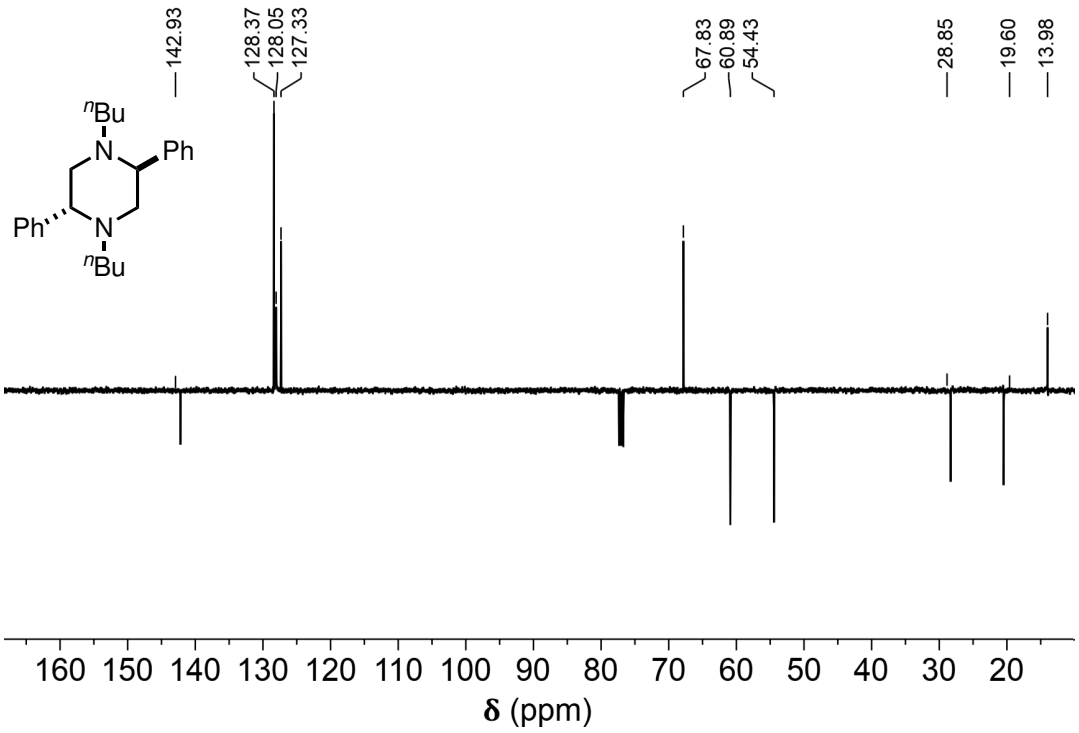

Figure A.134: *^{13}C APT NMR spectrum of meso -* ***P2a*** *(primary and tertiary carbons produce positive peaks, secondary and quaternary carbons produce negative peaks).*

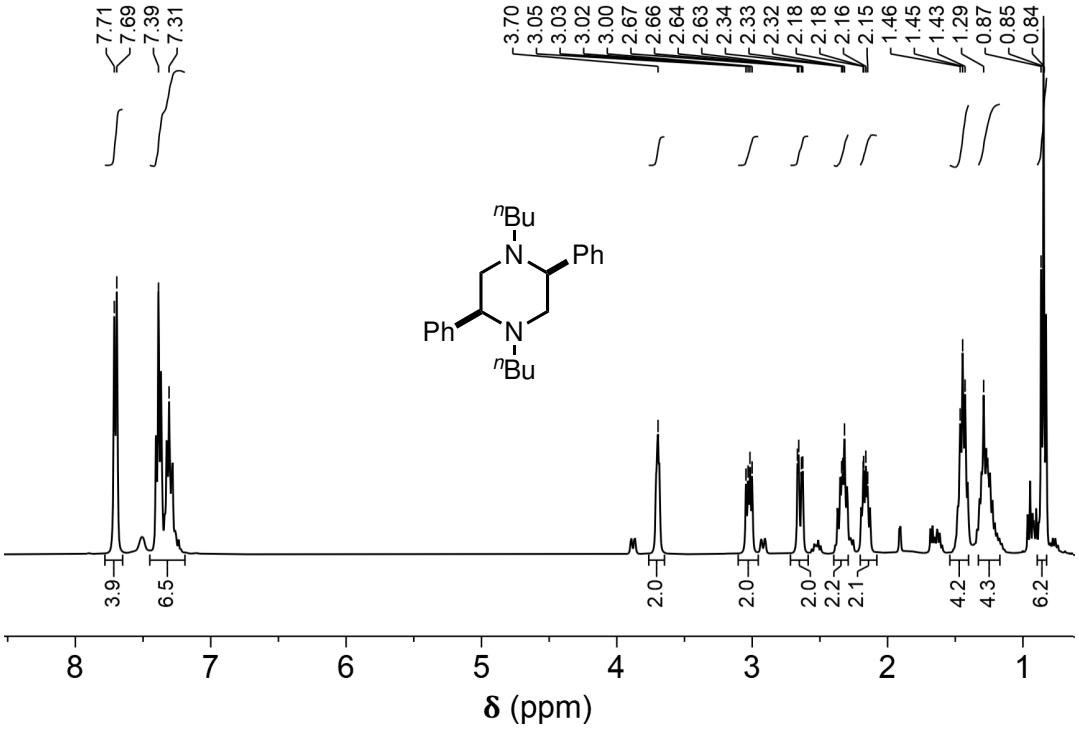

Figure A.135: *^{1}H-NMR spectrum of* (±) - ***P2a***.

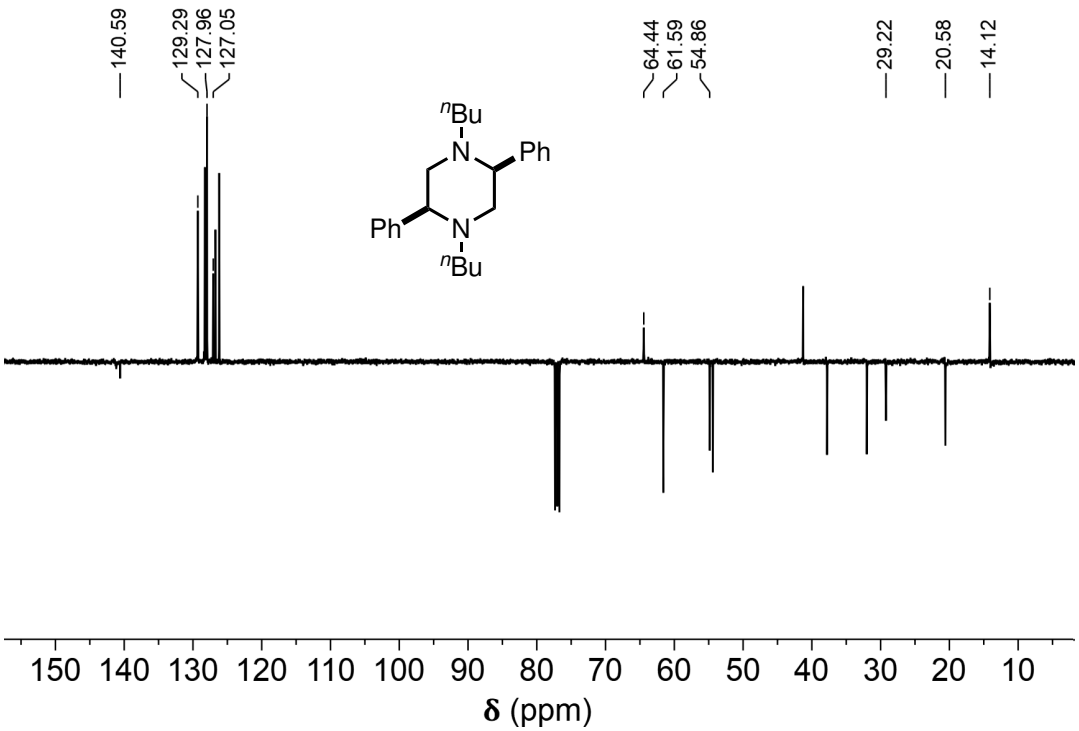

Figure A.136: *^{13}C APT NMR spectrum of* ± - ***P2a*** (*primary and tertiary carbons produce positive peaks, secondary and quaternary carbons produce negative peaks*).

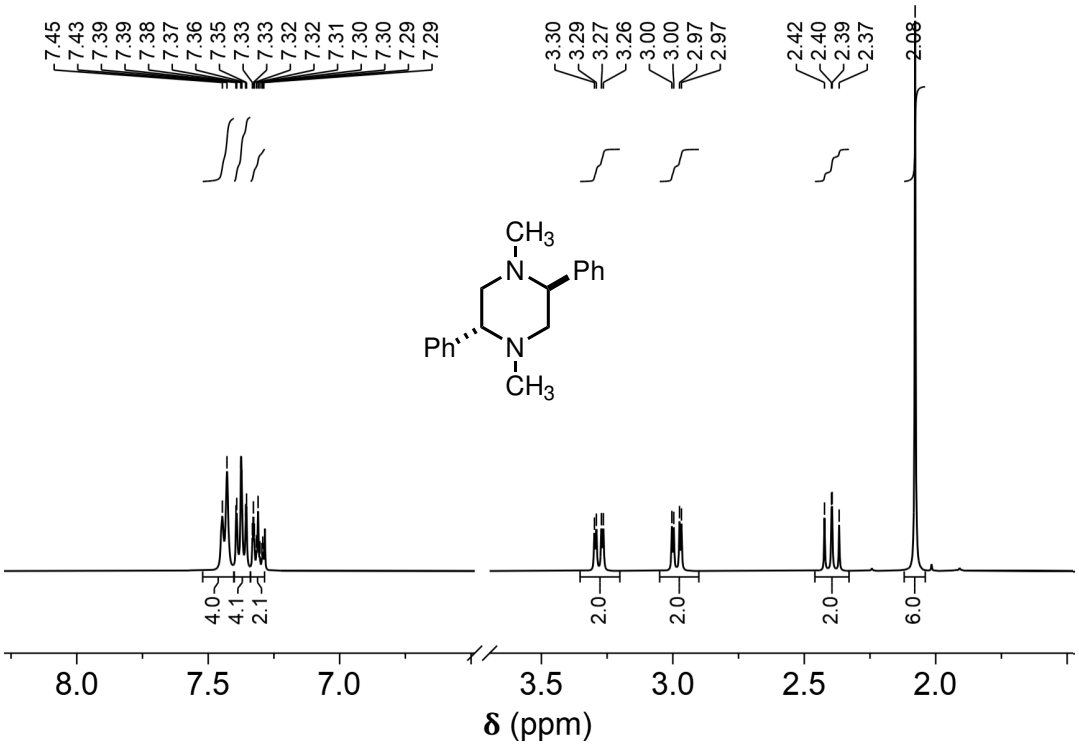

Figure A.137: *^{1}H-NMR spectrum of meso -* ***P2b****.*

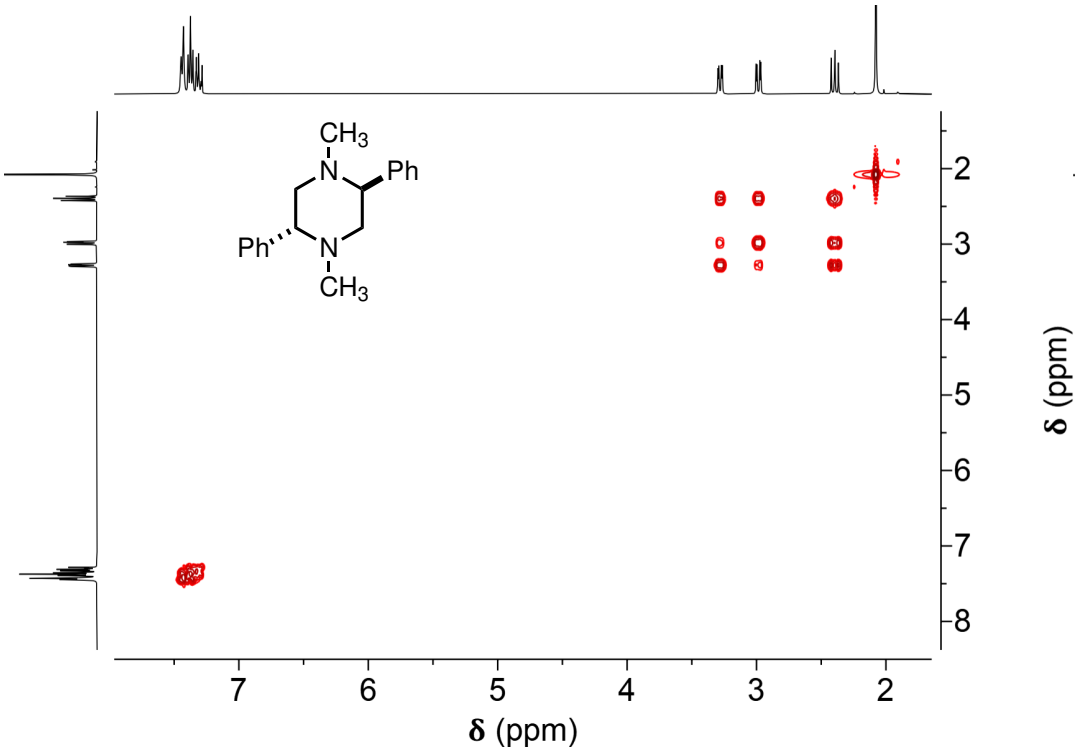

Figure A.138: *^{1}H COSY NMR spectrum of meso -* ***P2b****.*

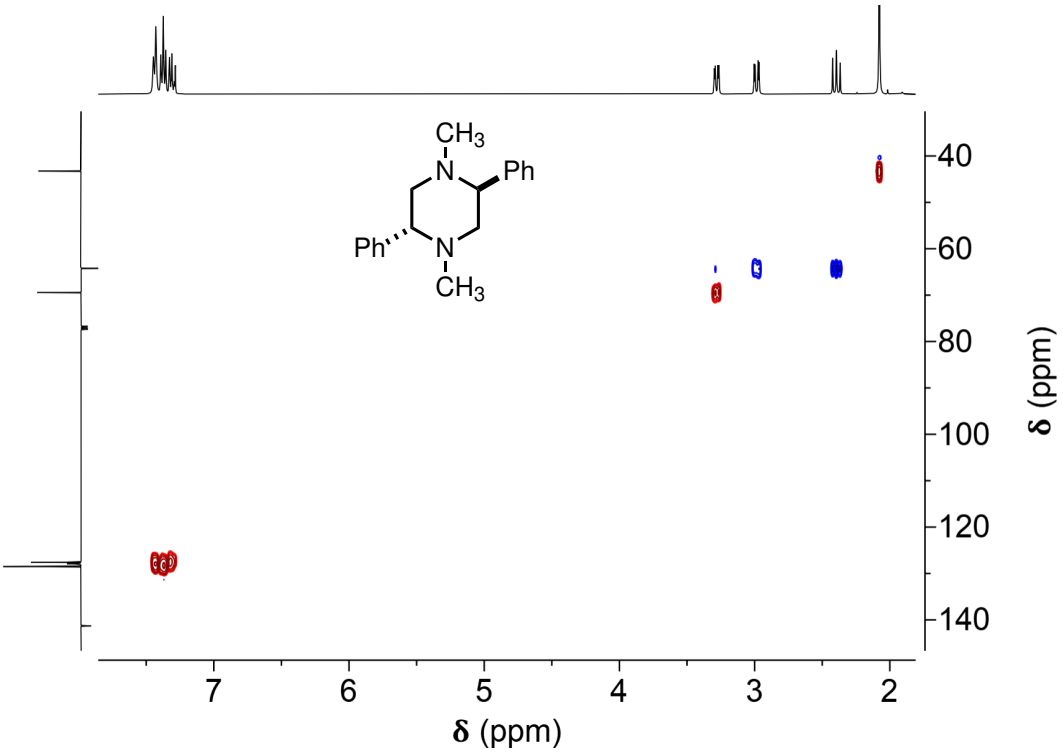

Figure A.139: *^{1}H-^{13}C HSQC NMR spectrum of meso - **P2b** (short range, primary and tertiary carbons produce red peaks, while secondary carbons produce blue peaks).*

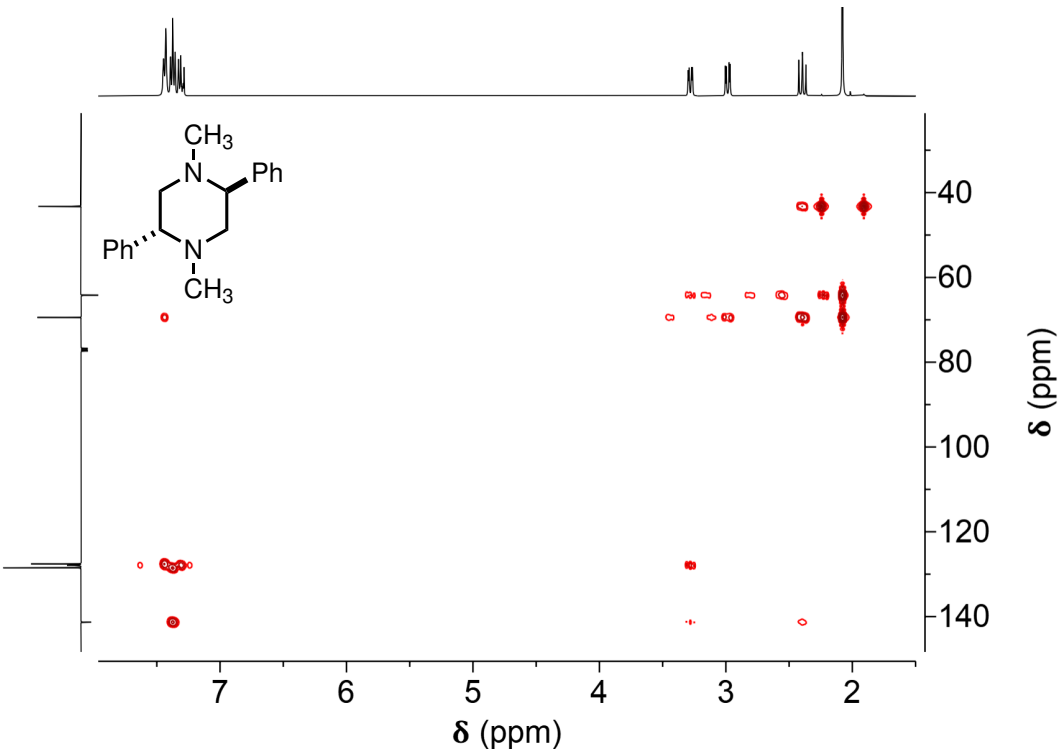

Figure A.140: *^{1}H-^{13}C HMBC NMR spectrum of meso - **P2b** (long range).*

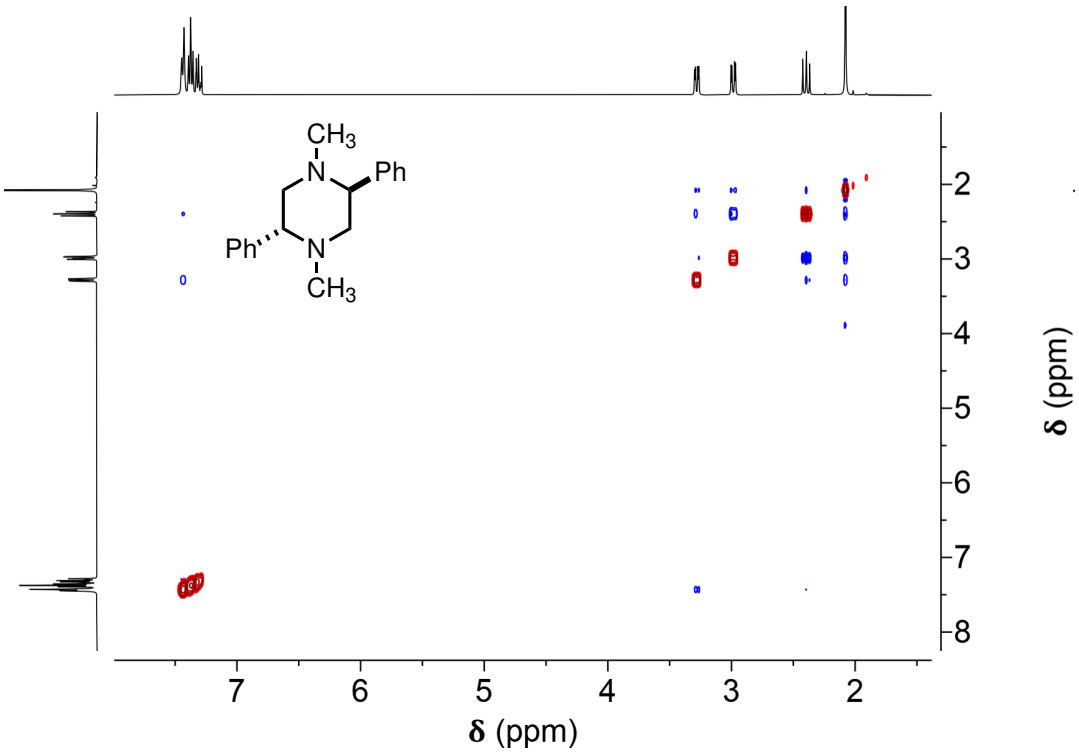

Figure A.141: *^{1}H NOESY NMR spectrum of meso - **P2b**.*

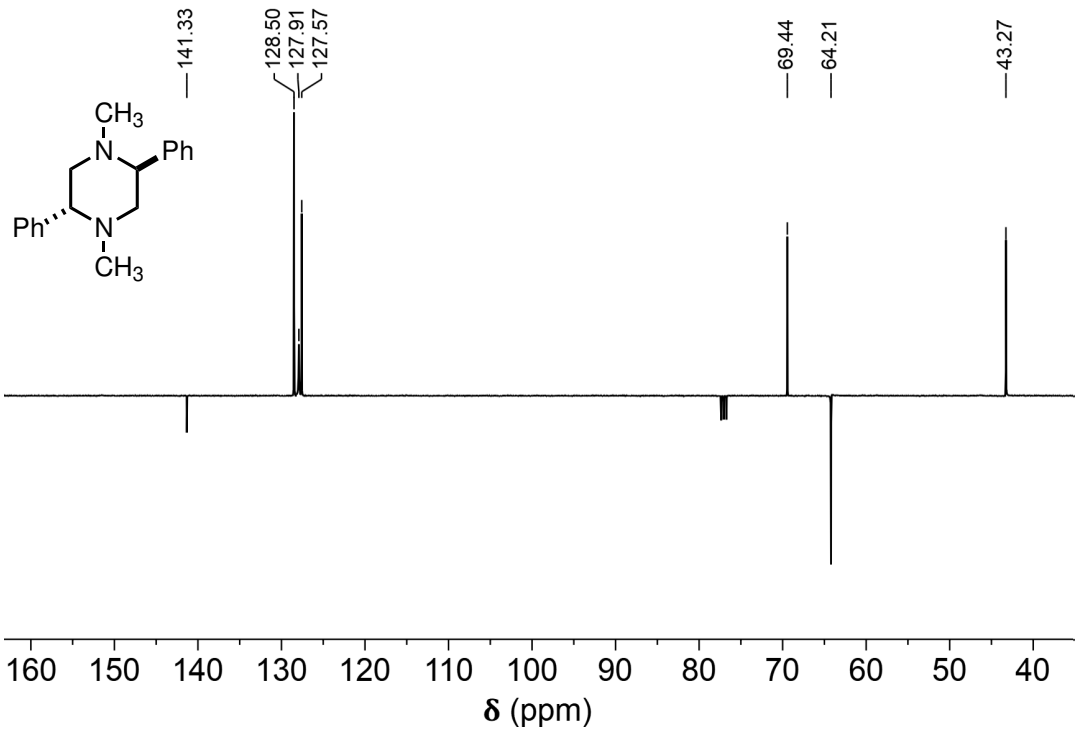

Figure A.142: *^{13}C APT NMR spectrum of meso - **P2b** (primary and tertiary carbons produce positive peaks, secondary and quaternary carbons produce negative peaks).*

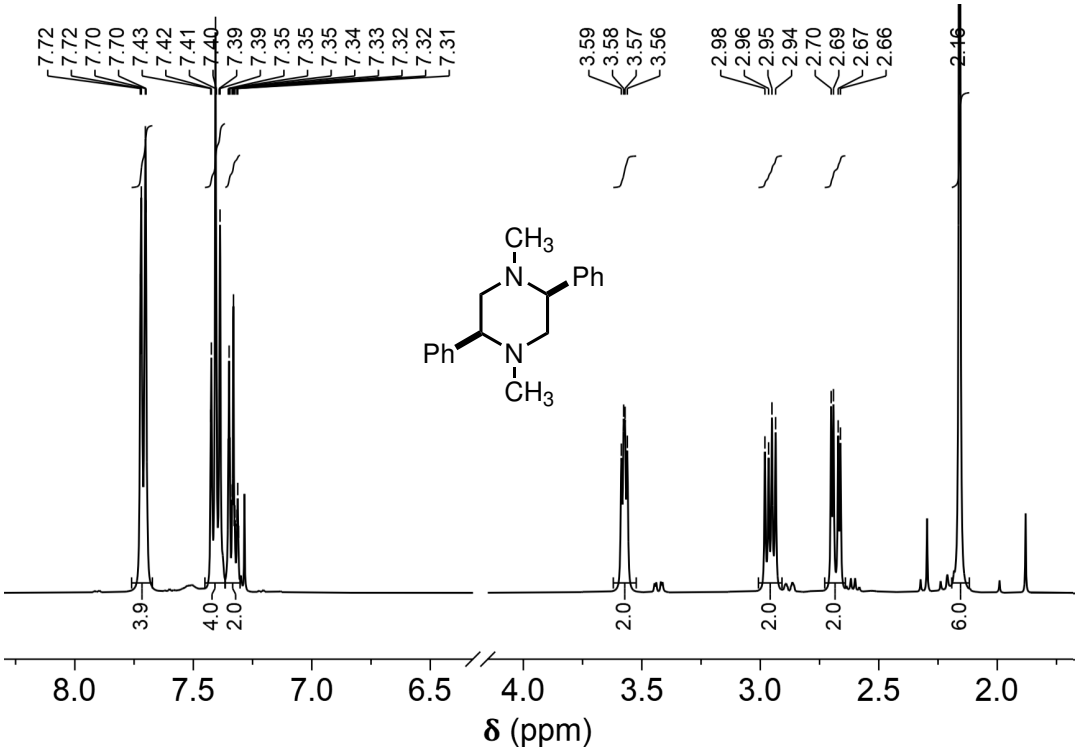

Figure A.143: *^{1}H-NMR spectrum of* (±) - ***P2b***.

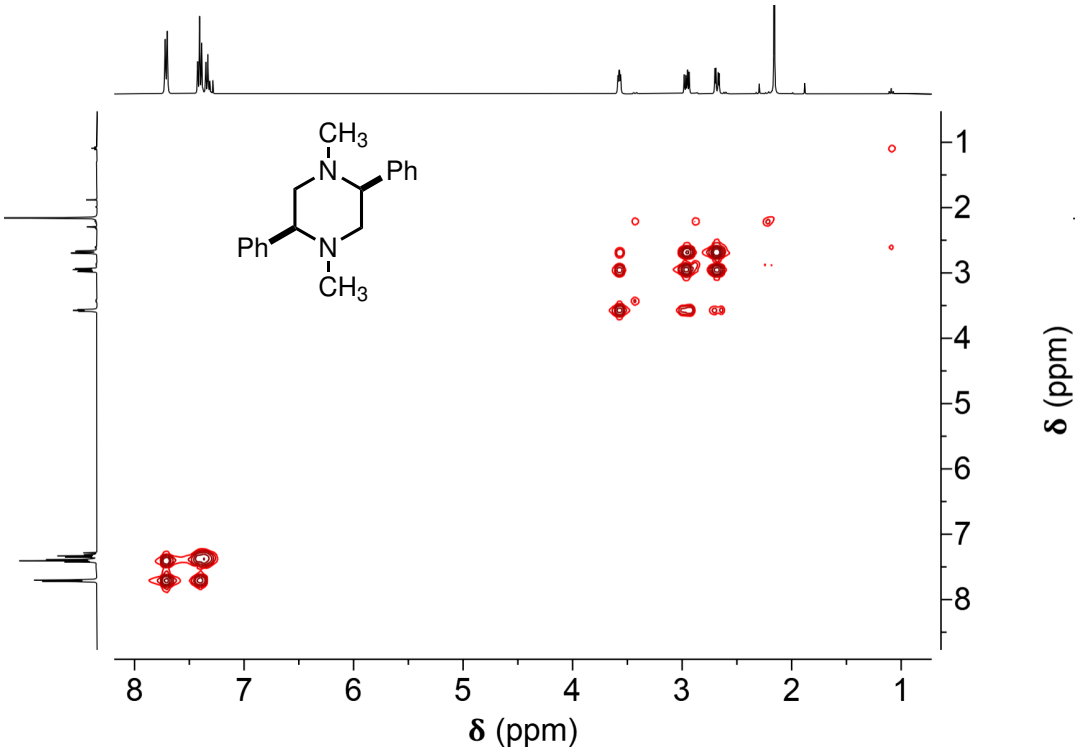

Figure A.144: *^{1}H COSY NMR spectrum of* (±) - ***P2b***.

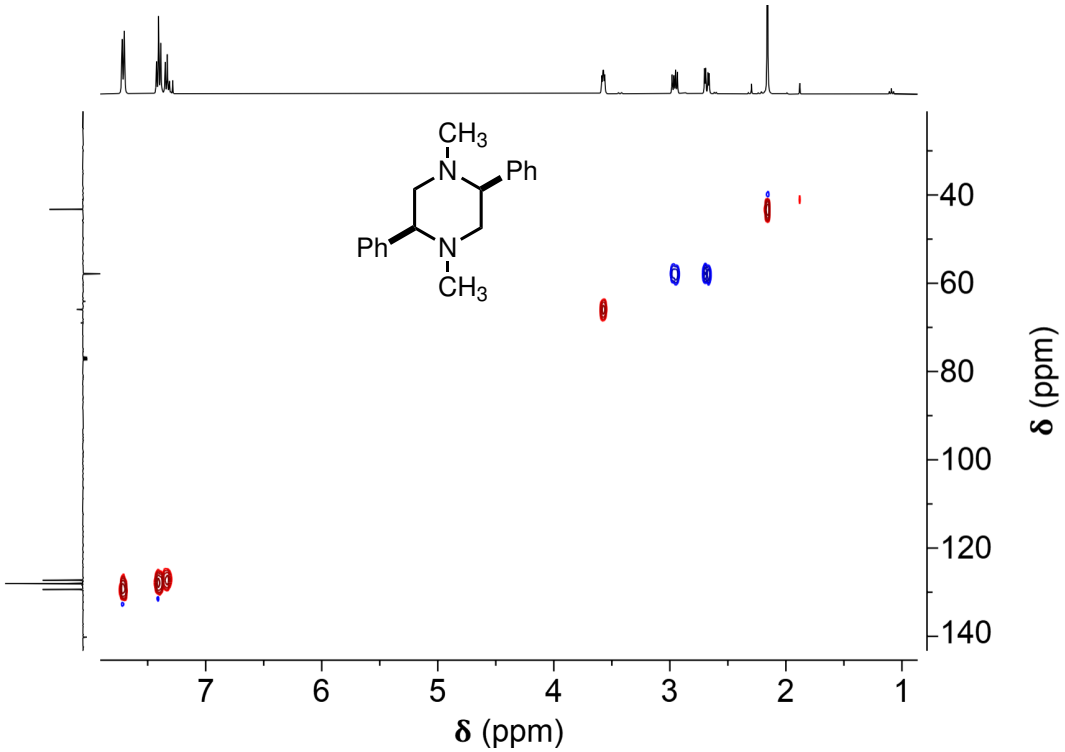

Figure A.145: *^{1}H-^{13}C HSQC NMR spectrum of* (±) - ***P2b*** *(short range, primary and tertiary carbons produce red peaks, while secondary carbons produce blue peaks).*

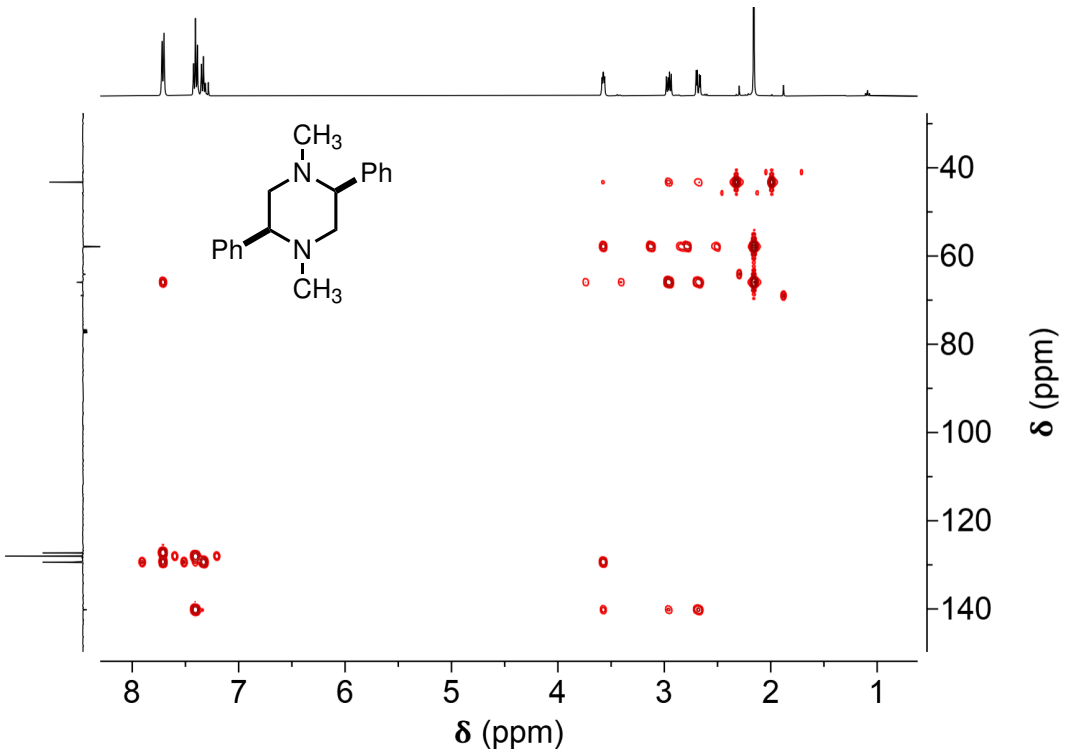

Figure A.146: *^{1}H-^{13}C HMBC NMR spectrum of* (±) - ***P2b*** *(long range).*

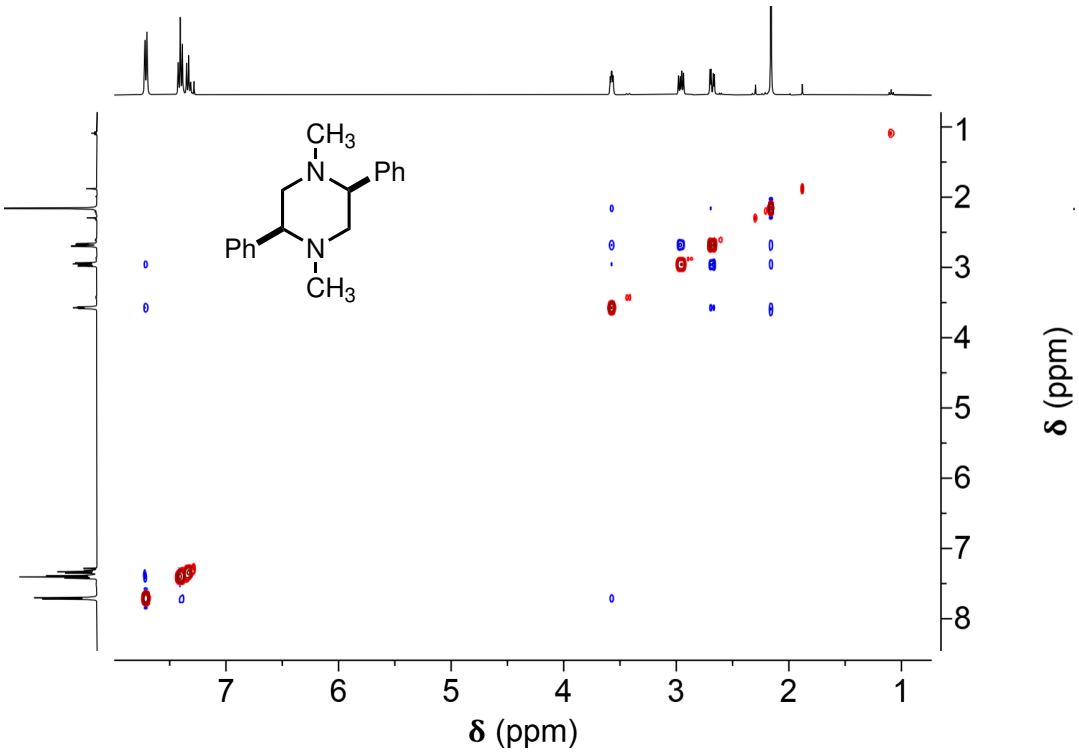

Figure A.147: *^{1}H NOESY NMR spectrum of* (±) - ***P2b***.

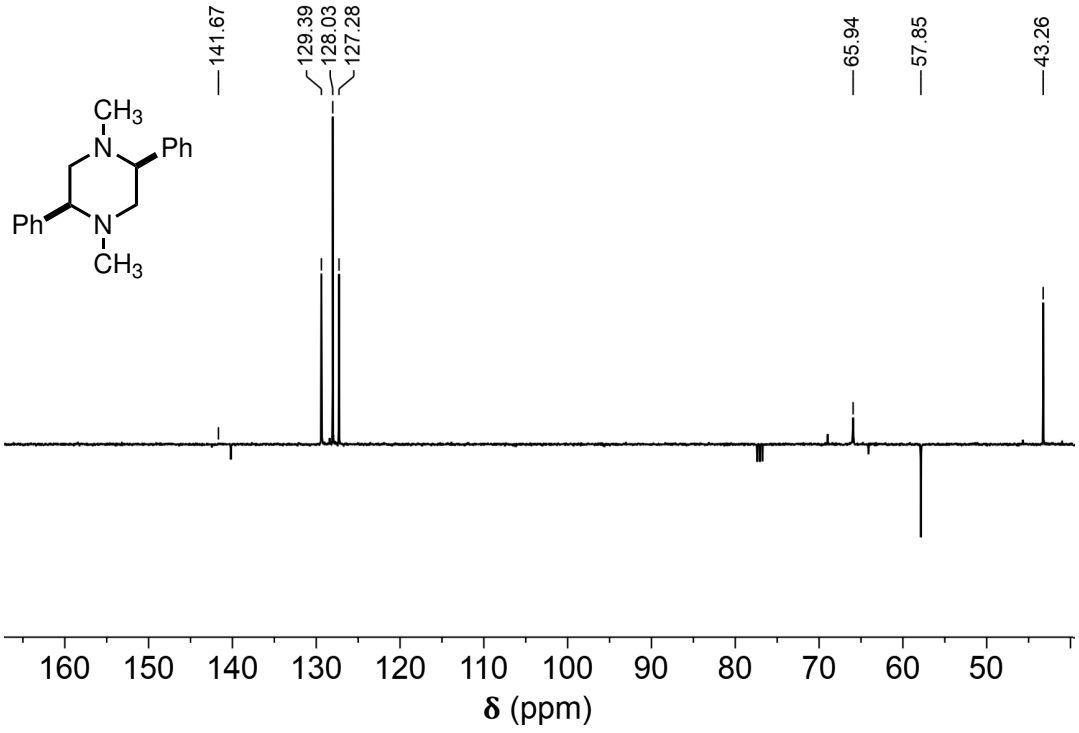

Figure A.148: *^{13}C APT NMR spectrum of* (±) - ***P2b*** (*primary and tertiary carbons produce positive peaks, secondary and quaternary carbons produce negative peaks*).

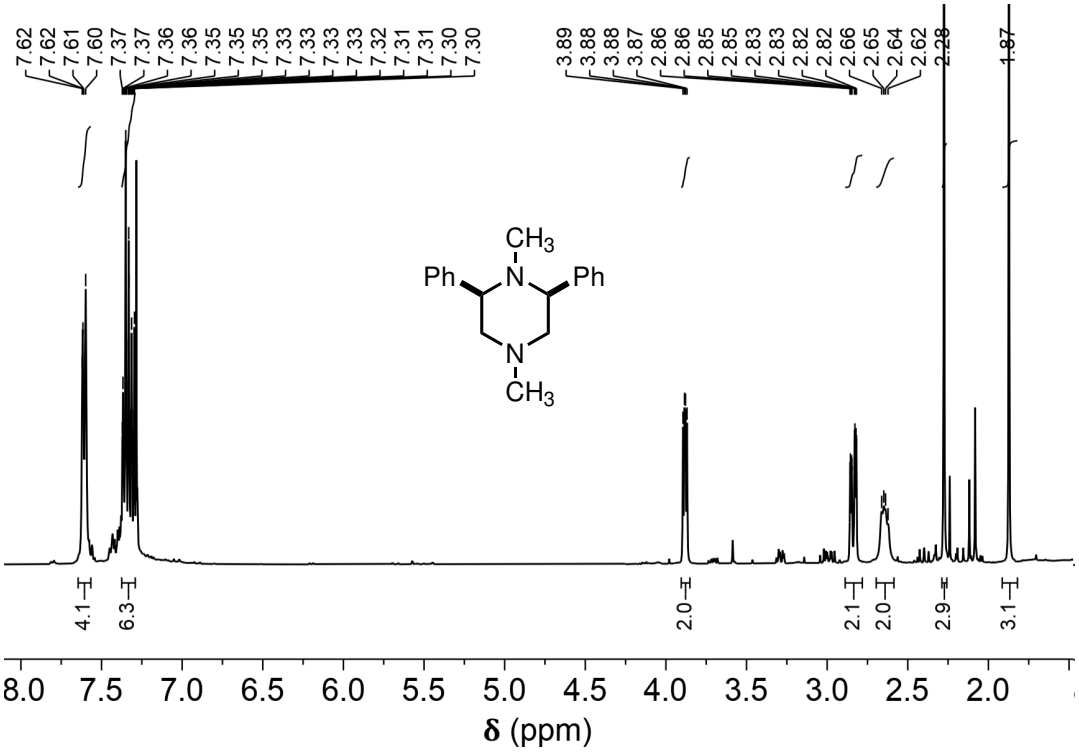

Figure A.149: *^{1}H-NMR spectrum of meso - **P2b'**.*

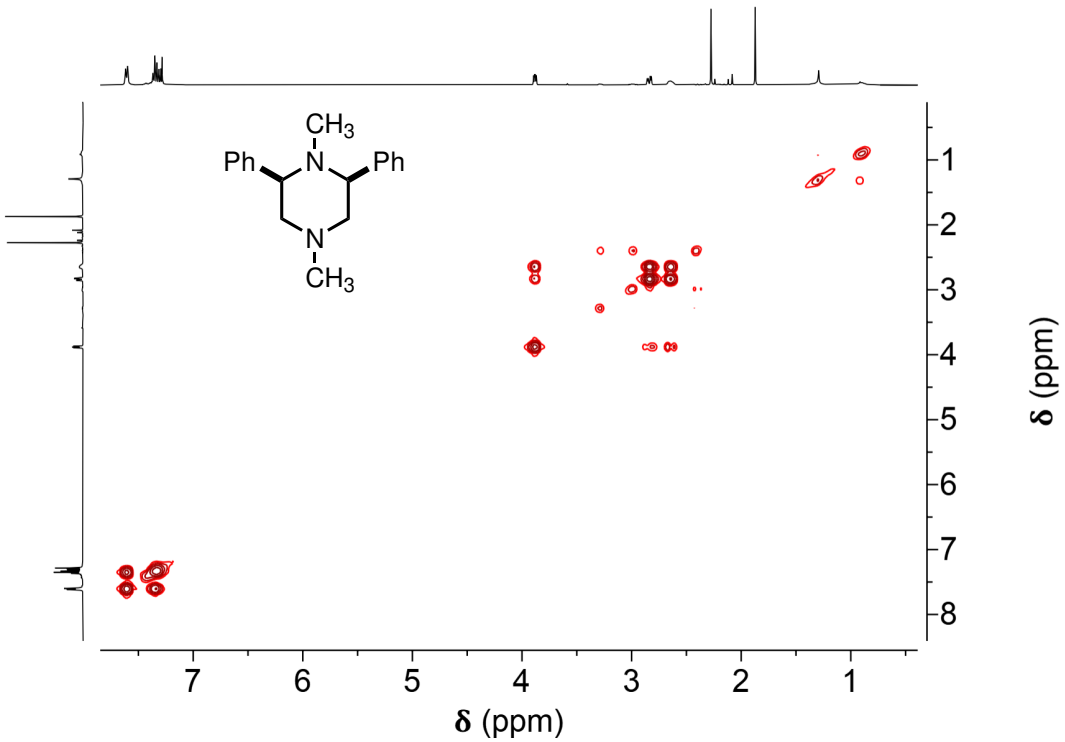

Figure A.150: *^{1}H COSY NMR spectrum of meso - **P2b'**.*

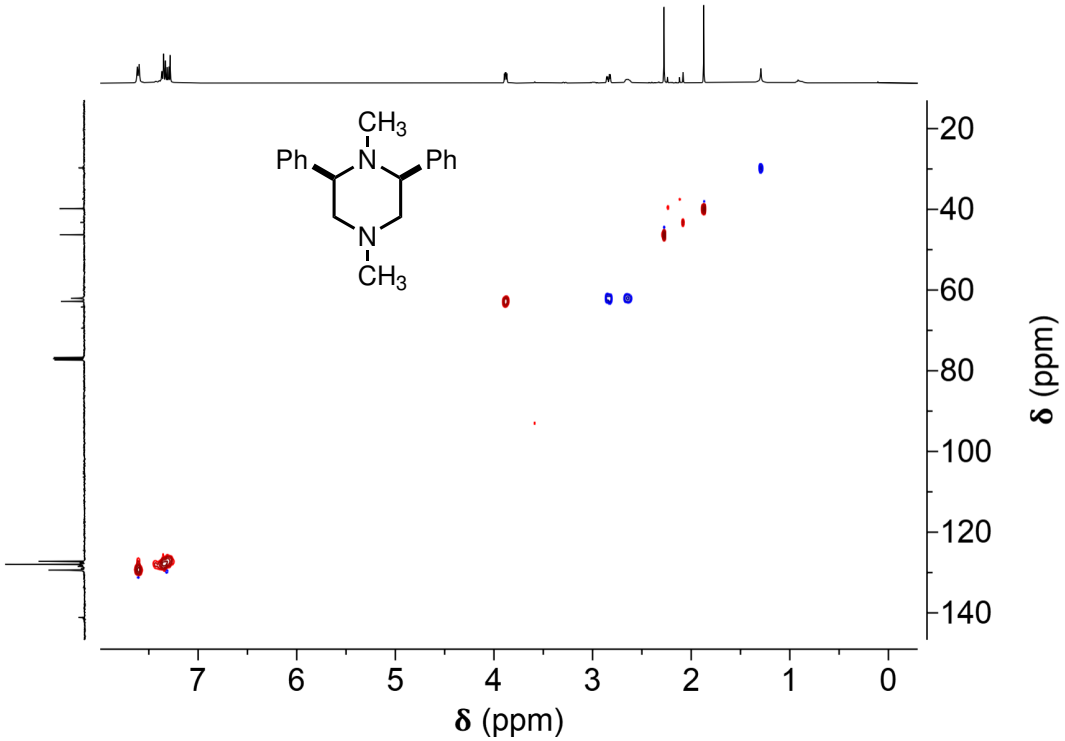

Figure A.151: *^{1}H-^{13}C HSQC NMR spectrum of meso - **P2b'** (short range, primary and tertiary carbons produce red peaks, while secondary carbons produce blue peaks).*

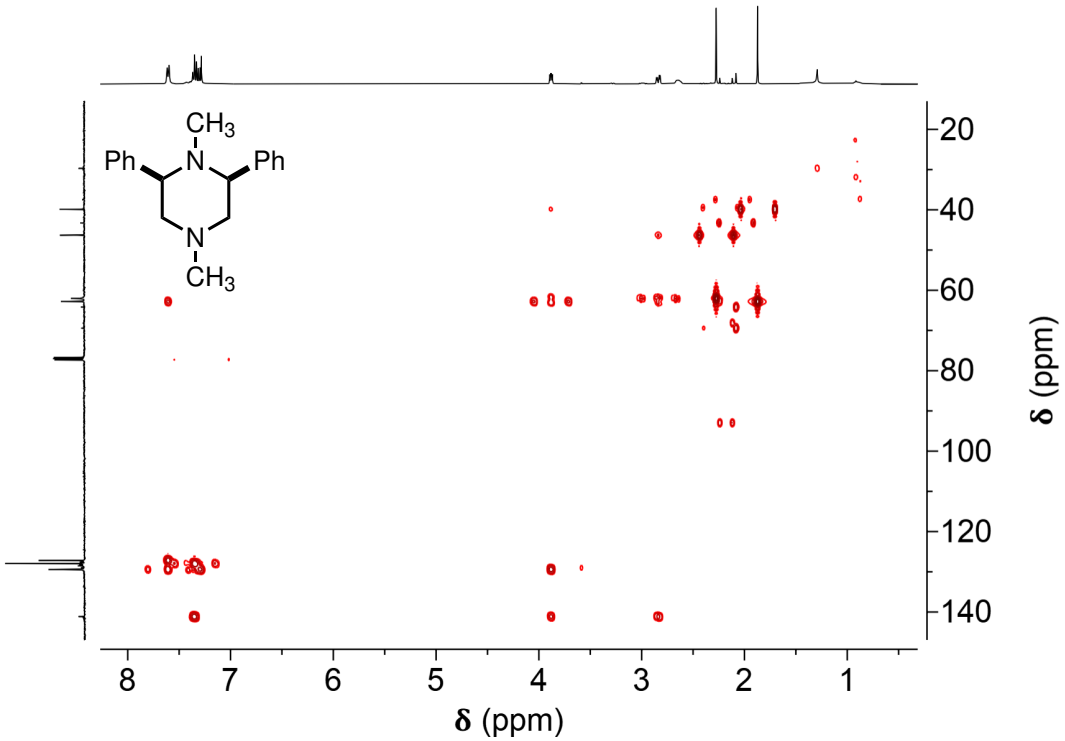

Figure A.152: *^{1}H-^{13}C HMBC NMR spectrum of meso - **P2b'** (long range).*

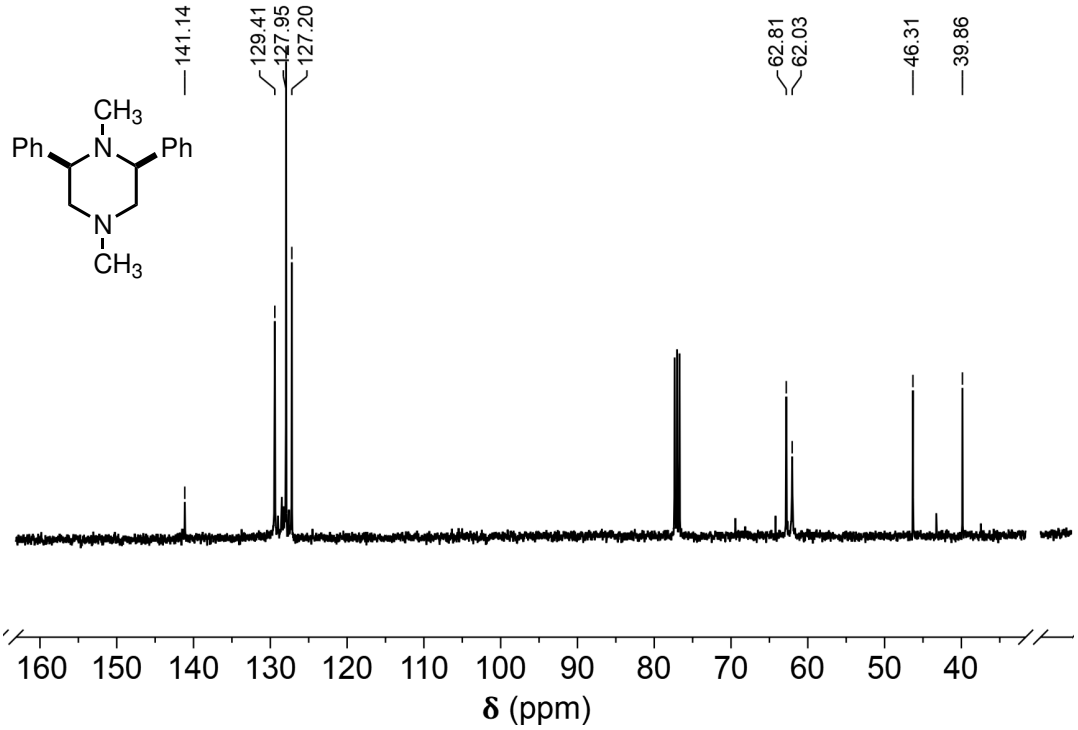

Figure A.153: *^{13}C-NMR spectrum of meso - **P2b′**.*

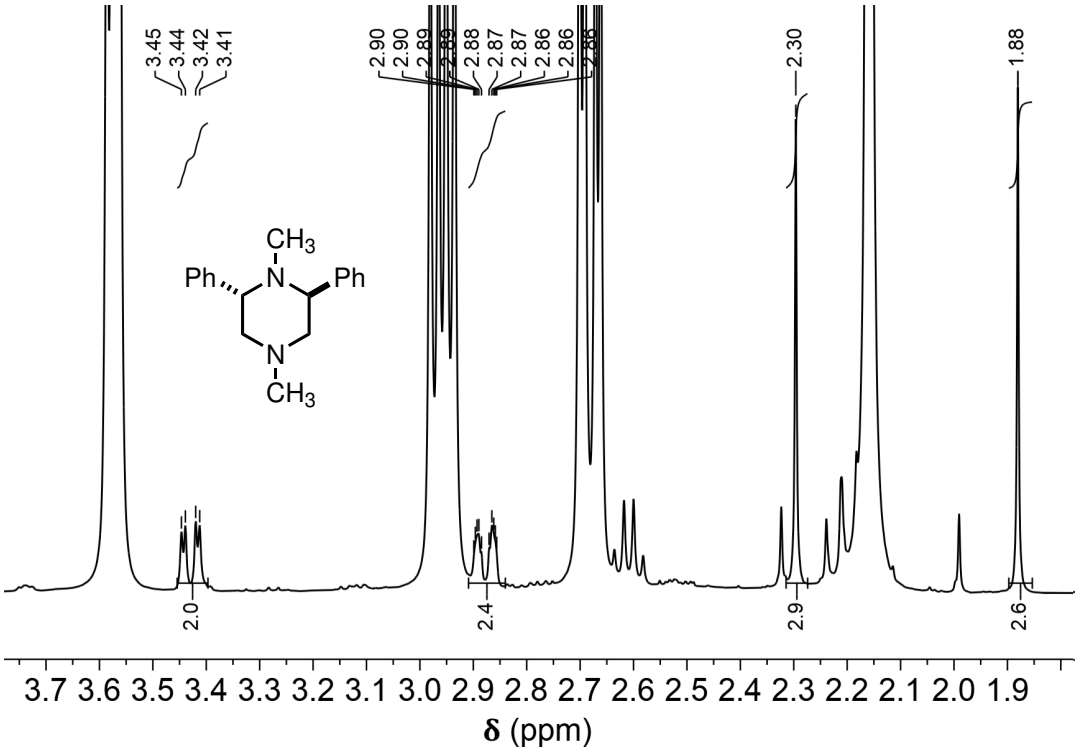

Figure A.154: *^{1}H-NMR spectrum of* (±) - ***P2b′***, *isolated together with* (±) - ***P2b***.

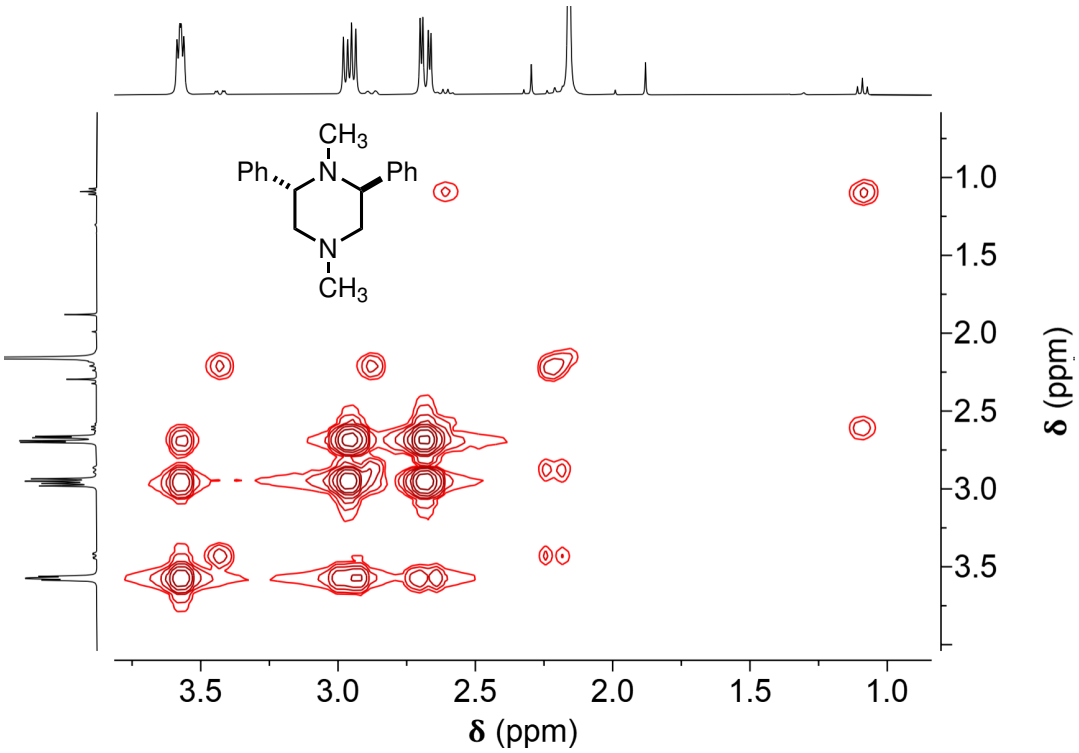

Figure A.155: *^{1}H COSY NMR spectrum of* (±) - ***P2b'***, *isolated together with* (±) - ***P2b***.

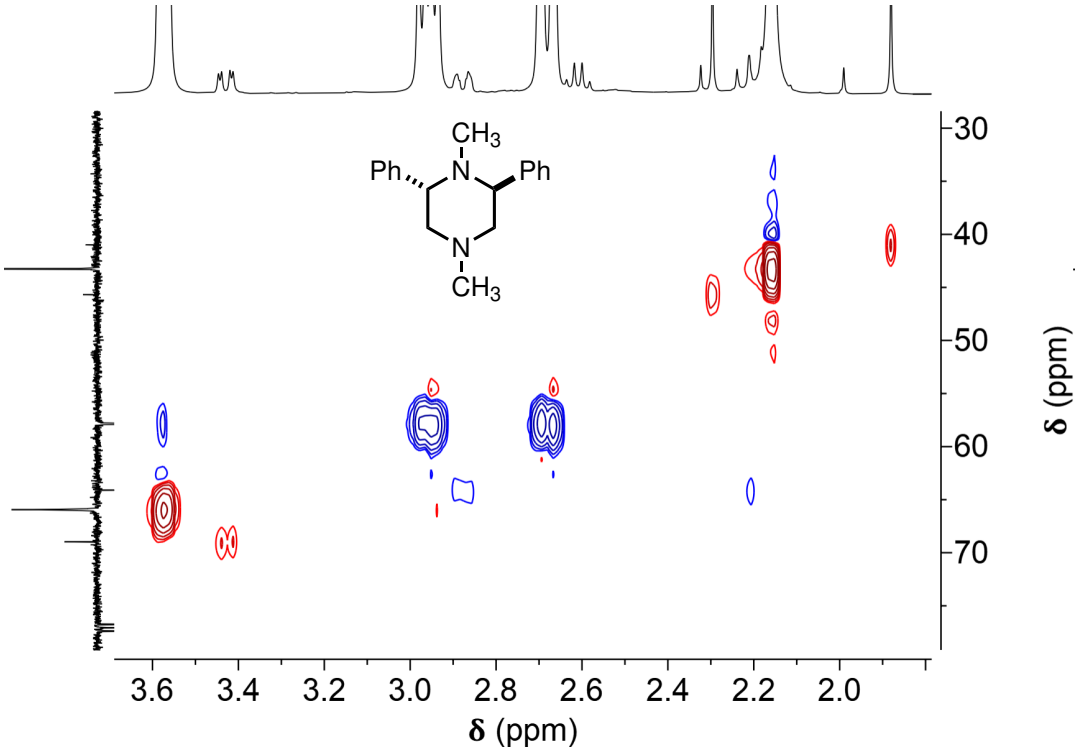

Figure A.156: *^{1}H-^{13}C HSQC NMR spectrum of* (±) - ***P2b'***, *isolated together with* (±) - ***P2b*** (*short range, primary and tertiary carbons produce red peaks, while secondary carbons produce blue peaks*).

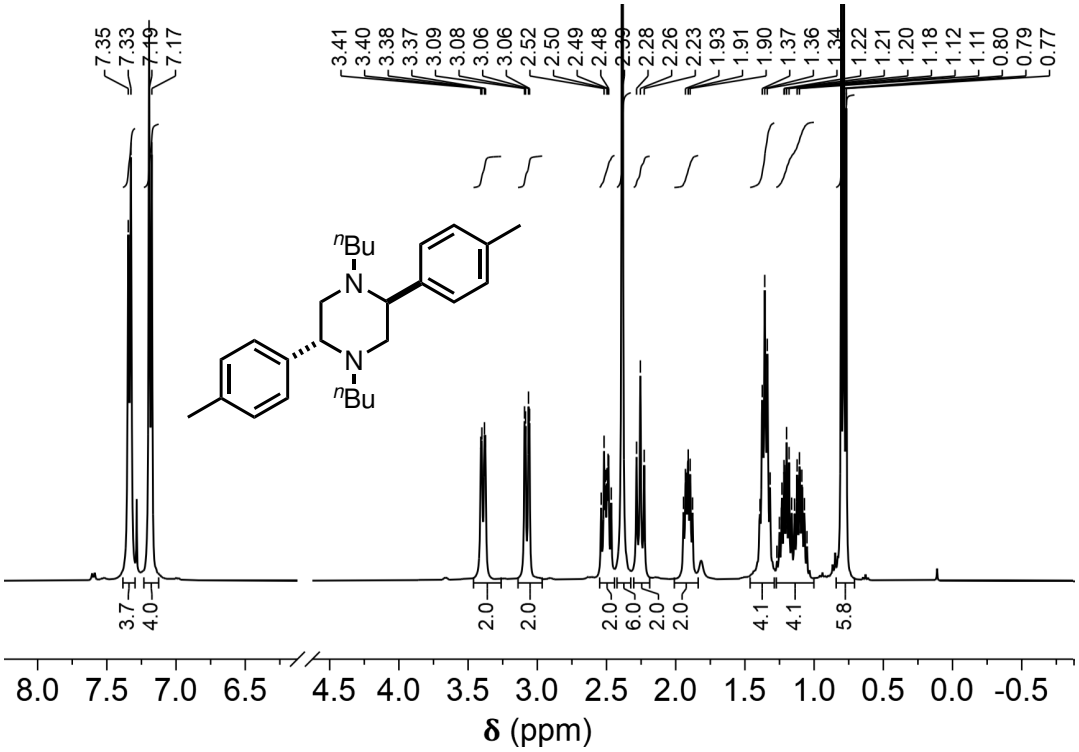

Figure A.157: *^{1}H-NMR spectrum of meso - **P2h**.*

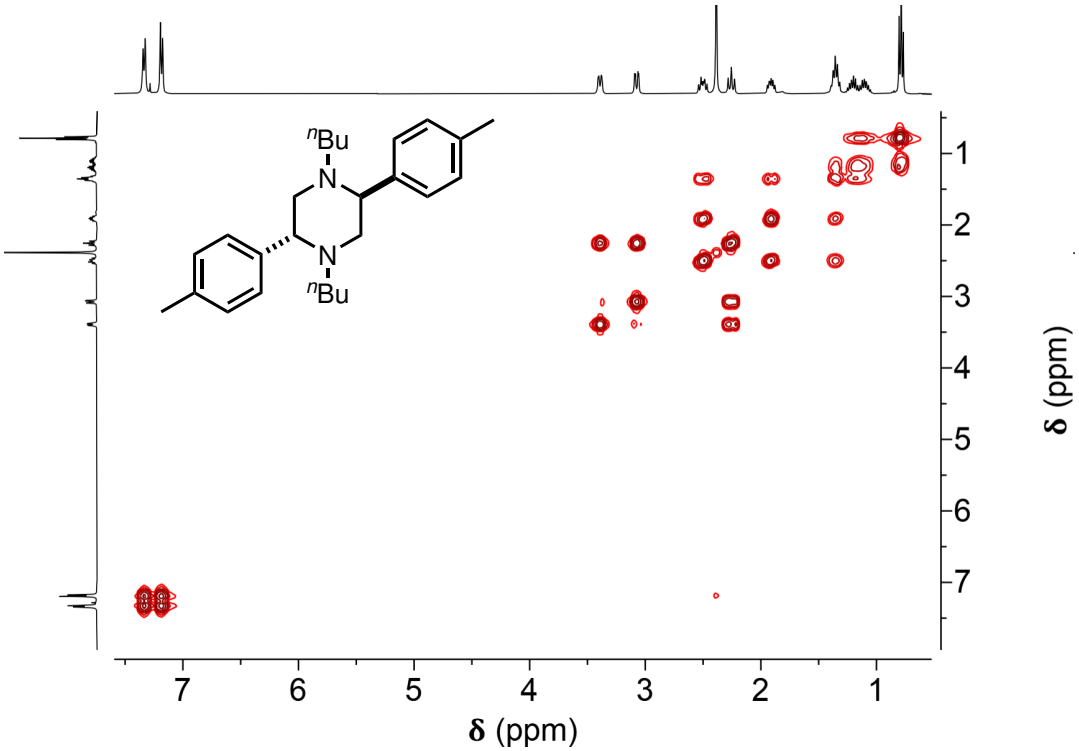

Figure A.158: *^{1}H COSY NMR spectrum of meso - **P2h**.*

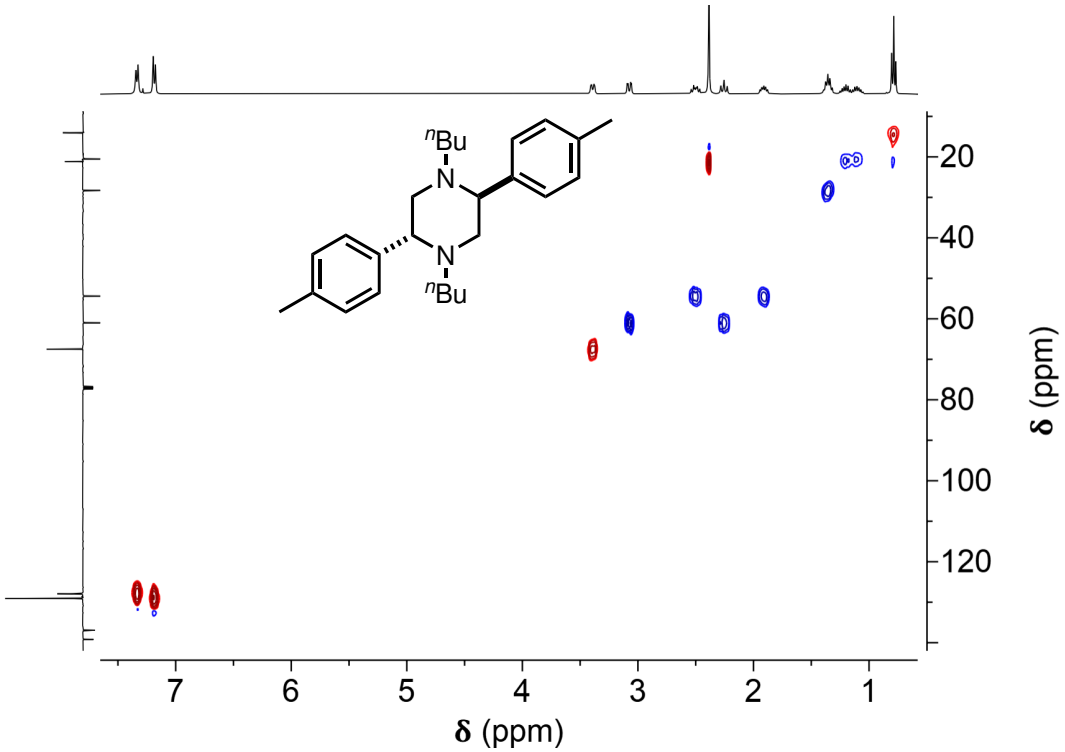

Figure A.159: *^{1}H-^{13}C HSQC NMR spectrum of meso -* ***P2h*** *(short range, primary and tertiary carbons produce red peaks, while secondary carbons produce blue peaks).*

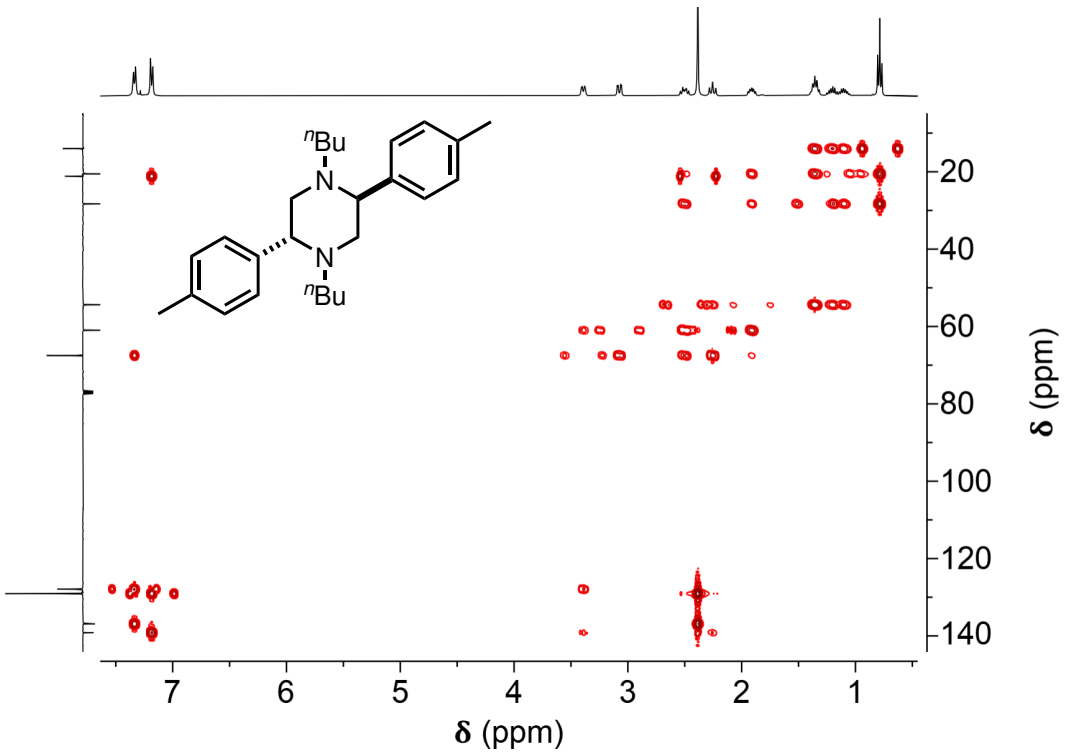

Figure A.160: *^{1}H-^{13}C HMBC NMR spectrum of meso -* ***P2h*** *(long range).*

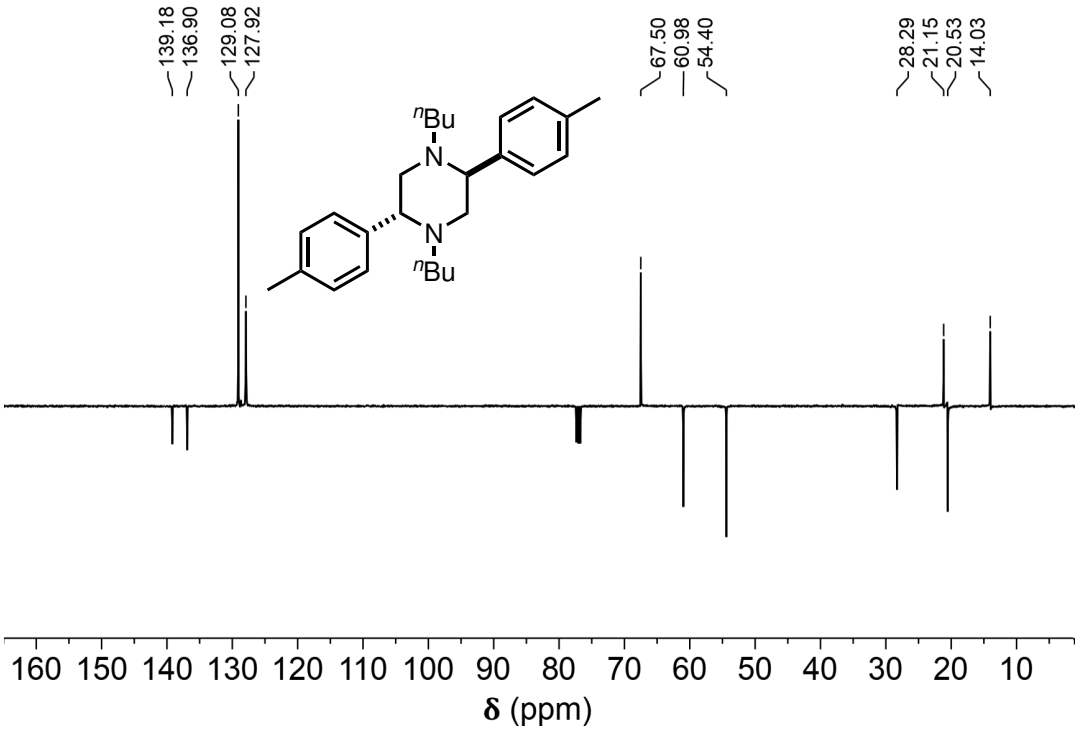

Figure A.161: *^{13}C APT NMR spectrum of meso -* ***P2h*** *(primary and tertiary carbons produce positive peaks, secondary and quaternary carbons produce negative peaks).*

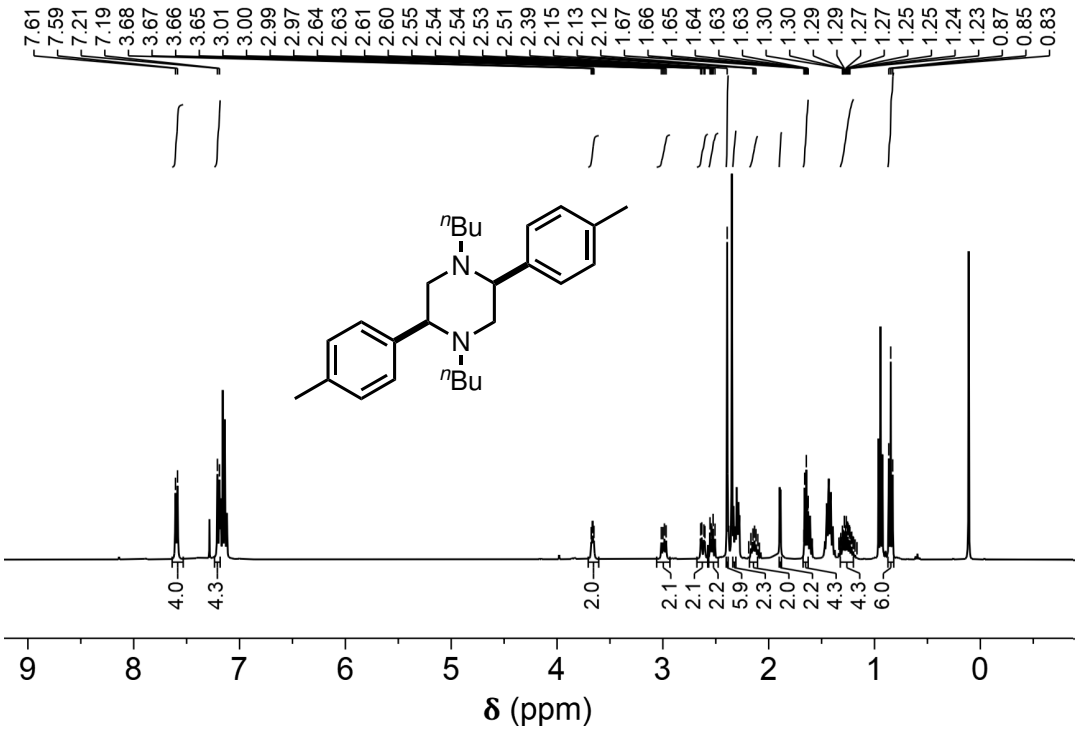

Figure A.162: *^{1}H-NMR spectrum of* (±) - ***P2h***.

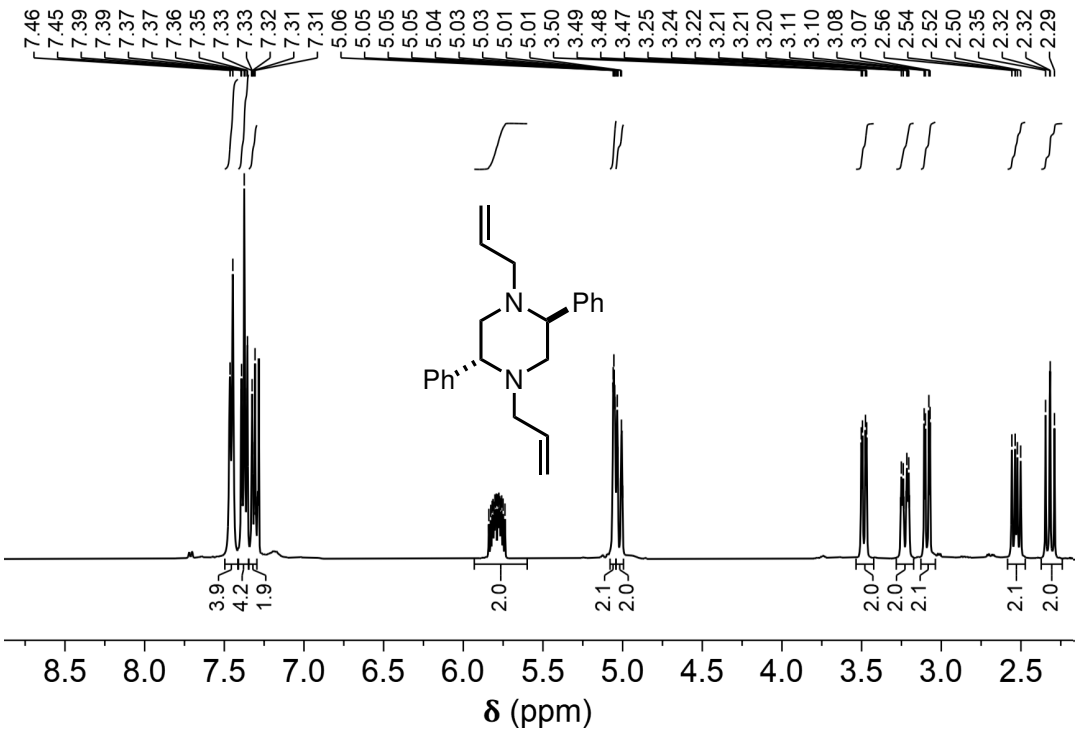

Figure A.163: *^{1}H-NMR spectrum of meso - **P2i**.*

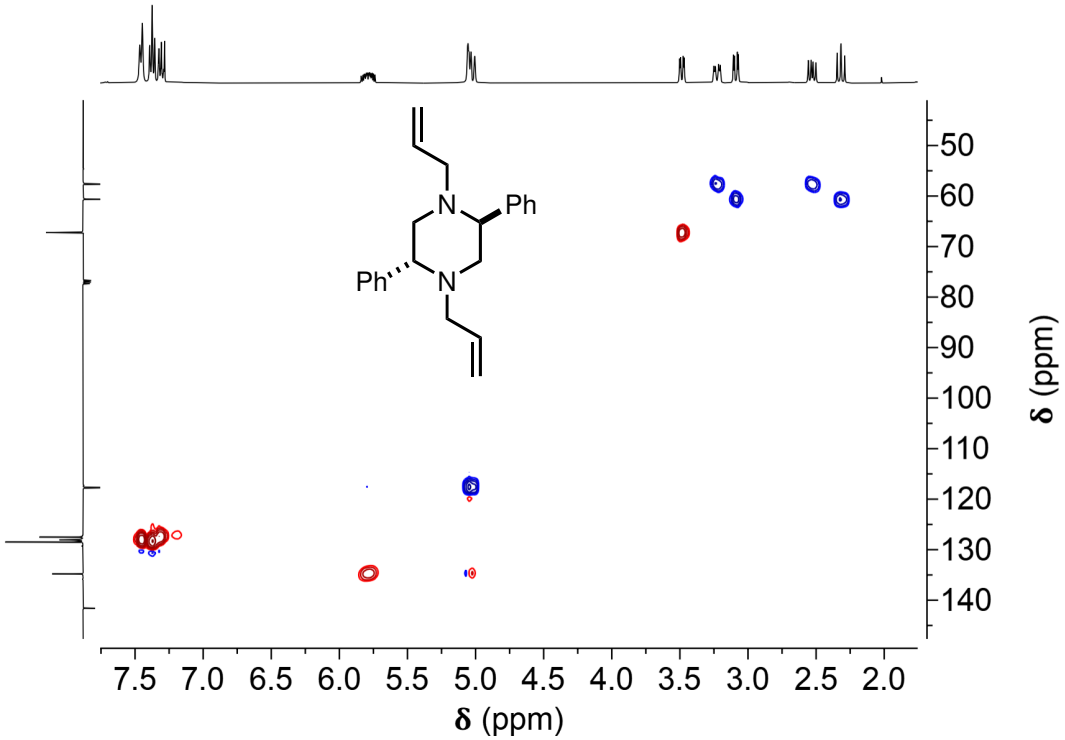

Figure A.164: *^{1}H-^{13}C HSQC NMR spectrum of meso - **P2i** (short range, primary and tertiary carbons produce red peaks, while secondary carbons produce blue peaks).*

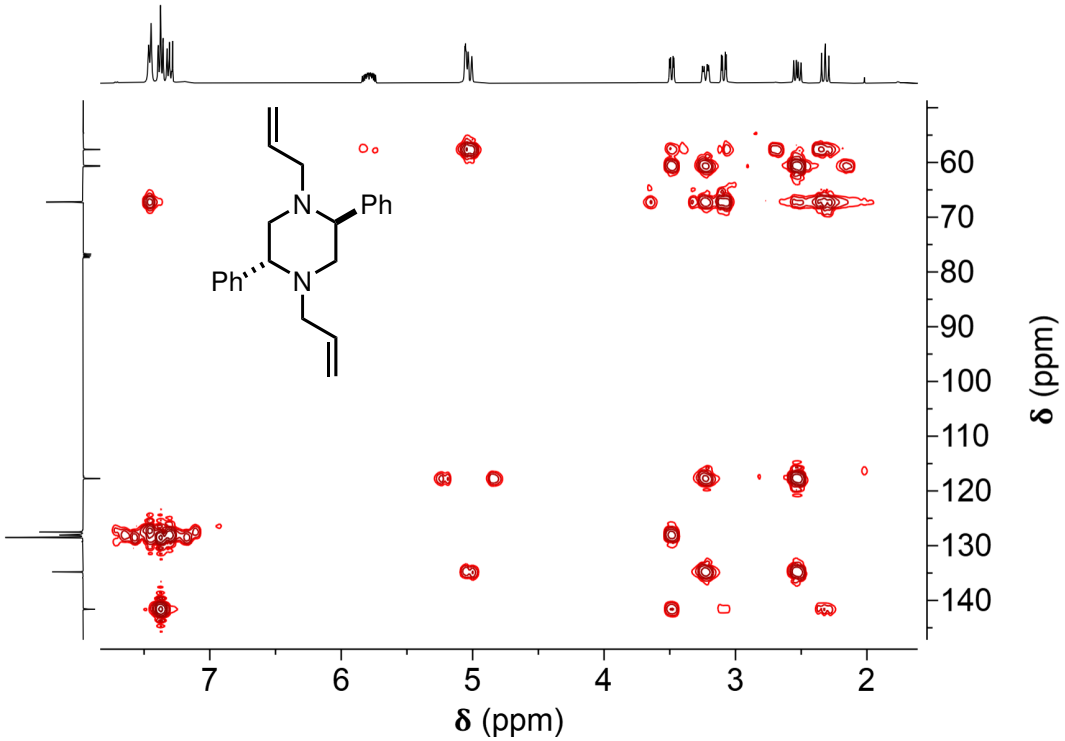

Figure A.165: *^{1}H-^{13}C HMBC NMR spectrum of meso - **P2i** (long range).*

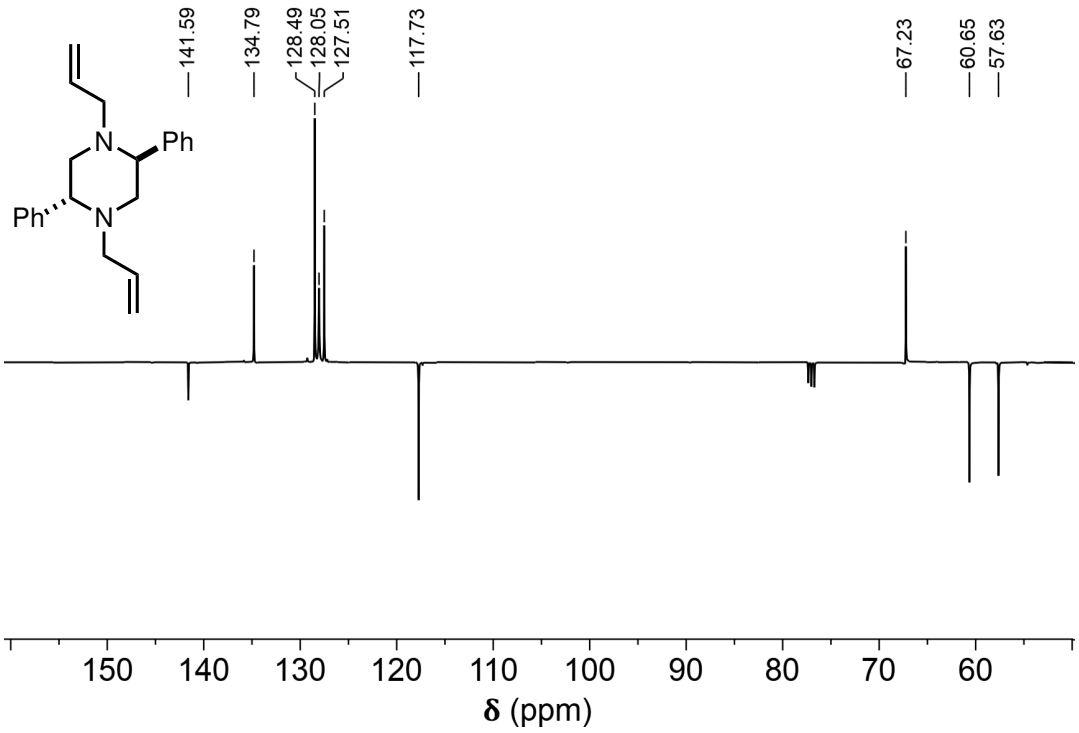

Figure A.166: *^{13}C APT NMR spectrum of meso - **P2i** (primary and tertiary carbons produce positive peaks, secondary and quaternary carbons produce negative peaks).*

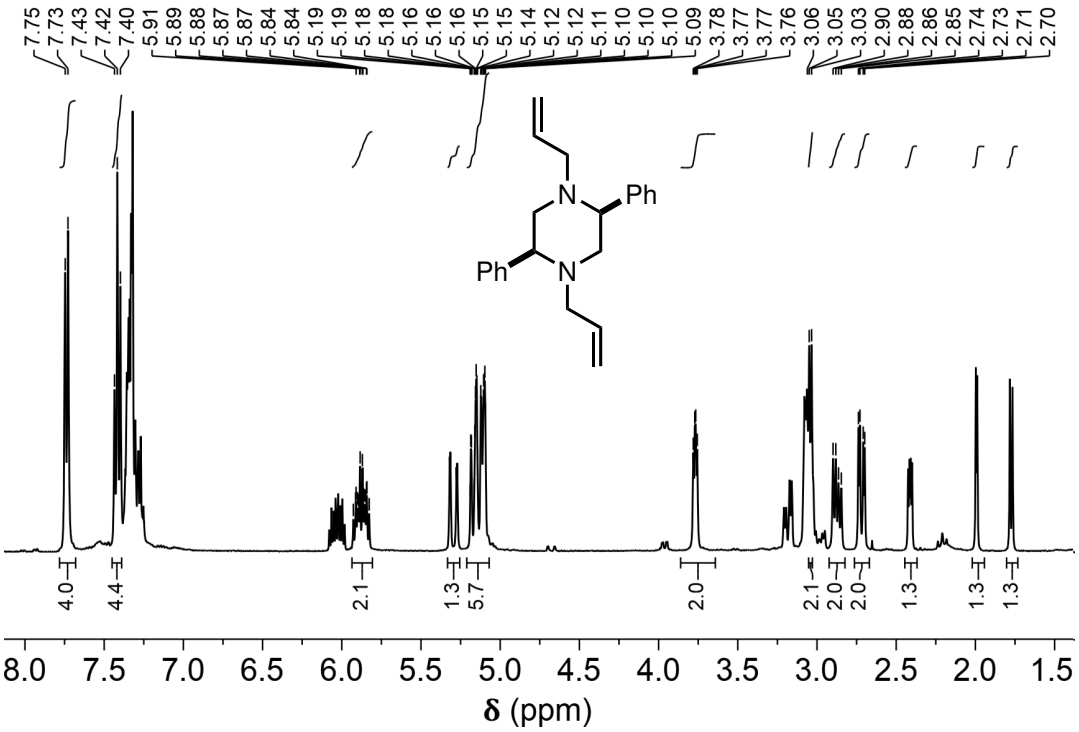

Figure A.167: ^{1}*H-NMR spectrum of* (±) - ***P2i***.

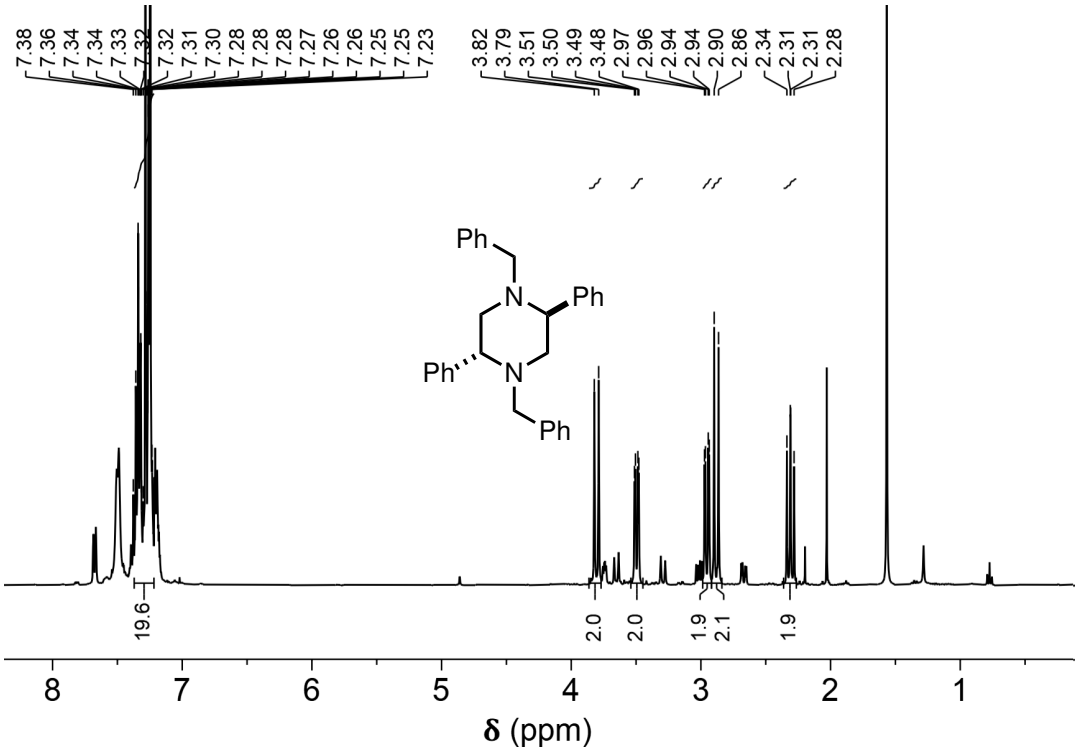

Figure A.168: ^{1}*H-NMR spectrum of meso* - ***P2j***.

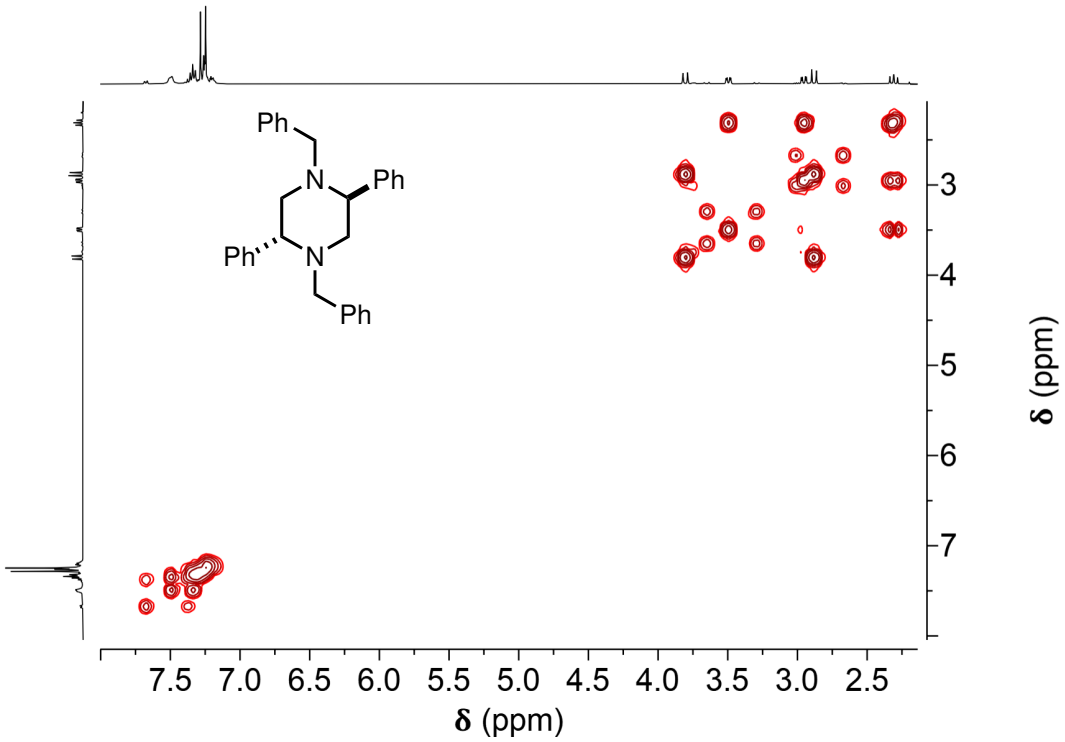

Figure A.169: *^{1}H COSY NMR spectrum of meso - **P2j**.*

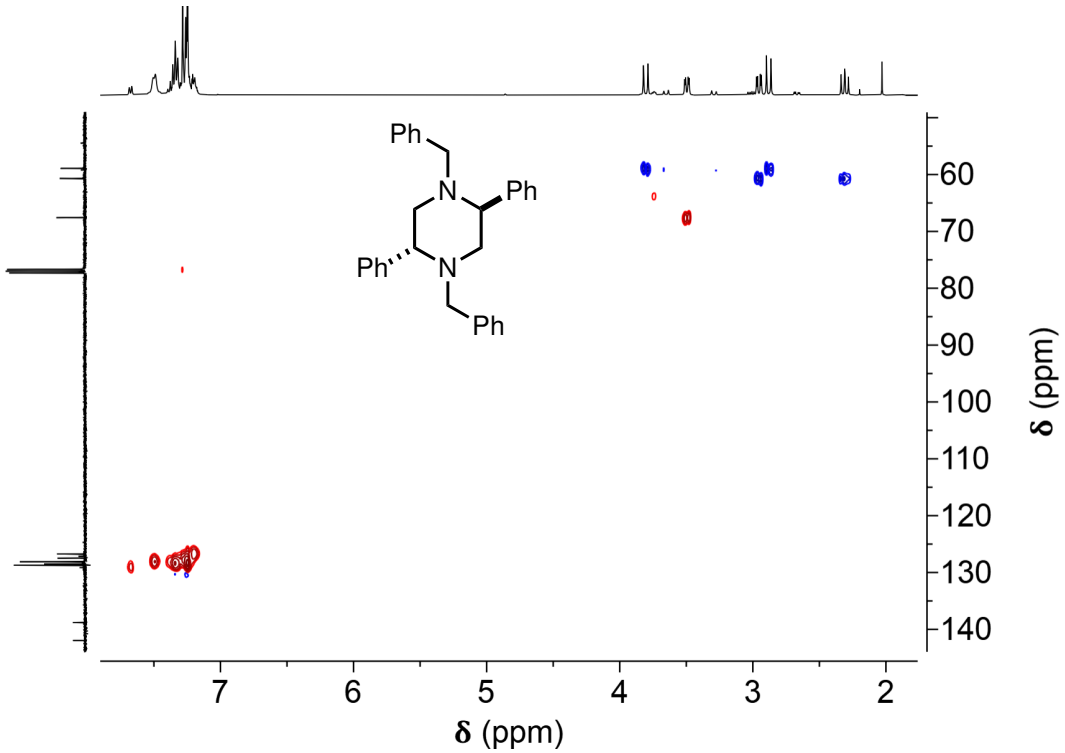

Figure A.170: *^{1}H-^{13}C HSQC NMR spectrum of meso - **P2j** (short range, primary and tertiary carbons produce red peaks, while secondary carbons produce blue peaks).*

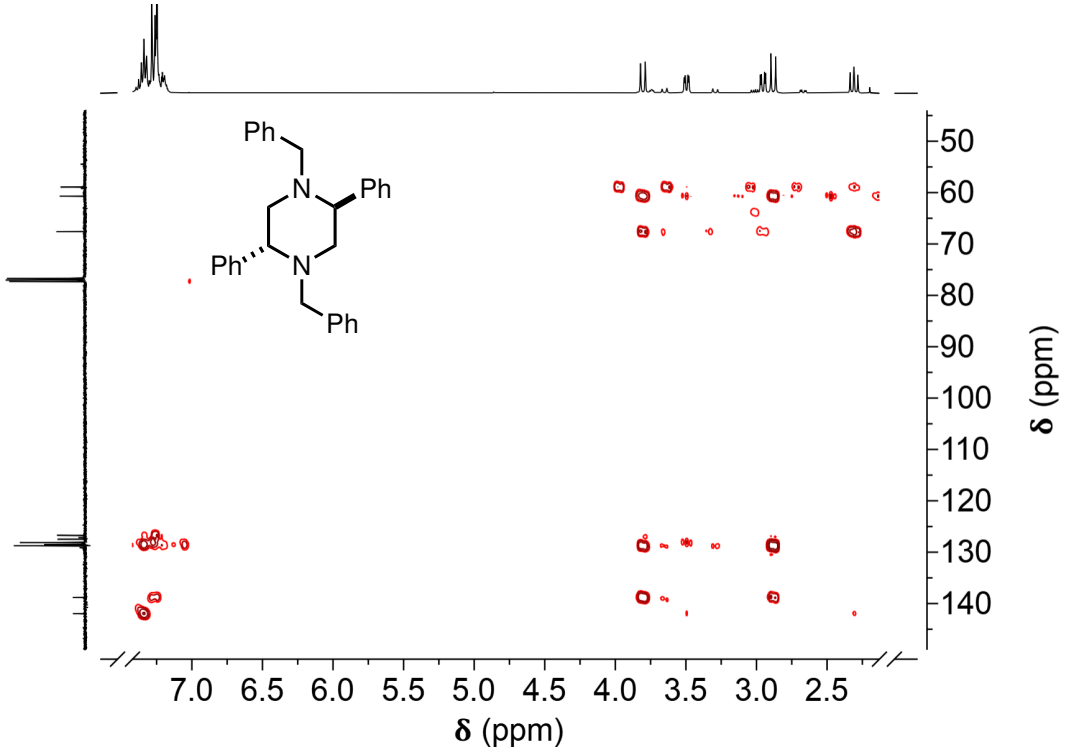

Figure A.171: *^{1}H-^{13}C HMBC NMR spectrum of meso - **P2j** (long range).*

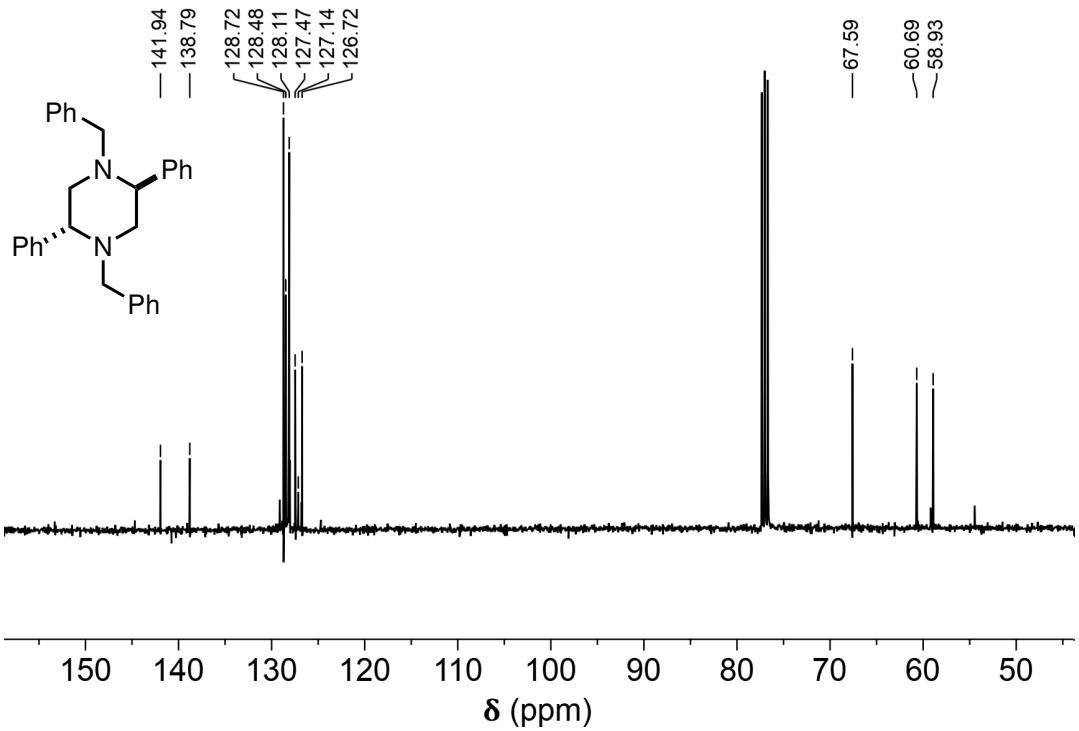

Figure A.172: *^{13}C-NMR spectrum of meso - **P2j**.*

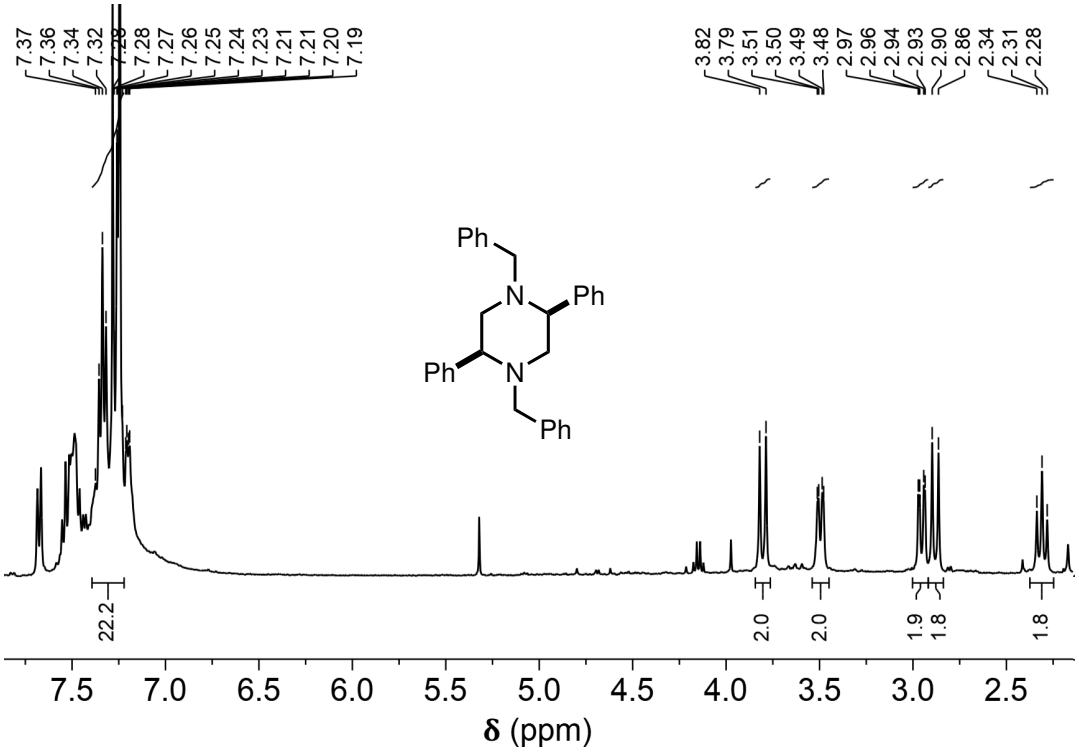

Figure A.173: *^{1}H-NMR spectrum of* (±) - ***P2j***.

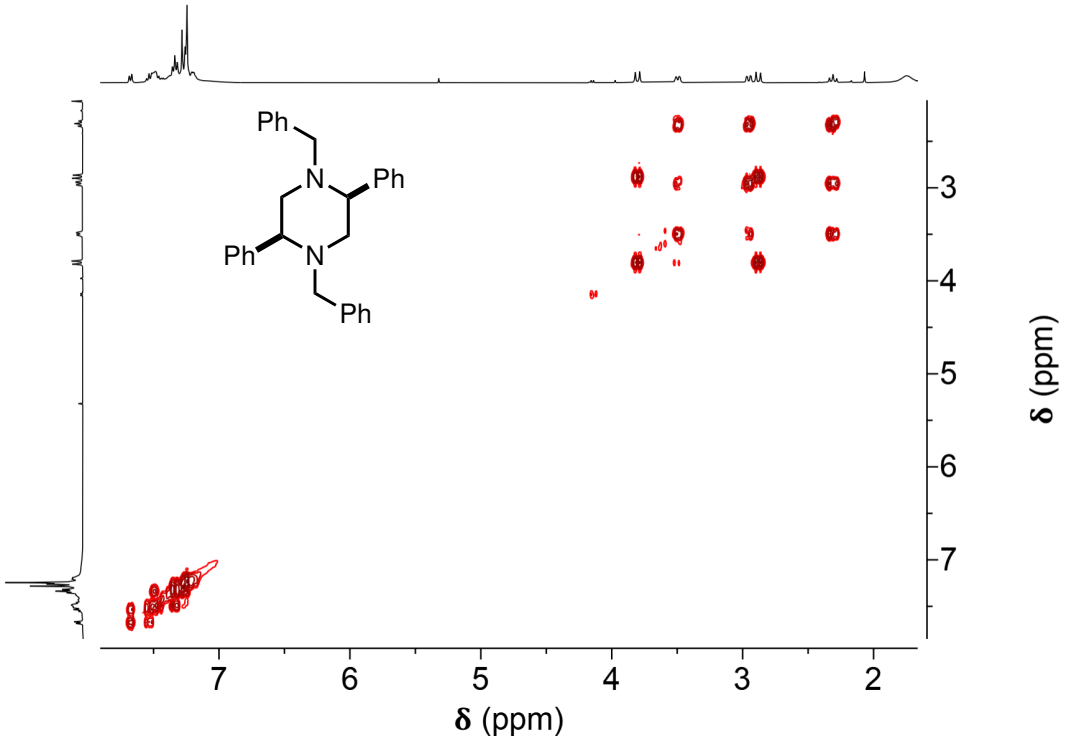

Figure A.174: *^{1}H COSY NMR spectrum of* (±) - ***P2j***.

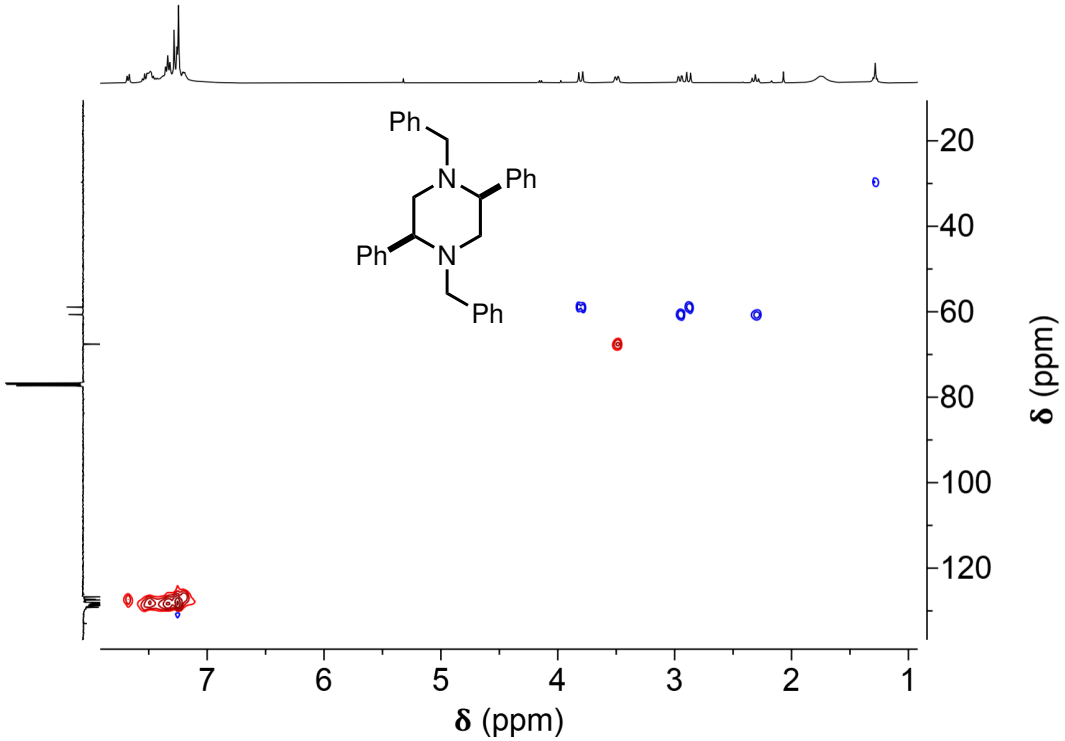

Figure A.175: *^{1}H-^{13}C HSQC NMR spectrum of* (±) - ***P2j*** *(short range, primary and tertiary carbons produce red peaks, while secondary carbons produce blue peaks).*

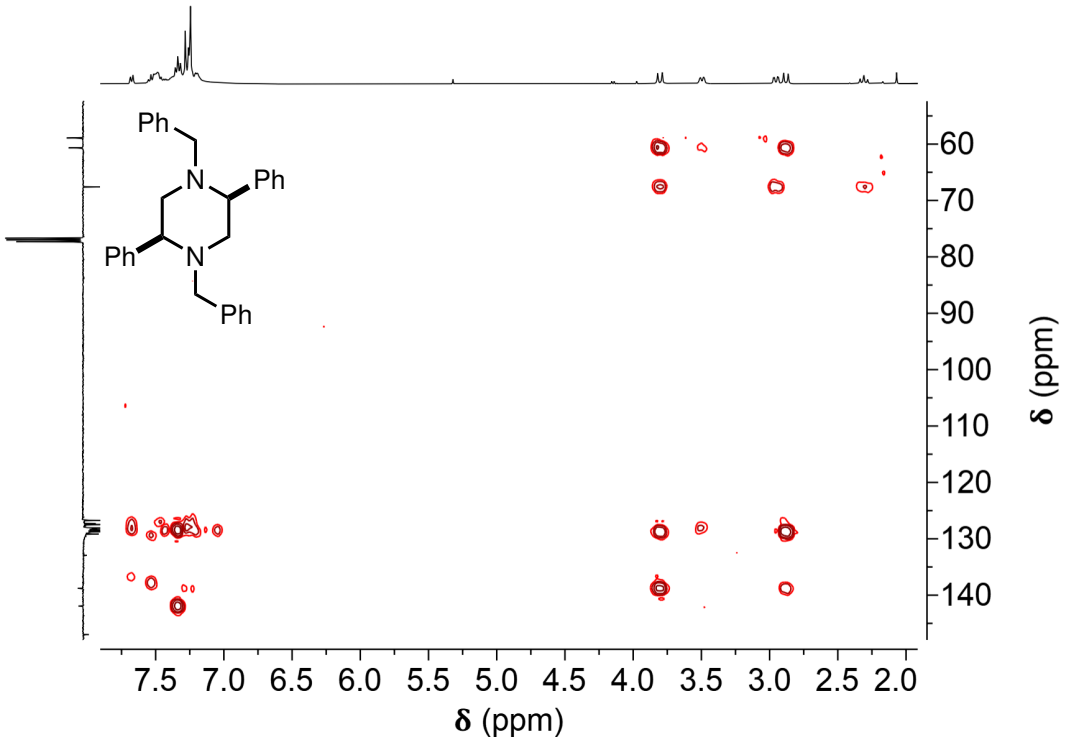

Figure A.176: *^{1}H-^{13}C HMBC NMR spectrum of* (±) - ***P2j*** *(long range).*

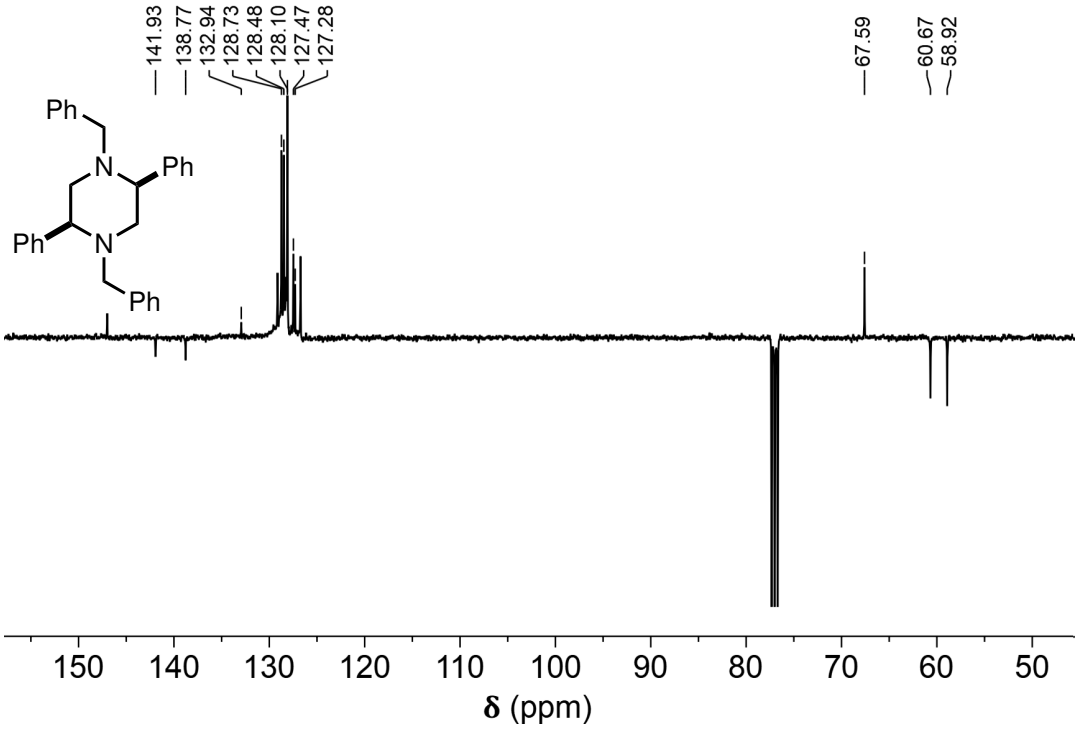

Figure A.177: *^{13}C APT NMR spectrum of* (±) - ***P2j*** (*primary and tertiary carbons produce positive peaks, secondary and quaternary carbons produce negative peaks*).

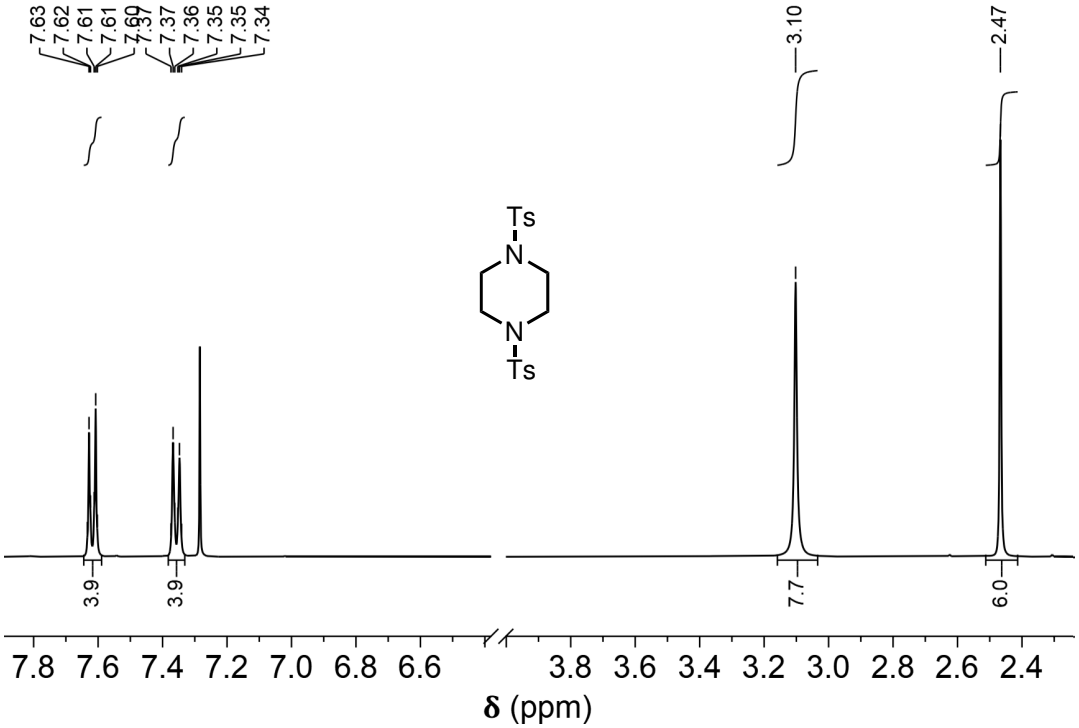

Figure A.178: *^{1}H-NMR spectrum of* ***P2m***.

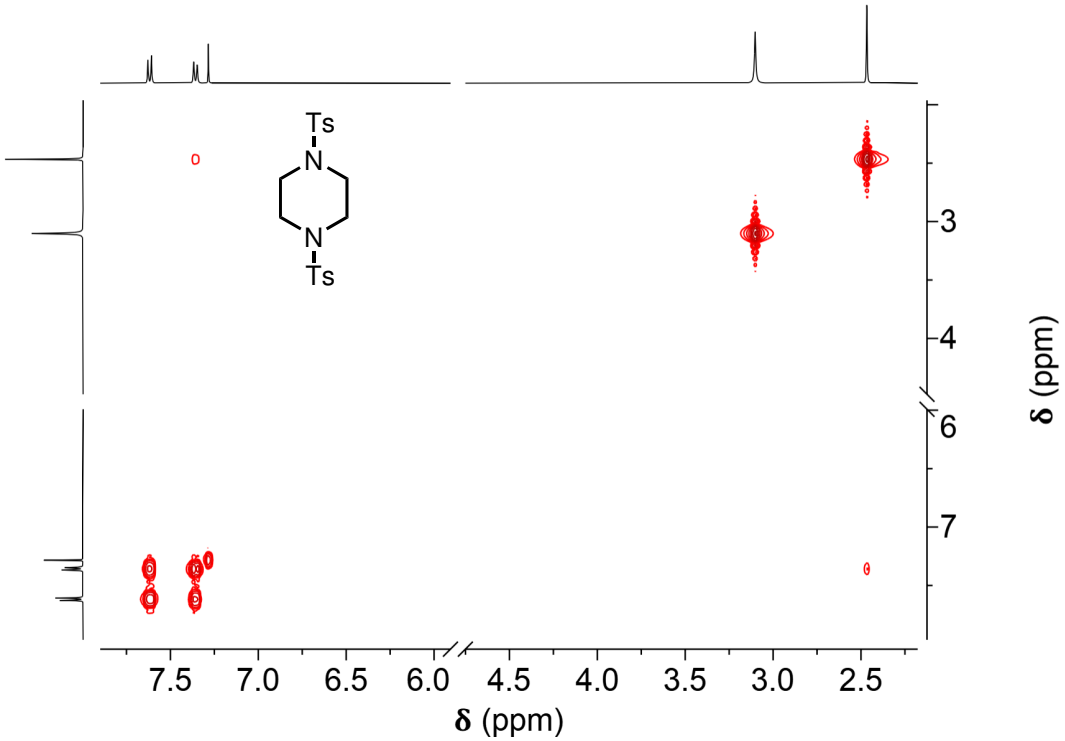

Figure A.179: *^{1}H COSY NMR spectrum of **P2m**.*

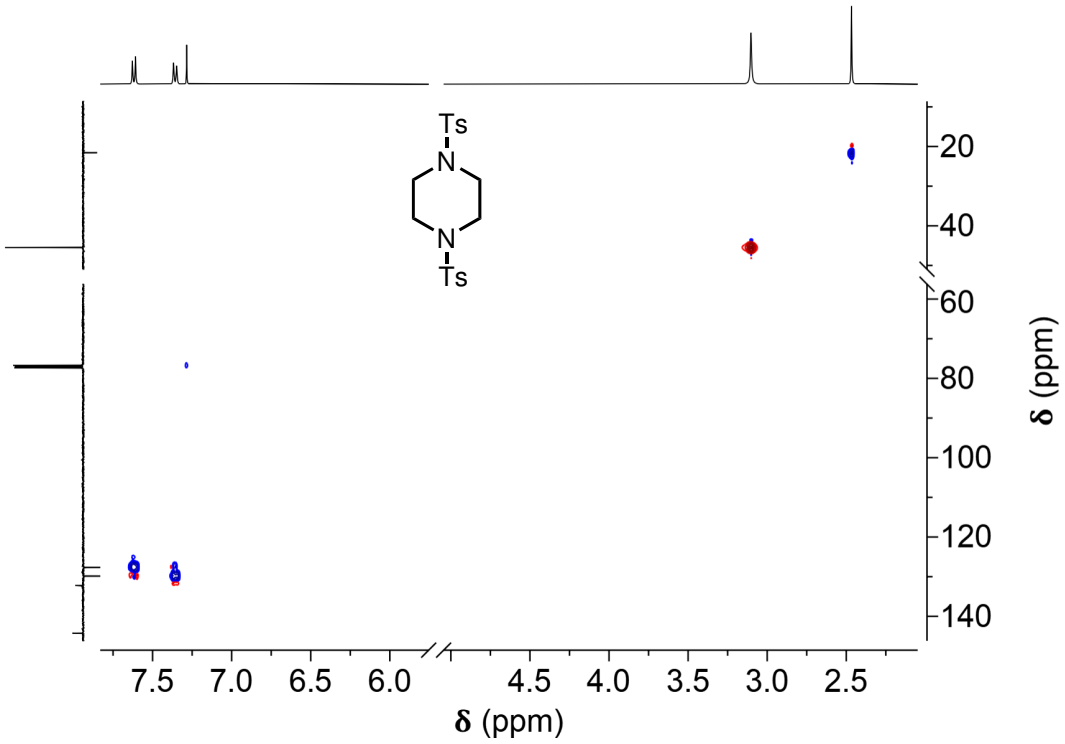

Figure A.180: *^{1}H-^{13}C HSQC NMR spectrum of **P2m** (short range, primary and tertiary carbons produce blue peaks, while secondary carbons produce red peaks).*

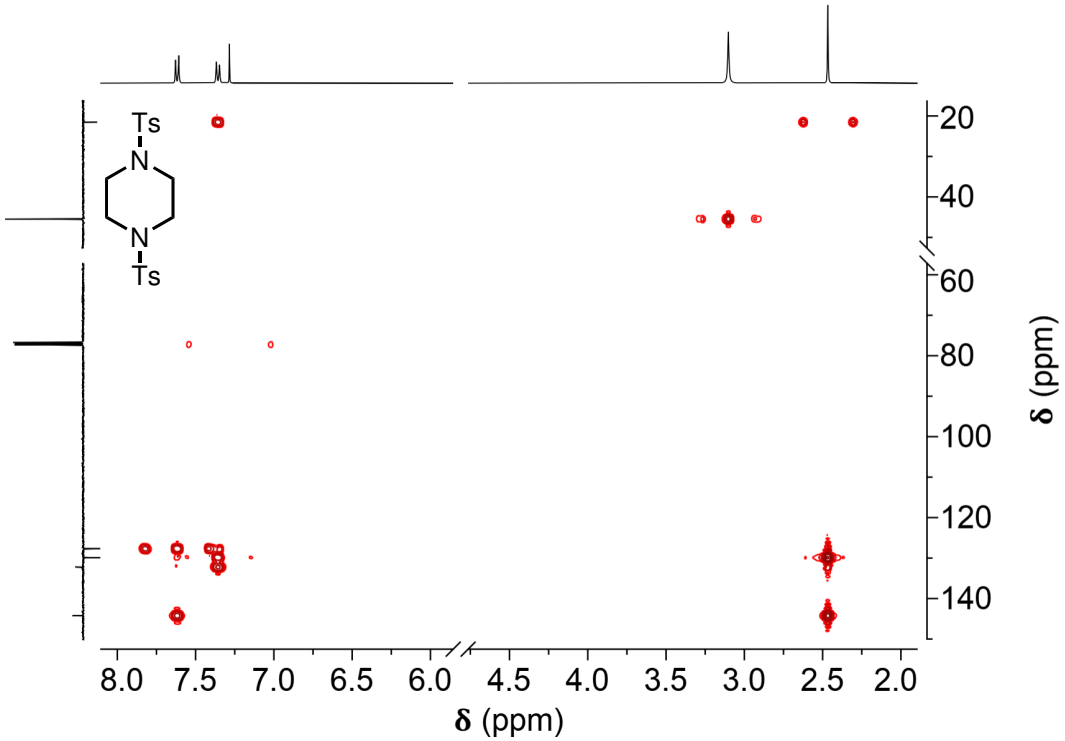

Figure A.181: *^{1}H-^{13}C HMBC NMR spectrum of* ***P2m*** *(long range).*

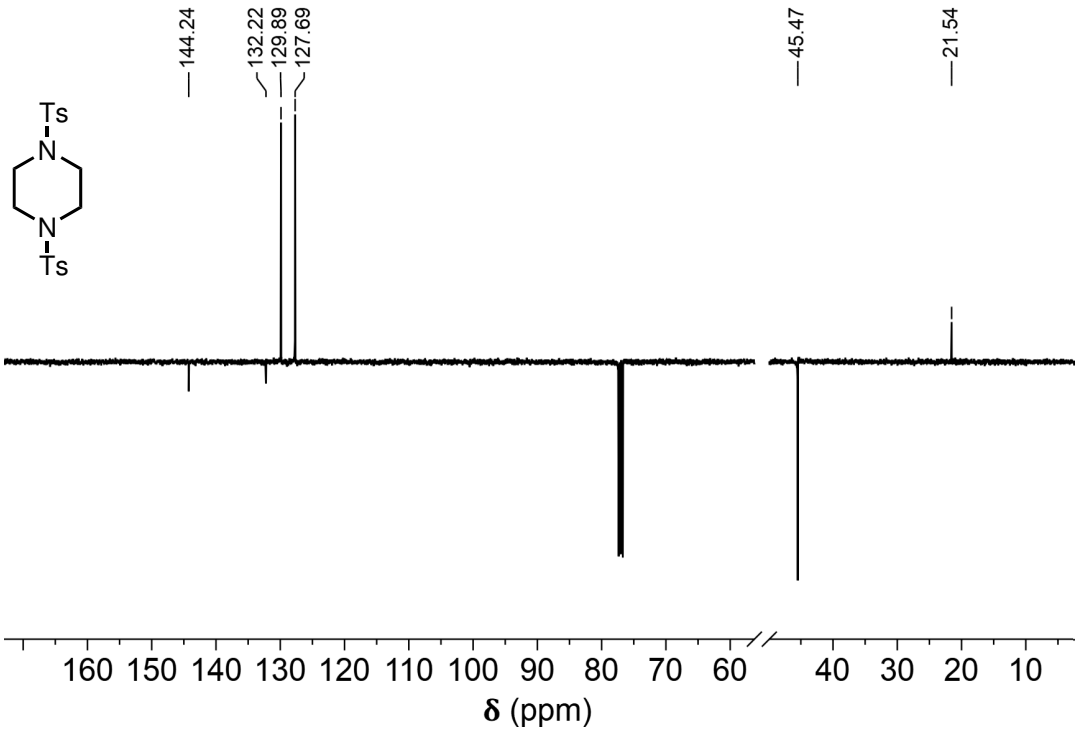

Figure A.182: *^{13}C APT NMR spectrum of* ***P2m*** *(primary and tertiary carbons produce positive peaks, secondary and quaternary carbons produce negative peaks).*

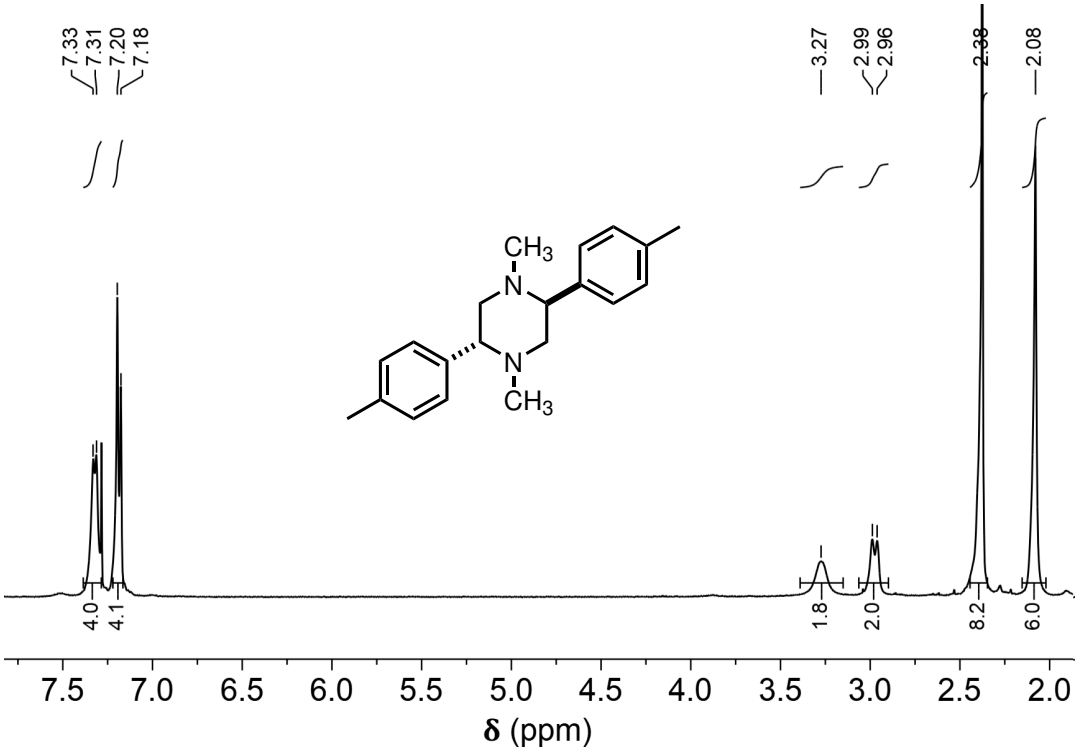

Figure A.183: *^{1}H-NMR spectrum of meso -* ***P2p****.*

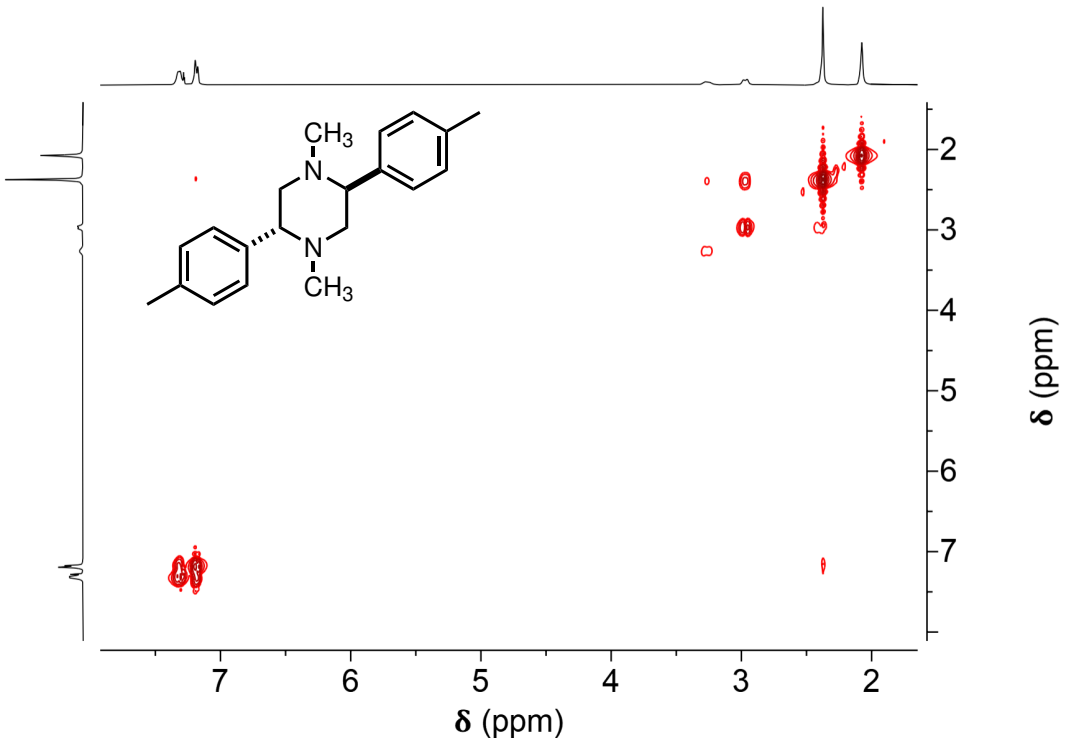

Figure A.184: *^{1}H COSY NMR spectrum of meso -* ***P2p****.*

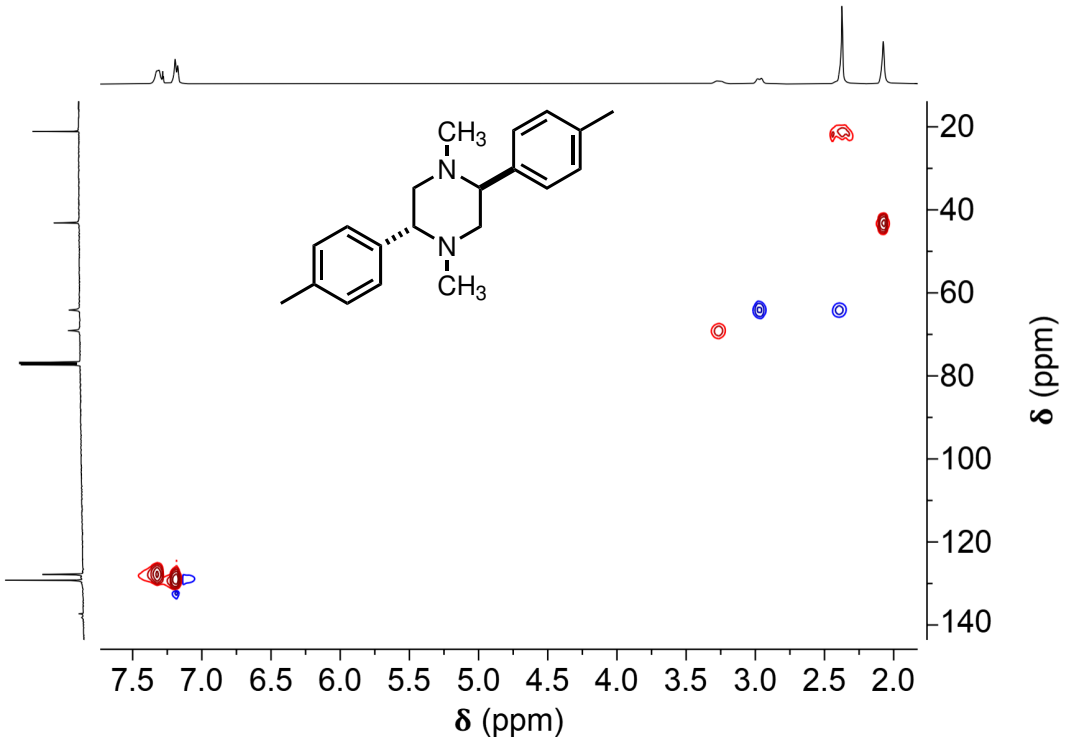

Figure A.185: *^{1}H-^{13}C HSQC NMR spectrum of meso - **P2p** (short range, primary and tertiary carbons produce red peaks, while secondary carbons produce blue peaks).*

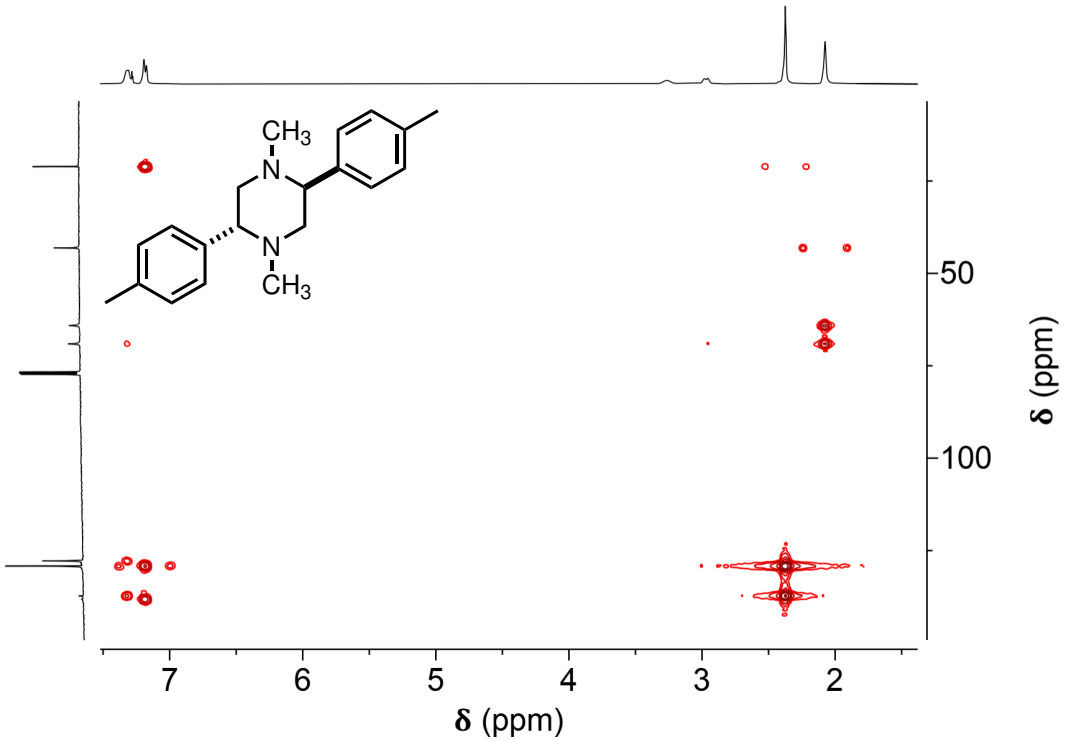

Figure A.186: *^{1}H-^{13}C HMBC NMR spectrum of meso - **P2p** (long range).*

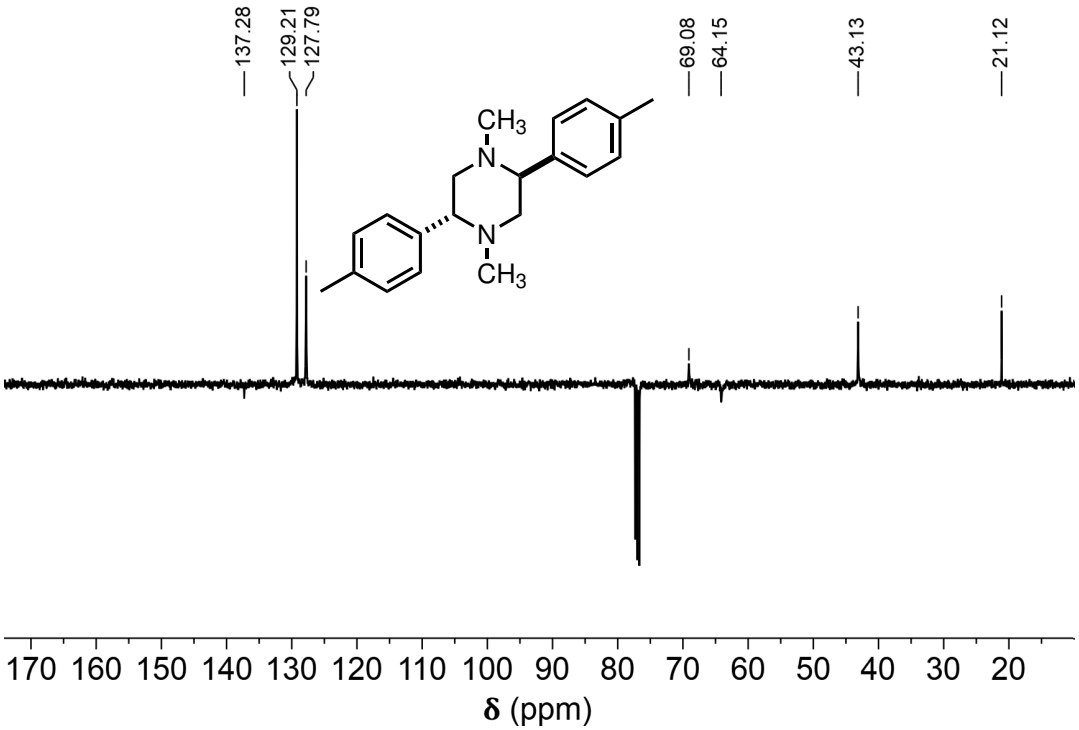

Figure A.187: *^{13}C APT NMR spectrum of meso -* ***P2p*** *(primary and tertiary carbons produce positive peaks, secondary and quaternary carbons produce negative peaks).*

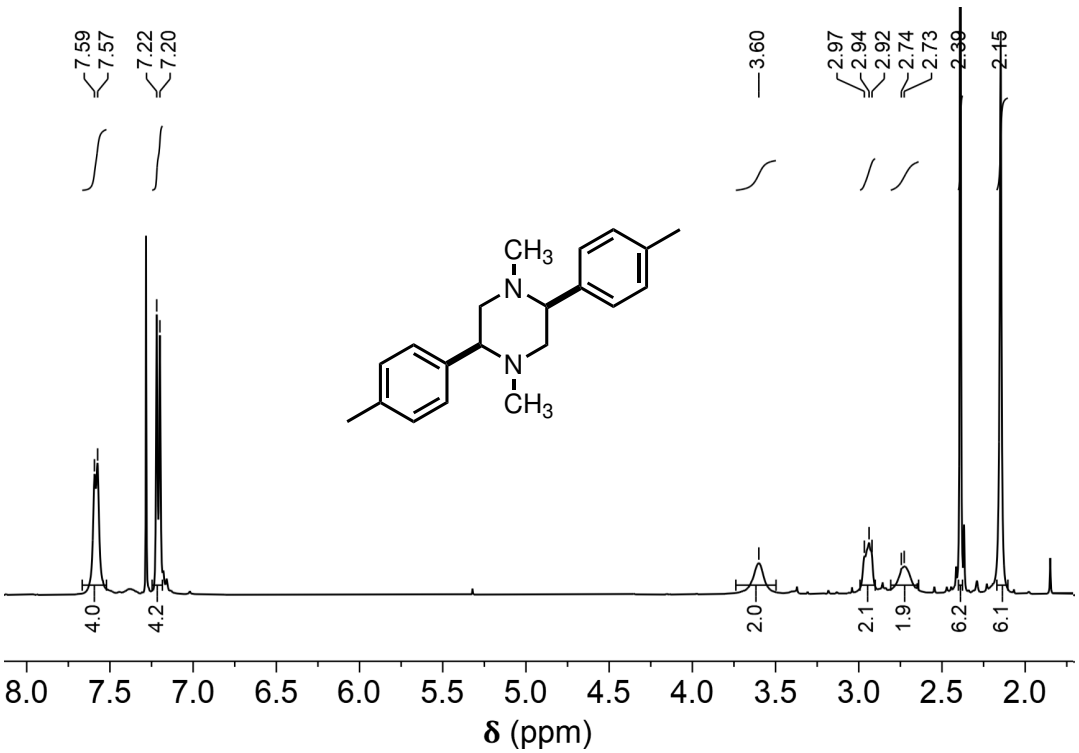

Figure A.188: *^{1}H-NMR spectrum of* (±) - ***P2p***.

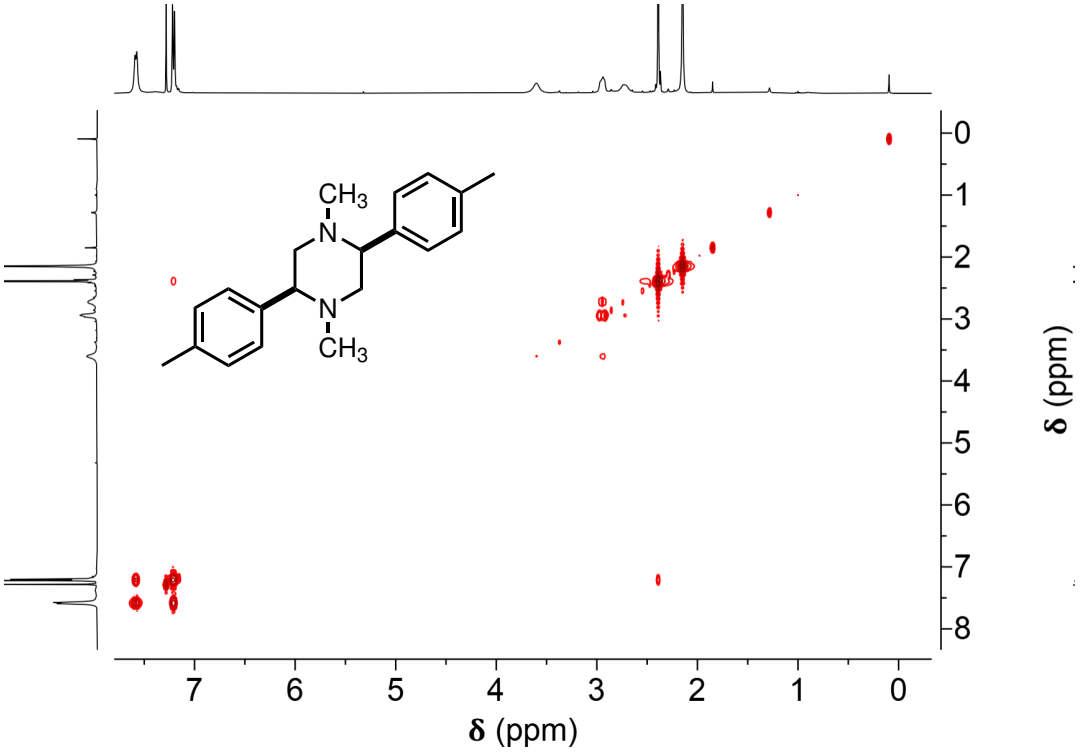

Figure A.189: *^{1}H COSY NMR spectrum of* (±) - ***P2p***.

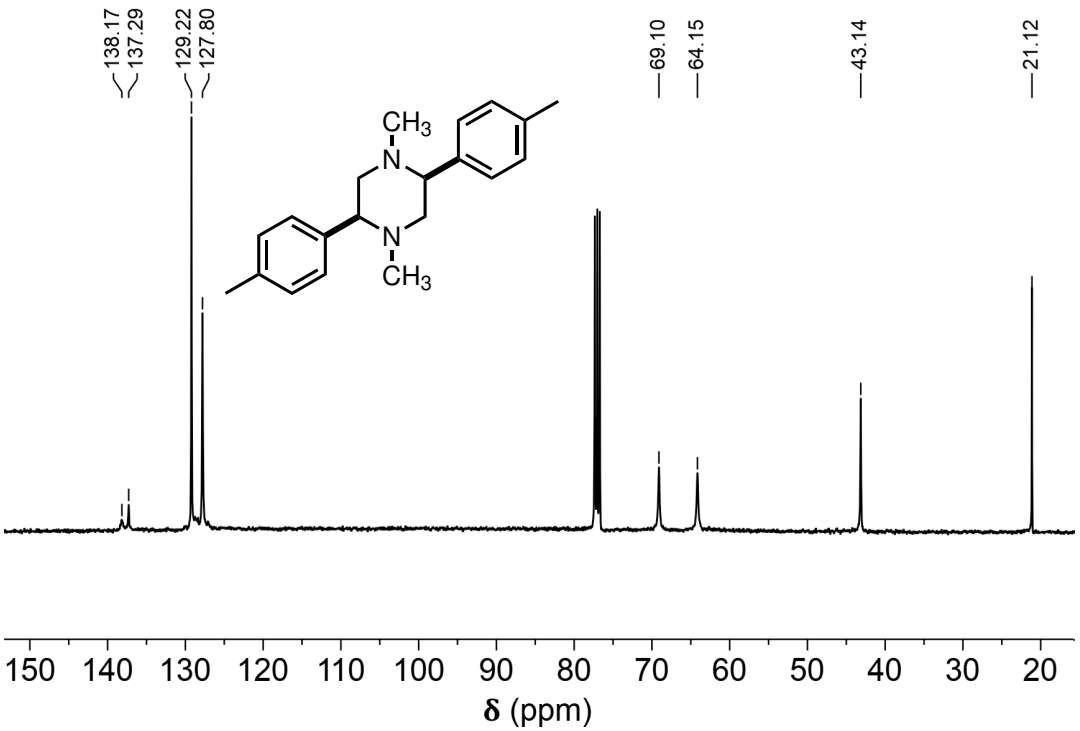

Figure A.190: *^{13}C-NMR spectrum of* (±) - ***P2p***.

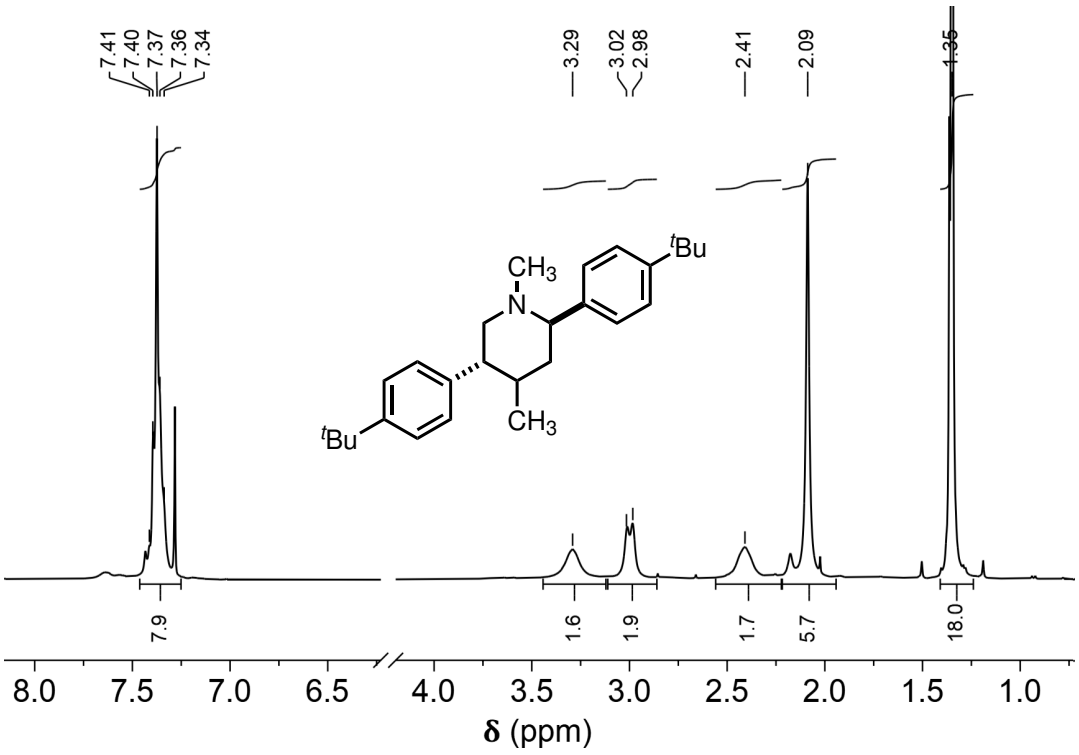

Figure A.191: *^{1}H-NMR spectrum of meso -* ***P2q****.*

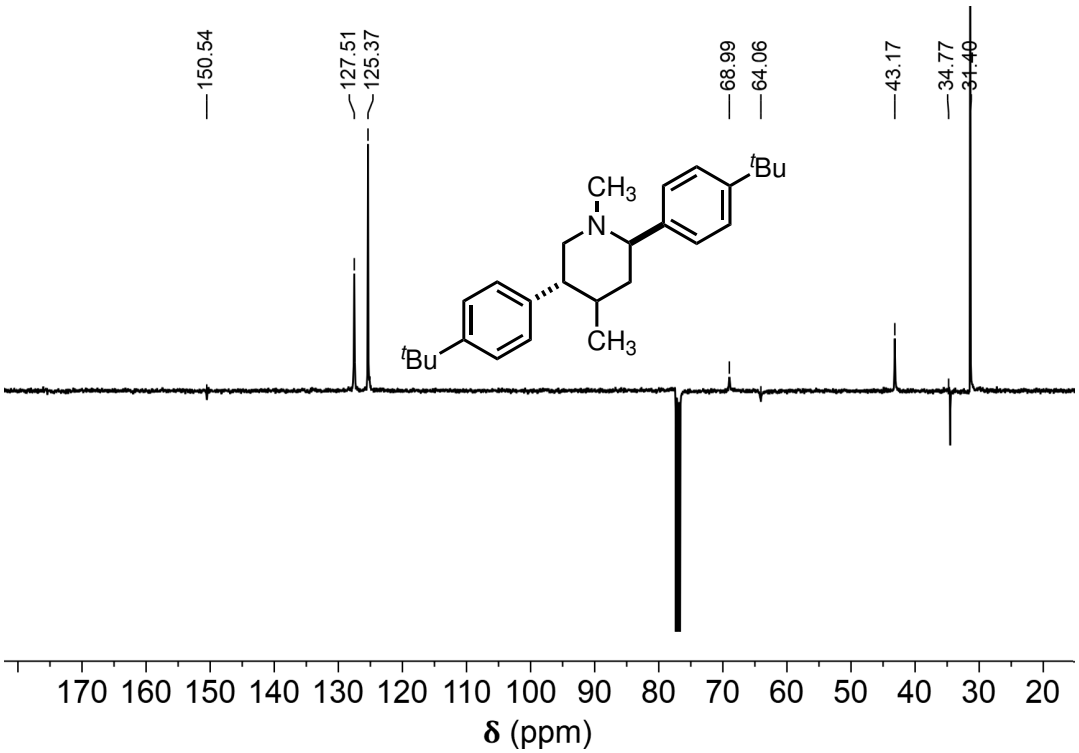

Figure A.192: *^{13}C APT NMR spectrum of meso -* ***P2q*** *(primary and tertiary carbons produce positive peaks, secondary and quaternary carbons produce negative peaks).*

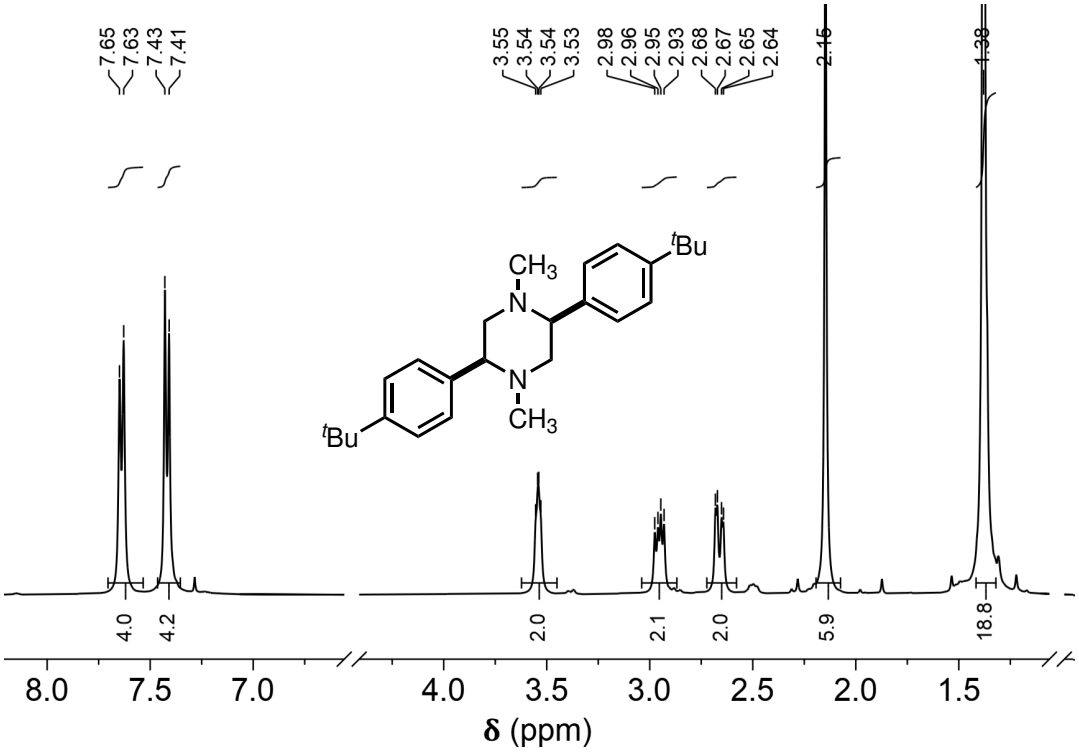

Figure A.193: *^{1}H-NMR spectrum of* (±) - ***P2q***.

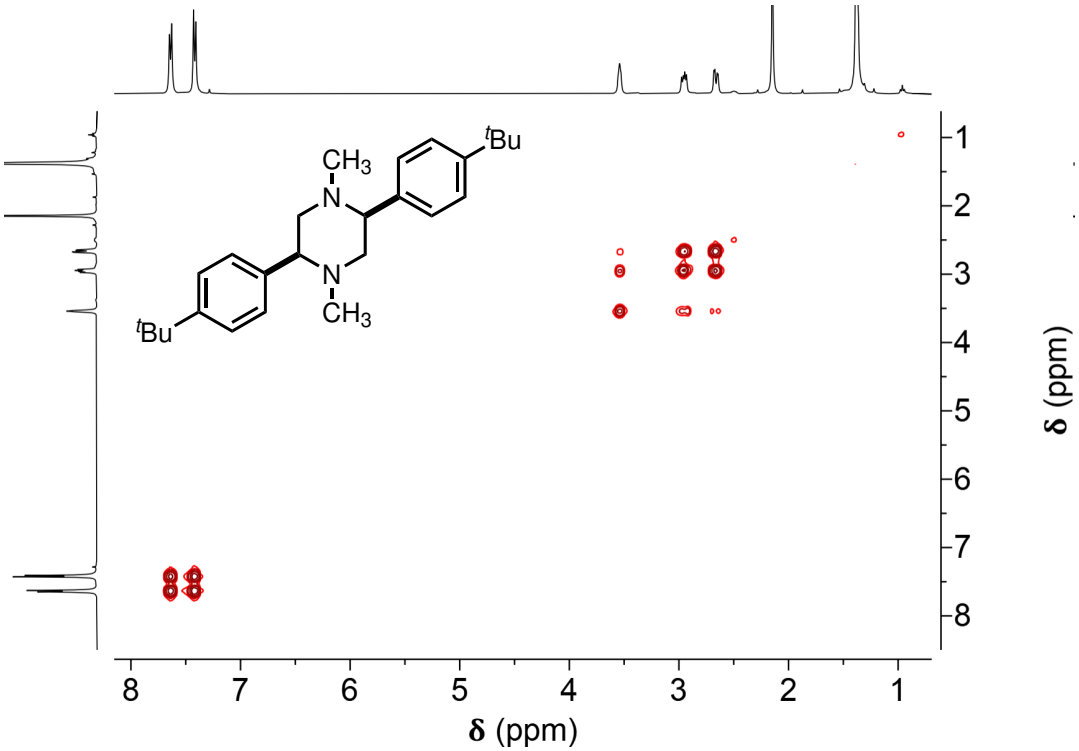

Figure A.194: *^{1}H COSY NMR spectrum of* (±) - ***P2q***.

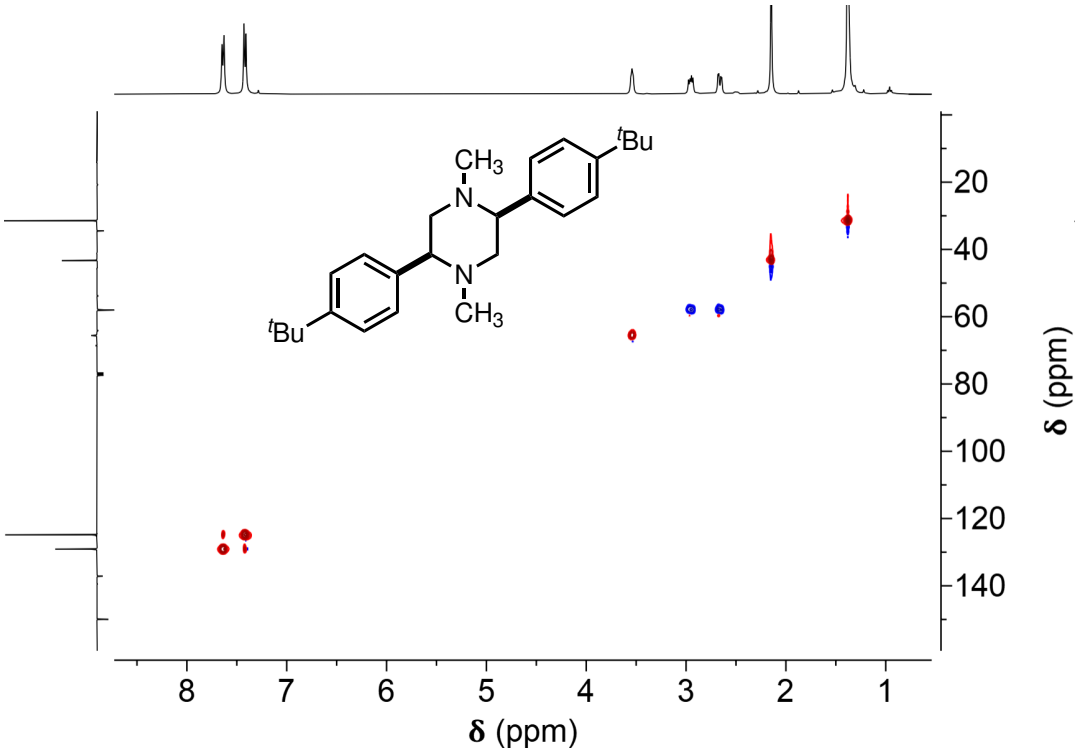

Figure A.195: *^{1}H-^{13}C HSQC NMR spectrum of* (±) - ***P2q*** *(short range, primary and tertiary carbons produce red peaks, while secondary carbons produce blue peaks).*

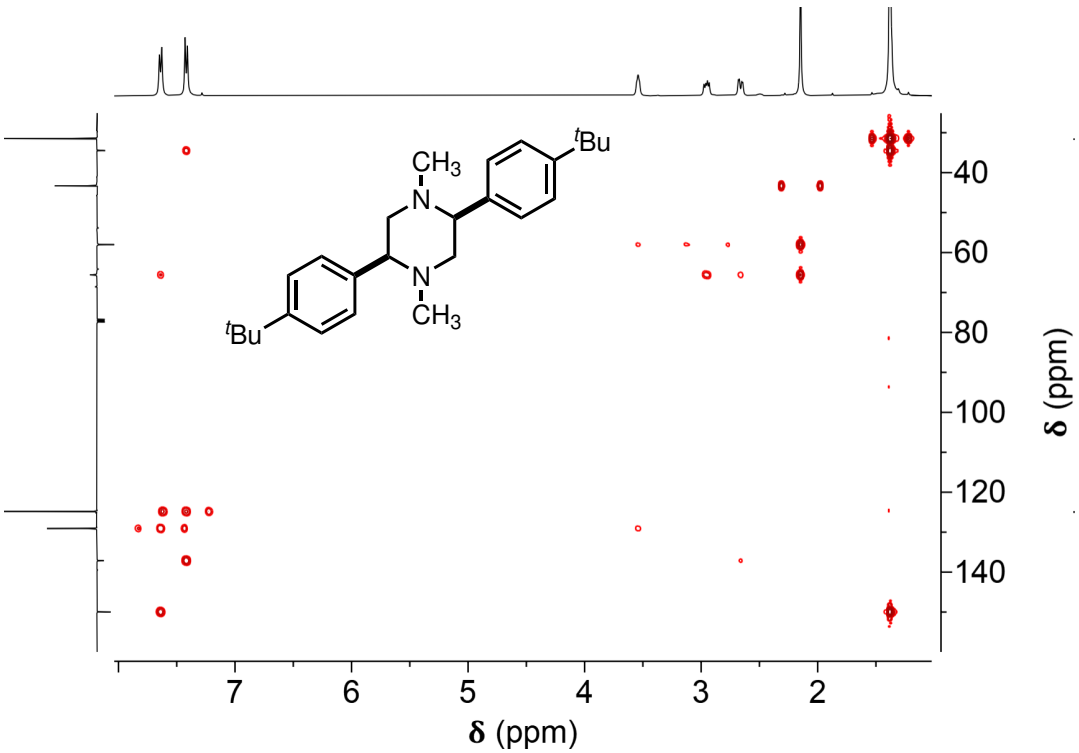

Figure A.196: *^{1}H-^{13}C HMBC NMR spectrum of* (±) - ***P2q*** *(long range).*

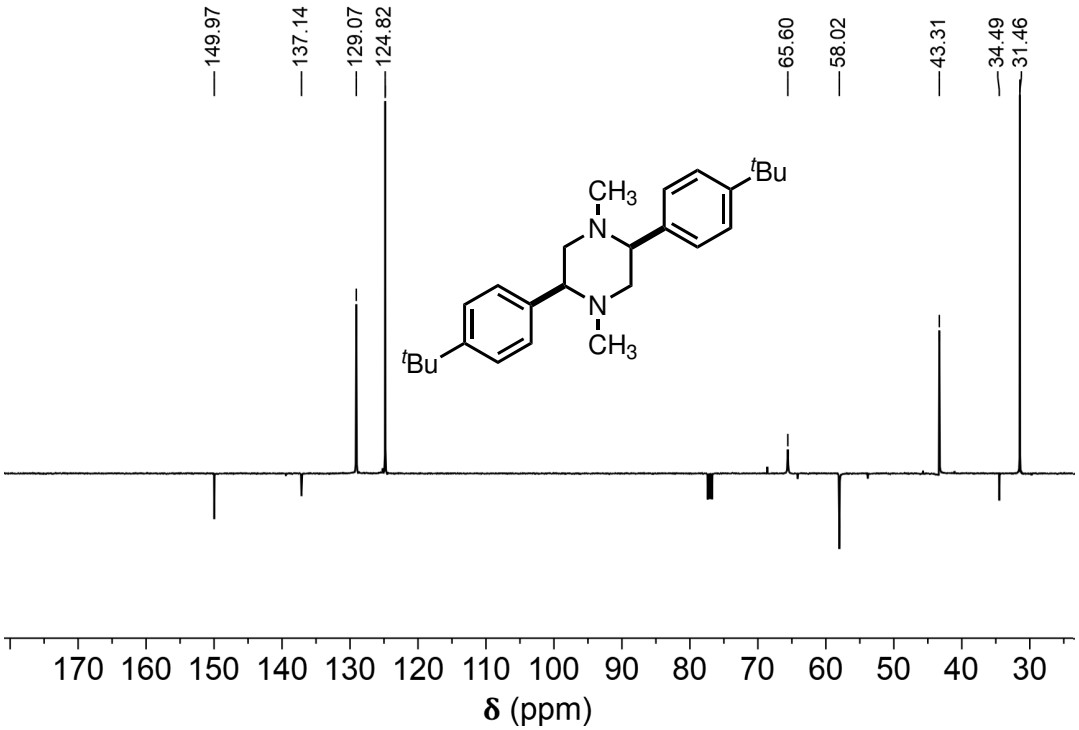

Figure A.197: *^{13}C APT NMR spectrum of* (±) - ***P2q*** (*primary and tertiary carbons produce positive peaks, secondary and quaternary carbons produce negative peaks*).

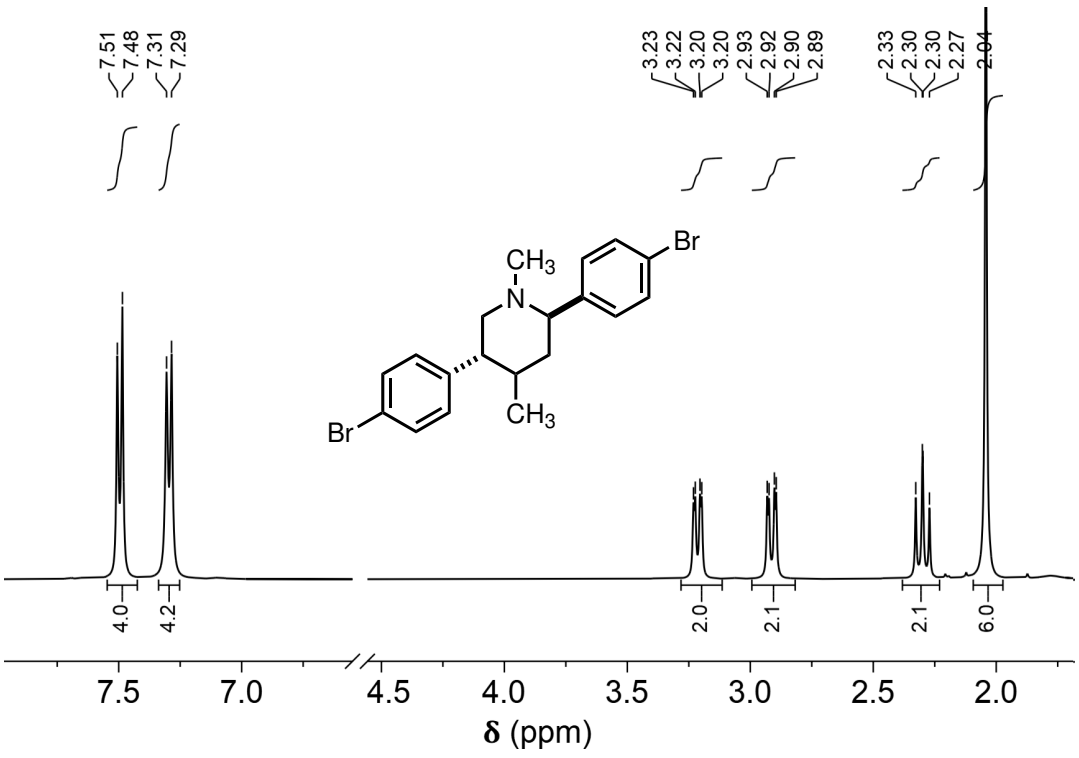

Figure A.198: *^{1}H-NMR spectrum of meso -* ***P2r***.

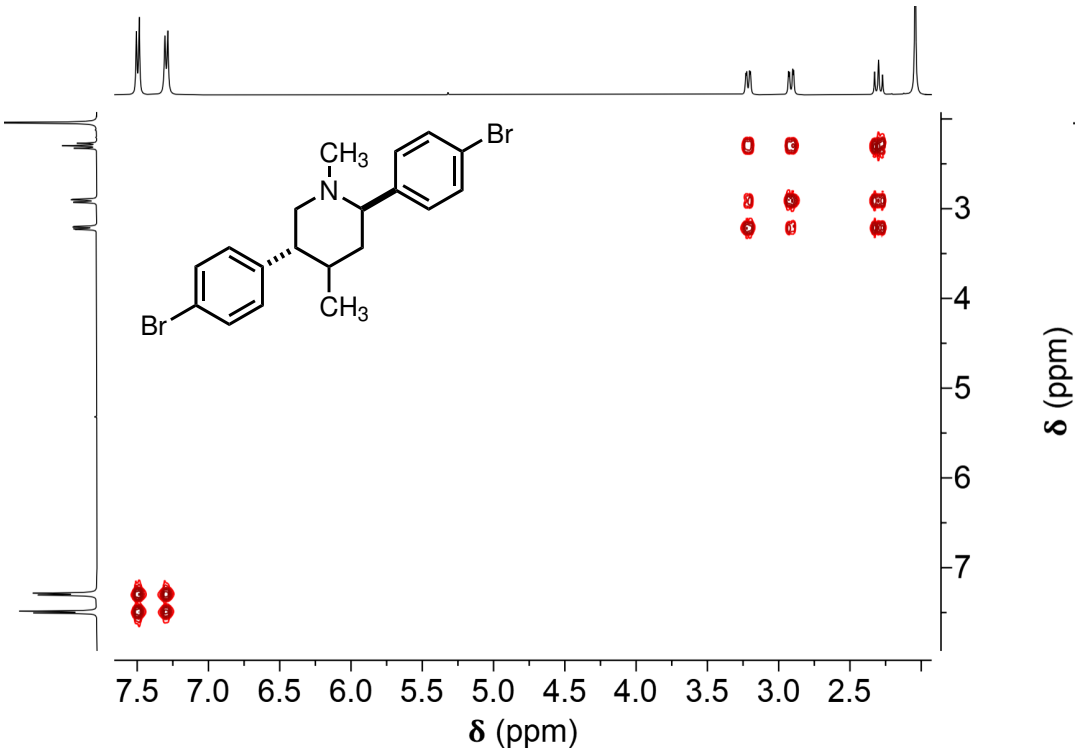

Figure A.199: *^{1}H COSY NMR spectrum of meso - **P2r**.*

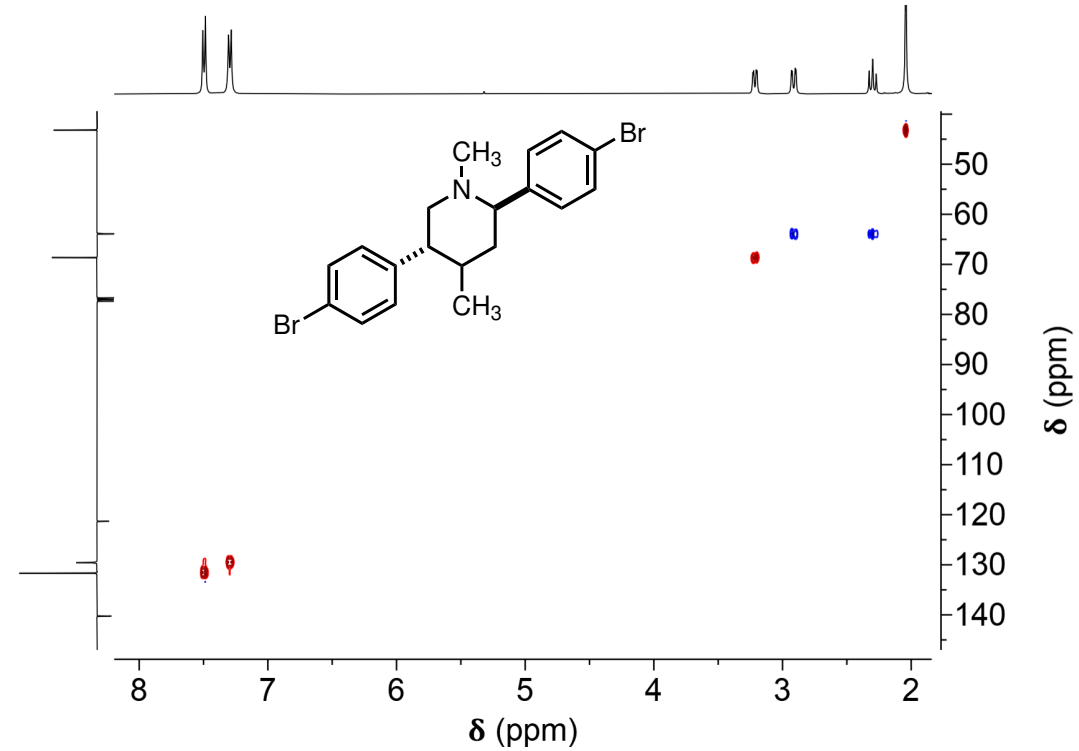

Figure A.200: *^{1}H-^{13}C HSQC NMR spectrum of meso - **P2r** (short range, primary and tertiary carbons produce red peaks, while secondary carbons produce blue peaks).*

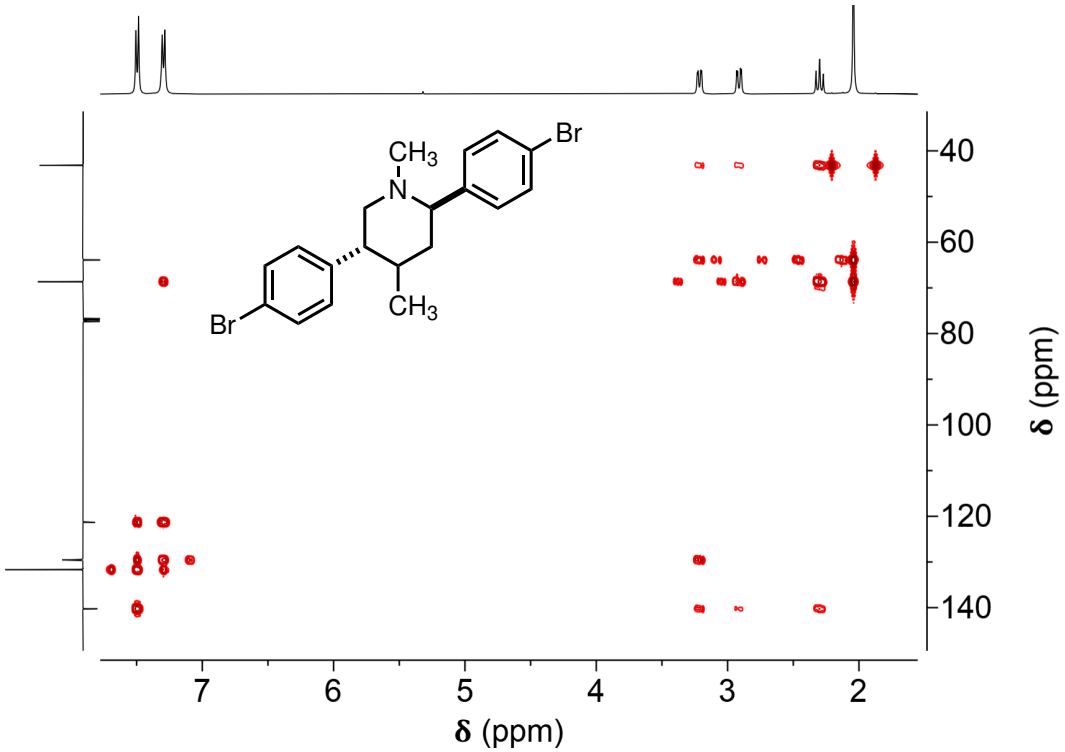

Figure A.201: *^{1}H-^{13}C HMBC NMR spectrum of meso - **P2r** (long range).*

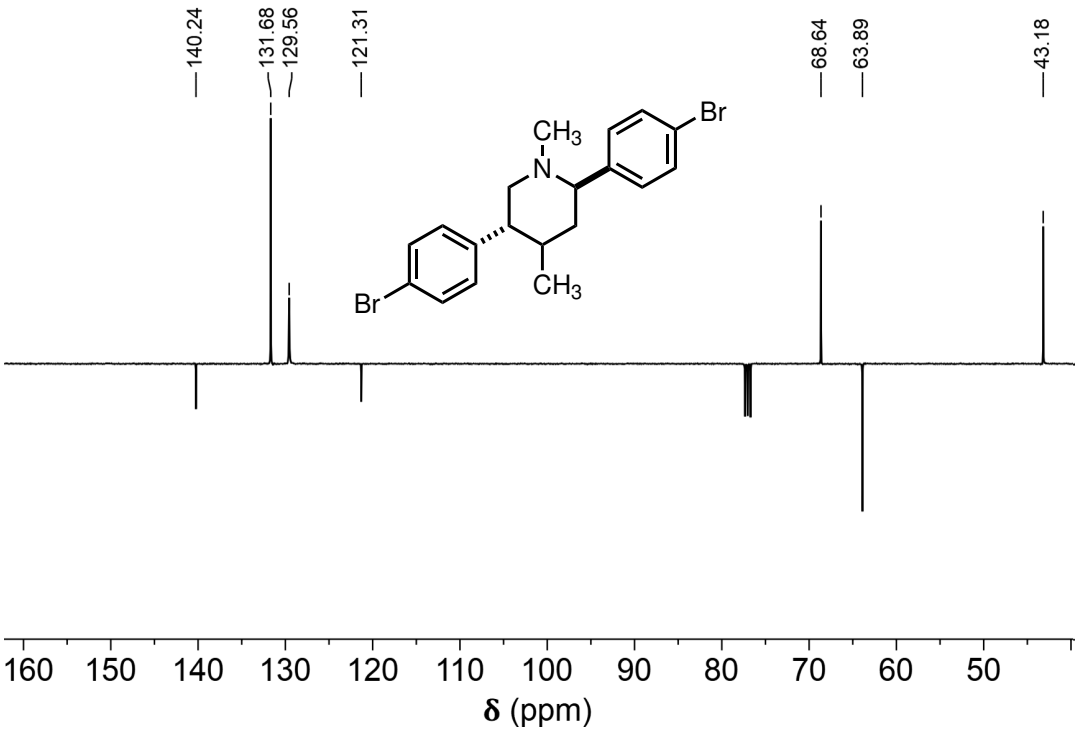

Figure A.202: *^{13}C APT NMR spectrum of meso - **P2r** (primary and tertiary carbons produce positive peaks, secondary and quaternary carbons produce negative peaks).*

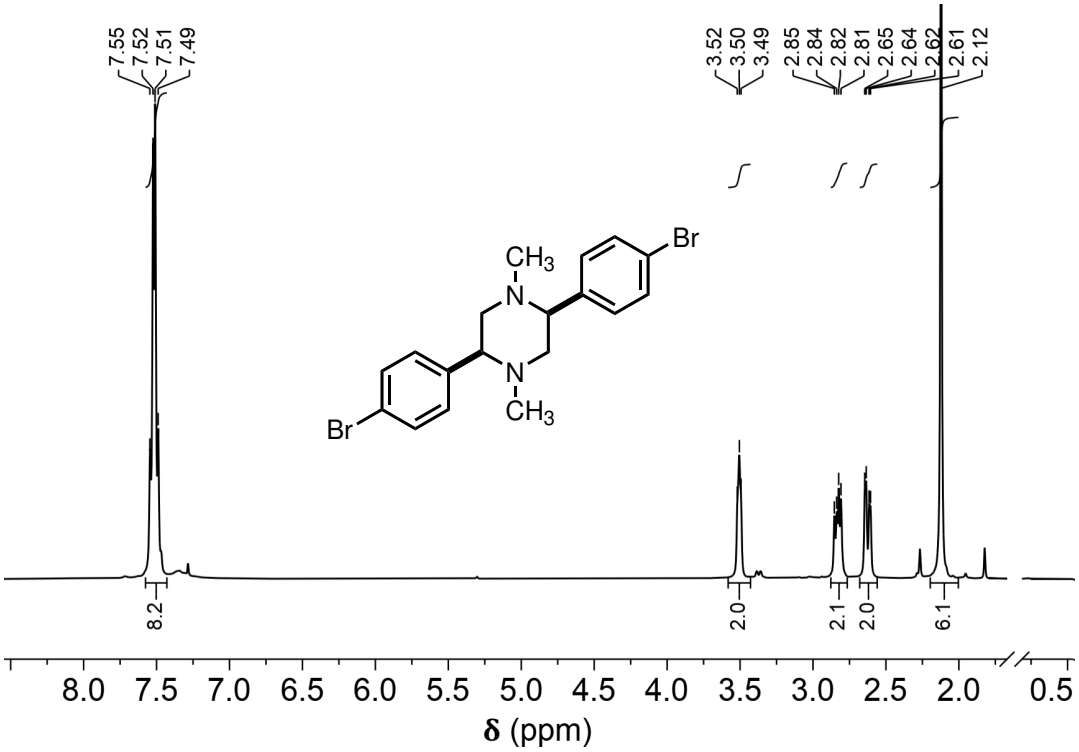

Figure A.203: *^{1}H-NMR spectrum of* (±) - ***P2r***.

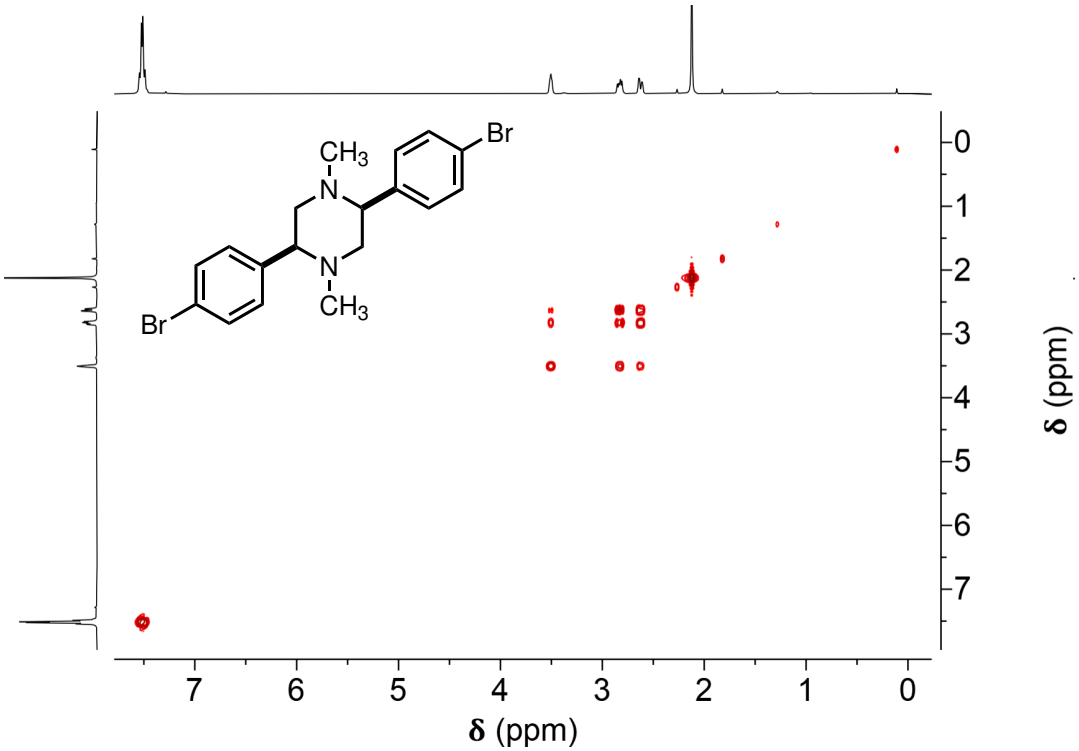

Figure A.204: *^{1}H COSY NMR spectrum of* (±) - ***P2r***.

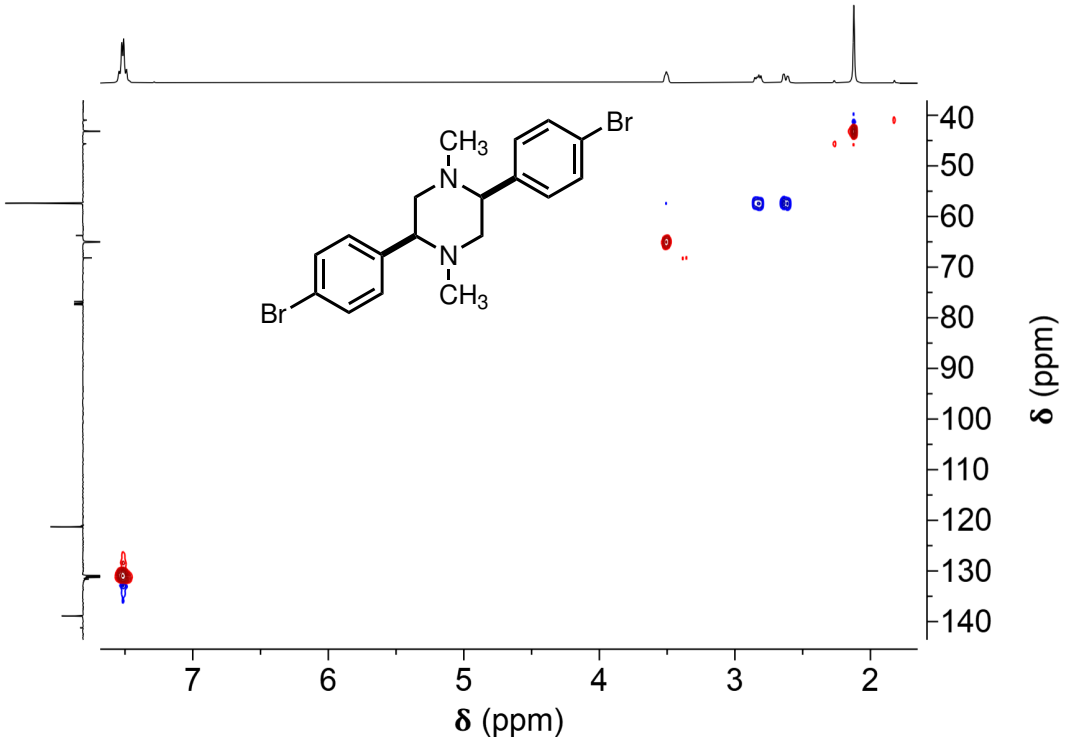

Figure A.205: *^{1}H-^{13}C HSQC NMR spectrum of* (±) - ***P2r*** (*short range, primary and tertiary carbons produce red peaks, while secondary carbons produce blue peaks*).

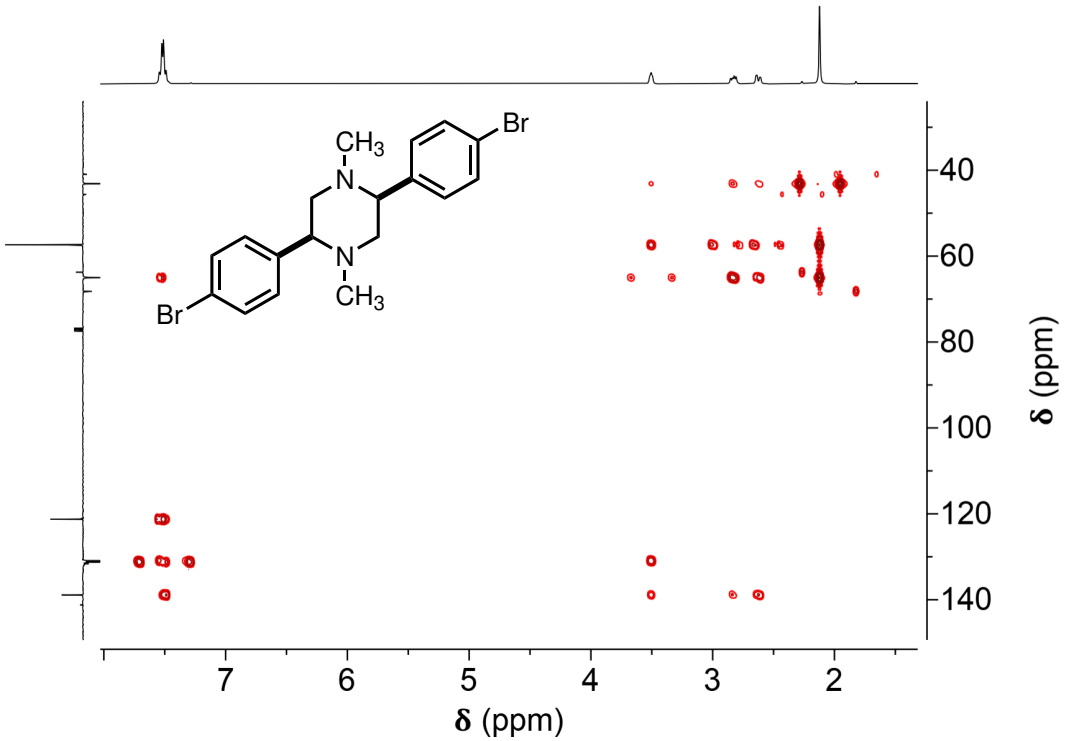

Figure A.206: *^{1}H-^{13}C HMBC NMR spectrum of* (±) - ***P2r*** (*long range*).

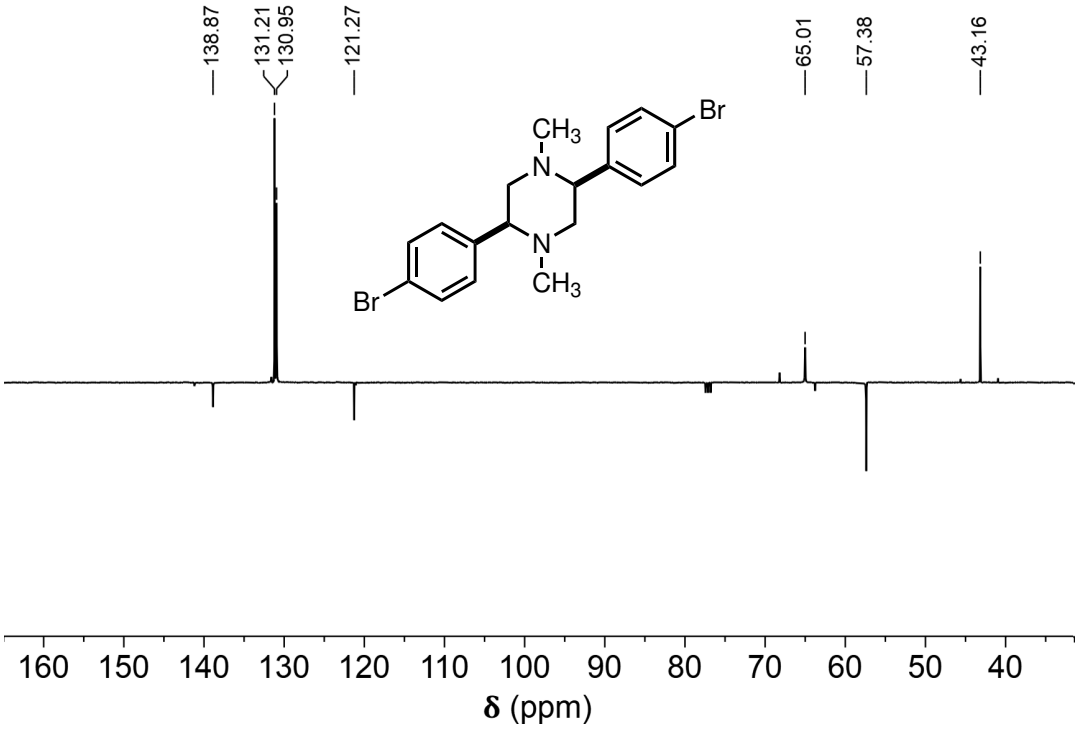

Figure A.207: *^{13}C APT NMR spectrum of* (±) - ***P2r*** (*primary and tertiary carbons produce positive peaks, secondary and quaternary carbons produce negative peaks*).

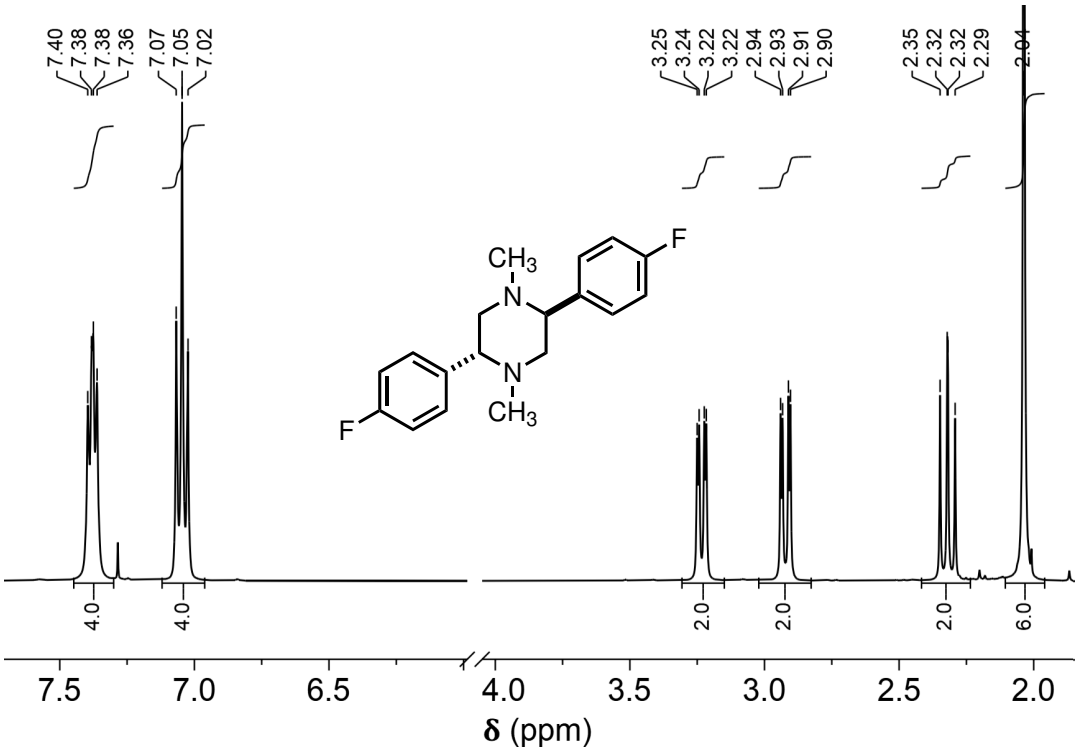

Figure A.208: *^{1}H-NMR spectrum of meso -* ***P2s***.

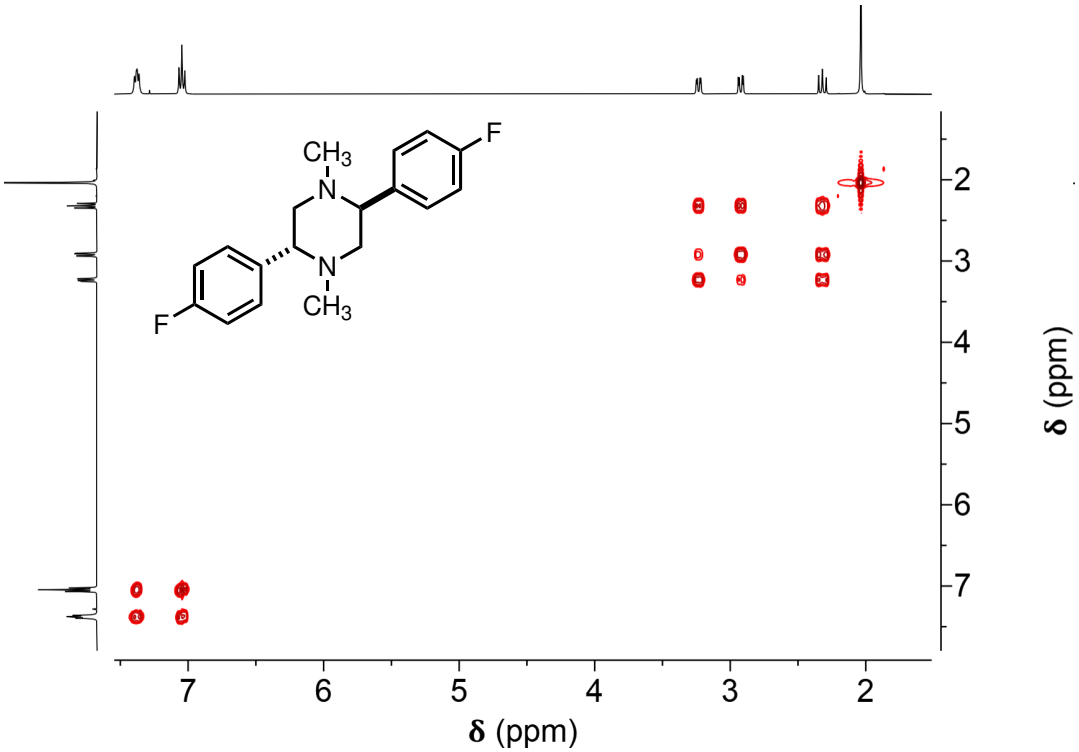

Figure A.209: *^{1}H COSY NMR spectrum of meso - **P2s**.*

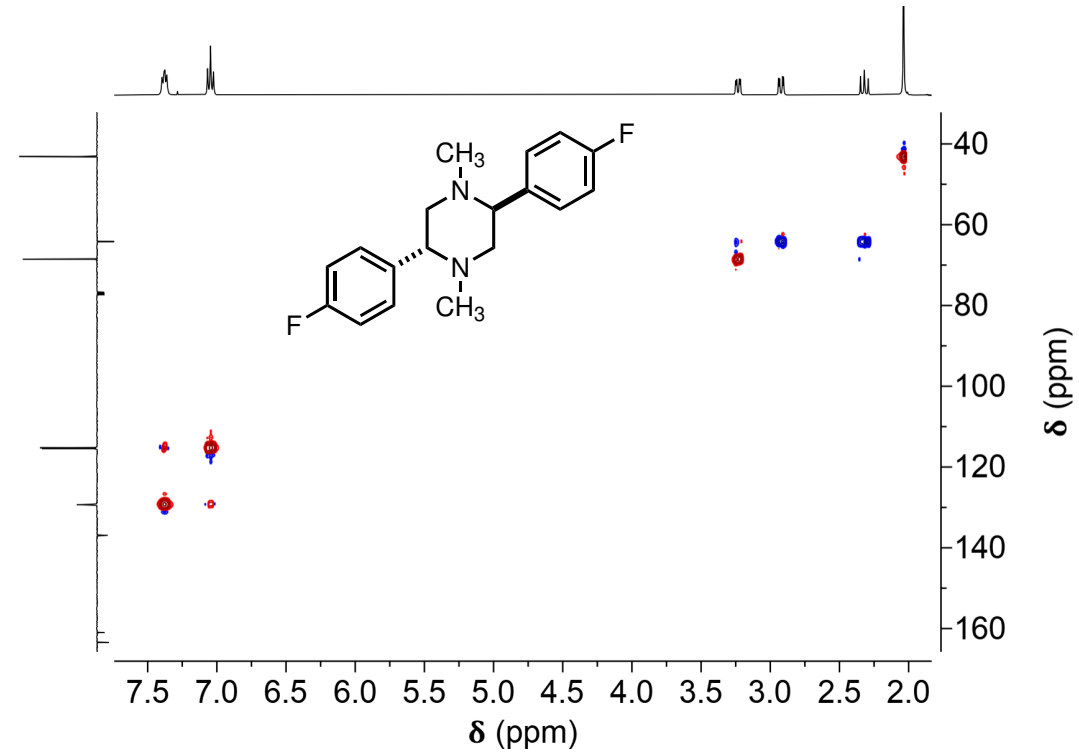

Figure A.210: *^{1}H-^{13}C HSQC NMR spectrum of meso - **P2s** (short range, primary and tertiary carbons produce red peaks, while secondary carbons produce blue peaks).*

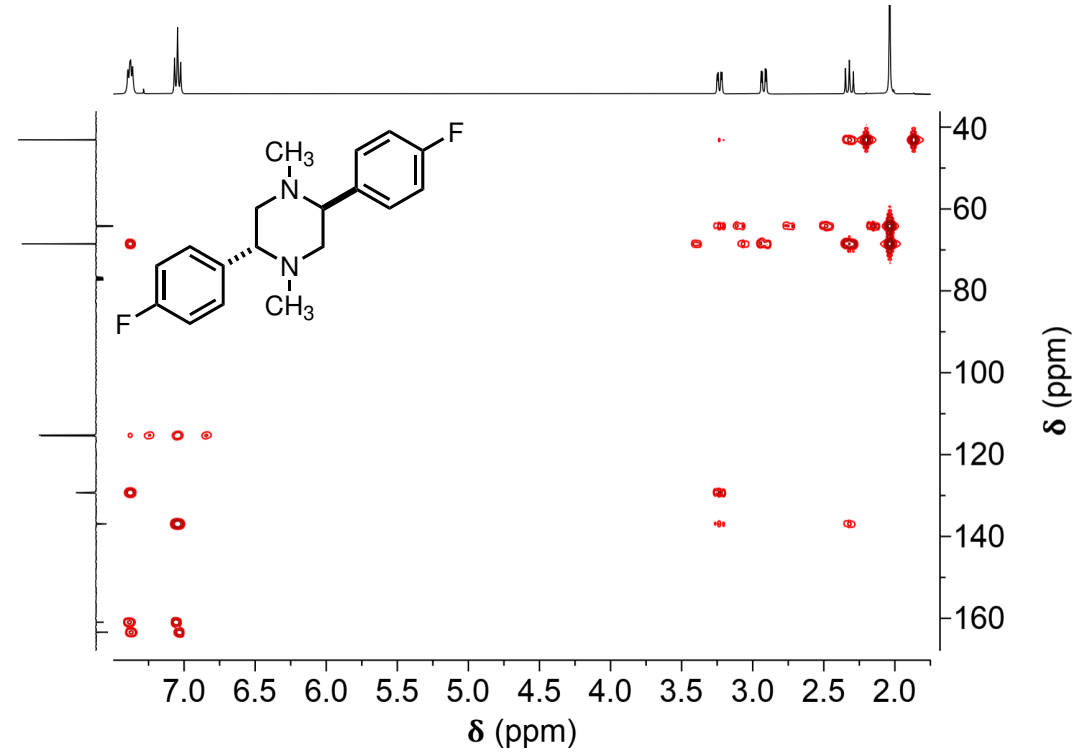

Figure A.211: *^{1}H-^{13}C HMBC NMR spectrum of meso - **P2s** (long range).*

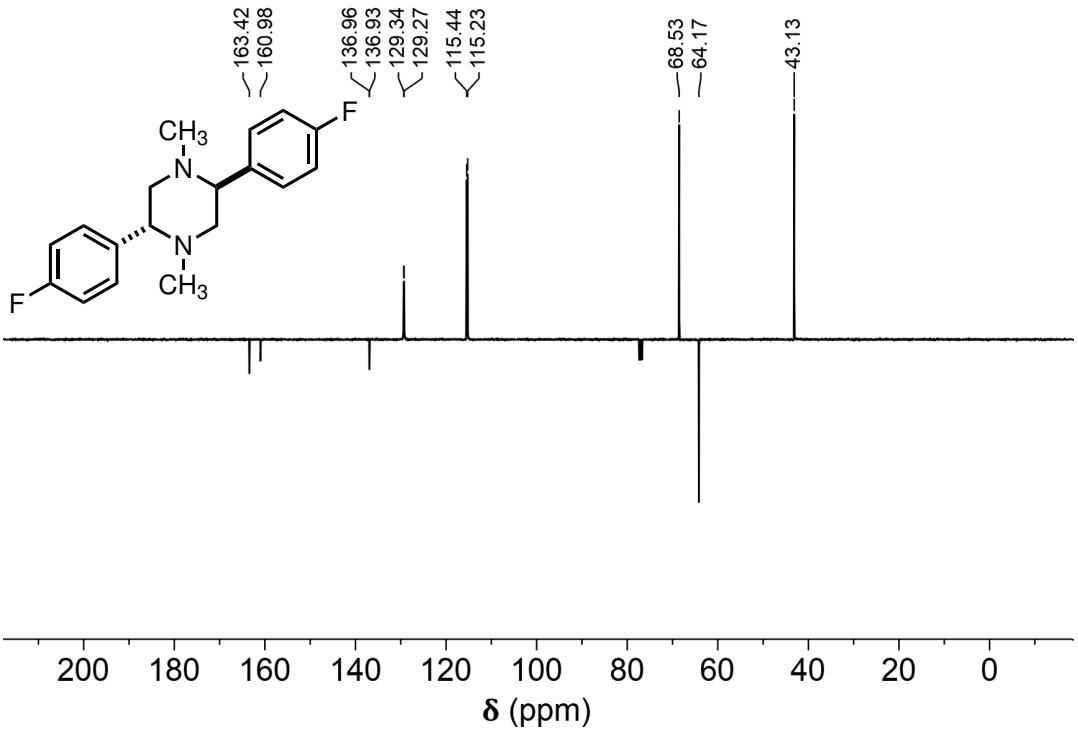

Figure A.212: *^{13}C APT NMR spectrum of meso - **P2s** (primary and tertiary carbons produce positive peaks, secondary and quaternary carbons produce negative peaks).*

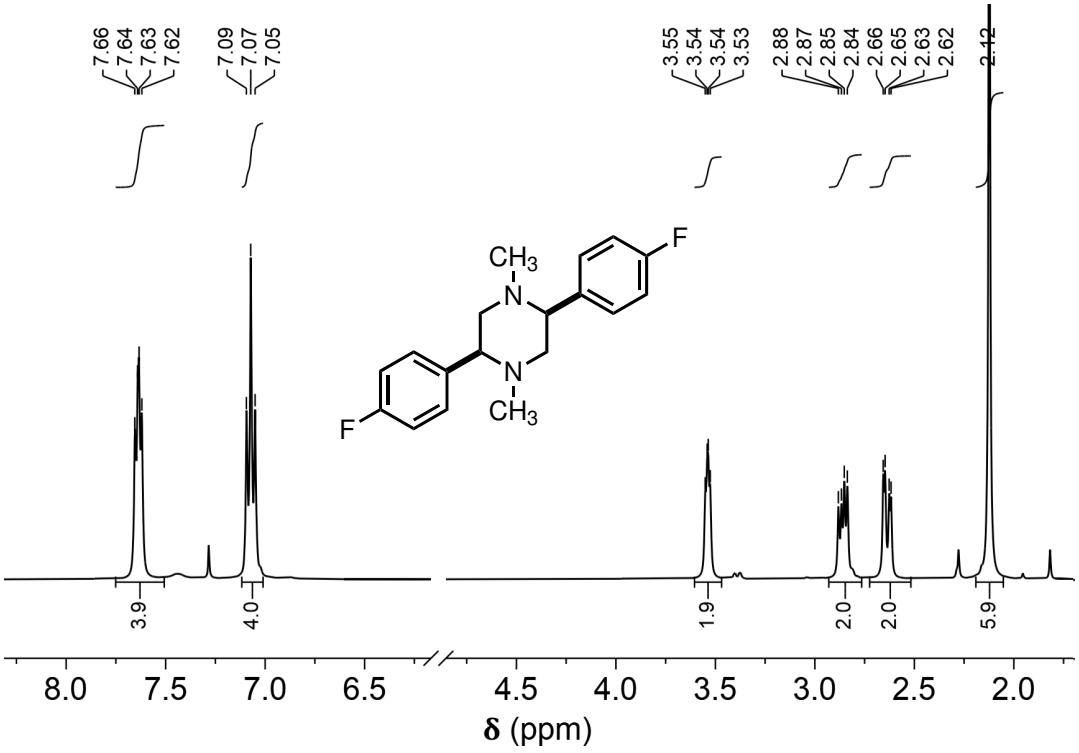

Figure A.213: *^{1}H-NMR spectrum of* (±) - ***P2s***.

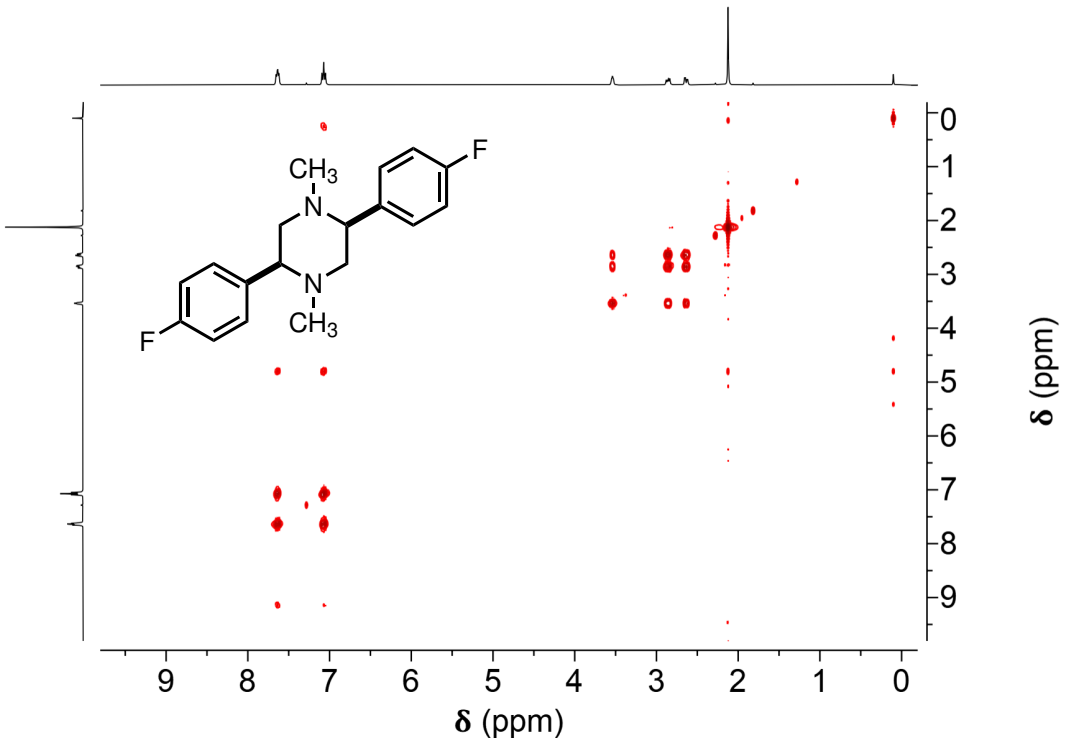

Figure A.214: *^{1}H COSY NMR spectrum of* (±) - ***P2s***.

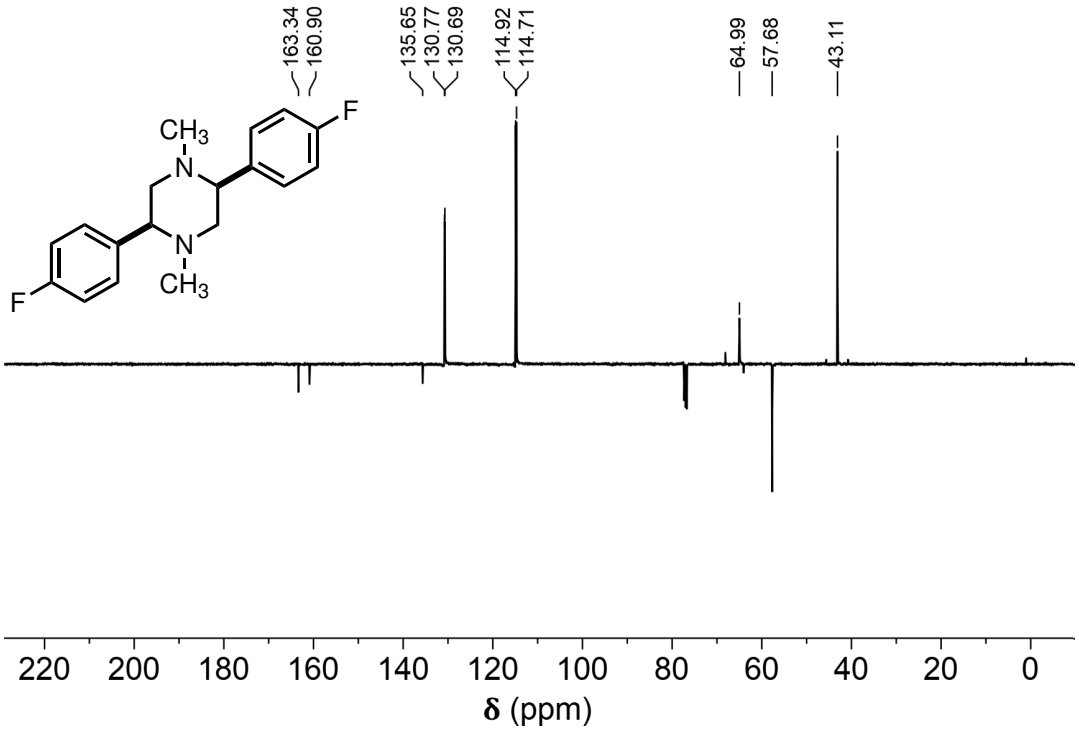

Figure A.215: *^{13}C APT NMR spectrum of* (±) - ***P2s*** (*primary and tertiary carbons produce positive peaks, secondary and quaternary carbons produce negative peaks*).

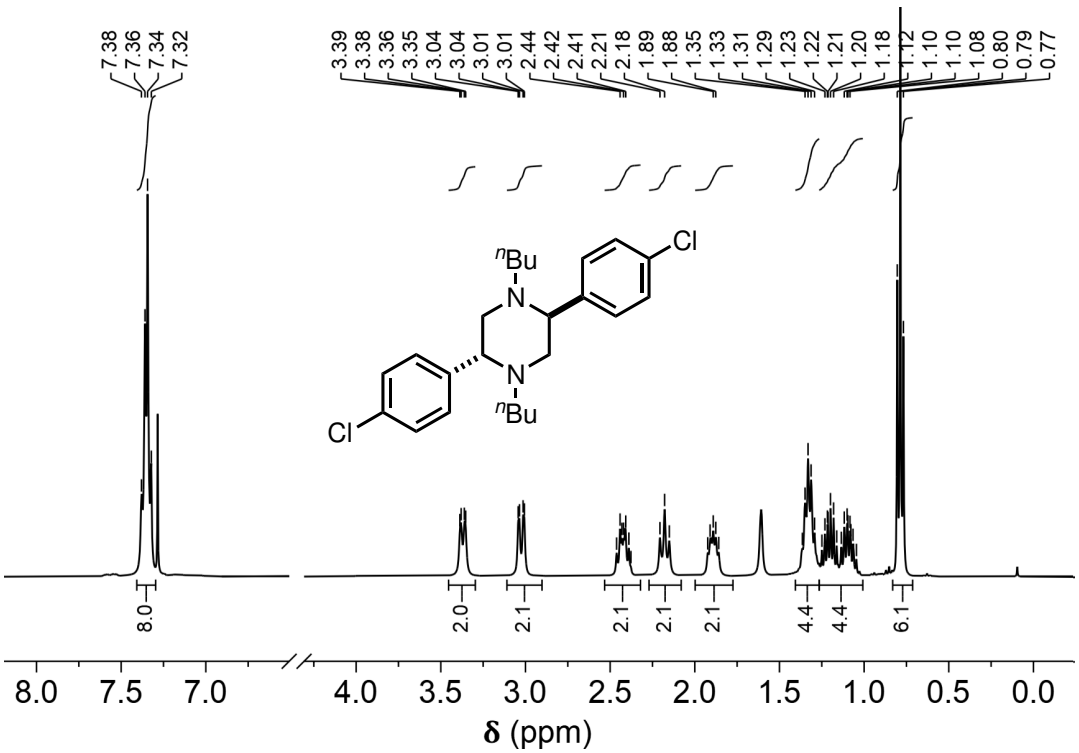

Figure A.216: *^{1}H-NMR spectrum of meso -* ***P2t***.

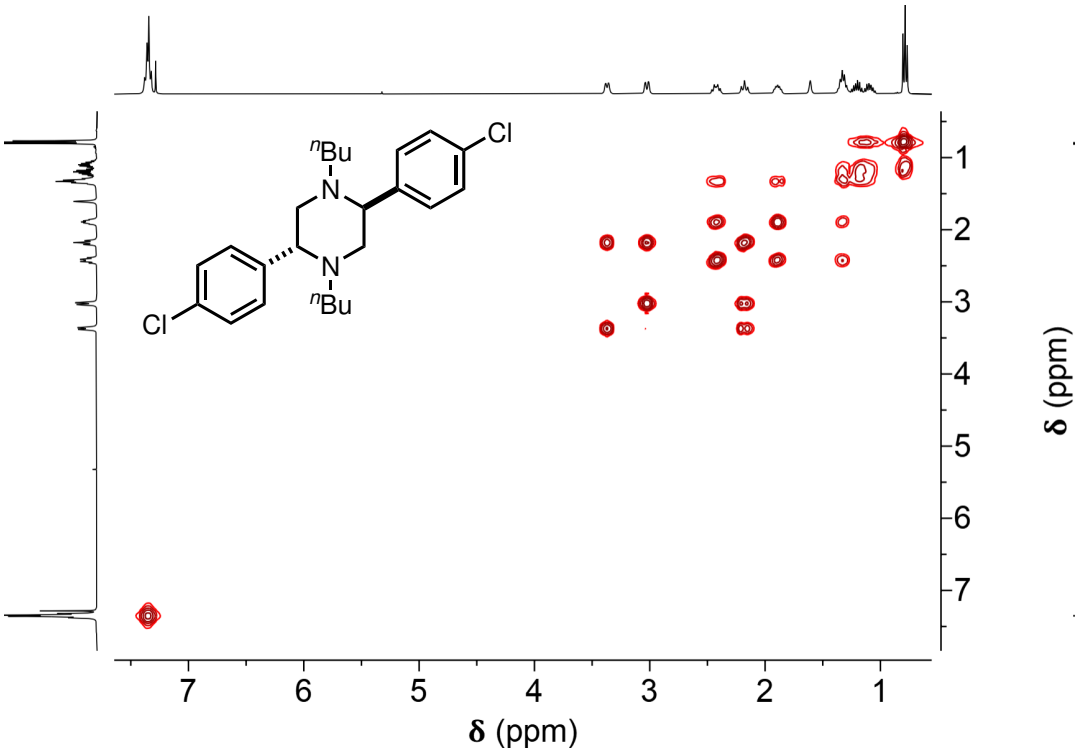

Figure A.217: *^{1}H COSY NMR spectrum of meso -* ***P2t****.*

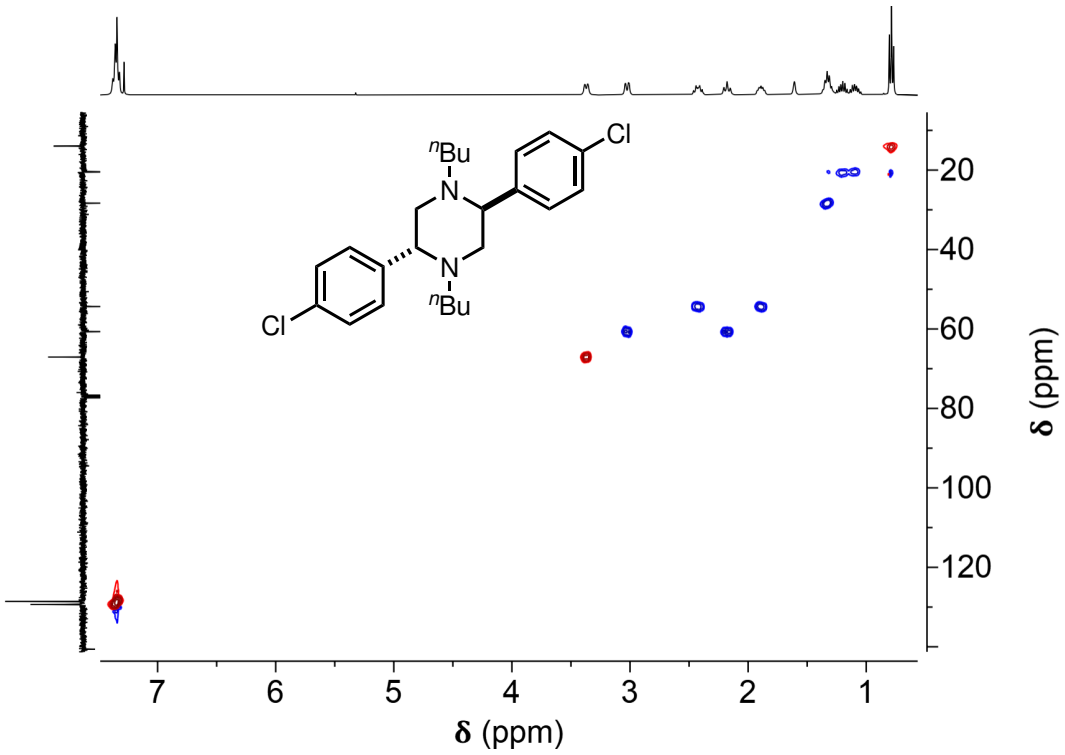

Figure A.218: *^{1}H-^{13}C HSQC NMR spectrum of meso -* ***P2t*** *(short range, primary and tertiary carbons produce red peaks, while secondary carbons produce blue peaks).*

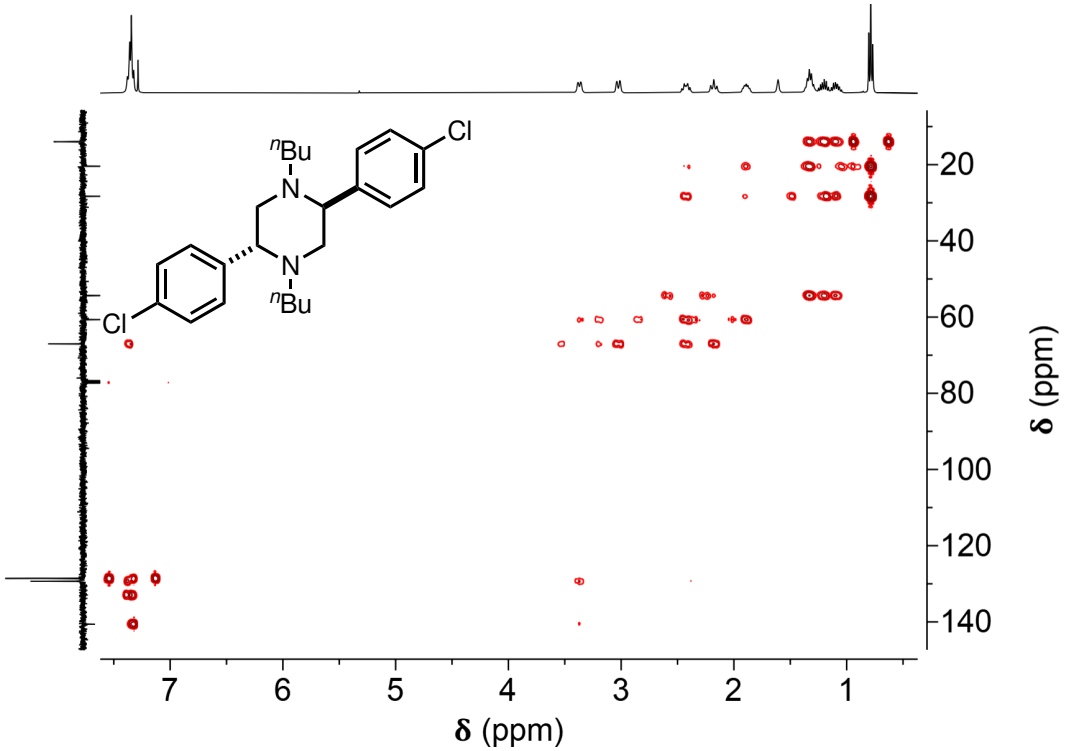

Figure A.219: *^{1}H-^{13}C HMBC NMR spectrum of meso - **P2t** (long range).*

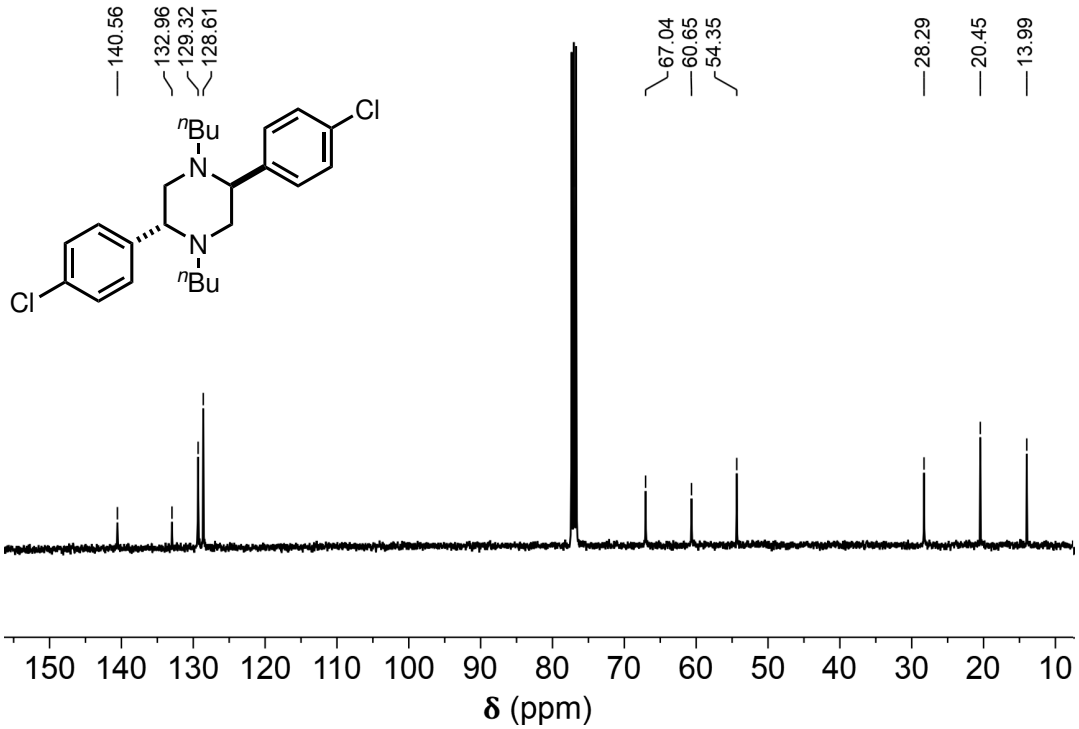

Figure A.220: *^{13}C-NMR spectrum of meso - **P2t**.*

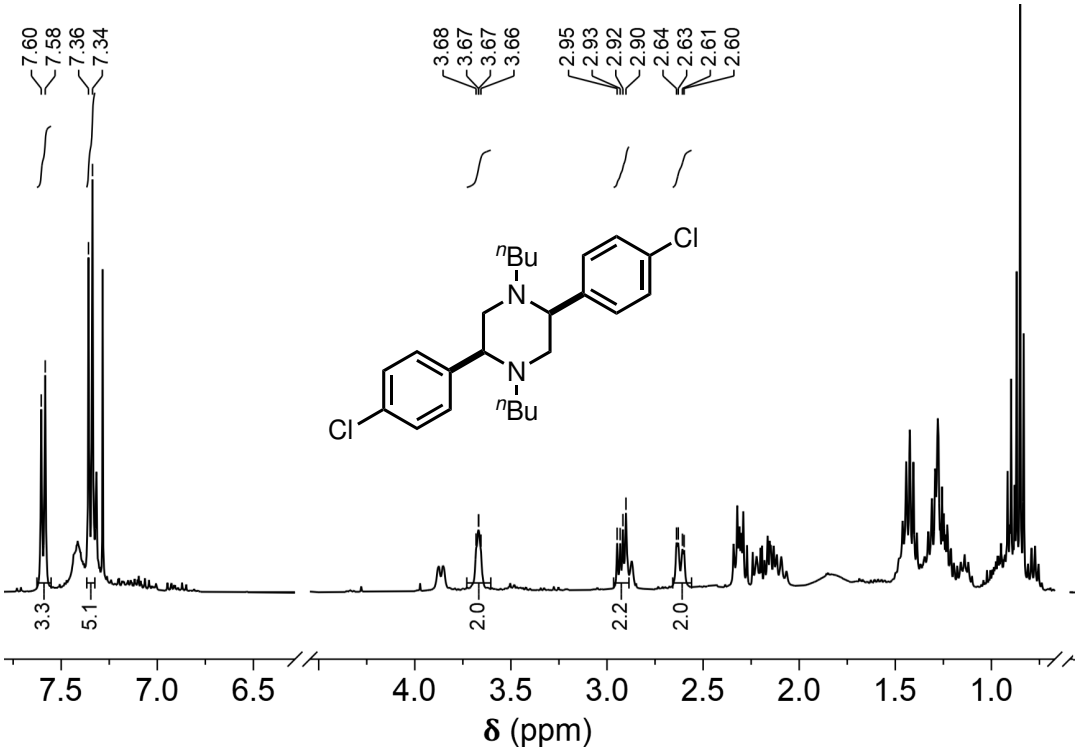

Figure A.221: *^{1}H-NMR spectrum of* (±) - ***P2t***.

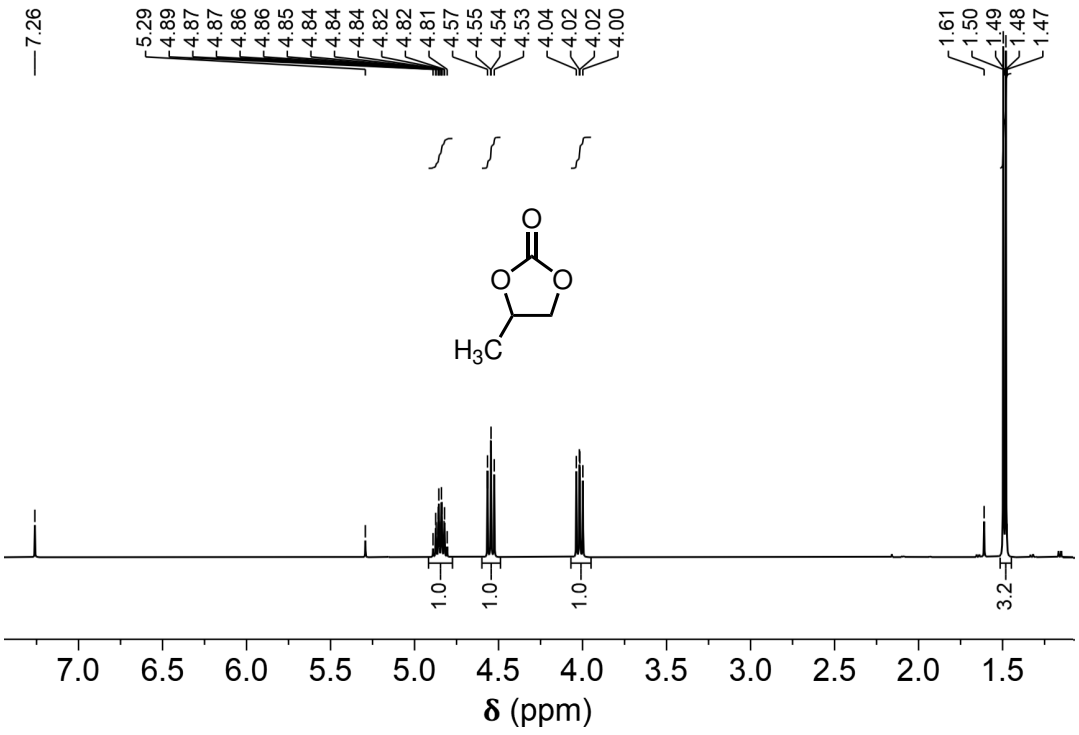

Figure A.222: *^{1}H-NMR spectrum of* ***P3a***.

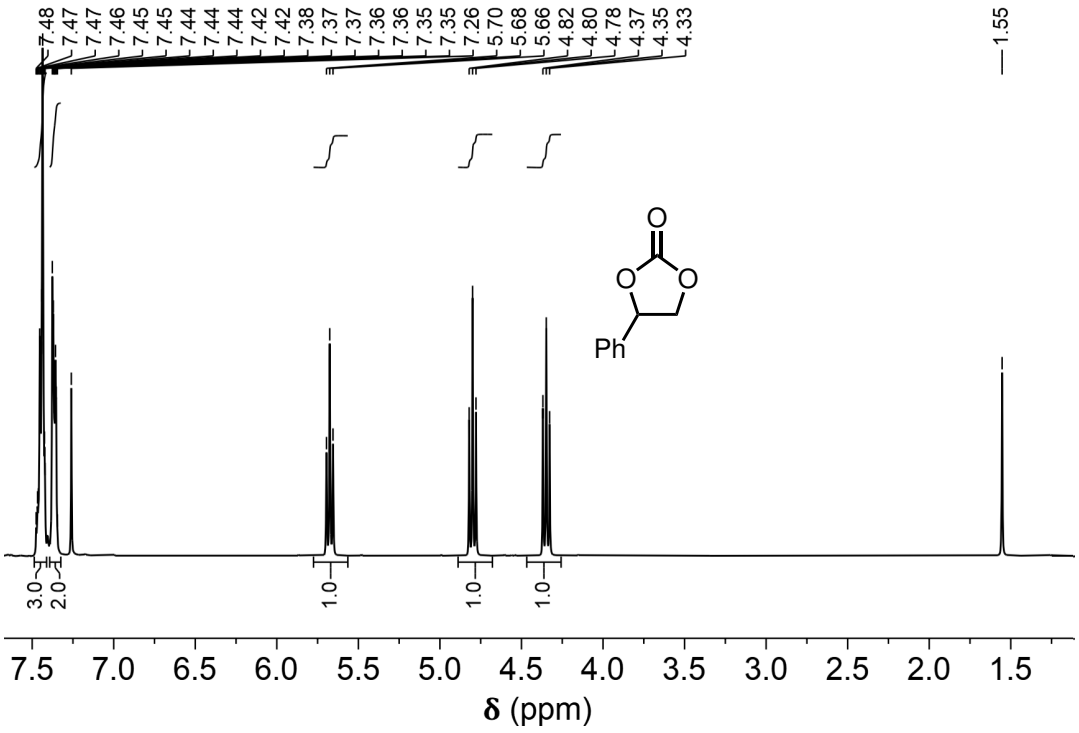

Figure A.223: *^{1}H-NMR spectrum of **P3b**.*

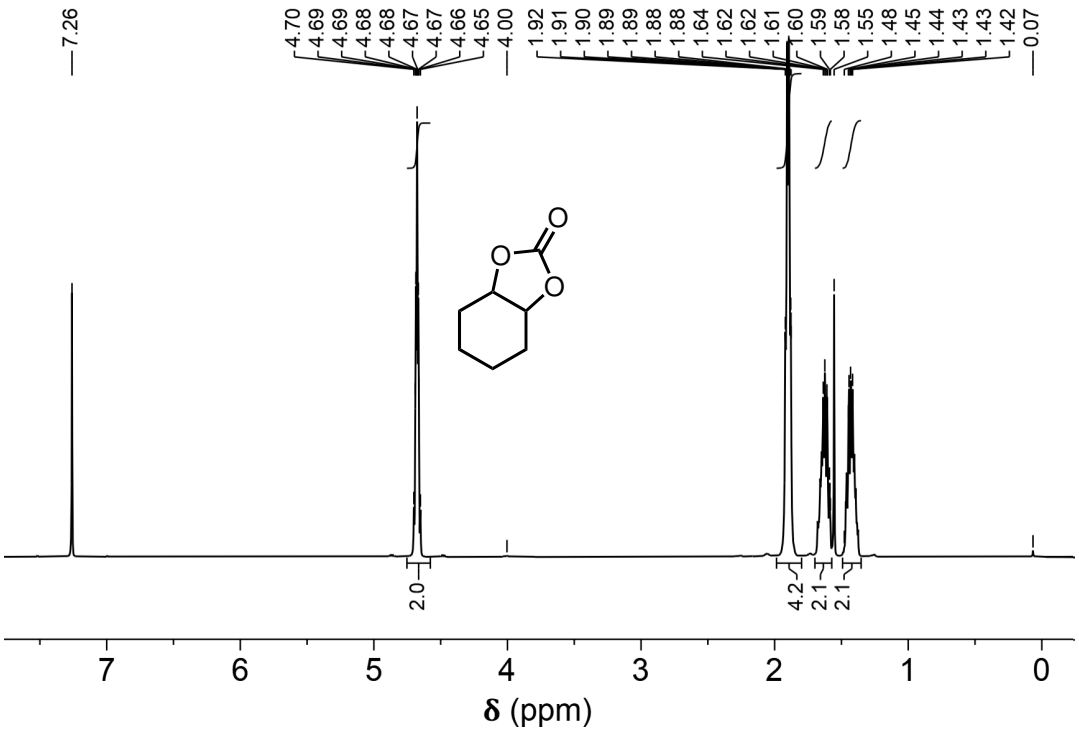

Figure A.224: *^{1}H-NMR spectrum of **P3c**.*

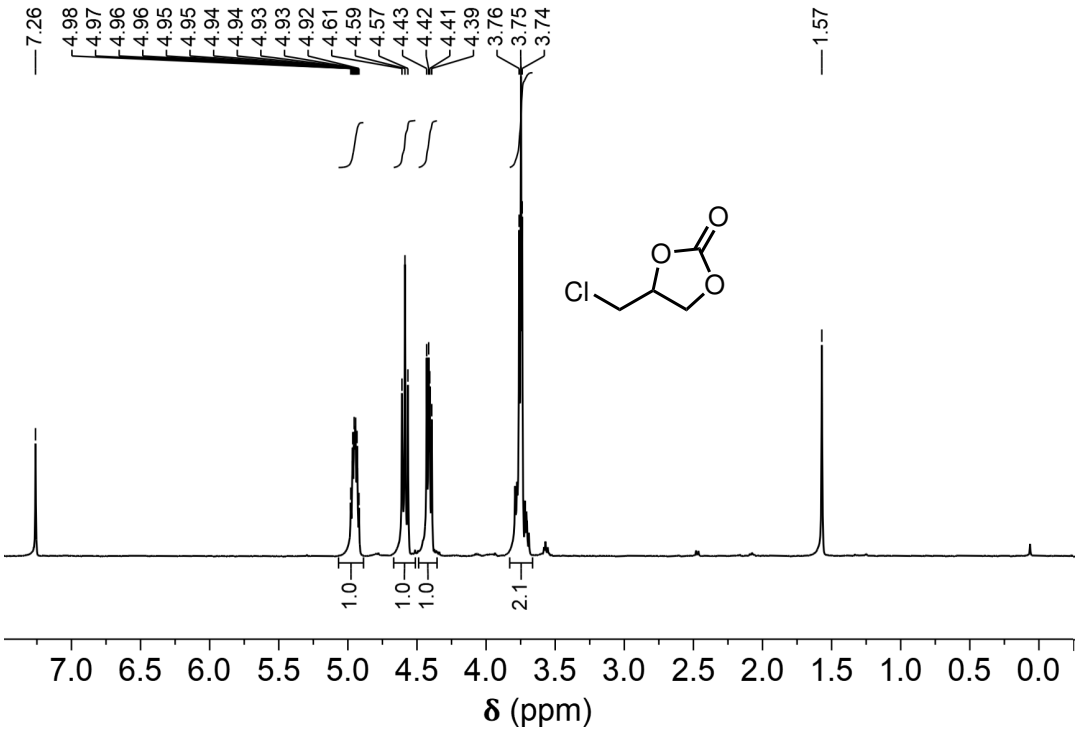

Figure A.225: *^{1}H-NMR spectrum of **P3d**.*

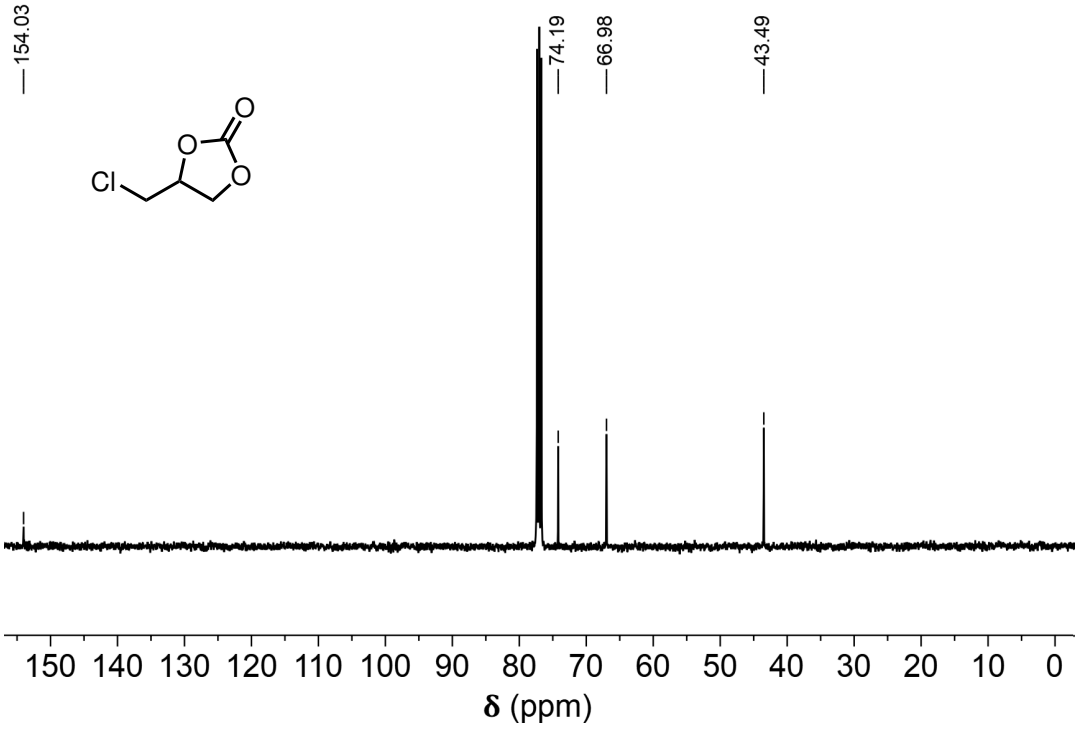

Figure A.226: *^{13}C-NMR spectrum of **P3d**.*

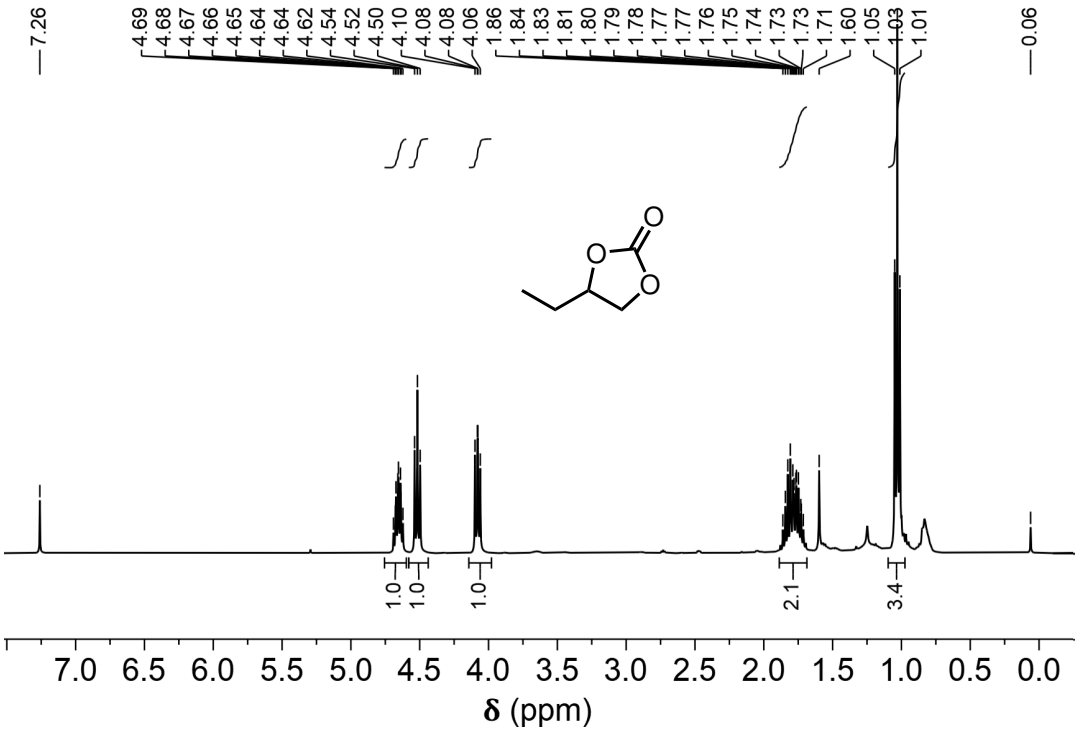

Figure A.227: *^{1}H-NMR spectrum of **P3e**.*

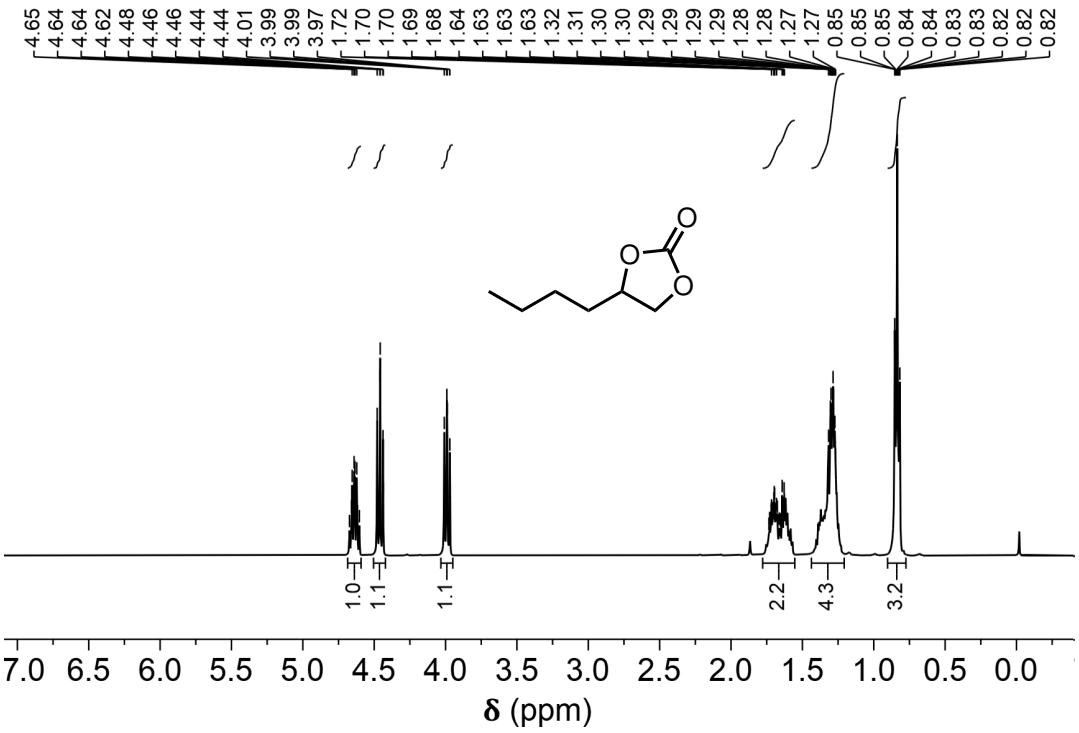

Figure A.228: *^{1}H-NMR spectrum of **P3f**.*

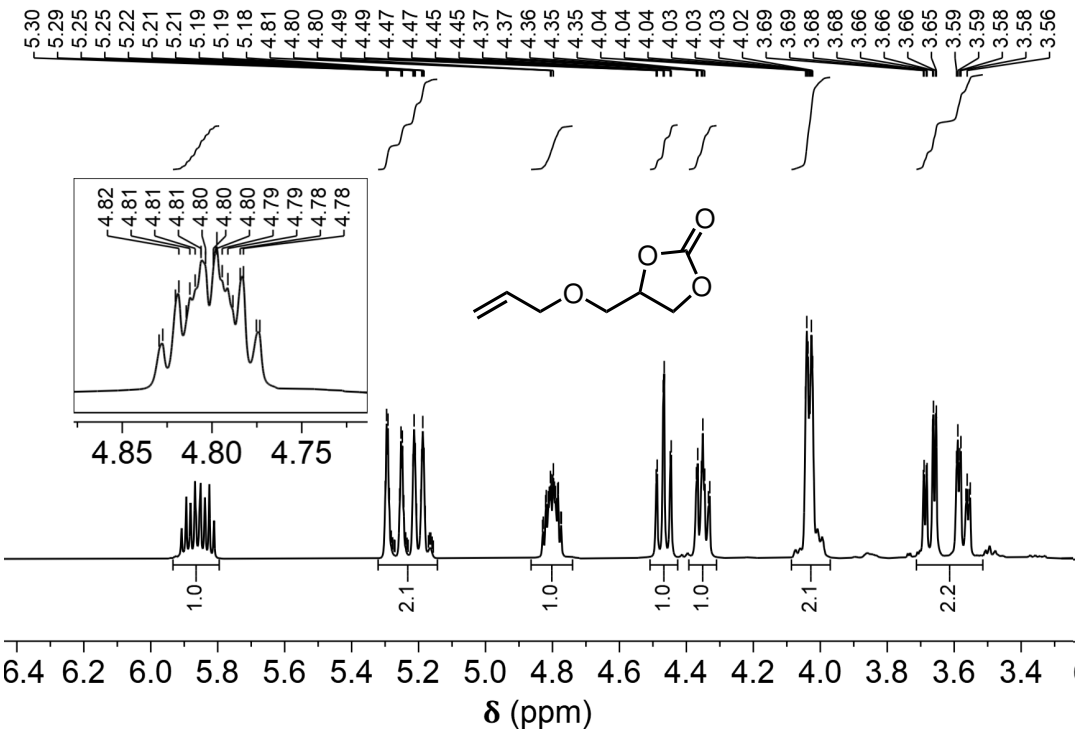

Figure A.229: *^{1}H-NMR spectrum of **P3g**.*

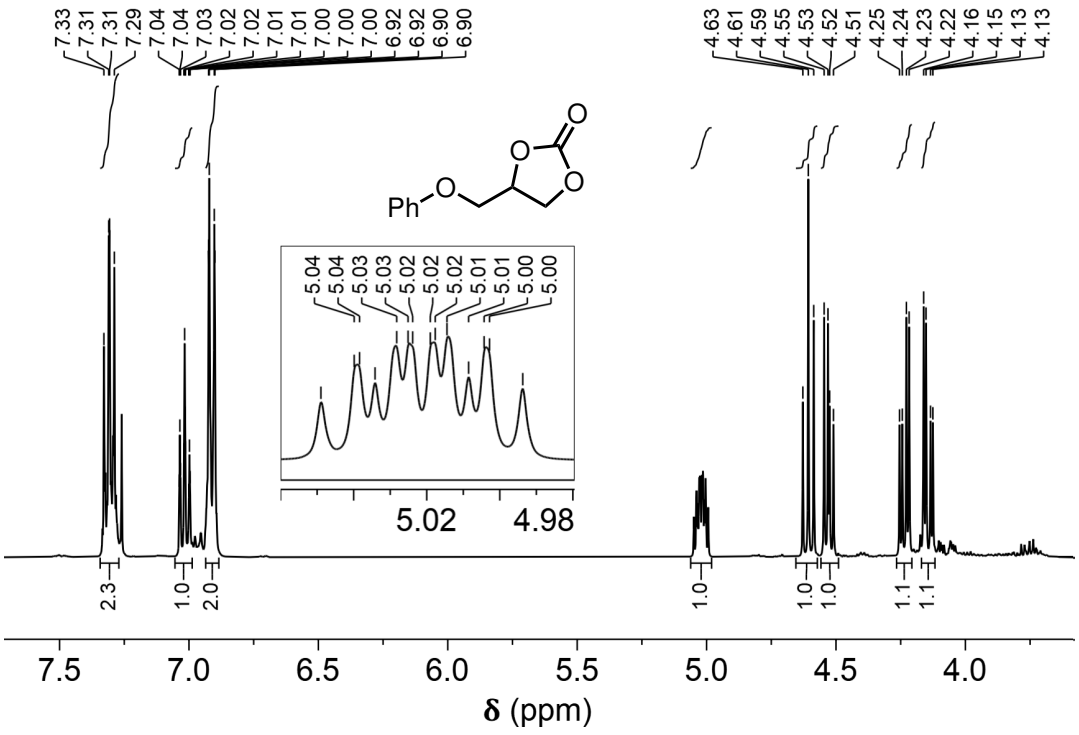

Figure A.230: *^{1}H-NMR spectrum of **P3h**.*

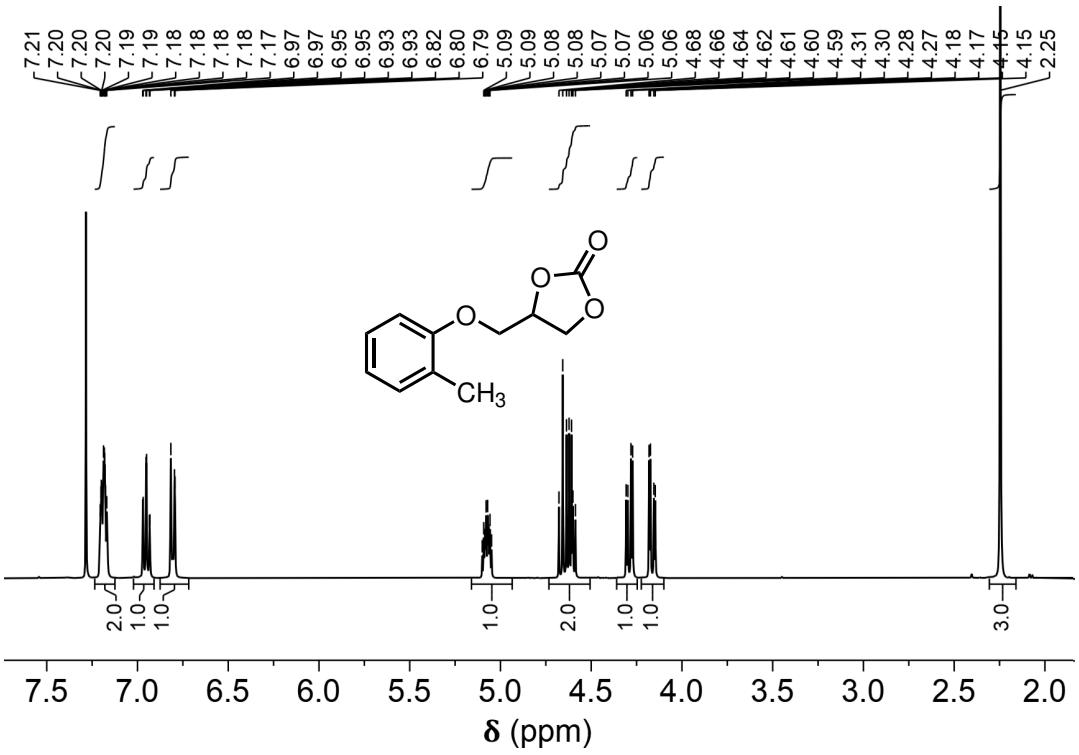

Figure A.231: *^{1}H-NMR spectrum of **P3i**.*

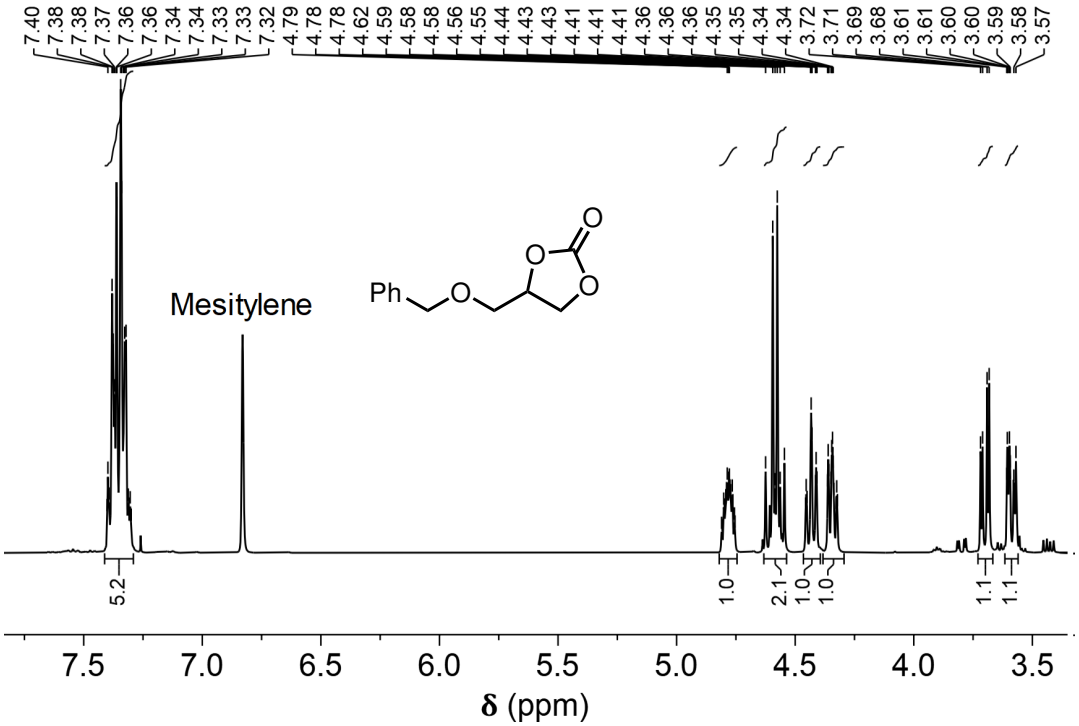

Figure A.232: *^{1}H-NMR spectrum of **P3j**.*

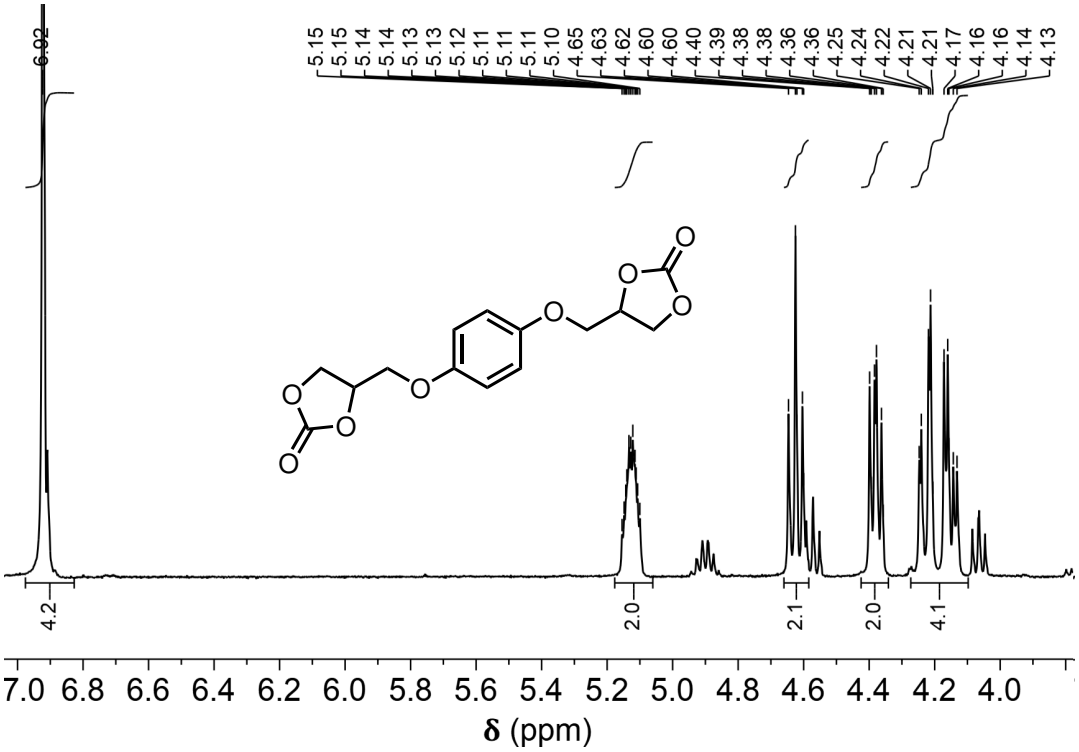

Figure A.233: *^{1}H-NMR spectrum of **P3k**.*

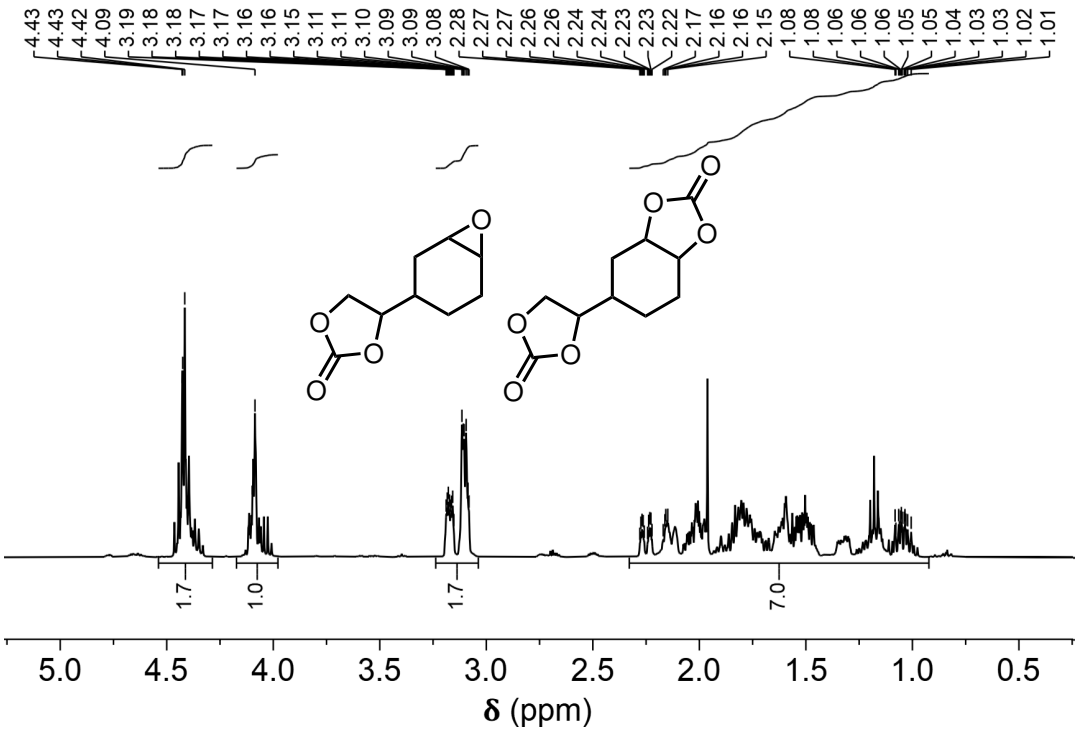

Figure A.234: *^{1}H-NMR spectrum of **P3l** + **P3l′**.*

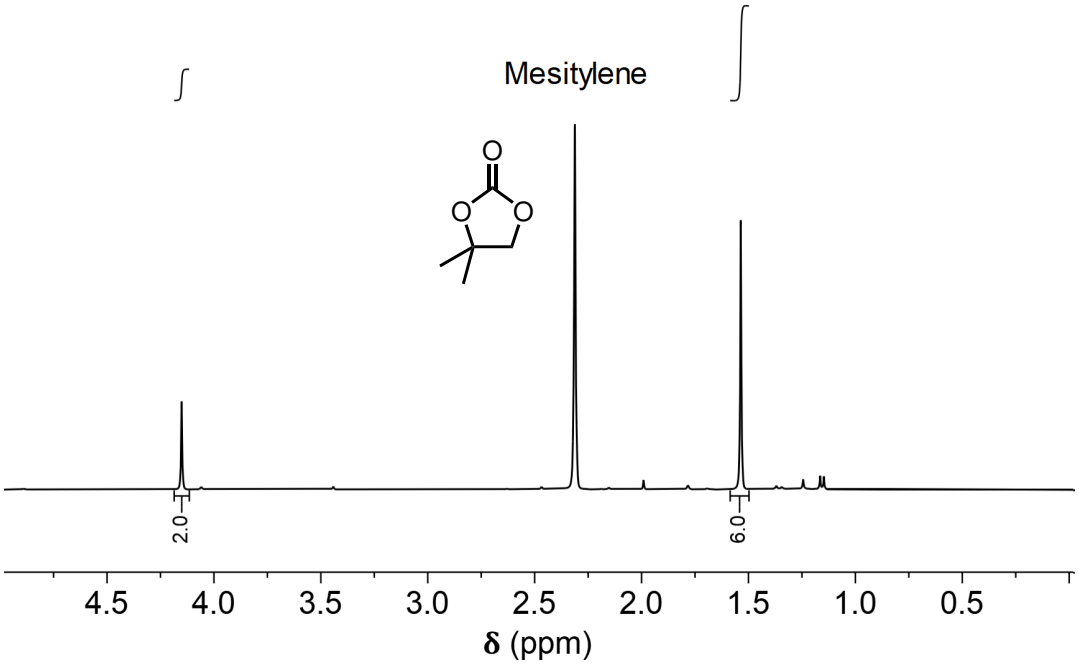

Figure A.235: *^{1}H-NMR spectrum of **P3m**.*

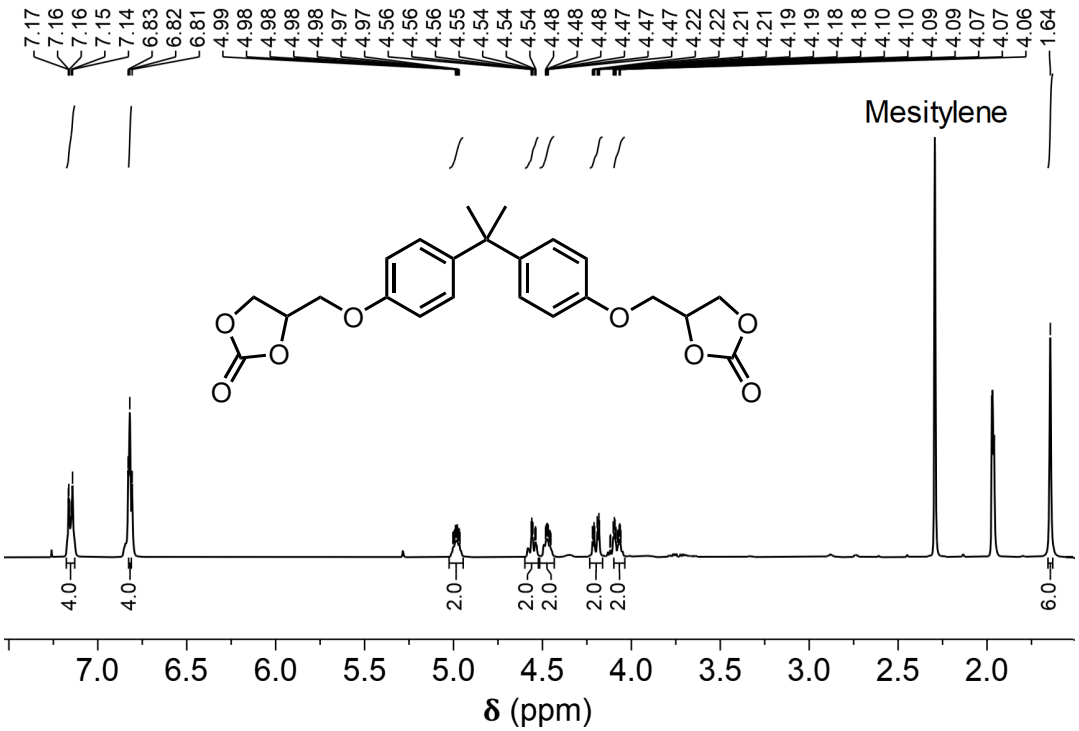

Figure A.236: *^{1}H-NMR spectrum of **P3r**.*

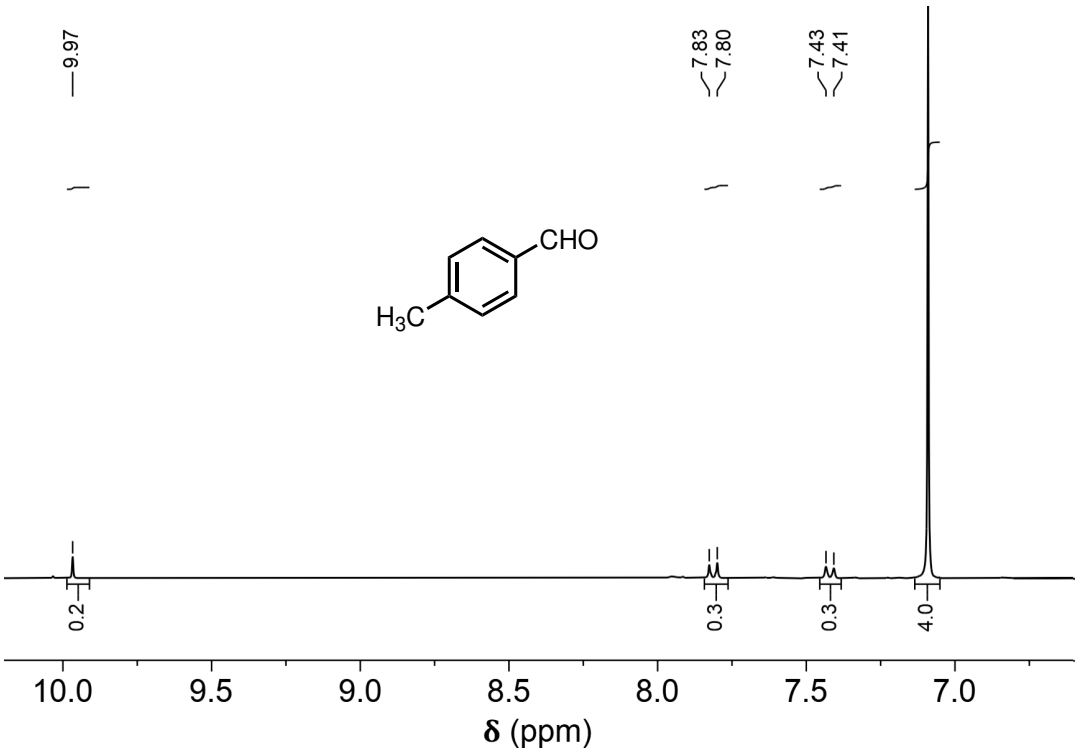

Figure A.237: *^{1}H-NMR spectrum of **P4** reaction crude.*

A.11 Photoreactor: electrical scheme and technical drawings

The next pages include the technical drawings (Figures A.238 and A.239) and the electronic scheme (Figure A.240) of the photoreactor that I designed and built.

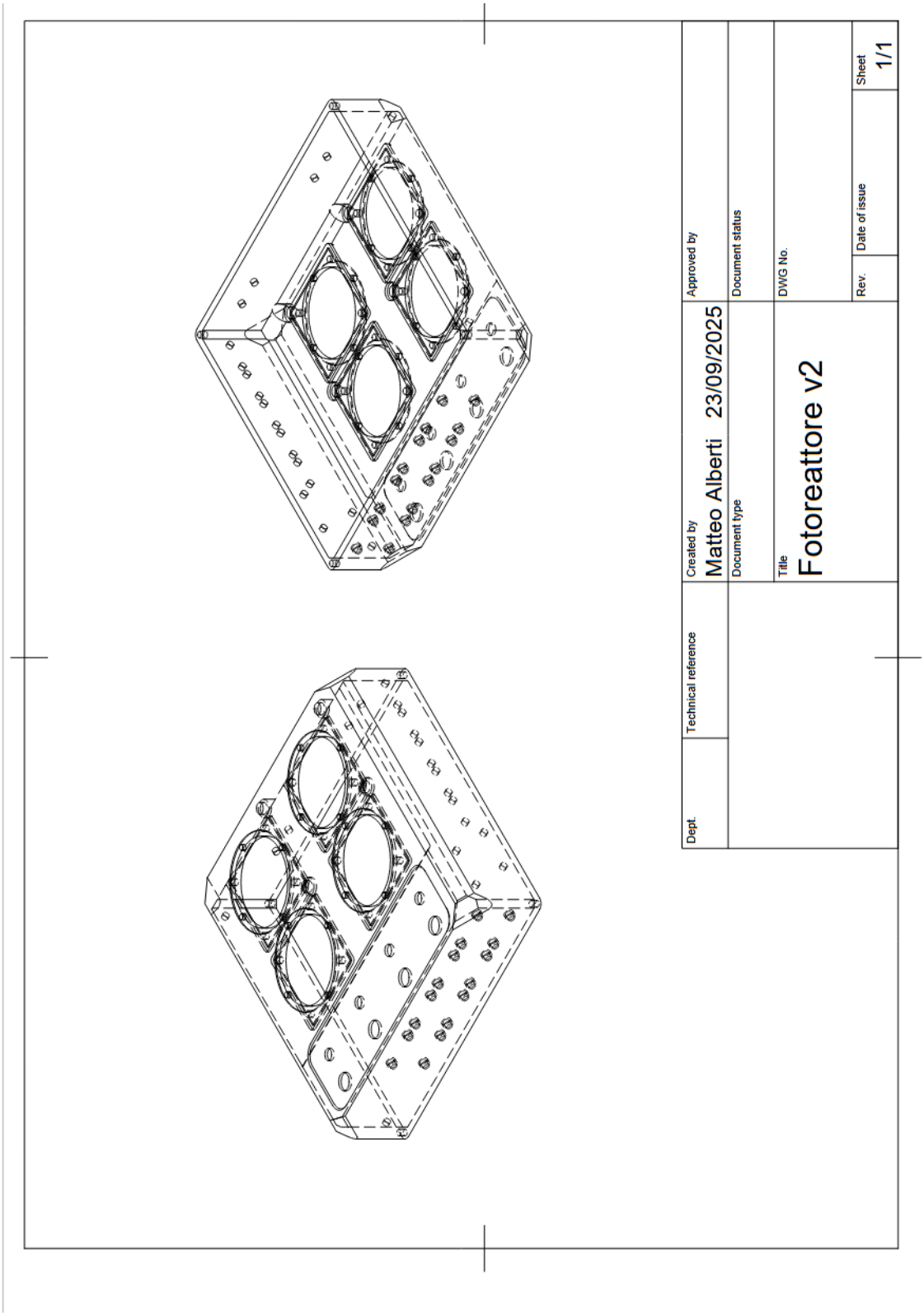

Figure A.238: *Technical drawings of the reactor's body.*

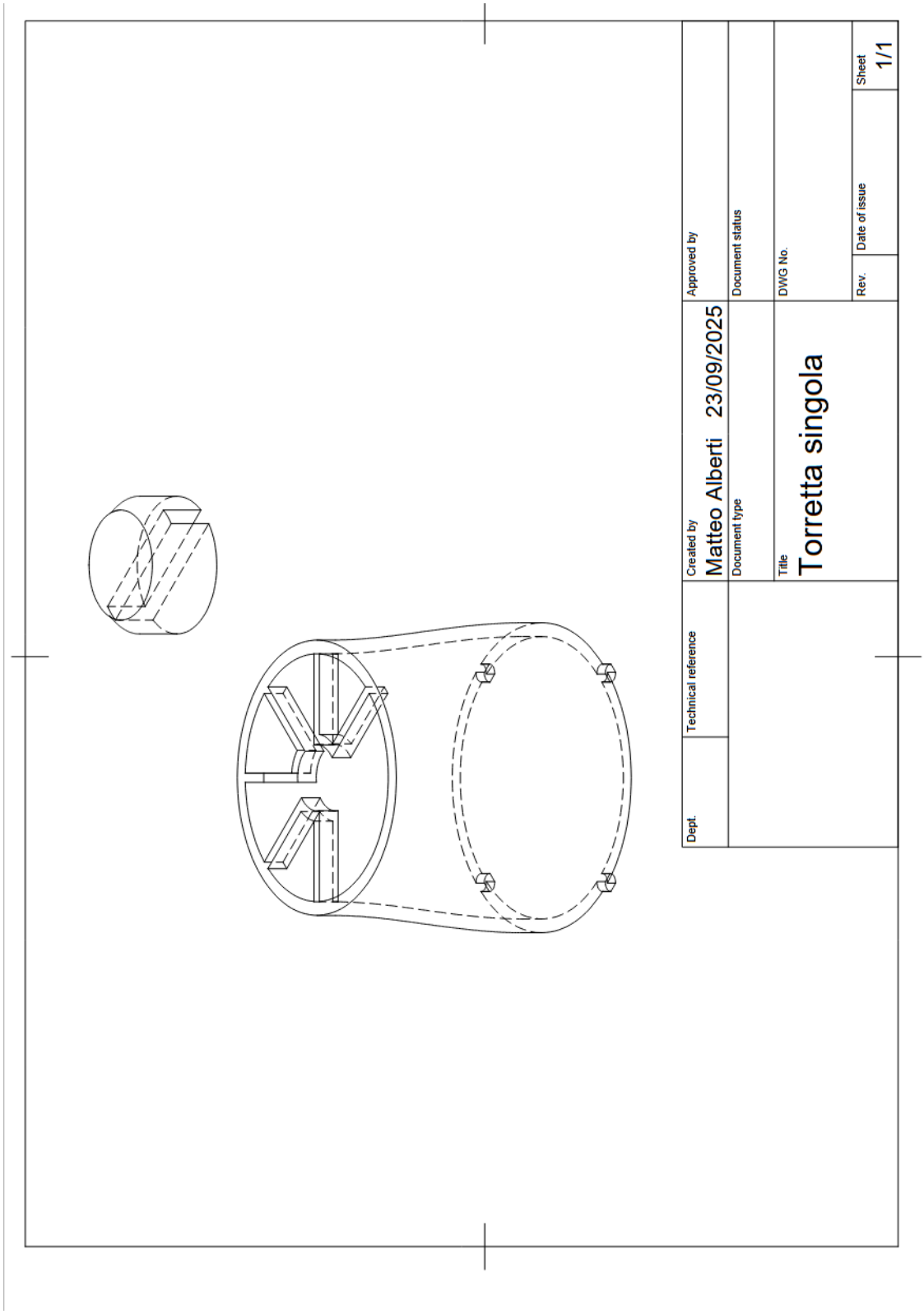

Figure A.239: *Technical drawings of the light emitting modules.*

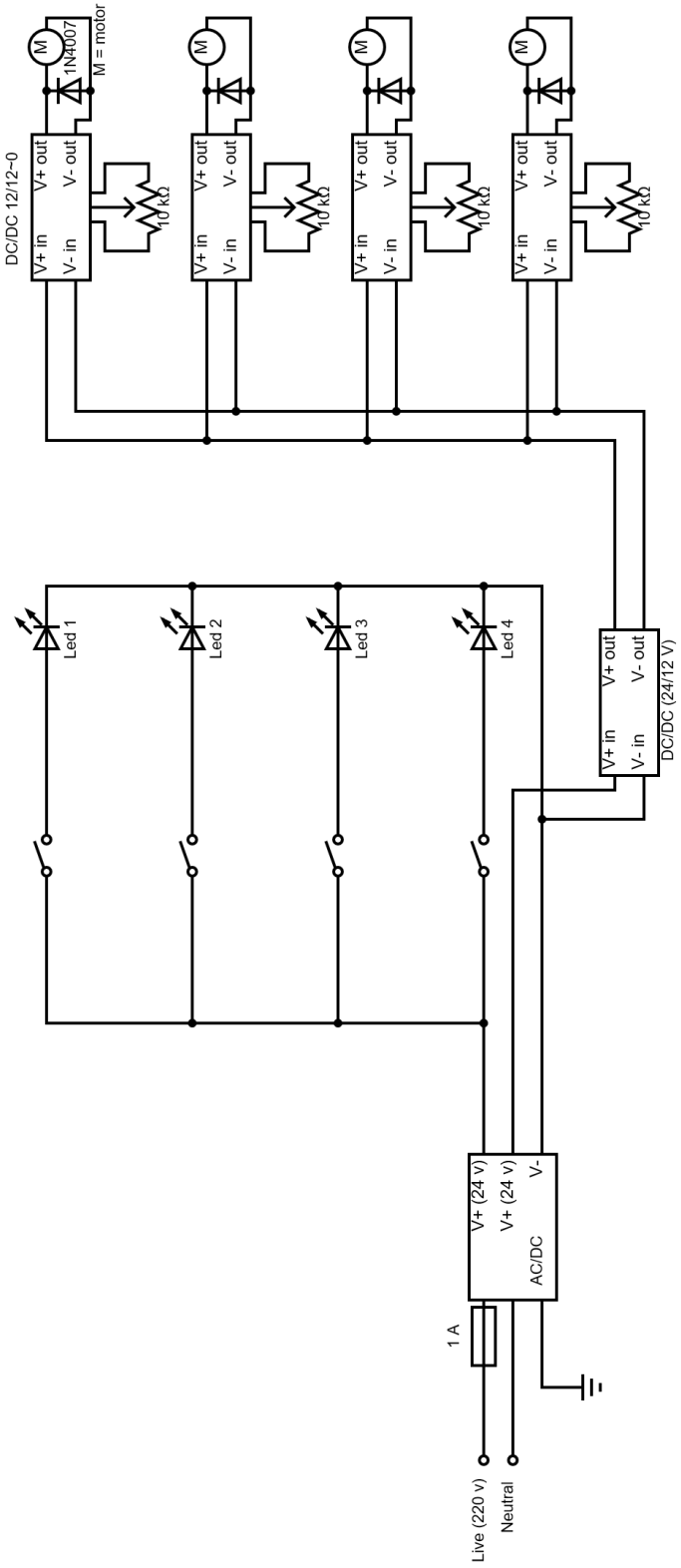

Figure A.240: *Wiring scheme of the photoreactor.*

B

Summary of the compounds nomenclature

Reading guidance

The next table summarizes the structure of the compounds that are described in the whole thesis.

Table B.1: *Schemes of all the compounds.*

Comp.	Scheme	Comp.	Scheme
1	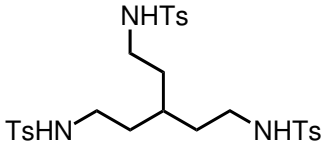	**2**	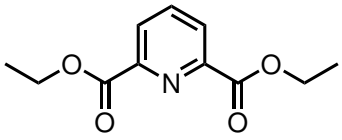
3	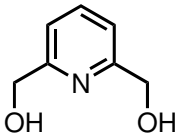	**4**	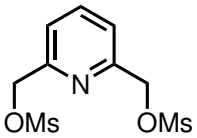
5	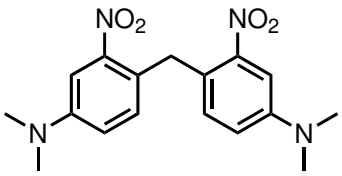	**6**	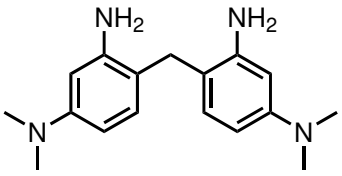
7	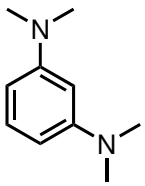	**L1**	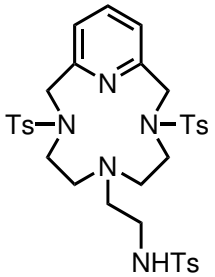

Continues on next page

Table B.1 – continued from previous page

Comp.	Scheme	Comp.	Scheme
L2	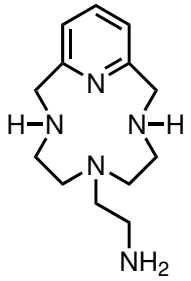	**L3**	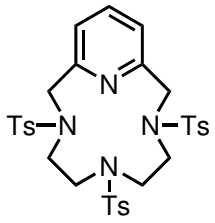
L4	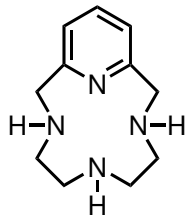	**L5**	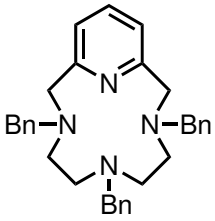
L6	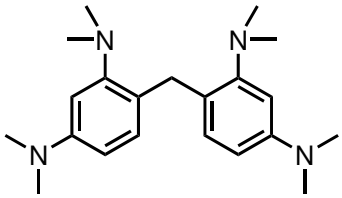	**L7**	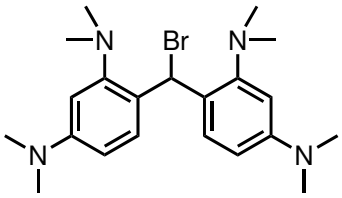
C1a	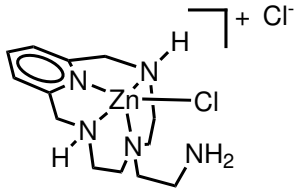	**C1b**	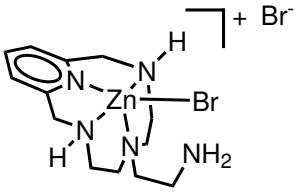
C2a	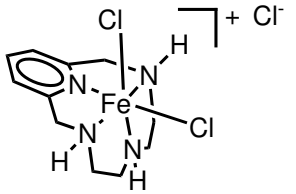	**C2b**	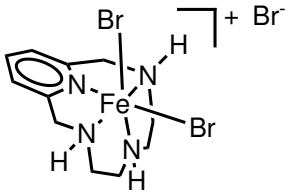
C2c	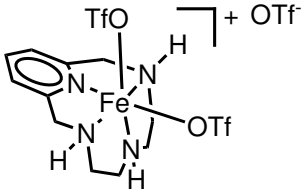	**C2d**	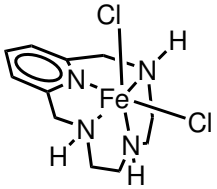
C2e	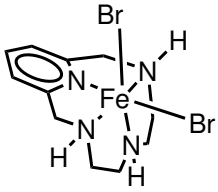	**C2f**	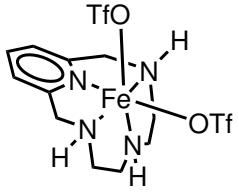

Continues on next page

Table B.1 – continued from previous page

Comp.	Scheme	Comp.	Scheme
C2a′	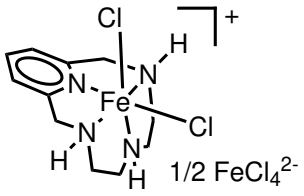	**C3a**	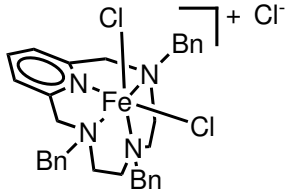
C3b	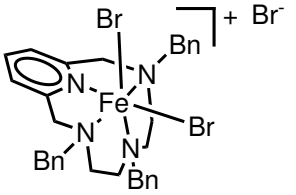	**C3c**	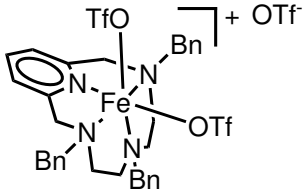
C3d	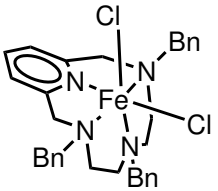	**C3e**	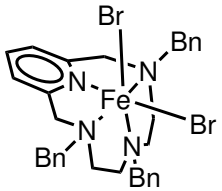
C3f	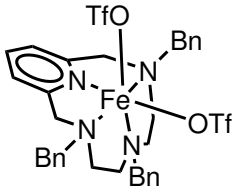	**C4a**	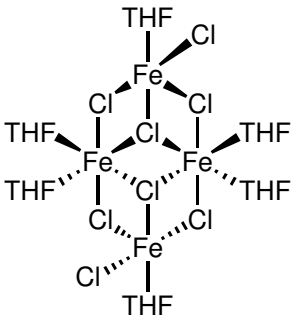
C4b	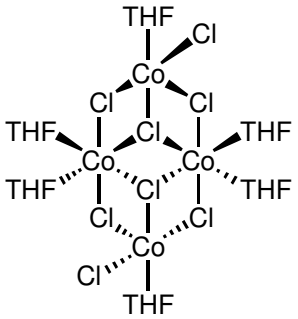	**C4c**	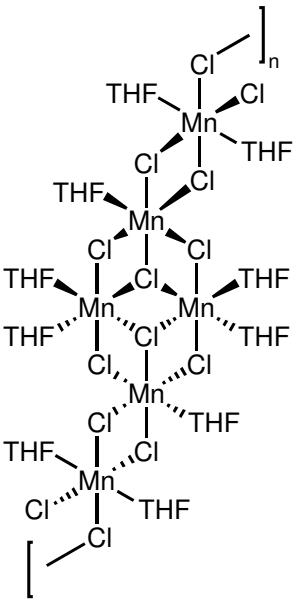

Continues on next page

Table B.1 – continued from previous page

Comp.	Scheme	Comp.	Scheme
C5a	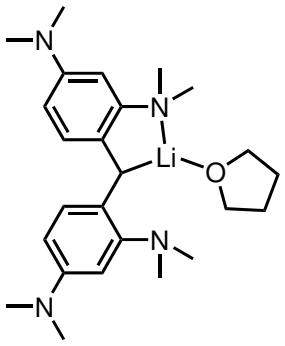	**C5b**	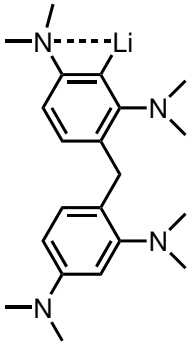
C2b′	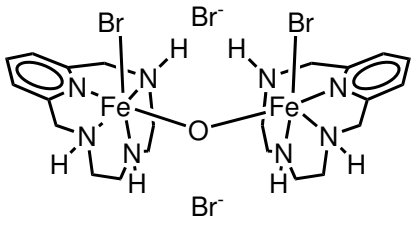		
C2d′	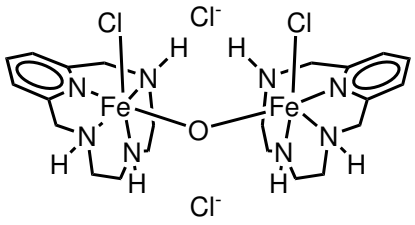		
S1a	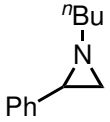	**S1b**	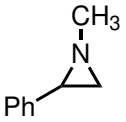
S1c	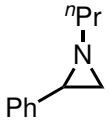	**S1d**	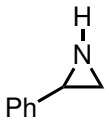
S1e	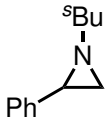	**S1f**	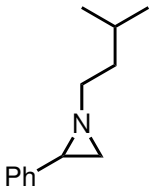
S1g	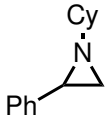	**S1h**	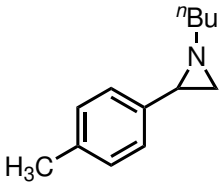

Continues on next page

Table B.1 – continued from previous page

Comp.	Scheme	Comp.	Scheme
S1i	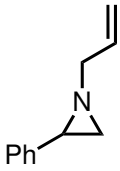	**S1j**	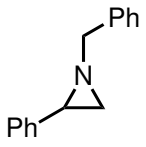
S1k	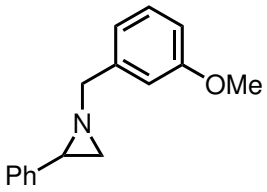	**S1l**	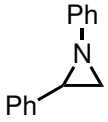
S1m		**S1n**	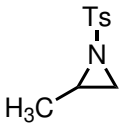
S1o	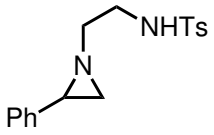	**S1p**	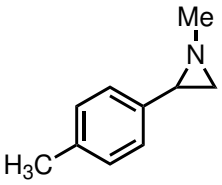
S1q	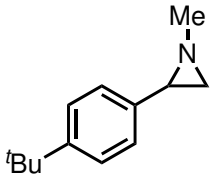	**S1r**	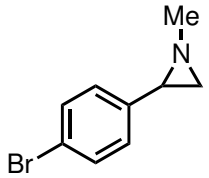
S1s	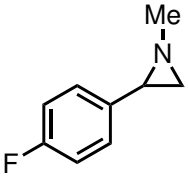	**S1t**	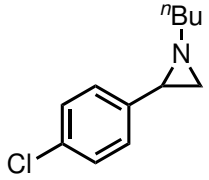
S1u	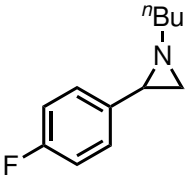		
P1a	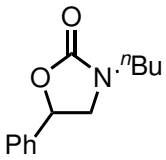	**P1b**	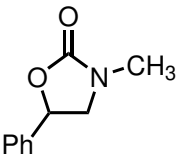

Continues on next page

Table B.1 – continued from previous page

Comp.	Scheme	Comp.	Scheme
P1c	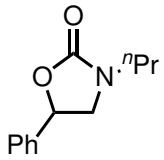	**P1d**	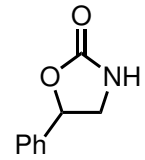
P1e	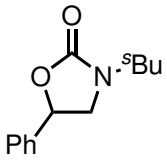	**P1f**	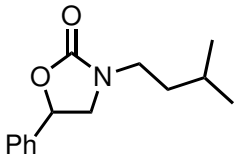
P1g	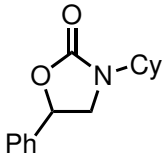	**P1h**	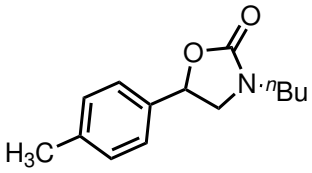
P1i	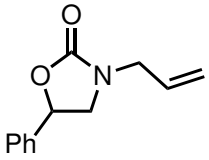	**P1j**	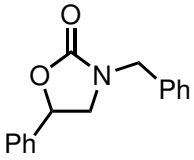
P1k	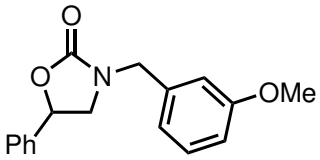	**P1l**	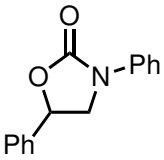
P1m	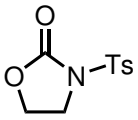	**P1n**	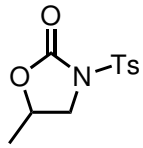
P1n′	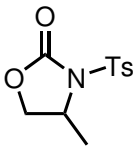		
meso **- P2a**	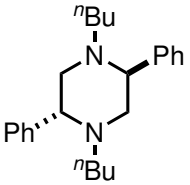	(±) - **P2a**	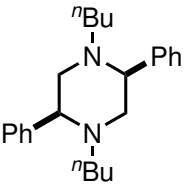
meso **- P2b**	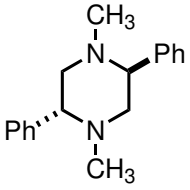	(±) - **P2b**	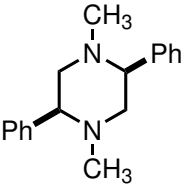

Continues on next page

Table B.1 – continued from previous page

Comp.	Scheme	Comp.	Scheme
meso - **P2b′**	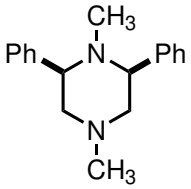	(±) - **P2b′**	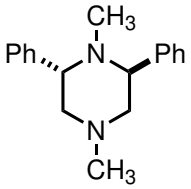
meso - **P2h**	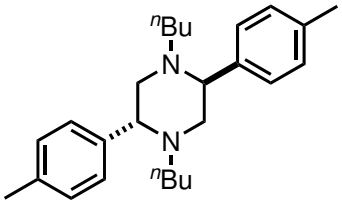	(±) - **P2h**	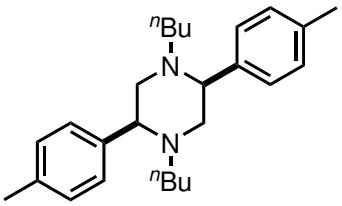
meso - **P2i**	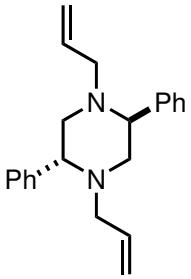	(±) - **P2i**	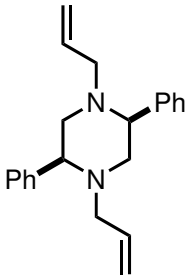
meso - **P2j**	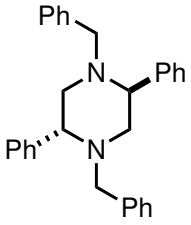	(±) - **P2j**	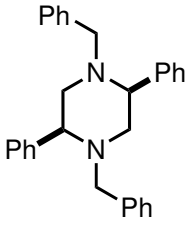
P2m	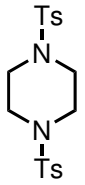		
meso - **P2p**	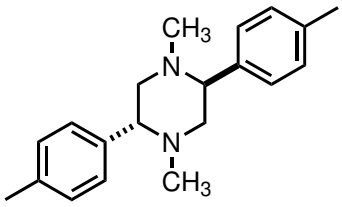	(±) - **P2p**	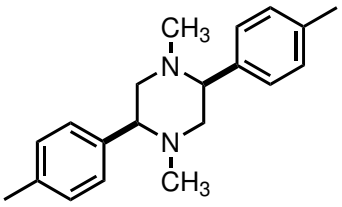
meso - **P2q**	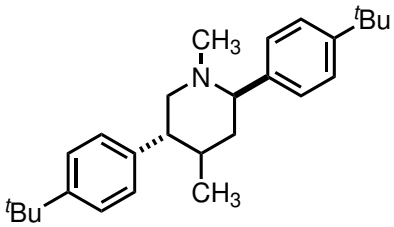	(±) - **P2q**	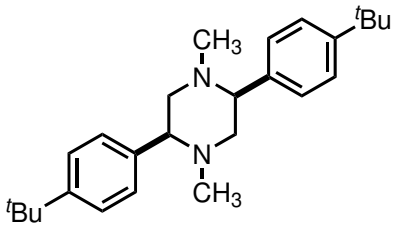

Continues on next page

Table B.1 – continued from previous page

Comp.	Scheme	Comp.	Scheme
meso **- P2r**	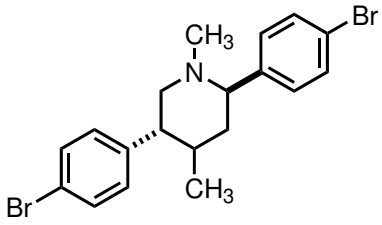	(±) - **P2r**	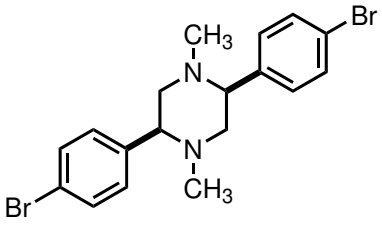
meso **- P2s**	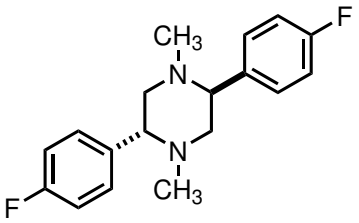	(±) - **P2s**	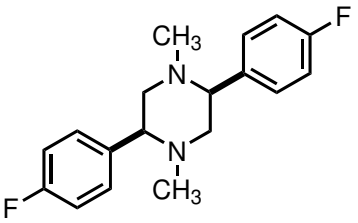
meso **- P2t**	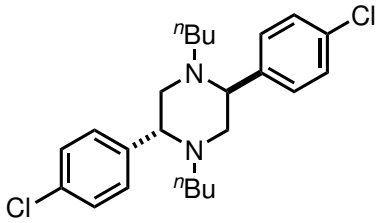	(±) - **P2t**	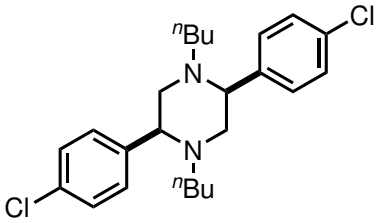
P3a	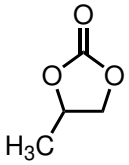	**P3b**	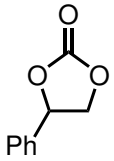
P3c	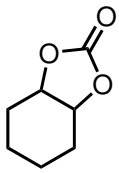	**P3d**	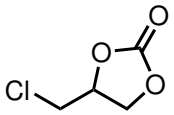
P3e	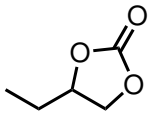	**P3f**	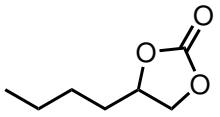
P3g	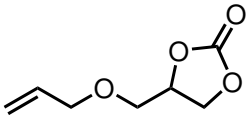	**P3h**	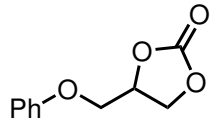
P3i	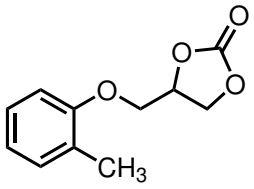	**P3j**	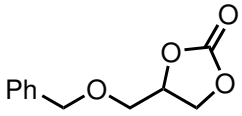

Continues on next page

Table B.1 – continued from previous page

Comp.	Scheme	Comp.	Scheme
P3k	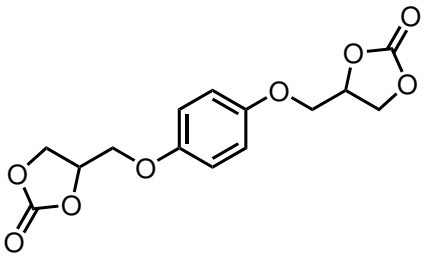	**P3l**	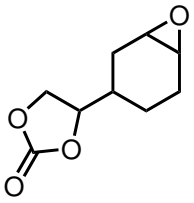
P3l′	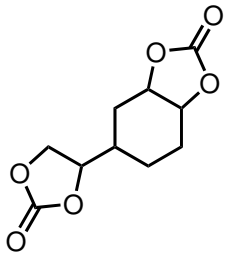	**P3m**	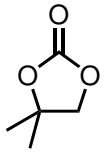
P3n	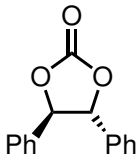	**P3o**	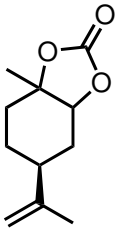
P3p	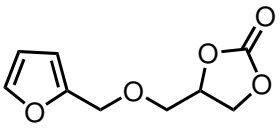	**P3q**	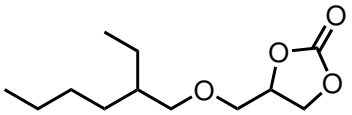
P3r	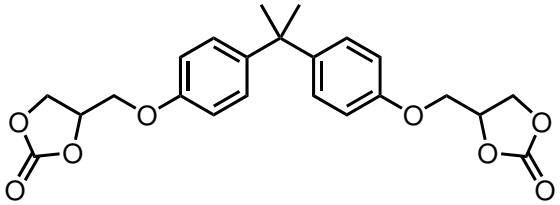		

C

Abbreviations and Symbols

A26 Commercial anion-exchange resin code A26 (used for resin-supported catalysts).

AIBN Azobisisobutyronitrile (radical initiator).

BMPO 5-tert-Butoxycarbonyl-5-methyl-1-pyrroline *N*-oxide (EPR spin-trapping agent).

CH_3CN Acetonitrile.

COD 1,5-Cyclooctadiene.

cosy / COSY Homonuclear correlation spectroscopy (2D NMR experiment).

DCM Dichloromethane.

DCE 1,2-Dichloroethane.

DME 1,2-Dimethoxyethane.

DiPEA *N*,*N*-Diisopropylethylamine (Hunig's base).

DMT Dimethyl terephthalate (analytical internal standard where used).

DMF Dimethylformamide.

DMSO Dimethyl sulfoxide.

EDX Energy-dispersive X-ray spectroscopy (elemental analysis by SEM-EDX).

EI Electron ionization (mass spectrometry ionization mode).

Eq. Equivalent(s).

ESI Electrospray ionization (mass spectrometry ionization technique).

Et_2O Diethyl ether.

EW Electron-withdrawing.

Fab / FAB Fast atom bombardment (mass spectrometry ionization technique).

FC Field-cooled (magnetometry measurement protocol).

GC-FID Gas chromatography with flame ionization detector.

HMBC Heteronuclear multiple-bond correlation spectroscopy (2D NMR experiment).

HPLC High-performance liquid chromatography.

HRMS High-resolution mass spectrometry.

HSQC Heteronuclear single quantum coherence spectroscopy (2D NMR experi-

ment).

Hz Hertz.

ICP-OES Inductively coupled plasma optical emission spectroscopy.

IRA-400 Commercial anion-exchange resin code IRA-400 (used for resin-supported catalysts).

IS Internal standard (analytical standard used for GC or NMR quantification).

K Kelvin (temperature).

KO^{t}Bu Potassium tert-butoxide.

L Ligand (general notation).

LED Light-emitting diode (irradiation source; e.g., 405 nm LED).

m Multiplet (NMR notation).

M$^+$ Molecular ion peak.

MeLi Methyllithium.

MHz Megahertz (for NMR spectrometer frequency).

Moessbauer ^{57}Fe Moessbauer spectroscopy (iron isotope spectroscopic technique).

MS Mass spectrometry.

NBS *N*-Bromosuccinimide (brominating reagent).

NCN Pincer ligands bearing donating atoms in this order; Nitrogen, Carbon, Nitrogen.

NMR Nuclear magnetic resonance.

NOESY Nuclear Overhauser effect spectroscopy (2D NMR experiment).

Oe Oersted (magnetic field unit).

OTf Trifluoromethanesulfonate (triflate anion, $CF_3SO_3^-$).

PcL Pyridine-containing macrocyclic ligand (notation used in text).

PC(sp^3)P Pincer ligands bearing donating atoms in this order: Phosphor, sp^3 Carbon and Phosphor.

PF_6 Hexafluorophosphate anion (PF_6^-), when used as counterion.

PXRD Powder X-ray diffraction.

Pyclen Name of the macrocyclic ligand family used in Chapter 3 (pyclen-based ligands).

Raman Raman spectroscopy.

rt Room temperature.

SCXRD Single-crystal X-ray diffraction.

SEM Scanning electron microscopy.

THF Tetrahydrofuran.

TBA Tetrabutylammonium cation (abbrev. for tetrabutylammonium salts).

TD-DFT Time-dependent density functional theory (when computational excited-state methods are referenced).

TOF Turnover frequency (catalysis; e.g., h^{-1}).

TOF-MS Time-of-Flight mass spectrometry (mass analyzer type).

TLC Thin-layer chromatography.

UV-Vis Ultraviolet-visible spectroscopy.

V Volt (electric potential unit).
VSM Vibrating sample magnetometry (magnetometry technique).
W Watt (power).
wt% Weight percent.
XRD X-ray diffraction (generic).
ZFC Zero-field-cooled (magnetometry measurement protocol).

χ Magnetic susceptibility (dimensionless in SI when specified appropriately).
χ_{M} Molar magnetic susceptibility.
χ_{T} Temperature-corrected molar susceptibility product ($\chi_{\mathrm{M}}T$).
μ_{eff} Effective magnetic moment.
μ_{B} Bohr magneton.
emu Electromagnetic unit (CGS unit for magnetic moment).
T (mag) Tesla (magnetic flux density).

This page intentionally left blank.